Deutsche Geophysikalische Gesellschaft e. V.

Protokoll über das 24. Schmucker-Weidelt-Kolloquium für Elektromagnetische Tiefenforschung

Neustadt an der Weinstraße 19.-23. September 2011

ISSN 0946-7467

herausgegeben von

Ralph-Uwe Börner
Institut für Geophysik und Geoinformatik
TU Bergakademie Freiberg
Gustav-Zeuner-Straße 12
09599 Freiberg

Katrin Schwalenberg
Bundesanstalt für
Geowissenschaften und Rohstoffe
Stilleweg 2
30655 Hannover

Vorwort

Das 24. Schmucker-Weidelt-Kolloquium für Elektromagnetische Tiefenforschung fand vom 19. bis 23. September 2011 im Herz-Jesu-Kloster in Neustadt an der Weinstraße statt. Zum Gedenken an Ulrich Schmucker (1930-2008) und Peter Weidelt (1938-2009) trägt das seit 1963 ausgerichtete Kolloquium für Elektromagnetische Tiefenforschung (EMTF-Kolloquium) erstmalig diesen neuen Namen.

Andreas Junge und sein Team von der Universität Frankfurt haben das Kolloquium hervorragend organisiert. Das Herz-Jesu-Kloster erwies sich aufgrund seiner bequemen und günstigen Räumlichkeiten und nicht zuletzt auch wegen der guten Hausmannskost als ideale Tagungsstätte. So ähnelte das Kolloquium mit seiner entspanntfamiliären Atmosphäre sehr einem Landschulheimaufenthalt mit wissenschaftlichem Programm. Auch der ungewöhnlich warme und sonnige Altweibersommer wird sicher allen im Gedächtnis haften bleiben. Bis tief in die Nacht verweilten die meisten im Klostergarten und genossen die letzten warmen Nächte des Jahres.

Die 84 Teilnehmer des Kolloquiums kamen überwiegend aus Deutschland, aber auch aus der Schweiz, Tschechien, Irland, Dänemark und Spanien. Insgesamt waren 19 Institutionen vertreten, wobei die Universität Köln und das GFZ Potsdam mit jeweils 17 Teilnehmern gefolgt von der TU Bergakademie Freiberg mit 12 Teilnehmern die stärksten Gruppen bildeten.

Der vorliegende Kolloquiumsband umfasst 38 Beiträge. Es ist sehr erfreulich, dass die Zahl der eingereichten Beiträge im Verlauf der letzten Jahre nahezu konstant geblieben ist, obwohl der Druck, die Diplom-, Master- oder Doktorarbeit innerhalb eines meist zu knapp bemessenen Zeitraums fertigzustellen oder die wissenschaftlichen Ergebnisse in einer internationalen Fachzeitschrift zu publizieren, immer größer wird. Ein gelungener Beitrag im Blauen Band kann ein erster guter Schritt in diese Richtung sein.

Das Themenspektrum ist vielfältig und deckt die verschiedenen Aufgaben und Anwendungsmöglichkeiten der elektromagnetischen Methoden ab: Case studies, numerische Verfahren und oberflächennahe Anwendungen stehen zwar im Vordergrund, aber auch Neuigkeiten zu interessanten Geräteentwicklungen und zunehmend mehr Beiträge aus dem marinen Bereich sind zu verbuchen.

Es gab einen Wechsel in der Sprecherfunktion des DGG-Arbeitskreises für Elektromagnetische Tiefenforschung: Oliver Ritter, der seit 2005 unser Sprecher war, hat sein Amt niedergelegt und wird sich fortan als Sprecher des lokalen Organisatonskomitees für den *22nd International Workshop on Electromagnetic Induction in the Earth* (EMIW2014) engagieren.

Seine Nachfolger sind Ralph-Uwe Börner (TU Bergakademie Freiberg) und Katrin Schwalenberg (BGR Hannover).

Schließlich möchten wir den Firmen Metronix Braunschweig und KMS Technologies sowie der Universität Frankfurt herzlich für ihr Sponsoring danken. Die großzügige finanzielle und organisatorische Unterstützung hat in sehr hohem Maße zum Gelingen des Kolloquium beigetragen.

Wir bedanken uns ebenso herzlich bei Herrn Bertelmann von der Bibliothek des Geoforschungszentrums Potsdam für die Gewährleistung der Online-Verfügbarkeit unseres Kolloquiumsbandes.

Ralph-Uwe Börner und Katrin Schwalenberg
Freiberg und Hannover, im Juni 2012

Inhaltsverzeichnis

MT Field Campaign in Lower Saxony Basin, Germany, and electrical conductivity measurements on black shale rock samples

***Filipe Adao*[1,2], *Oliver Ritter*[1,2], *Erik Spangenberg*[1]**
1 - GFZ Potsdam 2- Freie Universität Berlin

Abstract

A Magnetotelluric (MT) field campaign was carried out in the SE Lower Saxony Basin, Germany, with the main goal of testing this method on imaging the regional Posidonia black shale sediments. Eighty-three MT stations were deployed along a sixty-three kilometer long profile. Data was acquired successfully and we show examples of apparent resistivity and phase curves before and after remote reference processing. Also, in an attempt to correlate microscale with regional, macrosale electrical resistivity models, electrical resistivity measurements were made on a series of black shale samples from boreholes to study how electrical resistivity varies with different thermal maturity levels, organic carbon and mineral content, measurement orientation and water content. Results show that black shale conduct electrical currents highly anisotropic and that water content is a main controlling factor. So far, we cannot establish a simple correlation between electrical conductivity and intrinsic properties of black shale, like organic carbon, mineral composition, and thermal maturity.

Methodical Information

Magnetotelluric Field Measurements

The MT method is a passive geophysical method of exploration that allows for imaging the electrical conductivity (or its inverse resistivity) of the Earth's subsurface using natural electromagnetic field variations. These field variations, which are generated by ionospheric current systems and worldwide lightning activity, penetrate the Earth and induce secondary EM fields depending on the conductivity distribution (e.g. the geology) of the subsurface. Measurements of these EM field variations at the Earth's surface are accomplished using a GPS-synchronised datalogger, three induction coil magnetometers and non-polarizing electrodes. The electrodes are set up to form two 50-60m long dipoles, in North-South and East-West directions, respectively. The magnetometers are used to measure two horizontal components of the magnetic field variations, while the third records the vertical component. The EM time series are recorded with the datalogger in a frequency range of 0.001Hz-1 KHz for 4-5 days.

Rock Sample Electrical Resistivity Measurements

The magnetotelluric (MT) field experiment is accompanied by laboratory investigations on black shale samples. Electrical resistivity measurements are performed using a Zahner's Electrochemical Workstation ZENNIUM (for detailed information, see: http://www.zahner.de/workstations.html), on cylindrical samples, with a 3 cm diameter and 4 cm to 10 cm length, using a four-point electrode configuration, with two outer current electrodes and two inner potential electrodes. An alternating current in a frequency range of 1Hz – 10 kHz is injected into the sample. Using Ohm's Law, electric resistance for a specific frequency can be obtained. To derive the electric resistivity of the rock sample, the resistance value is multiplied by the cross-section area of the sample and divided the distance between the potential electrodes. First, the samples are dried in a vaccum cell at 60°C to extract any fluids contained in fissures and pores. Afterwards, the samples come in vaccum desiccator with a 2 mBar vaccum environment, in which a solution is progressively inserted until full submersion is reached. Samples are removed after a week.

Magnetotelluric field experiment in the Lower Saxony Basin

To study the regional electrical conductivity structure and to characterise the Early-Jurassic Lower-Toarcian Posidonia black shales located in the sedimentary basin of Lower Saxony (see Figure 1), a magnetolluric (MT) field survey was carried out November / December 2011, within the framework of the multi-disciplinary project GASH. Magnetotelluric data was collected along a 65 km-long profile, approximately perpendicular to the main geological strike direction.

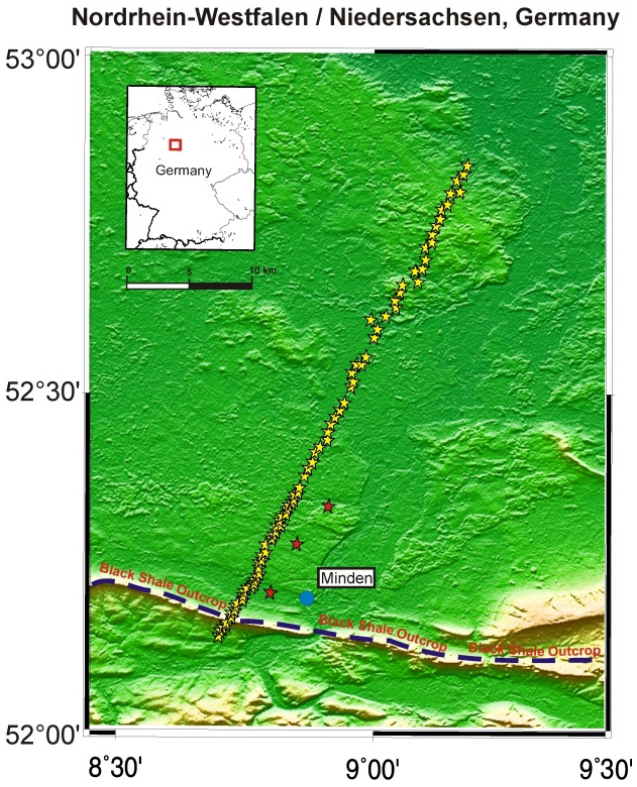

Figure 1. Southwest Lower Saxony Basin, Germany. A magnetotelluric field campaign was done under the GASH multidisciplinary project to test the MT method in the exploration of the local Posidonia black shale. Yellow and red stars represent the passive MT stations and controlled source transmitter's locations, respectively.

At the southern end of the profile southwest of Minden, the Posidonia black shale crops out. The black shale dips northward, and is it expected to reach maximum depths of approximately 3 km (Baldschuhn et al., 2001), just below the city of Nienburg. Eighty-three MT sites at a spacing of 500 m in the southern part and 1000 m in the northern part of the profile were set up. MT data was acquired in the frequency range 0.001 Hz - 10 kHz, which permits imaging shallow sediments as well as the deeper crust. Based on previous surveys of black shales (Weckmann et al., 2007) we anticipated to resolve internal resistivity variations of the Posidonia black shales in addition to its location and depth. Where the shales are at shallow depth, we also tested controlled-source MT surveying. For the CSMT measurements, currents were injected into the ground at three locations, and the resulting electromagnetic fields were recorded with the same MT stations that are used for passive MT surveying (Streich et al., 2011).

Data Processing

Using the time series processing method described in Ritter et al. (1998), with modifications included in Weckmann et al. (2005), apparent resistivity and phase curves were obtained for the acquired data. As can be seen in figure 2a, the near-field effect of the controlled source fields is evident in the period

band from 1 to 10s. After removing it, using the frequency domain selection scheme which allows manually exclude time segments from the time-series that contain undesirable events. The quality of the curves was slightly improved (see figure 2b).

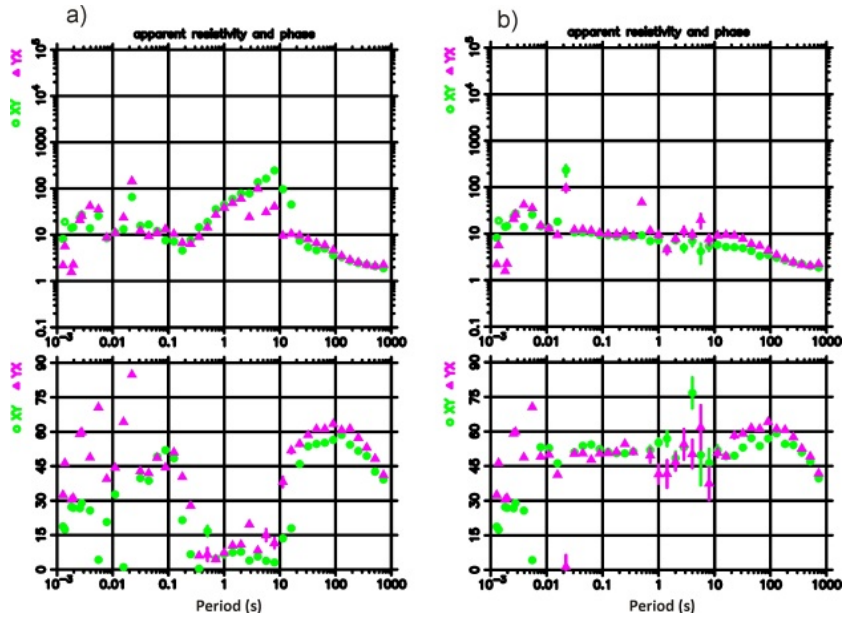

Figure 2. Apparent resistivity and phase for site 036 a) including CSMT signal and b) excluding CSMT signal.

Remote reference processing was then applied to the same data (see figure 3a) using the permanent MT reference station data acquired near Wittstock, Germany. Remote reference processing improves the results considerably (see figure 3b). At the time of writing, MT data processing is still on-going.

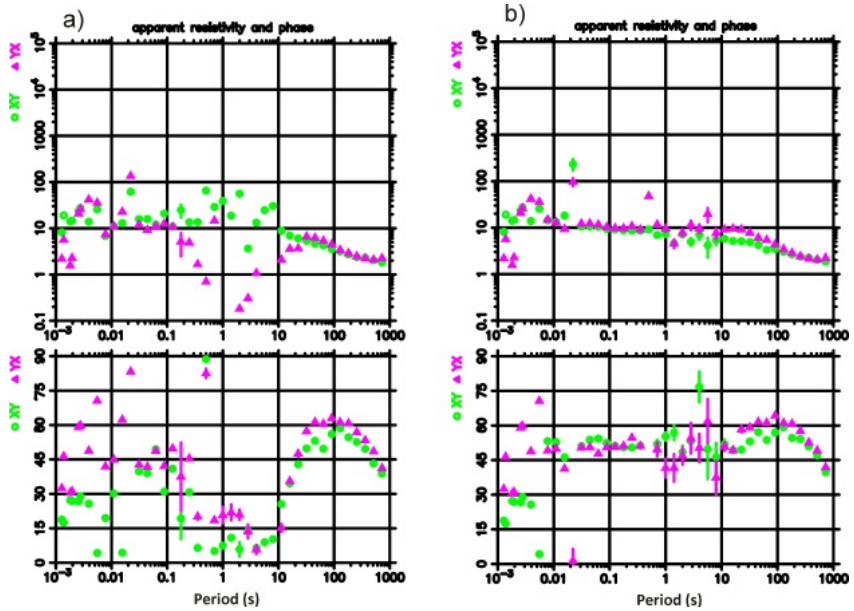

Figure 3. Apparent resistivity and phase for site 036 a) without Remote Reference processing and b) with Remote Reference processing.

Measuring electrical resistivity of black shale rock samples

Sample Description

Black shale rock samples were analysed for electrical resistivity from the Hils Syncline, Lower Saxony, Germany and for comparison from the Barnett shale, Texas, US (see Table 1 and 2 for detailed information).

1. Hils Syncline Samples

Wells	Samples	Rock Type	Depth (m)	TOC (%)	Ro (%)
Wickensen	W1	Black Shale	39.2	9.74	0.53
Wickensen	W2	Black Shale	48.8	9.79	0.53
Wickensen	W3	Black Shale	58.2	9.86	0.53
Harderode	HR1	Black Shale	42.5	7.22	0.88
Harderode	HR2	Black Shale	55.7	11	0.88
Harderode	HR3	Black Shale	76.1	9.97	0.88
Harderode	HR4	Black Shale	77.3	4.8	0.88
Haddensen	HD1	Black Shale	37.6	7.5	1.45
Haddensen	HD2	Black Shale	51.1	5.04	1.45
Haddensen	HD3	Black Shale	51.7	5.54	1.45
Haddensen	HD4	Black Shale	52.3	6.12	1.45

2. Barnett Samples

Wells	Samples	Rock Type	Depth (m)	S1 (mg/g)	TOC (%)	Dolomite (%)	Kaolinite (%)	Ro (%)
Mesquite	BN1	Mudstone	3660.4	0.31	0.79	1.58414	0	0.79
Mesquite	BN2	Mudstone	3690.9	0.79	1.53	1.148469	0	1.53
Mesquite	BN3	Black Shale	3699.8	1.19	1.62	7.460579	5.470771	1.62
Mesquite	BN4	Black Shale	3708.3	4.03	3.81	7.447475	3.004805	3.81
Mesquite	BN5	Black Shale	3736.9	3.19	6.31	5.080723	10.884463	6.31
Mesquite	BN6	Black Shale	3749.2	2.73	7.53	4.473192	13.08725	7.53
Mesquite	BN7	Mudstone	3769.1	1.73	2.48	6.365124	2.931621	2.48
Mesquite	BN8	Mudstone	3800.2	1.89	3.98	7.775465	7.19065	3.98
Mesquite	BN9	Mudstone	3817.7	1.92	2.47	6.178809	8.89889	2.47

In the Hils Syncline area, just south of the city of Hannover, Lower Toarcian, early Jurassic, black shale sediments have risen from deep burial to shallow depths, and even cropped out. A series of wells, namely Wickensen, Harderode and Haddensen, crossing the black shale formation at depths of 40 to 70 meters depths, were drilled to retrieve sample material. The mineral composition is comparable between the boreholes and hence, the progressive evolution of the black shale sediments with thermal maturation can be studied (Mann, 1987). The second area is located in the Fort Worth Basin, North-East Texas, and is known as one of the biggest gas producing black shale in the United States (Jarvie, 2007). Samples were retrieved from the Mesquite well, which crosses black shale of Early Silurian age at 3600 meters depth; the shale has a thickness of 200m.

Results

The samples extracted from the Wickensen, Harderode and Haddensen wells show an increase of electrical resistivity, at comparable depths, between the wells Wickensen and Harderode, reaching values as high as 600000 Ohm.m, and a decrease between the boreholes Harderode and Haddensen, reaching values as low as 100 Ohm.m (see Fig 4a). The Mesquite well sample series is not entirely composed of black shale but also includes mudstones. Within the black shale group, values as high as 60000 Ohm.m were measured. A simple relation between electrical resistivity and depth is not seen (see Fig 4b).

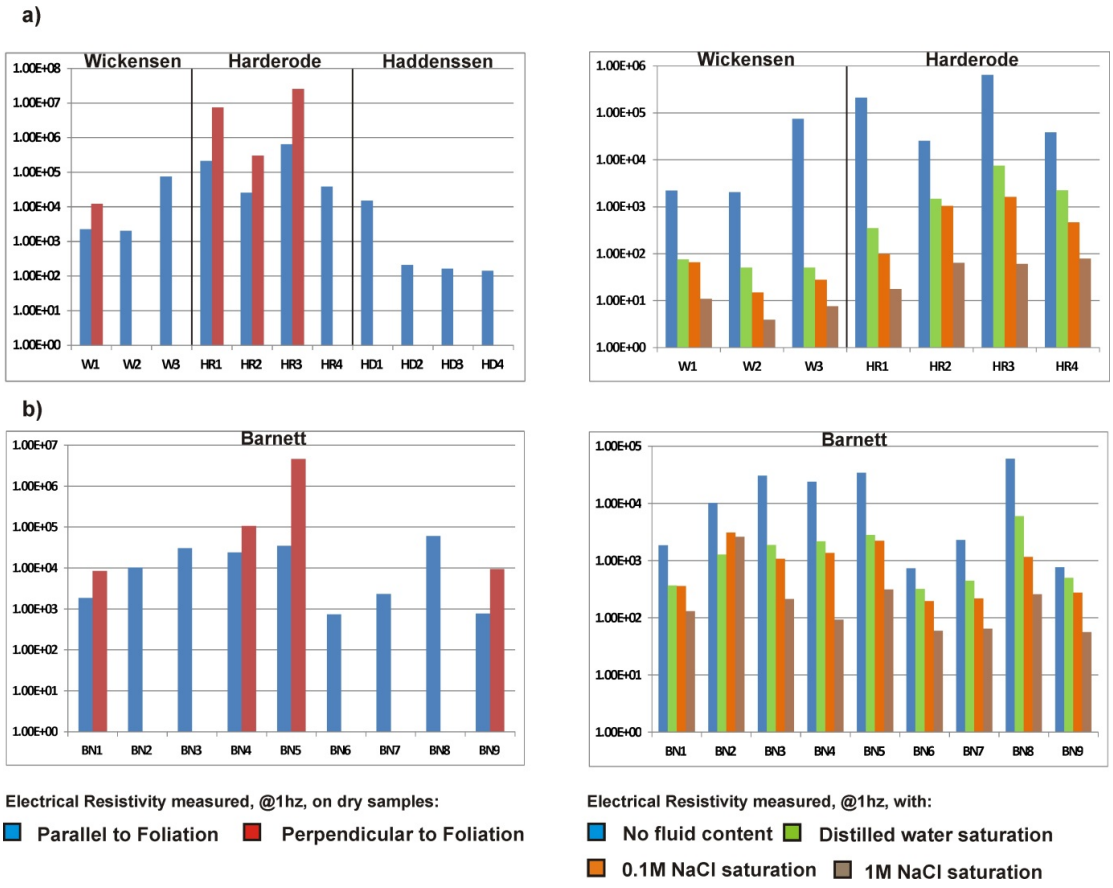

Figure 4. Results for the electrical resistivity measurements on the samples from the a) Hils Syncline and b) Barnett areas.

Samples were drilled parallel and perpendicular to the rock foliation and saturated with distilled water and two different solutions of salty water, with concentrations of 0.1M and 1M, respectively. Samples are consistently more resistive perpendicular to foliation. Saturation with distilled water and two distinct NaCl solutions decreased the electrical resistivity in a consistent fashion. This effect was overall bigger on the samples from the Hils Syncline, as the verified electrical resistivity drop was higher.

Discussion

The results suggest a complex relation between total organic carbon (TOC), mineral content and/or thermal maturity levels (Ro) and electrical resistivity; a simple (i.e. linear) correlation between these two intrinsic properties and electrical resistivity is not observed. For the Hils Syncline samples, it is interesting to note that between wells Wickensen and Harderode sample material evolves from the immature to mature state (oil window), electrical resistivity increases, and between wells Harderode and Haddensen sample material evolves from mature to overmature (gas window), and electrical resistivity decreases, to the lowest values measured. TOC levels decrease with thermal maturation (Ro), but electrical resistivity does not follow this behaviour. The presence of hydrocarbons sorbed in the rock matrix due to kerogen and bitumen cracking during maturation cannot be accounted for since the drying process extracts any remnants into the vacuum atmosphere. Structural information on the iron sulphide distribution is unknown. Thermal maturation values for the Mesquite samples are mainly between the immature and oil window states and they hint no correlation with electrical resistivity as well. Black shale are similarly resistive when compared with the over- and underlying mudstones even though they have higher TOC and clay content, namely Chlorite and Kaolinite. The results obtained saturating all the samples with distilled water showed a significant drop of resistivity at every sample. Distilled water is an insulator, but can become conductive if minerals are dissolved from the pore

matrix and by dissociation and desorption of ions from the mineral surfaces. Then, ionic conduction between interconnected pores and fractures takes control of the bulk conductivity of the rock. Obviously, fluid content is important as a controlling factor for the bulk electrical resistivity of black shale. And it is a permeable rock as both NaCl water solutions used circulated through all the rocks, lowering its bulk conductivity even further. This observation is linked to the porosity and interconnectivity of the pores of the samples. Porosity estimates still have to be determined but it seems reasonable to say that samples from the Mesquite well are less porous as the fluid content decreasing effect on electrical conductivity is smaller comparatively. From the results, within the available thermal maturity range, seems to be an electrically resistive rock. Should it be saturated with water or brine it would appear to be more conductive due to its permeable nature. Whether or not such black shale can be distinguished from over and underlying formations with magnetotelluric soundings seems to depend on many controlling factors and their interplay.

Acknowledgments

We would like to gratefully thank our colleagues at the German Research Centre for Geosciences, Potsdam, Germany, Rita Streich, Diane Eydam, Danielle Tölg, Ute Weckmann, Gerard Munoz, Paul Saß, Reinhard Klose, Norbert Ebel, Alexander Grayver, Dirk Brändlein, Sissy Kütter, Naser Meqbel, Mangal Bhatt, Stefan Rettig, Martin Baumann, and also Felicia Winter, from the Alfred-Wegener Institut, Bremerhaven, Germany, Bastian Wichand, from the BGR, Hannover, Germany, and Jan Schmoldt, PhD graduate, for helping with the planning, scouting, land access permitting, and ultimately, the field work. We also thank Kai Jasper, Dorit Kerschke and Hans-Martin Schultz for providing us with the black shale rock samples, and Alex Reichard, Christina Rudolph and Scott Angus Maclennan, from the University of Cape Town, for helping with the laboratory working envolving the preparation and saturation of the black shale rock samples. Acknowledgements go out also to land owners for granted access to their properties. All equipment was provided by the GIPP-MT (Geophysical Instrumental Pool Potsdam). Funding was from GFZ and GeoEn, a project from the German Federal Ministry of Education and Research, BMBF.

References

Baldschuhn, R.; Binot, F.; Fleig, S.; Kockel, F.: Geotektonischer Atlas von Nordwest-Deutschland und dem deutschen Nordsee-Sektor. Hannover, 2001.

Jarvie et al. (2007): Unconventional shale-gas systems: The Mississipian Barnett Shale of north-central Texas as one model for thermogenic shale-gas assessment. AAPG Bulletin, V. 91, NO. 4, 475-499.

Mann, U. (1987): Veränderungen von Porosität und Porengröße eines Erdölmuttergesteins in Annäherung an einen Intrusivkörper. Facies 17, 181-188.

Ritter, O.; Junge, A.; Dawes, G. J. K. (1998): New equipment and processing for magnetotelluric remote reference observations. Geophys. J. Int., 535-548.

Streich, R. (2011): Strategies for land-based controlled-source electromagnetic surveying in high-noise regions. The Leading Edge, 1174-1181.

Weckmann, U.,Jung, A.,Branch,T.,Ritter,O. (2007b): Comparison of electrical conductivity structures and 2D magnetic modelling along two profiles crossing the Beattie magnetic anomaly. South African Journal of Geology 110, 449–464.

Weckmann et al. (2005): Effective noise separation for magnetotelluric single site data processing using domain selection scheme. Geophysical Journal International 161, 635-652.

Wilkin & Barnes, (1996): Formation processes of framboidal pyrite. Geochimica et Cosmochimica, Vol 61, No. 2, pp. 323-339

Untersuchung von Schlammvulkanen in Perekishkul, Aserbaidschan mit Transient-Elektromagnetik (TEM) und Radiomagnetotellurik (RMT)

J. Adrian[1], H. Großbach, B. Tezkan (Institut für Geophysik und Meteorologie, Universität zu Köln), A. Novruzov, A. Mamedov (Baku State University); [1] *adrian@geo.uni-koeln.de*

Zusammenfassung

Ziel des Projektes ist es den inneren Aufbau von Schlammvulkanen mithilfe von elektromagnetischen Methoden zu untersuchen und bestehende Modelle zu bestätigen und ggf. zu verbessern. Dazu wurden eine Reihe von TEM und Radiomagnetotellurik Messungen an Schlammvulkanen in Perekishkul, Aserbaidschan durchgeführt. Die RMT-Ergebnisse werden in *Großbach et al. (2012)* besprochen.
Schlammvulkanismus ist ein in Aserbaidschan sehr verbreitetes Phänomen, welches häufig mit Erdölvorkommen in Verbindung steht. Die verwendeten Messmethoden ermöglichen es Aussagen über die Verteilung des spezifischen Widerstands der oberen 150 m zu treffen. Die TEM-Daten wurden mit Geräten der Firma Zonge Engineering, dem Sender NT-20 und dem Empfänger GDP-32 II, aufgezeichnet. Die Daten wurden mit 1D Inversionsalgorithmen ausgewertet, darunter auch der Laterally Constrained Inversion Algorithmus. Es konnten die oberen 100 - 150 m der Widerstandsverteilung aufgelöst werden.
Insgesamt zeigten sich im Messgebiet spezifische Widerstände zwischen 1 - 20 Ωm. Trotz der relativ geringen Widerstandskontraste ist es möglich die Lokation der Schlammvulkane, insbesondere in lateraler Richtung, in den Ergebnissen zu erkennen. Die Ergebnisse decken sich mit bereits bestehenden Modellen des inneren Aufbaus von Schlammvulkanen.

1 Das Projekt

Das Phänomen des Schlammvulkanismus tritt weltweit auf und ist dennoch relativ unbekannt. Dabei ist die Erforschung von Schlammvulkanen durch den Gasaustritt und die Verbindung mit Erdölvorkommen von ökologischem und ökonomischen Interesse.
Die bisher gewonnenen geophysikalischen Erkenntnisse über den Schlammvulkanismus in Aserbaidschan stammen größtenteils aus seismischen und gravimetrischen Messungen. Ziel des *ELMUD*-Projektes (Electromagnetic methods to study the inner structure of mud volcanoes in Perekishkul, Azerbaijan) ist es, die Anwendbarkeit Elektromagnetischer Methoden an Schlammvulkanen zu überprüfen. Es soll also die Verteilung des spezifischen Widerstands der inneren Struktur der Schlammvulkane und deren Umgebung untersucht werden. Im ersten Teil des Projektes wurden die Methoden der RMT [*Großbach et al., 2012*] und TEM angewendet, um den oberen Teil der Widerstandsverteilung bis etwa 150 m Tiefe aufzulösen. Im zweiten Teil des Projektes soll durch Anwendung der Long Offset Transient Electromagnetic (LOTEM) der aufgelöste Tiefenbereich mehrere Kilometer betragen.

2 Schlammvulkanismus

Schlammvulkanismus ist ein in Aserbaidschan weit verbreitetes Phänomen, bei dem Schlamm und Gas aus dem Erdboden austreten. Der austretende Schlamm besteht aus einer Dispersion von feinkörnigem Material. Das Gas besteht zu mehr als 85 % aus Methan.
Die drei untersuchten Schlammvulkane gehören zum Chikishlar-Typ, welcher sich durch eine mäßige und kontinuierliche Aktivität auszeichnet. Abb. 1 zeigt eine Aufnahme der

mit Vulkan 1 bezeichneten Schlammvulkangruppe in Perekishkul. Vulkan 1 besitzt mehrere Schlammaustrittsstellen, welche sich mehr oder weniger auf einer ca. 120 m langen Linie aufreihen und eine Höhe von bis zu 3 m besitzen.

Abbildung 1: *Vulkan 1, Ausmaße: ca. 120 m lang, bis zu 3m hoch, kontinuierlicher Schlamm- und Gasautritt.*

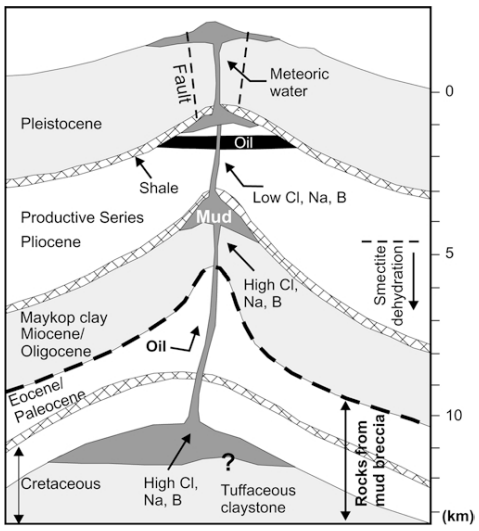

Abbildung 2: *Aufbau eines Schlammvulkans [Plancke, 2003].*

Abbildung 3: *Ölschlieren im Schlamm.*

In Aserbaidschan sind die Enstehungsbedingungen für Schlammvulkanismus optimal erfüllt. Zu den wichtigsten Bedingungen zählt das Vorhandensein einer mächtigen Sedimentdecke aus feinkörnigem, wenig verfestigten Material, welches einer lateralen tektonischen Kompression unterliegt [*Milkov, 2005*]. Die Sedimente weisen eine relativ kleine Dichte auf und können mehr Wasser aufnehmen als das umgebende Gestein. Das Sediment-Wasser Gemisch - der Schlamm - erlangt durch seine geringe Dichte einen Auftrieb. Ein weiterer wichtiger Antriebsmechanismus ist die Gashydrat-Dissoziation. Im Erdboden gebundene Gashydrate, meist Methanhydrat, sind nur unter bestimmten Druck-Temperatur Bedingungen stabil. Verändern sich diese Bedingungen kommt es zur Gashydrat-Dissoziation, bei der sich die Gashydrate in Gas und Wasser aufspalten. Durch die so enstehenden Gase ensteht ein zusätzlicher Auftrieb des nun vorliegenden Schlamm-Gas Gemisches. Bei beiden Prozessen spricht man von Dichteinversion [*Scholte, 2005*].

In Aserbaidschan stellt das Südkaspische Becken die Basis für eine bis zu 20 km mächtige Sedimentdecke dar, welche aus den umliegenden Gebirgen gespeist wird. Da Erdöl ähnliche Enstehungsbedingungen aufweist, treten - insbesondere in Aserbaidschan - Erdölvorkommen häufig in Verbindung mit Schlammvulkanismus auf. Ein Modell des inneren Aufbaus eines Schlammvulkans ist in Abb. 2 dargestellt. Unterhalb einer mehreren Kilometer mächtigen Sedimentschicht befindet sich ein Schlammreservoir. Das aufsteigende Schlamm-Gas Gemisch fördert weiteres leichtes Material, wie z.B. Erdöl, an die Oberfläche. Abb. 3 zeigt dunkle Ölschlieren im Schlamm eines Schlammvulkans im Messgebiet.

3 Messkampagne

Die Messkampagne fand im April 2010 in Perekishkul, 45 km von der aserbaidschanischen Hauptstadt Baku entfernt, statt. In Abb. 4a ist die Verteilung bekannter Schlammvulkane in Aserbaidschan und dem Kaspischen Meer dargestellt. Die Lage des Messgebietes ist rot markiert. Eine Satellitenaufnahme des Messgebietes zeigt Abb. 4b. Im Messgebiet befinden sich 3 Schlammvulkane. Diese sind in der Abb. 4b durch Vulkansymbole markiert. Bei den Vulkanen 1 und 3 handelt es sich um Schlammvulkangruppen (vgl. Abb. 1). Vulkan 2 besteht lediglich aus 2 Schlammaustrittsstellen mit einem Durchmesser von ca. 50 cm. Grüne und blaue Markierungen zeigen die Lage der 72 TEM Stationen auf 6 Profilen. Es wurden der Transmitter NT-20 und der Receiver GDP-32 II der Firma Zonge Engineering benutzt. Die verwendete Inloop Konfiguration mit einem 50 m x 50 m transmitter loop und einem 20 m x 20 m receiver loop sind in Abb. 4c skizziert.

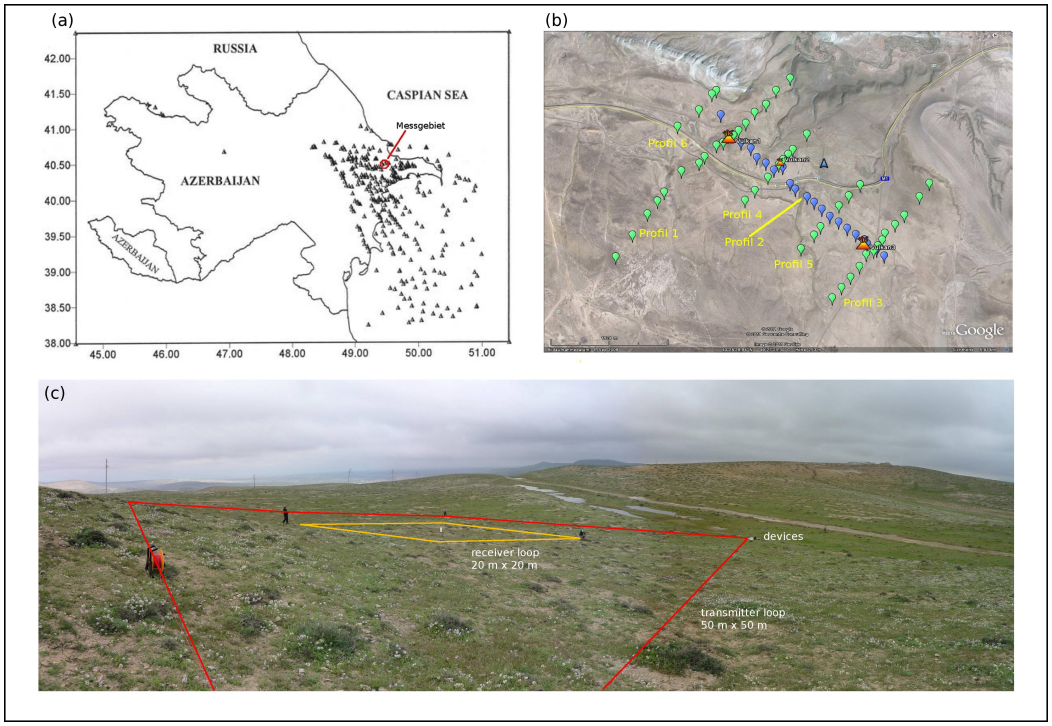

Abbildung 4: *(a) Schlammvulkane in Aserbaidschan und das Messgebiet [verändert nach Feyzullayev at al., 2005], (b) TEM Stationen (blau und grün markiert) und Schlammvulkane (Vulkansymbole), Entfernung von Vulkan1 (im Nordwesten) zu Vulkan3 (im Südosten) ca 2,4 km, (c) Messaufbau der Inloop-TEM Konfiguration.*

3.1 Daten

An allen Stationen wurden beide Moden, die der GDP-32 II zur Verfügung stellt, benutzt. Im NanoTEM Modus wurden induzierte Spannungen im Zeitbereich von 0,7 μs bis 2 ms mit einem Sendestrom von 1,5 A aufgezeichnet. Der aufgezeichnete Zeitbereich im ZeroTEM Modus betrug 40 μs - 6 ms und der Sendestrom 9,5 A.
Der Einfluss der endlichen Abschaltzeit des Transmitters wurde durch eine Dekonvolution entfernt [*Fittermann and Anderson, 1987; Helwig et al., 2003*]. Außerdem wurden unbrauchbare Datenpunkte entfernt. Anschließend konnten die Transienten des NanoTEM und ZeroTEM Modus zu einem Transienten zusammengesetzt werden, welcher einen Zeitbereich von 13 μs bis 6 ms abdeckt. Ein Datenbeispiel ist in Abb. 5 dargestellt. Es zeigt die Transienten der unterschiedlichen Moden, sowie den aus den prozessierten Einzeltransienten zusammengesetzten Transienten, welcher für die weitere Auswertung benutzt wurde. Außerdem ist das Noiselevel für beide Moden abgebildet.

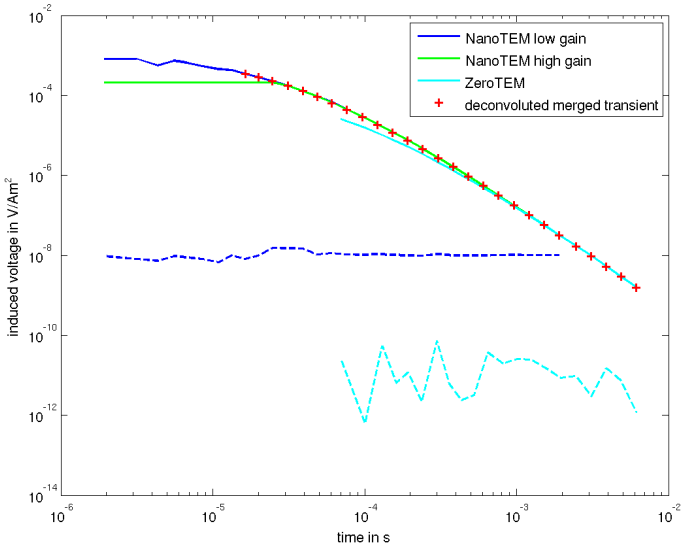

Abbildung 5: *Datenbeispiel für Punkt 02p11 (1350 m südöstlich von Vulkan 1 auf Profil 2). Die Daten des NanoTEM Modus mit kleiner Verstärkung sind in dunkelblau dargestellt, die des NanoTEM Modus mit großer Verstärkung in grün und die des ZeroTEM Modus in hellblau. Der aus den dekonvolvierten Daten zusammengesetzte Transient ist durch rote Kreuze gekennzeichnet. Die gestrichelten Linien zeigen das Noiselevel im NanoTEM Modus (dunkelblau) und im ZeroTEM Modus (hellblau).*

Die aufgezeichneten induzierten Spannungen $U(t)$ können mithilfe der latetime Näherung [*Strack, 1985*], welche für späte Zeiten nach der Abschalten gilt, in scheinbare Widerstände $\rho_a^{lt}(t)$ umgerechnet werden:

$$\rho_a^{lt} = \left(\frac{I A_T A_R}{U}\right)^{\frac{2}{3}} \cdot \frac{1}{20^{\frac{2}{3}} \cdot \pi} \cdot \left(\frac{\mu_0}{t}\right)^{\frac{5}{3}}$$

Dabei ist A_T die Senderfläche, A_R die Empfängerfläche und I der Sendestrom.
Ein Vergleich der Transienten der Station 01n01, welche sich direkt auf Vulkan 1 befand, und Station 01z07, welche sich in 170 m Entfernung südwestlich von Vulkan 1 befand, ist in Abb. 6 abgebildet. Im Zeitbereich von ca. $2 \cdot 10^-5$ s bis $1 \cdot 10^-3$ s weichen die beiden

Transienten deutlich voneinander ab. Somit sollten sich auch die Inversionsergebnisse der Stationen auf den Vulkanen von den übrigen Stationen unterscheiden lassen.

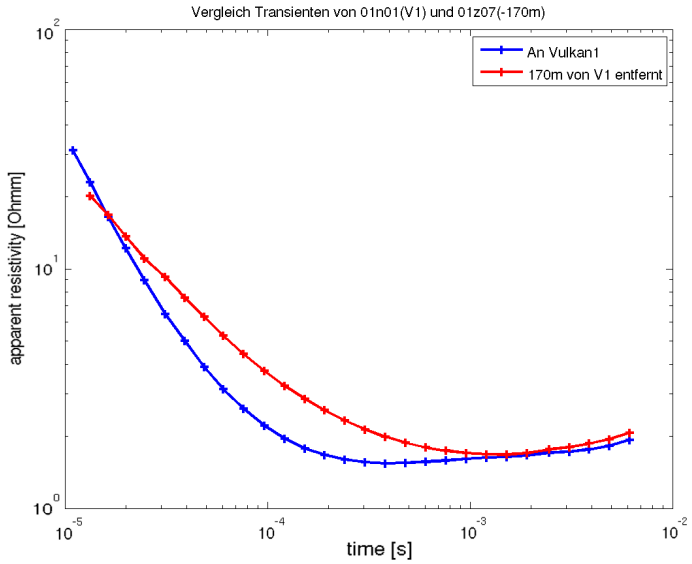

Abbildung 6: *Vergleich der Transienten der Stationen 01n01 (auf Vulkan 1) und 01z07 (170 m von Vulkan 1 entfernt), umgerechnet nach der latetime Näherung in scheinbare Widerstände.*

Die Ergebnisse der RMT Messungen, welche während derselben Messkampagne durchgeführt wurden, werden in dem Beitrag von *Großbach et al. (2012)* besprochen.

4 Ergebnisse

Die TEM Daten wurden mit verschiedenen 1D Inversionsalgorithmen ausgewertet, darunter Occam und Marquardt Inversionen, sowie der Quasi-2D Laterally Constrained Inversion (LCI) nach *Auken et al. (2005)*. Die Ergebnisse können ausführlich in *Adrian (2011)* nachgelesen werden.
Allgemein zeigen die Inversionsergebnisse spezifische Widerstände von 1 - 20 Ωm. Bezeichnungen wie gutleitend und schlechtleitend sind also innerhalb dieses Intervalls zu verstehen. In Abb. 7 und Abb. 8 sind beispielhaft die Occam und Marquardt Ergebnisse der Stationen 01n01 (auf Vulkan 1) und 01z07 (170 m südwestlich von Vulkan 1) dargestellt. Die Occam Modelle der Station auf Vulkan 1 (Abb. 7a) stimmen bis zu einer Tiefe von ca. 115 m gut überein. Die Marquardt Inversion resultiert in einem Zweischichtfall mit einer 14 m mächtigen 1,5 Ωm-Deckschicht über einem homogenen Halbraum mit spezifischem Widerstand von 3,5 Ωm. Die Äquivalenzmodelle weichen nur geringfügig voneinander ab. Dies zeigt sich auch in den Importances, welche mit 1,00 und 0,99 für den spezifischen Widerstand der ersten und zweiten Schicht eine sehr gute Auflösung dieser Parameter anzeigen. Auch die Schichtgrenze ist mit einer Importance von 0,86 noch gut aufgelöst. Die Datenanpassung der Marquardt Inversion ist mit einem RMS Fehler von 2,04 % gut (Abb. 7b).
Die Occam Modelle der Station in 170 m Entfernung von Vulkan 1 (Abb. 8a) stimmen in den oberen 10 m nicht gut überein. Das Marquardt Modell besitzt jedoch mit einem RMS Fehler von 1,73 % eine gute Datenanpassung (Abb. 8b). Im Vergleich zum Modell

auf Vulkan 1 zeigt das Marquardt Modell hier eine 7,5 m mächtige schlechtleitende Deckschicht mit einem spezifischen Widerstand von 6 Ωm. Darunter folgt eine 31 m mächtige gutleitende Schicht mit 1,8 Ωm, sowie eine Schicht mit 4,3 Ωm. Die Importance des spezifischen Widerstands der ersten Schicht zeigt mit 0,38 eine mäßige Auflösung. Allerdings zeigen die Äquivalenzmodelle ähnliche Widerstände. Die Importances der übrigen Parameter zeigen eine gute Parameterauflösung.
Das Ergebnis der Station auf dem Vulkan unterscheidet sich also hauptsächlich dadurch, dass keine schlechtleitende Deckschicht vorhanden ist.

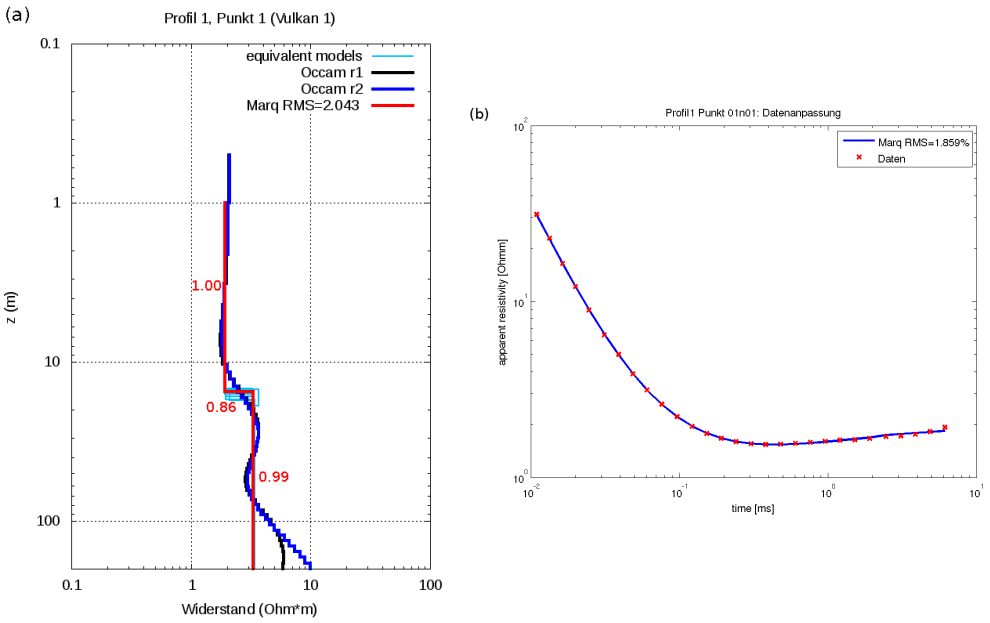

Abbildung 7: *Inversionsergebnisse für Punkt 01n01 auf Profil 1 an Vulkan 1; (a): Occam Modelle in dunkelblau und schwarz, Äquivalenzmodelle in hellblau, bestfit Marquardt Modell und Importances in rot; (b): Datenanpassung des Marquardt Modells in blau an die Messdaten in rot.*

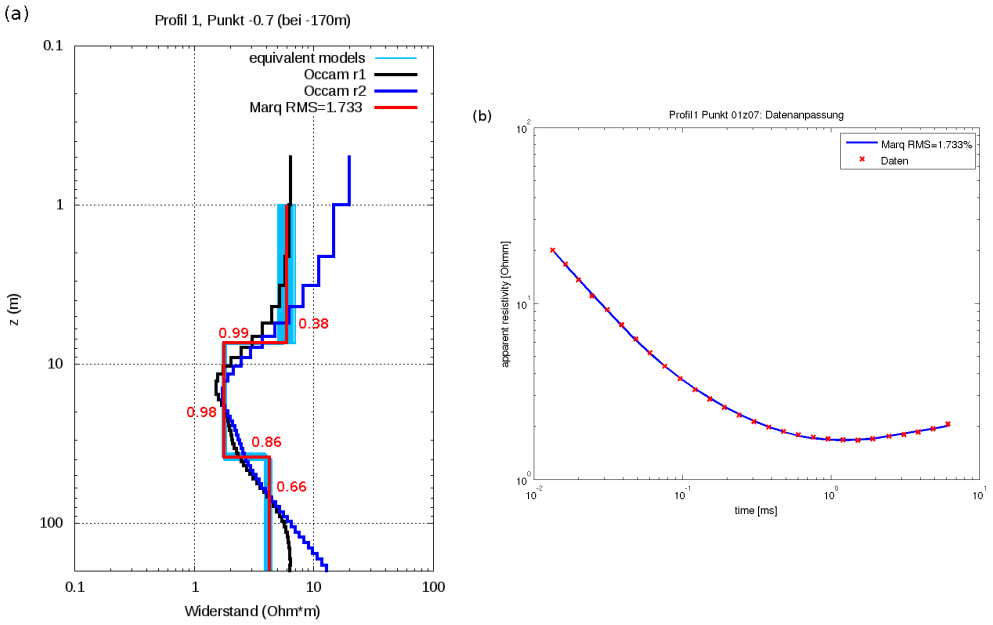

Abbildung 8: *Inversionsergebnisse für Punkt 01z07 auf Profil 1 170m südlich von Vulkan 1; (a): Occam Modelle in dunkelblau und schwarz, Äquivalenzmodelle in hellblau, bestfit Marquardt Modell und Importances in rot; (b): Datenanpassung des Marquardt Modells in blau an die Messdaten in rot.*

4.1 Laterally Constrained Inversion

Bei der LCI handelt es sich um eine Quasi-2D Inversion nach *Auken et al. (2005)*, bei der die Daten aller Stationen eines Profils als ein System invertiert werden und bei der benachbarte eindimensionale Modelle durch Constraints miteinander verknüpft sind. Ein Constraint von 0,1 bedeutet dabei, dass Nachbarparameter wie z.B. der spezifische Widerstand der ersten Schicht um 10 % voneinander abweichen dürfen. Nach einer Untersuchung an synthetischen Daten wurde die Stärke der Constraints auf 0,1 für alle Parameter - also spezifische Widerstände und Mächtigkeiten - festgelegt.
Das LCI Ergebnis für Profil 2, also das Verbindungsprofil der Vulkane 1 und 3 (vgl. Abb. 4b), ist in Abb. 9 dargestellt. Die Schichtgrenzen sind durch gestrichelte Linien markiert. Die Depth of Investigation (DOI) nach *Christiansen und Auken (2010)* ist als durchgezogene Linie dargestellt und liegt meist zwischen 100 - 130 m. Insgesamt zeigt sich eine gutleitende Schicht, welche einen spezifischen Widerstand von 2 - 4 Ωm und eine Mächtigkeit von ca. 15 - 30 m besitzt. Diese Schicht ist von einer schlechtleitenden Deckschicht mit einem spezifischen Widerstand von ca. 5 - 20 Ωm und einer Mächtigkeit von ca. 5 m bedeckt. Die dritte Schicht besitzt mit 4 - 6 Ωm leicht erhöhte Widerstände im Vergleich zur 2. Schicht. Die Stationen auf den Vulkanen 1 und 3 zeichnen sich durch eine laterale Variation des spezifischen Widerstands der ersten Schicht aus. Dort liegt keine schlechtleitende Deckschicht vor, sondern der gute Leiter von ca. 1,6 - 3 Ωm zieht sich bis zur Oberfläche hoch. Der Übergang zum schlechten Leiter liegt bei Vulkan 1 in 15 m und bei Vulkan 3 in 20 - 25 m Tiefe.

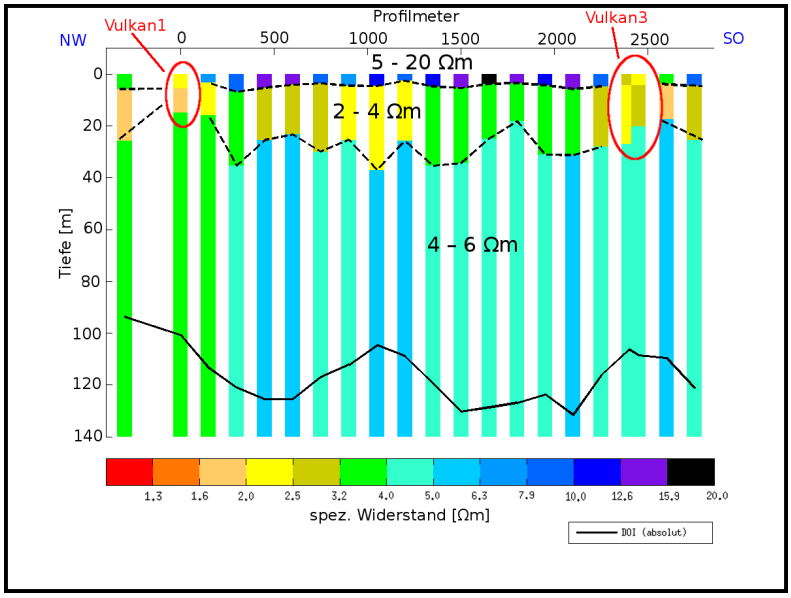

Abbildung 9: *LCI Ergebnis Profil2 (Verbindungsprofil, blau markiert in Abb. 4b), Constraints der Widerstände und Mächtigkeiten sind jeweils 0,1. Schichtgrenzen sind als gestrichelte Linien dargestellt, der DOI als durchgezogene Linie.*

5 Diskussion

Zusammenfassend kann man sagen, dass die Detektierung von Schlammvulkanen mithilfe der TEM erfolgreich durchgeführt wurde. Trotz der absolut betrachtet kleinen Widerstandskonstraste (1 - 20 Ωm), unterscheiden sich die Inversionsergebnisse der Stationen auf den Schlammvulkanen von denen der Stationen in der Umgebung. Insbesondere in lateraler Richtung ist ein Kontrast in der Verteilung des spezifischen Widerstands zu erkennen. Im Gegensatz zur Umgebung fehlt auf den Schlammvulkanen die mit 5 - 20 Ωm schlechtleitenden Deckschicht.

Es wird vermutet, dass der komplette untersuchte Tiefenbereich von maximal 150 m aus feinkörnigen Sedimenten besteht. Die vorgefundenen spezifischen Widerstände lassen sich nach *Reynolds (1997)* und *Telford et al. (1990)* beispielsweise mit Mergel (3 - 70 Ωm), Tonen (1 - 100 Ωm), Schlamm und Sand (10 - 800 Ωm) oder Boden mit 40 %igen Tonanteil (8 Ωm) in Verbindung bringen. Dabei gehen wir davon aus, dass die Bereiche mit einem geringeren spezifischen Widerstand - also die zweite Schicht - einen größeren Wasser- bzw. Salzwasseranteil besitzen als z.B. die Deckschicht. Bei der Deckschicht ist davon auszugehen, dass der Wassergehalt durch Verdunstung bzw. Versickerung des in den Sedimenten enthaltenen Wassers relativ gering ist. Das Fehlen dieser trockenen und somit weniger leitfähigen Schicht an den Vulkanen ist durch das Aufsteigen von feuchtem Schlamm, sowie die Bedeckung der Oberfläche durch den austretenden Schlamm zu erklären. Die TEM Ergebnisse lassen keine Interpretation eindeutiger Schlote oder Schlammkammern zu.

6 Ausblick

Im Rahmen des Projektes wurde im September 2011 eine Long Offset Transient Electromagnetic (LOTEM) Kampagne im gleichen Messgebiet durchgeführt. Ziel ist es den

spezifischen Widerstand größerer Tiefen aufzulösen. Außerdem sollen die LOTEM Ergebnisse mit den RMT- und TEM-Ergebnissen verbunden werden. Die Daten befinden sich nach aktuellem Stand in der Auswertung.

7 Danksagung

Unser Dank gilt der Volkswagenstiftung für die finanzielle Unterstützung, sowie den Messhelfern und aserischen Projektpartnern für die Unterstützung vor Ort.

8 Referenzen

Adrian, J., Untersuchung von Schlammvulkanen in Perekishkul, Aserbaidschan mit der Transient-Elektromagnetik, Diplomarbeit, Insitut für Geophysik und Meteorologie, Universität zu Köln, 2011.

Auken, E., A. V. Christiansen, B. H. Jacobsen, N. Foged und K. I. Sorensen, Piecewise 1D laterally constrained inversion of resistivity data, *Geophysical Prospecting*, 53, 497-506, 2005.

Christiansen, A. V. und E. Auken, A global measure for Depth of Investigation in EM and DC Modeling, in *ASEG 2010 - Sydney, Australia*, 2010.

Feyzullayev, A. A., F. A. Kadirov und C. S. Aliyev, Mud Volcano Model Resulting from Geophysical and Geochemical Research, in *Mud Volcanoes, Geodynamics and Seismicity*, herausgegeben von G. Martinelli und B. Panahi, NATO Science Series, Springer, 2005.

Fittermann, D. V. und W. L. Anderson, Effect of Transmitter Turn-Off Time on Transient Soundings, *Geoexploration*, 24, 131-146, 1987.

Großbach, H., J. Adrian, B. Tezkan, A. Novruzov und A. L. Mamedov, Erste Anwendung der Radiomagnetotellurik (RMT) und Transient-Elektromagnetik (TEM) auf Schlammvulkanen in Perekishkul, Aserbaidschan, in *Protokoll üder das 24. Schmucker-Weidelt-Kolloquium für Elektromagnetische Tiefenforschung*, 2012.

Helwig, S. L., J. Lange und T. Hanstein, Kombination dekonvolvierter Messkurven zu einem langen Transienten, in *Tagungsband der 63. Jahrestagung der Deutschen Geophysikalischen Gesellschaft*, 2003.

Milkov, A. V., Global Distribution of Mud Volcanoes and their Significance in Petroleum Exploration as a Source of Methane in the Athmosphere and Hydrosphere and as a Geohazard, in *Mud Volcanoes, Geodynamics and Seismicity*, herausgegeben von G. Martinelli und B. Panahi, NATO Science Series, Springer, 2005.

Planke, S., H. Svensen, M. Hovland, D. A. Banks und B. Jamtveit, Mud and fluid migration in active mud volcanoes in Azerbaijan, *Geo-Marine Letters*, 23, 258-268, 2003.

Reynolds, J. M., *An Introduction to Applied and Environmental Geophysics*, John Wiley and Sons, 1. Auflage, 1997.

Scholte, K. H., *Hyperspectral Remote Sensing and Mud Volcanism in Azerbaijan*, Dissertation, Department of Geotechnology, Delft University of Technology, 2005.

Strack, K. M., *Das Transient-Elektromagnetische Tiefensondierungsverfahren angewandt auf die Kohlenwasserstoff- und Geothermie-Exploration*, Dissertation, Institut für Geophysik und Meteorologie, Universität zu Köln, 1985.

Telford, W. M., L. P. Geldart und R. E. Sheriff, *Applied Geophysics*, Cambridge University Press, 2. Auflage, 1990.

A 3-D finite difference forward modelling framework for MT and CSEM applications

Börner, R.-U.[1], Ernst, O. G.[2], Spitzer, K.[1]
[1] Institute of Geophysics and Geoinformatics, TU Bergakademie Freiberg, Germany
[2] Institute of Numerical Analysis and Optimization, TU Bergakademie Freiberg, Germany

1 Introduction

In this paper we present a versatile 3-D forward operator for MT and CSEM applications. The boundary value problem of electromagnetic induction is expressed in terms of the electric field. The spatial discretization is carried out on a finite difference grid exploiting the well-known Yee scheme which positions the components of the electric field at the edges and the magnetic field components at the faces of an elementary Yee cell. To allow for a straightforward numerical calculation of the response of a 3-D conductivity structure for multiple applications, such as MT, and airborne CSEM, we apply the secondary field method, where the simulated field is split into a primary and secondary part. The primary electric field is generated by electromagnetic induction of a radiating source over a simple, e. g., one-dimensional conductivity structure with $\sigma = \sigma_0(z)$. The anomalous conductivity distribution $\Delta\sigma(x, y, z) = \sigma(x, y, z)\sigma_0(z)$ acts – together with the driving primary electric field – as a source density distribution causing a secondary anomalous electric field. We further present an adaptive grid refinement technique exploiting an *a-posteriori* error indicator on the basis of the divergence of the magnetic field. We give two numerical examples: First, a 3-D magnetotelluric model is considered. Second, an airborne EM example shall demonstrate how multiple sources can be handled efficiently. Our results agree well with those of other independent EM modelling codes.

2 The continuous boundary value problem in $\mathbb{R}^3$

We consider the quasi-static curl-curl equation for the secondary electric field $\boldsymbol{E}_s(\boldsymbol{r})$ arising from Maxwell's equations in the frequency domain with respect to a spatial distribution of electrical conductivity, $\sigma(\boldsymbol{r})$, and a source current density defined by $\boldsymbol{J}^e(\omega, \boldsymbol{r})$, such that

$$\nabla\times\nabla\times\boldsymbol{E}_s(\boldsymbol{r}) + i\omega\mu_0\sigma(\boldsymbol{r})\boldsymbol{E}_s(\boldsymbol{r}) = -i\omega\mu_0\,\boldsymbol{J}^e(\omega,\boldsymbol{r}) \qquad \text{in } \Omega\subset\mathbb{R}^3 \tag{1}$$

$$\boldsymbol{n}\times\boldsymbol{E}_s = 0 \qquad \text{on } \partial\Omega \tag{2}$$

$$\boldsymbol{J}^e(\omega,\boldsymbol{r}) = (\sigma - \sigma_0(z))\boldsymbol{E}_0(\omega,\boldsymbol{r}|\boldsymbol{r}_0) \tag{3}$$

$$\boldsymbol{E} = \boldsymbol{E}_0 + \boldsymbol{E}_s \tag{4}$$

$$\boldsymbol{H} = \frac{i}{\omega\mu_0}\nabla\times\boldsymbol{E}. \tag{5}$$

A time dependency of $e^{i\omega t}$ is assumed. At the artificial boundaries of the computational domain simple homogeneous Dirichlet boundary conditions apply.
The primary field $\boldsymbol{E}_0(\omega, \boldsymbol{r}|\boldsymbol{r}_0)$ is the solution of a 1-D Helmholtz equation for $\sigma_0(z)$ and a dipole source located at $\boldsymbol{r}_0$.
In the MT case, electromagnetic induction is exaggerated by temporal variations of the magnetic field. Any primary magnetic field can be decomposed into two linearly independet components along the horizontal coordinate axes. We refer to these horizontal directions as polarizations. The corresponding pairs of magnetic and electric field components are mutually orthogonal. Consider an x-oriented primary magnetic field, H_x. It follows from Maxwell's equations, that the corresponding electric field is E_y. The second polarization can be obtained by rotating the primary magnetic field around the vertical z-axis. For a primary H_y we obtain $E_x = -E_y$. The primary field simplifies to $\boldsymbol{E}_0(\omega, z)$ and, as a function of z, is independent of the cartesian coordinates x and y.
We note that the solution of (1) is usually desired for multiple frequencies ω.

3 Discrete Solution

We use a 3-D finite difference scheme on a graded tensor product grid. Spatial discretization of the boundary value problem defined by (1) and (2) yields the matrix operators

$$\begin{aligned}\boldsymbol{A}(\boldsymbol{m}) &= \boldsymbol{C}^H\boldsymbol{C}^E + i\omega\mu_0\boldsymbol{S}(\boldsymbol{m})\\ \boldsymbol{S}(\boldsymbol{m}) &= \mathrm{diag}(\boldsymbol{M}\boldsymbol{m})\\ \boldsymbol{m} &= (m_1,\ldots,m_M)^\top, \quad m_i = \sigma_i,\end{aligned}$$

where $\boldsymbol{C}^H$ and $\boldsymbol{C}^E$ are the discrete curl operators applied to the magnetic and electric field:

$$\boldsymbol{C}^H = \begin{bmatrix} 0 & -\mathbf{G}_z^H & \mathbf{G}_y^H \\ \mathbf{G}_z^H & 0 & -\mathbf{G}_x^H \\ -\mathbf{G}_y^H & \mathbf{G}_x^H & 0 \end{bmatrix}, \quad \boldsymbol{C}^E = \begin{bmatrix} 0 & -\mathbf{G}_z^E & \mathbf{G}_y^E \\ \mathbf{G}_z^E & 0 & -\mathbf{G}_x^E \\ -\mathbf{G}_y^E & \mathbf{G}_x^E & 0 \end{bmatrix}.$$

The 3×3 block matrices $\boldsymbol{C}^H$ and $\boldsymbol{C}^E$ represent discrete curl operators. More specifically, the $(1,2)$-block of $\boldsymbol{C}^H$, $-\mathbf{G}_z^H$, yields the x-component of the discrete curl by taking the negative z-derivative of the y-component of the magnetic field $\boldsymbol{H}$.
The matrix $\mathbf{M}$ maps the cell conductivities onto the unknown field positions by applying a volume weighting scheme. This *averaging operator* represents the action of the actual grid within the weighting scheme. $\mathbf{M}$ and $\boldsymbol{m}$ are related by a linear operation, i. e., a matrix-vector product. $\boldsymbol{S}$ can be understood as a spatially weighted conductivity projected onto the space of the discrete unknowns.
The right-hand side

$$\boldsymbol{b}(\boldsymbol{m}) = -i\omega\mu_0\boldsymbol{S}(\boldsymbol{m}-\boldsymbol{m}_0)\boldsymbol{u}_0$$

represents the contribution of the source current density. It is related to the transmitter position, frequency, and the anomalous conductivity distribution exaggerated by the primary field. A discretization of the primary field is represented by $\boldsymbol{u}_0$. Since the primary field usually depends on $\boldsymbol{r}_0$, the resulting right-hand side vectors change with different transmitter positions, or source field polarizations and have to be arranged as a block matrix consisting of linearly independent column vectors associated with the transmitter position.
Finally, the unknown secondary electric field $\boldsymbol{u}_s$ is obtained from the solution of the linear system

$$\boldsymbol{A}(\boldsymbol{m})\boldsymbol{u}_s = \boldsymbol{b}(\boldsymbol{m}), \tag{6}$$

where the system matrix $\boldsymbol{A}$ is complex-valued, large, sparse, and symmetric.
The projection of the discrete solution onto the data space is finally obtained by

$$\boldsymbol{d}(\boldsymbol{r}) = \boldsymbol{Q}(\boldsymbol{r})[\boldsymbol{u}_0+\boldsymbol{u}_s] = \boldsymbol{Q}(\boldsymbol{r})[\boldsymbol{u}_0+\boldsymbol{A}^{-1}\boldsymbol{b}]$$

with acting as a mapping or observation operator. Since the receiver points defined in the data space generally do not coincide with the grid lines of a FD grid defined in the solution space, a suitable interpolation scheme is necessary.
Moreover, if in addition to the electric field $\boldsymbol{E}$ the magnetic field $\boldsymbol{H}$ is required, then $\boldsymbol{Q}^H = \boldsymbol{Q}\boldsymbol{C}^E$ is the appropriate mapping operator yielding $\boldsymbol{d}^H = \boldsymbol{Q}^H[\boldsymbol{u}_0+\boldsymbol{u}_s]$.
For the solution of (6) we use the parallel direct solver package PARDISO (Schenk & Gärtner, 2004, 2006).

4 Mesh Refinement

It is well-known that numerical convergence can be achieved by several steps of grid refinement ultimately yielding a fine grid at which the numerical solution is close to the exact solution. In the FD case, a sequence of uniform grid refinement steps would quickly lead to systems of linear equations too large to be solved efficiently. A substantial improvement of the numerical solution can be obtained

by a grid refinement strategy where only a subset of the grid will be refined. To identify, which part of the grid has to be included in a mesh refinement step, a numerical measure of inaccuracy has to be defined. This measure shall be derived from an existing numerical solution obtained on a coarser grid. Therefore, we refer to this measure as *a-posteriori* error indicator. There exist strategies to quantify the residual between numerical and analytical solutions. This is, however, not feasible when no analytical solutions is available, which is the case for arbitrary 3-D conductivity structures. An alternative approach shall be derived in the following.
It is well-known that the magnetic field is divergence-free. However, when dealing with finite grids, we usually observe non-vanishing results for $\nabla \cdot \boldsymbol{B}$.
To assess how a coarse grid may influence deviations from the expected result, we evaluate the discrete divergence of the magnetic field and associate the quantity

$$d_{i,j,k} = \int\limits_{V_{i,j,k}} |\nabla \cdot \boldsymbol{B}|_{i,j,k} \, dV$$

with each cell (i, j, k). Note that by integrating over the whole cell volume $V_{i,j,k}$ more weight is put on large cells where a tendency towards larger deviations from the exact numerical solution might be expected *a-priori*.
With the help of the quantity d introduced above we define an *a-posteriori* error indicator:

Find all cells with indices (i, j, k) that satisfy the relation $d_{i,j,k} \geq c \cdot \max(d_{i,j,k})$, $0 < c \leq 1$.

All cells that meet this condition will be uniformly refined. The threshold parameter c controls what fraction of the cells shall be considered in the refinement step.

5 Numerical Examples

In this section, we carry out numerical experiments which demonstrate the accuracy of our numerical approach. Moreover, the efficiency of the error indicator is demonstrated. As a benchmark, we consider two models which are typical for MT and airborne EM applications.

5.1 The MT Example

We use the well-known COMMEMI model 3D-2 (cf. Figure 1a) for which secondary electric field responses have been calculated at a period of $T = 100$ s. A single polarization associated with a primary magnetic field of $H_x = 1$ A/m is considered. For this polarization, we expect galvanic effects at the conductivity jumps prependicular to the primary electric field. This expectation manifests itself in the observed discontinuities of the electric field component normal to those jumps. In Figure 1b the electric field component E_y normalized to the undisturbed 1-D response $E_y(y \to -\infty)$ at the outer model boundary is indicated. The observation operator $\boldsymbol{Q}^E(\boldsymbol{r})$ is defined in such a way that equidistant measurements can be produced from the numerical solution. Our results agree well with the reference data taken from Zhdanov et al. (1997). The computational results from 8 steps of grid refinement. Figure 2 shows horizontal sections of the first layer below the Earth's surface. Starting with the coarsest grid (Figure 2a) with 60 cells, the proposed grid refinement strategy yields a final grid with 91,728 cells (Figure 2b). We note, that our error indicator yields small cells in the vicinity of conductivity jumps. The observed asymmetry of the grid lines at the left and right boundaries of the conductive bodies in Figure 2b is due to numerical errors connected with the *ad-hoc* choice of the threshold parameter c.

5.2 The HEM Example

To further validate our code we have simulated an airborne EM survey crossing a conductive block embedded in a layered half-space (Siemon et al., 2009). A vertical section of the conductivity distribution

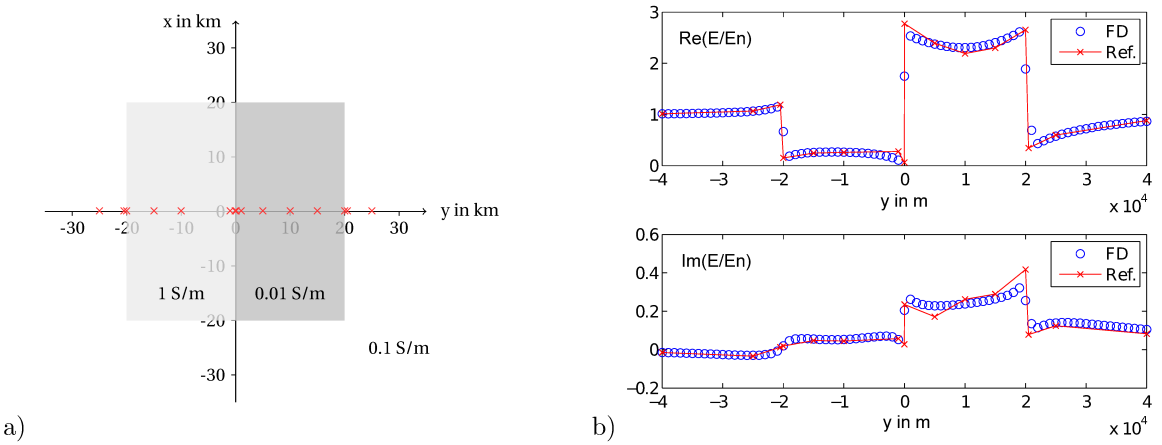

a) b)

Figure 1: Top view of the COMMEMI model 3D-2 (a), and normalized electric field response at a profile along the y-axis. Dots (o) indicate positions where measurements have been simulated, whereas asterisks (x) are related to positions where reference data was available.

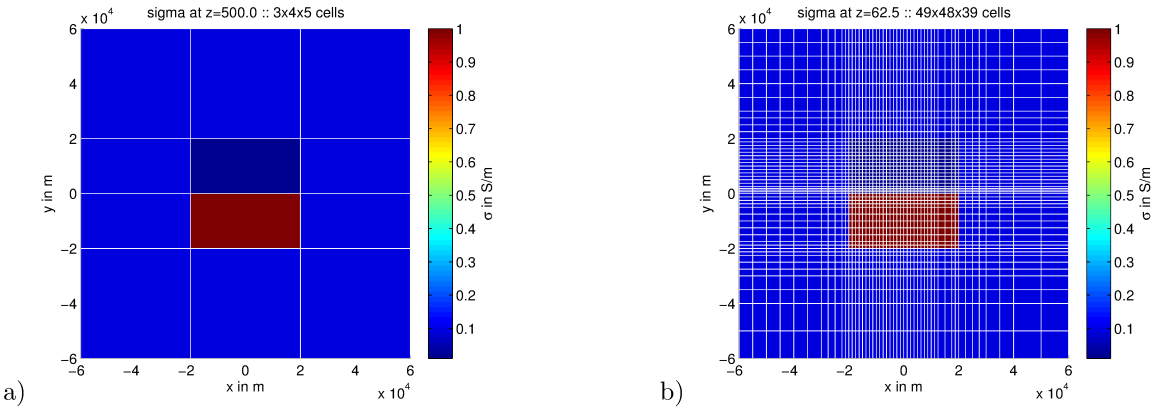

a) b)

Figure 2: Effect of the adaptive grid refinement strategy for the MT case. Shown are the first layer below Earth's surface for the initial grid (a), and the grid after 7 refinement steps (b). The horizontal section is located at the respective vertical midpoint of the first layer within the discretized Earth. Note that the vertical grid spacing is also affected by the mesh refinement strategy.

is displayed in Figure 3. Responses are calculated for five frequencies and 79 transmitter/receiver pairs. We define as response the quantities

$$R := \mathrm{Re}\left(\frac{H_z - H_z^0}{H_z^0}\right) \cdot 10^6 \qquad \text{and} \qquad Q := \mathrm{Im}\left(\frac{H_z - H_z^0}{H_z^0}\right) \cdot 10^6,$$

where R and Q are real and imaginary part of the measured magnetic field normalized to the free-space primary magnetic field

$$H_z^0 = -\frac{m}{4\pi r^3}.$$

In our case the distance between transmitter and receiver coils is $r = 8$ m. Responses are shown in Figure 4 for the lowest ($f = 387$ Hz), highest ($f = 133,200$ Hz), and one intermediate frequency ($f = 8,225$ Hz).

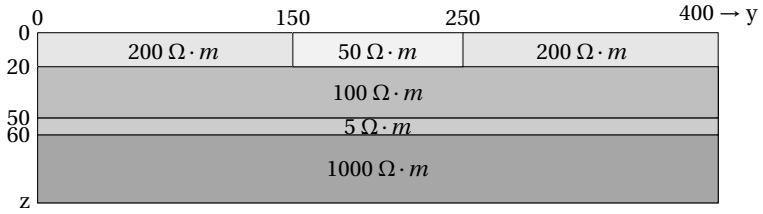

Figure 3: Vertical section across the model at $x = 0$. Axis labels are given in m. The block with $\rho = 50$ Ω·m has a lateral extent of ±200 m perpendicular to the y-z-plane.

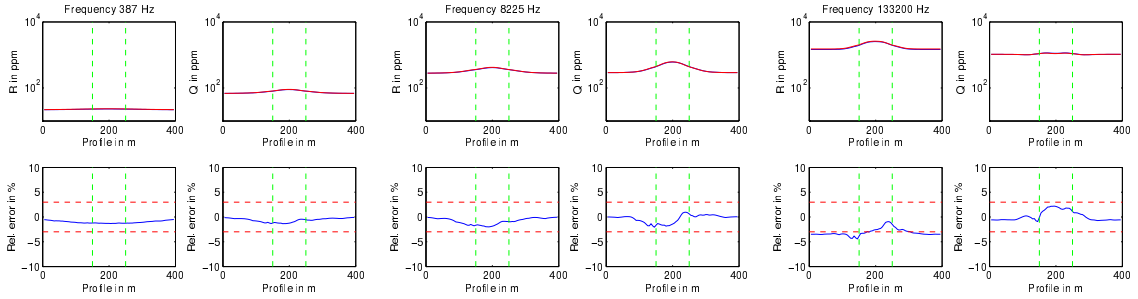

Figure 4: Real (R) and imaginary (Q) response in ppm obtained from our finite difference implementation (top row) for three frequencies $f = 387$ Hz (left), $f = 8,225$ Hz (middle), and $f = 133,200$ Hz (right), in comparison to the results of an integral equation code of Avdeev et al. (1998). Relative errors are indicated at the bottom row.

The calculated responses agree very well with results obtained by the integral equation code of (Avdeev et al., 1998). Compared with the reference data, relative errors are mostly less than ±5 %. The discrepancy at the highest frequency is due to a different primary field formulation.
In Figure 5 we illustrate the effectiveness of the proposed automatic grid refinement strategy for the airborne EM modelling. Similar to the MT case, cells are refined where lateral changes in conductivity occur. The initial coarse grid consists of 90 cells (Figure 5a). After 6 refinement steps, the final grid consists of 22,176 cells (Figure 5b). It is indicated by the thickness of the first layer within the conducting Earth, that the proposed refinemt strategy also affects the vertical grid.

6 Conclusion

We have presented an FD modelling code that is able to simulate magnetotelluric as well as dipole induction in a three-dimensional conductivity distribution. The accuracy of the numerical solution

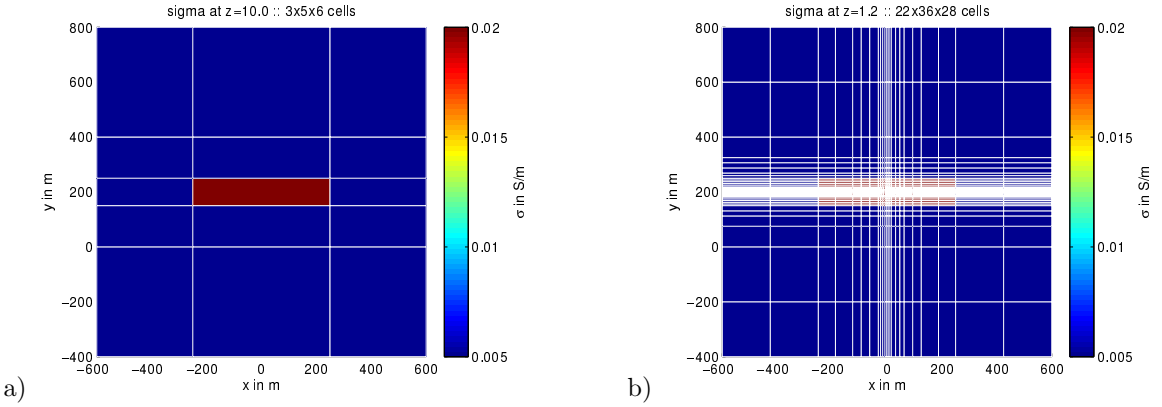

Figure 5: Effect of the adaptive grid refinement strategy. Shown are the initial grid (a), and the grid after 6 refinement steps (b). The horizontal section is located at the respective vertical midpoint of the first conducting layer within the discretized Earth. Note again, that the thickness of the first layer is also affected by the mesh refinement strategy.

has been improved by a mesh refinement strategy on the basis of an *a-posteriori* error indicator. More specifically, as error indicator the divergence of the magnetic field has been used. By successive refinement of the cells where the assumption of a divergence-free magnetic field is violated, the accuracy of the numerical solution has been improved. In addition, the total number of unknowns within the computational domain has been reduced in comparison with a uniform grid refinement technique.

References

Avdeev, D., Kuvshinov, A., Pankratov, O., & Newman, G. (1998). Three-dimensional frequency-domain modeling of airborne electromagnetic responses. *Exploration Geophysics*, *29*(2), 111–119.

Schenk, O., & Gärtner, K. (2004). Solving unsymmetric sparse systems of linear equations with pardiso. *Future Generation Computer Systems*, *20*(3), 475–487.

Schenk, O., & Gärtner, K. (2006). On fast factorization pivoting methods for sparse symmetric indefinite systems. *Electronic Transactions on Numerical Analysis*, *23*, 158–179.

Siemon, B., Auken, E., & Christiansen, A. (2009). Laterally constrained inversion of helicopter-borne frequency-domain electromagnetic data. *Journal of Applied Geophysics*, *67*(3), 259–268.

Zhdanov, M., Varentsov, I., Weaver, J., Golubev, N., & Krylov, V. (1997). Methods for modelling electromagnetic fields results from commemithe international project on the comparison of modelling methods for electromagnetic induction. *Journal of applied geophysics*, *37*(3), 133–271.

Electrical resistivity of the mantle at the South American subduction system in Northern Chile.

Dirk Brändlein[1,2], Oliver Ritter[1,2]

[1] *GFZ German Research Centre for Geosciences, Potsdam, Germany*

[2] *Freie Universität Berlin, Fachrichtung Geophysik, Berlin, Germany*

Introduction

In order to investigate the electrical resistivity of the upper mantle and mantle transition zone at the South American subduction system in North Chile we use data from the magnetotelluric (MT) network of the Integrated Plate Boundary Observatory Chile (IPOC). The IPOC is a permanent array of geophysical and geodetic multi parameter stations located in the Coastal Cordillera and Longitudinal Valley in Northern Chile. MT data is gathered at nine of the nineteen observation sites, with an average site spacing of approximately 50 km. The IPOC is operated since 2006 by the GFZ German Research Centre for Geosciences.

From long term observations of electromagnetic fields at two MT monitoring sites we compute MT transfer functions in the period range between 10 and 100,000 seconds. 2D forward modelling indicates that the apparent resistivities and phases at periods between 20,000 and 100,000 seconds are sensitive to the electrical conductivity structure of the upper to mid mantle. We present preliminary 2D inversion results which reveal a drastic decrease of electrical resistivity by two orders of magnitude between 100 and 250 km depth. Between 250 and 400 km depth the electrical resistivity decreases by another order of magnitude.

Data

The set-up of an IPOC MT monitoring site consists of a three component long period fluxgate magnetometer (GeoMagnet) and non-polarizing Ag/AgCl electrodes to measure all three components of the magnetic field and both horizontal components of the electric field. The monitoring sites (Figure 1) are connected via satellite link to the GFZ in Germany. The objective of the project is to monitor and analyse electromagnetic data to decipher possible temporary changes in the subsurface resistivity distribution, e.g. as a consequence of large scale fluid relocation.

Due to the extreme dry ground of the Atacama Desert continuous monitoring of the electric field is difficult. Contact resistances are on the order of MΩ and electrolyte is leaking. After a range of tests with various electrode installations we found a solution in December 2010. A plastic tube is buried vertically in the ground. At the bottom it is open and filled with a layer of bentonite where the electrode is pressed in. The space above is filled with water and serves as reservoir. The top is sealed with a lid.

We processed MT data of 150 subsequent days using the EMERALD processing package (Ritter et al. 1998). The resulting

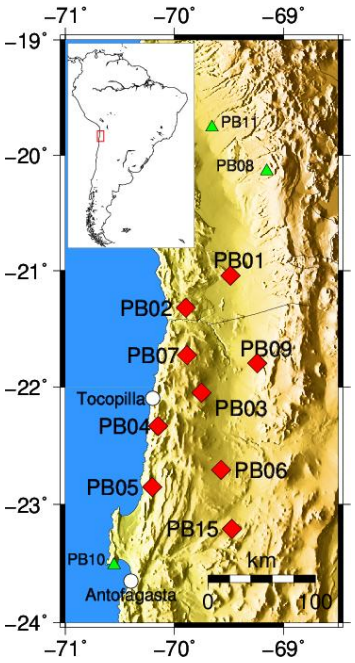

Figure 1: The IPOC-MT network in Northern Chile with sites PB01 to PB07, PB09 and PB15 (red symbols). The green symbols indicate locations of multi parameter sites without an MT component.

apparent resistivity and phase curves range from periods of 10 s to 100,000 s. We chose sites PB01 and PB09 for this study because the sites have relatively good data quality in both, the XY- and YX-components (Figure 2).

At both sites the YX component of apparent resistivity and phase exhibits smooth variation and small errors at periods longer than 10,000 s, at PB09 even 100,000 s are covered. In contrast, the XY component is usable only from approximately 20 to several thousand seconds.

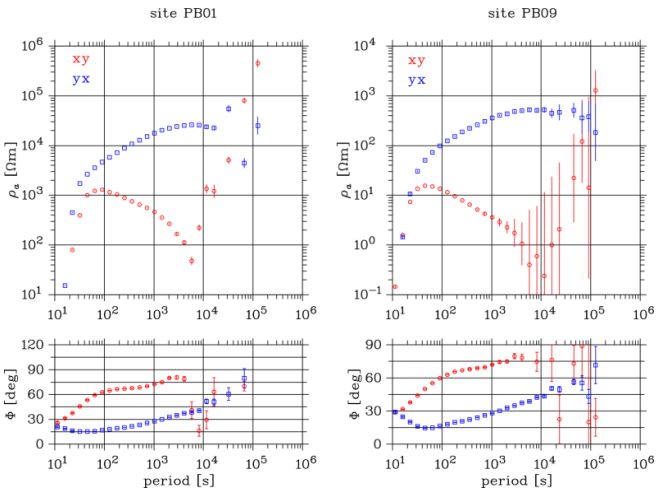

Figure 2: Apparent resistivities and phases for sites PB01 and PB09.

Depth resolution and directional dependency

To test the sensitivity of the MT data to certain depth ranges, we used 2D forward modelling using the software package WinGLink (Mackie et al. 1997). A 2D approach is necessary as the XY and YX components of apparent resistivity split up (Figure 2) in a way which is typical for the coast effect and which cannot be explained with 1D modelling.

We created an east-west orientated 2D background model including topography and ocean (not shown) and calculated the forward response at two synthetic sites which represent the minimum and maximum distance of the IPOC MT sites to the coast (A-150 and A-240 resembles sites PB01 and PB09, respectively). Background resistivity is set to 100 Ωm and the

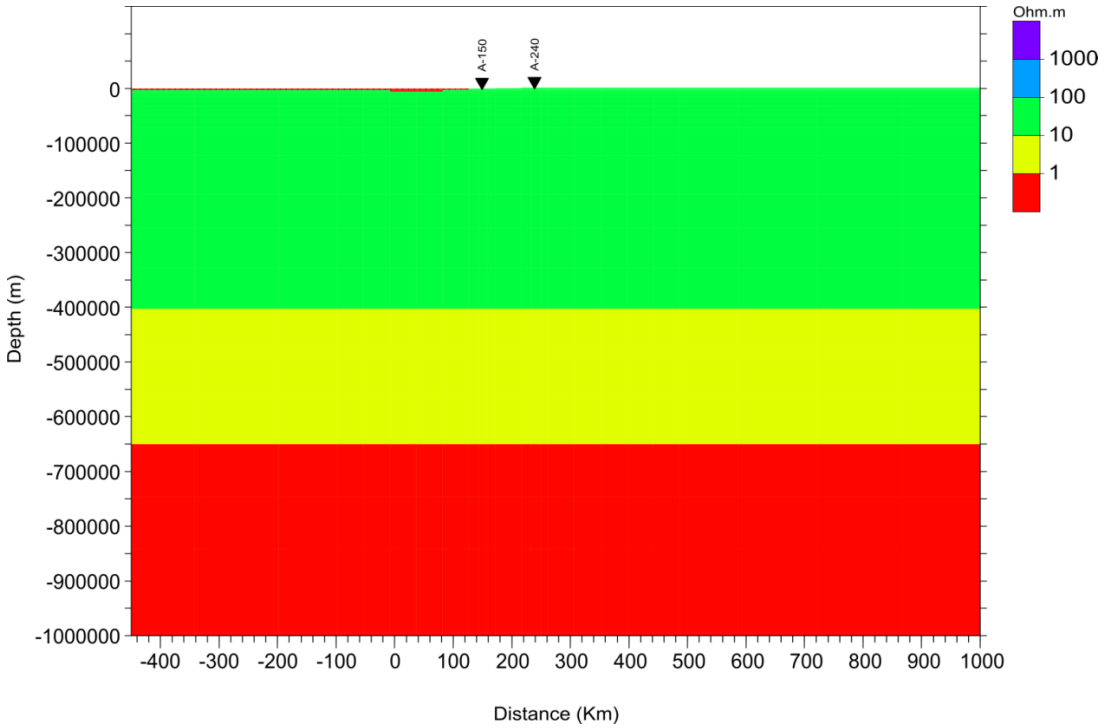

Figure 3: The 2 D forward model includes electrical resistivity structures which represent phase transitions in the mantle according to Utada et al. (2003). The distance to the coast of the two synthetic sites is similar to IPOC sites PB01 and PB09.

ocean to 0.3 Ωm. Figure 4 (upper panels) shows resulting apparent resistivity and phase curves which exhibit the expected split up between TE (XY component) and TM (YX component) modes. The split up is larger at the site closer to the coast.

In an alternative model we include two horizontal resistivity layers at 400 and 650 km depth with 10 and 1 Ωm, respectively (Figure 3). These discontinuities of electrical resistivity in the mantle were observed by Utada et al. (2003). These deep conductors are interpreted to reflect mineral phase transitions from olivine (α-phase) to wadsleyite (β-phase) and from material of the upper mantle to silicate perovskite or magnesiowüstite of the lower mantle, respectively. Comparing apparent resistivities and phases generated by the background model (Figure 4, upper panels) to those of the model including conducting layers at mantle depths (Figure 4, lower panels),

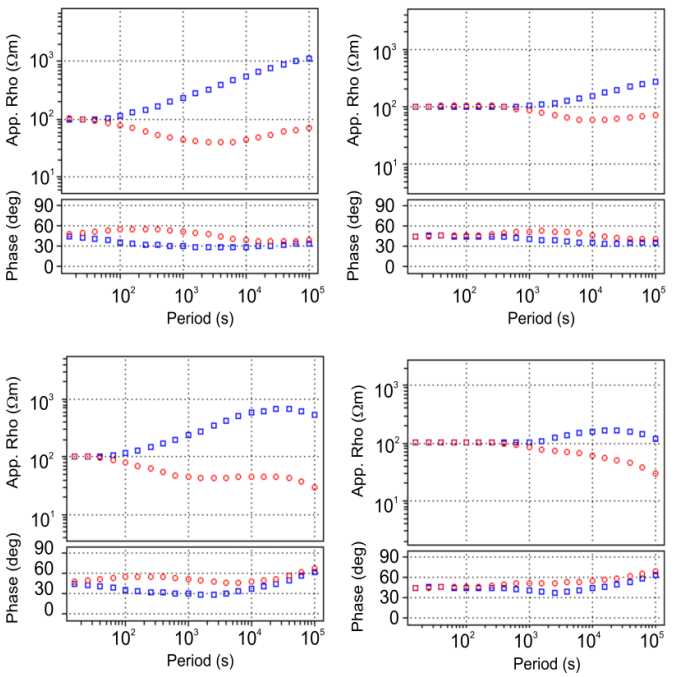

Figure 4: 2D forward model results for a simple 2D model featuring an conductive ocean in a homogeneous background (upper panels) and a model which includes two conductive layers in the mantel (lower panels). The left hand sides show results of site A-140 (PB01), the panels to the right show results of A-240 (PB09).

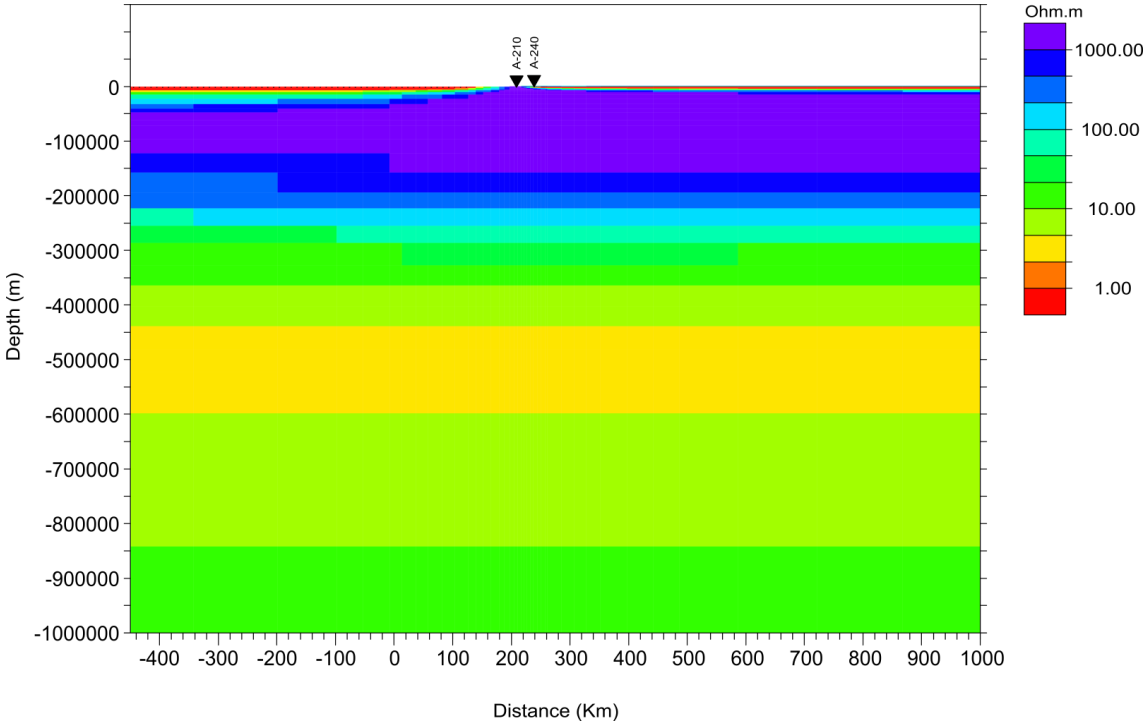

Figure 5: Preliminary result of inversion of apparent resistivity and phase of two sites. We inverted for TE and TM mode apparent resistivity and phase.

confirms that the influence of the deep structures (> 400 km) is observed at periods above 20,000 seconds and affects both, the TE and the TM mode.

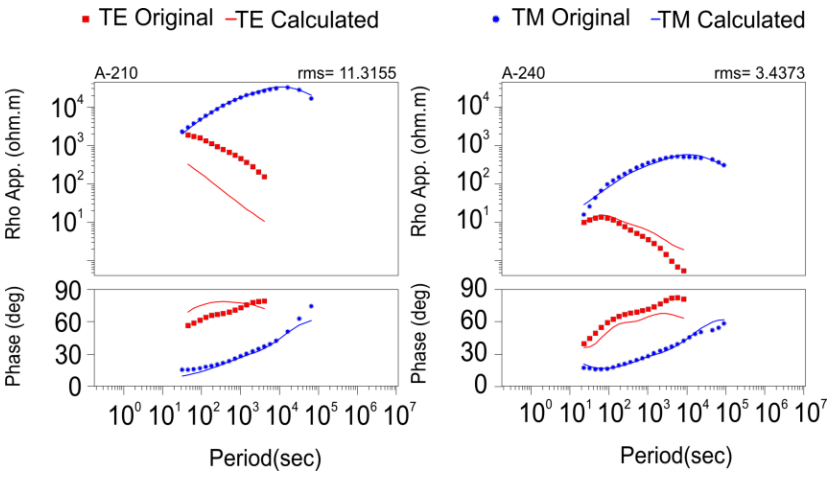

Figure 6: Data misfit of 2D inversion of sites PB01 and PB09, using a conductive ocean in a homogeneous background as starting model. The fit of the TM mode is better than the fit of the TE mode, which is noisy at long periods.

2D Inversion

To test if a phase transition zone in the mantle can be detected with the long term recordings of MT data in northern Chile we carry out a 2D inversion of apparent resistivities and phases for the IPOC sites PB01 and PB09. As a starting model we used a homogeneouse background with a conductive ocean. The distance of the sites to the coast is similar to PB01 (A-210) and PB09 (A-240). For the inversion we fixed the position and resistivity of the ocean. Unresolved TE mode data at longer periods are masked prior to the inversion. To attenuate the scattering of apparent resistivity and phase curves at the longest periods we smoothed the data.

Figure 5 shows the inversion result after inverting apparent resistivity and phase of TE and TM mode. The error floors were set to 10 % for apparent resistivity and 2% for phase data. After 200 iterations a RMS of 8.0 was achieved. The fit curves are plotted in figure 6. The high RMS is mainly caused by static shift of the TE mode of site PB01. We observe the largest gradient of decreasing apparent resistivity approximately between 100 and 250 km depth. From 250 to 400 km the gradient is smaller and from approximately 400 to 550 km the electrical resistivity shows nearly constant values of approximately 5 Ωm.

Discussion

Processing of 150 subsequent days of continuous MT data results in MT transfer functions with periods from 10 to 100,000 seconds. A strong split up between TE and TM modes is caused by the Pacific Ocean. The 2D forward modelling also indicates that the phase transition zone as suggested by Utada et al. (2003) is reflected in the MT transfer functions at periods between 20,000 to 100,000 seconds.

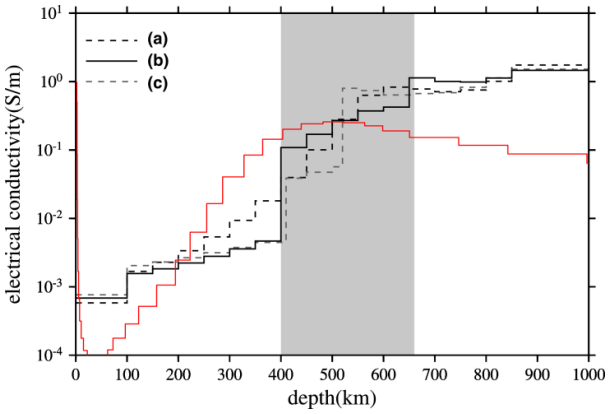

Figure 7: Conductivity values extracted from the 2D inversion model (Figure 5) derived as a vertical column between the two sites (red curve) compared to 1D inversions carried out by Utada et al. (2003) where (a) is unconstrained, (b) is constrained with contrasts at 400 and 660 km depths and (c) is also constrained with contrasts at 400, 550 and 650 km depths. Modified after Utada et al. (2003).

Preliminary 2D inversion results of apparent resistivities and phases of two IPOC monitoring sites are generally in agreement with the previous geophysical studies. The strong gradient of electrical

resistivity between 100 and 250 km depth could indicate the transition from the lithosphere of the down going Nazca plate to the asthenosphere (e.g. Giese et al., 1999). Between 400 and 550 km depth, which represents the upper part of the mantle transition zone, a nearly constant apparent resistivity of approximately 5 Ωm is observed. The semi-global reference model by Utada et al. (2003) shows a similar constant value of electrical conductivity in this depth range (Figure 7). In our inversion model, the minimum value of 4 Ωm is reached at 550 km depth.

References

-Giese, P., E. Scheuber, F. Schilling, M. Schmitz, and P. Wigger, Crustal thickening processes in the central Andes and the different natures of the Moho-discontinuity, J. S. Am. Earth Sci., 12, 201-220, 1999.

-Mackie, R., S. Rieven, and W. Rodi, Users manual and software documentation for two-dimensional inversion of magnetotelluric data, GSY-USA, Inc., San Francisco, Calif., 1997.

-Ritter, O., A. Junge, and G. J. K. Dawes, New equipment and processing for magnetotelluric remote reference observations, Geophys. J. Int., 132, 535– 548, 1998.

-Utada, H., T. Koyama, H. Shimizu, and A. D. Chave, A semi-global reference model for electrical conductivity in the mid-mantle beneath the north Pacific region, Geophys. Res. Lett., 30(4), 1194, doi:10.1029/2002GL016092, 2003.

Imaging of conductivity anomalies at Lazufre volcanic complex, Northern Chile, through 3-D inversion of magnetotelluric data

Ingmar Budach[1], Heinrich Brasse[1], Daniel Díaz[2]
[1]*Freie Universität Berlin, Fachrichtung Geophysik*
Malteserstr. 74-100, 12249 Berlin, Germany
[2]*Departamento de Geofísica, Universidad de Chile*
Blanco Encalada 2002, Santiago, Chile.

Abstract

Through an Interferometric Synthetic Aperture Radar (InSAR) survey, surface deformation was observed at Lazufre volcanic center in the Central Andes, Northern Chile / Northwestern Argentina. Uplift started there after 1998 and increased dramatically in the following time up to a rate of 3 cm/yr. Lazufre is now one of the largest deforming volcano systems on Earth, but the cause for uplift – likely influx of magmatic material into the crust – is still poorly understood.

In the beginning of 2010 a magnetotelluric survey was conducted to understand this process. Several LMT sites and two BBMT sites were set up on an EW trending profile crossing the volcanic center. Furthermore some LMT sites were arranged circularly around Lazufre complex and adjacent Lastarria volcano. Data were processed using an algorithm for robust and remote reference transfer function estimation. Electrical strike directions were estimated and induction arrows were derived. A 2-D resistivity model was then calculated. The most prominent feature of this model is a well conducting structure rising from the upper mantle to the shallow crust beneath the center of elevation. This can be interpreted as partial melts ascending from the asthenospheric wedge and feeding a potential magma reservoir beneath Lazufre volcanic center. A 3-D inversion model was then calculated which supports this feature. We assume that these rising melts are the source of the observed uplift at Lazufre complex.

1 Introduction

The evolution of volcanoes and the adjacent volcanic centers is of broad scientific interest. Recent insights into their spatio-temporal development are provided through images of Satellite Interferometric Synthetic Aperture Radar (InSAR). Pritchard and Simons (2002) created radar interferograms for about 900 of the approximately 1100 volcanic edifices in the Central Andes. Active deformation at four roughly axisymmetric volcanic centers was observed. In this work we focus on the area in the vicinity of the volcanoes Lastarria and Cordon del Azufre, which is often termed "Lazufre", an acronym of Lastarria and Azufre (Pritchard and Simons, 2002). This volcanic complex is situated in the Western Cordillera of the Central Andes, the location of the present magmatic arc, at approximately 25.1°S. The magmatic arc has developed due to subduction of the Nazca plate and has migrated 200 km eastwards since 120 Ma (Scheuber et al., 2006). Eruptions of caldera complexes resulted in immense Late Miocene to Pliocene ignimbrite deposits in the magmatic arc and the southern end of the Altiplano plateau (Allmendinger et al., 1997; de Silva, 1989).

Surprisingly the center of surface deformation at Lazufre is not associated with any known volcanic edifice, but lying between Lastarria and Cordon del Azufre. Both volcanic edifices are considered to be "potentially active". While no historical activity has been recorded

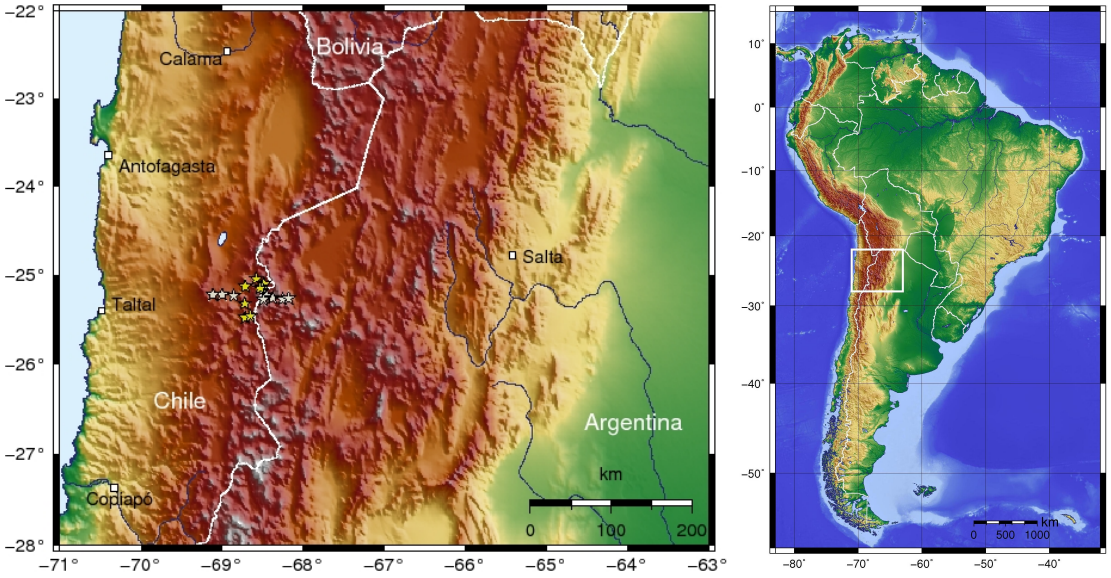

Figure 1:
Study zone and location of sites in the Central Andes, Northern Chile/Western Argentina. White stars indicate those sites which were used for 2-D modeling. Yellow stars indicate stations, which were arranged circularly around Lazufre volcanic complex.

at Cordon del Azufre, Lastarria shows persistent fumarolic activity (de Silva and Francis, 1991). The activity at Lastarria is thought to move to the north (Naranjo and Francis, 1987), although deformation has been observed to the south (Pritchard and Simons, 2004a). Surface elevation at Lazufre volcanic complex is time-depending. While no deformation was observed in the interferograms before 1998, there was a clear signal in three interferograms afterwards. Uplift at Lazufre increased drastically up to a rate of about 3 cm/yr and a spatial extent of 1800 km^2, with a long axis up to 50 km (Ruch et al., 2009). It is now one of the largest deforming volcano systems on earth, comparable in size with Yellowstone and Long Valley (both USA). Two possible scenarios explaining the inflation were hypothesized: It could either be a new intrusion of a sill expanding laterally at depth or a pre-existing magma chamber inflating at depth (Ruch et al., 2008).

2 Data evaluation and strike directions

During a field campaign in January/February 2010 a magnetotelluric experiment was conducted in the Central Andes of Northern Chile and Northwestern Argentina. As part of this experiment twelve long-period magnetotelluric (LMT) and two broadband magnetotelluric (BBMT) stations were arranged at the Lazufre volcanic complex. The other part of the experiment was centered around Lascar volcano farther north and is described in Díaz et al. (2012). Seven of the LMT stations and the two AMT stations were arranged along an approximately 100 km long EW trending profile at 25.1°S latitude, crossing the Western Cordillera with the present magmatic arc. The other stations were set circularly around the Lazufre volcanic complex (cf. figure 1). The LMT instruments cover a period range between T = 10s - 10000s and the BBMT a period range between T = 0.005s - 1000s, respectively. Since we faced serious logistic problems in the beginning of our field campaign, not as many stations as planned could be installed. Hence there is a lack in station coverage, especially in the eastern part of the measuring area.

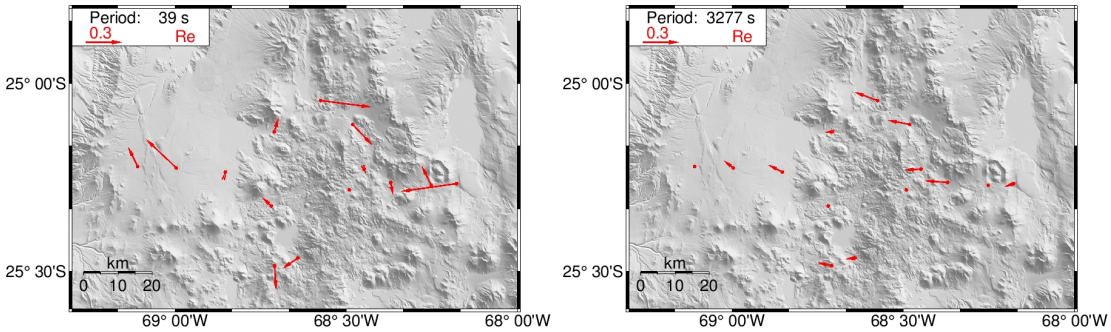

Figure 2: Map of the Lazufre volcanic complex imaging induction arrows calculated from the ratio of vertical to horizontal magnetic fields. The chaotic behavior for short periods (39s, left) is due to well-conducting salars at the surface. For long periods (3277s, right) induction vectors indicate a good conductor west of the profile. Note that red dots indicate stations where bad data was excluded.

Remote reference and robust techniques were used for data processing (Egbert and Booker, 1986). Electrical strike directions were calculated using the algorithm of Smith (1995), resulting in ambiguous directions for different periods. However, for the complete period range an electrical strike direction of approximately N30°E was estimated (Budach, 2011).

Induction arrows were calculated from the ratio of vertical to horizontal magnetic fields and were plotted according to the convention of Wiese (1962), i.e. the real parts of the induction vectors point away from well conducting structures in a 2-D setting (cf. figure 2). Similar to the strike directions after Smith (1995), they show an ambiguous behavior for short periods. They are aligned towards a northwest direction for intermediate periods and show influences of coastal effects for periods near 10000s. The chaotic behavior at short periods is probably caused by the presence of numerous salars in that region, internally drained basins filled with highly conductive brines (see section below).

3 Two-dimensional Model and Interpretation

A 2-D model was calculated employing the non-linear conjugate gradient algorithm of Rodi and Mackie (2001). All components (TE mode, TM mode and tipper) were used for the inversion, with a focus on smooth inversion employing a regularization factor of $\tau = 10$. Error floors were set to 20% for apparent resistivities and 5% for phases, in order to avoid static shift problems by assigning a higher weight to phases. A starting model was used with a homogenous half-space, the Pacific Ocean and the subducting Nazca plate (using contours for the subducting slab after Cahill and Isacks (1992)). The values for resistivities were set for the half-space 100 Ωm, for the ocean 0.3 Ωm and for the dipping Nazca-Plate 1000 Ωm. The inversion was performed with 200 iterations without weighting for static shift and 50 additional iterations with weighting for static shift enabled. The best fitting model achieved an RMS of 2.18 (Budach, 2011).

A highly resistive block is resolved beneath sites l08 and l04 at the western margin of the profile (marked as A in figure 3). This can be interpreted as a Late Cretaceous plutonic intrusion, which has also been observed at the southern part of the Salar de Atacama basin (Díaz, 2011; Díaz et al., 2012) and SW of the Salar de Atacama (Oncken et al., 2006).

In the center of the profile several well conducting structures (marked as B and associated arrows in figure 3) are observed. They are resolved at the surface down to shallow depths and show resistivities of a few Ωm. In the investigation area, as well as in other parts of the

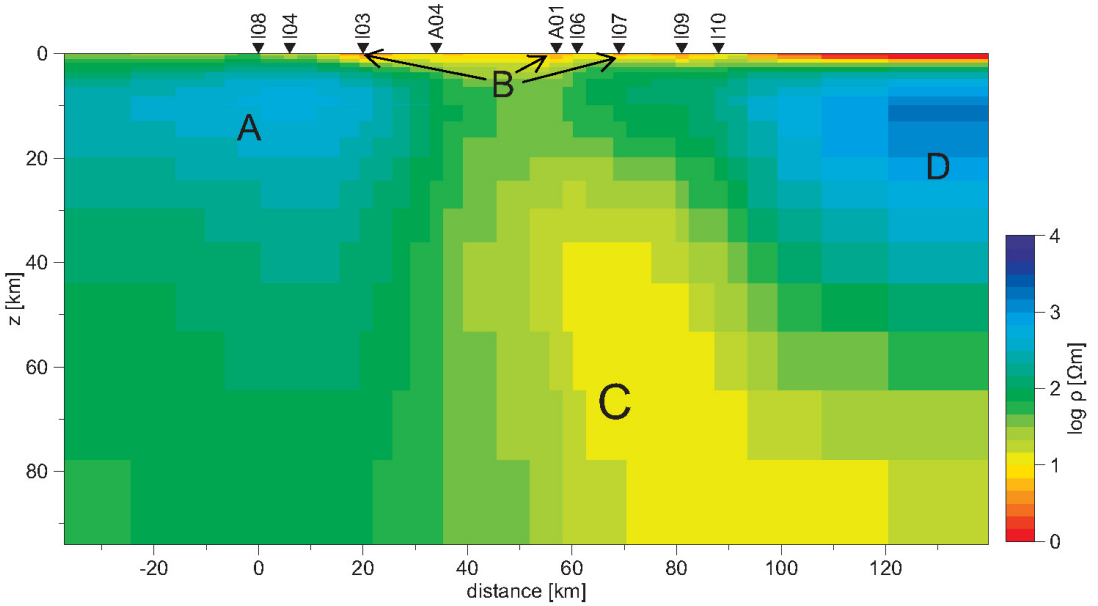

Figure 3:
2-D model of the Lazufre volcanic complex. The most prominent feature is a well conducting structure ascending the upper mantle. RMS for this model is 2.18.

Central Andes, numerous salars (salt pans) are found (Allmendinger et al., 1997). These are internally drained basins filled with evaporites and highly conductive brines, which can reach thicknesses of several hundred meters. Assuming them to be humid would explain the high conductivity of these structures.

The most striking and most important feature of this study is a well conducting structure marked as C in figure 3. It rises from the upper mantle towards the shallow crust and is showing a resistivity of around 10 Ωm with increasing resistivity towards the crust (some tens of Ωm). Note that an average depth to Moho of about 70 km is determined for this region (Wölbern et al, 2009). This feature appears in all tested models, with slightly different shapes. However, the rise from the upper mantle and the pathway towards shallow depths were observed in each model.

Taking these arguments into account we assume this structure to be an image of partial melts rising from the upper mantle and feeding an intracrustal magma reservoir. These rising melts are likely to be the source of surface deformation at Lazufre.

Another highly resistive feature was resolved east of the profile at midcrustal depths with a resistivity of approximately 1000 Ωm (marked as D in figure 3). Interpretation of this structure is somewhat doubtful, since it is lying outside the profile and, generally, model fit is worse at the eastern part of the profile.

4 Three-dimensional modeling of Lazufre data

In a second step, a 3-D inversion was performed applying the 3-D inversion code of Siripunvaraporn et al. (2005). This program is an extension of the 2-D data space Occam's inversion (Siripunvaraporn and Egbert, 2000) and inverts the eight components of the impedance tensor. In order to reduce computational time, the algorithm uses the data space method, where all computations depend on the size of data N, not the size of model parameters M. Since

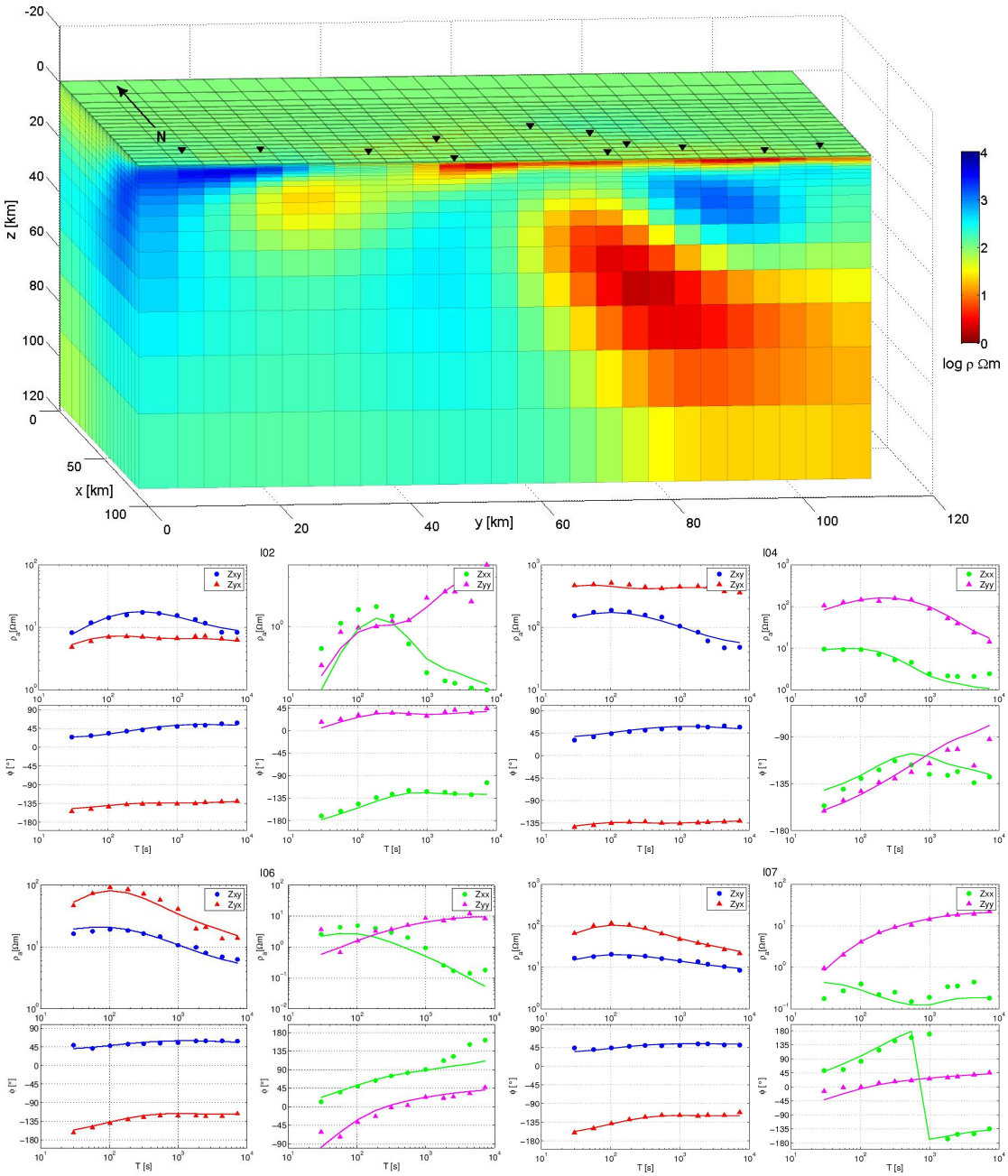

Figure 4:
3-D model of Lazufre volcanic complex showing the same prominent features like the 2-D model. RMS for this model is 1.449. Below the 3-D inversion result, the comparison between measured (dots) and modeled data (continuous lines) at four sites is shown. Minor diagonals are drawn in red and blue, major diagonals in green and purple. Site l04 is in the Precordillera in the western part of the profile, l02 in the center of the profile and l06 and l07 are in the eastern part of the profile in Argentina.

the general case for MT data is N << M, the computational efficiency can be increased significantly and thus makes it practical to be used on standard PCs.

A subset of data was chosen, eliminating data points of poor quality and selecting 4 periods per decade. Hence the size of the data N is limited to a reasonable value and therefor memory size and computational time.

The model was discretized into 49 cells in N-S and E-W direction, spanning an area of 3200 km in each direction, and 31 cells in z-direction up to a depth of 560 km. The cell size in the center of the grid was set to 4 x 4 km. A homogeneous 100 Ωm half-space and the Pacific Ocean with crude bathymetry and 0.3 Ωm resistivity was used as a starting model. Error tolerance levels were set to the double of the default value. After 9 iterations a best fitting model with an RMS of 1.449 was achieved (cf. figure 4 for inversion result and corresponding data fit plots).

Through the 3-D inversion similar results as discussed in the section above are achieved. Particularly the well conducting structure beneath the center of the profile is imaged, showing a similar shape and a slightly higher conductivity as for the 2-D model. Note that in the 3-D case, this well conducting structure appears to rise from a southwestern direction towards the center of profile. The well conducting structure at the western margin of the profile at shallow depth is in disagreement with the result of the 2-D inversion and is not yet constrained.

5 Conclusions

2-D and 3-D inversion of long-period and broadband magnetotelluric data image a well conducting anomaly beneath the Lazufre volcanic complex. It ascends from the upper mantle towards the shallow crust and has minor resistivities of a few Ωm till some tens of Ωm. This structure is imaged in all tested models, in 2-D as well as in 3-D inversions. The orientation of induction vectors supports this feature.

The spatial extent of this feature is in good agreement with surface deformation detected at the Lazufre volcanic complex (Pritchard and Simons, 2002, 2004a,b; Ruch et al., 2008, 2009; Ruch and Walter, 2010). Therefore we suggest that a major cause of uplift at Lazufre is due to partial melts ascending from depth and feeding an intracrustal magma reservoir.

It would be of interest in a future campaign to conduct more measurements towards the east in order to account for the eastern extension of the good conductor beneath Lazufre.

6 Acknowledgments

We are grateful towards H. Wilke and G. Chong (Universidad Católica del Norte, Antofagasta) for their help in logistical issues. Thanks to Dana Weichelt, Faustino Ticona and the Chilean students who helped us during the field campaign in 2010. The 3-D inversion code was provided by Siripunvaraporn. Most of the plots were prepared using the GMT package of Wessel and Smith (1998). This work has been funded by German Research Foundation (DFG).

References

Allmendinger, R.W., Jordan, T.E., Kay, S.M., Isacks, B.L., 1997. The evolution of the AltiplanoPuna plateau of the Central Andes, Ann. Rev. Earth Planet. Sci. 25, 139174.

Budach, I., 2011. Preliminary 2D inversion of the Lazufre volcanic area in the Central Andes, Northern Chile, B.Sc. thesis, Fachrichtung Geophysik, FU Berlin.

Cahill, T., Isacks, B., 1992. Seismicity and Shape of the Subducted Nazca Plate. J. Geophys. Res., 97 (B12), 1750317529. doi:10.1029/92JB00493.

de Silva, S.L., 1989. AltiplanoPuna volcanic complex of the Central Andes, Geology 17, 11021106.

de Silva, S.L., Francis, P.W., 1991. Volcanoes of the Central Andes, Springer-Verlag, New York.

Díaz, D., 2011. Magnetotelluric study of the Western Cordillera (Northern Chile), with a focus on Lascar volcano, Ph.D. thesis, FU Berlin

Díaz, D., Brasse, H., Ticona, F., 2011. Conductivity distribution beneath Lascar volcano (Northern Chile) and the Puna, inferred from magnetotelluric data. J. Volc. Geotherm. Res. 217218. doi:10.1016/j.jvolgeores.2011.12.007

Egbert, G.D., Booker, J.R., 1986. Robust estimation of geomagnetic transfer functions. Geophys. J. R. astr. Soc. 87, 173-194.

Mackie, R.L., Smith, J.T., Madden, T.R., 1994. Three-dimensional electromagnetic modeling using unite difference equations: The magnetotelluric example, Radio Sci. 29, 923-935.

Naranjo, J.A., Francis, O., 1987. High velocity debris avalanche at Lastarria volcano in the north Chilean Andes. Bull. Volc. 49, 509-514.

Oncken, O., Hindle, D., Kley, J., Elger, K., Victor, P., Schemmann, K., 2006. Deformation of the Central Andean Upper Plate System - Facts, Fiction, and Constraints for Plateau Models. In: O. Oncken et al. (Editors), The Andes: Active Subduction Orogeny, Frontiers in Earth Sciences, Springer, Berlin, 3-27.

Pritchard, M.E., Simons, M., 2002. A satellite geodetic survey of large-scale deformation of volcanic centers in the Central Andes, Nature, 418, doi:10.1038/nature00872.

Pritchard, M.E., Simons, M., 2004. An InSAR-based survey of volcanic deformation in the southern Andes. G3 5 (2), 142., doi:10.1029/2003GC000610

Pritchard, M.E., Simons, M., 2004b. Surveying Volcanic Arcs with Satellite Radar Interferometry: The Central Andes, Kamchatka and Beyond. GSA Today 14 (8), doi:10.1130/1052-5173(2004)014<4:SVAWSR>2.0.CO;2

Rodi, W., Mackie, R.L., 2001. Nonlinear conjugate gradients algorithm for 2-D magnetotelluric inversions, Geophysics 66, 174-187.

Ruch, J., Anderssohn, J., Walter, T.R., Motagh, M., 2008. Caldera-Scale inflation of the Lazufre volcanic area, South America: Evidence from InSAR. J. Volc. Geotherm. Res, 174, doi:10.1016/j.jvolgeores.2008.03.009

Ruch, J., Manconi, A., Zeni, G., Solaro, G., Pepe, A., Shirzaei, M., 2009. Stress transfer in the Lazufre volcanic area, central Andes, Geophys. Res. Lett. 36, doi:10.1029/2009GL041276

Ruch, J., Walter, T.R., 2010. Relationship between the InSAR-measured uplift, the structural framework, and the present-day stress field at Lazufre volcanic area, central Andes, Tectonophysics 492, doi:10.1016/j.tecto.2010.06.003

Scheuber, E., Mertmann, D., Harald, E., Silva-Gonzalez, P., Heubeck, C., Reutter, K.J., Jacobshagen, V., 2006. Exhumation and basin development related to formation of the central Andean plateau, 21°S. In: O. Oncken et al. (Editors), The Andes: Active Subduction Orogeny, Frontiers in Earth Sciences, Springer, Berlin, 285-301.

Siripunvaraporn, W., Egbert, G., 2000. An efficient data-subspace inversion method for 2-D magnetotelluric data. Geophysics 65, 791-803.

Siripunvaraporn, W., Egbert, G., Lenbury, Y., Uyeshima, M., 2005. Three-dimensional magnetotelluric inversion: data-space method. Phys. Earth Planet. Inter. 150, 3-14.

Smith, J.T., 1995. Understanding telluric distortion matrices. Geophys. J. Int., 122, 219-226.

Wessel, P., Smith, W.H.F., 1998. New, improved version of the generic mapping tools released. EOS Trans. AGU, 79, 579.

Wiese, H., 1962. Geomagnetische Tiefentellurik Teil II: die Streichrichtung der Untergrundstrukturen des elektrischen Widerstandes, erschlossen aus geomagnetischen Variationen. Pure App. Geophys., 52, 83-103.

Wölbern, I., Heit, B., Yuan, X., Asch, G., Kind, R., Tawackoli, S., Wilke, H., 2009. Receiver function images from the Moho and the slab beneath the Altiplano and Puna plateaus in the Central Andes, Geophys. J. Int., 177, 296-308.

Vorbereitende Untersuchungen für eine fliegende unbemannte VLF-Messung

Rudolf Eröss[1], Bülent Tezkan[1], Rainer Bergers[1],
Johannes B. Stoll[2]

[1]Universität zu Köln
[2]Mobile Geophysical Technologies - Celle

Zusammenfassung

Ziel dieser Arbeit ist es VLF/LF-Messungen mit einem unbemannten Flugsystem (Unmanned Aerial System (UAS)) durchzuführen. Hierfür müssen sowohl Modifikationen an Sensor und Logger als auch eine entsprechende Aufhängung für den Hubschrauber entwickelt werden. Der Super High Frequency Tripple (SHFT)-Sensor wurde 2008 von Metronix vorgestellt. Er kann elektromagnetische Felder von VLF/LF- und Radiosendern in einem Frequenzbereich von 10kHz bis 250kHz erfassen, wodurch eine feine Tiefenauflösung erreicht wird. Der ADU-07 Logger wird ebenfalls von Metronix bereit gestellt. Der SHFT-Sensor fand bereits Verwendung in einem von *Pedersen und Dynesius* (2008) durchgeführten schwedischen, aerogeophysikalischen Forschungsprojekt.
Es wird die effektive und flächenhafte Untersuchung von Leitfähigkeitsanomalien angestrebt. Hierfür muss das entsprechende Prozessing entwickelt werden.
Bisher wurden verschiedene bodengebundene Messungen durchgeführt, um eine geeignete Messlokation für die UAS/VLF- Messungen zu finden. Außerdem wurden Tests gemacht, bei denen der Sensor kontrolliert rotiert wurde, um herauszufinden welchen Einfluss Drehungen des Sensors auf die magnetische Übertragungsfunktion haben. Des weiteren wurden verschiedene Tests durchgeführt, um den Einfluss des Hubschraubers auf das Messgerät und den Datenlogger zu ermitteln.

1 Einleitung

In einem Pilotprojekt 2009/2010, welches von der Deutschen Forschungsgemeinschaft gefördert wurde, wurden zum ersten Mal mit einem Unmanned Aerial System (UAS) aeromagnetische Messungen durchgeführt (Abb.1). Hierbei wurden die Anwendungsmöglichkeiten und die Messgenauigkeit untersucht (Abb.2) (*Tezkan et al.*, 2011).

Abbildung 1: UAS - Magnetfeldmessungen bei Köln

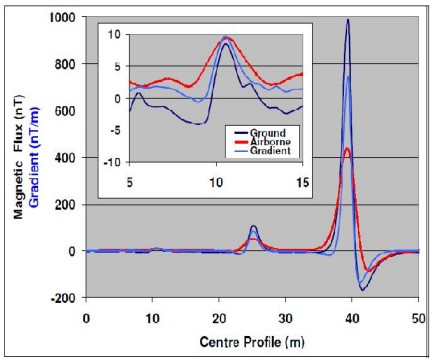

Abbildung 2: Totalfeldmessung - Boden und UAS-Magnetik Daten.

Es wurden verschiedene, vergrabene, künstliche Anomalien sowohl am Boden als auch mit dem UAS vermessen. Alle eingegrabenen Störkörper konnten mit UAS-Magnetik detektiert werden (Abb.2).

Ein UAS kann aufgrund seiner computerkontrollierten Steuerung präzise navigieren und daher auch Messungen bei geringer Flughöhe durchführen. Es kann schweben oder Messlokationen mit langsamer Geschwindigkeit überfliegen.

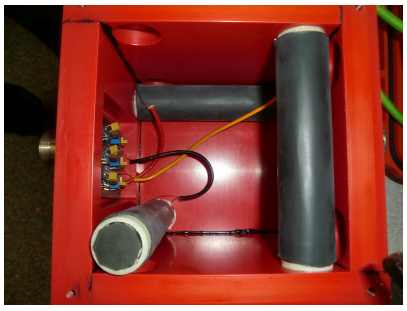

Abbildung 3: SHFT-Sensor der Firma Metronix

Abbildung 4: ADU-07 Logger der Firma Metronix

Nach der erfolgreichen UAS-Magnetik Messung ist in einem vom Bundesministerium für Bildung und Forschung geförderten Projekt geplant, VLF/LF-Messungen mit einem UAS durchzuführen. Dazu soll auf dem UAS ein Induktionsspulentriple (Abb.3) und ein Datenlogger (Abb.4) der Firma Metronix integriert werden. Mit diesen lassen sich die elektromagnetischen Felder von Sendern im Frequenzbereich von 10 kHz bis 250 kHz messen. Durch die große Anzahl der zur Verfügung stehenden Sender, welche ein breites Frequenzband abdecken, wird eine feine Tiefenauflösung erreicht.

Ziel der UAS-gestützten Messungen ist die Entwicklung einer neuen Messplattform für die VLF-Messungen bzw. neuer Inversionsalgorithmen für effiziente, flächenhafte Leitfähigkeitsuntersuchungen.

2 Noisemessungen

Abbildung 5: Aufbau des Hubschraubers bei der Noisemessung in Luzern ohne Logger und Sensor.

Für die UAS/VLF-Messungen muss eine neue Aufhängung entwickelt werden. Hierfür ist es notwendig zu wissen welchen Einfluss der Hubschrauber auf die Messgeräte hat. Um diesen Einfluss zu untersuchen, wurde daher ein Experiment durchgeführt, bei welchem für verschiedene Abstände (0, 0.85, 1, 1.5, 2, 2.5 ... 6 m) des Logges bzw. des Sensors vom Hubschrauber Zeitreihen aufgenommen wurden (Abb. 5). Dabei war der Motor ständig in Betrieb. Hier wird aus Platzgründen nur der Einfluss auf den Sensor dargestellt, der Logger stand bei dieser Messung in 10 m Entfernung, um eine Beeinflussung durch den Hubschrauber zu vermeiden.

In (Abb. 6) ist der Noise in dB gegen die Entfernung des Sensors zum Hubschrauber für drei VLF-Nutzfrequenzen bezogen auf eine Nullmessung in 6 m Entferung vom Hubschrauber dargestellt. Je nach Frequenz wird dabei der rauschfreie Bereich in einer unterschiedlichen Entfernung erreicht. Dies hängt mit der Amplitude der jeweiligen Sender zusammen, in den hier nicht gezeigten Frequenzspektren sieht man deutlich ob der Noiselevel über der Amplitude der jeweiligen Frequenzen liegt. Da wo der 23,4 kHz Sender schon bei 2 m über dem Noiselevel ist, sind die 18,3 kHz und 37,5 kHz Sender noch verrauscht. Den Bereich in dem der Noise des Hubschraubers keinen messbaren Einfluss mehr hat erreichen diese erst ab ca. 3 m. Für die Konstruktion der Aufhängung ist jedoch zu beachten, dass die hier gezeigte Messung seitlich vom Hubschrauber stattfand (Abb. 6). Während des Fluges wird der Sensor natürlich unterhalb des Hubschraubers hängen, was evtl. dazu führt, dass der Noise mit einer anderen Rate abnimmt als seitlich des Hubschraubers. Bei der Konstruktion der Aufhängung ergibt sich hieraus ein Mindestabstand von sensor zu Hubschrauber von 3-4 m.
Für den Logger haben die Untersuchungen einen Mindestabstand von 2 m ergeben.

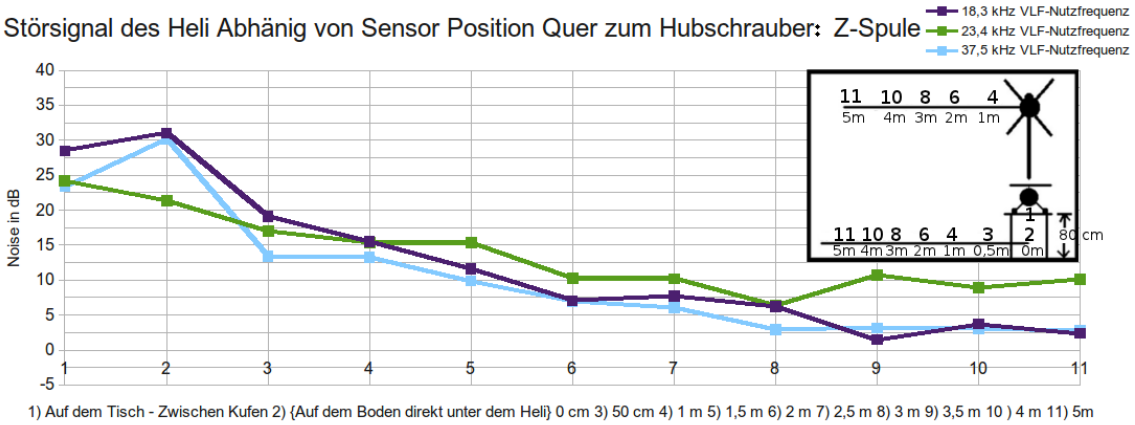

Abbildung 6: Aufgetragen ist die Überlagerung des VLF-Signals mit dem Noise des Hubschraubers (Motor an) in dB, gegen den Abstand des SHFT-Sensors für verschiedene VLF-Frequenzen, bezogen auf eine Nullmessung in 6 m Entferung vom Hubschrauber.

3 Drehexperiment mit dem SHFT Sensor

Das UAS wird nicht in der Lage sein, den Sensor vollkommen rotationsfrei entlang eines Profils zu bewegen. Vielmehr wird der Sensor voraussichtlich Pendelbewegungen entlang der x-Achse (schwarzer Pfeil Abb.7) und y-Achse (zeigt in die Blattebene hinein) und Drehbewegungen um die z-Achse (orangener Pfeil in Abb.7) ausführen. Um diese zu untersuchen, wurde der Sensor mit einem Gestell (Abb.8)

zunächst von -90 bis +90 Grad kontrolliert rotiert. Die Auswirkungen solcher Bewegungen auf die Daten ist in Abbildung 7 zu sehen: rot/blau bei Rotation um die y-Achse, grün/rosa für geringfügige Drehung um z-Achse und anschließender Rotation um die y-Achse.

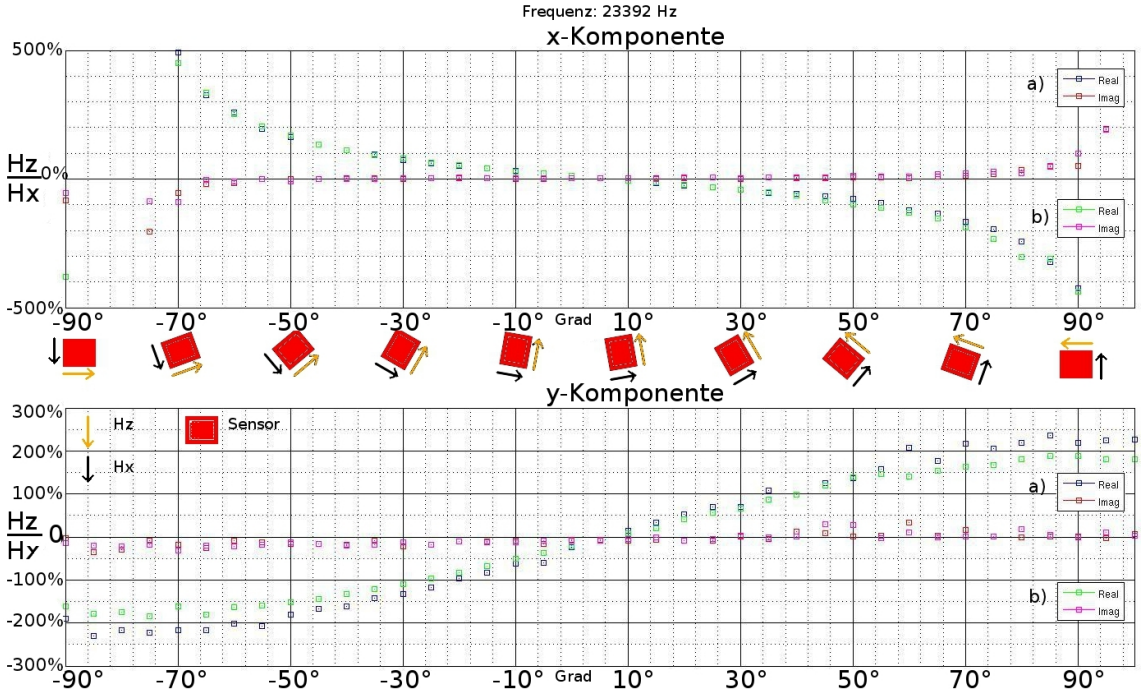

Abbildung 7: Übertragungsfunktion als Funktion der Sensordrehungen um die y-Achse (pitch angle) -90 bis +90 Grad. Dabei zeigt a) Realteil (blau) und Imaginärteil (rot) die Übertragungsfunktion vor der Rotation um die z-Achse (yaw angle) und b) Realteil (grün) und Imaginärteil (rosa) die Übertragungsfunktion nach der Rotation um die z-Achse (yaw angle) um 8 Grad.

Abbildung 8: Gestell zum kontrollierten drehen des Sensors

Man erkennt, dass bereits kleine Drehungen um die y-Achse (pitch angle), erheblichen Einfluss auf die Übertragungsfunktion des Realteils haben. Daher sollte die Gyration des Sensors während des Fluges gemessen werden, um Sensordrehungen nicht fälschlicherweise als Anomalie zu deuten. Es ist zu prüfen ob es auch möglich ist Drehungen aus der Übertragungsfunktion herauszurechnen und so Anomalien leichter zu identifizieren.

4 Verhalten der magnetischen Übertragungsfunktion für verschiedene Flughöhen

Um eine geeignete Flughöhe für das UAS zu ermitteln, wurden Modellierungen für den Realteil (Abb.9) und den Imaginärteil (Abb.10) der magnetischen Übertragungsfunktion durchgeführt. Dabei wurde untersucht, wie die Amplitude von verschiedenen Anomalien mit steigender Flughöhe (und damit größer werdenden Luftschicht) abnimmt.

In dem Modell werden vier lange Anomalien, mit einem Querschnitt von 1x1 Meter, bei Profilmeter 20, 80, 120 und 150 in 5 m Tiefe betrachtet. Sie haben einen spezifischen Widerstand von 1 Ω m, 10 Ω m, 100 Ω m bzw. 1000 Ω m und sind in einen 200 Ω m Halbraum eingebettet. Die Luftschicht wird mit 1 000 000 Ω m modelliert. Die Modellrechnungen wurden mit dem Programm MT3D erstellt (Alain Tabbagh, Marcus Gurk, personal communication, 2011).

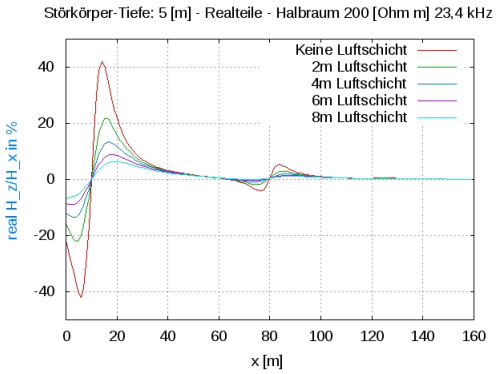

Abbildung 9: Realteil der magnetischen Übertragungsfunktion für verschiedene Flughöhen.

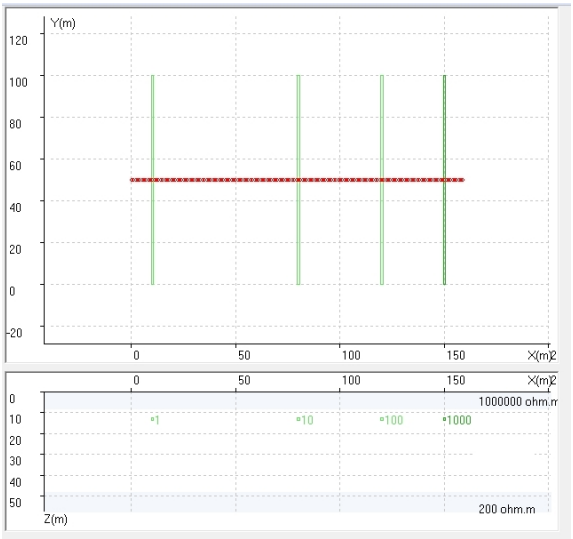

Abbildung 10: Exemplarisches Modell für eine der berechneten Flughöhen. Hier für die 8 m mächtige Luftschicht.

Fliegt der Sensor auf einer Höhe von 2 m, verringert sich die Amplitude der magnetischen Übertragungsfunktion für die stärkste Anomalie (1 Ω m) gegnüber der Messung an der Erdoberfläche um 50 %. Die Anomalie ist jedoch weiterhin klar zu erkennen. Auch für größere Flughöhen (4 m bis 8 m) ist die stärkste Anomalie (1 Ω m) noch klar in der Übertragungsfunktion zu sehen. Bei weniger starken Anomalien (z.B. 10 Ω m) d.h. weniger starkem Kontrast von Anomalie zu Halbraum, ist die Amplitude der Übertragungsfunktion schon bei einer Flughöhe von 2 m unter 5 % und damit unter dem voraussichtlichen Rauschniveau.
Mit diesem Ergebnis erwarten wir, dass wir mit dem VLF/UAS für eine Flughöhe von ca. 5m Anomalien detektieren können, welche einen Kontrast zur umgebenden Halbraum in der Größenordnung von etwa 1 zu 100 haben.

5 Suche nach geeigneten Messlokationen für UAS/VLF Messungen bei Cuxhaven

Um eine geeignete Messlokation für die UAS-VLF-Messung zu finden, wurden bisher verschiedene bodengebundene RMT- und VLF/LF-Messungen bei Cuxhaven und im Harz durchgeführt. Diese Lokationen wurden anhand einer Hubschrauber-Elektromagnetik(HEM)-Karte des BRG ausgewählt. Hier wird zunächst auf die Lokation bei Cuxhaven eingegangen.

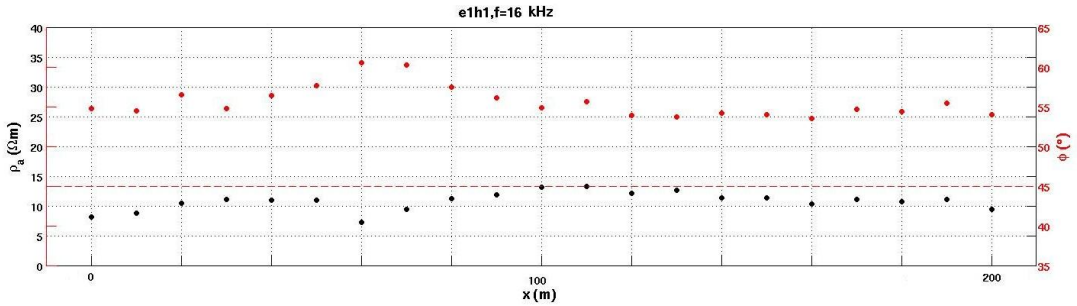

Abbildung 11: RMT-Messung bei Cuxhaven - Telefonkabel bei 60m als Anomalie zu sehen.

Sowohl die RMT- als auch die VLF-Daten, von einem Messgebiet aus der Nähe von Cuxhaven, zeigen bei ca. 55 m eine Anomalie. Es handelt sich laut Ortskundigen um ein Telefonkabel. Die Anomalie welche das Telefonkabel erzeugt (Abb.11 und 12), wurde modelliert (vgl. Abb.12). Die modellierten Übertragungsfunktionen stimmen gut mit der gemessenen Anomalie überein. Die Werte der spezifischen Widerstände des Hintergrundes des Modells orientieren sich hierbei an den Werten der RMT-Messung. Die Modellrechnung wurde mit dem Programm Inv2DVLF erstellt (*Santos et al.*, 2006). Da es mit dem Programm Inv2DVLF nicht möglich war ein dünnes und leitfähiges Telefonkabel zu modellieren, wurden für die Modellierung Dimension und spezifischer Widerstand des Kabels angepasst. Für einen analytischen Ansatz der für ein Telefonkabel verwendt werden könnte, vergleiche *Pedersen et al.* (1994).
Eigentliches Ziel war es jedoch eine natürliche Anomalie, wie etwa der Übergang von Süß- zu Salzwasser zu detektieren. Eine solche Anomalie ist in den Daten nicht zu erkennen.

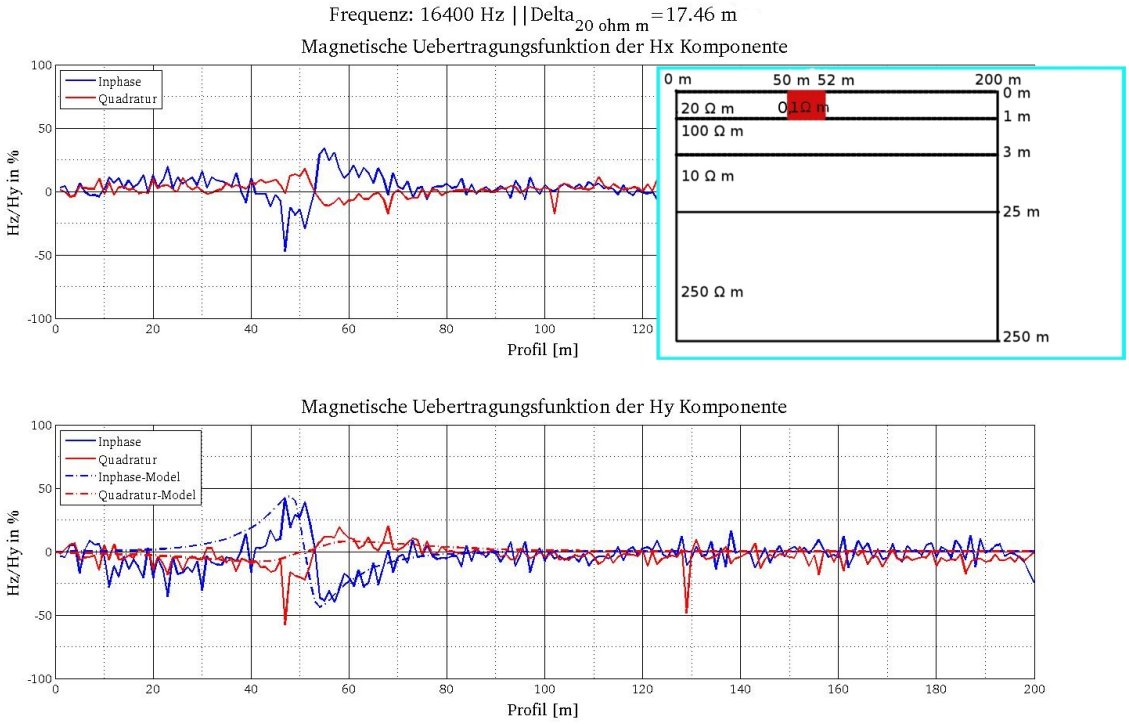

Abbildung 12: Magnetische Transferfunktion für VLF-Bodenmessung bei Cuxhaven - Telefonkabel deutlich als Anomalie zu erkennen. Gestrichelt: Magnetische Transferfunktion für ein Modell des Telefonkabels in Cuxhaven. (Rechtsoben) Modell.

Eine Besonderheit des SHFT-Sensors ist, dass er gleichzeitig die magnetischen Übertragungsfunktionen

der Hx- als auch der Hy-Komponente aufzeichnet. Das in (Abb.12) die Anomalie in beiden Komponenten zu sehen ist, liegt wahrscheinlich sowohl an der nicht 100 %ig realisierten TE-Mode der Hy-Komponente (d.h. Senderrichtung ist nicht parallel zur Streichrichtung) als auch daran, dass das die Profilrichtung nicht senkrecht zur Streichrichtung des Kables liegt (2D/3D Effekte).

6 Suche nach geeigneten Messlokationen für UAS/VLF Messungen im Harz

Als zweite potentielle Messlokation wurde ein Übergang von kreidezeitlichen zu quartären Ablagerungen im Harz vermessen. Auch diese Lokation wurde anhand einer Hubschrauber-Elektromagnetik(HEM)-Karte des BRG ausgewählt (Abb.13).

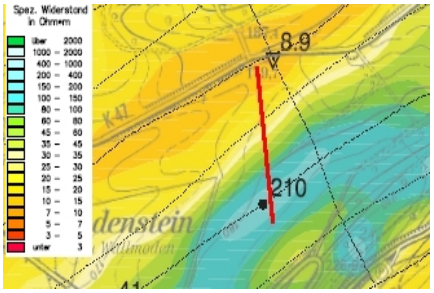

Abbildung 13: BGR-HEM Karte (*Siemon et al.*, 2002) aufgenommen bei 41,3 kHz. In Rot eingezeichnet das 360 m lange Profil. Man sieht hier wie der spezifische Widerstand schrittweise von Nord nach Süd (was der Profilrichtung entspricht) zunimmt. Dieser Verlauf des spezifischen Widerstandes wird im Folgenden als Modellannahme verwendet (Abb.16).

Auf zwei aufeinander folgenden Profilen wurden hierzu VLF-Messungen im Walking-Modus (d.h. kontinuierlich aufzeichnend mit dem Sensor in der Hand zu Fuß das Profil entlang gehend) durchgeführt (Abb.14 und 15).Im Imaginärteil der magnetischen Übertragungsfunktionen sieht man ein wellenförmiges Verhalten bei 140 bis 160 m (Abb.14) und bei 265 bis 305 m (Abb.15). Hier wurden zunächst Anomalien vermutet. Der Realteil zeigt starke Streuung, welche als Messeffekt (vlg. Abb.7) des Walking-Modus interpretiert wird.
Um zu untersuchen ob es sich um natürliche Anomalien handeln könnte, wurden Modellrechnungen für den Verlauf des Imaginärteils durchgeführt. Die Werte der spezifischen Widerstände wurden hierbei von Hubschrauber-Elektromagnetik(HEM)-Karte des BRG (Abb.13) abgelesen. Das auf diese Weise erstellte Modell hat mehrere vertikale Schichten mit stufenweise steigendem spezifischen Widerstand.

Da das Modell, welches aus (Abb.14) abgeleitet wurde, eine im Vergleich zu den Messdaten (Abb.14 und 15) schwach ausgeprägte Wellenbewegung zeigt, wurden verschiedene Alternativmodelle gerechnet. Dabei wurde das Original BGR-Modell modifiziert. Einige der gerechneten Modelle sind in (Abb.16 und Abb.17) zu sehen. Die Wellenbewegung und der Verlauf des Imaginärteils lassen sich zwar modellieren (Abb.16), es wurden jedoch bisher keine realistischen Modelle, welche die Amplitude des Imaginärteils so hoch wie in der Messung (ca. 50 %) bringen gefunden (Abb.17). Es folgen weitere Modellierungen. Die Modellrechnung wurde mit dem Programm Inv2DVLF erstellt.

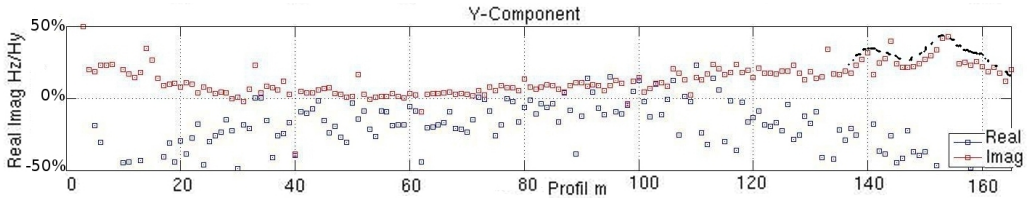

Abbildung 14: VLF-Bodenmessung im Harz. Übertragungsfunktion Hz/Hy. Anomalien bei Profilmeter 140 bis 160. Für f = 18,3 kHz.

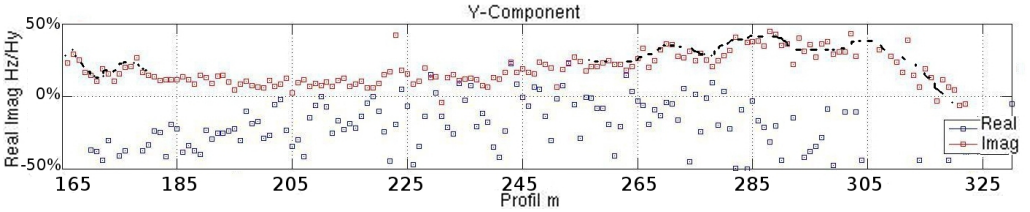

Abbildung 15: Fortsetzung von Abb.15 für Profilmeter $\geq$ 165.

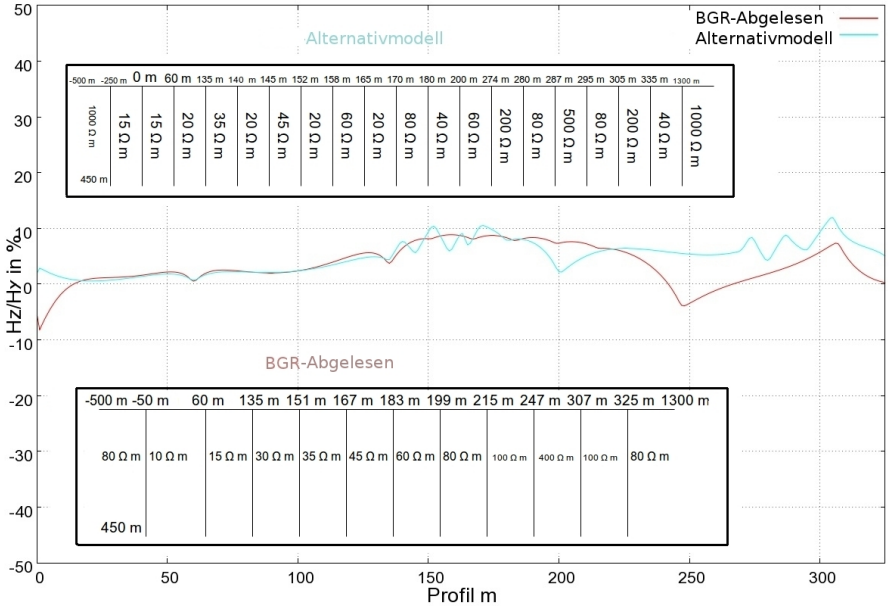

Abbildung 16: Modell des Untergrundes entlang der Profile in (Abb.14 und 15). Die Werte der spezifischen Widerstände für das BGR-Abgelesen Modell wurden aus (Abb.13) entnommen.

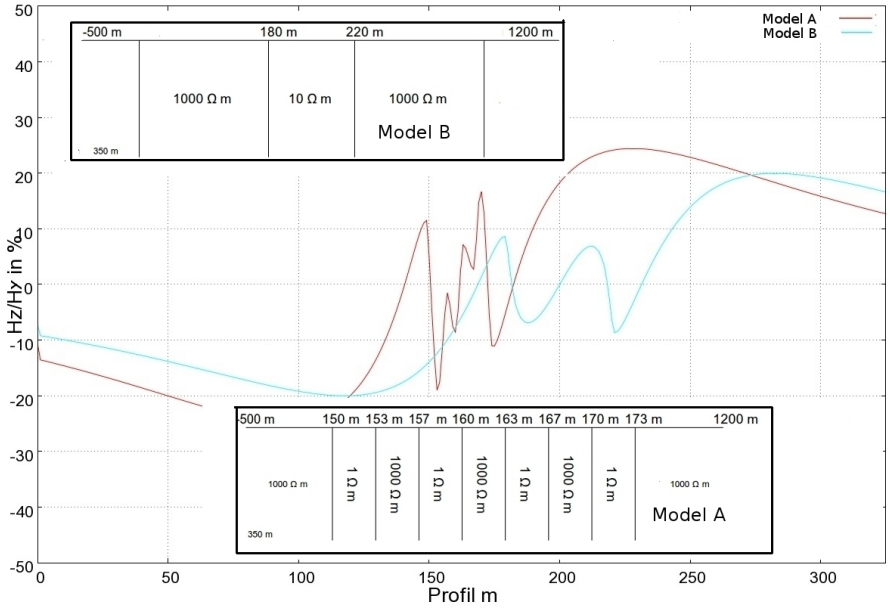

Abbildung 17: Alternativmodelle zur Untersuchung der mit vertikalen Schichten erreichbaren Amplitude des Imaginärteils.

7 Ausblick

Wir planen zunächst eine UAS/VLF-Messung über einer deutlichen und eindeutig bekannten anthropogogenen Anomalie, um die auftretenden Phänomene und Nebenbedingungen näher untersuchen zu können. Anschließend soll eine Messung über eine natürliche Anomalie in einem Gebiet, das bereits vom BGR beflogen wurde (d.h. BGR-HEM Karte vorhanden), durchgeführt werden.
Außerdem wird der Auswertealgorithmus weiterentwickelt. Zusätzlich sind weitere Noisemessungen und Messungen mit stillstehendem, sauber ausgerichtetem Sensor im Vergleich zum Walkingmodus geplant. Es soll ein Simulationsalgorithmus für UAS/VLF-Messungen entwickelt werden.

8 Danksagung

Diese Arbeit wird im Projekt AIDA (From Airborne Data Inversion to In-Depth Analysis) als Teil des BMBF/DFG-Sonderprogramms GEOTECHNOLOGIEN durchgeführt und durch dieses gefördert.

Literatur

Pedersen, L. B., W. Qian, L. Dynesius und P. Zhang, An airborne tensor vlf system. from concept to realization1, *Geophysical Prospecting*, *42*, (8), 863–883, 1994.

Pedersen, L. B. und L. Dynesius, Final report on the multi frequency vlf/lf receiver (mfr) project,, 2008.

Santos, F. M., A. Mateus, J. Figueiras und M. A. Gonçalves, Mapping groundwater contamination around a landfill facility using the vlf-em method - a case study, *Journal of Applied Geophysics*, *60*, (2), 115 – 125, 2006.

Siemon, B., W. Voß, B. Röttger, H.-J. Rehli und J. Pielawa, Forschungsvorhaben "Detaillierte aerogeophysikalische Landesaufnahme"(DAGLA), Messgebiet Rhüden - Lutter a. B., Juni 2000, *BGR-Bericht*, *Archiv-Nr. 0121613*, 2002.

Tezkan, B., J. Stoll, R. Bergers und H. Grossbach, Unmanned aircraft systems: a new geophysical measuring platform for aeromagnetic surveys., *First Break*, *V. 29*, 103–105, 2011.

The Permanent Magnetotelluric Remote Reference Station

D. Eydam & G. Muñoz from GFZ Potsdam

Summary

Magnetotellurics is a so called passive method where *natural* electromagnetic variations are used as signal excitation. The convenience of passive methods works at the expense of signal - to - noise ratios which are generally poor due to the absence of control of signal strengths.

The Remote - Reference - Technique is an effective way to improve magnetotelluric data quality by referencing the local fields to simultaneously recorded and undisturbed fields at a remote reference site. In areas where noise level is high remote reference processing is required but finding and maintaining a reference site during a campaign is expensive and time consuming.

Therefore a permanent and self - sustaining reference station simplifies MT measurements which are carried out in a radius where source fields are still coherent, which depends on the frequency. For high frequencies up to 1000 Hz this coherency radius can amount to over 800 km, which was proven by referencing data from the Black Forest to Rügen (Schill *et al.*, 2011).

Locating appropriate reference sites across Germany was not an easy task. We found high quality data in the urban forest of Wittstock where the permanent reference station was installed end of 2011. Reference data is being permanently recorded with sampling rates up to several kilohertz since 2010. Meantime the Wittstock station operated repeatedly as reference and magnetotelluric data from northern and eastern Germany could significantly be improved. Access to the reference site data is open to the MT community.

1 - Introduction

The magnetotelluric (MT) method uses amplitude - and phase - relations of quasi homogeneous electromagnetic (EM) fields at the earth's surface to obtain resistivity information of the subsoil. Inhomogeneous fields of nearby current sources overlie intrinsically proper MT - signals and disturb passive recordings. If any noise is present in one field component, it is amplified by calculating auto - power spectra which causes impedances to be biased. Considering that the uncontaminated natural part of the induced field is coherent over many kilometres whereas noise is generally random and incoherent, bias effects can be removed by substitution of local magnetic variations with simultaneously recorded, undisturbed magnetic variations at a remote reference site (for more detail

Figure 1: Test - areas across Germany: Rügen, northern Brandenburg, northern Bavaria, Eifel, Westerwald and Allgäu.

see, ex. Gamble *et al.*, 1979).

A remote reference site is thus located far away from current sources such as settlements, gas and power lines, electric fences etc. Among the variety of noise sources, noise influence is different since it can disturb just some definitive frequencies or a broad frequency range such as ground leakage currents arising from electric fences. Promising test sites are preferably located above well - conducting subsoil considering that disturbing fields propagate over shorter distances here. Geographic and geologic maps were used to decide about testing areas. Long term recording requires year - round accessibility which disqualifies sites at agricultural crop land, high altitudes or coastal areas. We concentrated our search on woodlands where we focused at clearances to ensure future power supply by photovoltaics.

2 - Locating appropriate remote reference sites in Germany

Data quality of about 25 locations across Germany was tested (fig. 1). Data was commonly recorded for at least three days with sampling rates between 500 to 6000 Hz. Geographic coordinates of the test - sites are listed in the appendix.

A site was qualified as a reference if the time series of the electromagnetic field components particularly the magnetic ones do not contain any obvious noise signal and if the local transfer functions are reasonable smooth and continuous especially in the *MT dead band*, the natural excitation minimum between 10 Hz and 10 s.

2.1 – Allgäu

Site *Mol* near Kempten was used as a fairly good reference for MT measurements in the southern Black Forest. However magnetic data is quite disturbed (fig. 3) and important annual snowfalls disqualify the site for long - term recordings.

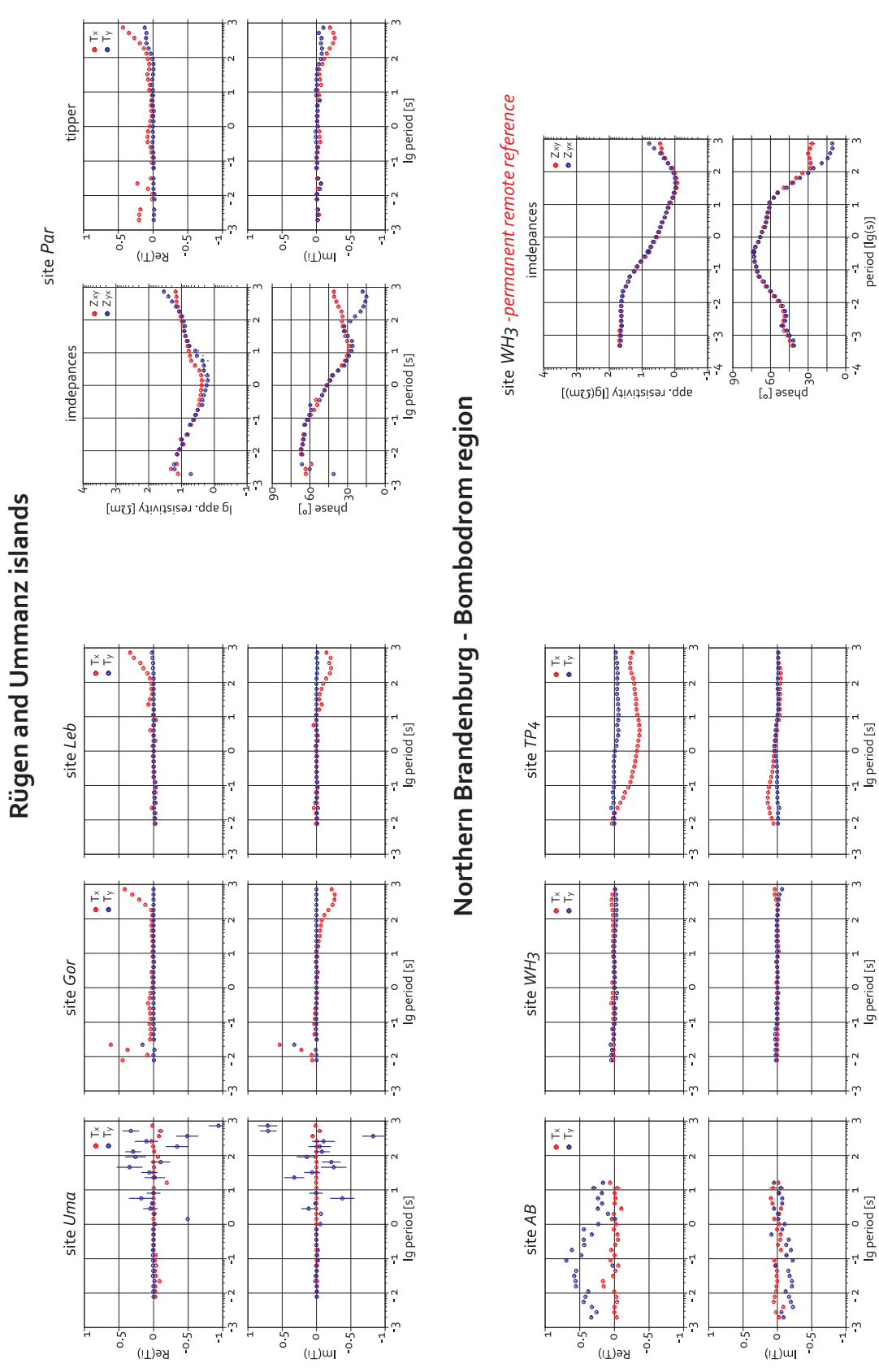

Figure 2: Overview about data quality for tested areas: Rügen and Brandenburg. Shown are magnetic transfer functions (left) for exemplarily chosen sites and qualitive best magnetotelluric transfer functions of the area (right). Corrupt high frequency data points at site *Par* (upper right corner) are due to enabling induction coil chopper which improves low frequency data at the expense of high frequency recording. At site *WH3* the permanent remote reference station has been set up.

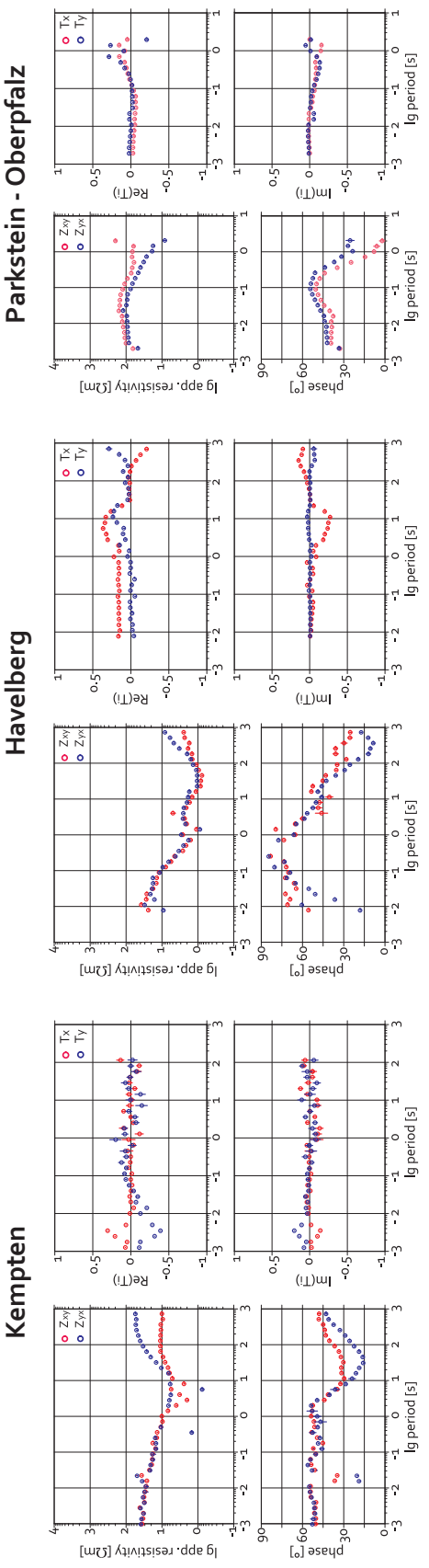

Figure 3: Overview about data quality for tested areas: Kempten, Havelberg and Parkstein. Shown are impedances (left) and tipper values (right). Note that at the Parkstein-site the quality decrease for periods longer than one second is due to disabling the induction coil chopper.

2.2 – Rügen & Ummanz islands

Islands should be preferable for an undisturbed recording of natural electromagnetic fields as the sea's conductivity is low so that tidal effects are negligible. Inspired by results from Schäfer (2010) who found good data quality at northern Rügen, we tested four sites at Rügen and Ummanz (fig. 4).

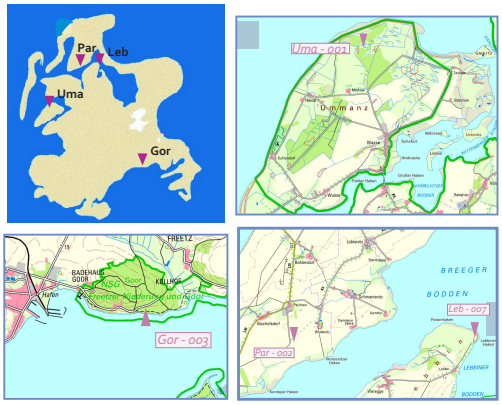

Figure 4: Test-sites at Rügen and Ummanz islands.

The quality of magnetic data is commonly good but deteriorates southward since population density increases which is demonstrated by a distinct 50 Hz signal and its harmonics at site *Gor* (fig. 2).

At northern Rügen as well as at Ummanz transfer functions are smooth even in the *MT dead band* and time series are without any obvious noise; regarding that disturbed long periods at Ummanz (*Uma*) are probably just due to a nearby, mobile electric fence. Notable are the small apparent resistivities which may shield nearby noise signals effectively (fig. 2). The congruent curvature up to periods of 100 s indicates horizontal layering of the subsoil which is confirmed by the vanishing geomagnetic transfer functions.

Site *Par* operated repeatedly as reference but is situated on agricultural crop land which is not year-round accessible. Since both islands are in intensive agricultural use, alternative sites for *Par* and *Uma* are difficult to find. *Leb* lies next to *Par* but at the other side of the indentation and data quality is still good, however time series of the magnetic fields show a minor 50 Hz signal. The influence of the recently built Baltic Sea-gas line has not been identified yet.

2.3 – northern Brandenburg

Eastern Germany is poorly settled and power and gas lines are less dense in northern Brandenburg and Mecklenburg-Vorpommern. The polish DC-railways are an important noise source in easternmost Germany so that this region was expected to be inappropriate as reference area.

2.3.1 – Havelberg

Tests were carried out in the woodland area east of Havelberg. Data quality of all five

Figure 5: Test - sites in northern Brandenburg - Bombodrom and Wittstock region. Site *AB* is located near the highway A24, sites *WH1-4* are in the urban forest of Wittstock and sites *TP1-4* adjoin to the former military drill ground Bombodrom (red line). Red circle: chosen permanent reference site.

sites is poor and data scatters especially in the *MT dead band* representing a more regional than local noise character (fig. 3). Major gas and power lines are more than 5 km away, but could still affect the quality of long period data. Middle to high frequencies are influenced by a distinct $16\frac{2}{3}$ Hz signal of the nearby ICE - railway.

2.3.2 – the Bombodrom - region

Bombodrom is a former military drill ground in the Kyritz - Ruppiner Heide. The terrain is an open and priory wild area of 144 km^2 but is severely mined and maintains the judicial status of a military safety zone. A petition for permission of test measurements was filed at the Bundeswehr service centre in Potsdam but has not been answered. Therefore we sidestepped to adjacent woodlands as well as to an extended forestry area north of Wittstock (fig. 5).

Data quality differs: Distinct local noise sources are present along the highway (site *AB*) and adjacent to the Bombodrom (sites *TP1-4*) where time series show 50 Hz signals with temporally varying amplitudes (fig. 2). Noise sources might be underground cables (sites *AB*, *TP2*), electric fences (site *TP1*) and minor gas pipelines which were not included in the maps we used (sites *TP3-4*).

Data recorded at all four sites in the urban forest north of Wittstock are quite undisturbed; transfer functions are reasonable and smooth (fig. 2) and time series are without any distinct noise. However spectra show minor 16 Hz and 50 Hz signals which is slightly more pronounced in the Zyx - component (see fig. 8). Similar to northern Rügen, impedances curve shapes are congruent up to periods of 100 s indicating horizontal layering of upper earth levels which concurs with the vanishing magnetic transfer function. Apparent resistivities are comparatively low and may shield noise signals.

2.4 – northern Bavaria

Test measurements in northern Bavaria were carried out just to get a brief overview about the local noise situation. Against a general high noise contamination in the Fränkische Schweiz, extended measurements in the Oberpfalz near Parkstein might be worthwhile (fig. 3). A short two days test carried out by IGEM (institute of geothermal resource management) reveal comparatively stable and smooth curves in the *MT dead band*.

2.5 – Eifel and Westerwald

Tests in the Eifel and Westerwald were carried out by IGEM. Data of all four test-sites is locally highly disturbed and quality is insufficient.

2.6 – Summary

Germany is widely exposed to artificial ground leakage currents. Location Fränkische Alb and Havelberg as well as tested sites in the Allgäu, Eifel and Westerwald had to be discarded due to insufficient data quality. Oberpfalz has promisingly good high frequent data and quality of longer periods, especially in the *dead band*, will be checked in more detail. High data quality was recorded at northern Rügen and northern Brandenburg. Alternative locations for site *Par* at Rügen or site *Uma* at Ummanz have still to be found; the sites are situated on agricultural crop land or swampy area and are not year-round accessible. We found high quality data in a forest north of Wittstock where we installed the first permanent magnetotelluric reference station.

3 – The permanent magnetotelluric reference station at Wittstock

The chosen permanent reference site *WH3* (red circle at fig. 5) is located in a natural clearance of the 7 km wide urban forest of Wittstock, 10 km north of the downtown (fig. 6). The site is easy to access and a two hours drive from Potsdam.

Figure 6: Clearance in the urban forest of Wittstock with permanent reference station.

Data recording was prolonged from May to November 2010 to assure the stability of data quality. End of 2010 the complete set-up has been installed: cables, sensors and the sensorbox are buried in tubes and a hut had been set up for the loggers and power supply system (fig. 7). The ground is being rented from the town Wittstock by GFZ.

Figure 7: Hut of the permanent station. Data is recorded broad - band with two Spam IV data loggers.

Data quality varies slightly in the *dead band* between 10 Hz and 10 s which could not be related to extern noise sources. This might be caused by variations in the source strength of MT signals.

Equipment and Configuration

In order to provide broad - band magnetotelluric reference data, the station is equipped with two sets of Metronix induction coils (MFS06/07) measuring middle to high frequency variations of the horizontal field as well as with a fluxgate magnetometer recording slow magnetic variations. Sampling rate is up to 6-12 kHz. Data is recorded with two Spam IV loggers and transfer is planned via telemetry infrastructure. The required energy is mainly provided by a 5 m^2 wide solar panel loading two 230 Ah batteries and is supported by a methanol fuel cell for additional needs in winter. This results in a self - sustaining recording during several months.

Recent changes in noise situation

During last year a solar park has been built 6 km away from the reference site. Reference data is now disturbed by a distinct 50 Hz signal though its amplitude is minor. Spectra of horizontal EM fields show a rosen 50 Hz content after the construction of the solar park (fig. 8) but the increased artificial signals do not affect the data quality very serverely; transfer functions are still smooth even in the *MT dead band*. Probably the noise signal will increase during summer season which has to be checked then.

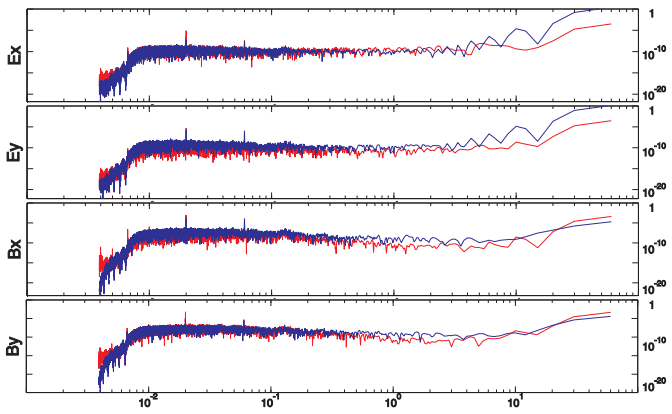

Figure 8: Comparison of field spectra measured in august 2010 (blue) and december 2011 (red). The red spectra show increased 16Hz and 50 Hz peaks due to the installation of the solar park. Shown is the frequency content of one minute of data sampled with 500 Hz .

4 – Application of reference site data

The Wittstock site operated successfully as reference for passive as well as active (controlled-source (CS)) MT measurements in northern and eastern Germany.

Ketzin area is worst case for passive MT: The profile was passing a transformer station, a subterranean gas storage, major gas and power lines as well as windmills. Streich *et al.* (2011) focused on the development of the CS - MT method in a noisy area, however a large dataset of passive MT data was collected as well by parallel and continuous, high frequent sampling at 40 passive MT receiver stations.

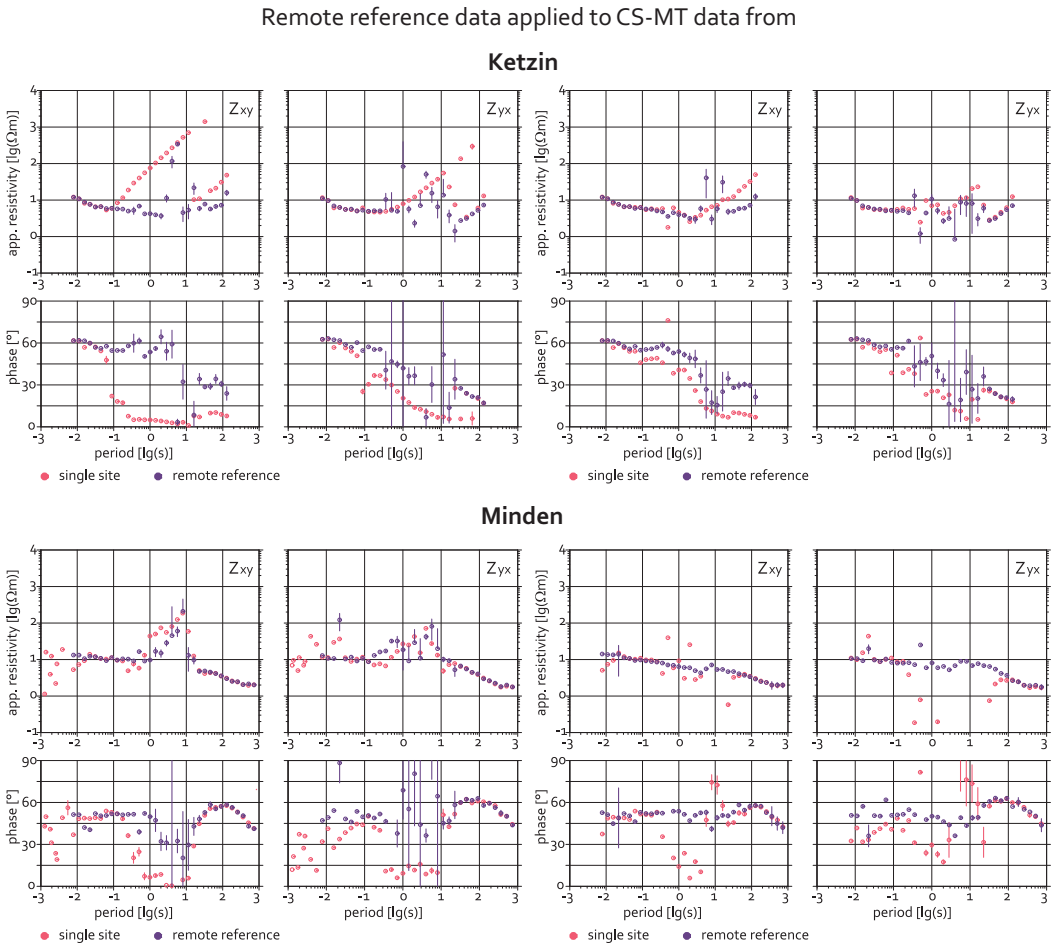

Figure 9: Results of referencing data from Ketzin (above) and Minden (below) to the permanent reference site at Wittstock for time segments when CS-MT signals where transmitted (left) compared to the same time segment with CS-MT transmission periods cut out (right). Transmitter - receiver - distance was less than one kilometre for the Ketzin station and about 4 km for the Minden station. All data is delay filtered at 16 2/3 Hz.

Data quality is absolutely poor and locally blur into point-clouds but quality improves southward. Applying the Remote-Reference-Technique data in the south can be improved even during emission periods of CS-MT signals which were transmitted just nearby (fig. 9) whereas data in the central and northern part of the Ketzin profile could just be improved in terms of raising phases and reducing non-physical steep slopes of

the apparent resistivities.

Minden area is much less exposed to artificial current sources which are mainly high voltage power lines beside some electric fences and gas lines. Data quality is comparable with the Ketzin southernmost stations and improves significantly by applying the remote reference processing even though high voltage CS-MT signals were transmitted some kilometres away (fig. 9 below). Improvement is minor in the *MT dead band* between 10 Hz and 10 s where natural excitation is low.

Conclusion

High quality reference data is being continuously recorded in a broad frequency range since end of 2010. Operating such a self - sustaining station simplifies MT campaigns across Germany by reducing the logistics and costs emerging by servicing a remote station. New methods of telemetry infrastructure will be developed for an easy data transfer to Potsdam. We are envisaging an open access of the data to the MT community by developing an effective data bank system. There is the equipment for more permanent reference stations and we are looking forward to proceed with the test measurements.

Beyond the function as magnetotelluric reference, a long-term recording of undisturbed homogeneous electromagnetic variations may offer new insights into the behaviour of MT source signals such as the investigation of field coherencies over distance and a wide spectrum.

Acknowledgement

Test measurements were carried out with the support of the institute of geothermal resource management IGEM. It was during a collaboration between GFZ and IGEM when the idea and necessity of a permanent reference station arose. Thanks for all helpers of IGEM & of the GFZ magnetotelluric group & to Anja Schäfer. Thanks to Dr. Henri Brasse for suggesting the Oberpfalz region. Thanks to all rangers and the management of the urban forest of Wittstock for supporting our work.

Appendix – Coordinates of tested sites

Test Area/Site Name	Site Number	Geographic Latitude (N)	Geographic Longitude (E)
Rügen			
Uma	001	54° 29.211'	13° 10.364'
Par	002	54° 34.632'	13° 17.361'
Gor	003	54° 20.500'	13° 31.612'
Leb	007	54° 34.664'	13° 22.190'
Northern Brandenburg – Havelberg			
*HB*1	006	52° 50.755'	12° 07.789'
*HB*2	008	52° 50.898'	12° 08.779'
*HB*3	009	52° 52.363'	12° 09.345'
*HB*4	010	52° 51.207'	12° 11.417'
*HB*5	011	52° 49.671'	12° 12.821'
Northern Brandenburg – urban forest of Wittstock			
AB	012	53° 06.014'	12° 31.434'
*WH*1	013	53° 15.038'	12° 33.699'
*WH*2	014	53° 12.832'	12° 31.300'
*WH*3	016	53° 14.341'	12° 32.854'
*WH*4	017	53° 15.242'	12° 32.342'
Northern Brandenburg – Bombodrom			
*TP*1	015	53° 13.244'	12° 40.443'
*TP*2	018	53° 12.536'	12° 41.145'
*TP*3	019	53° 10.779'	12° 45.087'
*TP*4	020	53° 11.136'	12° 43.798'
Allgäu – Kempten			
Mol	004		
Eifel & Westerwald			
Koll	023	50° 15.421'	7° 14.887'
Brohl	024	50° 11.986'	7° 16.621'
Lieg	025	50° 8.6590'	7° 19.258'
Rans	026	50° 26.527'	7° 43.981'
Northern Bavaria – Fränkische Schweiz and Oberpfalz			
Pot	021	49° 47.967'	12° 00.254'
Pas	022	49° 43.938'	11° 19.426'

References

Gamble, T.D., Goubau, W.M., & Clarke, J. 1979. Magnetotellurics with a remote magnetic reference. *Geophysics*, **44(1)**, 53–68.

Schäfer, A. 2010. *Magnetotellurische Untersuchung der Transeuropäischen Suturzone auf einer Traverse von Südschweden nach Nordostdeutschland*. Diploma Thesis at Technical University of Berlin, department for applied geophysics.

Schill, E., T., Kohl, H., Deckert, & et al. 2011. EGS Technologie Entwicklung: Risikominimierung bei der Exploration. *Technische Informationsbibliothek Hannover (TIB)*, **4.1**, 84–107.

Streich, R., Becken, M., Matzander, U., & Ritter, O. 2011. Strategies for land-based controlled-source electromagnetic surveying in high-noise regions. *The Leading Edge*, **30(10)**, 838–843.

Convergence studies for the 2D finite element simulation of the MT boundary value problem

A. Franke-Börner, R.-U. Börner and K. Spitzer
TU Bergakademie Freiberg, Germany

1 Summary

We use convergence studies that examine the accuracy of a numerical solution as a function of the computational effort in terms of computer memory requirements to assess the quality of a finite element approach to simulate the magnetotelluric boundary value problem arising from Maxwell's equations. Since three-dimensional simulation requires considerable computing power and memory capacity, first, the two-dimensional boundary value problem is analysed to verify the expectations according to convergence theory. The equation of induction is solved in a bounded two-dimensional domain Ω with appropriate Dirichlet boundary conditions. For models of the homogeneous and the layered halfspace, the error of the numerical solution with respect to the analytical solution is considered for a hierarchy of nested unstructured triangular meshes. Moreover, we also analyse the deviation of the numerical result from the finest-grid solution that is supposed to be close to the true solution. We determine the convergence behaviour with increasing number of degrees of freedom in dependence of the order p of the finite elements (p = 1, 2, 3), the frequency f of the electromagnetic fields (f = 0.01, 0.1, 1 Hz), and also the mesh refinement strategy applied. Our computations illustrate that the convergence behaviour of the numerical solution varies with the conductivity distribution in the model. Different convergence rates are obtained for the homogeneous and the layered halfspace models. Furthermore, global convergence results do not necessarily apply to local convergence that can be observed for, e.g., arbitrary data points on the earth's surface.
Keywords: magnetotellurics, finite element method, boundary value problem, 2D, numerical simulation

2 Introduction

Since the 1970s classical approaches such as the finite-difference (FD), integral-equation (IE) and finite-element (FE) method have been used to develop two-dimensional (2D) and three-dimensional (3D) numerical simulation algorithms for geo-electromagnetic applications. Brewitt-Taylor and Weaver (1976) provided a revision of the theory of 2D FD approximations which had been introduced by Jones and Price (1970) and Jones and Pascoe (1971) with respect to an extension towards 3D modeling that was later developed by Mackie, Madden, and Wannamaker (1993). The IE technique was rapidly advanced from 2D applications (Hohmann, 1971) to the 3D formulation (Wannamaker, Hohmann, & San Filipo, 1984). The application of the FE method to geo-electromagnetic simulation was first established by Coggon (1971). Mogi (1996) applied the FE approach to 3D simulation of magnetotelluric (MT) data. More recently, advances in software development have been focused on the flexibility, accuracy and efficiency of the simulation algorithms (e.g. Siripunvaraporn, Egbert, & Lenbury, 2002, Aprea, Booker, & Smith, 1997, Wannamaker, 1991, Mitsuhata & Uchida, 2004, Key & Weiss, 2006, Franke, Börner, & Spitzer, 2007, Nam et al., 2007, Farquharson & Miensopust, 2011) which are desirable for incorporating the forward operator into an inversion scheme as described for instance by Baranwal, Franke, Börner, and Spitzer (2011), Mackie and Madden (1993) as well as Avdeev and Avdeeva (2009).
We perform convergence studies, i.e., consider the accuracy of the numerical solution as a function of degrees of freedom of the linear system of equations to be solved, in order to assess the efficiency of our finite-element simulation approaches of the MT boundary value problem. Theory of the finite-element method provides estimates of convergence rates. Since 3D simulation requires considerable computing power and memory capacity, we restrict ourselves for now to analysing the 2D boundary value problem to verify these expectations. First, a 2D homogeneous halfspace model is considered. Using several steps of uniform or adaptive mesh refinement (h-refinement) and increasing the polynomial degree p of the basis functions (p-refinement) up to $p = 3$ the convergence of the FE solution towards the analytical solution is demonstrated for the frequencies $f = 0.01$, 0.1, 1 Hz. Since in general

the true solution is unavailable, second, after having ensured convergence to the analytical solution the convergence of the numerical result towards the finest-grid solution is analysed. Third, convergence studies for a 2D layered halfspace model are carried out.

3 Boundary Value Problem

In the case of 2-D isotropic structures Maxwell's equations yield two independent modes. If y is the strike direction of a 2-D body and assuming a harmonic time dependency $e^{i\omega t}$ with frequency f and angular frequency $\omega = 2\pi f$, they reduce to

$$\frac{\partial H_x}{\partial z} - \frac{\partial H_z}{\partial x} = (\sigma + i\omega\varepsilon)E_y, \tag{1a}$$

$$-\frac{\partial E_y}{\partial z} = -i\omega\mu H_x, \tag{1b}$$

$$\frac{\partial E_y}{\partial x} = -i\omega\mu H_z, \tag{1c}$$

and

$$-\frac{\partial H_y}{\partial z} = (\sigma + i\omega\varepsilon)E_x, \tag{2a}$$

$$\frac{\partial H_y}{\partial x} = (\sigma + i\omega\varepsilon)E_z, \tag{2b}$$

$$\frac{\partial E_x}{\partial z} - \frac{\partial E_z}{\partial x} = -i\omega\mu H_y \tag{2c}$$

for a homogeneous region of the electrical conductivity σ, magnetic permeability μ, and dielectric permittivity ε. The occurence of the electric field component E_y and the magnetic field components H_x, and H_z in eqs (1a)-(1c) is referred to as E-Polarisation, whereas eqs (2a)-(2c) hold for the case of H-Polarisation. Combining eqs (1a)-(1c) in a bounded domain $\Omega \in \mathbb{R}^2$ the following 2-D boundary value problem can be formulated for E-polarisation

$$-\frac{\partial}{\partial x}\mu^{-1}\frac{\partial E_y}{\partial x} - \frac{\partial}{\partial z}\mu^{-1}\frac{\partial E_y}{\partial z} + (i\omega\sigma - \omega^2\varepsilon)E_y = 0 \quad \text{in} \quad \Omega \tag{3a}$$

$$E_y = E_n(x,z) \quad \text{on} \quad \Gamma_{\mathrm{D}} \tag{3b}$$

$$\mathbf{n}_1 \times \mathbf{H}_1 + \mathbf{n}_2 \times \mathbf{H}_2 = \mathbf{n}_1 \cdot (\mu_1^{-1}\nabla E_{y,1}) + \mathbf{n}_2 \cdot (\mu_2^{-1}\nabla E_{y,2}) = 0 \quad \text{on} \quad \Gamma_{\text{int.}} \tag{3c}$$

Eqs (2a)-(2c) yield the 2-D boundary value problem for H-polarisation

$$-\frac{\partial}{\partial x}(\sigma + i\omega\varepsilon)^{-1}\frac{\partial H_y}{\partial x} - \frac{\partial}{\partial z}(\sigma + i\omega\varepsilon)^{-1}\frac{\partial H_y}{\partial z} + i\omega\mu H_y = 0 \quad \text{in} \quad \Omega \tag{4a}$$

$$H_y = H_n(x,z) \quad \text{on} \quad \Gamma_{\mathrm{D}} \tag{4b}$$

$$\mathbf{n}_1 \times \mathbf{E}_1 + \mathbf{n}_2 \times \mathbf{E}_2 =$$

$$\mathbf{n}_1 \cdot \left((\sigma_1 + i\omega\varepsilon)^{-1}\nabla H_{y,1}\right) + \mathbf{n}_2 \cdot \left((\sigma_2 + i\omega\varepsilon)^{-1}\nabla H_{y,2}\right) = 0 \quad \text{on} \quad \Gamma_{\text{int.}}, \tag{4c}$$

For the outer boundaries Γ_D to which inhomogeneous boundary conditions of the Dirichlet type apply a layered-halfspace model is assumed and the field values E_n and H_n are computed according to Wait's algorithm (Wait, 1953).

Once the strike-parallel components E_y and H_y have been computed, the remaining components H_x, H_z, E_x, and E_z can be derived from eqs (1b)-(2b) by numerical differentiation in a subsequent procedure which is generally referred to as post-processing.

4 Finite Element Method

4.1 Weak Form

We seek for solutions E_y and H_y of the boundary value problems described by eqs (3a)–(3c) and (4a)–(4c), respectively. An equivalent formulation of the boundary value problem for E-polarisation on the domain Ω requires the validity of eq. (3a) only in the sense of the L^2 inner product $(u, v) = \int_\Omega u\bar{v}\, d\mathbf{x}$ with an arbitrary complex test function v of a function space V and its complex conjugate $\bar{v}$. If $v \equiv 0$ on the Dirichlet boundary Γ_D, the original problem of solving eqs (3a)-(3c) can be replaced by the so-called weak formulation which consists of finding $E_y \in U$ such that:

$$b(E_y, v) = \int_\Omega \left(\mu^{-1}\nabla E_y \cdot \nabla\bar{v} + (i\omega\sigma - \omega^2\varepsilon)E_y\bar{v}\right)\, d\mathbf{x} = 0 \quad \forall v \in V, \tag{5}$$

where

$$U := \{E_y \in H^1(\Omega) : E_y = E_n(x, z) \quad \text{on} \quad \Gamma_\mathrm{D}\} \quad \text{and} \tag{6}$$
$$V := \{v \in H^1(\Omega) : v \equiv 0 \quad \text{on} \quad \Gamma_\mathrm{D}\} \tag{7}$$

are the trial and the test space, respectively. H^1 denotes the finite-dimensional Hilbert space

$$H^1(\Omega) := \{v \in L^2(\Omega), \nabla v \in (L^2(\Omega))^2\} \tag{8}$$

that is linear with respect to the scalar product $(u, v) = \int_\Omega (u\, v + \nabla u \cdot \nabla v)\, d\mathbf{x}$. For the solution E_y of the weak form (5) and its first partial derivatives ∇E_y it is sufficient to be square integrable instead of twice continuously differentiable ($E_y \in C^2(\Omega)$, cf. eq. 3a). The material parameters $\sigma, \mu, \varepsilon \in L^2(\Omega)$ are required to be square integrable. Satisfying eqs (3a)-(3c), the electromagnetic fields are solutions to eq. (5) as well.
In the H-Polarisation case, the weak form of the boundary value problem described by eqs (4a)-(4c) is: Find $H_y \in U$ such that

$$b(H_y, v) = \int_\Omega \left((\sigma + i\omega\varepsilon)^{-1}\nabla H_y \cdot \nabla\bar{v} + i\omega\mu H_y\bar{v}\right)\, d\mathbf{x} = 0 \quad \forall v \in V, \tag{9}$$

where

$$U := \{H_y \in H^1(\Omega) : H_y = H_n(x, z) \quad \text{on} \quad \Gamma_\mathrm{D}\} \quad \text{and} \tag{10}$$
$$V := \{v \in H^1(\Omega) : v \equiv 0 \quad \text{on} \quad \Gamma_\mathrm{D}\} \tag{11}$$

with the same finite-dimensional Hilbert space H^1 as above

$$H^1(\Omega) := \{v \in L^2(\Omega), \nabla v \in (L^2(\Omega))^2\}. \tag{12}$$

4.2 Finite Element Analysis

To find the discrete form of eqs (5) and (9), preliminarily, the solution $u := E_y, H_y$ and the test function v are both required to belong to the same infinite-dimensional function space V, i.e. $E_y, H_y \equiv 0$ on Γ_D . The inhomogeneous Dirichlet boundary conditions will be taken into account later. Projection of the weak form onto an N-dimensional function subspace V_N means requiring $u, v \in V_N$. Taking N test functions $\psi_i \in V_N$ that form a basis of V_N and u^h as a linear combination of these basis functions and the scalar complex expansion coefficients U_i

$$u^h(\mathbf{x}) = \sum_{i=1}^{N} U_i\psi_i(\mathbf{x}) \tag{13}$$

the discrete formulation of eqs (5) and (9) can be written as

$$(\mathbf{K} + \mathbf{M})\mathbf{U} = \mathbf{0}, \tag{14}$$

with stiffness ($\mathbf{K}$) and mass ($\mathbf{M}$) matrix

$$K_{i,j} = \int_\Omega (c\,\nabla\psi_i)\cdot\nabla\bar{\psi}_j d\mathbf{x}, \qquad M_{i,j} = \int_\Omega a\,\psi_i\bar{\psi}_j d\mathbf{x} \quad i,j = 1,...,N. \tag{15}$$

where $\mathbf{U}$ and the coefficients c and a are denoted as follows

E-Polarisation: $\mathbf{U} := E_{y,i}, \quad c := \mu^{-1}, \quad a := i\omega\sigma - \omega^2\varepsilon,$

H-Polarisation: $\mathbf{U} := H_{y,i}, \quad c := (\sigma + i\omega\varepsilon)^{-1}, \quad a := i\omega\mu.$

In the 2D MT case, i.e. for simulating scalar field components in source-free regions, Lagrange elements whose degrees of freedom $l_n(\psi_i)$ are defined as values $\psi_i(\mathbf{x})$ at location $\mathbf{x}$ are well suited. Furthermore, we choose V_N to be a space of piecewise linear (p = 1), quadratic (p = 2), or cubic (p = 3) functions. The basis functions are designed such that

$$l_n(\psi_i) = \delta_{n,i} = \begin{cases} 1 & \text{if} \quad n = i \\ 0 & \text{if} \quad n \neq i \end{cases} \quad \text{and} \quad \sum_n l_n(\psi_i) = 1 \quad i = 1,...,N. \tag{16}$$

Solving eq. (14) yields values of the approximate solution $u^h(\mathbf{x})$ for all DOF. In the case of linear basis functions DOF are placed in the vertices of the triangles. Additional DOF appear on the edges for quadratic and cubic basis functions. The integrals in eqs. (15) are computed on each triangle ϑ by numerical quadrature. The system matrices $\mathbf{K}$ and $\mathbf{M}$ are assembled from the local matrices $\mathbf{K}^\vartheta$ and $\mathbf{M}^\vartheta$, respectively.
The inhomogeneous Dirichlet boundary conditions still need consideration. So far, the vector $\mathbf{U}$ contains $N_{\Omega\setminus\Gamma_\mathrm{D}}$ elements for the interior points in region $\Omega\setminus\Gamma_\mathrm{D}$ and N_{Γ_D} elements for the points on Γ_D whose values vanish. Eqs (3b) and (4b) provide the N_{Γ_D} non-zero values on Γ_D in $\mathbf{U}_{\Gamma_\mathrm{D}}$ which comprises $N_{\Omega\setminus\Gamma_\mathrm{D}}$ zero-elements for all the interior points. Applying

$$\mathbf{U} = \mathbf{U}_{\Omega\setminus\Gamma_\mathrm{D}} + \mathbf{U}_{\Gamma_\mathrm{D}} \tag{17}$$

to eq. (14), we derive a system of linear equations for $\mathbf{U}_{\Omega\setminus\Gamma_\mathrm{D}}$:

$$(\mathbf{K}+\mathbf{M})\mathbf{U}_{\Omega\setminus\Gamma_\mathrm{D}} = -(\mathbf{K}+\mathbf{M})\mathbf{U}_{\Gamma_\mathrm{D}}. \tag{18}$$

Eq. 18 is assembled and solved using COMSOL Multiphysics™ (COMSOL, 2006). UMFPACK (Davis, 2004) a direct solver of the Gauss elimination type is applied.

4.3 Convergence of the Finite Element Solution

Assuming the exact solution with regularity $u \in H^k(\Omega)$ and $u^h \in V_N$ being the FE solution, for a family of quasiuniform meshes the error $e_h := u - u^h$ of the numerical solution can be estimated in terms of the L^2-norm by

$$||e_h||_{L^2} = ||u - u^h||_{L^2} \leq CN^\alpha \tag{19}$$

where C is a constant that is dependent on the regularity of the exact solution, the polynomial degree p of the basis functions, the modelling domain Ω, and the triangulation but does not depend on the exact solution u itself and the number N of degrees of freedom (Babuška & Szabo, 1982). In the case of quasiuniform meshes, the ratio of size $h_{\max}$ of the largest element to the size $h_{\min}$ of the smallest element is bounded, i.e. the refinement applies to all parts of the mesh. The number N of degrees of freedom is proportional to h^{-2} in the 2D case whereas h denotes the mesh size, e.g. the circumdiameter of a triangle. Considering N instead of h for the standard error bound in eq. (19) allows to examine the convergence of the numerical solution not only in dependence on the mesh size (h-refinement) but also on the polynomial order of the finite elements (p-refinement).

The exponent

$$\alpha = -\frac{1}{2}\,\min\{k, p+1\} \tag{20}$$

is called the asymptotic rate of convergence or simply convergence rate. Sufficient regularity of the exact solution provided, i.e. $k > p+1$, the convergence rate α is governed by the order of the finite elements. Theoretical values are listed in table 1. Note, that the derived field components are approximated by polynomials of order $p-1$ and, hence, exhibit different convergence behaviour than the FE solution itself.

p	FE solution	derivative
1	-1.00	-0.50
2	-1.50	-1.00
3	-2.00	-1.50

Table 1: Convergence rate α for the simulated field components ("FE solution") and the derived field components ("derivative") in dependence of the dimensionality d and the polynomial order p of the finite elements.

For further details on the finite element method and a-priori error estimates the reader is referred to Babuška and Aziz (1972), Ciarlet (1978), and Strang and Fix (1973).
The quality of the FE solution might be improved by increasing the number of degrees of freedom N if the exact solution provides sufficient regularity. This is achieved by (i) increasing the number of mesh elements, i.e. reducing the size h of the mesh elements (h-refinement) or (ii) choosing higher-order basis functions (p-refinement). We restrict ourselves to $p = 1$ (linear basis functions), $p = 2$ (quadratic basis functions), and $p = 3$ (cubic basis functions). The h-refinement can be applied globally so that each element of the FE mesh is refined (uniform mesh refinement). On the basis of an error indicator function elements with large errors can be chosen for refinement such that the mesh is refined adaptively in regions only where strong variations of the solution occur. The initial mesh is created by the COMSOL Multiphysics™ mesh generator based on a Delaunay triangulation algorithm.

5 Convergence Studies

In the following the convergence curves display the error of the numerical solution with respect to the analytical solution as a function of the number of degrees of freedom (DOF). The relative root mean square (rms) error is calculated by

$$\text{relative rms}^2 = \frac{\sum_{i=1}^{N} |u_i^h - F_i|^2}{\sum_{i=1}^{N} |F_i|^2}, \tag{21}$$

where u_i^h denotes the numerical solution for all DOF i ($i = 1, ..., N$) including boundary DOF represented by Dirichlet boundary conditions and $F_i = E_i, H_i$ is the analytical solution for the electric and magnetic field, respectively. The relative rms error is determined on the finest grid of each hierarchy, i.e. each FE solution is mapped onto the finest grid and the error is computed for each DOF location there. Hence, for one hierarchy of meshes F_i ($i = 1, ..., N$) and, thus, its norm $|F_i|$ ($i = 1, ..., N$) are constant. Therefore, the estimates of convergence rates presented in section 4.3 are expected to apply for the discrete relative rms error measure (eq. 21) in the same manner as for the L^2-norm $||\cdot||_{L^2}$ that performs an area integration.
Note, that for the H-polarisation case the magnetic field H_i is considered whereas we examine the electric field E_i in the E-polarisation case in order to estimate the errors of the simulated fields first. In a second step the errors for the derived field components (H-polarisation: E_i, E-polarisation: H_i) are computed.
From eq. (19) the asymptotic convergence rate α_{as} is determined as the slope of a linear function

$$\log(\text{relative rms}) = \alpha_{\text{as}} \log(N) + \beta, \tag{22}$$

fitting the data for sufficiently large numbers N of DOF in a least-squares sense. $\log(\cdot)$ denotes the common logarithm. Additionally, a limiting convergence rate α_{lim} is computed by

$$\alpha_{\text{lim}} = \frac{\log(\text{relative rms}(n)) - \log(\text{relative rms}(n-1))}{\log(N(n)) - \log(N(n-1))}, \tag{23}$$

for the finest (n) and the second-finest $(n-1)$ grid of the appropriate hierarchy of meshes. If α_{lim} is significantly smaller than α_{as}, a stagnation of the relative rms error is indicated and, hence, the limit of the discretisation error of the boundary value problem is achieved.
Considering the convergence to the finest-grid solution, a relative rms deviation is calculated by

$$\text{relative dev}^2 = \frac{\sum_{i=1}^{N} |u_i^h - u_i^{h,n}|^2}{\sum_{i=1}^{N} |u_i^{h,n}|^2}, \tag{24}$$

where $u_i^{h,n}$ is the numerical solution on the finest (n) grid of the hierarchy. Assuming that the finest grid yields the most accurate solution, the coarser-grid solutions need to converge to the finest-grid solution. The asymptotic convergence rate is then obtained as the slope of

$$\log(\text{relative dev}) = \alpha_{\text{as}} \log(N) + \beta, \tag{25}$$

and the limiting convergence rate α_{lim} can be computed as

$$\alpha_{\text{lim}} = \frac{\log(\text{relative dev}(n-1)) - \log(\text{relative dev}(n-2))}{\log(N(n-1)) - \log(N(n-2))}. \tag{26}$$

for the second-finest $(n-1)$ and the third-finest $(n-2)$ grid.

5.1 The 2D homogeneous halfspace model: Comparison with the Analytical Solution

The following convergence studies are carried out for a homogeneous halfspace of the electrical conductivity $\sigma = 0.01\,\text{Sm}^{-1}$. The 2D model extends from x_1 = -100 km to x_2 = 100 km. The homogeneous halfspace is chosen to be 100 km deep. In the case of E-polarisation, an air space of 50 km height is added.

5.1.1 h-refinement vs. p-refinement

Figure 1 displays convergence curves for E-polarisation (left-hand side) and H-polarisation (right-hand side), respectively. The polynomial order of the finite elements varies among $p = 1$ (+), $p = 2$ (×), and $p = 3$ (□).
Obviously, the relative rms error decreases with increasing number N of DOF for E- and H-polarisation. Since for a given mesh, the number of DOF is enlarged by raising the polynomial order p of the finite elements higher-order basis functions yield smaller errors. The convergence rate, i.e. the slope of the linear trend line, however, is also increased with the polynomial degree of the shape functions. Hence, even with a similar number of DOF the relative rms error is smaller using higher-order basis functions. Note, that the computational effort is not only increased with the number N of DOF but also depends on the sparsity pattern of the system matrix which becomes more complex for higher-order finite elements. The number of non-zero elements grows with the polynomial degree of the basis functions (cf. Figure 2).
The convergence rates α_{as} and α_{lim} listed in Table 2 reflect the expected behaviour. The asymptotic convergence rate α_{as} is calculated as the slope of a linear function that fits the data for appropriate numbers N of DOF in a least squares sense. Data that do not exhibit a linear trend are neglected. In the present case, this applies to very coarse grids (N < 300). The asymptotic convergence rate is approximately the same for E- and H-polarisation and increases with the order of the finite elements as expected from section 4.3. The linear trends are displayed as black lines (–) in figure 1. The limiting convergence rate α_{lim} is computed as the slope between the largest and the second-largest number N of DOF. It does not differ by orders of magnitude from the asymptotic convergence rate α_{as} in all cases ($p = 1, 2, 3$, E- and H-polarisation). Hence, the limit of the discretisation error which will be indicated by a stagnation of the convergence curves, i.e. a small limiting convergence rate, is smaller than $2.4 \cdot 10^{-9}$ and $1.0 \cdot 10^{-8}$ for E- and H-polarisation, respectively.

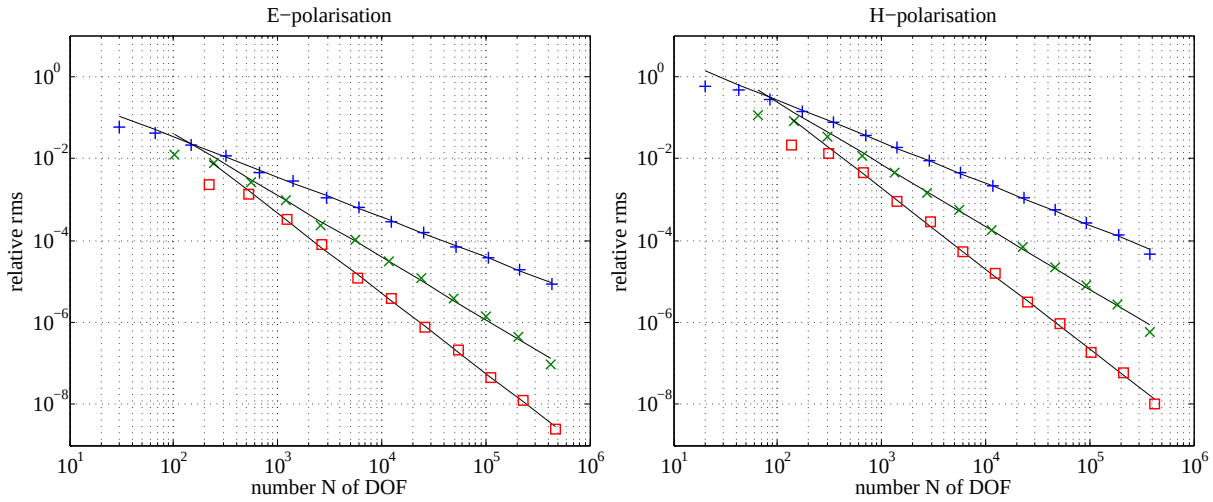

Figure 1: Convergence curves of the global relative rms error for E-polarisation (left-hand side) and H-polarisation (right-hand side) using linear ($p = 1$, +), quadratic ($p = 2$, ×) and cubic ($p = 3$, □) finite elements. Black lines (–) indicate the linear trend of each convergence curve for sufficiently large N. The frequency is $f = 0.1$ Hz.

	asymptotic conv. rate α_{as}			limiting conv. rate α_{lim}		
p	1 (linear)	2 (quadratic)	3 (cubic)	1 (linear)	2 (quadratic)	3 (cubic)
E-polarisation	-0.98	-1.51	-1.95	-1.06	-2.22	-2.32
H-polarisation	-1.01	-1.52	-1.96	-1.59	-2.23	-2.54

Table 2: Asymptotic (α_{as}) and limiting (α_{lim}) convergence rate for E- and H-polarisation depending on the polynomial degree p of the basis functions.

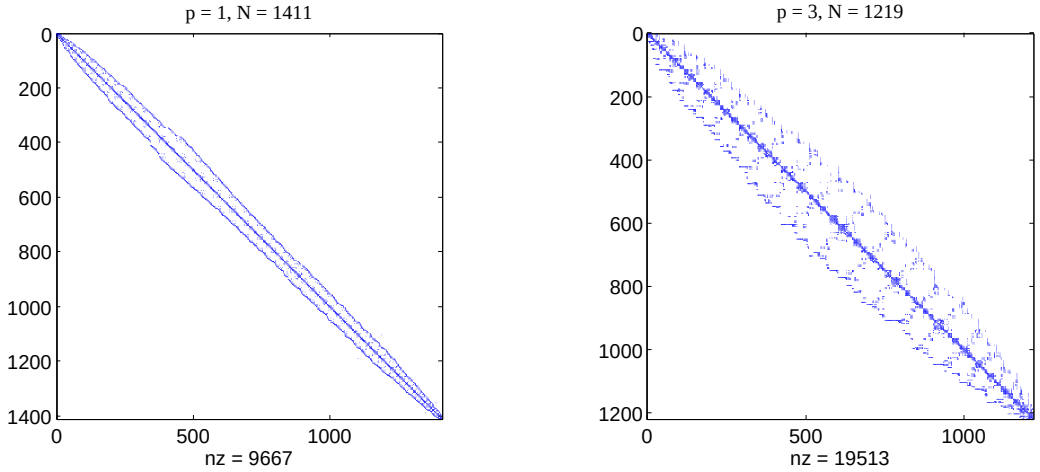

Figure 2: Sparsity patterns for the system matrices $\mathbf{K} + \mathbf{M}$ for linear ($p = 1$, N = 1411, left-hand side) and cubic ($p = 3$, N = 1219, right-hand side) finite elements. Numbers nz of non-zero elements are 9687 and 19513 for $p = 1$ and $p = 3$, respectively.

5.1.2 Frequency dependence

The size of the model used for the presented computations is well suited for the frequency of 0.1 Hz. The model boundaries are chosen to be 5 ... 10 times the skin depth away from the center of the model (cf. P. E. Wannamaker, 1989). Since exact bondary conditions are applied in the case of the homogeneous halfspace, we ensure that no error is introduced by boundary effects. Therefore, the dependence of the discretisation error on the frequency exclusively is examined in the following. The frequency is choosen to be $f = 0.01$, 0.1, or 1 Hz.
Figure 3 shows that for a given mesh the relative rms errors decrease if the frequency is reduced. This is due to an enlarged skin depth δ ($\delta \propto f^{-1}$) in which a larger number of DOF is distributed for a fixed mesh. The asymptotic convergence rate α_{as}, however, is almost independent of the frequency.

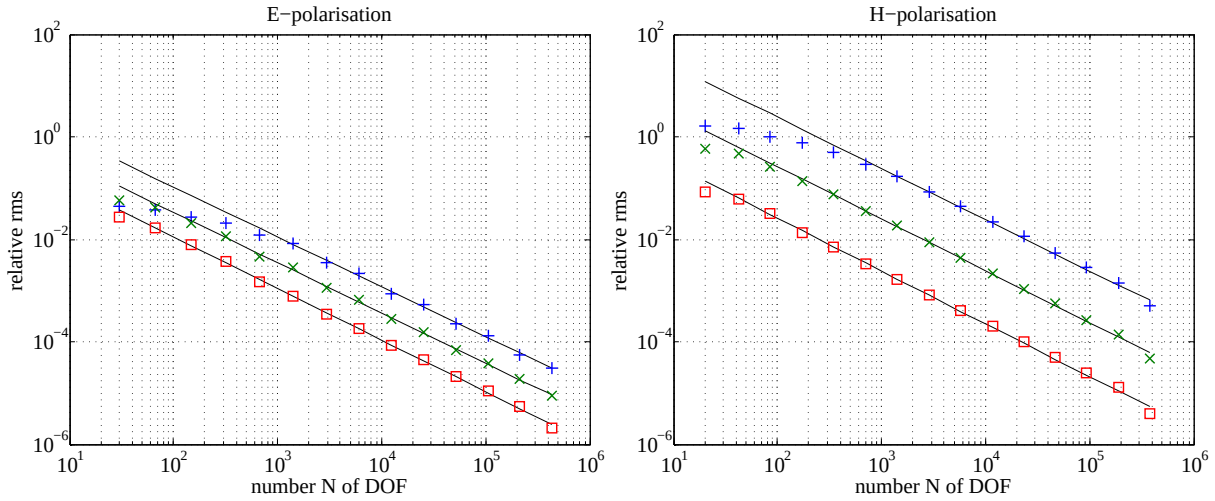

Figure 3: Convergence curves of the global relative rms error for E-polarisation (left-hand side) and H-polarisation (right-hand side) using linear ($p = 1$) finite elements. Frequencies are $f_1 = 1$ Hz (+), $f_2 = 0.1$ Hz (×), $f_3 = 0.01$ Hz (□). Black lines (–) indicate the linear trend of each convergence curve for sufficiently large N.

5.1.3 Grid refinement methods

All convergence studies presented so far have been performed applying a uniform longest-edge bisection as mesh refinement strategy. To compare this with other methods, Figure 4 displays convergence curves for linear shape functions using the longest-edge bisection (+), the regular refinement method (×), the adaptive mesh refinement in combination with the longest-edge bisection (□), and the adaptive regular mesh refinement (△), respectively, for generating the family of grids. In general, the regular mesh refinement (× and △) yields smaller errors than the longest-edge bisection (+ and □) considering both techniques for uniform (+ and ×) or adaptive mesh refinement (□ and △). Adaptive mesh refinement strategies do not prove to be advantageous here.

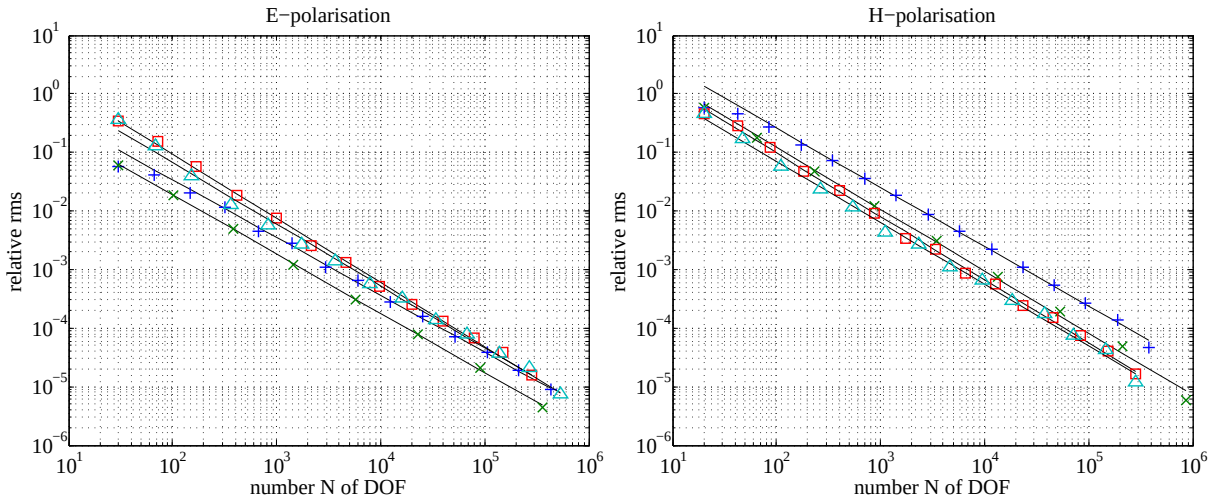

Figure 4: Convergence curves of the global relative rms error for E-polarisation (left-hand side) and H-polarisation (right-hand side) using linear ($p = 1$) finite elements. For generating the family of grids, the longest-edge bisection (+), the regular refinement method (×), the adaptive mesh refinement in combination with the longest-edge bisection (□), and the adaptive regular mesh refinement (△) are applied, respectively. The frequency is $f = 0.1$ Hz. Black lines (–) indicate the linear trend of each convergence curve for sufficiently large N.

5.1.4 Derived field components

After having discussed the convergence behaviour for the simulated field components, we will switch to the derived field components, i.e. the horizontal electric field for H-polarisation and the horizontal magnetic field for E-polarisation, respectively. In general, they show the same behaviour as the simulated field components. However, the relative rms errors are larger (cf. Figure 5 and Figure 1) and the convergence rates are lower for the derived field components (cf. Table 3 and Table 2). The asymptotic convergence rates α_{as} are in good agreement with those listed in Table 1 in section 4.3. Slightly reduced limiting convergence rates α_{lim} might indicate that the relative rms errors are approaching their limits. Due to limited computer memory capacity it is not possible to perform further refinement steps to assess the limit of the relative rms error.

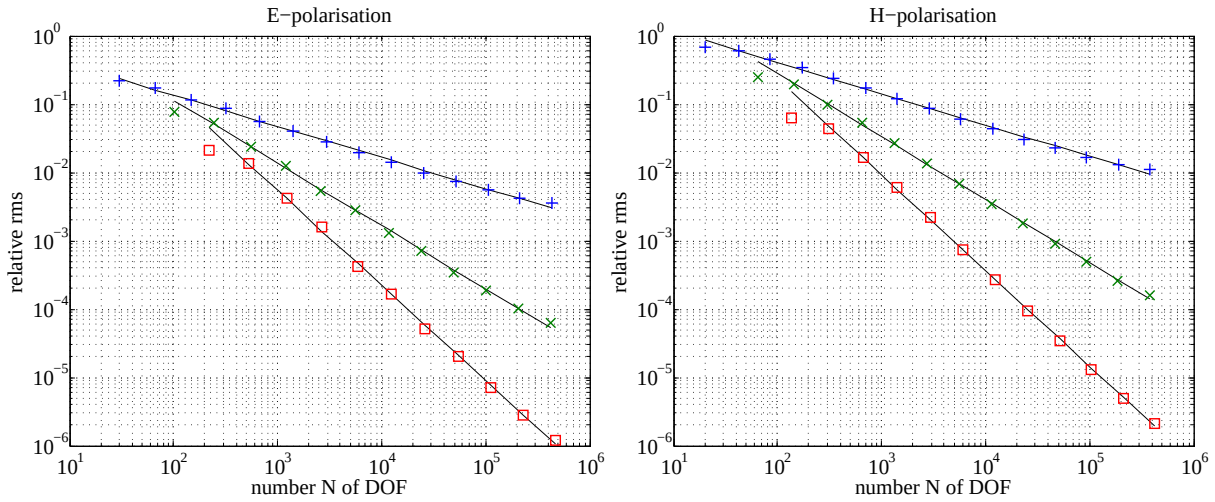

Figure 5: Convergence curves of the global relative rms error of the derived field components for E-polarisation (left-hand side) and H-polarisation (right-hand side) using linear ($p = 1$, +), quadratic ($p = 2$, ×) and cubic ($p = 3$, □) finite elements. Black lines (–) indicate the linear trend of each convergence curve for sufficiently large N. The frequency is $f = 0.1$ Hz.

	asymptotic conv. rate α_{as}			limiting conv. rate α_{lim}		
p	1 (linear)	2 (quadratic)	3 (cubic)	1 (linear)	2 (quadratic)	3 (cubic)
E-polarisation	-0.46	-0.92	-1.39	-0.23	-0.69	-1.21
H-polarisation	-0.46	-0.93	-1.40	-0.25	-0.73	-1.20

Table 3: Asymptotic (α_{as}) and limiting (α_{lim}) convergence rate of the derived field components for E- and H-polarisation depending on the polynomial degree p of the basis functions.

5.1.5 Local convergence

In contrast to the global convergence that we have verified in the last section, we focus on the local convergence in this section. The convergence curves for all DOF located at the earth's surface are compared to those for one point (0,0) at the earth's surface that is choosen independently of the positions of the DOF. From the geophysical point of view, local convergence, i.e. convergence of the solution in some arbitrary data points, is even more important than global convergence that includes DOF in regions of the model, e.g. at large depths, where no measured data exist.

Considering the left-hand and right-hand diagram of Figure 6 quite similar convergence behaviour is obtained for all DOF located at the earth's surface (left-hand side) and for the point (0,0) (right-hand side) in the case of E-polarisation for the frequency of $f = 0.1$ Hz. The appropriate convergence rates are listed in Table 4. They are

similar to the global convergence rates in Table 2. Convergence theory is not applicable in a local sense, however, in most cases local convergence rates are similar to global ones. Here, the asymptotic convergence rates α_{as} for the DOF on the earth's surface are lower than those for all DOF (cf. Table 2). For the point (0,0), the asymptotic convergence rates α_{as} are as high as the global ones, however, the relative rms error exhibits a more and more non-linear behaviour with increasing order of the finite elements (cf. Figure 6, right-hand side).

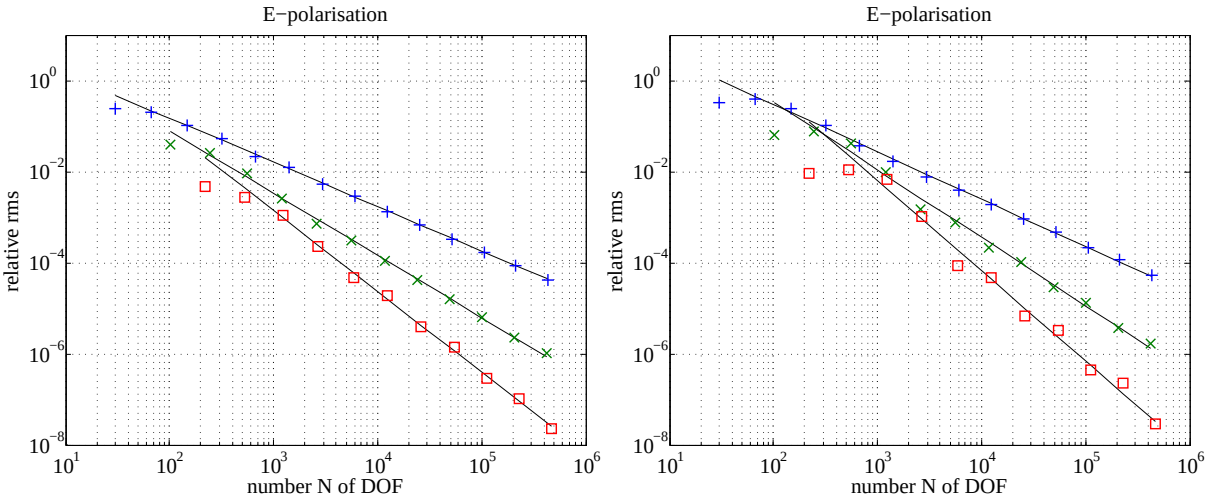

Figure 6: Convergence curves of the local relative rms error of the electric field for E-polarisation for all DOF on the earth's surface (left-hand side) and for the point (0,0) (right-hand side) using linear ($p = 1$, +), quadratic ($p = 2$, ×) and cubic ($p = 3$, □) finite elements. Black lines (–) indicate the linear trend of each convergence curve for sufficiently large N. The frequency is $f = 0.1$ Hz.

	asymptotic conv. rate α_{as}			limiting conv. rate α_{lim}		
p	1 (linear)	2 (quadratic)	3 (cubic)	1 (linear)	2 (quadratic)	3 (cubic)
earth's surface	-0.97	-1.36	-1.78	-0.99	-1.11	-2.07
point (0,0)	-1.04	-1.49	-1.98	-1.13	-1.09	-2.88

Table 4: Asymptotic (α_{as}) and limiting (α_{lim}) convergence rate of the electric field for E-polarisation at all DOF on the earth's surface and at the point (0,0) depending on the polynomial degree p of the basis functions.

Anomalous convergence behaviour can be observed in Figure 7 for the derived field components. Here, the application of cubic basis functions does not yield the smallest errors for all numbers N of DOF. Especially, regarding the convergence in the point (0,0) (right-hand diagram) more accurate results are obtained from the numerical solution computed with quadratic basis functions than from that computed with cubic basis functions for all N. Moreover, the relative rms error for quadratic basis functions does not decrease strictly monotonically.
For completeness, Figure 8 shows the local convergence of the derived field components for H-polarisation. Here, the local convergence behaviour is as expected from the global convergence studies (cf. Table 5). For the simulated magnetic fields the error on the earth's surface is zero because the boundary conditions for the numerical solution is represented by the analytical solution on the air-earth-interface.

5.2 The 2D homogeneous halfspace model: Comparison with the numerical finest-grid solution

In most cases, especially considering models that are close to reality, the true solution is unavailable to compare with and to estimate the discretisation error of the numerical solution. Therefore, in this section, the convergence of the numerical solution to the finest-grid solution of the 2D homogeneous-halfspace model introduced in section

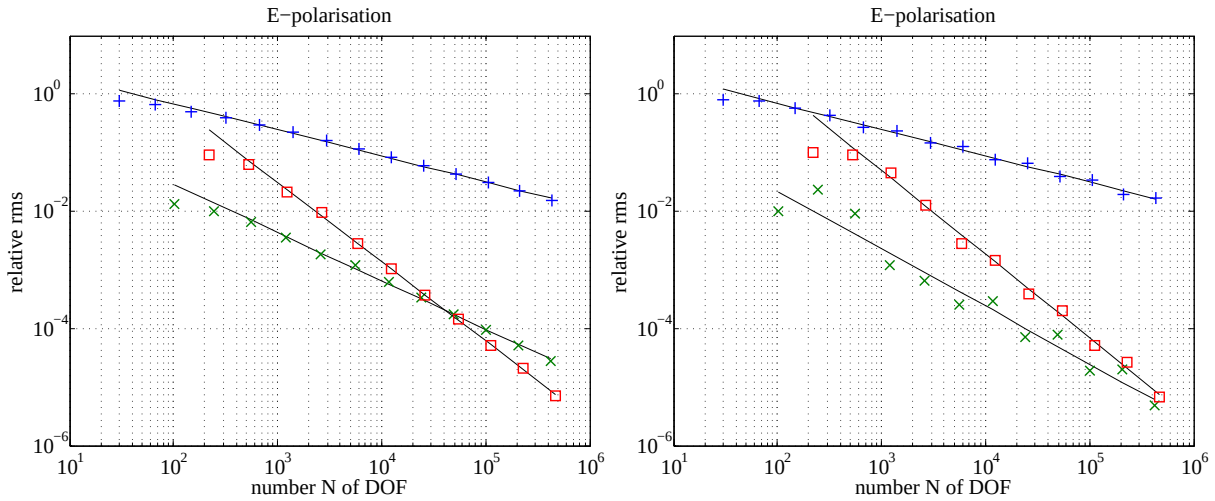

Figure 7: Convergence curves of the local relative rms error of the magnetic field for E-polarisation for all DOF on the earth's surface (left-hand side) and for the point (0,0) (right-hand side) using linear ($p = 1$, +), quadratic ($p = 2$, ×) and cubic ($p = 3$, □) finite elements. Black lines (–) indicate the linear trend of each convergence curve for sufficiently large N. The frequency is $f = 0.1$ Hz.

	asymptotic conv. rate α_{as}			limiting conv. rate α_{lim}		
p	1 (linear)	2 (quadratic)	3 (cubic)	1 (linear)	2 (quadratic)	3 (cubic)
earth's surface	-0.44	-0.91	-1.36	-0.46	-0.84	-1.20
point (0,0)	-0.45	-0.89	-1.35	-0.69	-1.14	-1.51

Table 5: Asymptotic (α_{as}) and limiting (α_{lim}) convergence rate of the electric field for H-polarisation at all DOF on the earth's surface and at the point (0,0) depending on the polynomial degree p of the basis functions.

5.1 is examined. We expect the numerical finest-grid solution to be close to the analytical solution and, hence, similar convergence behaviour for the relative deviation as shown in the previous section for the relative rms error. Figure 9 and Table 6 show the same convergence behaviour and convergence rates as Figure 1 and Table 2, respectively. Note, that the convergence curves for the comparison with the numerical finest-grid solution are supported by one point less than the ones for the comparison with the analytical solution since the finest-grid solution is needed to compute the relative deviation (eq. 24).

	asymptotic conv. rate α_{as}			limiting conv. rate α_{lim}		
p	1 (linear)	2 (quadratic)	3 (cubic)	1 (linear)	2 (quadratic)	3 (cubic)
E-polarisation	-1.01	-1.47	-1.95	-1.21	-1.67	-1.80
H-polarisation	-1.01	-1.49	-1.98	-1.02	-1.72	-1.67

Table 6: Asymptotic (α_{as}) and limiting (α_{lim}) convergence rate for E- and H-polarisation depending on the polynomial degree p of the basis functions.

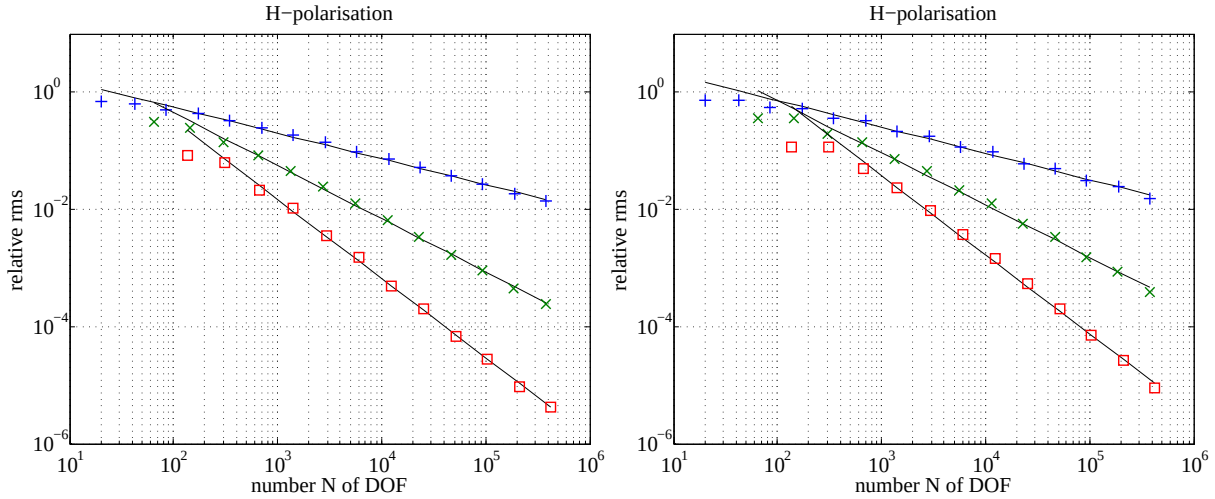

Figure 8: Convergence curves of the local relative rms error of the electric field for H-polarisation for all DOF on the earth's surface (left-hand side) and for the point (0,0) (right-hand side) using linear ($p = 1$, +), quadratic ($p = 2$, ×) and cubic ($p = 3$, □) finite elements. Black lines (–) indicate the linear trend of each convergence curve for sufficiently large N. The frequency is $f = 0.1$ Hz.

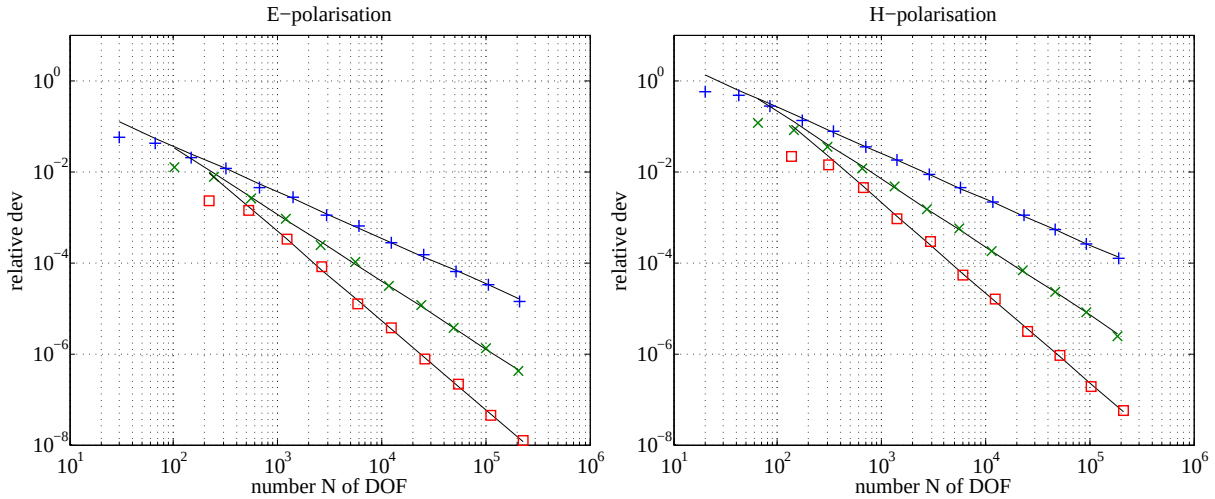

Figure 9: Convergence curves of the global relative deviation from the finest-grid solution for E-polarisation (left-hand side) and H-polarisation (right-hand side) using linear ($p = 1$, +), quadratic ($p = 2$, ×) and cubic ($p = 3$, □) finite elements. Black lines (–) indicate the linear trend of each convergence curve for sufficiently large N. The frequency is $f = 0.1$ Hz.

5.3 The 2D layered halfspace model

In this section, the model of a layered halfspace consisting of three layers of conductivities $\sigma_1 = 0.1\,\mathrm{Sm}^{-1}$, $\sigma_2 = 0.01\,\mathrm{Sm}^{-1}$, and $\sigma_3 = 100\,\mathrm{Sm}^{-1}$ and thicknesses $d_1 = 10\,\mathrm{km}$, $d_2 = 20\,\mathrm{km}$ is examined regarding the convergence behaviour of the numerical solution. We restrict ourselves to the comparison with the finest-grid solution since for the homogeneous-halfspace model in the previous section these results have proved to reflect the convergence behaviour with respect to the true solution that is usually unknown for close-to-reality models. At vertical conductivity contrasts the horizontal components of the electric and magnetic fields are continuous, however, the horizontal magnetic field component is not continuously differentiable (cf. eq. 2a) which affects the regularity of the numerical solution. Hence, the convergence behaviour is expected to be different from that for the homogeneous halfspace.

Figure 10 displays convergence curves for linear ($p = 1$, +), quadratic ($p = 2$, ×) and cubic ($p = 3$, □) finite elements in the case of E-polarisation (left-hand diagram) and H-polarisation (right-hand diagram) at a frequency of $f = 0.1\,\mathrm{Hz}$. The convergence rate, i.e. the slope of the convergence curves, does not vary with p in the same way as for the homogeneous halfspace model (cf. Figure 9). Table 7 illustrates that the convergence rate α_{as} is almost constant for $p \geq 2$ in the E-polarisation case and for even all p in the case of H-polarisation. This observation is in accordance with the expectations from section 4.3. If the true solution is not sufficiently smooth an increase of the polynomial order of the finite elements does not result in a higher convergence rate. For $f = 1\,\mathrm{Hz}$ (Figure 11) and $f = 0.01\,\mathrm{Hz}$ (Figure 12) the convergence behaviour is almost similar to that for the homogeneous halfspace model due to the small skin depth for $f = 1\,\mathrm{Hz}$ and the large skin depth $f = 0.01\,\mathrm{Hz}$ for which the layered halfspace model appears to be a homogeneous halfspace of σ_1 or σ_3, respectively.

Applying adaptive mesh refinement strategies, the convergence rates increase with the order p of the finite elements independently of the frequency (cf. Figure 13 and Table 8) to even higher values than predicted by eq. (20) and Table 1 in section 4.3.

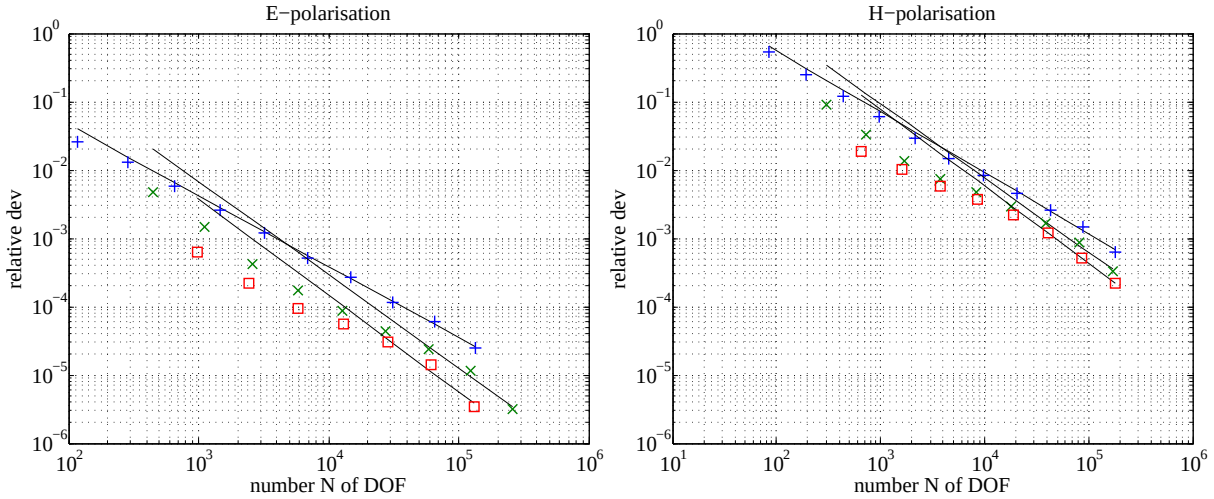

Figure 10: Convergence curves of the global relative deviation for E-polarisation (left-hand side) and H-polarisation (right-hand side) using linear ($p = 1$, +), quadratic ($p = 2$, ×) and cubic ($p = 3$, □) finite elements. Black lines (–) indicate the linear trend of each convergence curve for sufficiently large N. The frequency is $f = 0.1\,\mathrm{Hz}$.

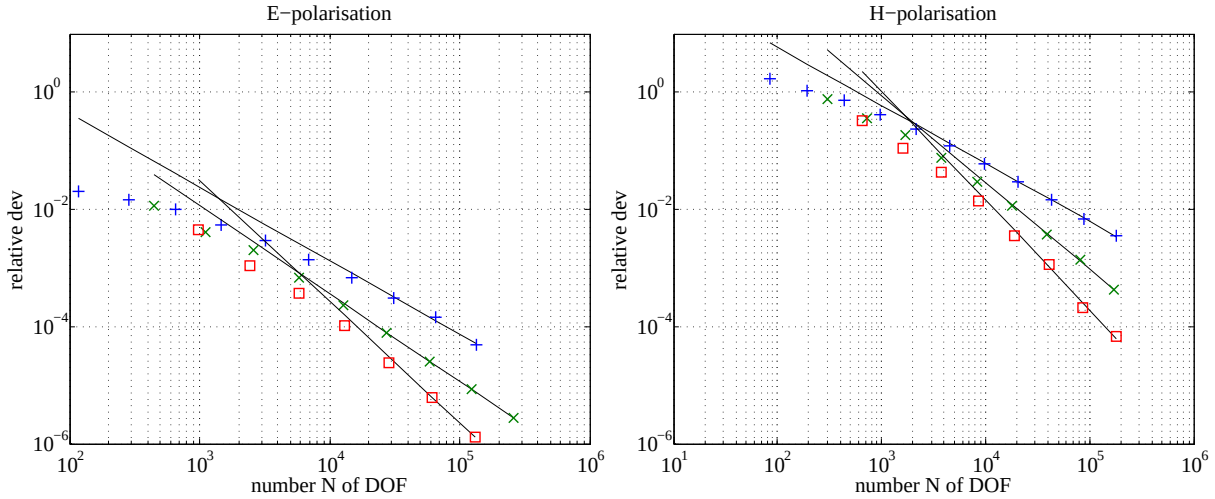

Figure 11: Convergence curves of the global relative deviation for E-polarisation (left-hand side) and H-polarisation (right-hand side) using linear ($p = 1$, +), quadratic ($p = 2$, ×) and cubic ($p = 3$, □) finite elements. Black lines (–) indicate the linear trend of each convergence curve for sufficiently large N. The frequency is $f = 1$ Hz.

		asymptotic conv. rate α_{as}			limiting conv. rate α_{lim}		
f [Hz]	p	1 (linear)	2 (quadratic)	3 (cubic)	1 (linear)	2 (quadratic)	3 (cubic)
0.01	E-polarisation	-1.18	-1.66	-1.72	-1.02	-1.68	-1.72
(fig. 12)	H-polarisation	-1.06	-1.38	-1.80	-1.34	-1.44	-2.09
0.1	E-polarisation	-1.04	-1.36	-1.41	-1.24	-1.75	-1.86
(fig. 10)	H-polarisation	-0.89	-1.09	-1.13	-1.17	-1.34	-1.15
1	E-polarisation	-1.26	-1.50	-2.06	-1.48	-1.52	-2.06
(fig. 11)	H-polarisation	-0.99	-1.49	-1.87	-0.90	-1.62	-1.54

Table 7: Asymptotic (α_{as}) and limiting (α_{lim}) convergence rate for E- and H-polarisation depending on the polynomial degree p of the basis functions.

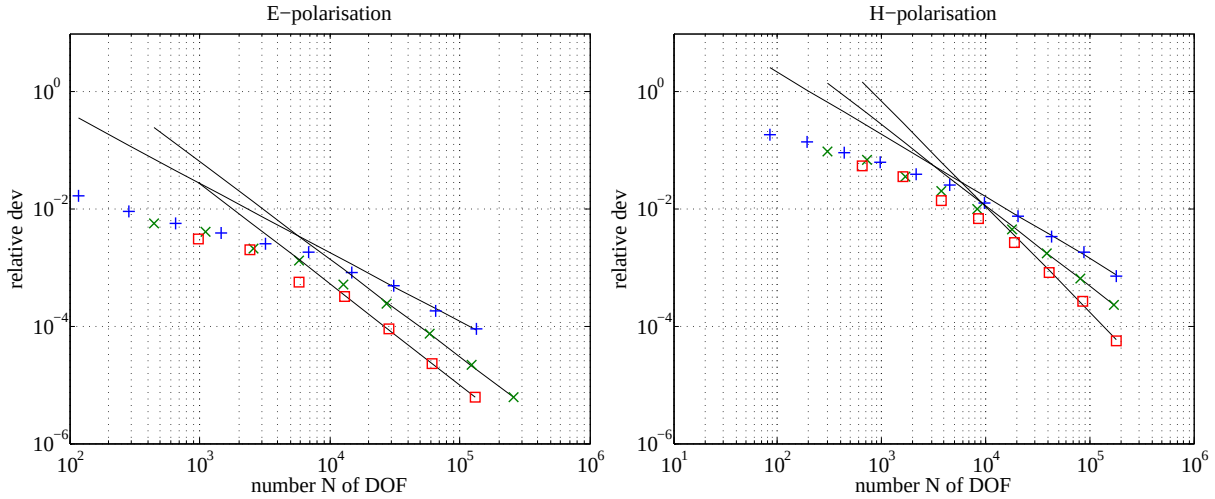

Figure 12: Convergence curves of the global relative deviation for E-polarisation (left-hand side) and H-polarisation (right-hand side) using linear ($p = 1$, +), quadratic ($p = 2$, ×) and cubic ($p = 3$, □) finite elements. Black lines (–) indicate the linear trend of each convergence curve for sufficiently large N. The frequency is $f = 0.01$ Hz.

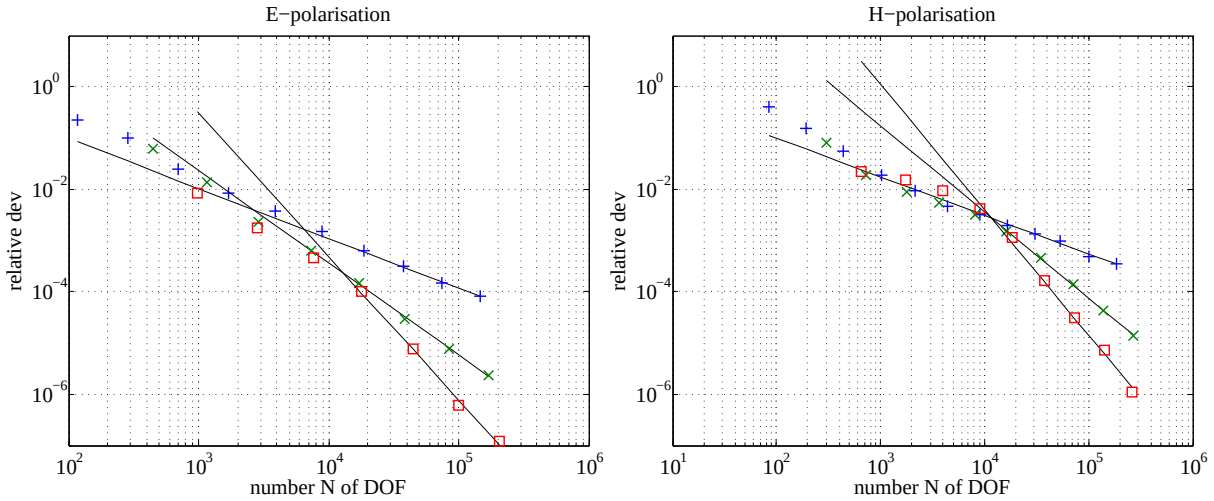

Figure 13: Convergence curves of the global relative deviation for E-polarisation (left-hand side) and H-polarisation (right-hand side) using linear ($p = 1$, +), quadratic ($p = 2$, ×) and cubic ($p = 3$, □) finite elements. Black lines (–) indicate the linear trend of each convergence curve for sufficiently large N. The frequency is $f = 0.1$ Hz. Adaptive mesh refinement.

	asymptotic conv. rate α_{as}			limiting conv. rate α_{lim}		
p	1 (linear)	2 (quadratic)	3 (cubic)	1 (linear)	2 (quadratic)	3 (cubic)
E-polarisation	-0.97	-1.80	-2.79	-0.82	-1.75	-2.24
H-polarisation	-0.75	-1.69	-2.44	-0.59	-1.80	-3.05

Table 8: Asymptotic (α_{as}) and limiting (α_{lim}) convergence rate for E- and H-polarisation depending on the polynomial degree p of the basis functions. Adaptive mesh refinement.

6 Conclusions

For the global convergence of the simulated and the derived field components of the 2D MT boundary value problem, we have verified the expectations according to the theory of the finite-element method. The convergence rate is independent of the frequency and, sufficient regularity of the true solution provided, increases with the polynomial degree of the basis functions. In general, if conductivity structures are involved, the exact solution is not expected to be sufficiently regular. In this case, adaptive mesh refinement strategies have proved to be advantageous. We have also demonstrated that the comparisons with the analytical and the numerical finest-grid solutions yield the same convergence rates. Hence, even if the true solution is unkown, a reasonable estimate of the accuracy of the FE solution can be obtained by convergence studies. However, global convergence rates do not necessarily apply to local convergence. We expect similar results for 3D FE simulation approaches.

References

Aprea, C., Booker, J., & Smith, J. (1997). The forward problem of electromagnetic induction: accurate finite-difference approximations for two-dimensional discrete boundaries with arbitrary geometry. *Geophysical Journal International*, *129*, 29-40.

Avdeev, D., & Avdeeva, A. (2009). 3d magnetotelluric inversion using a limited-memory quasi-newton optimization. *Geophysics*, *74*, F45-F57.

Babuška, I., & Aziz, A. K. (1972). *Survey lectures on the mathematical foundations of the finite element method with applications to partial differential equations* (A. K. Aziz, Ed.). Academic Press, New York.

Babuška, I., & Szabo, B. (1982). On the rates of convergence of the finite element method. *International Journal for Numerical Methods in Engineering*, *18*(3), 323–341.

Baranwal, V., Franke, A., Börner, R.-U., & Spitzer, K. (2011). Unstructured grid based 2-d inversion of vlf data for models including topography. *Journal of Applied Geophysics*, *75*, 363?372.

Brewitt-Taylor, C. R., & Weaver, J. T. (1976). On the finite difference solution of two-dimensional induction problems. *Geophysical Journal of the Royal astronomical Society*, *47*, 375-396.

Ciarlet, P. G. (1978). *The finite element method for elliptic problems*. North-Holland.

Coggon, J. H. (1971). Electromagnetic and Electrical Modeling by the Finite Element Method. *Geophysics*, *36*, 132-155.

COMSOL. (2006, August). COMSOL Multiphysics™ User's Guide, Version 3.5a [Computer software manual].

Davis, T. A. (2004, June). Algorithm 832: Umfpack - an unsymmetric-pattern multifrontal method. *ACM Transactions on Mathematical Software*, *30*(2), 196-199.

Farquharson, C. G., & Miensopust, M. P. (2011). Three-dimensional finite-element modelling of magnetotelluric data with a divergence correction. *Journal of Applied Geophysics*, *75*, 699-710.

Franke, A., Börner, R.-U., & Spitzer, K. (2007). Adaptive unstructured grid finite element simulation of two-dimensional magnetotelluric fields for arbitrary surface and seafloor topography. *Geophysical Journal International*, *171*, 71-86.

Hohmann, G. (1971). Electromagnetic scattering by conductors in the earth near a line source of current. *Geophysics*, *36*, 101-131.

Jones, & Pascoe, L. (1971). A gerneral computer program to determin the perturbation of alternating electric currents in a two-dimesnional model of a region of uniform conductivity with an embedded inhomogeneity. *Geophysical Journal of the Royal astronomic Society*, *24*, 3-30.

Jones, & Price. (1970). The Perturbations of Alternating Geomagnetic Fields by Conductivity Anomalies. *Geophysical Journal of the Royal astronomic Society*, *20*, 317-334.

Key, K., & Weiss, C. (2006). Adaptive fiinite-element modeling using unstructured grids: The 2d magnetotelluric example. *Geophysics*, *71*, G291-G299.

Mackie, R., & Madden, T. (1993). Three-dimensional magnetotelluric inversion using conjugate gradients. *Geophysical Journal International*, *115*, 215-229.

Mackie, R., Madden, T., & Wannamaker, P. (1993). Three-dimensional magnetotelluric modeling using finite-difference equations - theory and comparison to integral equation solutions. *Geophysics*, *58*, 215-226.

Mitsuhata, Y., & Uchida, T. (2004). 3D magnetotelluric modelling using the T-Ω finite-element method. *Geophysics*, *69*(1), 108-119.

Mogi, T. (1996). Three-dimensional electromagnetic modeling of magnetotelluric data using finite element method. *Journal of Applied Geophysics*, *35*, 185-189.

Nam, M., Kim, H., Song, Y., Lee, T., Son, J.-S., & Suh, J. (2007). 3d magnetotelluric modelling including surface topography. *Geophysical Prospecting*, *55*, 277-287.

Siripunvaraporn, W., Egbert, G., & Lenbury, Y. (2002). Numerical accuracy of magnetotelluric modeling: a comparison of finite difference approximations. *Earth, Planets and Space*, *54*, 721-725.

Strang, G., & Fix, G. J. (1973). *An analysis of the finite element method*. Prentice-Hall, Inglewood Cliffs.

Wait, J. R. (1953). Propagation of Radio Waves over a Stratified Ground. *Geophysics*, *20*, 416-422.

Wannamaker. (1991). Advances in three-dimensional magnetotelluric modeling using integral equations. *Geophysics*, *56*, 1716-1728.

Wannamaker, Hohmann, G., & San Filipo, W. (1984). Electromagnetic modeling of three-dimensional bodies in layered earths using integral equations. *Geophysics*, *49*, 60-74.

Wannamaker, P. E. (1989). PW2DIS Finite Element Program for Solution of Magnetotelluric Responses and Sensitivities of two-dimensional Earth Resistivity Structures, User Documentation [Computer software manual].

3D CSEM inversion: strategy and synthetic studies

Alexander Grayver and Rita Streich
Helmholtz Centre Potsdam - German Research Center for Geosciences, Germany
agrayver@gfz-potsdam.de, rstreich@gfz-potsdam.de

Abstract

We have developed a three-dimensional inversion scheme for controlled-source EM data in the frequency domain. The forward problem is solved using a finite-difference frequency-domain algorithm that efficiently solves the vector-Helmholtz equation for the electric field exploiting a secondary field approach and a parallel distributed direct solver. The forward algorithm is stabilized by explicitly enforcing a divergence condition and proved to be robust for low frequencies and high conductivity contrasts. The direct solution offers advantages over iterative approaches for multi-source modeling, and makes the algorithm well-suited for inversion.

For the inversion algorithm, we have implemented an inexact Gauss-Newton approach with the model update being calculated using either an LSQR or conjugate-gradient iterative solver. To stabilize the inversion, we use a Tikhonov additive regularization approach with a smoothing functional based on finite-difference discretization of the Laplacian operator. We apply a bounded logarithmic transform to the model parameters, which allows us to efficiently include *a priori* knowledge about the lower and upper bounds of model conductivity, such that the ambiguity of the ill-posed inverse task is reduced. To take advantage of distributed multi-core systems, a multilevel parallelization scheme has been implemented using the MPI and PETSc libraries. In the first level, we parallelize the computations over frequencies, and in the second level, we decompose the model grid. The distributed strategy of computation and data storage in connection with a parallel direct solver make this code scalable and suitable for inverting large models on high-performance systems.

Initial tests with synthetic data show that conductors as well as resistors can be recovered. However, absolute values of resistivity and exact locations of resistive objects are more difficult to resolve.

Inversion algorithm

The inversion scheme employs a forward modeling algorithm that is based on a finite-difference frequency-domain discretization of Maxwell's equations as described in Streich (2009). The discrete nonlinear inverse problem is formulated as the minimization of the objective function

$$\Phi(\mathbf{m}) = \Phi_d(\mathbf{m}) + \beta\Phi_m(\mathbf{m}) = ||\mathbf{W}_d\delta\mathbf{d}||^2 + \beta||\nabla^2\mathbf{m}||^2, \quad (1)$$

where vector $\delta\mathbf{d}$ contains the residuals between the observed and predicted data. $\mathbf{W}_d$ is a data weighting matrix, and vector $\mathbf{m}$ contains the model parameters. Presently, we use a finite-difference approximation of the Laplacian operator in 3D space as a smoothing stabilizer. The regularization parameter β is determined using a cooling approach, starting from a large value

and reducing it as the inversion proceeds (Newman and Alumbaugh, 1997). By using this strategy, we initially enforce a relatively large regularization in order to handle noisy data, establish larger-scale structure first and prevent the optimization process from producing unstable, physically unreasonable results. As the inversion proceeds, we gradually decrease the influence of the regularization to allow for smaller-scale structure being added to the model.

We use a direct solver in our forward algorithm, which is highly efficient in computing solutions for multiple sources once an expensive matrix factorization is completed. Because the factorization has to be repeated for every new model, optimization techniques that require a small number of model updates are best-suited for combination with the direct solver. Therefore, we use a Gauss-Newton approach, which exhibits super-linear convergence properties (Habashy and Abubakar, 2004). At the n^{th} iteration we solve a system of normal equations for the model update $\delta\mathbf{m}$

$$\mathbf{H}_n \delta\mathbf{m}_n = -\mathbf{g}_n, \tag{2}$$

where the gradient vector $\mathbf{g}_n$ of the objective functional (1) is given by

$$\begin{aligned}\mathbf{g}_n = \nabla\Phi_n(\mathbf{m}) &= \nabla\Phi_{d(n)}(\mathbf{m}) + \beta\nabla\Phi_{m(n)}(\mathbf{m}) \\ &= Re\{\mathbf{J}_n^T\mathbf{W}_d^T\mathbf{W}_d(\mathbf{d}_n^{pred} - \mathbf{d}^{obs})^*\} + \beta\mathbf{W}_n^T\mathbf{W}_n(\mathbf{m}_n - \mathbf{m}_{ref}),\end{aligned}$$

and the approximate Hessian matrix is

$$\mathbf{H_n} = \nabla\nabla\Phi_n(\mathbf{m}) = Re\{\mathbf{J}_n^T\mathbf{W}_d^T\mathbf{W}_d\mathbf{J}_n^*\} + \beta\mathbf{W}_n^T\mathbf{W}_n.$$

Here, $\mathbf{J}$ is the sensitivity matrix representing the partial derivatives of the data with respect to the model parameters, $\mathbf{W}_d$ is a data weighting matrix, vector $\boldsymbol{d}_n^{pred}$ is the predicted data at iteration n, d^{obs} is the observed data vector, m_{ref} is a reference model, which may be set to zero, and matrix $\mathbf{W}_n$ is a weighted finite-difference discretization of the Laplacian operator. Each row of this matrix corresponds to the discretization of the second-order spatial derivative for one model parameter. Multiplying different rows by different scalars allows us to weight the model parameters during the inversion. The symbol '*' denotes complex conjugate and superscript T denotes transpose.

A line-search procedure (Zhdanov, 2002) is used to determine a suitable step length α and compute the model at the next iteration as $\mathbf{m}_{n+1} = \mathbf{m}_n + \alpha\delta\mathbf{m}$. The line search ensures that the objective function decreases and prevents the inversion from taking too large steps between iterations. The system of normal equations (2) is solved using iterative methods such as conjugate gradients. In this way, we avoid explicit formation of the (huge) Hessian matrix. Alternatively, the model update can be determined in a least-squares framework using methods such as LSQR (Sasaki, 2001). The LSQR approach is more robust than the system of normal equations, since it avoids the explicit product $\boldsymbol{J}^H\boldsymbol{J}$ of the Jacobian. This product is known to be an ill-conditioned matrix, because the condition numbers of $\boldsymbol{J}$ and $\boldsymbol{J}^H\boldsymbol{J}$ are related as $\text{cond}(\boldsymbol{J}^H\boldsymbol{J}) = \text{cond}(\boldsymbol{J})^2$ (Paige and Saunders, 1982).

We also apply a bounded logarithmic transform to the model parameters (Commer and Newman, 2008). This allows us to include a priori knowledge about the lower and upper conductivity bounds efficiently, such that the ambiguity of the ill-posed inverse problem is reduced.

Synthetic study I: Cross-well configuration

We first invert cross-well EM data for a model containing a conductive blocky object (Figure 1a). Fifteen receivers and 15 transmitters are located in two wells. The operating frequency is 10 Hz and we record the vertical electric field. In computing model updates, we down-weight the cells containing the sources and receivers by applying low weights to the rows in the regularization matrix that correspond to these model parameters.

Inversion results are shown in Figure 1b and c. An overall misfit of 1.9 was achieved after ten iterations. Examples of data fit for transmitters above and near the vertical center of the anomaly are shown in Figure 2. The data fit for the source located in the center is better than that for the transmitter above the object. This is anticipated, because current flow through the object is stronger and thus its influence on the data is better constrained if the transmitter is located near the center of the object. Also notice that differences between the data for the initial and final model are much larger for source s08 than source s03.

For a similar model containing a resistor (Figure 3a), 15 iterations were required to achieve a misfit of 2.5 (Figure 3e, f). The position of the object is recovered reasonably well, but the resistivity is underestimated. This can have two reasons. Firstly, resistive objects are generally harder to resolve than conductive ones (Constable, 2010). Configurations with galvanic sources that excite strong TM-mode fields are best suited to highlight resistors (Cox, 1980; Weidelt, 2007; Constable, 2010). Secondly, our smoothing constraints that regularize the ill-posed inversion problem always favor smoothly varying conductivity models without sharp contrasts.

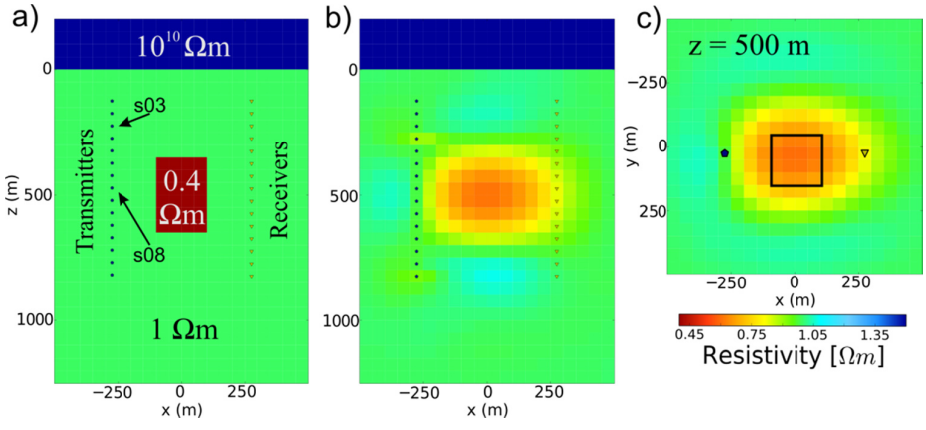

Figure 1: (a) True and (b, c) inverted models for a conductor. The position of the original object is outlined in (c).

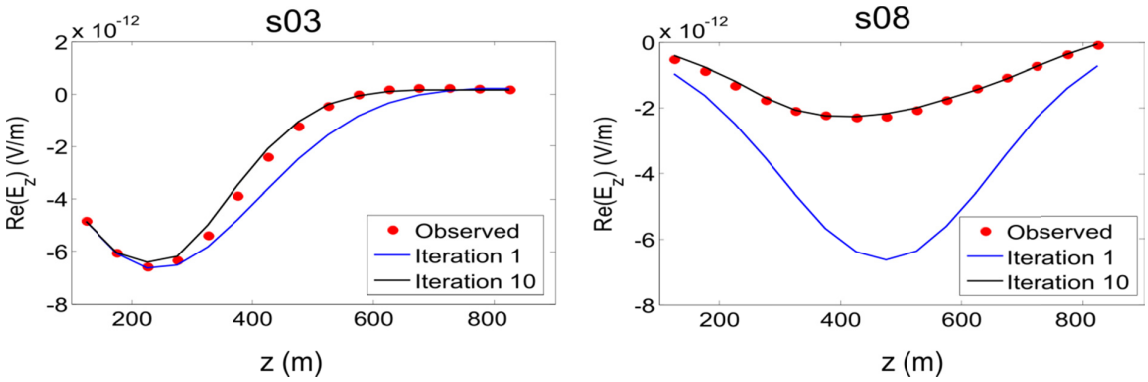

Figure 2: Data fit at each receiver for the two sources indicated in Figure 1a.

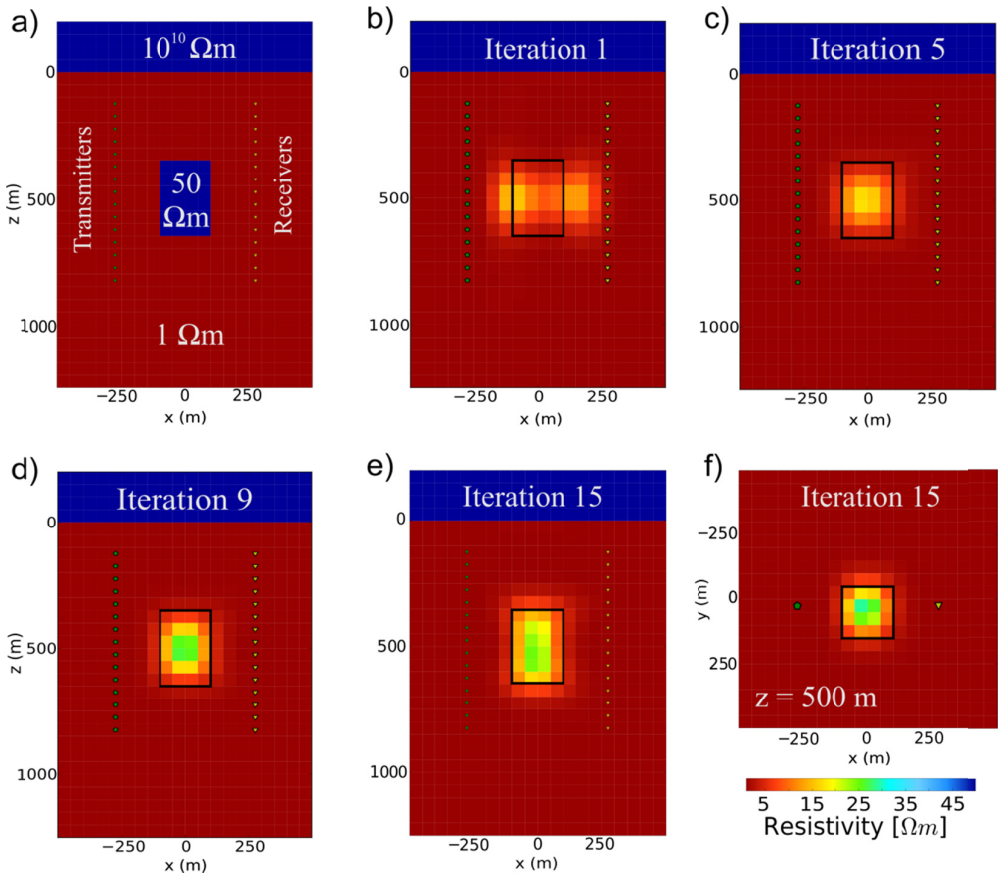

Figure 3: (a) True model containing a resistive object and (b – f) inversion models at four different iterations. The position of the original object is outlined.

Synthetic study II: Marine survey

We now apply our inversion scheme to a marine CSEM survey configuration (Figure 4a). Twenty-four receivers and 52 transmitters are deployed on and 50 m above the seafloor, respectively. The operating frequency is 0.75 Hz. The inline components of the electric and magnetic fields E_x and H_y for source-receiver offsets larger than 2.2 km were used, resulting in 840 complex data values. We use a horizontal to vertical smoothing ratio of 2 to 1 for this

test to emphasize laterally continuous structures. The conductivities of the air and seawater are kept constant during the inversion.

Inversion results for this model are shown in Figure 4b and c. After 20 iterations, a misfit of 1.0 was achieved, corresponding to optimum fit for pre-set data errors of 1%. The horizontal position and resistivity of the object are well resolved; however, its depth is slightly underestimated.

Figure 5 shows the reduction of data misfit and simultaneous gradual increase of the model norm. The different magnitudes of the data misfit and model norm are balanced by choosing the initial regularization parameter β (Equation 1) appropriately. The regularization parameter was reduced from its initial value by a factor of 20 during the inversion. The model norm remains nearly constant after iteration 12, indicating that the chosen regularization produces a stable result.

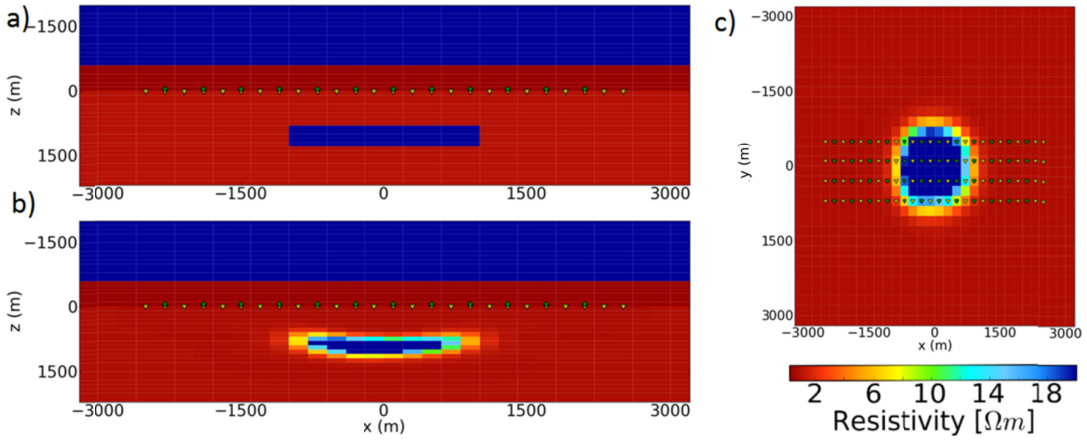

Figure 4: (a) True and (b, c) inverted models for a synthetic marine CSEM survey.

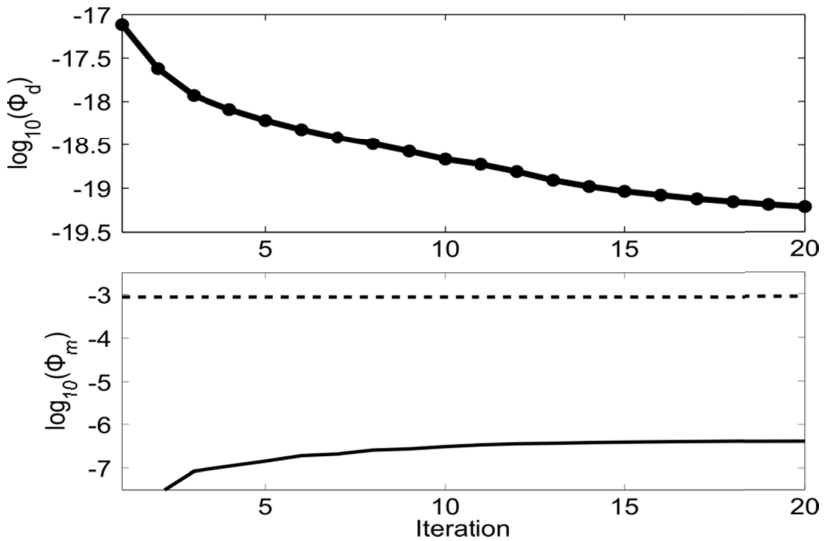

Figure 5: The data misfit Φ_d (top; see Equation 1) and values of the regularization functional Φ_m (bottom) as functions of iteration. The straight line indicates the value of the regularization term for the true model.

Computational cost

In Table 1, we summarize the computational time and memory required for the synthetic studies presented. The inversions were run in parallel on a distributed-memory platform. For both models, once the factorization is done, a single forward problem takes no more than 1% of the time spent on the factorization. For larger problems, the difference between factorization and solution times will be even larger, since the complexity of the factorization increases more rapidly than that of the forward elimination and backward substitution required to find the solution for one right hand side (Amestoy et al., 2006). Most of the remaining time during each inversion iteration is spent on computing background fields for 1D layered models and solving the system of normal equations. If a direct solver is used, the memory requirements are determined by the factorization. For our examples presented in Table 1, a four-fold increase in the number of model parameters results in a ten-fold increase in the memory requirements, demonstrating that the growth of memory consumption is a nonlinear function of the number of model parameters.

Conclusions

We have developed a 3D CSEM inversion scheme based on a direct forward solution approach, and demonstrated its performance in two different synthetic studies. Our examples show that using a direct solver for 3D inversion is computationally feasible.

As expected, we observe that it is crucial to choose source-receiver geometries and frequencies that maximize sensitivity in the region of interest. In addition, the choice of various inversion parameters (e.g., the starting model, conductivity bounds, regularization parameter) critically influences the convergence behavior.

The cooling approach for adjusting the regularization parameter results in good convergence behavior with smoothly decreasing data misfit and smoothly increasing model roughness. Furthermore, the accuracy of the sensitivities is crucial; regions of very high sensitivities near the sources and receivers had to be down-weighted to enforce model updates in the target regions. Strategies for improving the robustness of the algorithm need to be investigated further.

	Number of unknowns	Number of data points (complex)	Number of CPU cores	Size of system matrix	Time for factori-zation (s)	Time per forward solution (s)	Time per inversion iteration (s)	Total memory (GB)
Cross-well survey	19584	450	12	78336	6	0.05	55	2.5
Marine survey	80000	840	64	320000	30	0.2	350	27

Table 1: Computation time and memory required for inverting the two synthetic data sets.

Acknowledgments

This work is part of the MULTI-EM project, which is funded by the German Ministry of Education and Research, Grant 03G0746-MULTI-EM.

References

Amestoy, P. R., Guermouche, A., L'Excellent, J.-Y., and Pralet, S., Hybrid scheduling for the parallel solution of linear systems, Parallel Computing, 32, 136-156 (2006).

Commer, M. and Newman, G. New advances in three-dimensional controlled-source electromagnetic inversion. Geophysical Journal International, 172, 513-535 (2008).

Constable, S., Ten years of marine CSEM for hydrocarbon exploration, Geophysics, 75(5), 75A67–75A81 (2010).

Cox, C., Electromagnetic induction in the oceans and inferences on the constitution of the earth, Surveys in Geophysics, 4, 137-156 (1980).

Habashy, T. M., Abubakar, A., A general framework for constraint minimization for the inversion of electromagnetic measurements, Progress in Electromagnetics Research, 46, 265-312 (2004).

Newman, G. A. and Alumbaugh, D. L., Three-dimensional massively parallel electromagnetic inversion – I: Theory. Geophysical Journal International, 128, 345-354 (1997).

Paige, C. C. and Saunders, M. A., LSQR: An algorithm for sparse linear equations and sparse least squares, ACM Transactions on Mathematical Software, 8(1), 43-71 (1982).

Sasaki, Y., Full 3-D inversion of electromagnetic data on PC. Journal of Applied Geophysics, 46, 45-54 (2001).

Streich, R., 3D finite-difference frequency-domain modeling of controlled-source electromagnetic data: direct solution and optimization for high accuracy, Geophysics, 74, F95 (2009).

Weidelt, P., Guided waves in marine CSEM, Geophysical Journal International 171, 153–176 (2007).

Zhdanov, M. S., Geophysical inverse theory and regularization problems. Elsevier Science, 2002.

Erste Anwendung der Radiomagnetotellurik (RMT) und Transientelektromagnetik (TEM) auf Schlammvulkanen in Perekishkul/Aserbaidschan

H. Großbach[1], J. Adrian[1], B. Tezkan[1], A. Novruzov[2], A. Mamedov[2]

[1]Institut für Geophysik und Meteorologie, Universität zu Köln
[2]Baku State Universitity

grosbach@geo.uni-koeln.de

Zusammenfassung

Im Rahmen des von der Volkswagen-Stiftung finanzierten Projekts (ELMUD) wurde die innere Struktur von Schlammvulkanen erstmals mit RMT und TEM untersucht. Das Projekt wird in Zusammenarbeit mit der Baku State University durchgeführt.
Schlammvulkanismus ist ein in Aserbaidschan häufig auftretendes geothermales Phänomen, bei dem kontinuierlich Schlamm und Gas aus dem Erdboden austreten. Teilweise kommt es zudem zum Austritt von Erdöl.
Das Ziel dieses Projektteils ist die Auflösung der Leitfähigkeitsverteilung der oberen Schichten mit RMT und TEM und die Verbesserung der bisherigen Vorstellung des Aufbaus. In dieser Veröffentlichung werden die Ergebnisse der RMT-Messungen vorgestellt. *Adrian et al.* (2012) diskutiert die TEM-Ergebnisse.
Im Messgebiet nahe der aserbaidschanischen Hauptstadt Baku befinden sich 3 Schlammvulkangruppen, die auf 16 Profilen mit RMT untersucht wurden. Es wurden insgesamt 536 RMT Messpunkte gemessen.
Die RMT-Messungen wurden mit dem vierkanaligen RMT-F Gerät der Universität zu Köln durchgeführt, welches in einem Frequenzbereich von 10 kHz bis 1 MHz misst. Die Messdaten wurden mittels 1D und 2D Inversionen ausgewertet. Die Leitfähigkeitsverteilung der oberen 10 - 20 m konnte aufgelöst werden.
Trotz der geringen Eindringtiefen, aufgrund geringer Widerstände (im Bereich der Schlammvulkane $< 1\ \Omega$m), und geringen Kontrasten der Leitfähigkeit, konnten die Vulkane lateral detektiert werden. Die bisherigen Vorstellungen des Aufbaus der Schlammvulkane konnten verifiziert werden.

Schlammvulkanismus

Das Phänomen des Schlammvulkanismus wurde bereits im Mittelalter beschrieben und tritt weltweit auf. Auf Land sind mehr als 1000 Schlammvulkane bekannt und die Anzahl der Schlammvulkane im Meer wird auf über 5500 geschätzt [*Judd* (2005)].
Grundsätzlich kommt es bei Schlammvulkanen zu einem Ausfluss bzw. Auswurf von Schlamm, festem Gestein und Gasen. Die dabei freigesetzte Energie ist meist nur lokal messbar. Sowohl Größe als auch Form der so entstehenden Schlammvulkane können variieren.

Neben mächtig und schnell abgelagerten Sedimentschichten ist tektonischer Druck, den kollidierende Platten ausüben, eine wichtige Vorraussetzung für die Enstehung von Schlammvulkanismus [*Bohrmann et al.* (2006)]. Sind zudem große Mengen Flüssigkeit und Methan, welches sich aus dem organischen Material in den Ablagerungen bildet, im Erdboden vorhanden kommt es zur Bildung von Schlammvulkanen.
Man findet die meisten Schlammvulkane in Regionen tektonischer Kompression. Sie treten häufig in Verbindung mit Gashydrat- und Erdöllagerstätten auf, was sie zu einem möglichen Indikator der Lagerstätten macht.
Grundsätzlich werden bei einer schnellen Ablagerung von großen Mengen Ton Sedimentschichten mit einer ungewöhnlich hohen Porosität für die entsprechende Tiefe gebildet. Diese gering

kompaktierten Schichten stehen nach *Scholte* (2005) unter einem hohen Druck.
Gashydrate (Verbindungen mit z.B. Methan, Ethan und Propan) und Tonminerale existieren unter bestimmten Druck-Temperatur-Verhältnissen. Ändert sich dieses Verhältnis während der Sedimentation spalten sich die Gashydrate auf und Gas und Wasser werden freigesetzt. Die Freisetzung kann kontinuierlich oder plötzlich ablaufen, abhängig von der Schnelligkeit der Änderung des Druck-Temperatur-Verhältnisses. Schlammvulkanismus ist ein Mechanismus zur Entwässerung mächtiger Sedimentdecken in Kompressionszonen, in denen die Sedimentationsrate die Kompaktionsrate übersteigt.
Aufgrund der geringeren Dichte der Gase und Flüssigkeiten im Vergleich zu dem Umgebungsgestein steigen diese auf. Der Aufstieg folgt den tektonischen Gegebenheiten meist in Form eines dünnen Strahls. Wenn der Strahl dabei einen dünnen Riss in großer Tiefe durchfließt, kann dies die Ursache für eine Eruption sein [*Bohrmann et al.* (2006)].

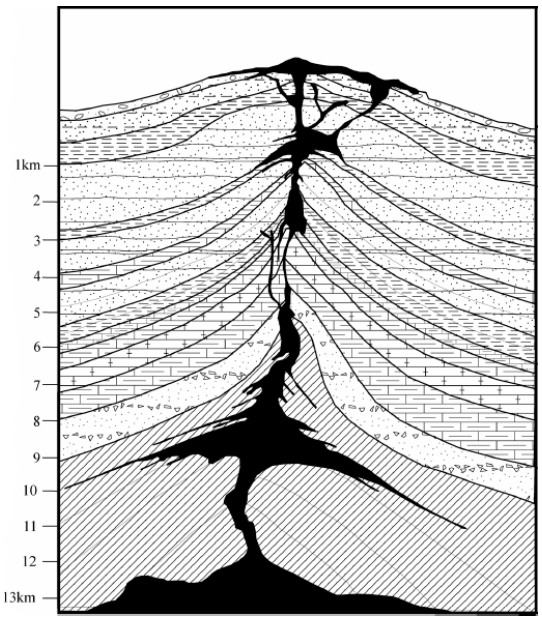

Abbildung 1: *Modell des Aufbaus eines Schlammvulkans in Aserbaidschan. Die Wurzel des Schlammvulkans reicht bis in mehr als 13 km Tiefe. Der aufsteigende Schlamm kann sich mit Material aus dem Jura bis zum Quartär vermischen und dieses an die Oberfläche befördern [Scholte (2005)].*

Nach *Feyzullayev* (2005) legen gravimetrische, radiometrische und Satelliten gestützte Messungen eine Tiefe der Schlammvulkanwurzeln in mehreren Kilometer Tiefe nahe. Davon geht auch *Scholte* (2005) in seinem Modell des Aufbaus von Schlammvulkanen in Aserbaidschan aus (siehe Abbildung 1). Die Wurzel des Schlammvulkans können in bis zu mehr als 13 km Tiefe reichen.

Bei seinem Aufstieg wählt der Schlamm den Weg des geringsten Widerstandes und folgt häufig Rissen im Untergrund. Während seismischer Aktivität kann es zu Bildung von Rissen kommen, was den Aufstieg des Schlamm begünstigt [*Panahi* (2005)].
Nach *Martinelli* (2005) scheint unabhängig von der Entfernung zu Ozeanen der Schlammvulkanismus von Salzwasser beeinflusst zu sein. Das Porenwasser in Subduktionszonen ist häufig mit Salzwasser und Kohlenwasserstoffen angereichert.

Für den unterirdischen Aufbau der Schlammvulkane gibt es verschiedene mögliche Modelle, wie in Abbildung 2 schematisch dargestellt. Es kann zu einer Diatremstruktur oder zur Ausbildung mehrerer Schlammvulkane oberhalb eines Schlammdiapirs kommen.
Bei einer Diatremstruktur verläuft der Schlotgang von der fluidreichen Schlammursprungsschicht bis zur Erdoberfläche und es kommt zur Ausbildung eines Schlammvulkans. Oberhalb eine Schlammdiapirs, einem aufsteigenden Körper aus Schlamm im Untergrund, bilden sich an der Erdoberfläche meist mehrere Schlammvulkane. Die Ausbildung der Struktur ist von den Gegebenheiten des Untergrundes abhängig, wobei die Diapirstruktur häufiger vorkommt.
Der sichtbare Aufbau der Schlammvulkane variiert je nach Menge und Art des Schlammaustritts. So kann der Durchmesser des Schlammvulkans einige Zentimeter bis zu mehreren Kilometern betragen. In der Höhe kann ein Schlammvulkan mehrere 100 Meter erreichen [*Bohrmann et al.* (2006)].
Ein langsamer, stetiger Schlammaustritt von dickflüssigem Material führt zu einer domartigen Struktur. In Abbildung 3 ist beispielhaft eine Seitenansicht eines domartigen Schlammvulkankegels abgebildet. Ein solcher Schlammvulkankegel wird auch als Gryphon bezeichnet. Tritt dünnflüssiges Material aus dem Schlammvulkan aus, bildet sich ein flacher oder fladenförmiger Kegel. Die Höhe des Kegels wird durch den Wasseranteil des austretenden Schlamms bestimmt. Je grö-

ßer der Wasseranteil desto flacher bleibt der Kegel des Schlammvulkans, welcher auch als Salse bezeichnet wird.
Bei heftigem und gasgeladenem Schlammaustritt kommt es zu kraterähnlichen Senken, in deren Zentrum sich häufig ein Kratersee aus sehr dünnflüssigem Schlamm bildet.
Trocknet der austretende Schlamm schnell, bilden sich Trockenrisse. Salz, welches im austretenden Schlamm enthalten ist, blüht dort aus [*Bohrmann et al.* (2006)].

Die Aktivität der bekannten Schlammvulkane variiert von stetigem leichtem Schlammausfluss bis zu heftigen Eruptionen. Man unterscheidet auf Grund der Aktivität drei Gruppen von Schlammvulkanen, die je nach einem beispielhaften Schlammvulkan benannt wurden [*Judd* (2005)]. Beim **Lokbatan Typ** handelt es sich um selten aktive Schlammvulkane, wobei die Ausbrüche kurzlebig und heftig sind. Durch leichte und kontinuierliche Aktivität verbunden mit einem fast ständigen Austritt von Gasblasen zeichnet sich der **Chikishlyar Typ** aus. Der Zwischentyp der beiden oben beschriebenen Typen wird als **Schugin Typ** bezeichnet.
Die Schlammvulkaneruptionen treten häufig in Verbindung mit Erdbeben auf. Nach *Panahi* (2005) gibt es einen Zusammenhang zwischen Erdbebenherd und Tiefe der Schlammkammer der Schlammvulkane. Die in Verbindung mit Schlammvulkanen auftretenden Erdbeben haben häufig einen Bebenherd in einer Tiefe von 8 bis 12 km [*Panahi* (2005)]. Dies ist ein weiterer Hinweis für die Tiefe der Wurzeln der Schlammvulkane.

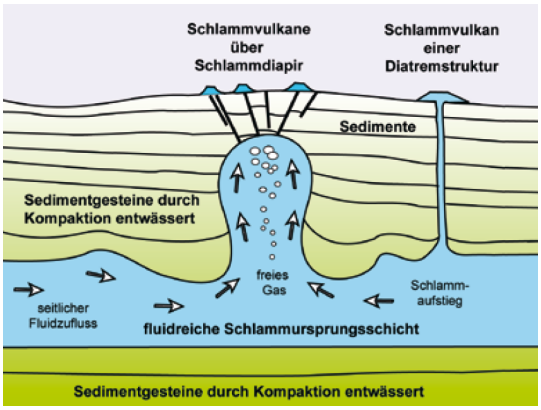

Abbildung 2: *Schemazeichnung von verschiedenartigem Schlammaufstieg aus einer Ursprungsschicht im tiefen Untergrund. Rechts ist ein Schlammvulkan mit einer Diatremstruktur skizziert. Die in der Mitte dargestellte Diapirstruktur kommt häufiger vor [Bohrmann et al. (2006)].*

Abbildung 3: *Durch langsamen und stetigen Schlammaustritt von dickflüssigem Material bildet sich ein domartiger Kegel (links). Flache Kegel werden durch den Austritt von flüssigem Material gebildet. Der Wasseranteil im austretenden Schlamm des rechts dargestellten Vulkans (ca. 2 m Durchmesser) ist höher als der des links abgebildeten Schlammvulkans. Die Bilder wurden an den untersuchten Schlammvulkanen in Perekishkul, Aserbaidschan während der Messung im April 2010 aufgenommen.*

Messung

Die Messungen fanden im April 2010 in Perekishkul, Aserbaidschan statt. Neben RMT-Messungen wurden auch TEM-Messungen durchgeführt. Im Folgenden werden die RMT-Messungen beschrieben und einige Ergebnisse beispielhaft vorgestellt. Die TEM-Messungen werden im Beitrag von *Adrian et al.* (2012) gesondert vorgestellt.

Messgebiet

Aserbaidschan liegt an der westlichen Flanke des Süd Kaspischen Beckens (siehe Abbildung 4), welches Teil des Alpen-Himalaya-Gürtels ist. Es grenzt an Russland, Georgien, Armenien, die Türkei und den Iran.

Wie in Abbildung 4 erkennbar, ist Aserbaidschan von dem Talysh Gebirge, dem Kaspischen Meer, dem großen Kaukasus und dem kleinen Kaukasus eingerahmt. Die beiden Flüsse Palaeo - Volga und Palaeo - Kura sorgten in der Vergangenheit für eine stete Sedimentzufuhr [*Scholte* (2005)].
Judd (2005) geht von 300 Schlammvulkanen in Aserbaidschan aus. Hauptsächlich handelt es sich dabei um den in Abschnitt *Schlammvulkanismus* beschriebenen *Chikishlyar Typ* mit einer kontinuierlichen, leichten Aktivität (z.B. die 3 untersuchten Schlammvulkane im Messgebiet).

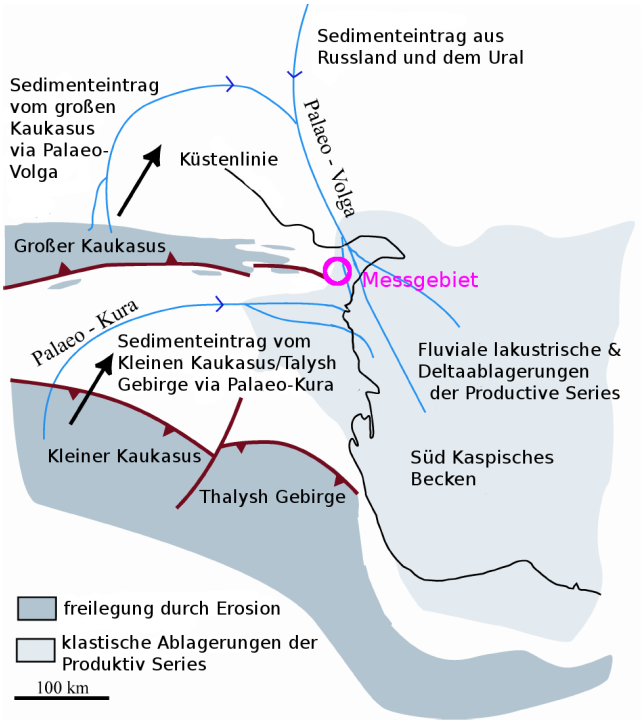

Abbildung 4: *Aserbaidschan liegt an der westlichen Flanke des Süd Kaspischen Beckens. Es ist vom Kaspischen Meer, dem großen und dem kleinen Kaukasus und dem Talysh Gebirge eingerahmt. Die beiden Flüsse Palaeo-Volga und Palaeo-Kura sorgten für eine stetige Sedimentzufuhr [bearbeitet Scholte (2005)].*

Aserbaidschan ist eine Region tektonischer Kompression, in der es zu Dichteinversion kommt. Dabei haben typische Mineralien wie Kalziumsulfat, Halit, Kaolinit, Smektit und Vermiculit kleinere Dichten als Quartz oder Feldspat. Zudem können sie große Mengen Wasser in ihrer Mineralstruktur speichern. Eine zweite treibende Kraft ist die hohe Last der Sedimente, welche in Aserbaidschan bis zu 20 km mächtig sein können.
Aserbaidschan ist besonders im Bereich des Süd Kaspischen Beckens von Brüchen durchzogen. Bruchhafte Verformungen gehen oft mit tektonischer Kompression einher. Die Lokationen der bekannten Schlammvulkangebiete korrelierien mit solchen tiefen Brüchen [*Panahi* (2005)].

Die Kombination der hohen Kohlenwasserstoffkonzentration und der geringen Wärmeleitfähigkeit des Schlammes führen zu einem kleinen Temperaturgradienten. Der austretende Schlamm hat Temperaturen zwischen 21 °C und 23 °C. Im Schlamm der drei im April 2010 untersuchten Schlammvulkane wurden Bakterien festgestellt. Zudem war im austretenden Schlamm sichtbar Erdöl vorhanden. Abbildung 5 zeigt sichtbares Erdöl im austretenden Schlamm auf dem linken Foto und Bakterienaktivität im rechten Foto.

Abbildung 5: *Im linken Foto ist deutlich Erdöl im austretenden Schlamm erkennbar. Der im Bild sichtbare Auschnitt ist ca. 30 cm x 20 cm groß. Das rechte Foto (Ausschnitt ca. 40 cm x 30 cm) zeigt Bakterienaktivität. Die Bilder wurden an Schlammvulkan 3 in Aserbaidschan während der Messung im April 2010 aufgenommen.*

Das Messgebiet befindet sich ca. 45 km entfernt von der Hauptstadt Baku. Untersucht wurden 3 Schlammvulkane, welche jeweils aus mehreren Gryphons bestanden.
Die Lage der Schlammvulkane und RMT-Profile ist in Abbildung 6 dargestellt. Insgesamt wurden auf 16 Profilen 536 Messpunkte aufgenommen. Der Messpunktabstand betrug zwischen 10 und 50 m. In 17 km Entfernung wurde westlich des Messgebiets ein Referenzprofil vermessen. Die Profile kreuzen die Vulkane. Profil 3 ist mit 8,5 km das längste gemessene Profil und das Referenzprofil mit 60 m das kürzeste.
Profil 2 verbindet die Vulkane 1, 2 und 3 und wird im folgenden als Verbindungsprofil bezeichnet. Es verläuft von West nach Ost entlang der vermuteten Streichrichtung und hat eine Neigung von 127° gegenüber Nord. Der Abstand zwischen Vulkan 1 und Vulkan 3 beträgt 2,4 km. Die weiteren Profile sind sowohl senkrecht als auch parallel zu dem Verbindungsprofil 2 angeordnet (siehe Abbildung 6). Diese Anordnung der Profile wird durch sichtbare Strukturen gestützt, welche an mehreren Stellen im Messgebiet sichtbar sind.
Die drei Schlammvulkane liegen jeweils auf einem ca. 100 m hohen Hügel.

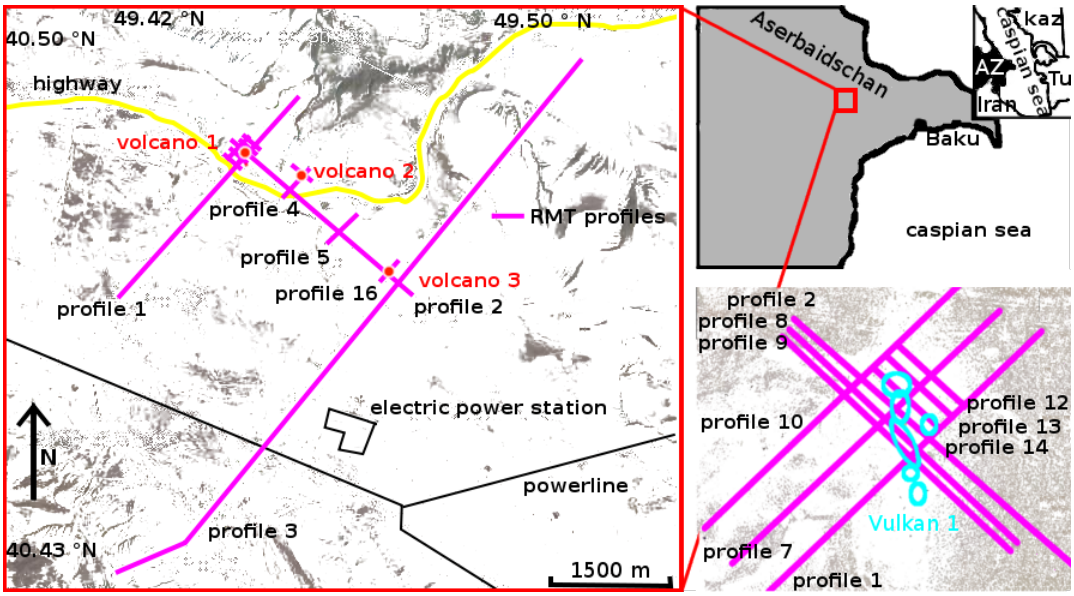

Abbildung 6: *Dargestellt ist die Lage der untersuchten Schlammvulkane und der Profile (magentafarbenen). Rechts unten ist eine vergrößtere Ansicht der Profile an Vulkan 1 abgebildet.*

Messinstrument

Bei der Radiomagnetotellurik handelt es sich um ein passives elektromagnetisches Verfahren, welches zur Erkundung der Leitfähigkeitsstrukturen des oberflächennahen Untergrundes geeignet ist.
Das Messprinzip ist in Abbildung 7 skizziert. Mit zwei Magnetfeldspulen und zwei kapazitiv angekoppelten Elektroden werden Sendesignale im Längst-, Mittel- und Langwellenbereich von 10 kHz bis 1 MHz registriert. Aus der magnetischen und der elektrischen Übertragungsfunktion werden der scheinbare spezifische Widerstand ρ_s [Ωm] sowie die Phase Φ [°] berechnet.

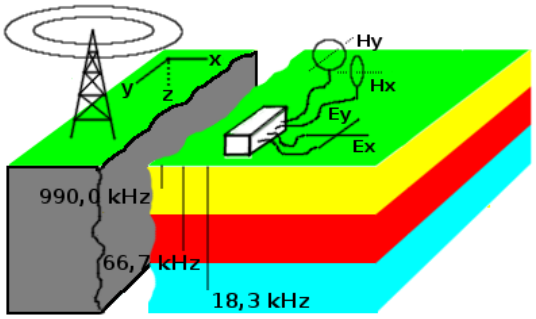

Abbildung 7: *Messprinzip der RMT*

Da hochfrequente elektromagnetische Wellen stärker gedämpft werden als niederfrequente Wellen, können durch die Verwendung unterschiedlicher Frequenzen verschiedene Eindringtiefen realisiert werden. Die maximale Eindringtiefe wird mit der niedrigsten gemessenen Frequenz erreicht. Bei der TE-Mode verläuft die gemessene elektrische Feldkomponente parallel zur Streichrichtung und die gemessene magnetische Feldkomponente senkrecht zu dieser. Die gemessene elektrische Feldkomponente der TM-Mode verläuft senkrecht und die gemessene magnetische Feldkomponente parallel zur Streichrichtung.

Als Messgerät wurde das in Kooperation mit der St. Petersburg State University entwickelte RMT-F-Gerät der Universität zu Köln verwendet [*Tezkan et al.* (2002)].

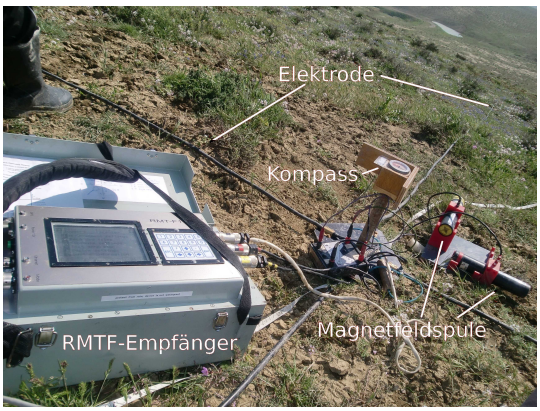

Abbildung 8: *Das RMT-F-Gerät besteht aus einem Empfänger mit vier Kanälen, zwei kapazitiv angekoppelten Elektroden (20 m lang) und zwei Iduktionsspulen. Die Magnefeldspulen werden in einem rechten Winkel zueinander aufgebaut. Parallel zu den Magnetfeldspulen und ebenfalls rechtwinklig zueinander werden die Elektroden ausgelegt.*

Mit zwei Induktionsspulen und zwei kapazitiv angekoppelten Elektroden werden Zeitreihen aufgezeichnet. Dies kann gleichzeitig über vier Kanäle geschehen und ermöglicht einen schnellen Messfortschritt.
Wie in Abbildung 8 erkennbar werden die Magnetfeldspulen in einem rechten Winkel zueinander aufgebaut. Die Elektroden werden parallel zu den Magnetfeldspulen ausgelegt.
In den aufgezeichneten Zeitreihen sind Informationen aller Frequenzen zwischen 10 kHz und 1 MHz enthalten. Die gemessenen Daten werden in zwei Frequenzbändern gespeichert. Das D2-Band (Sampling Frequenz: 312,5 kHz) beinhaltet die Frequenzen von 10 kHz bis 100 kHz und das D4-Band (Sampling Frequenz: 2,5 MHz) die Frequenzen von 100 kHz bis 1 MHz. Mit der Processingsoftware **sm25** kann später eine Frequenzauswahl entsprechend der Moden getroffen werden.
Im Messgebiet konnten Frequenzen der TE- als auch der TM-Mode empfangen werden. Zudem war die kleinste empfangene Frequenz 10,1 kHz und die größte empfangene Frequenz betrug 990,0 kHz. Es wurde somit eine gleichmäßige Auflösung der oberen 10 - 20 m erreicht.
Im Folgenden werden Ergebnisse der gemeinsamen Inversion beider Moden beispielhaft vorgestellt.

Ergebnisse

Nach dem Prozessieren der Rohdaten mit dem Programm **sm25** [*Tezkan et al.* (2002)] wurden 2D Inversionen mit dem Programm **rund2inv_nlcg2_fast** von *Mackie et al.* (1997) durchgeführt.
Bei der Interpretation der Ergebnisse werden für die 2D Inversionen nur Bereiche mit Sensitivitätsdichten kleiner 3 betrachtet, da diese Bereiche ausreichend gut aufgelöst sind [*Seher* (2005)]. Für die einzelnen Profile ist die Isolinie der Sensitivitätsdichten gleich 3 weiß eingezeichnet. Für die gemeinsame Darstellung der Profile für die Schlammvulkane werden die Bereiche mit Sensitivitätsdichten größer 3 transparent dargestellt. Die Lokation der Messpunkte ist durch schwarze Punkte gekennzeichnet und die der Gryphons der Schlammvulkane magentafarben.
Zusätzlich wurden für alle 536 Messpunkte der 16 Profile 1D Inversionen mit dem Programm **Emuplus** durchgeführt [*Großbach* (2011), *Wiebe* (2007)].

Beispielhaft werden die Ergebnisse der Profile 2 und 16 im Bereich des Schlammvulkans 3 vorgestellt (siehe Abbildung 6). Des Weiteren werden neun Profile im Bereich des Schlammvulkans 1 gezeigt (siehe Abbildung 6).

Vulkan 3

Das Profil 2 verläuft von West nach Ost und die Länge beträgt insgesamt 2,45 km. Es verbindet die Schlammvulkane 1 und 3. Die genaue Lage des Profils kann Abbildung 6 entnommen werden. Der Schlammvulkan 3 liegt im Bereich der Profilmeter 2100 bis 2120 (siehe Abbildung 13). In

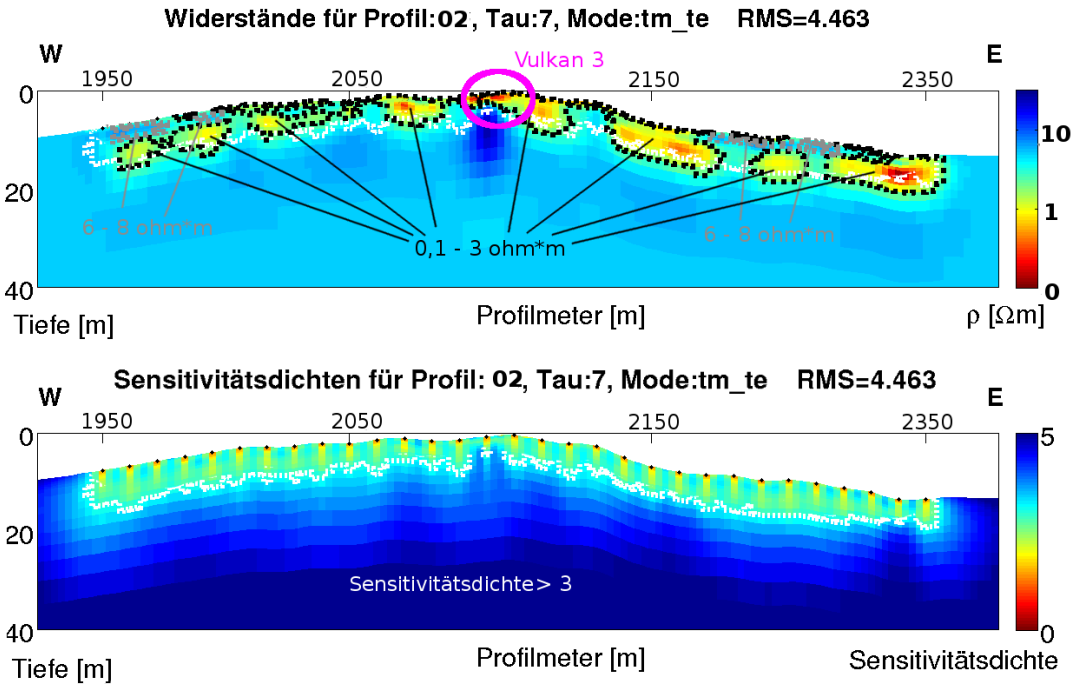

Abbildung 9: *Der spezifische Widerstand des 2D Inversionsergebnisses für Profil 2 ist für die Profilmeter 1950 bis 2350 dargestellt (oben). Bereiche spezifischer Widerstände zwischen 0,1 und 3 Ωm sind schwarz markiert. Graue Markierungen kennzeichnen Bereiche spezifischer Widerstände zwischen 6 und 8 Ωm. Die untere Abbildung zeigt die Sensitivitätsdichten des Inversionsergebnisses. Im Bereich der Profilmeter 2100 bis 2120 liegt der Schlammvulkan 3.*

Abbildung 9 sind die spezifischen Widerstände (oben) und die Sensitivitätsdichten (unten) der 2D Inversionsergebnisse für Profilmeter 1950 bis 2350 des Profils 2 dargestellt. Die spezifischen Widerstände liegen zwischen 0,3 und 8 Ωm. Bereiche spezifischer Widerstände zwischen 0,1 und

3 Ωm sind schwarz und Bereiche spezifischer Widerstände zwischen 6 und 8 Ωm grau markiert. Es ist keine durchgängige Schichtung erkennbar. Im Bereich des Schlammvulkans 3 ist der Untergrund mit 0,1 bis 1 Ωm leitfähiger als auf dem restlichen Profil.
Die Datenanpassung zwischen kalkulierten (rot) und gemessenen Daten (schwarz) ist beispielhaft für die Frequenz 45.9 kHz in Abbildung 10 dargestellt.

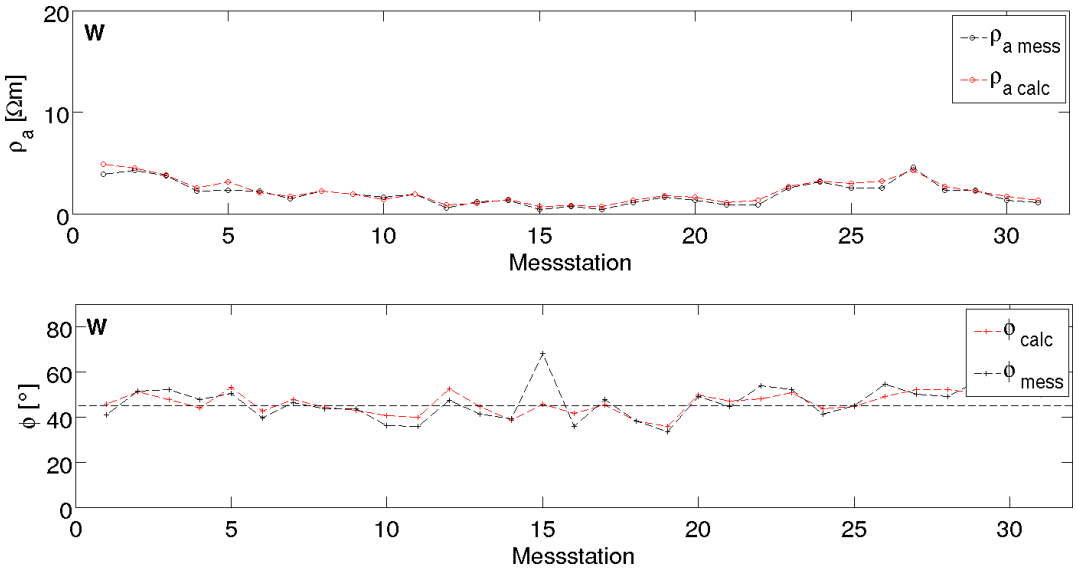

Abbildung 10: *Dargestellt ist die Anpassung zwischen kalkulierten (rot) und gemessenen Daten (schwarz) für die Frequenz 45.9 kHz für das in Abbildung 9 dargestellte Ergebnis.*

Das Profil 16 verläuft von Süd nach Nord über Schlammvulkan 3. Es hat eine Länge von 210 m. Die genaue Lage kann man Abbildung 6 entnehmen. Im Bereich der Profilmeter 50 bis 130 verläuft das Profil 16 auf dem Schlammvulkan 3. Das Ergebnis der 2D Inversion für Profil 16 ist

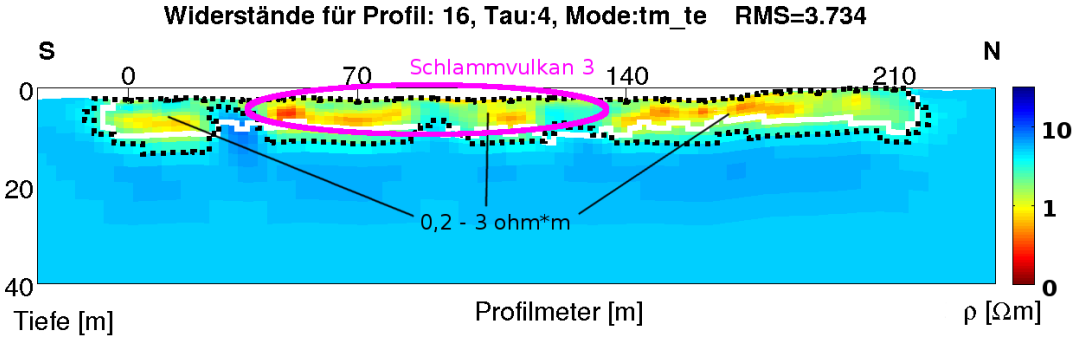

Abbildung 11: *Dargestellt ist das Ergebnis der 2D Inversion für Profil 16. Bereiche spezifischer Widerstände zwischen 0,2 und 3 Ωm sind schwarz markiert. Im Bereich der Profilmeter 50 bis 130 verläuft das Profil 16 auf dem Schlammvulkan 3.*

in Abbildung 11 zu sehen.
Entlang des Profils 16 liegen die spezifischen Widerstände des gesamten Untergrundes zwischen 0,2 und 3 Ωm. Im Bereich des Messpunktes 5 (Profilmeter 50) liegen die spezifischen Widerstände zwischen 0,2 bis 1 Ωm.
In Abbildung 12 sind die 2D Inversionsergebnisse der Profile 2 und 16 abgebildet. Bereiche mit Sensitivitätsdichten größer als 3 sind transparent dargestellt. Bereiche ähnlicher spezifischer Widerstände beider Profile sind durch schwarze Markierungen gekennzeichnet.
Die spezifischen Widerstände der 2D Inversionsergebnisse der Profile 2 und 16 liegen zwischen 0,1

und 8 Ωm. Dieser Wertebereich stimmt gut mit dem Wertebereich der spezifischen Widerstände des Referenzprofils 7 mit 0,1 bis 10 Ωm überein.
Im Bereich des Schlammvulkans 3 liegen die spezifischen Widerstände zwischen 0,1 und 1,5 Ωm.

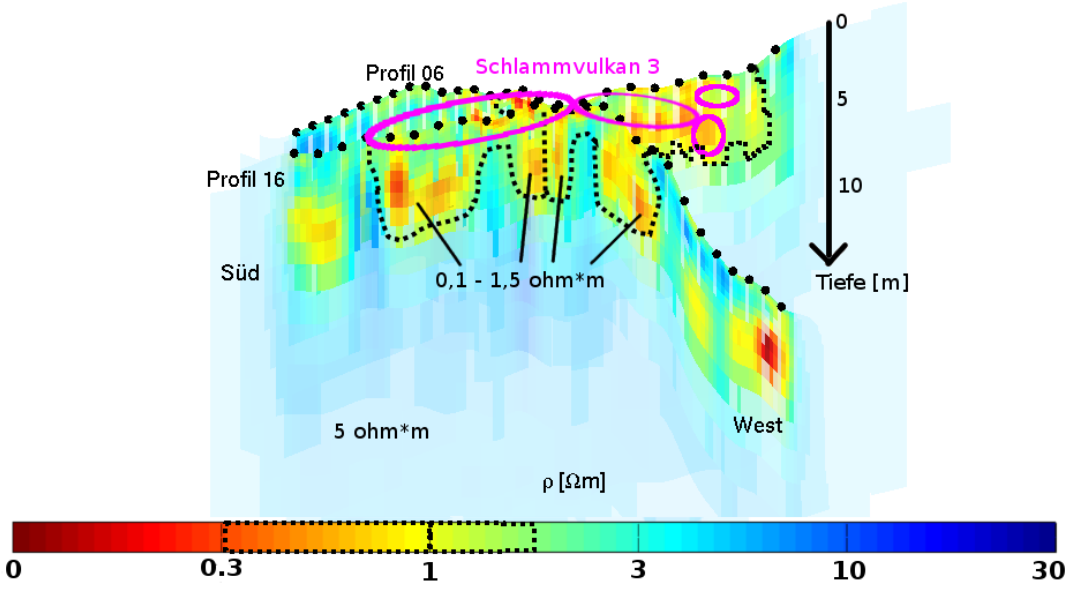

Abbildung 12: *Dargestellt sind die spezifischen Widerstände der 2D Inversionsergebnisse der Profile 2 und 16, wobei Bereiche mit Sensitivitätsdichten größer als 3 transparent sind. Die Inversionsergebnisse sind entsprechend ihrer Koordinaten angeordnet (in x-y-Ebene befindet sich Erdoberfläche, Tiefe auf z-Achse aufgetragen). Magentafarben sind die Umrisse der Gryphons eingezeichnet. Bereiche ähnlicher spezifischer Widerstände beider Profile sind durch schwarze Markierungen gekennzeichnet.*

Abbildung 13: *Abgebildet ist Schlammvulkan 3. Man erkennt die einzelnen Schlammaustrittsstellen. Das Bild wurde in Perekishkul, Aserbaidschan während der Messung im April 2010 aufgenommen.*

Vulkan 1

In Abbildung 14 sind die Ergebnisse der 2D Inversionen der Profile 1, 2, 7, 8, 9, 10, 12, 13 und 14 im Bereich des Schlammvulkans 1 (siehe Abbildung 15) gemeinsam dargestellt. Grundsätzlich zeigen die Ergebnisse der 2D Inversionen der einzelnen Profile ähnliche Strukturen im Untergrund. In der näheren Umgebung des Schlammvulkans 1 liegen die spezifischen Widerstände hauptsächlich zwischen 0,1 und 2 Ωm (grau markiert). Bereiche spezifischer Widerstände zwischen 0,1 und 1,5 Ωm in der Umgebung der Gryphons (magentafarben markiert) sind schwarz gestrichelt gekennzeichnet.

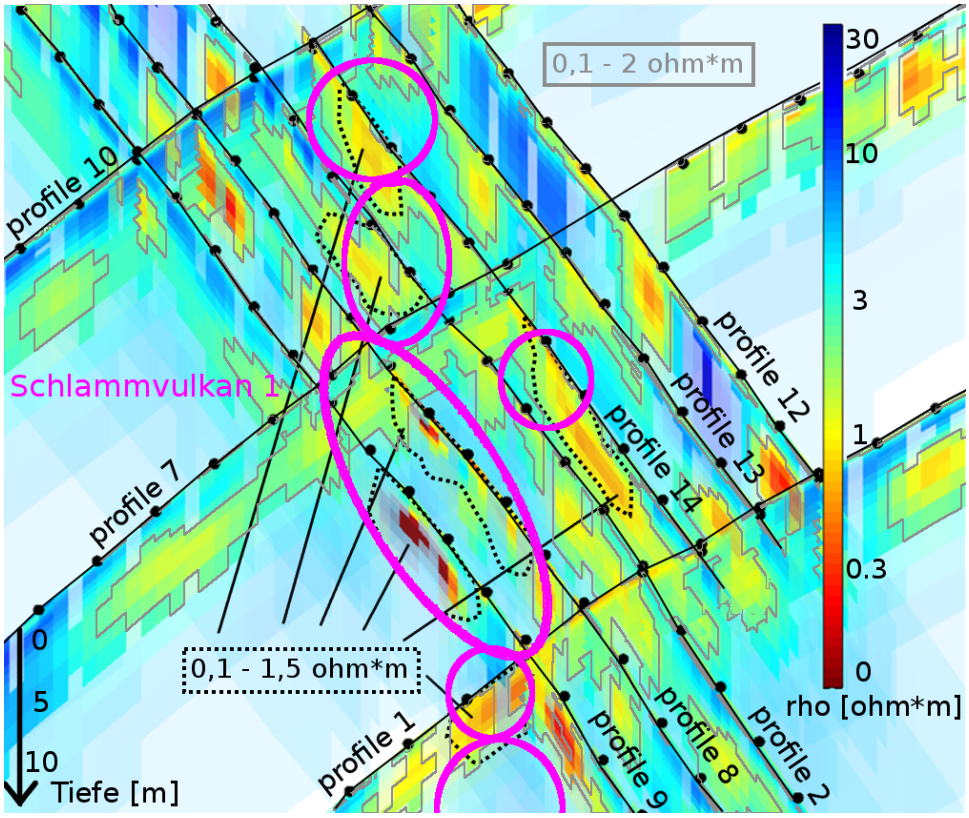

Abbildung 14: *Dargestellt sind die spezifischen Widerstände der 2D Inversionsergebnisse (Bereiche mit Sensitivitätsdichten > 3 transparent). Profile sind durch schwarze Striche gekennzeichnet, grau sind Bereiche zwischen 0,1-2 Ωm und Bereiche zwischen 0,1-1,5 Ωm in der direkten Umgebung der Gryphons (magentafarben) sind schwarz gestrichelt.*

Diskussion

Die Inversionergebnisse der Profile 1 bis 16 zeigen spezifische Widerstände zwischen 0,1 und 21 Ωm. In guter Korrelation zur oberflächlich sichtbaren Ausdehnung der Schlammvulkane sind im Untergrund gutleitende Bereiche mit spezifischen Wideständen zwischen 0,1 und 1,5 Ωm erkennbar (siehe Abbildung 12 und 14). Diese Bereiche können als gemeinsame Schlammkammer der Gryphons der einzelnen Schlammvulkane interpretiert werden. Die Werte der spezifischen Widerstände stimmen für die drei untersuchten Schlammvulkane sehr gut überein.

Abbildung 15: *Abgebildet ist Schlammvulkan 1. Man erkennt die einzelnen Schlammaustrittsstellen. Das Bild wurde in Perekishkul, Aserbaidschan während der Messung im April 2010 aufgenommen.*

Der Wertbereich stimmt gut mit dem durch geoelektrische Messungen ermittelten Bereich von 1 bis 25 Ωm überein [*Scholte* (2005)]. Auch im Bereich der Schlammkammern stimmen die spezifischen Widerständen mit Werten zwischen 1 bis 3 Ωm gut überein. Die Ergebnisse der TEM-Messungen zeigen ebenfalls einen Wertebereich von 1 bis 20 Ωm für den spezifischen Widerstand [*Adrian* (2011)].
Das Aufsteigen des guten Leiters an den drei im Rahmen dieser Arbeit untersuchten Schlammvulkanen kann man auch in dem Modell in Abbildung 1 erkennen.

Nach *Knödel et al.* (2005) erstreckt sich der Widerstandsbereich für Ton in Abhängigkeit seines Wassergehalts von 3 (erdfeucht) bis über 1000 Ωm (trocken). Schluff weist spezifische Widerstände zwischen 20 und 50 Ωm auf. Natürlich vorkommendes Wasser hat spezifische Widerstände zwischen 10 und 300 Ωm und Meerwasser ungefähr 0,25 Ωm.
Die gemessenen spezifischen Widerstände und die Korngrößen des austretenden Schlamms weisen auf Ton und Schluff hin. Als Hauptquelle der Schlammvulkane in Aserbaidschan dient unter anderem die im Miozän und im Oligozän abgelagerte Schicht, welche verschiedene Tone als Bestandteile enthält. Diese Schicht wird auch als erdölführende Schicht angesehen [*Scholte* (2005)].
Als Fluid des Schlammes ist ein Gemisch aus natürlich vorkommenden Wässern und Meerwasser am wahrscheinlichsten. Dafür sprechen die für natürliche Wässer zu geringen spezifischen Widestände mit bis zu 0,1 Ωm. Auch das im Messgebiet an den Schlammvulkanen ausblühende Salz bestätigt einen hohen Salzgehalt des austretenden Schlamms. Ein Teil der Sedimente besteht aus ozeansicher Kruste, welche Meerwasser als Porenwasser beinhaltet [*Scholte* (2005)].
Das im Schlamm sichtbare Erdöl konnte in den Messdaten nicht nachgewiesen werden.

Die geringen spezifischen Widerstände im Bereich der Schlammvulkane lassen sich unter anderem auf den höheren Wassergehalt relativ zum restlichen Messgebiet zurückführen.
Dies wird durch die großflächig feuchte Schicht im Bereich der Schlammvulkane wenige Zentimeter unterhalb der Erdoberfläche gestützt.

Eine unterirdische Verbindung der Schlammvulkane 1, 2 und 3 konnte nicht festgestellt werden. Im Bereich der einzelnen Schlammvulkane 1 und 3 scheint es jedoch gemeinsame Schlammkammern der verschiedenen Gryphons zu geben.

Trotz der geringen Eindringtiefen aufgrund der hohen Leitfähigkeiten konnte aufgrund des großen Spektrums von Frequenzen eine Auflösung der oberen 10 bis 20 m erreicht werden. Die Schlammvulkane konnten lateral detektiert werden, obwohl die große Anzahl von Schlammvulkanen im Messgebiet zu schwachen Kontrasten in der Leitfähigkeit führen.
Die bisherige Vorstellung des Aufbaus von Schlammvulkanen konnte verifiziert werden.

Ausblick

Im Rahmen des zweiten Teils des Projekts ELMUD wurden im September 2011 Long-Offset Transient Elektromagnetik Messungen (LOTEM) durchgeführt. Diese werden zur Zeit von A. Haroon im Rahmen seiner Masterarbeit am Institut für Geophysik und Meteorologie der Universität zu Köln ausgewertet. Dabei wurde eine Auflösung der oberen 5 km erreicht.
Es soll eine gemeinsame Interpretation der Ergebnisse von RMT, TEM und LOTEM stattfinden.

Danksagung

Wir danken der Volkswagen Stiftung für die Finanzierung des Projekts ELMUD sowie den aserischen Kollegen vor Ort.

Literatur

Adrian, J., Untersuchung von Schlammvulkanen in Perekishkul, Aserbaidschan mit der Transient-Elektromagentik, Diplomarbeit, Universität zu Köln, Institut für Geophysik und Meteorologie, 2011.

Adrian, J., H. Großbach, B. Tezkan, A. Novruzov und A. Mamedov, Untersuchung von Schlammvulkanen in Perekishkul, Aserbaidschan mit Transient-Elektromagnetik (TEM) und Radiomagentotellurik (RMT), in *EMTF 2012*, 2012.

Bohrmann, G., A. Kopf und V. Spiess, Vulkane, die Schlamm statt Lava speien, *Expedition Erde*, 336, 2006.

Feyzullayev, A. A., Mud Volcano Model Resulting from Geophysical and Geochemical Research, in *Mud Volcanoes, Geodynamics and Seismicity*, herausgegeben von G. Martinelli und B. Panahi, 251–262, Springer, 2005.

Großbach, H., Erste Anwendung der Radiomagnetotellurik auf Schlammvulkanen in Perekishkul/Aserbaidschan, Diplomarbeit, Universität zu Köln, Institut für Geophysik und Meteorologie, März 2011.

Judd, A., Gas Emissions from Mud Volcanoes, in *Mud Volcanoes, Geodynamics and Seismicity*, herausgegeben von G. Martinelli und B. Panahi, 147–157, Springer, 2005.

Knödel, K., H. Krummel und G. Lange, *Handbuch zur Erkundung des Untergrundes von Deponien: Geophysik*, Bd. 3, Springer Berlin, 2 Auflage, 2005.

Mackie, R., W. Rodi und S. Rieven, *Users Manual and Software Documentation for Two-Dimensional Inversion of Magentotelluric Data*, GSY-USA, Inc., San Francisco, California 94114, Juli 1997.

Martinelli, G., Geochemical Model of Mud Volcanoes from Reviewed Worldwide Data, in *Mud Volcanoes, Geodynamics and Seismicity*, herausgegeben von G. Martinelli und B. Panahi, 211–220, Springer, 2005.

Panahi, B., Mud volcanism, Geodynamics and Seismicity of Azerbaijan and the Caspian Sea Region, in *Mud Volcanoes, Geodynamics and Seismicity*, herausgegeben von G. Martinelli und B. Panahi, 89–104, Springer, 2005.

Scholte, K. H., *Hyperspectral Remote Sensing and Mud Volcanism in Azerbaijan*, Dissertation, Delf University of Technology, Department of Geotechnology, 2005.

Seher, T., Untersuchung von Feuchtbiotopen in Ostfriesland: Gefährdungsabschätzung mit Multielektroden-Geoelektrik und Radiomagnetotellurik, Diplomarbeit, Universität zu Köln, Institut für Geophysik und Meteorologie, 2005.

Tezkan, B., A. Saraev, A. Shuman, P. Georgescu und N. Christensen, *Final Report: INCO*, 2002.

Wiebe, H., 1d-Joint-Inversion von Geoelektrik und Radiomagnetotellurik, Diplomarbeit, Universität zu Köln, Institut für Geophysik und Meteorologie, 2007.

Comparison of 2D MT inversion approaches using spatially constant and locally varying regularization parameters

M. Jamie[1,2], B. Oskooi[1], M. Becken[2]

[1] Institute of Geophysics, University of Tehran,
Kargar shomali St., 14155-6466, Tehran, Iran
[2] Institute für Geophysik, WWU Münster
Corrensstraße 24, 48149, Münster, Germany
Contact:majid.jamie@uni-muenster.de

Summary

Inversion of magnetotelluric (MT) data is a non-linear ill-posed inverse problem, and is commonly solved with an iterative linearized approach. In order to solve the minimization problem a regularization parameter is employed to balance between the norm of the data misfit and the norm of the model. Determination of a suitable regularization parameter is necessary to achieve both resolution and stability in inversion. In most inversion schemes, the regularization parameter is applied globally to the entire model. In this study, we test the capability of active constraint balancing (ACB) approach, which was introduced by Yi et al. (2003). The approach determines a spatially varying regularization parameter $\lambda(x_i, y_i, z_i)$ via Backus-Gilbert spread function analysis for model parameters. Here, we use the 2D MT inversion code developed by Lee et al., (2009) to test the ACB on 2D synthetic and field MT datasets.

Key words: Active Constraint Balancing (ACB), Inversion, Regularization parameter, Magnetotelluric (MT), Model parameter

Introduction

The magnetotelluric inverse problem is ill-posed in that small errors in the measured data can lead to huge changes in the model. In order to stabilize the inversion and to produce useful solutions, regularization constraints are imposed on the model. A typical regularization scheme is to minimize the norm or a semi-norm of the model, such as the second derivatives. A trade-off (or regularization) parameter is introduced to balance between the data residuals and the model norm and is usually a single number that is globally applied to the entire model. Different strategies are used to determine the optimum regularization parameter. The OCCAM algorithm (deGroot-Hedlin and Constable, 1990) determines in each iteration a regularization parameter that yields the best data fit. The REBOCC algorithm (Siripunvaraporn and Egbert, 2000) searches for the optimum value of the regularization parameter through a predefined range at each iteration. Other approaches such as the conjugate gradient (CG) and nonlinear conjugate gradient (NLCG) schemes (Mackie and Madden, 1993; Rodi and Mackie, 2001) use a fixed regularization parameter, the inversion is then repeated for a range of regularization parameters, and the choice of suitable regularization parameter is based on e.g. the L-curve criterion or similar means. A method presented by Oldenburg and Li (1999), for DC resistivity and IP inverse problem, is based on using three different regularization terms for minimizing the conductivity update, minimizing the update variation in horizontal direction and minimizing the update variation in vertical direction. Instead of using a global regularization parameter, it could be

useful to define a spatially variable regularization parameter that scales with the resolution of model domains. This can be achieved implicitly by making the regularization model-grid-dependent (i.e. the model norms are computed in model domain rather than in space domain), or explicitly by investigating the resolution of model parameters and defining a resolution-dependent regularization parameter. Active Constraint Balancing (ACB) is a later approach which was introduced by Yi et al., (2003). In this approach the regularization parameter is determined from the model resolution matrix via Backus-Gilbert spread function analysis (Menke, 1989). This approach is generalized form of the approach introduced by Sasaki (1989) for Dc resistivity problem. Sasaki's (1989) method is based on pre-defined, spatially variable regularization parameters λ for model parameters according to theoretical expectation of their resolution, i.e. parameters located near to the electric source are expected to need smaller values of λ, due to their higher resolution, compared to parameters far from the source. The ACB approach defines λ as a spatial term $\lambda(x_i, y_i, z_i)$ which is computed in each iteration of the inversion from the current model resolution matrix. The idea is to assign higher values of λ to parameters with low resolution and vice versa. In this study we test ACB approach, using the MT2DInvMatlab code developed by Lee et al., (2009), for 2D synthetic and field MT datasets. The inversion results using ACB are then compared with inversion results using a global regularization parameter.

Active Constraint Balancing (ACB)

Let the forward problem be given by $d = G(m)$. Then, the regularized least-squares can be obtained by iterating over a sequence of linearized systems of equations of type,

$$m^{k+1} = [J_k^T J^k + \lambda^2 L^T L]^{-1} J_k^T \hat{d}^k \quad (1)$$

Where m^{k+1} is the solution in iteration $k+1$. J is sensitivity matrix for model parameters, L is a weighting matrix, and λ is regularization parameter. $\hat{d}^k$ is defined by $\hat{d}^k = d - G^k + J^k m^k$ which $G^k = G(m^k)$.
In order to take the λ as a spatial variable $\lambda(x_i, y_i, z_i)$, Yi et al., (2003) propose to rewrite the model update in eq.1 as

$$m^{k+1} = [J_k^T J^k + L^T \Lambda L]^{-1} J_k^T \hat{d}^k \quad (2)$$

Where $\Lambda = \mathrm{diag}(\lambda_\mathrm{i})$ and $\lambda_\mathrm{i} = \lambda(x_i, y_i, z_i)$.

$$m^{k+1} = J^\dagger \hat{d}^k \quad (3)$$

Where $J^\dagger$ is the generalized inverse,

$$J^\dagger = [J_k^T J^k + L^T \Lambda L]^{-1} J_k^T \quad (4)$$

Then the model resolution matrix R (Menke, 1989) for the current model is expressed as

$$R = J^\dagger J \quad (5)$$

The estimated model parameters can be conceived as weighted averages of the true model parameters with the rows of the model resolution matrix containing the weighting factors. Perfect resolution

corresponds to $R = I$. The width of the averaging functions are determined by the Backus-Gilbert spread function (Menke, 1989) as

$$Spread\ (R) = \sum_{i=1}^{M}\sum_{j=1}^{M} w(i,j)[R_{ij} - I_{ij}]^2 = \sum_{i=1}^{M}\sum_{j=1}^{M} w(i,j){R_{ij}}^2 \quad (6)$$

Where $w(i,j) = (i-j)^2$ is a weighting matrix that weights the (i,j) element of the model resolution matrix R according to its diagonal elements. In calculating the spread function the diagonal elements of R have no weight, i.e. $w(i,i) = 0$, hence the spread for the ith parameter is calculated by eq.7,

$$SP_i = \sum_{j=1}^{M} w(i,j){R_{ij}}^2 \quad (7)$$

High value of spread function for a definite model parameter indicates low resolution for that parameter and vice versa. In ACB approach regularization parameters are set in a logarithmic space between predefined upper and lower limits; λ for the ith parameter is calculated by e.q.8,

$$\log(\lambda_i) = \log(\lambda_{min}) + \frac{\log(\lambda_{max}) - \log(\lambda_{min})}{\log(SP_{max}) - \log(SP_{min})} \times [\log(SP_i) - \log(SP_{min})] \quad (8)$$

Where λ_i holds the value of regularization parameter for ith parameter. λ_{max} and λ_{min} are upper and lower limits for λ which are specified manually for the algorithm. SP_{max} and SP_{min} correspond to upper and lower boundaries of the spread function respectively. In practice the algorithm starts with a small value of λ (which is defined by the user), and calculates SP_i via eq.7, afterwards, having the boundary values for Largerabgian multiplier and spread function, the ACB algorithm depending on the dimension of the problem, automatically assigns λ as a spatial variable in one- two- or three dimensional space. Higher values of λ are allocated to parameters with poor resolution and vice versa.

Example with Synthetic Data

We tested ACB on two different models: 1- A synthetic model consisting of a Homogeneous half space with resistivity of 100 Ohm-m (Fig.1.a), and 2- A model containing a conductive zone with resistivity of 2 Ohm-m in a half space medium with resistivity of 100 Ohm-m (Fig.2.a). The 2D synthetic datasets for these two models were generated from forward modeling code of REBOCC for 36 stations with 3000 m spacing increment using 31 frequencies in range of 0.001 – 1.000 Hz. The synthetic datasets ere inverted using MT2DInvMatlab code (Lee et al., 2009) for TM mode with 10 iterations. Fig.1.a shows the anomaly for the first model. TM-mode inversion model for this anomaly using ACB approach with $\lambda_{min} = 0.5$, $\lambda_{max} = 100$ is depicted in Fig.1.b. Distribution of spread functions and regularization parameters for the last iteration are shown in Fig.1.c and Fig.1.d respectively. The anomaly for the second model is shown in Fig.2.a. Fig.2.b shows the TM-mode inversion model using traditional approach with fixed $\lambda = 4$. The inverted model using ACB approach with $\lambda_{min} = 0.5$, $\lambda_{max} = 100$ is in Fig.2.c. The inversion result for this synthetic anomaly using ACB is less smeared out compared with traditional approach with fixed regularization parameter. Distribution of spread function and also regularization parameter for the last iteration is depicted in Fig.2.d and Fig.2.e respectively. As the spread function analysis uses sensitivity matrix and sensitivities for model parameters are updated with iteration, the distribution of the spread

function and also regularization parameters are changing iteration to iteration. Distribution of λ for 1st -, 2nd -, 5th -, 8th - and 10th - iteration are shown in Fig.3.a, Fig.3.b, Fig.3.c and Fig.3.d respectively. This panel illustrates that λ-distribution changes significantly in primary iterations and converges in final iterations, as the model converges.

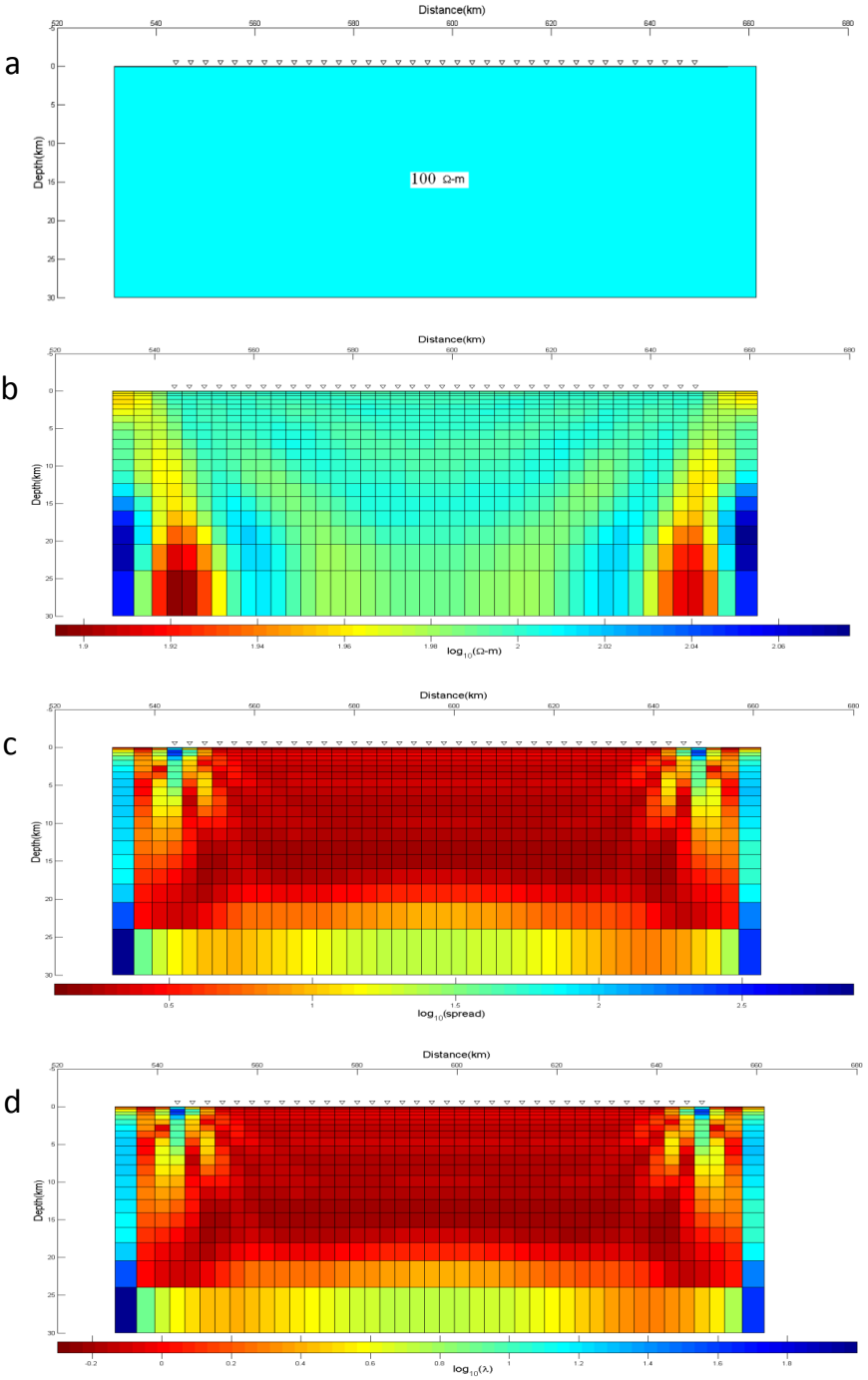

Fig.1. Homogeneous half space with Resistivity of 100 Ohm-m used as the model (a), the inversion model using ACB approach with $\lambda_{min} = 0.5$, $\lambda_{max} = 100$ for TM mode (b), distribution of spread function for the last iteration (c) distribution of λ for the last iteration (d).

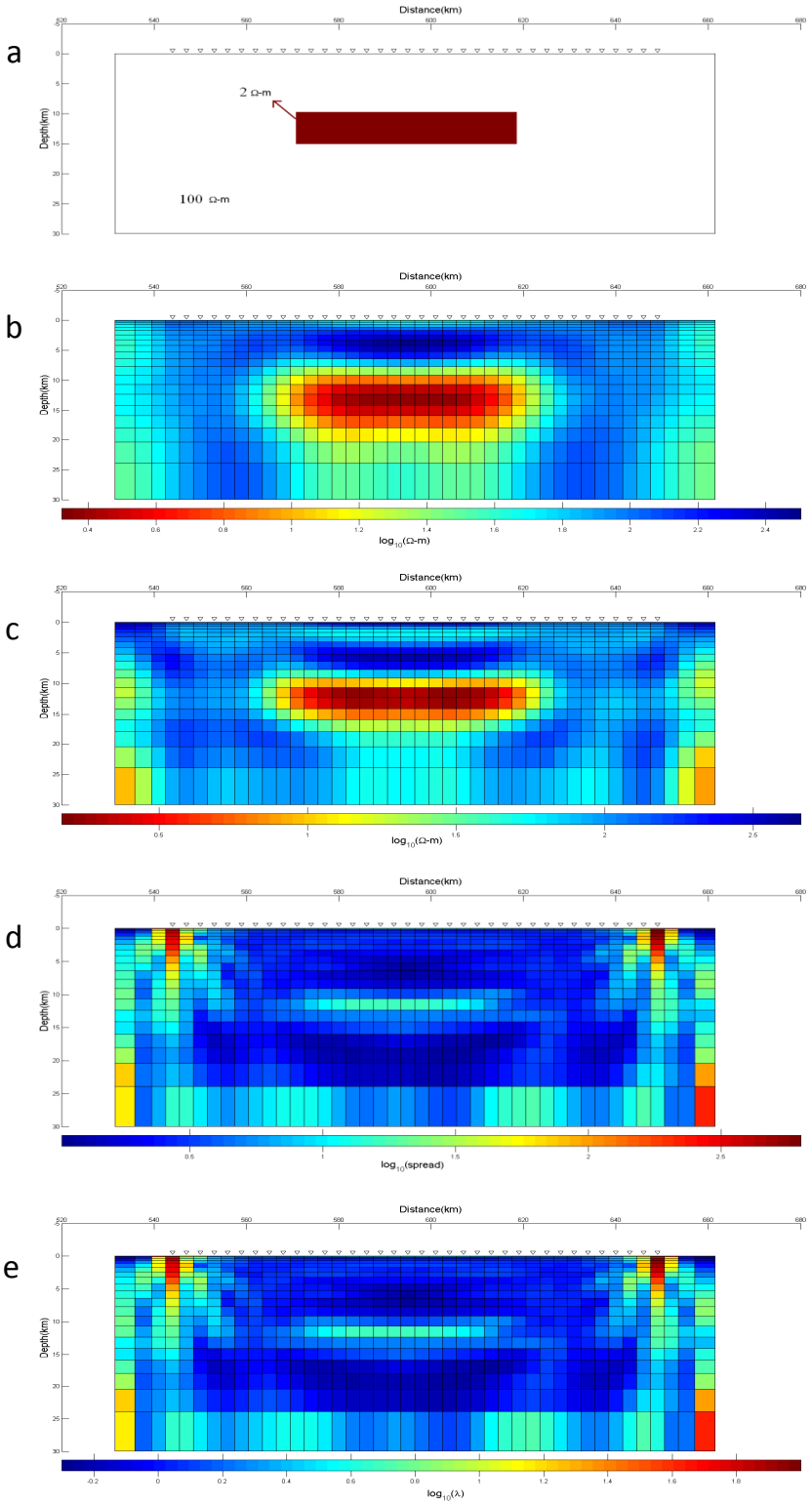

Fig.2. The conductive zone with resistivity of 2 Ohm-m, in a half space medium with resistivity of 100 Ohm-m used as synthetic model (a), the inversion model for TM mode using traditional approach with fixed $\lambda = 4$ (b), the TM-mode inversion model using ACB approach with $\lambda_{min} = 0.5$, $\lambda_{max} = 100$ (c), distribution of spread function for last iteration (d), distribution of λ for the last iteration (e).

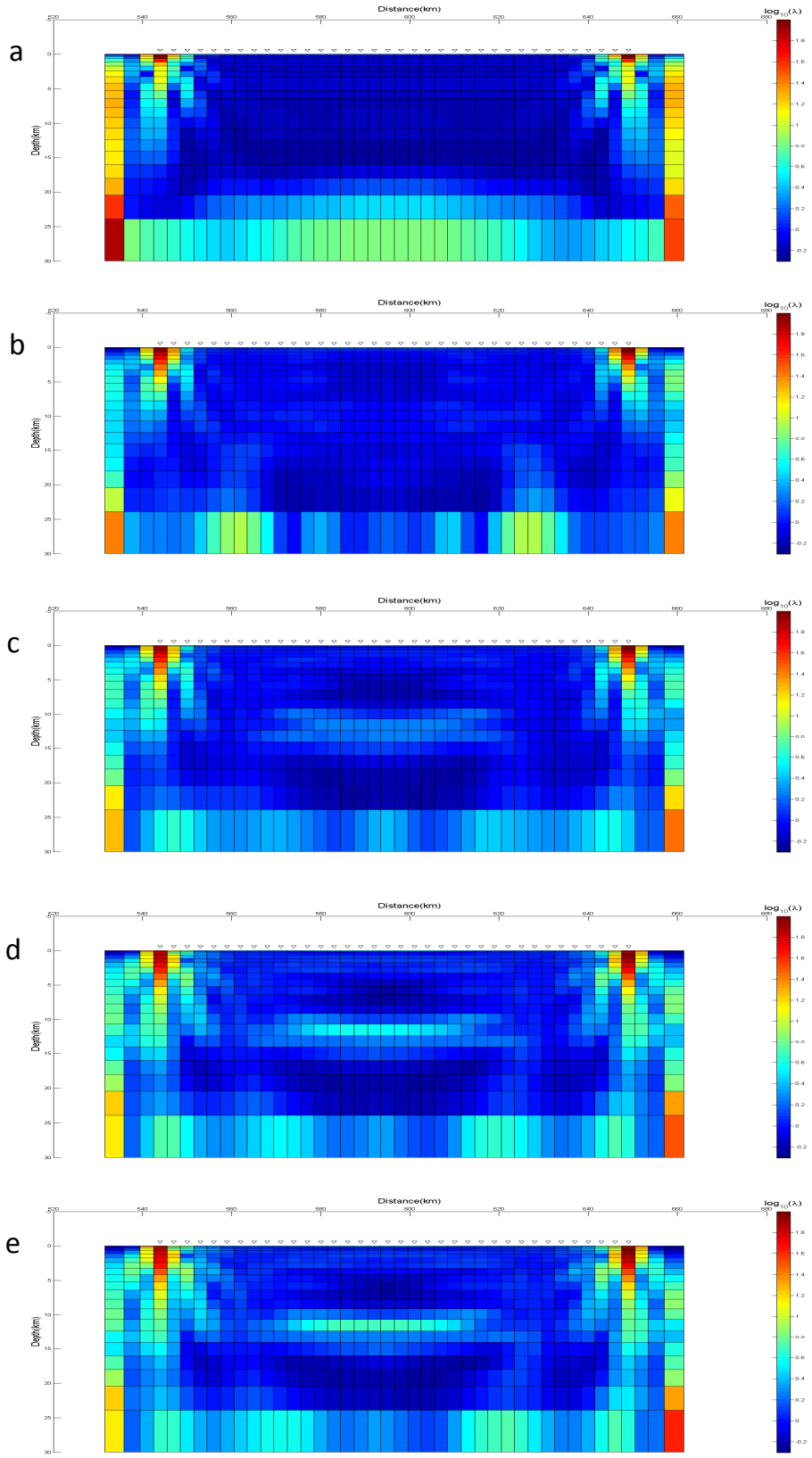

Fig.3. Distribution λ for 1st -, 2nd -, 5th -, 8th - and 10th – iteration are shown in (a), (b), (c), (d), and (e) respectively.

Example with Field Data

The ACB approach was also applied on MT field data for TE, TM, and joint inversion of TE&TM modes. The data is from a 2D MT profile conducted at NE margin of the Ejina Basin in NW China for basement studies (Becken et al., 2007). There are 22 stations along the profile with 180 m spacing increment using 33 frequencies with the range between 0.1-1000 Hz. MT2DInvMatlab code was used for inverting the dataset for three modes (TE, TM and Joint TE&TM) with 10 iterations. Inversion models for TE, TM, and joint inversion of TE&TM modes with fixed λ are shown in Fig.4.a, Fig.4.b, and Fig.4.c respectively. Inversion models for TE, TM, and joint inversion of TE&TM modes using ACB approach are shown in Fig.5.a, Fig.5.b, and Fig.5.c respectively. Regularization parameters for these models are assigned in the range of $\lambda_{min} = 0.5$ and $\lambda_{max} = 10$. The maximum value of 10 for λ is chosen by experience because λ_i has mostly values less than 10 for model parameters. Distribution of regularization parameters for the last iteration for TE, TM, and joint inversion for TE&TM modes are shown in Fig.6.

Conclusion

In this study a regularization approach called active constraint balancing (ACB) presented by Yi et al., (2003) for least-squares resistivity tomography inverse problem, was tested on 2D synthetic and field MT datasets. The approach assigns spatially varying regularization parameters to each model parameter with iteration. This approach is generalized form of the approach introduced by Sasaki (1989) for Dc resistivity problem, which defines regularization parameter λ as a spatial term $\lambda(x_i, y_i, z_i)$, which is computed in each iteration of the inversion from the current model resolution matrix. The idea is to assign higher values of λ to parameters with low resolution and vice versa. The inversion models using ACB approach for 2D synthetic and MT field datasets, in this study, are less smeared out compared with corresponding inversion models with fixed regularization parameter.

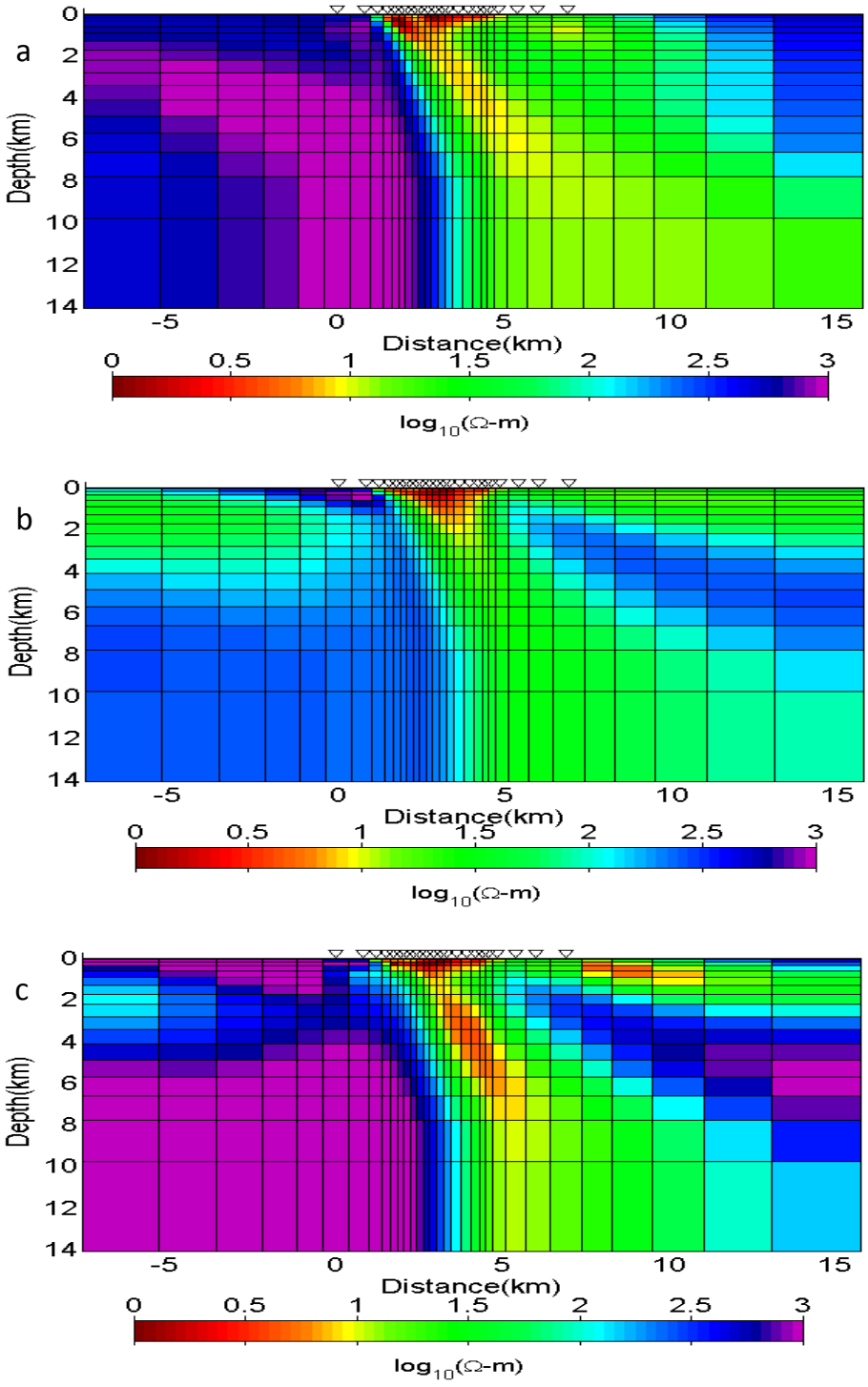

Fig.4. Inversion models for TE, TM, and joint inversion of TE&TM modes for fixed regularization parameter are shown in a, b and c respectively.

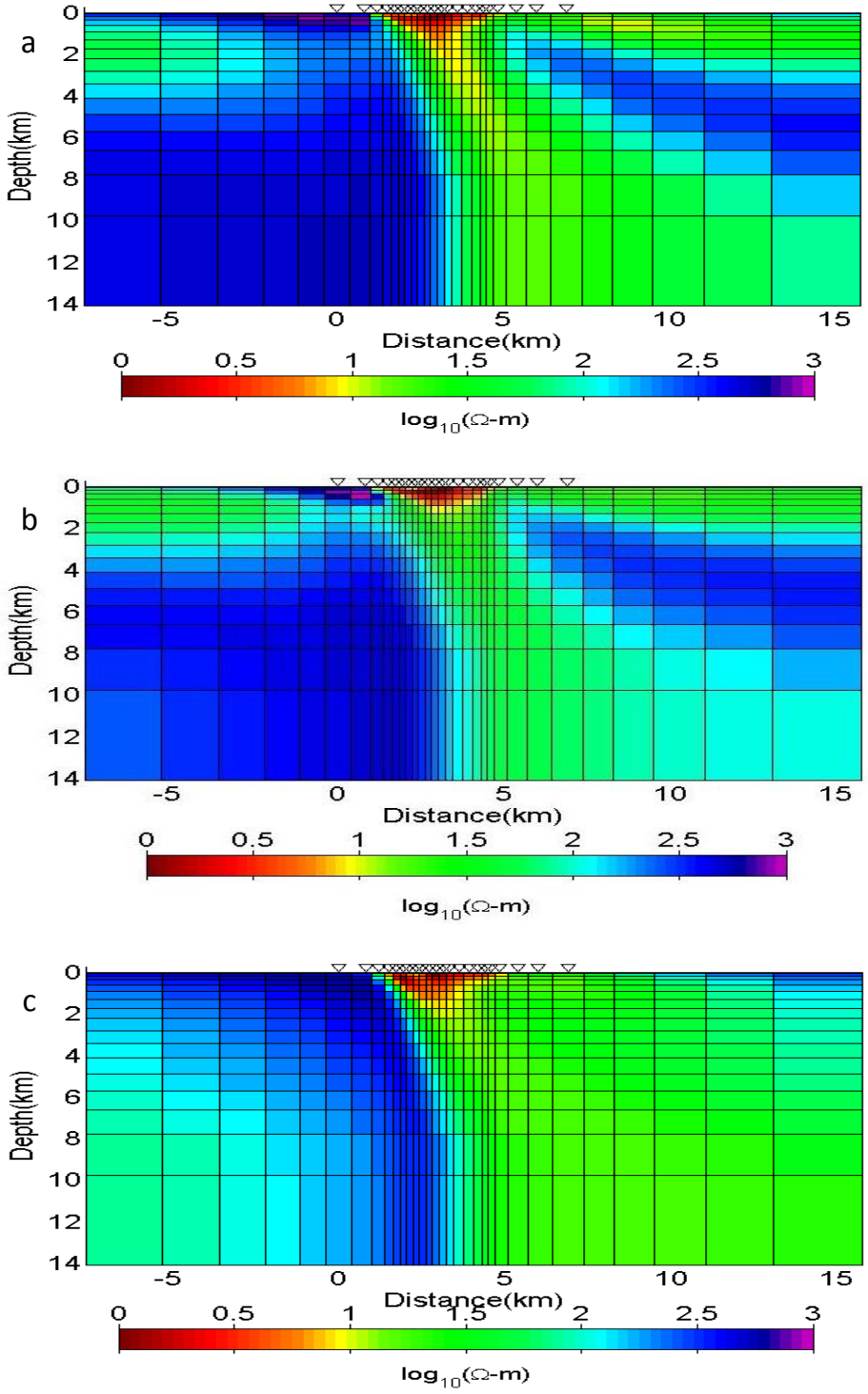

Fig.5. Inversion models after applying ACB for TE, TM, and joint inversion of TE& TM modes are shown in a, b and c respectively.

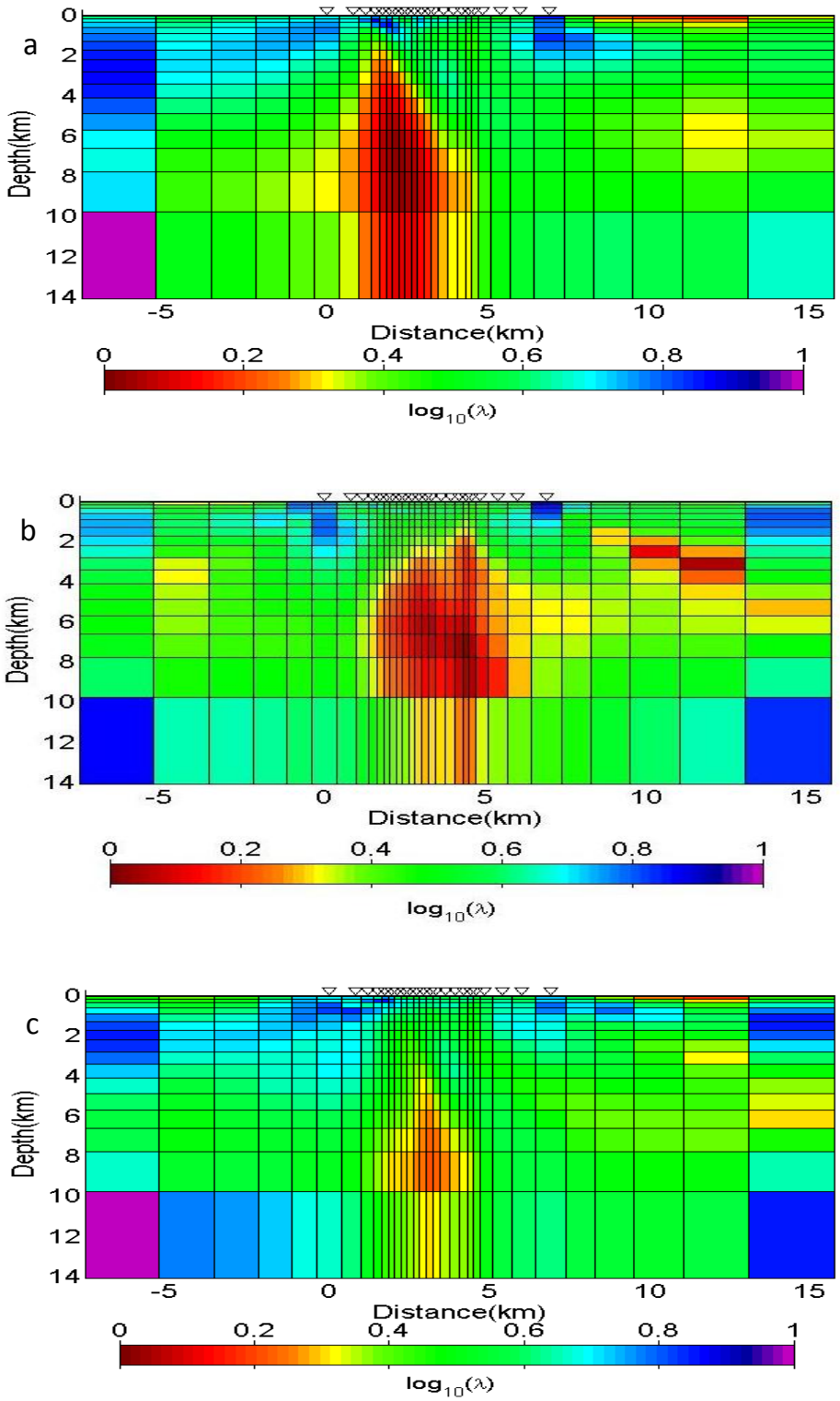

Fig.6. Distribution of λ in the last iteration for TE, TM, and joint inversion of TE&TM modes are shown in a, b and c respectively.

References

Backus G., Gilbert, F., 1970, Uniqueness in the inversion of inaccurate gross earth data. Philosophical Transactions of the Royal Society A, 266, 123–192.

Becken, M., S. Hölz, R. Fiedler-Volmer, K. Hartmann, B. Wünnemann, and H. Burkhardt, 2007, Electrical resistivity image of the Jingsutu Graben at the NE margin of the Ejina Basin (NW China) and implications for the basin development, Geophys. Res. Lett., 34, L09315.

deGroot-Hedlin, C., Constable, S. C., 1990, Occam's inversion to generate smooth, two-dimensional models from magnetotelluric data. Geophysics, 55, 1613–1624.

Engl, H. w., Hanke, M., Neubauer, A., 1996, Regularization of Inverse Problems. Kluwer Academic Publishers, Boston.

Jupp, D. L., Vozoff, K., 1975, Stable iterative methods for the inversion of geophysical data. Geophys. J. Roy. Astr. Soc., 42, 67–72.

Lee, S. K., Kim, H. J., Song, Y., Lee, C., 2009, MT2DInvMatlab-A program in MATLAB and FORTRAN for two-dimensional magnetotelluric inversion. Computers and Geosciences, 35(8), 1722-1734.

Mackie, R. L., Madden,T. R., 1993, Three-dimensional magnetotelluric inversion using conjugate gradients. Geophys. J. Internat., 115, 215-229.

McCarthy, P. J., 2003, Direct analytic model of the L-curve for Tikhonov regularization parameter selection. Inverse Problems, 19, 643–663.

Menke, W., 1989. Geophysical Data Analysis Discrete Inverse theory, revised ed. Academic Press Inc, San Diego, CA, 289pp.

Molinari, M., Blott, B., Cox, S., and Daniell, G., 2002, Optimal imaging with adaptive mesh refinement in electrical impedance tomography. *Physiol. Meas.*, **23**(1), 121–128.

Oldenburg, D., and Li, Y. (1999), Estimating depth of investigation in dc resistivity and IP surveys. Geophysics, 64(2), 403–416.

Rodi, W. L., Mackie, R. L., 2001, Nonlinear Conjugate Gradients Algorithm for 2-D Magnetotelluric Inversion. Geophys, 66(1), 174–187.

Sasaki, Y., 1989, Two-dimensional joint inversion of magnetotelluric and dipole-dipole resistivity data. Geophysics, 54, 254–262.

Siripunvaraporn,W., Egbert, G., 2000, An efficient data-subspace inversion method for 2D magnetotelluric data. Geophysics 65, 791–803.

Yi, M.-J., Kim, J.-H., Chung, S.-H., 2003, Enhancing the resolving power of least-squares inversion with active constraint balancing. Geophysics 68, 931–941.

A concept for 1D inversion of MT data using phase tensor invariants

Andreas Junge
Institute of Geosciences, Frankfurt University, Germany
Contact: junge@geophysik.uni-frankfurt.de

Motivation

The 1D inversion of MT data often gives a first impression about the conductivity structure of the underground and can be used as a start model for more complex 2D or 3D inversion schemes. However, it is often affected by static shift and the influence of large scale non 1D conductivity structures. Therefore the inversion results generally depend on the interpreter's subjective selection and manipulation of impedance tensor elements. Furthermore inverting data from a large period range, e.g. 10^{-3}-10^{5} s, aggravates the choice of proper layer thicknesses.

In this contribution an inversion scheme is presented which overcomes most of the mentioned difficulties: (1) it uses the phase tensor (Caldwell et al, 2004) and thus it is independent from static shift except for the scaling problem, (2) it uses the average of the modified phase tensor invariants Φ_{min} and Φ_{max} and thus it is independent from the instruments orientation, (3) it proceeds stepwise starting at the short period end and thus adapts to layer thicknesses increasing with depth.

Input data

Emanating from the phase tensor $\mathbf{\Phi} = \begin{pmatrix} \Phi_{11} & \Phi_{12} \\ \Phi_{21} & \Phi_{22} \end{pmatrix}$ according to (Caldwell et al, 2004), the invariant

$\varphi_{inv} = 0.5(\varphi_{min} + \varphi_{max})$ with $\varphi_{min} = tan^{-1}\Phi_{min}$ and $\varphi_{max} = tan^{-1}\Phi_{max}$ (details see Caldwell et al, 2004, Appendix) is calculated for each frequency $f_n = f_1, \dots, f_N$, N being the number of frequencies resp. data $\varphi_{inv}(f_n)$. Note that the phase tensor values φ are used instead of Φ, following (Häuserer and Junge, 2011), as averaging of Φ_{min} and Φ_{max} would lead to biased values due to the non-linearity of the tangent function.

In case of 2D anomalies, φ_{min} and φ_{max} correspond to the TE mode resp. TM mode phases showing opposite behaviour with varying period and distance from the anomaly boundary. Thus using φ_{inv} the influence of lateral conductivity inhomogeneity is decreased which can also be shown in case of 3D conductivity anomalies (cf Löwer and Junge, this volume).

Inversion scheme

The inversion follows a Gauss-Newton procedure with stepwise shifting a data subsample of size $N^{(k)}$ which is inverted for a 1D layered model with layer thicknesses $d_m = d_1, \dots, d_{M-1}$ and layer resistivities $\rho_m = \rho_1, \dots, \rho_M$, consisting of $M-1$ layers and ρ_M as half space resistivity underneath. If $k = 1, \dots, K$ are the number of steps, then $N^{(k)}$ and $M^{(k)}$ are the number of data and layers used in step k. In the following $N^{(k)}$ is kept constant.

If other information is not available, a homogeneous half space is taken as start model with resistivity ρ_{hom}. ρ_{hom} is calculated from the Berdichevsky-Invariant of all impedance tensors by taking the median of its apparent resistivity values ρ_a . Furthermore if static shift can be neglected, the first 2-3 short period ρ_a values may also be inverted.

It proved that starting with $M^{(1)} = 5$ and $N^{(1)} = 5$ is adequate in many cases. First the inversion is performed for ρ_m only, with equal layer thicknesses $d_1, \dots, d_{M-1} = {}^{p}/_{M-1}$ defined by the skin

depth $p = \sqrt{\rho_{hom}/f_2}$. In an alternating way the inversion is carried out for d and ρ resp. until significant improvement of the data fit ceases.

In the next step ($k = 2$) it is $M^{(2)} = M^{(1)} + 1 = 6$ and $N^{(2)} = N^{(1)}$, whereby the frequency window is shifted such that $\varphi_{inv}(f_n), n = 3, \dots, N^{(2)} + 2$ are inverted. The parameters of the first 2 top layers are kept constant, while the parameter values of the last inversion step serve as initial values of the current inversion which is performed in the same manner as in the first inversion step. The initial resistivity of the additional layer is determined by evaluating the conductance $\tau = \sum_{m=1}^{M-1} d_m/\rho_m$ and from that the average resistivity value $\bar{\rho} = \sum_{m=1}^{M-1} d_m/\tau$, which in turn is taken to define the initial value for thickness of the additional layer from the skin depth $p = \sqrt{\bar{\rho}/f_{N^{(2)}+2}}$. The inversion is carried out again until no significant improvement of the data fit is achieved. For the next step again one layer is added at the bottom and its parameters are calculated similarly as in step 2, while the parameters of the third layer from top are kept constant additionally. The phase interval to be inverted is shifted by 2 periods to the longer period end. The inversion procedure is performed until all the phases of all N frequencies are being considered.

Test and discussion

The inversion scheme was tested by generating a 1D data set using the Wait algorithm. The model consists of 4 layers of increasing thickness by a factor of 10 and alternating high and low conducting layers (cf Fig. 2), impedances were calculated for 30 periods between 0.01 s and 10000 s. For the first data set 1 % noise was added.

Fig.1 shows the performance of the inversion algorithm for $k = 1,4,11$. The top figures show the inverted models, the centre and bottom figures the simulated resistivity and phases (red stars) and the model responses (blue lines). The solid line marks the period interval for which the phases were inverted; the dashed line denotes that part estimated from the inversion model.

It is remarkable that the fit is very good not only for the phases but also for the resistivity values. This is probably due to the inclusion of the first 3 short period resistivity values in the inversion; however, the inversion is largely dominated by the phase values.

Fig.2 shows the inversion results for different noise levels (1% and 10%) and sample size (N=30 and 15). 5 phase values per decade and 1 % noise yields a model which outlines the true model very well considering the low resolution power of inductive methods for high resistive layers. Increasing the noise level up to 10% results in a larger phase scatter, however the algorithm is still able to resolve the input parameters. Subsequent smoothing certainly would carve out the significant model features. The algorithm loses the bottom layer when the number of frequencies per decade is reduced by half with similar noise level and the model gets somehow instable, still subsequent smoothing might again produce the major features adequately.

In conclusion the algorithm proves to be stable and it reproduces model features over large scales. It works completely automatically and it is independent from instrument orientation. Thus it liberates the interpreter from the often difficult choice of selecting or manipulating impedance tensor elements and thus approves its use for the generation of start models for 2D or 3D inversion schemes.

Literature

Caldwell, T.G., Bibby, H.M., Brown, C.: The magnetotelluric phase tensor, Geophys.J.Int. 158, 2004

Häuserer, M., Junge A.: Electrical mantle anisotropy and crustal conductor: A 3D conductivity model of the Rwenzori region in western Uganda, Geophys. J. Int. 185, 2011

Löwer, A., Junge, A.: Limits of 1D phase tensor inversion on 3D structures, Protokollband EMTF Neustadt/Weinstrasse, 2012 (this volume)

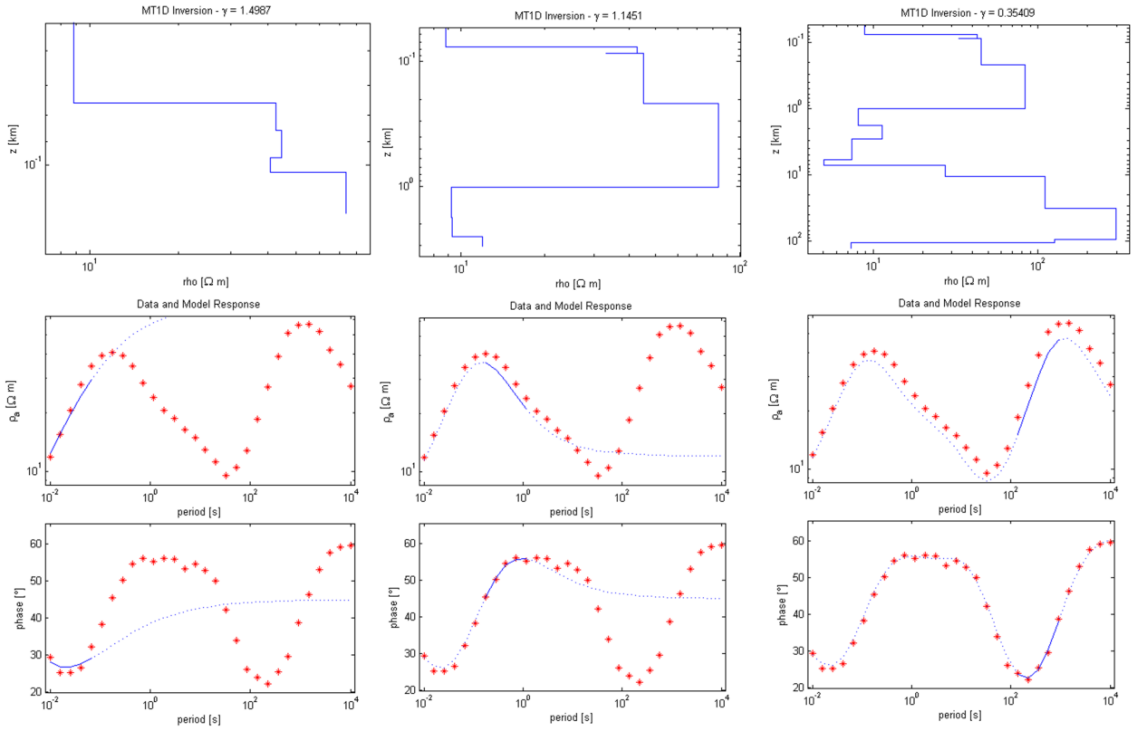

Fig.1: Inverted model (top), ρ_a values (middle), φ values (bottom), both for simulated (red stars) and model (blue lines) data. Inversion steps $k = 1$ (left), 4 (centre), 11(right). Further explanation see text.

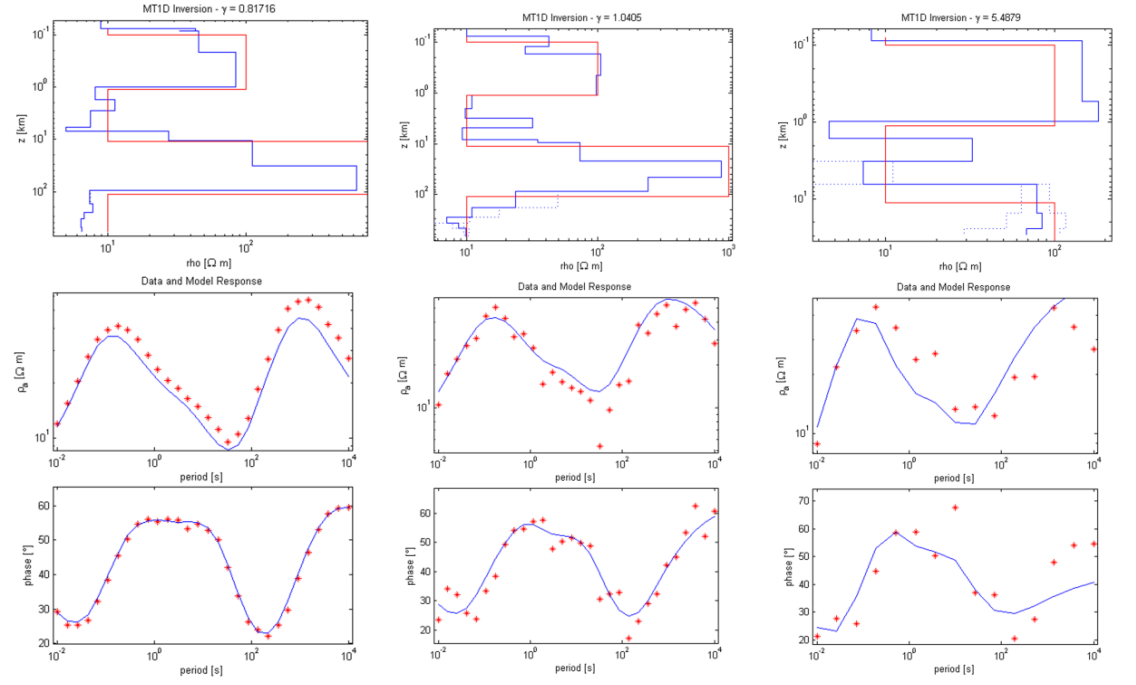

Fig.2: Inversion for N = 30 frequencies and 1% (left) and 10% (centre) noise; N = 15 frequencies and 10% (left). True models are marked by red lines. Further explanation see Fig.1 and text.

The effect of offsets on averaged in-loop transients

Ulrich Kalberkamp
Consulting Geophysicist, Hagen, Germany
kalberkamp@online.de

Introduction

In transient electromagnetic soundings slowly decaying voltages indicate conductors in which the induced current system can persist longer. Often this slow decay has been observed at the late time portion of the transient resulting in a nearly horizontal course. The following simulation shows that this slow late time decay can not only be caused by conductors at depth but also by small offset voltages caused e.g. by active receiving antennae. If present, this effect results in misleading model results with conductors at depth.

Based on the simulation results a simple approach is presented to overcome the effects caused by offsets introduced through pre-amplifier or other analogue signal conditioning devices attached to the TEM receiver.

Adding noise to the simulation suggests that the decay curve could even increase at late times due to the spectral distribution of the noise.

TEM acquisition

In the following the in-loop (or central loop) configuration is assumed. This configuration yields decay curves without sign reversals if non linear or frequency dependant effects (e.g. lateral inhomogeneities, IP effects) are absent.

Generally TEM transmitters deliver a 50% duty cycle signal with alternating polarity. During the current-off time the voltage decay is recorded by a receiver which converts the preconditioned (amplified and or band limited) signal into digital format by the use of an 16 or 24 bit A/D converter. Since the dynamic range of the voltage decay can span 8 decades it is common usage in the available commercial equipment to reverse the polarity of the sampling synchronized with the transmitter signal. Thus only one polarity is sampled and the full bit resolution can be used.

The disadvantage of this approach is that analogue offsets are not cancelled by the receiver rather than stacked coherently. As a result the decay curve becomes almost horizontal towards late times when the signal drops to the order of the offset. This effect is illustrated in figure 1.

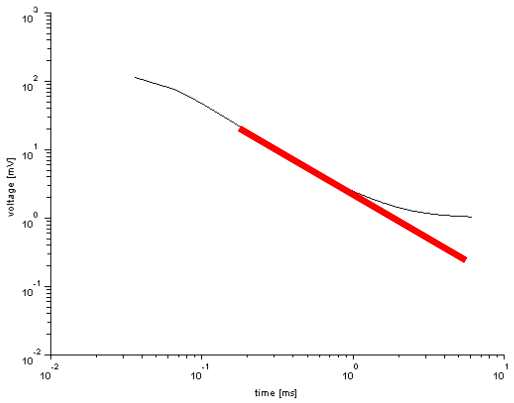

Figure 1: The black transient results from stacking including an offset of 1mV. The red curve indicates the transient without offset. At late times a considerable effect is obvious.

To cancel out any offset effect produced by the analogue front-end of the TEM receiver, including active antennae, two data sets have to be recorded: One data set with normal polarity of the source field and the other with reversed polarity of the source field. To achieve the cancelling effect it is necessary to maintain the internal polarity of the receiver so that the decay voltage will change its polarity while the offsets keep their polarity. Therefore it will not help to reverse the polarity of the receiver input rather than to reverse the source field, either by reversing the polarity of the transmitter loop or flipping the active receiving antenna upside down, as explained in figure 2.

In the latter cases the resulting two data sets can be averaged and the offset will cancel out (assuming that no substantial offset drift occurs during the recording time) as follows:

Normal polarity: $U_{out+} = U_{offset} + U_{decay}$
Reversed polarity: $U_{out-} = U_{offset} - U_{decay}$
Averaging yields: $Uout = (U_{out+} - U_{out-}) / 2 = (U_{offset} - U_{offset} + 2U_{decay}) / 2 = U_{decay}$

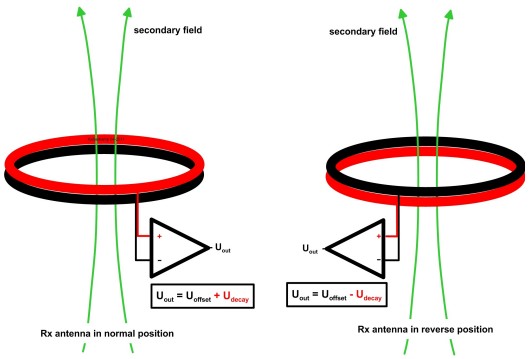

Figure 2: Acquiring two data sets with normal (left) and reversed (right) source, and thus secondary field polarity, while polarity of the inherent offsets are retained by flipping the receiving coil upside down.

This cancelling effect has been simulated for various offsets and added noise. In figure 3 the recorded transients are shown in red and the averaged transient in black for offsets of 0.5 mV (figure 3a) and 1 mV (figure 3b). It can be seen that the offset is cancelled when the approach as explained above is applied, regardless of the offset level. Figure 3c) shows the result of the superposition of an analogue offset of 1 mV and a transient distorted by an offset of 1 mV offset of other origin. Applying the averaging procedure will then yield erroneous results (black curve). When white noise of ±0.5 mV is added to a transient with 1 mV offset, the result is shown in figure 3d). If the noise is not white but coloured (e.g. pink-, 1/f-, $1/f^2$-noise) the spectral energy increases with lower frequency and the decay curve may even increase towards later times.

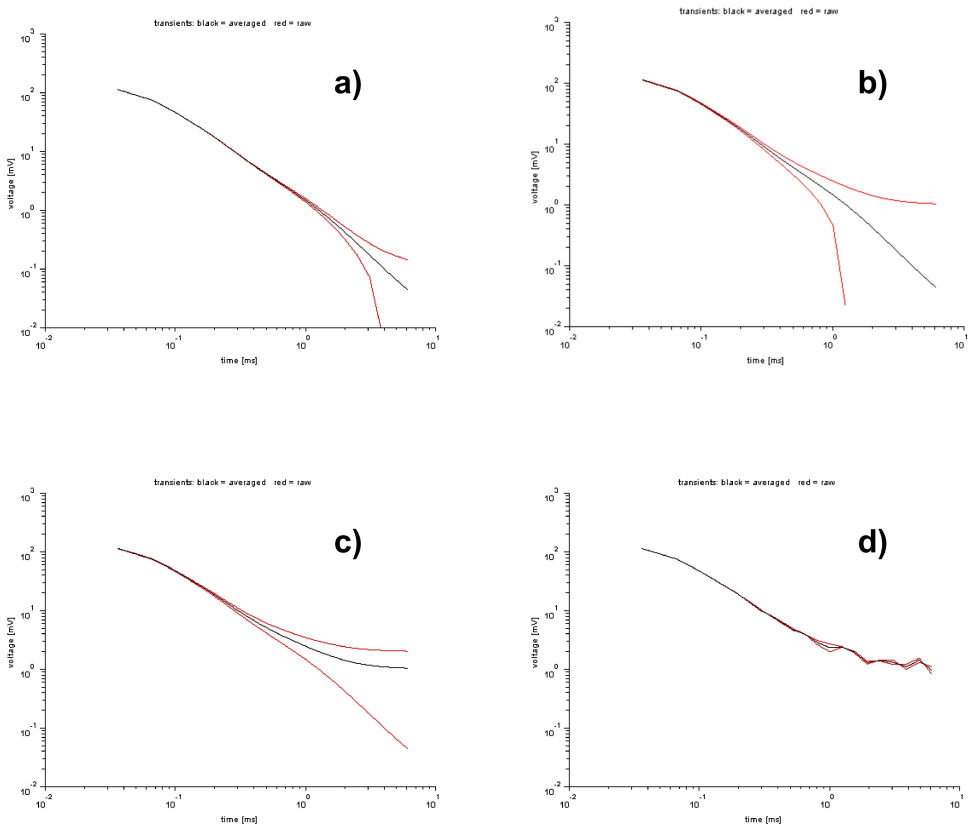

Figure 3: Result of averaging (black) of offset affected transients. a) Offset: 0.5 mV. b) Offset: 1 mV. c) superposition of 1 mV (analogue) offset and 1 mV offset of other origin. d) Offset: 1 mV, white noise added.

Reduction of offset effect

Best practice would be to modify the acquisition procedure as explained above: Record at least two data sets, one with normal orientation of the source field, one with reversed orientation. The reverse orientation can be achieved by changing the transmitter polarity, by flipping the receiving coil upside down or reversing the synchronisation polarity between receiver and transmitter. In the latter case the result on the transmitter current flow has to be verified. When during the overall recording time offset variations are to be expected, reversing should be performed in shorter intervals.

Transient recordings with flat responses towards late times due to assumed offset effects can be corrected to a certain extent also if only one data set is available. Then the offset can be estimated by the asymptote to the late times of the decay curve, as depicted in figure 4a). Depending on the noise the offset recovered from the affected transient may be slightly overestimated. A noise measurement recorded with the TEM receiver without a transmitted signal should also show the offset present in the decay data and can assist in estimating the offset. The original voltage decay can then be reduced by the estimated offset. In figure 4b) the flat decay has been removed from the corrected transient using the asymptote method. The usable late time range is extended by more than half a decade due to the offset correction applied and thus allows an interpretation of the decay to later times avoiding false interpretation as conductive structures at depth.

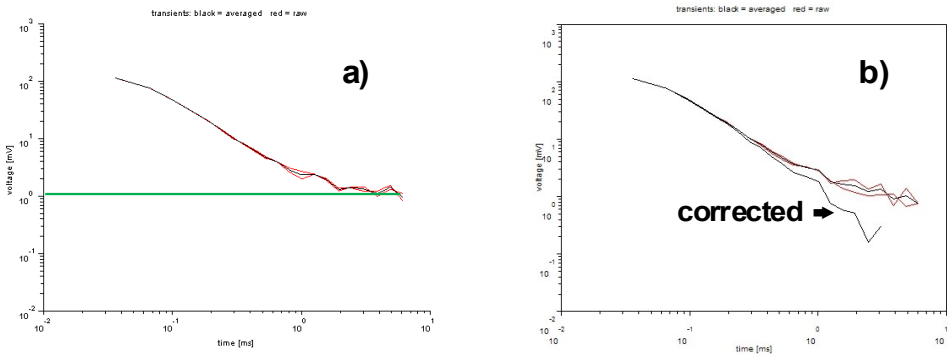

Figure 4: a) Estimation of offset through late time asymptote (green). A 1 mV offset and ±0.5 mV noise have been added to the transient. The offset of 1 mV can be recovered from the affected transient but may be slightly overestimated. b) The corrected transient avoids false interpretation as conductive structures at depth.

Summary and recommendations

A flat, almost horizontal, voltage decay curve of in-loop TEM soundings can be caused by offsets introduced by analogue front-end electronics in the receiving path. Due to the sampling procedure this offset effects are not generally cancelled out be the alternating transmitted waveform. Instead both the decay voltage and the amplifier voltage are reversed in polarity in usual sampling procedures. Therefore the stacking of transients leads to approximately constant values at late times, stabilized around the amplifier offset.

The offset effect can be cancelled by averaging of datasets of normal and reversed polarity of the primary field while the internal polarity of the receiver is maintained. This can be established by reversing the transmitted current, by flipping the active receiving antenna upside down or by reversing the polarity of the synchronization between receiver and transmitter.

Already recorded transients may be corrected later using an estimated offset, deduced from a late time asymptote. Additional noise measurements are helpful to identify any biasing due to offsets and the noise distribution with decay time.

The offset correction allows interpretation towards later times and avoids misleading model results with arbitrary conductors at depth.

Offshore magnetotellurics in the presence of bathymetry

Gerhard Kapinos [1], Heinrich Brasse [2]
Freie Universität Berlin, Fachrichtung Geophysik

1 Introduction

Offshore magnetotelluric (MT) investigations attract more and more attention. During the last years several offshore MT projects were carried out worldwide in marine environments and on the seaside of continental margins in order to estimate the conductivity distribution beneath the seafloor, particularly at ocean-continent subduction zones, where fluids and melts are known to control the subduction process. However, magnetotelluric responses obtained at the ocean bottom beneath a conductive ocean layer can be affected strongly by changes of seafloor topography. Synthetic 2-D studies, based on magnetotelluric investigation at the south Chilean continental margin, reveal that a changing ocean relief affects the impedances in TE mode, producing cusps in apparent resistivities curves and phases exceeding the normal quadrant. Likewise tipper transfer functions get very large. These effects can also be confirmed by real, measured data. We show that such disturbed responses cannot be connected together via Kramers-Kronig dispersion relations, as is the case with the causal (analytical) responses at the surface. An inspection of the distribution of electromagnetic fields shows that the non-validity or limited validity of these relations is due to the behavior of the bathymetry-affected magnetic field on the ocean bottom.

2 Offshore magnetotelluric and magnetic transfer functions in presence of bathymetry

The behavior of electromagnetic responses of a synthetic amphibious model was presented in (Kapinos and Brasse, 2010; Kapinos, 2011) and is shown in Figs. 1, 2.

A model incorporating a homogeneous half space with a resistivity of 100 Ωm and a conductive ocean with bathymetry of that observed at the South Chilean continental

[1]Now *Deutsches GeoForschungsZentrum GFZ*, kapinosg@gfz-potsdam.de
[2]heinrich.brasse@fu-berlin.de

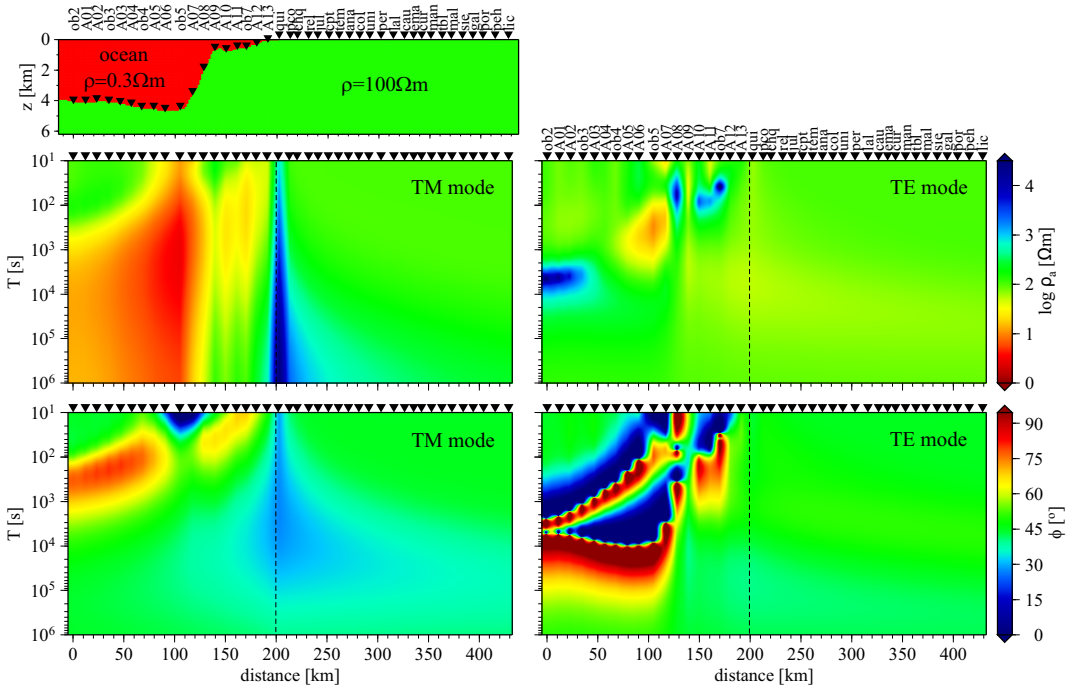

Figure 1: Responses of a synthetic amphibious model shown in the upper panel. Middle panel: resistivity of TM and TE modes. Bottom panel: phases of TM and TE modes. Dashed line separates the profile into offshore and onshore parts. Site locations correspond to the South Chile experiment; further sites are introduced for equidistant coverage.

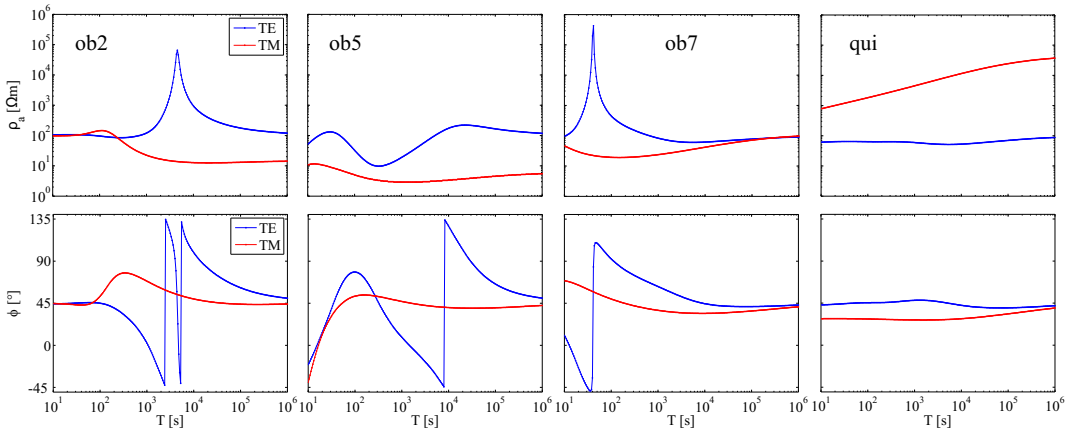

Figure 2: Apparent resistivities and phases on the sea floor and at a continental margin, derived at four selected points from the model presented in Fig. 1. The bathymetric rise has a huge distorting effect on the electric and magnetic fields on the seafloor, which results in anomalous transfer functions in TE mode, like sharp upward peaks in apparent resistivity and phases leaving quadrants. Note that phases, for reasons of clarity, are plotted in a range between 135° and -45°.

margin produces dramatic anomalous effects in the ocean, which can be observed in the phases and apparent resistivities of the TE mode. In TM mode, the phases are largely unaffected, the apparent resistivities seem to be diminished by an order of magnitude however, which is typical for galvanic distortion, and *static shift effect* in onshore magnetotellurics (Constable et al., 2009). The effects which occur only in the ocean appear clearly by plotting apparent resistivities and phases at representative points, as shown in Fig. 2. In TE mode the distorting effect of bathymetric rise is more spectacular. The resistivity in TE mode rises and falls dramatically, producing cusps in the image and phases in excess of -180° and 180°. Note that phases, for reasons of clarity, are plotted in a range between 135° and -45°, with exception of station *ob7*, so that phases that attain extreme values jump to another quadrant. The coast effect on land (right of the dashed line) is of only marginal significance compared to the anomalous transfer functions on the ocean floor. Similar anomalous features can be observed in modeled magnetic trans-

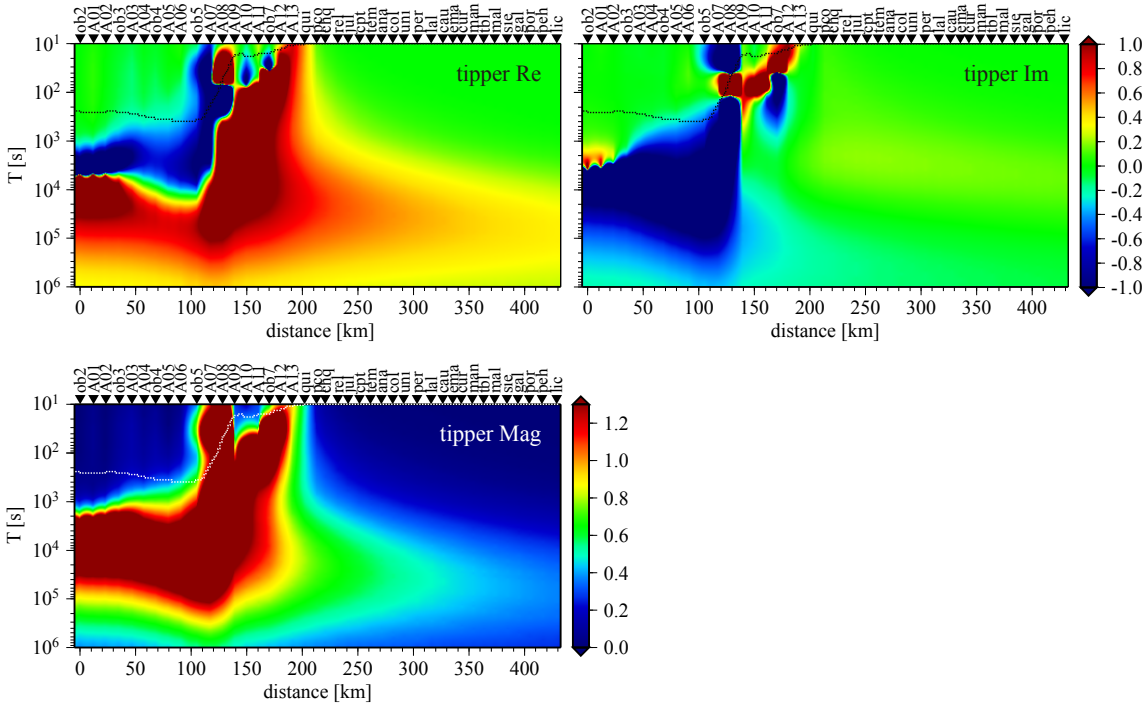

Figure 3: In the upper panel: the real (left) and the imaginary (right) parts; in the lower panel: the magnitude of the tipper calculated for the synthetic amphibious model shown at the top of figure 1. The dotted lines indicate the model bathymetry.

fer functions; the real and imaginary parts of which, as well as magnitude, are presented in Fig. 3. Jumps from very high positive to very high negative values in both real and imaginary parts dominate in the slope region. However, high values, often exceeding the color scale, in the left half of the images also show clearly that the tipper in the ocean is affected by the bathymetry, which is adumbrated by a dotted line, even far away from the slope. The unusually high imaginary values compared to what would be expected of

a land survey indicate a large phase shift between the vertical and horizontal magnetic fields at the seafloor; they are, in addition to the anomalous effects in magnetotelluric responses, like peaks in apparent resistivity and phases below -180° and over 180°, a typical feature for magnetotelluric surveys at the continental margin. Note the sharp threshold from high negative to moderate values: especially in the imaginary, but also in the real part, at point *A09* which marks the beginning of a plateau on the shelf. It is obvious that strong bathymetric changes cause correspondingly strong responses in tipper. Nevertheless, even slight changes in the shape of the seafloor are reflected by dramatic variations in the magnitude of the induction arrows, as becomes evident by inspecting the smooth bathymetric change between stations *A09* and *A13* and its large impact on the magnitude of the induction vectors. On the other hand, the ocean effect at onshore stations is limited to long periods and to near-coastal regions. This distorting effect of bathymetry seems to be confirmed by magnetic transfer functions measured at the offshore station *ob7*, the only station at the continental slope of the South Chilean margin. The real parts of the induction vectors shown in Fig. 4 are remarkable for their considerable amplitude, exceeding 1, and correspond roughly, at middle and long periods, with magnitude values calculated by the simple amphibious model. For short periods (up to 100 s), a comparison is impossible due to unavailable data.

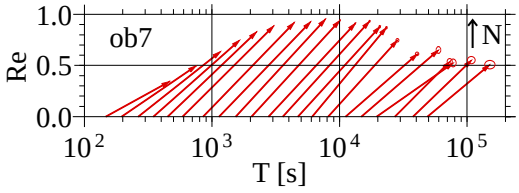

Figure 4: Real parts of the observed induction vectors at station *ob7*, deployed on the continental margin off Southern Chile. Induction vectors observed land-side are presented by Brasse et al. (2009). Much larger vectors were observed at the Costa Rican margin by T. Worzewski (pers. comm.)

Considering these anomalous responses, two questions arise:

- Does exist a relation between the anomalous phases and apparent resistivites in the TE mode?
- What causes this phenomenon, and how can it be explained?

3 Kramers-Kronig dispersion relations

The first question can be addressed by the *Kramers-Kronig dispersion relations* (*K-K relations*). Derived by R. de Laer Kronig and H. A. Kramers (de Kronig R. L., 1926; Kramers, 1927) the relations connect the real and the imaginary parts of any causal response function which is analytic in the upper half of the complex plane. These relations are well known and are widely used in different branches of physics, and their dereviation can be found in current literature and is also presented by Kapinos (2011). Such

relations also exist between the real and imaginary parts of a complex magnetotelluric impedance Z as long as Z satisfies the condition of causal response. The causality principle postulates that the response of a system is zero before an impulse is applied. In the context of electromagnetic induction in the Earth it implies that observed internal magnetic and electric fields at time t cannot be the effect of external magnetic field inducing at the time $t + dt$. Based on this causality principle, Weidelt (1972) also shows that the magnitude and the argument of the complex impedance function are not independent, but rather related to each other similarly to the way the real and the imaginary part are connected, i.e. in a causal system $\phi(T)$ can be calculated using values of $\rho_a(T)$, and vice versa:

$$\phi(\omega_0) = \frac{\pi}{4} + \frac{2\omega_0}{\pi} \wp \int_0^\infty \frac{\ln\left(\sqrt{\omega\mu_0\sigma(0)}\,|c(\omega)|\right)}{\omega^2 - \omega_0^2} d\omega. \tag{1}$$

Since the magnetotelluric transfer functions are conventionally presented on a periodic logarithmic scale, relation 1 can be expressed as (Fischer and Schnegg, 1980):

$$\phi(T_0) = \frac{\pi}{4} - \frac{1}{2\pi} \wp \int_{-\infty}^{+\infty} \ln\left|\frac{T_0 + T}{T_0 - T}\right| \frac{d\ln\left(\frac{\rho_a(T)}{\rho_0}\right)}{d\ln T} d(\ln T), \tag{2}$$

where $\omega = \frac{2\pi}{T}$ is the angular frequency, $\wp$ is the Cauchy principal value and $\rho_0 = \frac{1}{\sigma(0)}$ a reference resistivity. For magnetotelluric applications, relations between the apparent resistivity and the phase are more interesting than relations between the real and imaginary parts. The fact that the phase $\phi_{ij}(T)$ can be derived from the resistivity $\rho_{a_{ij}}(T)$, and vice versa, can be now used to study the relationship between the anomalous apparent resistivities and phases at the continental margin, disscussd and presented in (Kapinos and Brasse, 2010; Kapinos, 2011) and in Figs. 1, 2.

3.0.1 Application of the Kramers-Kronig relations to magnetotelluric 2-D models

Weidelt (1972), Fischer and Schnegg (1980, 1993) and Weidelt and Kaikkonen (1994) have already presented examples which quantitatively prove the validity of these relations for 1-D and 2-D structures in TM mode. Another example relating to an offshore model is presented in Fig. 5 (top). The model is a usual 2-D scenario and includes a conductive half layer (0.3 Ωm) embedded in a 100 Ωm resistive background. The half layer is bounded to the right by an oblique conductivity contrast, which would correspond to a slope in a offshore model; however, this is not a offshore model, but rather a 2-D onshore model with stations on the model surface.

The phases' responses on the surface, computed directly from the model, and presented in Fig. 5 in the middle panel, correlate very well with phases in the lower panel, which are calculated numerically from apparent resistivities via the Kramers-Kronig relations. Fig. 5 suggests that in 1-D (approximately station *A22* on the right edge on the model) or 2-D conditions the K-K relations is valid in TM as well as TE mode. The quality of the correlation can be more precisely evaluated by taking into account phase curves at

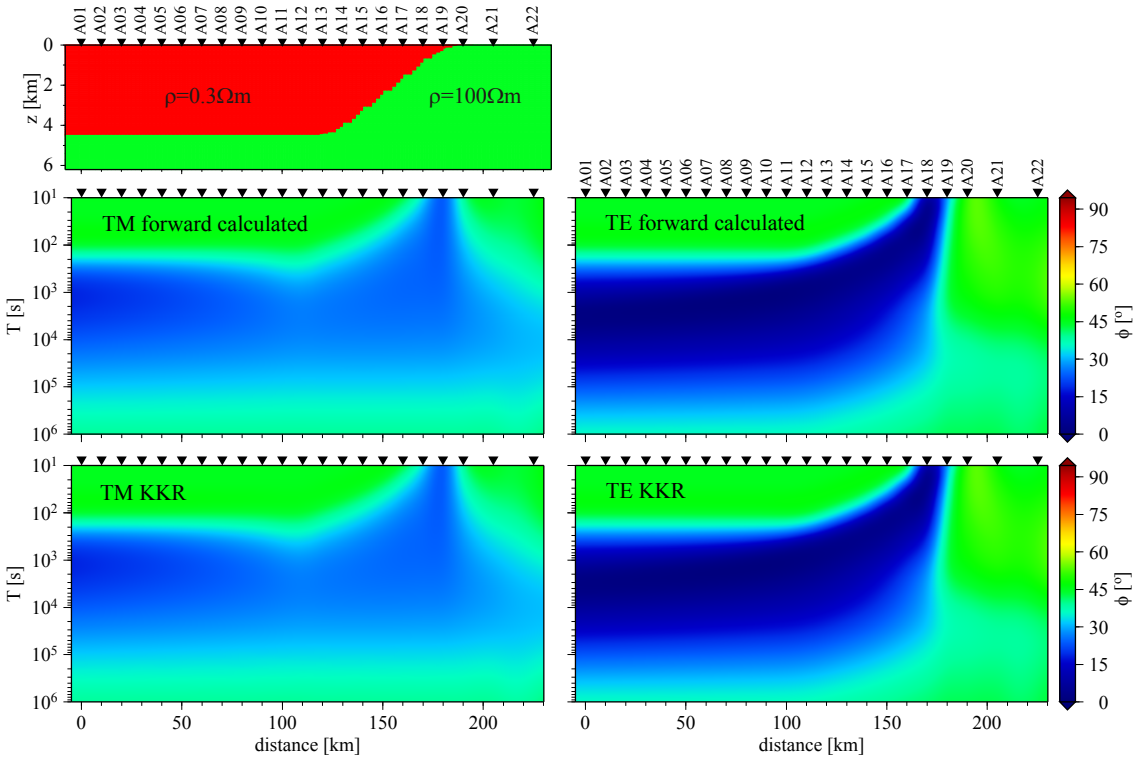

Figure 5: Responses in the form of pseudo sections calculated for a 2-D onshore model that is shown in the upper panel. Middle panel: phases of TM and TE modes derived directly from this model. Bottom panel: phases of TM and TE modes calculated from the Kramers-Kronig relations via eq. 2.

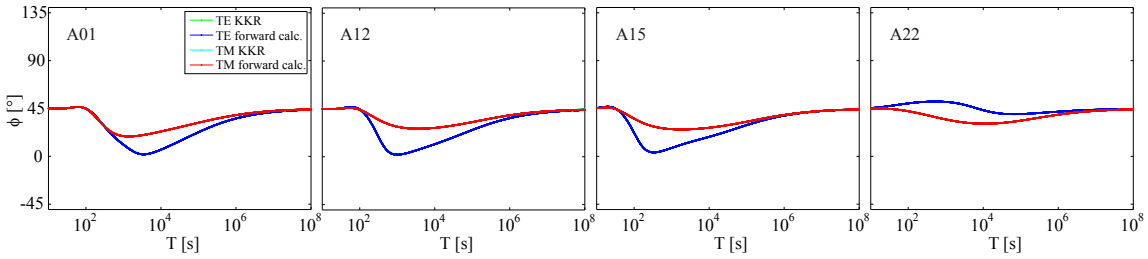

Figure 6: Phase curves calculated at four representative profile points for the 2-D onshore model shown in Fig. 5. In blue and red: phases in TE and TM mode derived directly from the model; in green and cyan: phases in TE and TM mode calculated from the Kramers-Kronig relations via eq. 2; no difference is seen.

four representative stations selected from different profile sections, as shown in Fig. 6. A discrepancy of less than a few tenths of one degree between phases calculated with the Kramers-Kronig relations and phases derived directly from the model is due to numerical inaccuracies and thus confirms the validity of the Kramers-Kronig relations

for the presented 2-D model.

Having verified the validity of these relations for a 2-D onshore model, we return to the anomalous magnetotelluric responses in TE mode in Fig. 1 prepared to address the question asked at the end of the previous section, which we here restate more precisely: Do the anomalous phases on the seafloor in the presence of bathymetry, derived directly from the model, correspond with phases calculated from anomalous offshore resistivities via the Kramers-Kronig relations? Weidelt (1994) qualitatively illustrated the induction process in the vicinity of strong bathymetry, as found at a continental margin, and suggested anomalous behavior of phases in the TE mode might occur if inhomogeneous anomalous sources control the induction.

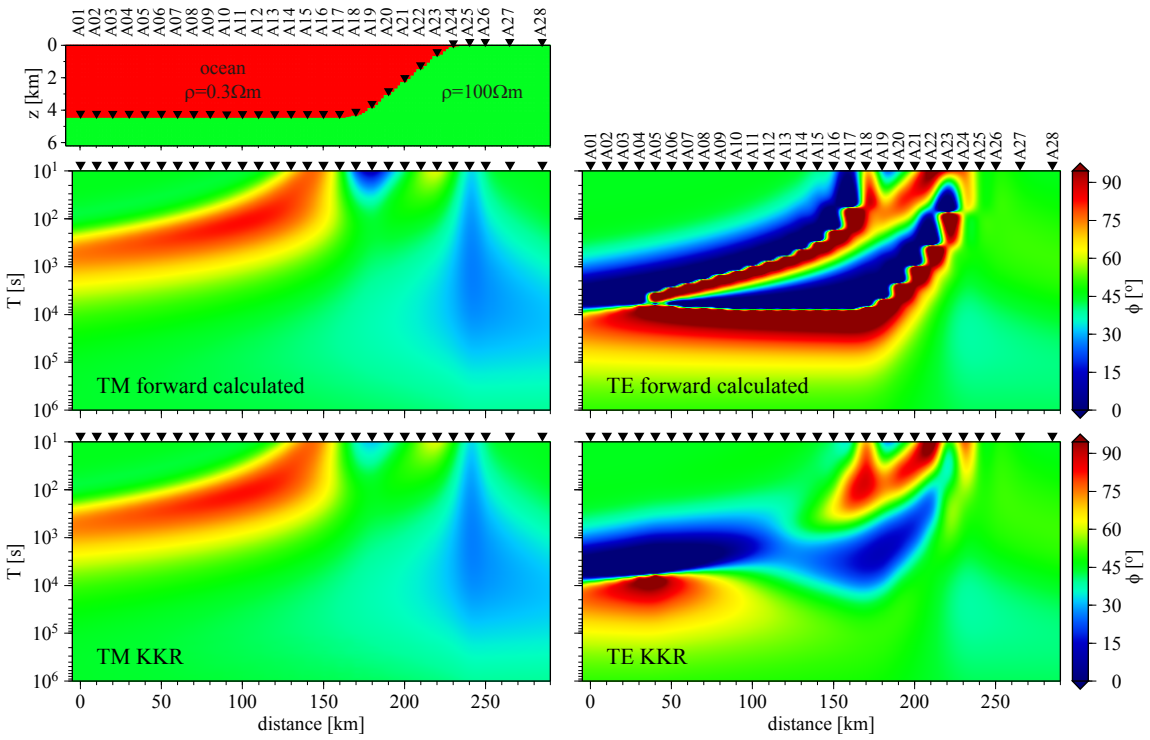

Figure 7: Responses in the form of pseudosections, calculated for the 2-D amphibious model shown in the uppermost panel. The model consists of a highly conductive ocean (0.3 Ωm), and a resistive homogeneous half space (100 Ωm) with a step bathymetry. Middle panel: phases of the TM and TE modes derived directly from this model. Bottom panel: phases of TM and TE modes calculated from the Kramers-Kronig relation via eq. 2.

For a quantitative evaluation an amphibious model, presented in Fig. 7, was constructed. It incorporates a conductive ocean (0.3 Ωm) with simple bathymetry and a resistive background (100 Ωm). The model geometry is as in Fig. 5, but unlike the onshore model, the stations are not placed on the model surface, but on the seafloor and on the continental slope, i.e. below highly conductive sea water.

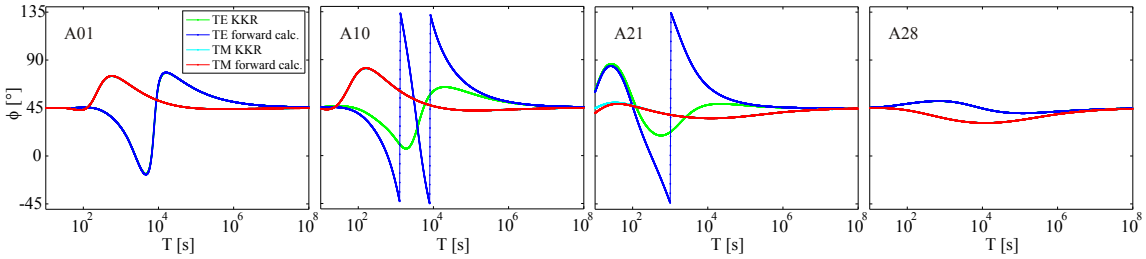

Figure 8: Phase curves calculated at four representative profile points for the 2-D amphibious model shown in Fig. 7. While at sites located far enough from the bathymetric changes (*A01*, *A28*), the phases derived directly from model agree very well with the phases calculated from the Kramers-Kronig relations via eq. 2, this is not the case at sites located close to the slope (*A10*, *A21*). Note that at sites *A01* and *A28* the curves calculated via K-K relations presented in green and cyan are covered by curves obtained directly from the model and thus are difficult to recognize.

In TM mode the phases calculated via the Kramers-Kronig relations agree very well with those derived directly from the model. Some discrepancies can be observed at very short periods in the vicinity of the slope, and may be caused by numerical inaccuracies due to discontinuous TM responses across a strong conductivity gradient. More interestingly, TE mode phases derived directly from the model and those calculated via Kramers-Kronig relations yield substantially different results. The images agree only on the flanks, far away from bathymetric changes, where the induction is not affected by the shape of the seafloor. In the central part there is no correlation between phases derived from the model and by the Kramers-Kronig relation. A more detailed view of the phases in the TE and TM modes at selected single points of the profile is presented in Fig. 8. It is clear from these figures that the spikes in apparent resistivities and reversal phases in the TE mode cannot be reproduced via the Kramers-Kronig relations. Note that the amphibious profile has been extended by 60 km on the sea side, compared to the onshore profile, by adding 6 additional stations, in order to investigate how far from the slope the offshore impedances are affected. Fig. 7 reveals that at long periods, even responses more than 100 km away from the bathymetric onset are still strongly affected by heterogeneous fields induced in the vicinity of the slope.

4 Discussion

A thorough study verifying the validity of Kramers-Kronig relations for a typical synthetic 2-D onshore impedance tensor is given by Fischer (1992) and in Fischer and Schnegg (1993). The authors state that in 1-D case and in TM mode the external and internal magnetic fields are practically identical at the surface, and thus conclude that a 2-D model in TM mode justifies these relations. The TE mode is more complicated, since the fields are not identical, and thus the question of whether for a 2-D model in TE mode, the application of the Kramers-Kronig relations is justified seems to be legitimate.

A discussion about the necessary conditions for this is raised in Yee and Paulson (1988), who suggest adoption of the properties of Kramers-Kronig relations, valid for the 1-D case, for the general case of a 3-D impedance tensor. This assumption was seriously questioned by Egbert (1990). In a critical review, he raises doubts as to whether, for a general 3-D magnetotelluric impedance tensor, the Kramers-Kronig relations are still preserved; and shows that in a 3-D Earth, certain conductivity distributions can violate the fundamental conditions necessary to connect the modulus and phase of an impedance tensor. He argues that under certain circumstances, the linear relation between the horizontal electric and magnetic field vectors is not necessarily causal, and thus does not satisfy conditions required by the Kramers-Kronig relations. The crucial point of this argumentation is the need to distinguish between the physically obvious causality and passivity of the whole system and the causality and passivity of the impedance tensor, which is a ratio of the **total** (external and internal) magnetic and electric field at a single measurement point. While the causality is justified if the impulse arises from an external magnetic field, it is not the case if the total magnetic field is regarded. By way of example, he outlined a conductivity distribution in which the induced internal magnetic field cancels the external source field so that the causality principle at a single point fails. In a further example, Egbert (1990) contrives a conductivity distribution which causes a violation of the local passivity condition, defined here on the basis of simple energy conservation. Such failure can occur if the currents focus on a local conductor. The high concentration of current acts as an internal source, whose energy flux is larger than that of the external source, producing anomalous phases exceeding the quadrant, and not satisfying the passivity requirements of magnetotelluric impedance. This phenomenon, termed "current channelling", since currents are strongly bundled, violates the passivity conditions at a single point, and limits the usefulness of the Kramers-Kronig relations.

Although it is also generally possible to contrive a 2-D conductivity distribution leading to channelling of currents, Fischer (1992) suggests that they wouldn't result in a breakdown of the dispersion relations, and Egbert (1990) argues that for 2-D conductivities the impedance is in TM mode certainly and in TE mode almost certainly causal.

However, considering the special induction conditions in marine environment and the anomalous responses on the seafloor, the questions of the validity of the Kramers-Kronig relations in the TE mode or of the validity of the assumption of causality and passivity of such a system seem to be more current than ever. Berdichevsky (1999) postulated "to leave room for the possibility of violation of dispersion relations in the E-polarized 2-D models and 3-D models", and presented a model which reveals an obvious discrepancy between responses derived directly from this model and responses calculated via KK-relations. More interesting in the context of the present work is the amphibious 2-D model presented by Alekseev et al. (2009). The phases of this model leave the quadrant in the TE mode, at sites close to the continental slope, and they interpreted this behavior as indicator for the violation of the KK-relations in the TE mode.

The answer to the question for the reason of this phenomenon may be provided by studying the induction and distribution of electric currents and magnetic fields in the ocean, or particularly on the ocean bottom, in presence of bathymetric changes.

Due to the high sea water conductivity, the induced electric currents concentrate pri-

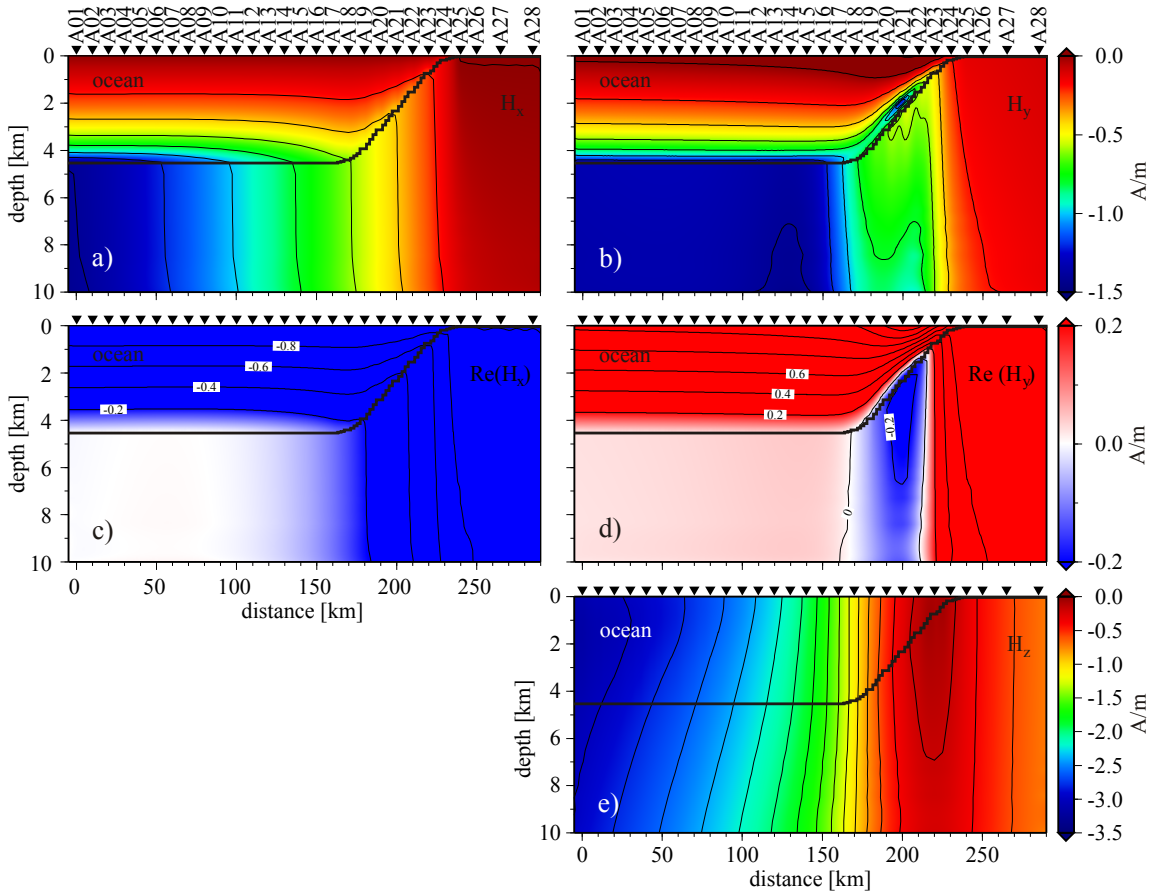

Figure 9: Distribution of magnetic fields at a period of $T = 315\,\mathrm{s}$ at on- and offshore parts of the continental margin. The left column shows magnetic fields in TM mode; right column in TE mode. The input reference magnetic intensity on the surface is $1\,\mathrm{A/m}$. In a)-b) and e) the logarithm of the field and current magnitude was taken, whereas in c)-d) a linear scale is used. a) Magnitude of H_x (TM mode), b) magnitude of H_y (TE mode), c) real part of H_x, d) real part of H_y; note that, at the slope in TE mode, $\Re(H_y)$ reverses on the ocean bottom (blue color corresponds to negative values), e) magnitude of vertical magnetic field H_z.

marily in the ocean, avoiding the more resistive subsurface and generate a secondary magnetic field. This opposes the primary field, so that the total magnetic field diminishes considerably, or even disappears completely in the case of an insulating substrate. The effect for the one dimensional case was discussed in detail in Kapinos and Brasse (2010) and Kapinos (2011). However, at continental margins, the conditions become two dimensional, and the bathymetric changes affect the distribution of electric currents and the electromagnetic fields. To study this, fields and electric currents were calculated for the model presented in Fig. 7 by applying the 2-D finite-difference algorithm of Pek and Verner (1997), and plotted for a period of $T = 315\,s$ in Fig. 9 and 10. Fig. 9, parts a)-b), show clearly once again that far enough from any bathymetric changes the hor-

izontal magnetic field in the ocean experiences a strong attenuation and decays on the ocean bottom, to a slight fraction of its surface value, whereas the horizontal electric field in Fig. 10 doesn't change significantly, in accordance with previous conclusions for one dimensional conditions. A striking feature is the different color patterns and the densities of field contours in the offshore and onshore model parts; or, respectively, in the highly conductive ocean and the less conductive background. The reason for this is higher attenuation and smaller skin depth for the fields in the highly conductive seawater on the left side (small distance between the contours) and smaller attenuation and larger skin depth in less conductive background on the right side (large space between the contours). Note that in Fig. 9 a)-b) and e) as well as in 10 the logarithm of the field and current magnitude is taken, whereas Fig. 9 c)-d) show the real parts of H_x and H_y using linear scale.

At a continental margin, where the seafloor shallows towards land, the density of the TE polarized electric currents j_x flowing in the ocean, i.e. above the ocean bottom and along the coast, increases as shown in Fig. 10 i) (brown color and higher density of contour lines). These squeezed currents induce a secondary, anomalous, and on the ocean bottom oppositely directed magnetic field, that becomes predominant in the shelf region in TE mode (Weidelt, 1994), not only below but also above the seafloor, in the deeper part of the ocean, as shown in Fig. 9 d) (blue color corresponds to reverse field). This effect is not seen in TM mode (Fig. 9 c)). According to Maxwell's equations this magnetic field curls around the electric current, so that a vertical magnetic field H_z also arises at the lateral conductivity gradient, as expected, and as shown in Fig. 9 e). This effect, known in terrestrial magnetotellurics as coast effect (Fischer, 1979), can also be seen in the contour pattern of the electric field in TE mode (E_x) in Fig. 10 g). The bending contours of constant E_x correspond to magnetic stream lines with a strong vertical component in TE mode around the slope. The contours of the magnitude of the electric field (or, equivalently, the streamlines of magnetic field) turn horizontal as the conditions becomes one dimensional.

The impact of bathymetric changes on the fields is reflected directly in the impedance relation. While the horizontal magnetic component vanishes accompanied by arising vertical magnetic field, as seen in Figs. 9 b) d) e), so that the denominator tends to zero, the electric field in the numerator is only marginally modified, and thus the impedance becomes singular; see Constable et al. (2009). Furthermore, resistivities in the TE mode increase, generating upward cusps, while the phase jumps by 180°, as presented in Fig. 8; and the tipper gets very large. The period at which these effects occur depends on the position of the probe in relation to the slope, and corresponds to the lateral distance at which a transfer function is sensitive to bathymetry. However, at high frequencies the field is generally unaffected by the bathymetry and the results are MT-like because the fields still look like plane waves. At low frequencies, the currents are below the ocean. At intermediate frequencies, the currents prefer to accumulate in the highly conductive ocean instead of the resistive ocean bottom, and this causes the responses to look like those due to infinite line currents right above the station. Note that if the MT responses are recorded at the top of the sea (Fig. 5), they behave as in a usual 2-D case, since all the currents are distributed below the sounding surface, instead of above, as is the case

in the presented marine model.

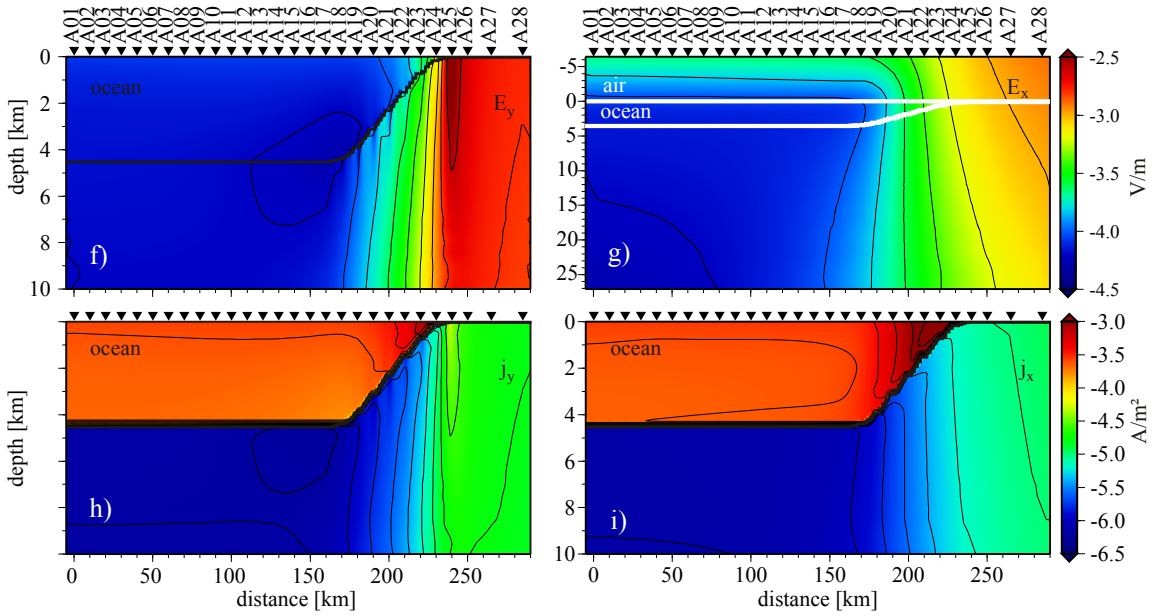

Figure 10: Distribution of electric fields and currents at a period of $T = 315\,s$ at on- and offshore parts of the continental margin. The left column shows electric fields and current in TM mode; right column in TE mode. f) magnitude of E_y, g) magnitude of E_x; note the different depth scale and that the contours of E_x bend above the surface in the supplementary air layer (the contours of the magnitude correspond with stream lines of H_y in Fig. 9), h) magnitude of electric currents j_y in TM mode, i) magnitude of electric currents j_x in TE mode. The density of j_x increases significantly in the shallow ocean, close to the coast (brown color and higher density of contour lines). Note that the currents are continuous across the interface, but due to the large conductivity contrasts between the ocean and the ocean bottom the density vary very rapidly.

The anomalous responses on ocean bottom are overcome or mitigated by introducing a very conductive layer below the seafloor, which must be at least several kilometers thick. However, the assumption of an oceanic crust being wholly conductive seems unrealistic. This is even more the case for the continental crust below the slope: every aquiclude would prohibit the intrusion of sea water into deeper layers. But another class of models makes the effect described above disappear, too: the association of the upper part of the downgoing plate with a good conductor (in accordance with standard models of subduction).

References

Alekseev, D. A., Palshin, N. A. and Varentsov, I. M.(2009). *Magnetotelluric dispersion relations in a two-dimensional model of the coastal effect.* Izvestiya, Physics of the Solid Earth, 45(2), 167–170.

Berdichevsky, M. N.(1999). *Marginal notes on magnetotellurics*. Surv. Geophys., 20, 341–375.

Brasse, H., Kapinos, G., Li, Y., Mütschard, L., Soyer, W. and Eydam, D.(2009). *Structural electrical anisotropy in the crust at the South-Central Chilean continental margin as inferred from geomagnetic transfer functions*. Phys. Earth Planet. In., 173, 7–16.

Constable, S. C., Key, K. and Lewis, L.(2009). *Mapping offshore sedimentary structure using electromagnetic methods and terrain effects in marine magnetotelluric data*. Geophys. J. Int., 176, 431–442.

de Kronig R. L.(1926). *On the theory of dispersion of X-rays*. J. Opt. Soc. Am., 12, 547–556.

Egbert, G. D.(1990). *Comments on 'Concerning dispersion relations for the magnetotelluric impedance tensor' by E. Yee and K.V. Paulson*. Geophys. J. Int., 102, 1–8.

Fischer, G.(1979). *Electromagnetic induction effects on the ocean coast*. Proc. IEEE, 67, 1050–1060.

Fischer, G.(1992). *Die kausalen Dispersions-Relationen in der Magnetotellurik*. In: V. Haak and H. Rodemann (Eds.), *Protokoll über das Kolloquium "Erdmagnetische Tiefensondierung" in Borkheide bei Berlin vom 25.-29. Mai 1992*, 31–41.

Fischer, G. and Schnegg, P. A.(1980). *The dispersion relations of the magnetotelluric response and their incidence on the inversion problem*. Geophys. J. R. astr. Soc., 62, 661–673.

Fischer, G. and Schnegg, P.-A.(1993). *The magnetotelluric dispersion relations over 2-D structures*. Geophys. J. Int., 115, 1119–1123.

Kapinos, G.(2011). *Amphibious Magnetotellurics at the South-Central Chilean Continental Margin*. Dissertation, Freie Universität Berlin. Fachbereich Geowissenschaften.

Kapinos, G. and Brasse, H.(2010). *Some notes on bathymetric effects in marine magnetotellurics, motivated by an amphibious experiment at the South Chilean margin*. In: O. Ritter and U. Weckmann (Eds.), *Prot. 22. Koll. Elektromagnetische Tiefenforschung*, 198–209, Heimvolkshochschule am Seddiner See, 28. September-2. October. 2009. ISSN 2190-7021.

Kramers, H. A.(1927). *La diffusion de la lumière par les atomes*. Atti Cong. Intern. Fisica, 2, 545–557.

Pek, J. and Verner, T.(1997). *Finite-difference modelling of magnetotelluric fields in two-dimensional anisotropic media*. Geophys. J. Int., 128, 505–521.

Weidelt, P.(1972). *The inverse problem of geomagnetic induction.* Z. f. Geophys., 38, 257–289.

Weidelt, P.(1994). *Phasenbeziehungen für die B-Polaristation.* In: Bahr, K. and Junge, A. (Eds.), *Protokoll über das Kolloquium "Erdmagnetische Tiefensondierung" in Höchst in Odenwald vom 28.-31. März 1994*, 60–65.

Weidelt, P. and Kaikkonen, P.(1994). *Local 1-D interpretation of magnetotelluric B- polarization impedances.* Geophys. J. Int., 117, 733–748.

Yee, E. and Paulson, K. V.(1988). *Concerning dispersion relations for the magnetotelluric impedance tensor.* Geophysical Journal, 95, 549–559.

What is SPAM four for?

R. Klose (reinhard.klose@gfz-potsdam.de), G. Schmidt, O. Ritter (oliver.ritter@gfz-potsdam.de), Helmholtz Centre Potsdam GFZ, German Research Centre for Geosciences,
G. Dawes, McD Systems, Edinburgh, UK

The short period automatic magnetotelluric (SPAM) data acquisition instruments are the backbone of the MT component of the Geophysical Instrument Pool Potsdam (GIPP). Here we introduce SPAM Mark IV of the instruments (SPAM4), designed and built by Graham Dawes, McD Systems, Edinburgh in close cooperation with the GeoForschungsZentrum (GFZ), Potsdam. Since 2008 SPAM4s have been used successfully in a number of field experiments. Currently, 40 SPAM4s are available from the GIPP free of charge to all members of the German scientific community.

GIPP-MT

The MT part of the GIPP provides instruments and sensors for magnetotelluric data acquisition. Instruments can be combined in various ways (Figure 1).

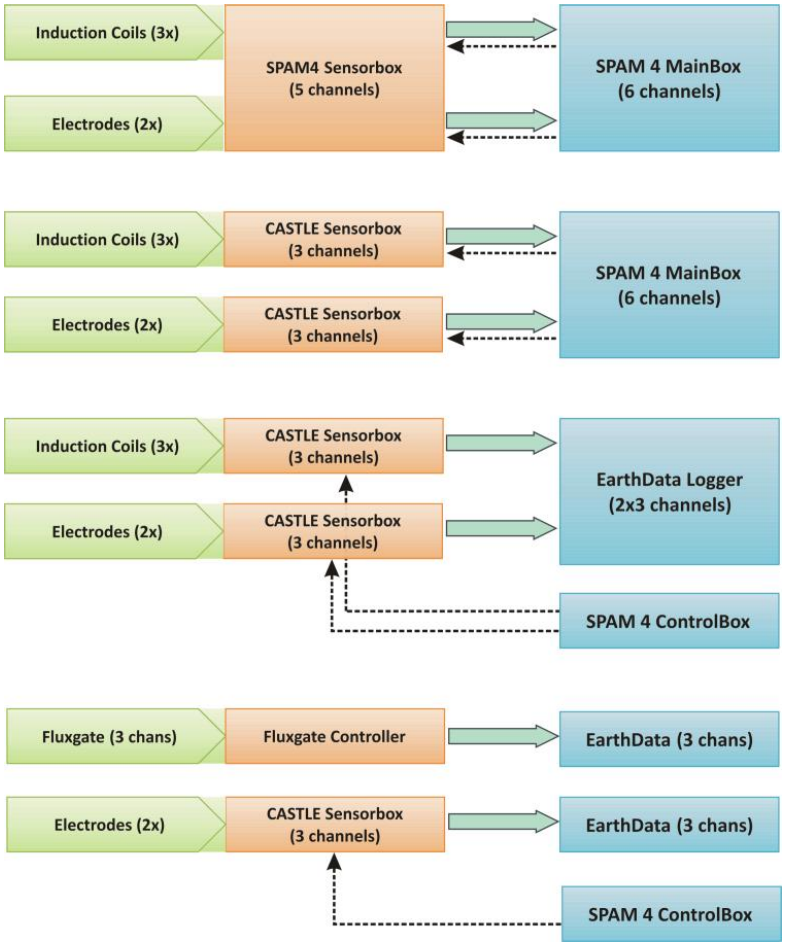

Figure 1: Possible combinations of instruments and sensors available from the GIPP-MT. Sensor level is marked in green, signal preconditioning in orange and data recording in blue.

Sensors available from the GIPP-MT are Metronix MFS05/06/07 induction coil magnetometers, Geomagnet fluxgate magnetometers, Pulz/Magson fluxgate magnetometers and GFZ-type Ag/AgCl non-polarizing electrodes. The sensors are connected to Sensor Boxes which provide power and signal preconditioning. Sensor Boxes available at the GIPP-MT include three channel CASTLE Sensor Boxes for magnetic or electric field sensors and the five channel SPAM4 Sensor Boxes, suitable for two electric and three magnetic (induction coil) sensors. All Sensor Boxes can be programmed (e.g. filter and gain settings) via SPAM4 Control Boxes or using the SPAM4 Main Boxes. Once programmed, all settings are stored internally (EEPROM) and all information is restored after re-powering.

SPAM4 and EarthData (EDL) data acquisition systems convert the (preconditioned) analogue sensor signals to digital data streams. EDL systems store time-series data of up to six channels. In addition to that, SPAM4 systems allow real-time quality control of time and frequency domain data and MT transfer function results. Up to 8 digitally filtered frequency bands can be recorded and analyzed concurrently. In the following, we concentrate on the SPAM4 data acquisition system.

SPAM4 Hardware

The SPAM4 system consists of a Main Box and a Sensor Box. The Sensor Box is used to power sensors and to precondition incoming analogue sensor signals. It can be connected to the Main Box via two Sensor Box cables. The Main Box digitizes the incoming signals on up to six channels and processes and stores the acquired data.

Figure 2 - a: SPAM4 Main Box with input sockets for 2 x 3 analogue channels (SBX1/2), GPS antenna, WLAN, power supply and LAN. LxWxH: 37.5x29.5x14.5 cm. Weight: 4.8 kg. - b: Sensor Box with input sockets for electric and magnetic field sensors and output sockets for Main Box connection. LxWxH: 26.0x18.5x9.3 cm. Weight: 2.9 kg.

SPAM4 Main Box

The Main Box (Figure 2a) is equipped with a low-pass filter and six 24-bit sigma-delta A/D converters, one for each channel. The low-pass filter can be set to 500 Hz or 50 kHz cutoff frequency. The A/D converters are GPS synchronized with an absolute accuracy of 150 ns. The highest possible sampling frequency is 100 kHz in burst mode. For continuous data acquisition sampling frequencies between 50 kHz and 500 Hz can be selected. Instrument noise level is at 16 nV/sqrt(Hz). All Main Box components can be tested with an inbuilt test signal generator (Figure 3).

The typical power consumption is about 7 W for the Main Box and approximately 1.5 W for the Sensor Box, depending on the type of sensors connected. The system runs on any 12 V DC power supply and supports hot-swapping of batteries.

The Main Box is equipped with a small PC (SBC) running on Microsoft Windows7, which communicates with the SPAM4 hardware components (Control Board, Clock/GPS Board, Castle Control Board) via USB interfaces (Figure 3). The SBC is accessible via Remote Desktop connection over Ethernet or WLAN. All USB storage solutions are supported, including hard disks, USB-sticks and solid-state disks.

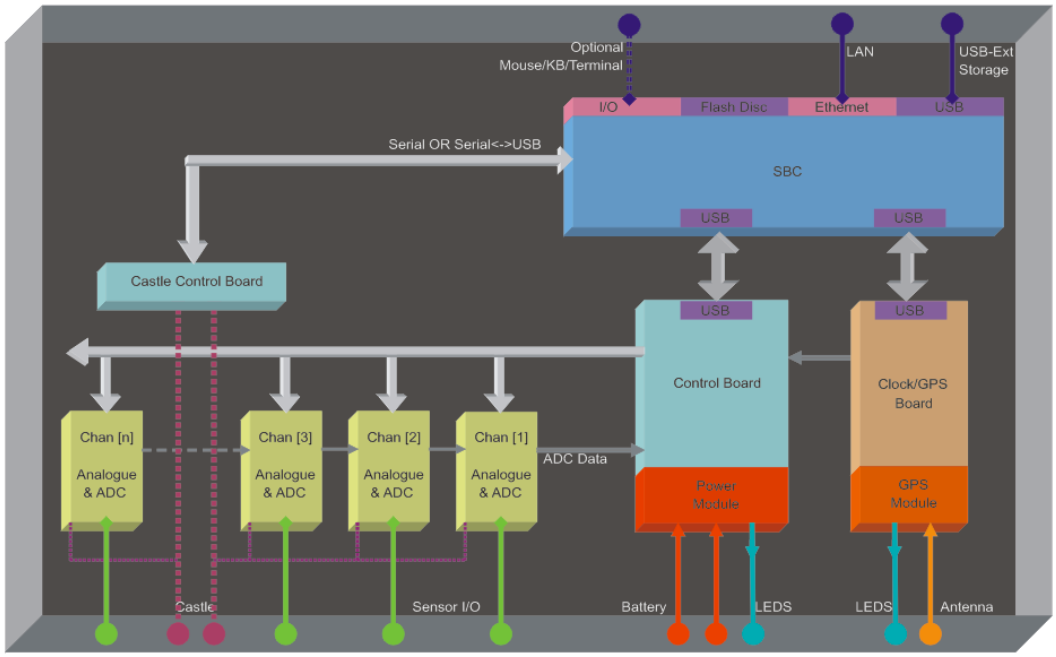

Figure 3: Block Diagram of a SPAM4 Main Box. The Control Board manages data acquisition (D/A converters) and overall system status. The GPS board provides a highly accurate, PLL-stabilized internal clock and location and time information. The Castle Control Board is used to control Sensor Box behaviour. All Boards communicate with the SPAM4 Board Computer (SBC) via USB interfaces. The SBC itself can be accessed via Ethernet.

Sensor Box

The SPAM4 Sensor Box (Figure 2b) is used to power connected sensors and precondition the incoming, analogue signals. For this purpose it is equipped with an input amplifier, an optional high-pass filter of 4 Hz, a low-pass filter of 2 kHz or 130 kHz, and an output amplifier. Each Sensor Box consists of five channels, three for connecting magnetic field sensors and two for connecting electrodes. Input and output gains can be set to 1, 2, 4 or 8 individually for each channel, reaching a total gain of up to 64. A test signal can be generated internally and fed in before the first amplifier (Figure 4).

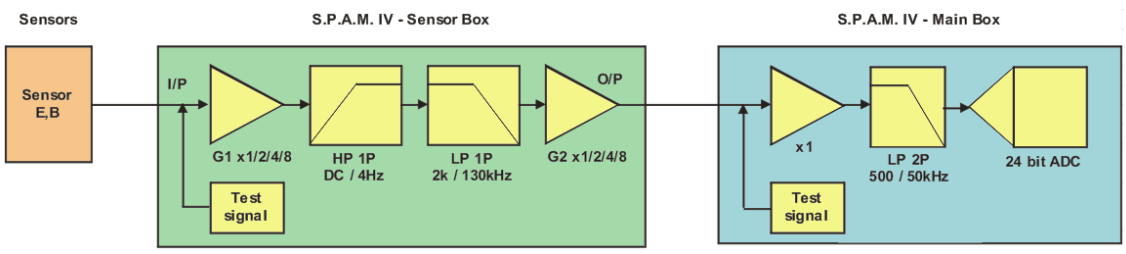

Figure 4: Block Diagram of the SPAM4 system with Sensor Box

SPAM 4 Software

The SPAM4 software (Figures 5 to 8) runs on the SBC of the SPAM4 Main Box. A graphical user interface provides access to system functionality. The SPAM4 software allows real-time quality control of time and frequency domain data and MT transfer function results. Up to 8 digitally filtered frequency bands can be recorded and analyzed concurrently (Figure 7). One can choose between periodically scheduled time segments or continuous data recording for each band.

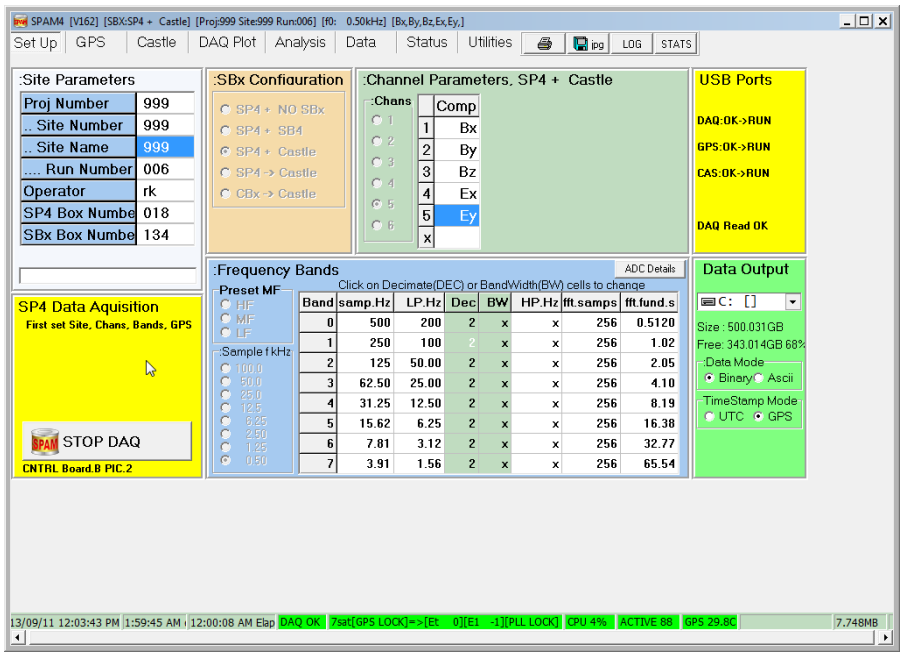

Figure 5: Setup screen of the SPAM4 software. In the example shown, the Main Box is connected to a CASTLE Sensor Box to record data of five channels with 500Hz sampling frequency. 8 concurrent frequency bands are selected. GPS lock has been obtained and data acquisition has started.

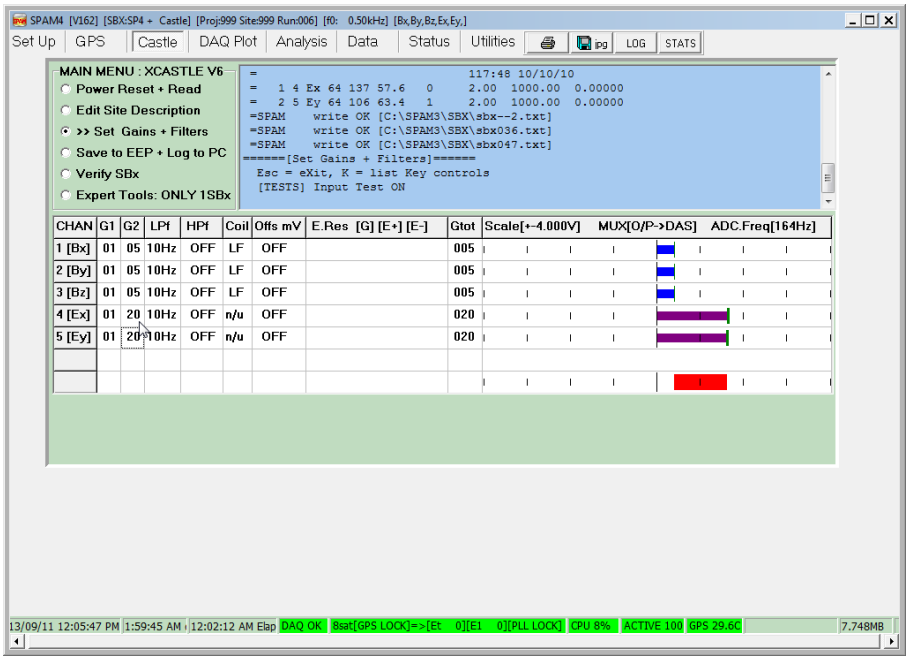

Figure 6: Setup of CASTLE Sensor Boxes using the SPAM4 system for communication and display. Gain, low-pass filter and DC-offset can be adjusted. The bar chart displays signal amplitudes; in the example a test signal is fed into the system. Ground contact resistances can be measured directly with the Sensor Box using an AC signal which does not polarize the electrodes.

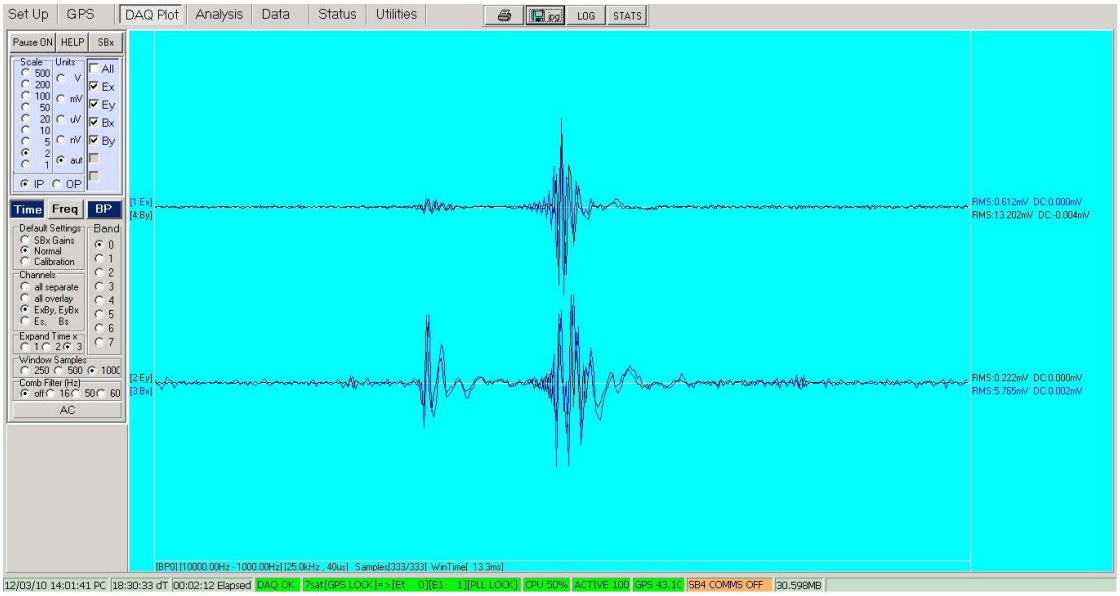

Figure 7: Viewing time-series in real-time. In the example, sampling rate is 25 kHz. BxEy and ByEx channels are superimposed. The operator can select combinations of channels, their scales, switch between low-pass and band-pass filtered time series, select frequency bands and display real-time frequency spectra.

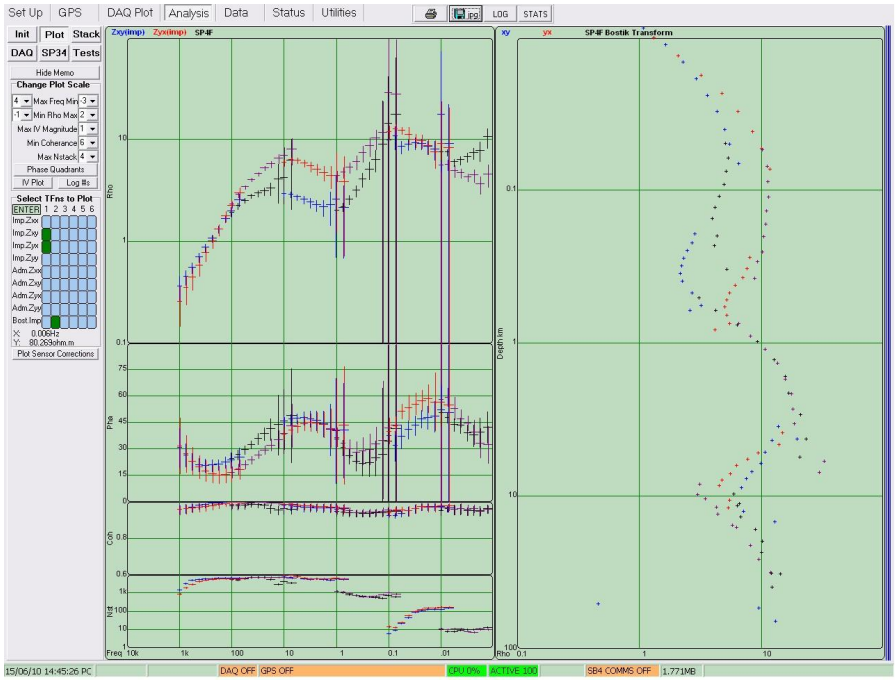

Figure 8: Real-time analysis of the data. Shown parameters are apparent resistivity and phase, coherency, number of stacks and Bostick transform.

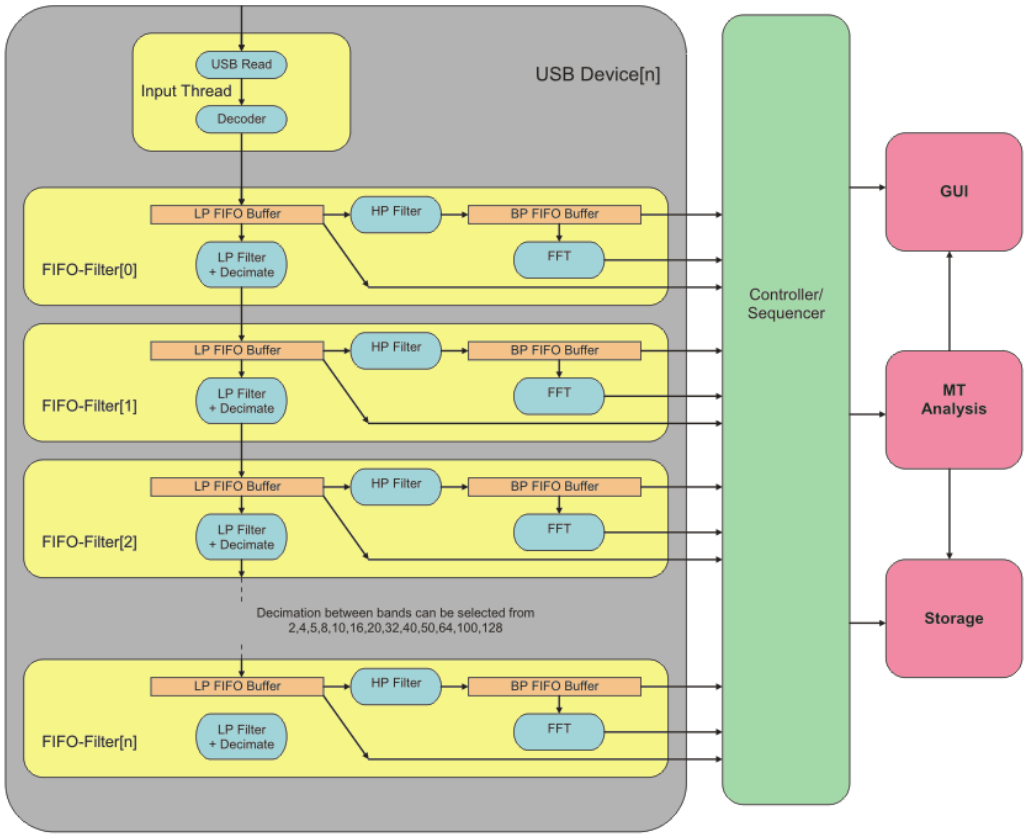

Figure 9: Block Diagram of the SPAM4 software operation. Input A/D data is fed into a cascade band-band decimation scheme. For each of up to 8 bands the data is digitally FIR low-pass filtered and IIR high-pass filtered. A Fast Fourier Transform is applied to the band-pass filtered data. A Sequencer manages the distribution of the buffered data to display, storage and processing modules.

Current and future Developments

Since we have access to all aspects of hard- and software, we can change the system as needed. With the introduction of controlled source magnetotellurics, we could extend the functionality of the system to adapt to the new requirements. In modern controlled-source geo-electromagnetic field campaigns it is essential for economic and organizational reasons to control and monitor an entire set of SPAM4s centrally. Therefore, we have developed a software package which automatically establishes a self-healing WLAN mesh over all SPAM4s in range. A central controlling computer is used to visualize data streams and status information from all sites. It is also possible to remote control the SPAM4s. As the original SPAM4 software has been built using now obsolete compiler libraries, switching to a new compiler was necessary. The opportunity was taken to restructure the existing software sources and to adapt new concepts. In addition to remote-controlling and monitoring the SPAM4 Main Boxes, a real-time time- and frequency domain stacking module is being implemented.

Self-healing WLAN mesh

The WLAN ad-hoc mesh network is built on cheap and easy to maintain, ordinary WiFi components, the LogiLink WiFi USB dongle and a 9 dBi omnidirectional antenna. Even under bad line of sight conditions (narrow tree corridors and antenna on ground level) we could achieve data rates of 1.3 MB/s on distances of more than 1 km. For the automatic mesh construction, each SPAM4 periodically broadcasts and listens for “sign of life” UDP-datagrams (User Datagram Protocol). Upon

receiving such a datagram, a TCP (Transmission Control Protocol) connection to its sender is established. The more robust TCP connection is then used for all data transfers. This mechanism is also applied for reconnecting ("self-healing") when a connection is lost. Every SPAM4 manages a list of TCP connections to its neighbors. Over these connections control messages can be (re)broadcasted to establish the telecommunication infrastructure over the mesh.

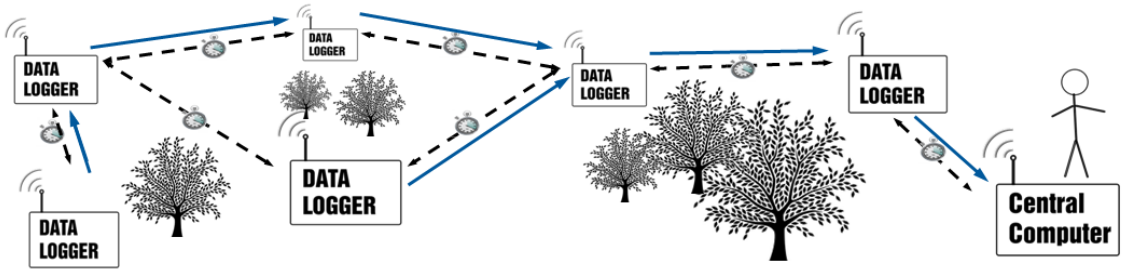

Figure 10: For transferring larger amounts of data to a central collector (re)broadcasting messages is inefficient. Dijkstra's graph search algorithm solves this single source shortest path problem for each data logger (blue arrows). The ping time measured by two adjacent data loggers (black arrows) is used as the connection quality parameter required by this algorithm. The maximum transfer rate is limited by the maximum bandwidth available (max. 3 MB/s) divided by the number of connections on the path to the collector.

WLAN mesh software package

The software package used to establish a WLAN mesh consists of two separate programs, a vertex and a central computer program. The vertex program (Figure 11) runs on and automatically tries to connect to adjacent SPAM4s. If successful, the program can broadcast, receive and process messages defined in a message protocol. It responds to control commands sent by the central computer. Subsequently, the vertex program periodically checks the local file system directories for new or updated SPAM4 data files which are then pushed to the central computer using a shortest path infrastructure (Figure 10).

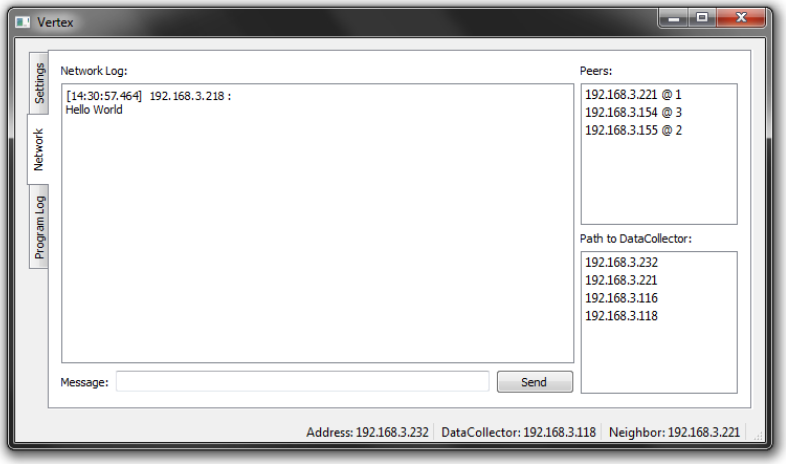

Figure 11: The vertex program can be used to inspect the network communication. On the right hand side, neighboring vertex computers with corresponding ping response time and path to the central computer are listed.

The central computer program (Figure 12 and 13) runs on a standard (field laptop) computer. Like the vertex program it also tries to find and connect to neighboring vertex programs to become part of the WLAN mesh. The main objective of the central computer program is to monitor SPAM4 status, data quality, and to control the SPAM4 operation. All information obtained from the SPAM4s is processed, displayed and automatically stored in a project / site specific directory structure.

Locations and current status, as well as the overall network structure and network activity are displayed on a survey map. Incoming (stacked) time or frequency domain data is shown and updated whenever a new data packet is received. It is also possible to remote-control the SPAM4 operation mode by broadcasting control files. The SPAM4 software periodically checks for these files and restarts data acquisition accordingly.

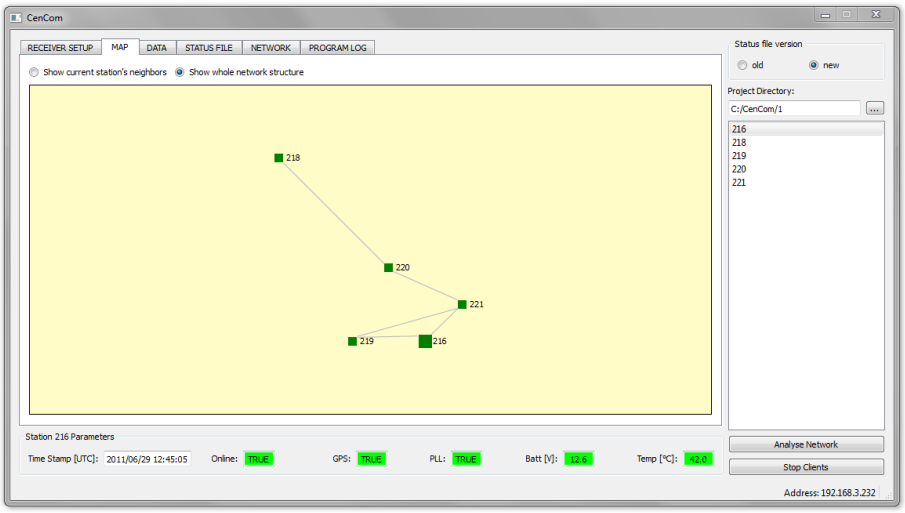

Figure 12: The central computer program. In map view all SPAM4 stations part of the mesh and their respective connections are displayed. Crucial state-of-health parameters are continuously updated in the status line (bottom of the screen) when a map symbol or the corresponding entry in the list is selected. More detailed SPAM4 information is available in the status tab.

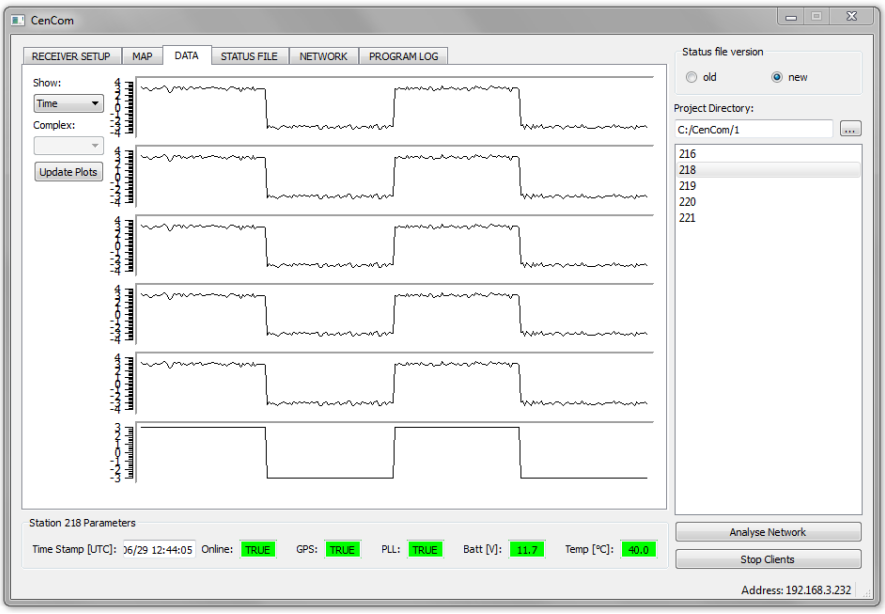

Figure 13: Time series received by the central computer program from one of the SPAM4 stations on the mesh. It is possible to monitor stacked time- or frequency data from all stations in quasi-real time.

Detektion oberflächennaher Störkörper mit elektromagnetischen Methoden - ein Vergleich zwischen Nano-TEM- und EM34-Messungen

Jan Köhler, Bülent Tezkan
Institut für Geophysik und Meteorologie, Universität zu Köln

Zusammenfassung

Ziel der Arbeit ist es, verschiedene elektromagnetische Methoden auf ihre Eignung zur Detektion leitfähiger Störkörper in geringer Tiefe zu testen. Bisher wurden entsprechende Messungen mit einer Nano-TEM-Apparatur und dem Zweispulensystem EM34 von Geonics durchgeführt. Zur Vorbereitung wurden Profile über eine Wasserleitung in Köln vermessen. Der in diesem Fall als unendlich ausgedehnt angenommene gute Leiter verursachte dabei für beide Methoden deutliche Leitfähigkeitsanomalien. Desweiteren wurden Messungen auf einem Testgelände in Greven bei Münster durchgeführt. Hier waren zwei bombenähnliche Störkörper von ca. 1 m Länge in ca. 2 bzw. 5 m Tiefe vergraben worden, welche ebenfalls mit den beiden Messgeräten detektiert werden sollten. Die TEM-Messungen beinhalteten zunächst eine Kartierung mit einer Sendespule von $10 * 10\ m^2$ und einer zentrierten Empfängerspule von $0,5 * 0,5\ m^2$. Außerdem wurde bei stationär verbleibendem Sender und wanderndem Empfänger gemessen. Das EM34 wurde bei einem Spulenabstand von 10 m sowohl im Vertikal- als auch im Horizontal-Dipol-Modus verwendet. Die Störkörper riefen erwartungsgemäß geringere Anomalien als die Wasserleitung hervor und konnten mit dem Zweispulensystem nicht zweifelsfrei nachgewiesen werden. Die Nano-TEM-Methode lieferte zumindest für den flacher gelegenen Störkörper bessere Resultate und eine Lokalisierung war möglich.

1 Messmethoden und -Geräte

1.1 Transientelektromagnetik

Die Transientelektromagnetik wurde mit dem Sender NT-20 und dem Empfänger GDP32 (beide von Zonge Engineering) durchgeführt. Es wurde stets mit einem Sendeloop von $10 * 10\ m^2$ und einem Empfängerloop von $0,5 * 0,5\ m^2$, welcher sich zumeist im Zentrum des Sendeloops befand, gemessen. Dabei wurde der sogenannte Nano-TEM-Modus verwendet, welcher im Vergleich zum Zero-TEM-Modus mit geringeren Stromstärken (bis $3\ A$) arbeitet, was kürzere Abschaltzeiten bedeutet und somit die Erkundung geringerer Tiefen ermöglicht. Die vom Gerät gemessenen Transienten der induzierten Spannung können mittels Late-Time-Näherung in scheinbare Widerstände umgerechnet werden und somit für einzelne Zeitpunkte der TEM-Messungen die scheinbaren Widerstände entlang des jeweiligen Profils dargestellt werden.

1.2 Zweispulensystem EM34

Es wurde das EM34-3XL von Geonics verwendet. Dieses wurde von der WWU Münster zur Verfügung gestellt. Dabei wurde ausschließlich mit einem Spulenabstand von $10\ m$ gearbeitet, da die ebenfalls möglich Auslagen von $20\ m$ und $40\ m$ für diesen Fall zu große Eindringtiefen zur Folge haben und für die Erkundung von Tiefen unter $10\ m$ somit nicht sinnvoll erscheinen. Das Gerät gibt als Messwert direkt die scheinbare Leitfähigkeit des Untergrundes aus.

2 Testmessungen in Köln

Es wurden zunächst Messungen über einer metallischen Wasserleitung in Köln durchgeführt, um die Geräte zu überprüfen und ihre generelle Fähigkeit zur Detektion positiver Leitfähigkeitsanomalien in vergleichsweise geringer Tiefe zu testen. Die Wasserleitung befand sich dabei in einer Tiefe von ca. 2 m und kann näherungsweise als unendlich ausgedehnter guter Leiter angesehen werden. Es wurden jeweils Profile vermessen, welche annähernd senkrecht zur Wasserleitung verliefen.

2.1 Nano-TEM-Messungen

Die Nano-TEM-Messungen wurden als Kartierungsmessungen durchgeführt bzw. ausgewertet, was bedeutet, dass der Empfängerloop sich im Zentrum des Sendeloops befindet und jeweils die gesamte Messanordnung entlang des Profils fortbewegt wurde (siehe Kapitel 3.1) und jeweils für einen bzw. jeden Zeitpunkt der aufgezeichneten Transienten die ermittelten scheinbaren Widerstände gegen die Profilmeter aufgetragen wurden. Es wurden 13 Messpunkte mit einem Abstand von je $1\ m$ vermessen. Abbildung 1 zeigt die aus den Transienten ermittelte scheinbare Leitfähigkeit entlang des Profils für den Zeitpunkt $1,986 * 10^{-5}\ s$. Die negative Widerstandsanomalie ist klar erkennbar und tritt erwartungsgemäß im Bereich des Verlaufs der Wasserleitung auf. Die Nano-TEM-Kartierungsmessungen erwiesen sich somit grundsätzlich als geeignet, Störkörper mit erhöhter Leitfähigkeit zu detektieren.

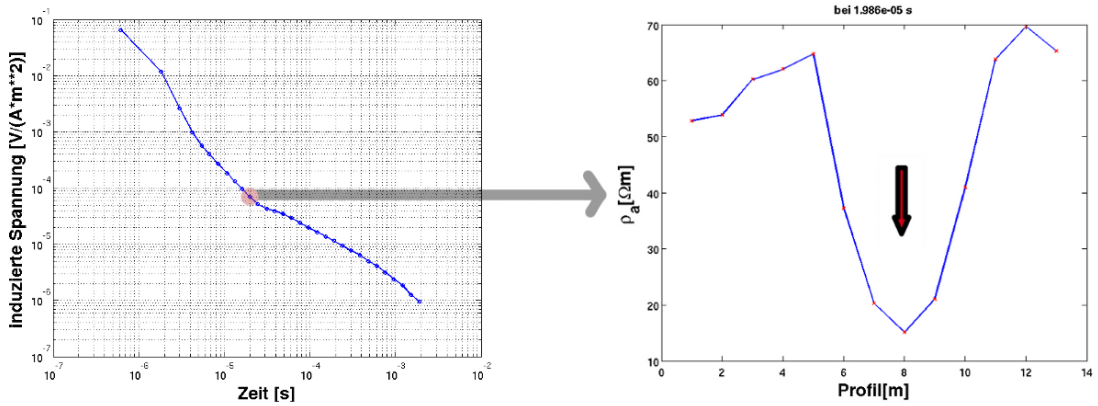

Abbildung 1: Ergebnisse der Nano-TEM-Kartierungsmessungen über der Wasserleitung, links ein exemplarischer Transient für einen Messpunkt, rechts der scheinbare Widerstand entlang des Profils für einen ausgewählten Zeitpunkt

2.2 EM34-Messungen

Mit dem EM34-Messgerät wurde ebenfalls überprüft, ob die Wasserleitung detektiert werden kann und außerdem, ob eine Ausrichtung von Sende- und Empfangsspule längs zum Profil oder quer zum Profil sinnvoller ist. Bei der Messung quer zum Profil, d.h. die Verbindungslinie zwischen Sende- und Empfangsspule verläuft senkrecht zum Profil, waren sowohl im Horizontal- als auch im Vertikal-Dipol-Modus ausgeprägte positive Leitfähigkeitsanomalien im Bereich der Wasserleitung zwischen Profilmeter 16 und 19 zu erkennen (Abb. 2). Das Einknicken der Leitfähigkeitskurve für den Vertikal-Dipol-Modus ist dabei durch die vom Gerät verwendete Näherung der kleinen Induktionszahlen zu erklären, welche bei den hohen Leitfähigkeiten der metallischen Leitung nicht mehr erfüllt ist (McNeill 1980).

Bei der Messung mit längs zum Profil ausgerichteten Spulen konnten hingegen keine erfolgsversprechenden Ergebnisse erzielt werden. Die Wasserleitung konnte nicht detektiert werden, teilweise war es nicht möglich, Messwerte zu erhalten. Dies ist eventuell ebenfalls auf die zuvor erwähnte Abweichung von der Näherung der kleinen Induktionszahlen zurückzuführen. Folglich wurde die senkrechte Ausrichtung der Spulen zum Profil für die weiteren Messungen als bevorzugte Messanordnung gewählt.

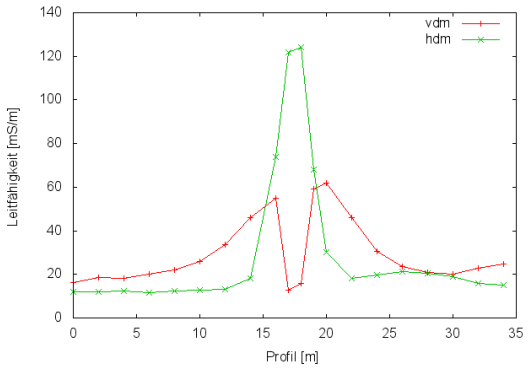

Abbildung 2: Scheinbare Leitfähigkeit aus den EM34-Messungen über der Wasserleitung

3 Messungen in Greven

Auf dem Testgelände in Greven, welches vom Unternehmen Tauber DeDeComp bereit gestellt wurde, waren zwei Störkörper in unterscheidlicher Tiefe vergraben, deren bekannte Postionen mit den elektromagnetischen Messungen bestätigt werden sollten. Es handelte sich dabei um ellispoide Körper von ca. $1\ m$ Länge und mit einem Durchmesser von ca. $0,70\ m$. Der eine Störkörper, im Folgenden Bombe 1, lag waagerecht in einer Tiefe von etwa $2\ m$, der zweite, im Folgenden Bombe 2, war bei einer senkrechten Ausrichtung in ca. $4,5\ -5,5\ m$ vergraben.

Abbildung 3: Übersicht über das Messgelände in Greven, Bombe 1 in 2 m Tiefe, Bombe 2 in 4,5 - 5,5 m Tiefe. Das Feld war von einem Metallzaun umgeben, welcher die Messungen teilweise beeinflusste

3.1 Nano-TEM-Messungen

Zunächst wurden wie bei den Tests in Köln über beiden Bomben Inloop-Messungen zu Kartierungszwecken durchgeführt. Die Abbildungen 4 und 5 zeigen den Messaufbau. Die gesamte Anordnung wird dabei jeweils entlang des Profils um einen Meter fortbewegt. Es wurden je Bombe 21 Profilpunkte vermessen, wobei die Bombe jeweils in der Mitte des Profils, also bei 11 m, vermutet wurde.

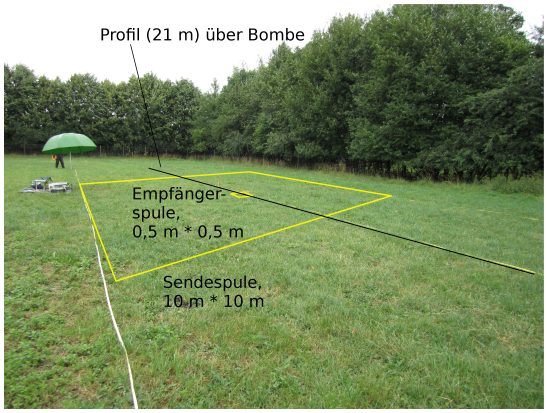

Abbildung 4: Messaufbau Nano-TEM-Messungen

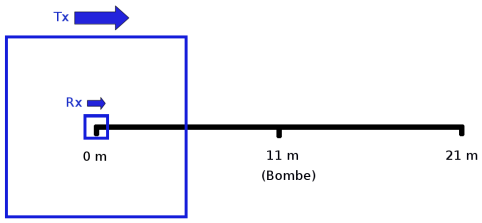

Abbildung 5: Schematischer Messaufbau der Nano-TEM-Kartierungsmessungen

In den Resultaten ist über Bombe 1 eine deutliche negative Widerstandsanomalie zu erkennen(Abb. 6). Dabei fällt jedoch auf, dass das Widerstandsniveau vor und hinter der Bombe sehr unterschiedlich ist. Dieses Verhalten ist auch bei Betrachtung der entsprechenden Transienten (Abb. 7) zu erkennen. Die Transienten hinter der Bombe knicken unter das Rauschniveau ab, ein Messverhalten, welches bei dem verwendeten Gerät bereits beobachtet wurde, allerdings nur bei Messungen in unterschiedlichen Polaritäten (Mollidor 2008). Bei den vorliegenden Messungen wurde die Polarität nur ein mal getauscht, bei Profilmeter 21. Der entsprechende Transient zeigt wiederum einen ähnlichen Verlauf, wie die Transienten aus dem Bereich vor der Bombe. Ob sich diese Ergebnisse reproduzieren lassen, soll bei weiteren Messungen überprüft werden.

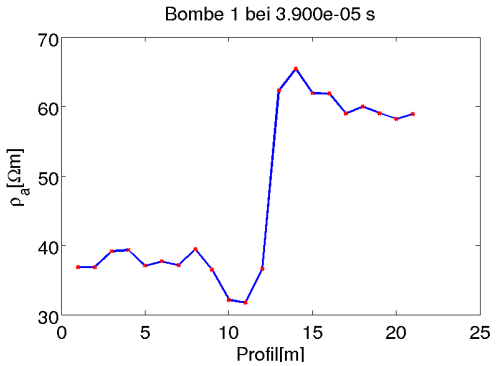

Abbildung 6: Scheinbarer Widerstand aus den Nano-TEM-Kartierungs-Messungen über Bombe 1 für einen ausgewählten Zeitpunkt

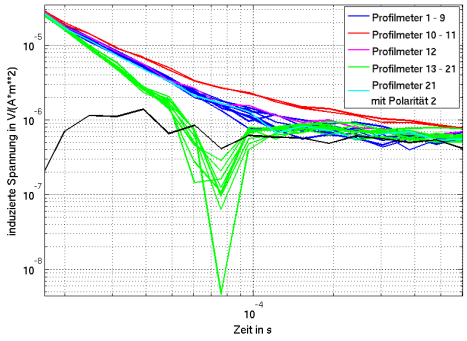

Abbildung 7: Ausschnitt aus dem Verlauf der über Bombe 1 gemessenen Transienten, in schwarz das Rauschniveau

Anders als Bombe 1 konnte die tiefere und senkrecht gelagerte Bombe 2 mit den Nano-TEM-Messungen nicht detektiert werden. Es gilt hier zu prüfen, ob eine Messung im Zero-TEM-Modus, also die Betrachtung späterer Zeitpunkte der Transienten, ein besseres Ergebnis zur Folge hat.

Desweiteren wurden über Bombe 1 Messungen mit einer stationären Sendespule von $10 * 10\ m^2$ und einer darin wandernden Empfangsspule von $0,5 * 0,5\ m^2$ durchgeführt. Der Messaufbau ist in Abbildung 8 dargestellt. Es wurde insgesamt bei drei verschiedenen Sendeloop-Positionen mit jeweils sieben Empfängerloop-Postionen gemessen. Die jeweiligen scheinbaren Widerstände sind ebenfalls in Abbildung 8 zu sehen. Wiederum ist bei Betrachtung der mittleren Postion(blau, mit der Bombe in der Mitte des Sendeloops) eine negative Anomalie über der Bombe zu erkennen, jedoch zeigen die Ergebnisse der beiden weiteren Sendeloop-Positionen ein noch geringeres Widerstandsniveau als diese Anomalie. Es ist zu vermuten, dass die Bombe auch hier Einfluss auf die Messungen nimmt, da sie sich jeweils direkt unter dem Rand der Transmitterspule befindet.

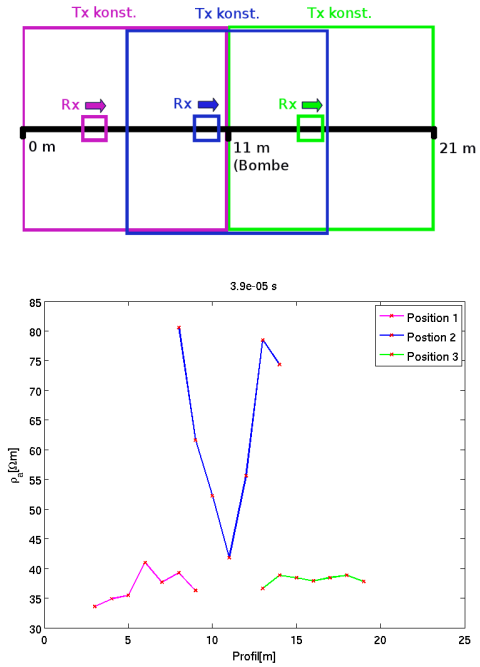

Abbildung 8: Schematischer Messaufbau der Nano-TEM-Messungen bei stationärer Sendespule und die zugehörigen Verläufe des scheinbaren Widerstands

3.2 EM34-Messungen

Mit dem EM34 wurden über beiden Bomben 30 m lange Profile vermessen. Der Messpunktabstand variierte dabei, so dass im Bereich der Bomben in geringeren Abständen gemessen wurde. Die Anordnung von Sende- und Empfangsspule ist den Abbildungen 9 und 10 zu entnehmen. Es wurde dabei wie erwähnt jeweils im Horizontal-Dipol-Modus, d.h. mit senkrecht auf dem Boden stehenden Spulen (siehe Abb. 9), und im Vertikal-Dipol-Modus mit waagerecht auf dem Boden aufliegenden Spulen gemessen.

Abbildung 9: Messanordnung der EM34-Messungen im Horizontal-Dipol-Modus

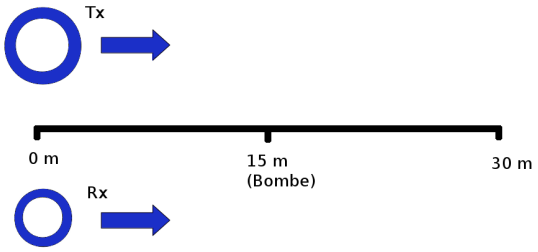

Abbildung 10: Schematischer Messaufbau der EM34-Messungen

Mit den EM34-Messungen konnte nur die tiefer gelegene Bombe 2 detektiert werden. Dies allerdings auch nur im Horizontal-Dipol-Modus. Abbildung 11 zeigt die Ergebnisse dieser Messung. Es ist eine positive Leitfähigkeitsanomalie zu erkennen, welche mit ca. 2 mS/m bzw. 8 % jedoch relativ gering ausfällt. Nach Herstellerangaben ist bei einem Messwert von 20 mS/m mit einem Fehler von 5 % zu kalkulieren, was das Ausmaß der Anomalie weiterhin relativiert. Im Vertikal-Dipol-Modus ist die Bombe nicht in den Ergebnissen zu erkennen, wie Abbildung 12 zeigt. Hier ist am Profilende der Einfluss des nahe gelegenen Metallzauns auszumachen, eine Leitfähigkeitsanomalie im Bereich der Bombe jedoch nicht. Bei einer Messung auf einem 10 m langen, senkrecht zum hier gezeigten Profil verlaufenden Profil konnten die Ergebnisse bestätigt werden. Bombe 1 war weder im Horizontal- noch im Vertikal-Dipol-Modus zu detektieren.

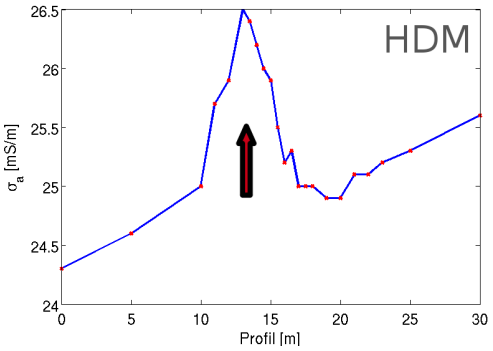

Abbildung 11: Scheinbare Leitfähigkeit aus den EM34-Messungen im Horizontal-Dipol-Modus über Bombe 2

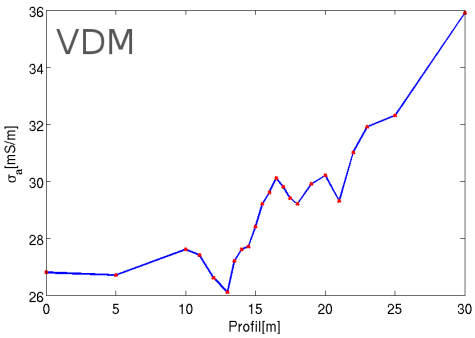

Abbildung 12: Scheinbare Leitfähigkeit aus den EM34-Messungen im Vertikal-Dipol-Modus über Bombe 2

4 Zusammenfassung und Ausblick

Sowohl Nano-TEM-Kartierungsmessungen als auch EM34-Messungen erwiesen sich bei den Tests in Köln als grundsätzlich geeignet, leitfähige Störkörper in geringer Tiefe zu detektieren. Die Messungen in Greven, bei denen über zwei Bomben in unterschiedlicher Tiefe gemessen wurde, brachten unterschiedliche Ergebnisse.
Mit der Nano-TEM-Methode konnte Bombe 1 in $2\,m$ Tiefe detektiert werden, Bombe 2 in $4,5-5,5\,m$ Tiefe konnte nicht detektiert werden. Möglicherweise würden Messungen im Zero-TEM-Modus hier zu besseren Ergebnissen führen. Bei den Ergebnissen der EM34-Messungen konnten über Bombe 2 im Horizontal-Dipol-Modus kleine Leitfähigkeitsanomalien beobachtet werden, Bombe 1 konnte nicht detektiert werden. Es stellt sich die Frage, ob für nocht tiefer gelegene Objekte bessere Resultate zu erwarten wären.
Es sollen weitere Messungen mit der TEM-Methode folgen, um weitere Daten zu erhalten und aufgetretene Fragestellungen zu beantworten. Modellierungen mit COMSOL Multiphysics mit variienden Mess- und Targetgeometrien sollen zur Interpretation der Ergebnisse angestellt werden. Außerdem soll als weitere Methode eventuell die Radiomagnetotellurik herangezogen werden.

Literatur

Adrian, J. (2011). *Untersuchung von Schlammvulkanen in Perekishkul, Aserbaidschan mit der Transient-Elektromagnetik*. Diplomarbeit, Universität zu Köln.

K. Knödel, H. Krummel G. Lange (1997). *Handbuch zur Erkundung des Untergrundes von Deponien und Altlasten, Band 3: Geophysik*. Springer-Verlag.

Koch, Olaf (2003). *Transient-elektromagnetische Messungen zur Erkundung einer Leitfähigkeitsanomalie am Vulkan Merapi in Indonesien*. Diplomarbeit, Universität zu Köln.

McNeill, J.D. (1980). *Electromagnetic terrain conductivity measurement at low induction number*. Geonics Limited.

Mollidor, Lukas (2008). *Central-Loop-TEM auf dem Holzmaar, Eifel*. Diplomarbeit, Universität zu Köln.

Report on a Magnetotelluric Study in Kangerlussuaq, West Greenland

L. Kother[1,2], A. Junge[3], A. Löwer[3], J. Matzka[1] and N. Olsen[1,2]

[1)] Danish National Space Center/DTU, Juliane Maries Vej 30, 2100 Copenhagen, Denmark
[2)] Niels Bohr Institute, Copenhagen University, Juliane Maries Vej 30, 2100 Copenhagen, Denmark
[3)] Institute of Geoscience at J.W.Goethe-University, Altenhöferallee 1, 60438 Frankfurt, Germany

Despite a well-mapped, interesting surface geology, deep sounding geophysical studies like seismics or magnetotellurics have been used very rarely in Greenland. The aim of this article is to present the preliminary results of a magnetotelluric study performed in the area of Kangerlussuaq, West Greenland. The estimated transfer functions will be used in the future for 2-D and 3-D modelling of subsurface resistivity structures, the influence of the electrically conductive ocean, as well as the source geometry in the auroral oval.

1. The MT-survey

We report on a magnetotelluric (MT) investigation in the Kangerlussuaq area performed in the period from 5^{th} of August 2010 to 17^{th} of September 2010. Five recording stations were evenly distributed along a 40 km profile with an approximate WSW-ENE orientation between Kellyville (SRI Incoherent Scatter Radar; DTU Space magnetometer station), station A, and the Greenland Ice Sheet (Fig. 1), station E. The telluric field variations were measured using Ag/AgCl electrodes (Junge, 1990) at all five stations, and magnetic field variations were recorded with 3-component fluxgate magnetometers at stations A and E. The sampling frequency was 4 Hz and standard robust processing (Löwer, 2010) was applied to the data to estimate MT transfer functions such as impedance tensors and tipper vectors.

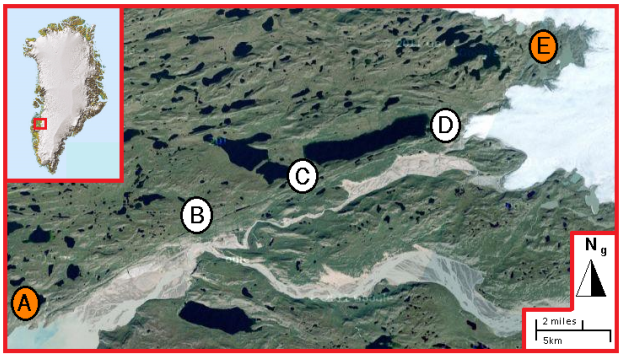

Figure 1: Map of Greenland (upper left panel) and detailed map of the Kangerlussuaq region including the locations of the five measurement stations. At stations A and E the three components of the magnetic field and the horizontal components of the telluric field were observed (orange circles), whereas at stations B, C and D only the telluric field was recorded (white circles). Source: www.google.com

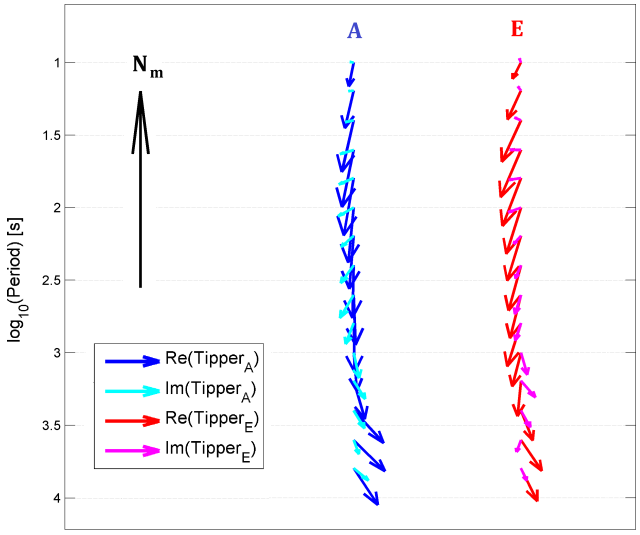

Figure 2: Tipper arrows for stations A (blue) and E (red). The corresponding calculations are due to the Wiese convention, thus the real tipper arrows point away from a good conductor. The local magnetic north points upwards. The black arrow indicates the unity arrow pointing towards local magnetic nord.

2. Data processing

Unstable transfer functions were observed during magnetic active periods. The survey period was therefore divided into halfdays and data from half days with a mean k-index value above 2 were excluded.

Comparing the measured tipper arrows (Fig. 2) and phase tensor bar orientations (Fig. 3) (Häuserer and Junge, 2011), the determined phase values could be assigned to the polarisation modes TE and TM (Fig. 4), under assumption of two-dimensionality. This is necessary before a 2-D subsurface resistivity model can be created.

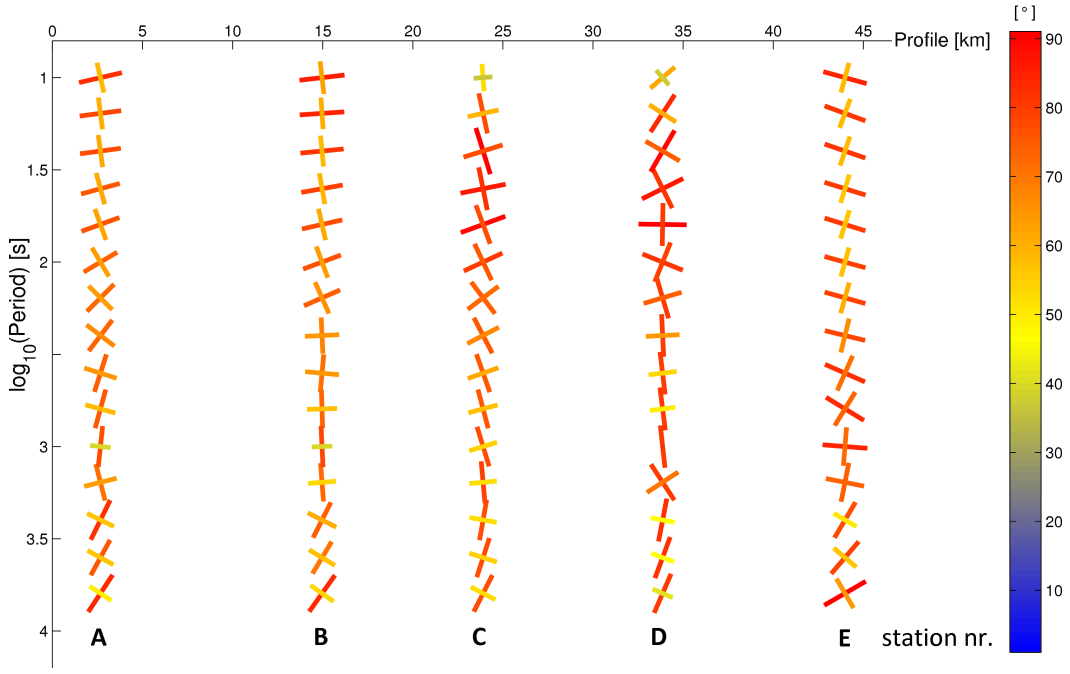

Figure 3: Phase tensor bars along the measurement profile, orientated in the local magnetic coordinate system. The bar colours and lengths correspond to the phase values.

3. Results

The orientation of the estimated tipper arrows in Fig. 2 is shown in the local magnetic coordinate system. Taking the westerly magnetic declination of 32 degrees into account, the real part of the tipper arrows points approximately towards geographic southeast.

The estimated phase tensor bar values (Fig. 4) show a distinctive split-up between the two polarisation modes as well as a cross over at periods around 100 sec. The measurements of station E differ from the general phase behaviour seen at the other stations. We suggest that this could be caused by a pronounced 3-D conductivity structure and/or anisotropy.

4. Discussion

The observed tipper orientations suggest a large and well conducting structure northwest to the measurement profile. Other magnetotelluric investigations from Finland (Korja et al., 1989) and Canada (Evans et al., 2005) reveal also good conducting structures of approximately $5\Omega m$ between 10 km and 40 km surface depth. The Kangerlussuaq area might be linked to the other two areas through a 1.9 Ga old foldbelt (Johansson, 2009), which encourages further investigations of our data set. In Greenland, this fold belt is called the Nagssugtoqidian orogen (e.g. Marker et al. (1995)).

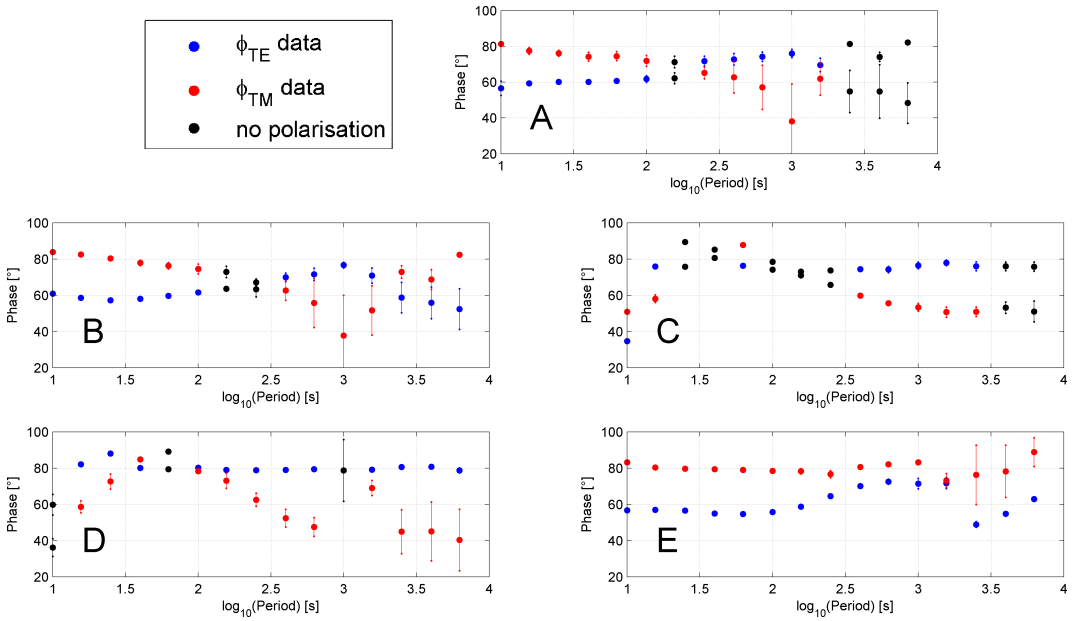

Figure 4: The estimated phase tensor bar values for stations A to E are illustrated with their corresponding polarisation mode affiliation for TE (blue) and TM (red). Black data points represent the measurements where a polarisation mode association was not possible.

5. Conclusion

The current study investigates the subsurface resistivity structure in the area around Kangerlussuaq, West Greenland. Magnetotelluric measurements were performed at five stations along a 40km WSW-ENE profile. As a first step, the corresponding transfer functions were estimated and are presented here. The orientation of the tipper vectors suggests a large and well conducting structure to the northwest, with a strike direction of similar orientation as the measurement profile. Future surveys should therefore aim at locations along a profile perpendicular to the strike direction identified here. Such studies could then be compared to similar MT-studies, especially from Canada, and reveal conductivity structures across the proterozoic orogen.
Further data treatment, including 2-D as well as 3-D inversion modelling, is already in progress.

References

Evans, S., Jones, A., Spratt, J., and Katsube, J. (2005). Central Baffin electromagnetic EXperiment (CBEX): Mapping the North American Central Plains (NACP) conductivity anomaly in the Canadian Arctic. *Physics of the Earth and Planetary Interiors*, 150:107–122.

Häuserer, M. and Junge, A. (2011). Electrical mantle anisotropy and crustal conductor: a 3-D conductivity model of the Rwenzori Region in western Uganda. *Geophysical Journal International*, 185:1235–1242.

Johansson, Å. (2009). Baltica, Amazonia and the SAMBA connection - 1000 million years of neighbourhood during the Proterozoic? *Precambrian Research*, 175:221–234.

Junge, A. (1990). A new telluric KCl probe using Filloux's AgAgCl electrode. *Pure and Applied Geophysics*, 134:589–598.

Korja, T., Hjelt, S.-E., Kaikkonen, P., Koivukoski, K., Rasmussen, T., and Roberts, R. (1989). The geoelectric model of the POLAR profile, northern Finland. *Tectonophysics*, 162:113–133.

Löwer, A. (2010). Die neue Frankfurter Magnetotelluric Processingsoftware am Datenbeispiel von Uganda. *Poster at DGG Jahrestagung Bochum*.

Marker, M., Mengel, F., and van Gool, J. (1995). Evolution of the Paleoproterozoic Nagssugtoqidian orogen: DLC investigations in West Greenland. *Rapport Grønlands Geologiske Undersøgelse*, 165:100–105.

24. Schmucker-Weidelt-Kolloquium
Neustadt an der Weinstraße, 19.–23. September 2011

Magnetotelluric measurements across the southern Barberton greenstone belt, South Africa: data improving strategies

S. Kütter[1,2] and U. Weckmann[1]

[1] *GFZ - German Research Centre for Geosciences, Potsdam, Germany*
[2] *University of Potsdam, Germany*

Magnetotelluric (MT) measurements in areas with electromagnetic (EM) noise sources such as electric fences, power and railway lines pose severe challenges to the standard processing procedures. In order to significantly improve the signal to noise ratio advanced filtering and processing techniques need to be applied. The presented MT data set from two field campaigns in 2009 and 2010 in the Barberton/Badplaas area, South Africa, was acquired within the framework of the German-South African geo-scientific research initiative Inkaba yeAfrica. Approximately 200 MT sites aligned along six profiles provide a good areal coverage of the southern part of the Barberton Greenstone Belt (BGB). Since it is one of the few remaining well-preserved geological formations from the Archean, it presents an ideal area to study the tectonic evolution and the role of plate tectonics on Early Earth. Comparing the electric properties, the surrounding high and low grade metamorphic rocks are characteristically resistive whereas mineralized shear zones are possible areas of higher electrical conductivity. Resolving their properties such as depth extent, width or inclination is a crucial step toward understanding the formation and the evolution of the BGB. Unfortunately, in the measurement area numerous EM noise sources were active, producing severe spikes and steps in the EM time series. These kinds of disturbances mainly affect long periods which are necessary for resolving the deepest structures. The Remote Reference technique as well as two filtering techniques are applied to improve the data in different period ranges. Adjusting their parameters for each site is necessary to obtain the best possible results.

1 Survey area

The MT survey area is located at the southern part of the Barberton Greenstone Belt (BGB), South Africa. Approximately 200 5-component sites were aligned along five short (≈ 85 km) and one long profile (≈ 115 km) with site spacings between 2 and 10 km. They were set up during two field campaigns in April/May 2009 and July/August 2010. A simplified geological map with the site locations indicated by blue markers is shown in Fig. 1.

The BGB is mainly composed of rocks with high electric resistivity. This allows the natural electro-

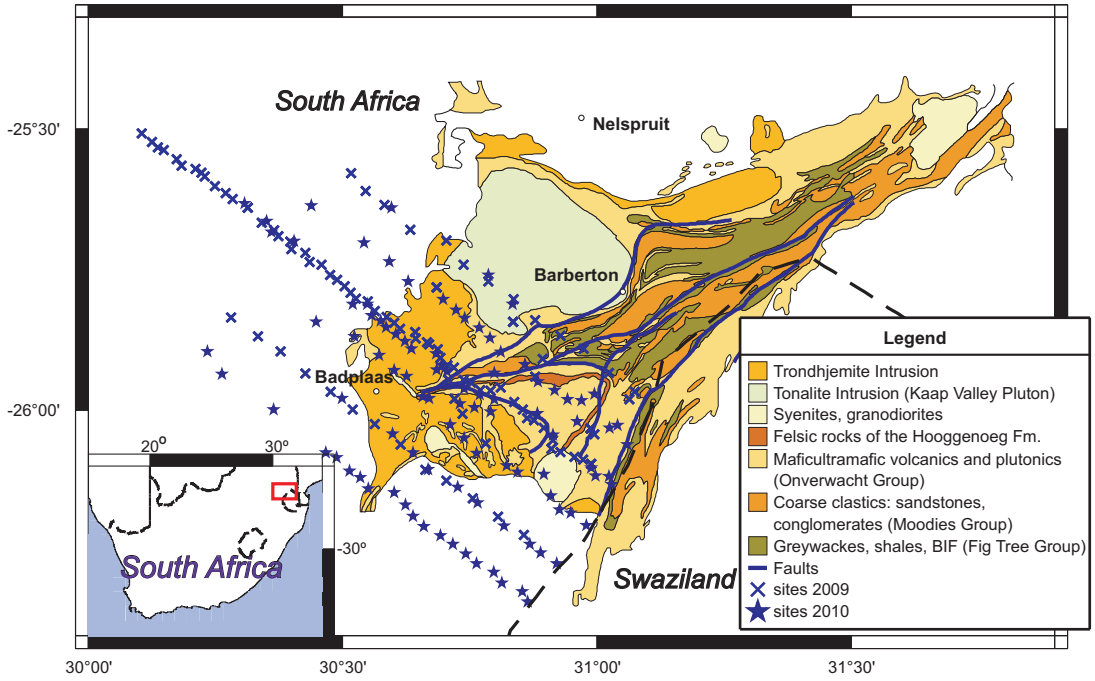

Fig. 1: Simplified geological map of the Barberton Greenstone Belt (colored areas, modified after Schoene et al. 2007 [2]). The BGB is surrounded by batholiths and younger sedimentary rocks (white areas). Site locations are marked in blue. The inset shows the location of the survey area in South Africa (red rectangle).

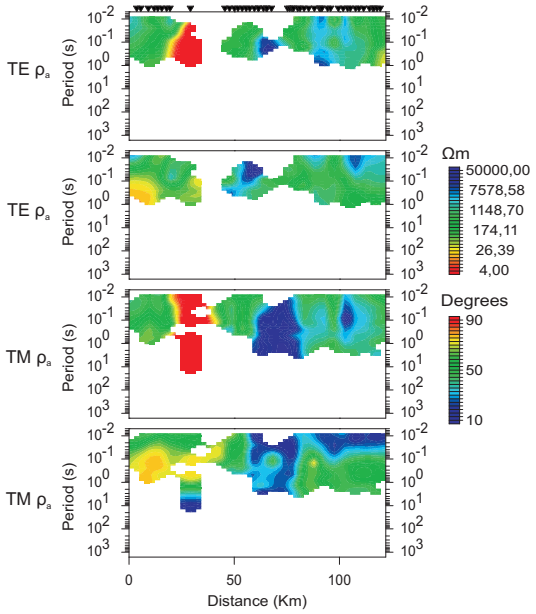

Fig. 2: Pseudosections of profile 4. Shown are only the periods that can be used for inversions.

magnetic (EM) source signals being in the far field state to penetrate deep into the earth and simultaneously to travel far laterally. Hence, numerous noise signals being in the near field state that are present in this area are hardly attenuated either. They influence the data in the entire period range but in particular long periods. To illustrate the limitation of usable data due to EM noise pseudosections of profile 4 are shown (Fig. 2, cp. Fig. 1 longest profile). Since data was recorded at each site for three to four days periods of 10^3 s should be resolved. However, only data from $0.01 - 1/10$ s have the necessary quality to be used for further analysis. Omitting longer periods limits our resolution to the upper crust ($\approx$ 5 km depth). There are also a number of sites that were excluded entirely which can be seen by comparing the site density of the pseudosections (marked by black triangles) with the site spacing of the longest profile in the map (Fig. 1).

2 Improving the data quality

Reducing the EM noise in the data throughout the entire period range is a time-consuming task. Filters need to be applied carefully since they are improving the data quality mostly in a rather narrow period band and sometimes worsen it in other bands. Hence, different methods are applied to different period bands.

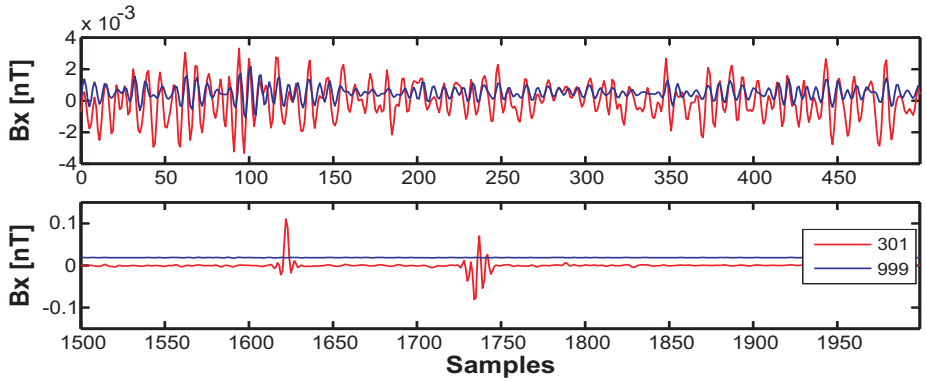

Fig. 3: Magnetic field time series of local site 301 and reference site 999. Signals of both sites correlate well in general (top) but also show uncorrelated parts with spikes in the local site 301 (bottom). Time series are bandpass filtered (16 s to DC), the sampling rate is 0.25 Hz. For both sites the same gain settings were used for Bx during the recording.

Remote referencing and delay filtering

In a first step to improve the data quality remote referencing (RR, Gamble et al., 1979 [3]) and a delay filter (Chen, 2008 [1]) are applied.

Based on the correlation of magnetic (B) fields even between distant sites the RR method uses the fields of a reference site to remove uncorrelated noise in the B channels of a local site. Plotting parts of the time series of Bx of sites 301 and 999 shows the correlation well (Fig. 3). However, it also reveals high amplitude spikes.

The delay filter is applied to remove noise with a known base frequency and its multiples, e.g. 50 Hz for powerlines. An example for periodograms before and after a delay filter with 50 Hz is used is shown for channel B_z of site 301 (Fig. 4).

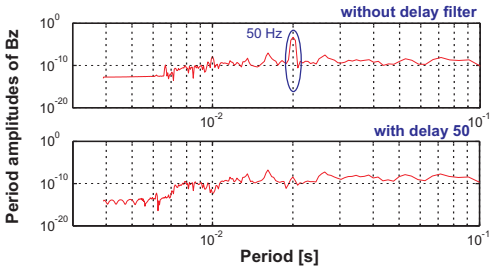

Fig. 4: Periodograms of channel B_z of site 301 before (top) and after (bottom) applying a delay filter with 50 Hz base frequency. Time series for spectra calculations have 512 samples and are bandpass filtered (128 Hz to DC). The sampling rate is 512 Hz.

Figure 5 shows a comparison between raw data (top row) and filtered data (bottom row). In the examples presented here the RR especially improved the data in period ranges from $0.1 - 1/10$ s (blue ellipses). Improvements by the delay filter are marked with green ellipses whereas red is used for parts that still have an insufficient data quality.

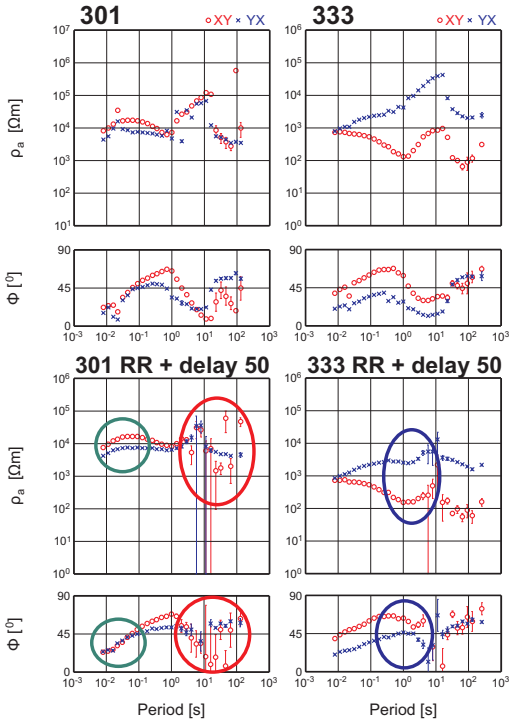

Fig. 5: Apparent resistivity ρ_a and phase Φ curves of site 301 and 333 after standard processing (top) and with applying Remote Referencing (blue ellipses) and delay filtering (green ellipses, bottom).

RVRWR filter

The **R**eference site **V**ariance **R**atio **W**iener-filter **R**eplacement (RVRWR) is based on a filter by Kappler (2012 [4]). It is designed to replace spikes that mainly occur in the magnetic channels of the data with calculated plausible data using one or more reference sites. The basic steps are listed below and are subsequently described further.

- Data parsing of two or more sites into windows of a user defined number of samples
- Calculation of the data variance for all windows
- Calculation of the variance ratios between the channels of the site
- Window flagging according to a user defined threshold for the value of the ratios
- Calculation of the Wiener filter coefficients and subsequently of the replacement data
- Replacement of the flagged windows

Data parsing and calculation of window variance

The first step is to parse the time series of all electric (E) and magnetic field components of two or more sites in windows (Fig. 6). The resulting number of windows n depends on the length of the time series and the window length chosen by the user, e.g. 128 or 256 samples. n also increases if an overlap (e.g. 16 samples) of succeeding windows is chosen. This overlap artificially increases the amount of windows and can help improving the data further by identifying also spikes that without overlap would be at the edge of adjacent windows and thus hard to identify.
For all windows a variance of the time series in that window is calculated. The variance describes how far data points lie from the expected value μ as defined in equation (1).

$$a_i \;\widehat{=}\; VAR(\mathbf{Y}) = \frac{1}{n}\sum_{i=1}^{n}(y_i-\mu)^2, \qquad \mu = \frac{1}{n}\sum_{i=1}^{n} y_i \tag{1}$$

where $\mathbf{Y}$ is the respective time series and y_i is one of its data points. The expected value is simply defined as the mean value of the time series.

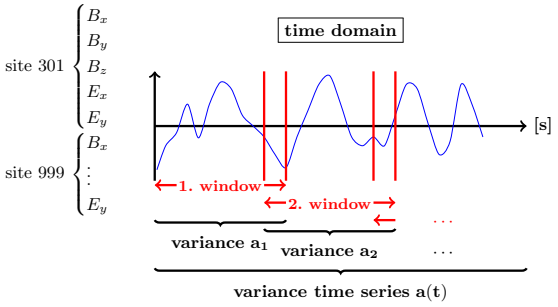

Fig. 6: Sketch to illustrate the parsing of time series of magnetic and electric channels of local site (e.g. 301) and reference site (e.g. 999) into windows (here with an arbitrary overlap). For every window the variance a is calculated.

Shown in Fig. 7 and 8 are variance time series where no windows are flagged and where 65 windows are flagged, respectively.

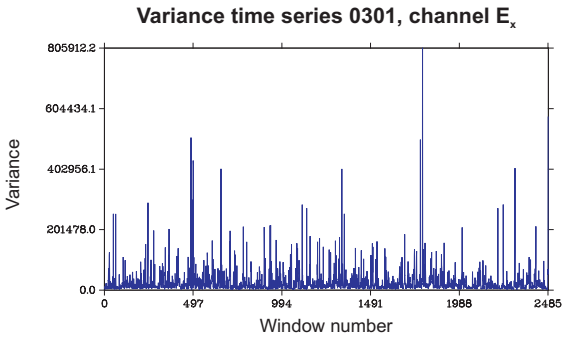

Fig. 7: Variance time series of site 301 (Ex). For this time series no windows are flagged by the algorithm due to the chosen threshold settings (cp. Fig. 9).

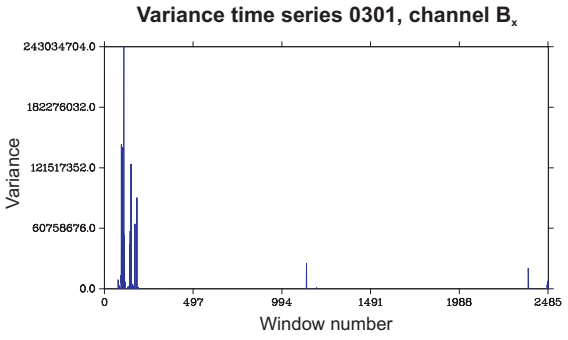

Fig. 8: Variance time series of site 301 (Bx). For this time series 65 windows are flagged by the algorithm (cp. Fig. 10). The activities of the unflagged windows are too small for the used scale to be seen.

Calculation of variance ratios

The next step is to calculate the variance ratio r (2) between the sites for all channels according to the following equation where i (e.g. site no. 301) and j (e.g. site no. 999) are the indices representing the sites.

$$r_{i,j} = log_{10}\left(\frac{a_i(t)}{a_j(t)}\right) \tag{2}$$

This ratio relates the variance of the channels of the local site to the reference site and determines whether a certain window of the local site is really affected by noise or just by a higher natural electromagnetic source activity. In the time series example given in Fig. 3 the signal is generally in the order of $\approx 10^{-3}$ nT wheras the spikes have amplitudes around 10^{-1} nT.

Window flagging

Fig. 9 and 10 are examples for the variance ratio r plotted for channels Bx and Ex with the thresholds for the window flagging marked by red lines. The threshold is defined as the standard deviation σ (3) of the ratio multiplied by a user defined value t_{user} to control the threshold. For both examples t_{user} was set to 5.

$$\sigma = \sqrt{\frac{\sum_{i=1}^{n}(a_i - \overline{a})^2}{n-1}} \tag{3}$$

The window with the higher variance a in the ratio $r_{i,j}$ is flagged.

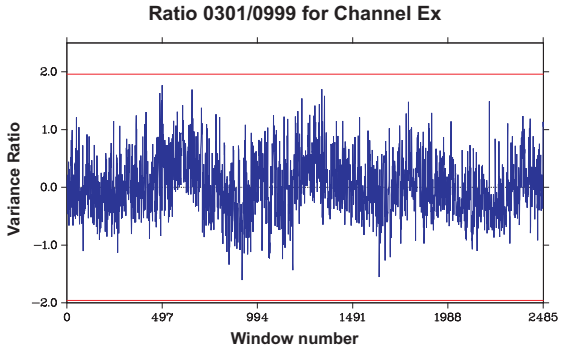

Fig. 9: Variance ratio 301/999 for channel Ex. Marked by red lines are the thresholds.

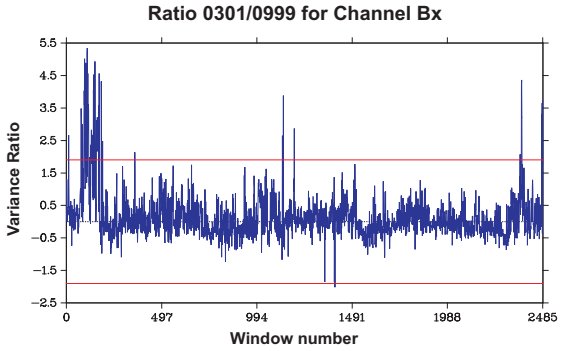

Fig. 10: Variance ratio 301/999 for channel Bx. Marked by red lines are the thresholds. All variance ratios that exceed the thresholds correspond to flagged windows.

Calculation of the replacement data

For calculating the replacing data the Wiener filter (Wiener, 1949 [5]) is used. Originally this filter is used in signal processing for noise reduction by comparing the noisy signal with the estimated noise-free signal. It was adapted to calculate replacement data in the following way.
In the first step the algorithm searches for unflagged training data in the time series to assemble the training data vector d_{tr} and the convolution matrix M (Fig. 11, left part). After transforming them into the frequency domain the Wiener filter coefficients Ψ are computed using

$$d_{tr} = M\Psi. \tag{4}$$

The use of unflagged training data in the calculations replaces the estimation of the noise-free signal in the original version of the Wiener filter.
Once the filter coefficients are computed the algorithm uses the unflagged data in the initial window to assemble M and the flagged data is replaced by the resulting $\mathbf{d_{calc}}(t)$ vector (Fig. 11, right part).

Replacement of the flagged windows

In the final step the calculated data is fitted to the adjacent windows by downweighing the calculated data and upweighing the original data in a transition zone on either side of the flagged window.

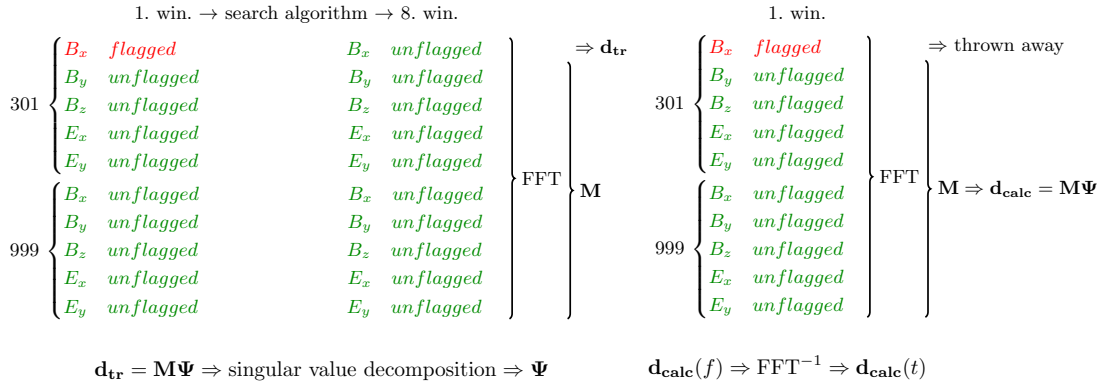

Fig. 11: Scheme for finding training data for the calculation of the Wiener filter coefficients Ψ (left) and for calculating the replacement data $\mathbf{d_{calc}}$ (right).

A flagged window with a dominant spike is shown in Fig. 12 and the calculated data to replace it is plotted in Fig. 13. Especially note the difference in the scale of the ordinate of the two figures.

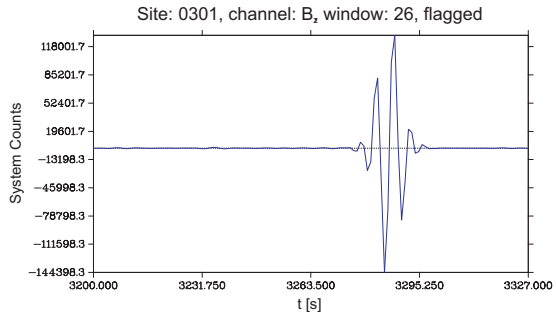

Fig. 12: Example for a flagged window of site 301 channel B_z.

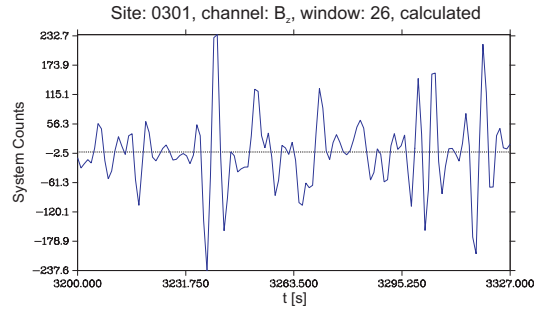

Fig. 13: Example for calculated data to replace the flagged window in Fig. 12.

Fig. 14 displays the apparent resistivity ρ_a and phase Φ of site 301. The curves in the left panel were calculated using just the raw data for the processing. The right panel shows the processing results after applying all of the three mentioned filtering methods. Marked with ellipses are the period ranges in which the different filters are most effective.

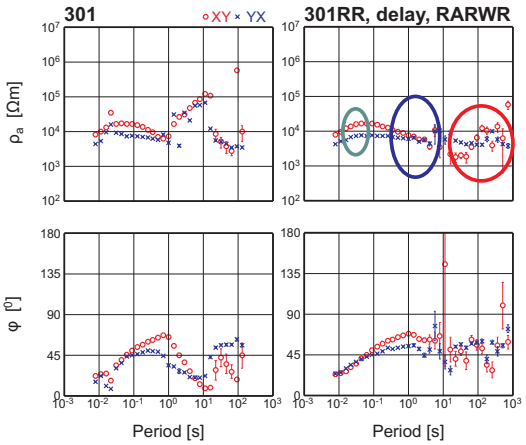

Fig. 14: Site 301 using standard processing (left) and filtering(right). Marked are the periods that are improved using delay filtering (green), Remote Referencing (blue) and RVRWR filter (red).

The RVRWR filter is still in the testing stage, hence, adjusting the parameters should further improve the data quality.

3 Conclusions

Areas interesting for geophysical research are often in populated regions. Avoiding all the various noise sources is therefore impossible. Hence, finding novel and improving existing methods is necessary to analyse disturbed MT data sets.

Presented in this work are three methods for removing different types of electromagnetic noise and improving the data quality in various period ranges. The delay filter is well suited for noise with a specific frequency whereas the Remote Referencing increases the data quality in a wider range. The given examples exhibited noise reduction especially for intermediate periods.
Depending on how severe the data is affected by noise other methods might need to be applied. For the longest periods the RVRWR filter is a useful technique. It employs a reference site that should have an overall good data quality to remove spikes mostly occuring in the magnetic fields. After adjusting its parameters it can be a good tool for further improving the data.

Acknowledgements

We like to thank: Rod Green, Corné Maritz, the farmers in the Mpumalanga region, the team of Travelport and managers of the game reserves for land access and their support, Abel Sihlongonyane for the permitting, the Geophysical Instrument Pool Potsdam for providing the instruments, all colleagues Manfred Schüler, Stefan Rettig, Paul Sass, Diane Eydam, Reinhard Klose, Gerald Schmidt, Norbert Ebel, Euston Witbooi and Brady Lob for their help in the field, the NRF and DST for their support of the experiment and the students, the DFG for funding the experiment (WE 2938/8-1), and the GFZ Potsdam for funding my PhD research.

Reference

[1] X. Chen. 2008. Filterung von geophysikalischen Zeitreihen mit periodisch auftretenden multifrequenten Störsignalen. MSc thesis.

[2] B. Schoene, S. A. Bowring. 2007. Determining accurate temperature–time paths from U–Pb thermochronology: An example from the Kaapvaal craton, southern Africa. Geochimica et Cosmochimica Acta 71(1), 165-185.

[3] T. D. Gamble, W. M. Goubau, and J. Clarke. 1979. Magnetotellurics with a remote magnetic reference. Geophysics, 44(1), 53-68.

[4] K. N. Kappler. 2012. A data variance technique for automated despiking of magnetotelluric data with remote reference. Geophysical Prospecting, 60, 179-191.

[5] N. Wiener. 1949. Extrapolation, interpolation, and smoothing of stationary time series: with engineering applications. Journal of the American Statistical Association, 47(258).

Detektion eines Aquifers unter dem Mittelmeer mit Long Offset Transient Elektromagnetik (LOTEM)

K. Lippert*, B. Tezkan*, R. Bergers*, M.Goldman**
* Institut für Geophysik und Meteorologie, Universität zu Köln
** Geophysical Institute of Israel

Abstract

Im Rahmen dieses BMBF-geförderten Projektes [1] kommt die Long-Offset Transient Elektromagnetik (LOTEM) Methode in mariner Umgebung zum Einsatz. Ziel ist die Kartierung eines relativ schlechtleitenden Aquifers unter den gutleitenden Meeressedimenten. In diesem Beitrag werden 1D Ergebnisse der Messungen aus den Jahren 2009 und 2011 vorgestellt.

Einleitung

Die Bedeutung von Offshore-Süßwasserleitern für das Grundwassermanagment nahm in den letzten Jahren stark zu. Das Vorhandensein dieser Aquifere, die sich bis zu mehreren Kilometern unter dem Meeresboden erstrecken können, wurde in der Fachliteratur beschrieben: z.B. an der Küste von Guyana *[Arad, 1983]* oder vor den Niederlanden *[Groen et al., 2005]*. Der israelische Küstenaquifer ist eine der Hauptgrundwasserresourcen des Landes (vgl. Fig. 2). Allerdings verschlechtert sich aufgrund der intensiven Nutzung die Wasserqualität zumehmend. Die Gründe hierfür liegen sowohl in der anthropogenen Verschmutzung aus dem Landesinneren, als auch in der Salzwasserintrustion vom Meer aus. Der Küstenaquifer besteht hauptsächlich aus kalkhaltigem Sandstein und Sanden und ist selbst noch in vier Sub-Aquifere unterteilt. Untersuchungen von *[Kafri und Goldman , 2006]* und *[Yechieli et. al, 2009]* deuten auf eine Fortsetzung des Aquifers unter dem Meer hin. So zeigen TEM-Messungen auf Land, nahe der Küste, einen schlechteren elektrischen Leiter eingebettet zwischen zwei guten elektrischen Leitern. Diese Schicht, in der Tiefe der unteren Sub-Aquifere, wird als grundwasserführende Schicht interpretiert.
Die Fragestellung an die LOTEM-Methode ist nun

1. die Prüfung der Existenz des unteren Sub-Aquifers in etwa 100m Tiefe unter den Meeressedimenten und
2. dessen Ausbreitung unter dem Mittelmeer.

[1] BMBF-Förderkennzeichen: 02WT0987

Messungen

Die Daten wurden in insgesamt 10 Schiffstagen in den Jahren 2009 und 2011 aufgezeichnet. Der 400 m lange Sendedipol und die Empfänger der elektrischen und magnetischen Felder wurden dabei stets auf dem Meeresgrund positioniert (vgl. Fig. 1). Der Sender wurde sowohl parallel als auch senkrecht zur Küstenlinie aufgebaut, gemessen wurden sowohl inline als auch broadside Komponenten. In Fig. 3 sind die Positionen aller Messungen in einer Nautischen Karte dargestellt. Ca. 2,5 km von der Küste entfernt befindet sich eine Nicht-Anker-Zone, in der kein Sender aufgebaut werden durfte. Außerdem ist die große Änderung der Wassertiefe in Küstennähe zu erkennen, was eine eindimensionale Interpretation erschwert hat.

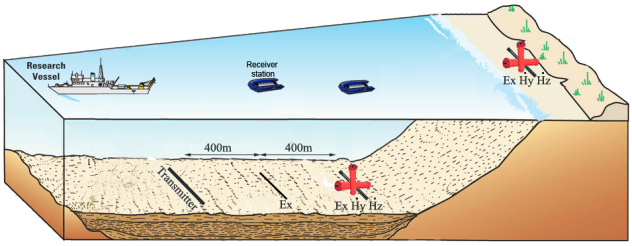

Figure 1: *Skizze einer Feldanordnung. Der Sender ist parallel zur Küste, gemessen wird in der broadside Konfiguration.*

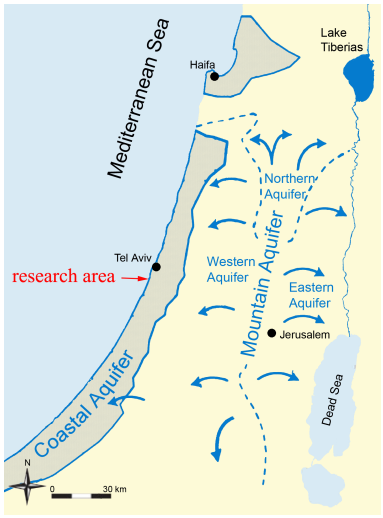

Figure 2: *Die wichtigen Aquifere der Region.*

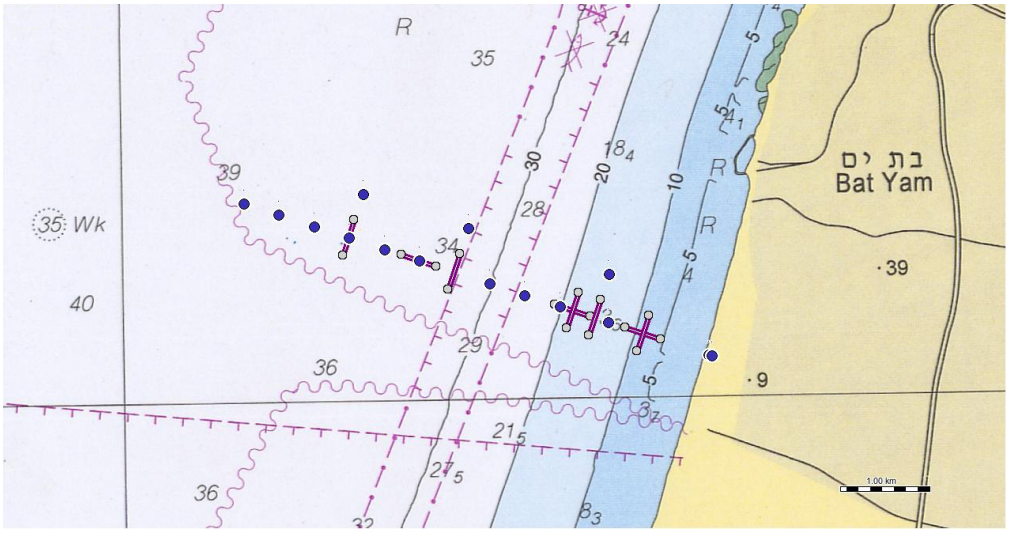

Figure 3: *Setup der Messungen: Lila Linien und graue Punkte stellen die Sender, blaue Punkte die Empfänger dar. Die Zahlen geben die Wassertiefe an.*

Datenprocessing

Als Sendestrom wird ein alternierender Gleichstrom mit bis zu 11 Ampere eingespeist. Die Periode dieses Signals (50%-Duty-Cycle) betrug im Jahr 2009 800 ms und im Jahr 2011 1600 ms. Nach dem Entfernen periodischer Störungen (hauptsächlich 50 Hz) wurden die Zeitreihen auf eine ganze Periode gelevelt. Normalerweise werden Ausschaltvorgänge auf die letzten Zeitpunkte gelevelt, mit der Annahme dass der Transient hier schon auf Null abgeklungen ist. Bei den vorliegenden kurzen Aufzeichnungszeiten ist dies jedoch nicht der Fall. Durch das Leveln auf eine komplette Periode hat man, z.B. bei den elektrischen Feldern, zweimal den Gleichspannungsanteil (mit unterschiedlichen Vorzeichen) und levelt somit die komplette Zeitreihe auf das richtige Null-Niveau. Anschliessendes Clustern, Zerschneiden, ggf. Multiplikation mit -1 und Stapeln der Zeitreihen führt zu auswertbaren Ausschalt-Transienten. Zwei Datenbeispiele inklusive Datenanpassung der eindimensionalen Occam-Inversion sind in Fig. 4 und 5 dargestellt (einmal westlich und einmal östlich der detektierten Kante des Aquifers).

Occam-Inversion

Die Ausschaltvorgänge wurden mittels eindimensionaler Occam-Inversion interpretiert. Es wurden jeweils zwei Regularisierungen verwendet: Roughness 1 und 2 (vgl. *Constable et al., 1987*). Die Güte der Datenanpassung wird mittels χ (ebenfalls z.B. *Constable et al., 1987*) abgeschätzt. Bei den Inversionen wird die Tiefe und der spezifische Widerstand des Wassers festgehalten. Hierbei wurde eine mittlere Wassertiefe zwischen Sender und Empfänger gewählt. Außerdem wurde wurde vor Ort die Systemantwort der Messapparatur gemessen. Im Inversionsprozess werden die berechneten Daten aus der Vorwärtsrechnung, vor dem Vergleich mit den gemessenen Daten, mit der Systemantwort gefaltet. Auch die Periodizität des Sendesignals wird im Inversionsprogramm berücksichtigt.

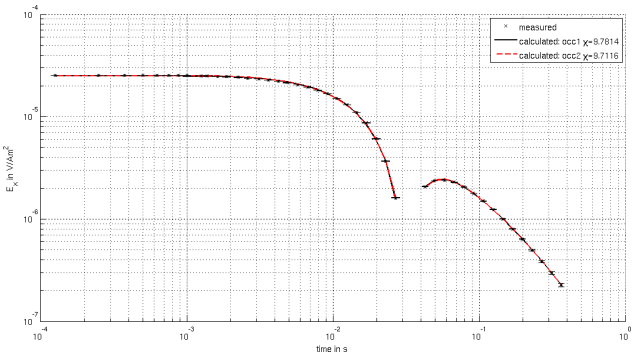

Figure 4: *Datenbeispiel östlich der detektierten Kante des Aquifers (mp 7 in Fig. 6). E_x-Komponente, broadside Konfiguration, Sender parallel Küstenlinie. Tx bei 1250 m, Rx bei 1650 m Entfernung von der Küste.*

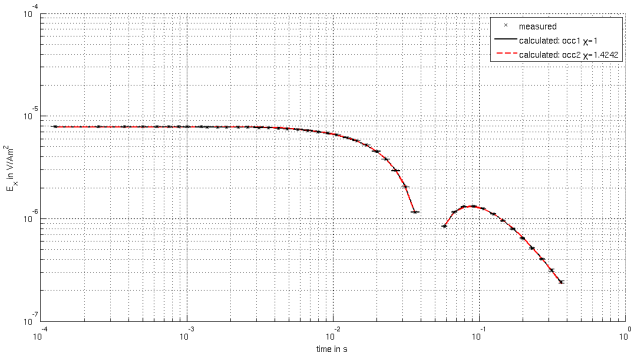

Figure 5: *Datenbeispiel westlich der detektierten Kante des Aquifers (mp 2 in Fig. 6). E_x-Komponente, broadside Konfiguration, Sender parallel Küstenlinie. Tx bei 4050 m, Rx bei 4450 m Entfernung von der Küste.*

Diskussion der Ergebnisse

Die Ergebnisse der eindimensionalen Inversionen sind in Fig. 6 als Profil dargestellt. Invertiert wurden die Daten der E_x-Komponente, broadside Konfiguration mit Sender parallel zur

Küstenlinie. Das jeweilige Erdmodell wurde unter die Position des Empfängers geplottet. Ab einer gewissen Tiefe zeigen die Ergebnisse der beiden Regularisierungen deutlich unterschiedliches Verhalten. Unterhalb dieser Tiefe wird das Modell nicht mehr von den Daten bestimmt, die Widerstände sind sehr schlecht aufgelöst. Bei den Messpunkten mp 1 und mp 2 liegt die aufgelöste Tiefe bei mind. 200 m. Bei den Messpunkten > 3 liegt die Tiefe bei mind. 400 m. Somit ist der relevante Tiefenbereich, in welchem der Aquifer liegt, dort gut aufgelöst. Bei Messpunkt mp 3 hingegen kann keine Aussage über den relevanten Tiefenbereich getroffen werden. Das Modell mit Roughness 2 ist außerdem unzureichend angepasst. Der gesuchte Aquifer, die schlechtleitende Schicht ($\rho_a > \sim 70\ \Omega m$), ist deutlich in den Messpunkten mp 4 bis mp 9 erkennbar: Die Schicht beginnt bei einer Tiefe von ca. 80 m und ist durchschnittlich etwa 100 m dick. Die Ergebnisse der Messpunkte mp 1 und mp 2 zeigen diese Schicht nicht. Die Daten von Messpunkt mp 3 können nicht zufriedenstellend mit einem 1D-Modell erklärt werden. Somit liegt das Ende des Aquifers zwischen ca. 3,2 km und ca. 4 km von der Küste entfernt.

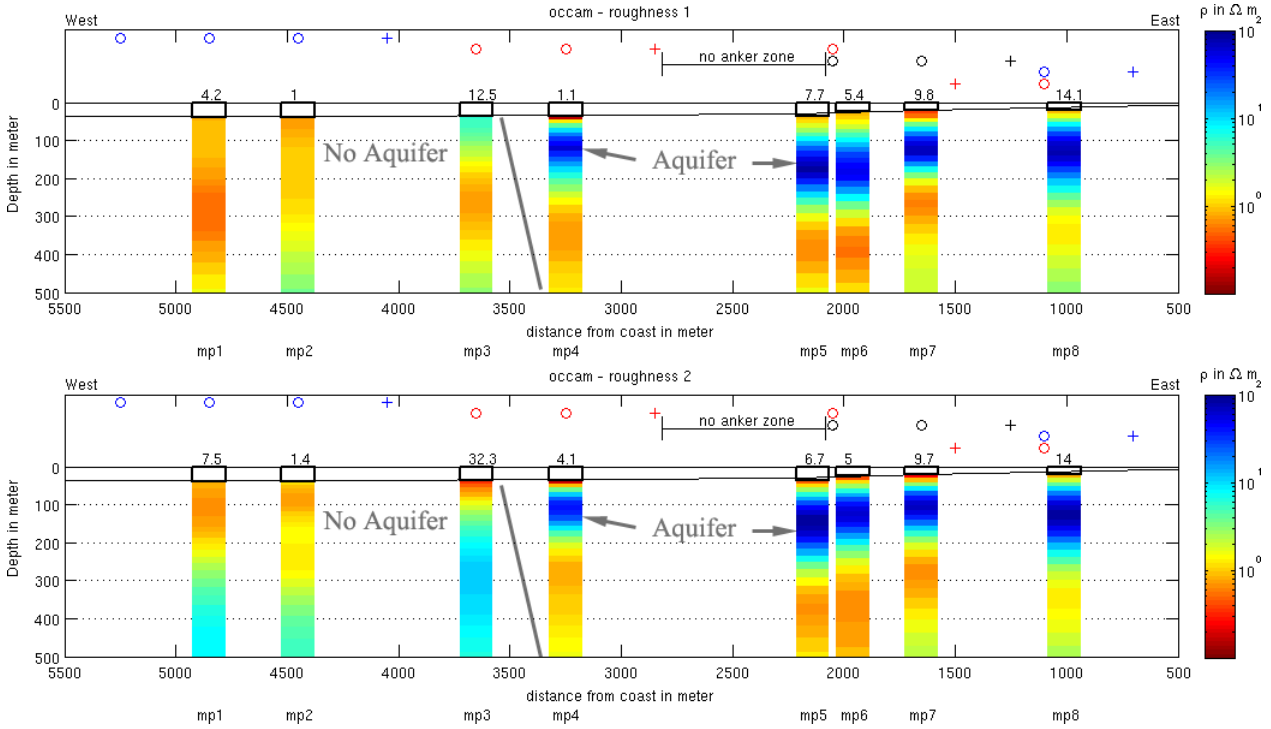

Figure 6: *1-D Occam Ergebnisse. Über den Modellen sind jeweils die Sender-(+) und Empfängerpositionen (○) eingezeichnet. Über den jeweiligen Stationen sind die χ-Werte der Datenanpassung angegeben. Die Küste befindet sich bei Profilmeter 0.*

Synthetische Modellierungen zur Form des Aquiferendes

Um die hydrologischen Randbedingungen am Ende des Aquifers zu verstehen ist die genaue Form interessant. Es kann sich um eine undurchdringliche, eine lithologische, Grenze handeln oder um eine hydrologische Grenze, bei der Meerwasser eindringt und sich eine schräge

Süß-/Salzwassergrenzschicht ausbildet. Diese beiden Situationen werden von den Modellen in Fig. 7 grob wiedergegeben: Modell 1 stellt einen geblockten Aquifer dar, die Modelle 2 und 3 beschreiben Aquiferenden mit Grenzschicht. Die Küste wurde mit einem einzigen Block angenähert. Die Schräge dieses Blocks stellt die Grenzschicht dar, deren Neigung durch die Ghyben-Herzberg-Näherung *[Bear et al., 1999]* beschrieben wird.

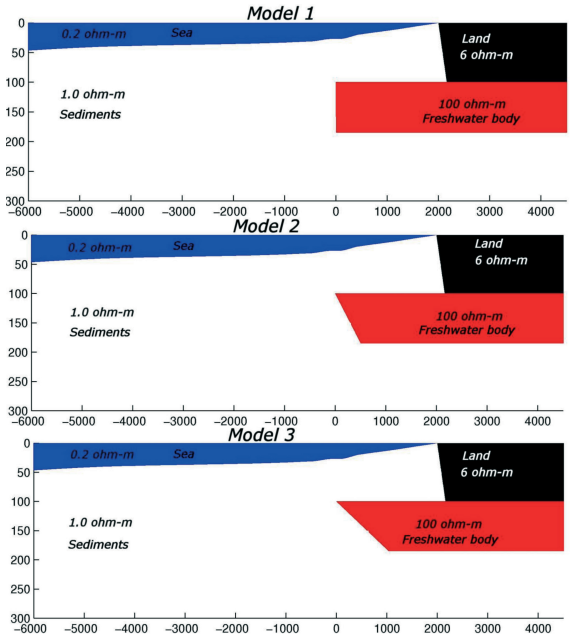

Figure 7: *Zweidimensionale Modelle die verschiedene Formen des Aquiferendes wiedergeben: lithologische Grenze (Modell 1) oder hydrologische Grenze (Modell 2 und 3).*

Die zweidimensionalen Modelle wurden mit SLDMEM3T *[Druskin und Knizhnermann, 1988]* gerechnet. Der Sender liegt horizontal bei Profilmeter 0, ist 400m lang und in die Zeichenebene hinein gerichtet. Der Empfänger befindet sich bei Profilmeter 310. Die E_x-Komponenten der drei Modelle aus Fig. 7 sind in Fig. 8 dargestellt. Es ist kein signifikanter Unterschied erkennbar.

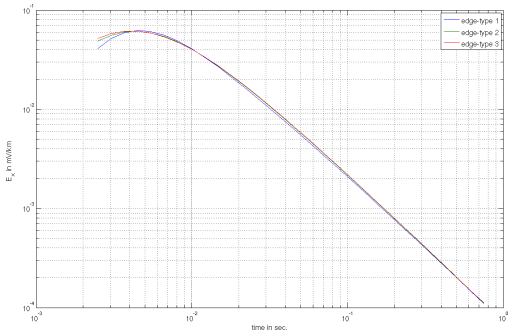

Figure 8: *Synthetische Daten der Modelle in Fig. 7 für einen horizontalen Sender parallel zur Küste, broadside Konfiguration, E_x-Komponente.*

Eine Möglichkeit die Form des Targetendes zu untersuchen wäre ein vertikaler elektrischer Dipol als Sender. In der Modellierung befindet sich dieser bei Profilmeter 0. Der Empfänger befindet sich bei Profilmeter 50. Die radialen Komponenten des elektrischen Feldes der drei Modelle aus Fig. 7 sind in Fig. 9 dargestellt. Die Transienten der verschiedenen Modelle unterscheiden sich deutlich. Somit ist mit Hilfe dieser Feldanordnung eine Interpretation über die Geometrie der Aquiferkante möglich.

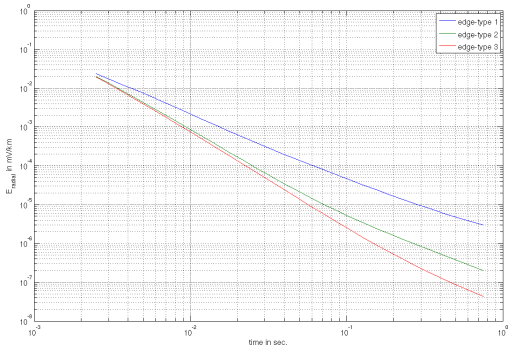

Figure 9: *Synthetische Daten der Modelle in Fig. 7 für den vertikalen elektrischen Dipol als Sender.*

Zusammenfassung

Der Aquifer unter dem Mittelmeer wurde mit der LOTEM-Methode detektiert und seine lat-

erale Ausdehnung konnte eingegrenzt werden. Für die hydrogeologisch interessante Frage nach der From der Abschlusskante des Aquifers scheint diese Methode nicht die geeignete Wahl zu sein, was synthetische Modellierungen zeigen.

Danksagung

Großer Dank geht an C.Scholl für sein "(MAR)ine (T)em (IN)version program" !

Literatur

Arad, A.: *"A summary of artesian coastal basin of Guyana."*, J.Hydrol. 1983.

Bear, J., Cheng, A.H.-D., Sorek, S., Ouazar, D. and Herrera, I. (Eds.): *"Seawater Intrusion in Coastal Aquifers - Concepts, Methods and Practices"*, Kluwer Academic Publishers, 1999.

Constable, S. C., R. L. Parker und C. G. Constable: *"Occams Inversion: A practical algorithm for generating smooth models from electromagnetic sounding data."*, Geophysics, 1987.

Druskin, V.L., Knizhnermann, L.A.: *"A spektral semi-discrete method for the numerical solution of 3d nonstationary problems in electrical prospecting."*, Phys. Solid Earth, 1988.

Groen J., Groen M., Post V., Kooi H., Mendizabal I. and Groot S.M.: *"Seaward continuation of groundwater flow systems along the coast of the Netherlands."*, GSA Salt Lake Ann.Meet. Abstract Paper No.211-9., 2005.

Kafri, U. and Goldman, M.: *"Are the lower subaquifers of the Mediterranean coastal aquifer blocked to seawater intrusion? Results of a TDEM (time domain electromagnetic) study."*, Isr.J.Earth Sci., 2006.

Yechieli et. al: *"The inter-relationship between coastal sub-aquifers and the Mediterranean Sea, deduced from radioactive isotopes analysis."* Hydrogeology, 2009.

Limits of 1D phase tensor inversion on 3D structures

Alexander Löwer, Andreas Junge
Institute for Geosciences, departement of Geophysics,
Goethe-University Frankfurt, Germany
contact: loewer@geophysik.uni-frankfurt.de

Methodical approach

The successfull and fast inversion of three dimensional magnetotelluric data benefits from a good start model for the electrical conductivity distribution. In this work we calculate pseudo-3D models constructed from a robust phase tensor (PT) inversion of average minimum and maximum PT values (AMMPT) [*Junge* 2011]. Each 1D model is scaled by the median resistivity gained from the Berdichevsky invariants over all periods. The AMMPT has three important features: It is not influenced by static shift, it is independent of instrument orientation and it reduces the impact of lateral conductivity inhomogenities on 1D model estimation. In the following the influence of 3D structures on the 1D PT inversion is shown. The 3D forward calculation of the magnetic and telluric field variations is done using *Comsol Multiphysics 4.2*. After computing the transfer functions up to 15% random error was added. The phase tensors are calculated after *Caldwell et al.* [2004]. Then 1D-AMMPT inversion was used to reconstruct the 3D conductivity distribution. In the following we present three model studies.

Single Block

The first model is a single good conducting block with a resistivity of $10\Omega m$ and dimensions of 100x100x10km in 30km depth (Fig. 1). The background resistivity is $1000\Omega m$. The 1D inversions detect the anomaly well (Profile #1, Fig. 1b). The upper boundary of the block is well resolved. However, the corners of the conductor (Fig. 1c) can not be located precisely. Besides the upper boundary the horizontal dimensions are also well resolved, but conductivity boundaries are displayed as smooth transition zones.

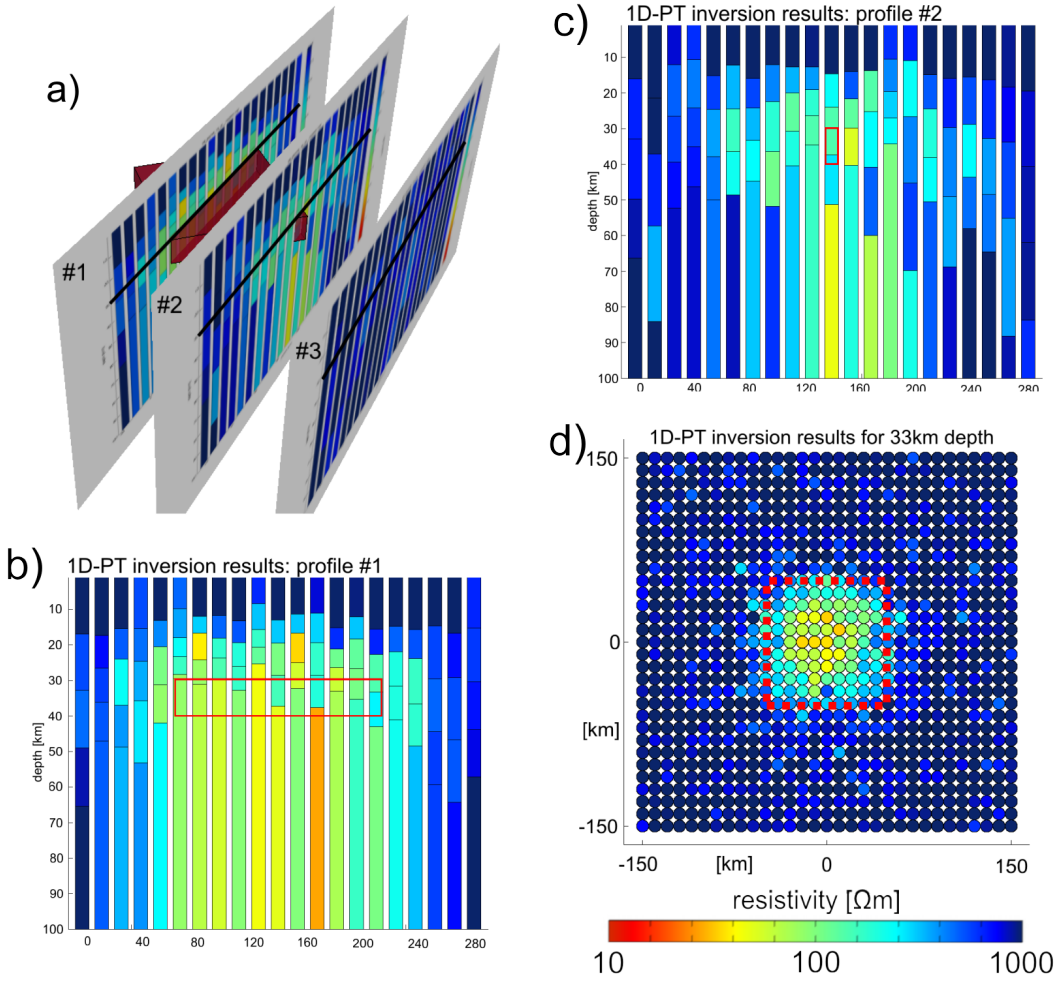

Figure 1: **a)** Overview of the model and the 2D profiles. The red block is the conducter with the dimensions of 100x100x10km at 30 km depth having a resistivity of $10\Omega m$, whereas the background resistivity is $1000\Omega m$. Black lines mark the upper boundary of the conductor.
The three profiles show 2D-depth-slices with the 1D PT inversion results. Profile #1 is shown in Fig. 1b, profile #2 in Fig. 1c, profile #3 is localized outside the good conducting area with a minimum distance of 30km to the conductor. The influence of the block cannot be noticed any more.
b) Profile #1 running diagonal through the center of the good conducting block. The red rectangle marks the position of the block.
c) Profile #2 parallel to profile #1 through the corner of the conductor. The red rectangle marks the corners position.
d) horizontal slice of the 1D PT inversion resistivities at a depth of 33km. Resistivities are indicated by the circle color. The station spacing is 10km. Red dotted lines show the dimensions of the good conductor.

Checkerboard test

Secondly a checkerboard test was performed. Each anomaly has the dimension of 100x100x10km and the resistivity of $10\Omega m$, the background resistivity being $1000\Omega m$. The upper boundary of the anomaly is at 30km depth. As in the previous test the top boundaries and the horizontal dimensions are well resolved (Fig. 2). However, the depth of the top layer is too shallow. The 1D approach fails in areas with high 3D effects (for instance at the corners).

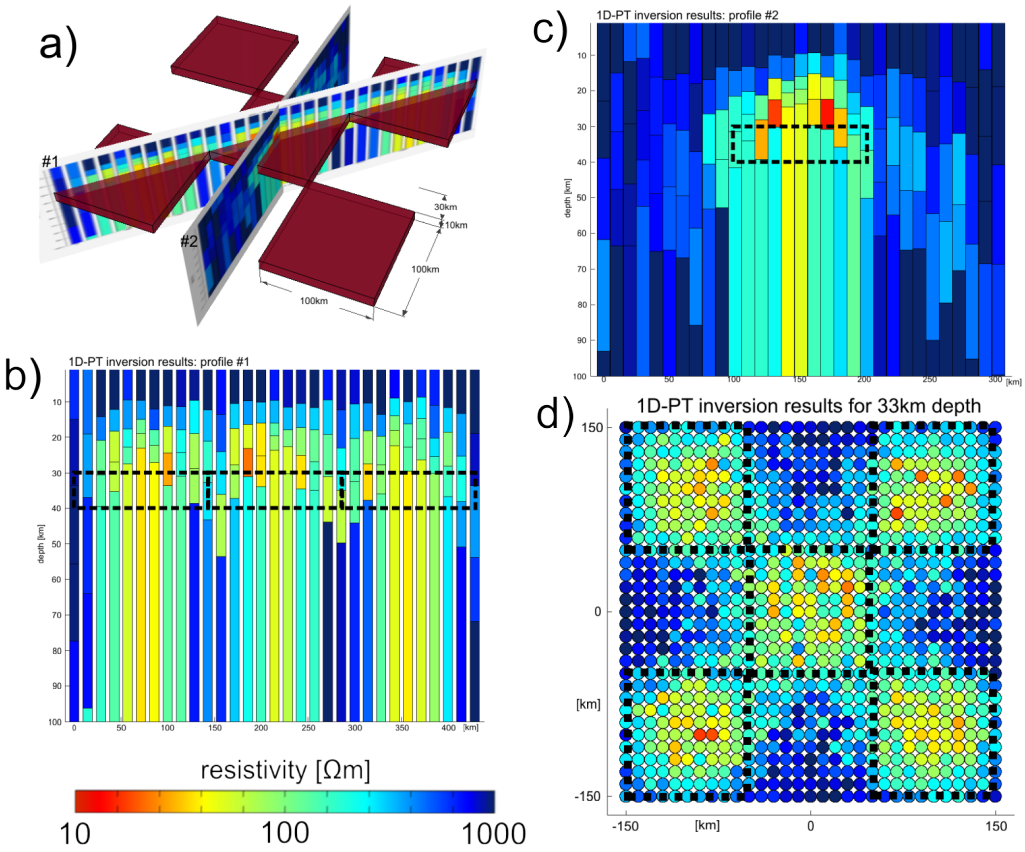

Figure 2: **a)** Overview of the model and the 2D depth sections. The red blocks are the conductors with dimensions of 100x100x10km each. They represent a checker board pattern at a depth of 30 km. Their resistivity is $10\Omega m$ whereas the background resistivity is $1000\Omega m$.
b) Profile #1 running diagonal through three conducting blocks. The dotted black rectangles mark the positions of the blocks. Their corners are close together.
c) Profile #2 parallel to the X-axis crossing the block in the center, its position is marked by the dotted black rectangle.
d) Horizontal 2D plane showing resistivities of the 1D PT inversion results at 33km depth. The resistivities are indicated by the circle colors. The station spacing is 10km. The locations of the good conductors are shown by the dotted black rectangles.

Overlapping blocks

As a third model we used two overlapping conducting blocks in different depths (Fig. 3a). One conductor is located at the depth of 30km and comprises the dimensions of 150x100x10km and a resistivity of $10\Omega m$, the second conductor also has a resistivity of $10\Omega m$ at a depth of 60km with the dimensions of 175x100x30km. The overlapping area is 100x100km. The geometry of the upper body is well resolved, as in the previous tests. However, the lower body is shielded and can not be distinguished from the upper anomaly. Because the vertical dimension of the total anomaly is larger than in the other models, the resistivity estimate is more realistic.

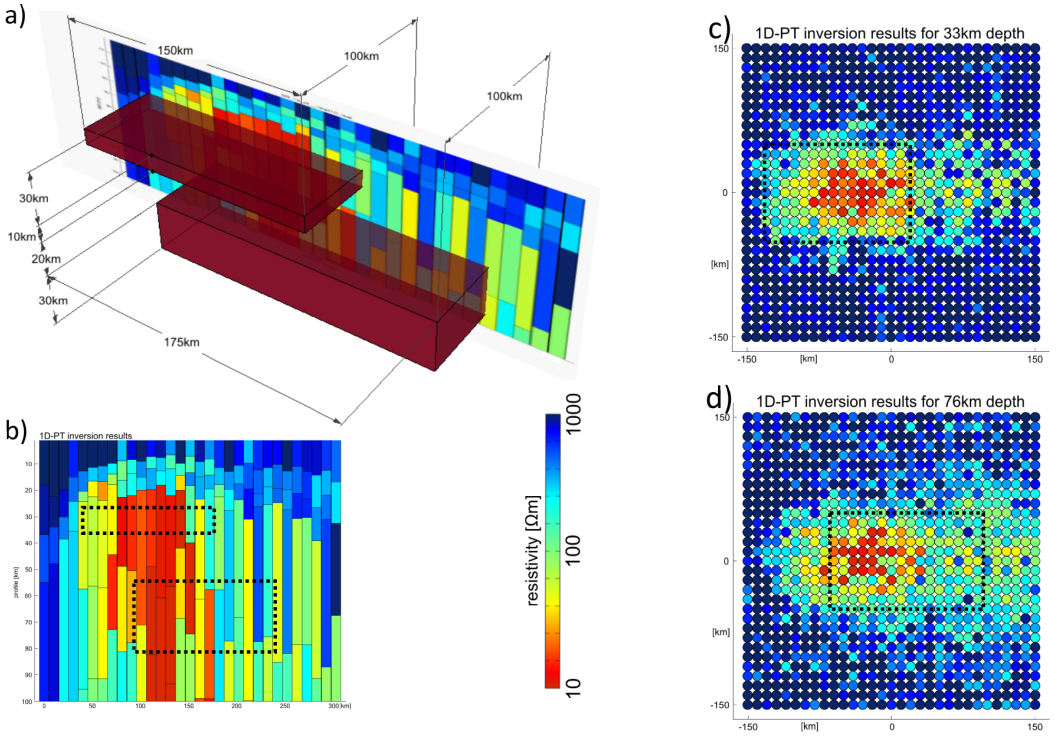

Figure 3: **a)** Overview of the model and the 2D depth section. The upper red block is a good conducter with dimensions 150x100x10km at 30km depth, the lower red block is a good conductor with dimensions 175x100x30km at 60km depth. Each block has a resistivity of $10\Omega m$, whereas the background resistivity is $1000\Omega m$. The overlapping area is 100x100km.
b) Profile #1 represents 1D-PT inversion results parallel to the x-axis cutting both blocks. The conductors are marked by dotted black rectangles.
c) Resistivities at 33 km depth. The upper good conductor is marked by the dotted black rectangle. The resistivities from the 1D PT inversion are represented by the colors of the circles, station spacing is 10km.
d) Resistivities at 76km depth similar to Fig. 3(c). The dottet black line marks the geometry of the lower conductor.

Conclusions

The 1D phase tensor inversion reflects 3D situations rather well and offers a quick first impression of the conductivity distribution. It resolves top boundaries of conductors and their lateral extensions. However, sharp boundaries are mapped into smooth transitions, internal structures dissapear and depth scaling might be biased. A selection of the stations based on parameters indicating three dimensional influences was not possible. Nevertheless, the general pattern of the resistivity structure, also of more complicated anomalies, is reproduced and thus can be used as a start model for 2D or 3D inversions.

References

Caldwell, T. G., H. M. Bibby and C. Brown, The magnetotelluric phase tensor, *Geophys. J. Int*, , (158), 457–469, 2004.

Junge, A., A concept of MT-data inversion using adaptive master Jacobians for spatially fixed model conductivity sampling points, *Abstract Volume, 24. Schmucker-Weidelt-Kolloquium für elektromagnetische Tiefenforschung Neustadt a.d.W.*, 2011.

ELECTROMAGNETIC INVESTIGATION OF THE RESISTIVITY STRUCTURES AROUND AND BENEATH THE EYJAFJALLAJÖKULL VOLCANO, SOUTHERN ICELAND: PRELIMINARY RESULTS

Marion P. Miensopust[1,2], Alan G. Jones[1], Gylfi P. Hersir[3] and Arnar M. Vilhjálmsson[3]

[1] Dublin Institute for Advanced Studies, School of Cosmic Physics, Dublin, Ireland
[2] Institut für Geophysik, Westfälische Wilhelms-Universität Münster, Germany
[3] Iceland GeoSurvey, Reykjavík, Iceland

ABSTRACT - Due to the recent eruptive and highly disruptive volcanic events in 2010 in Iceland, scientific and societal interest is overwhelming in gaining as much information as possible about the volcanic structures and processes to enhance the understanding of the partially glacier-covered Eyjafjallajökull and Katla volcanic systems. Numerous petrological, geochemical and geophysical investigations of these systems have already been published. However, to date no electrical or electromagnetic data have been acquired on these two volcanoes to attempt to image the resistivity structure beneath and around them, although electromagnetic methods are far more sensitive to fluid distribution (in this case partial melt) than any other geophysical method.
In July 2011, a pilot study took place to collect broadband magnetotelluric (MT) data around the Eyjafjallajökull. The MT data are supplemented with transient electromagnetic (TEM) measurements. This data set is the first one collected at these volcanic systems and will complement the existing geophysical data. Very fresh data and preliminary results from the experiment will be shown.

INTRODUCTION

Iceland has numerous active volcanoes, some of which are covered by glaciers. The Eyjafjallajökull volcano in southern Iceland has an ice-capped crater and its 'sister volcano', Katla, that erupted twice in historic times (within the last 1,100 years) synchronously with the Eyjafjallajökull, is mostly covered by a glacier. The volcanic system of Katla is one of the most active ones in Iceland with at least twenty eruptions within the central volcano and one in its fissure swarm during the past 1,100 years (Larsen, 2000). These eruptions have been quite regularly twice every century, but the last eruption in 1918 is almost 100 years ago. The volcano is mostly covered by the Mýrdalsjökull ice cap and, therefore, eruptions within the Katla volcano are phreato-magmatic in type and are capable of producing jökulhlaups (or glacier bursts), i.e., sudden glacial outburst floods (Sturkell et al., 2010). The neighbouring volcano, 25 km to the west, is Eyjafjallajökull, which is covered by a smaller and thinner glacier. It is less active than Katla with the most recent (in March/April 2010) and two historic eruptions recorded during the last 1,100 years. These two known historic events occurred in tandem, the first simultaneously with the Katla eruption of 1612, and the second being the eruption in 1821-1823 that was immediately followed by an eruption of Katla (Sturkell et al., 2010 and references therein in Icelandic). Both volcanoes are in proximity to populated areas and to international flight paths, which makes them both potent societal threats, although the erupted volume of Katla has been orders of magnitude larger than those of Eyjafjallajökull. The recent eruptive events of the Eyjafjallajökull volcano have focused major public interest - even more than ever before - on volcanic eruptions (not only on their local effects but also on potential long-distant effects on daily life). Scientific interest is

overwhelming in gaining as much information as possible about the volcanic structures and processes to enhance understanding. Based on the historic eruptive connections between these two volcanoes, there is the apprehension that the 2010 eruption of Eyjafjallajökull will be followed by a larger eruption of Katla. Therefore, interest in knowing the volcanic structures of both volcanoes and understanding the possible links between them is heightened.

Beside numerous petrological and geochemical studies also some geophysical investigations on the Eyjafjallajökull and Katla volcanoes have been published showing results from GPS measurements (e.g., Árnadóttir et al., 2008), earthquake studies (e.g., Dahm & Brandsdóttir, 1997; Einarsson & Brandsdóttir, 2000), radar altimetry and interferometry (e.g., Guðmundsson et al., 2007; Hooper et al., 2009), seismic surveys (e.g., Guðmundsson et al., 1994), and aeromagnetic measurements (e.g., Jónsson & Kristjánsson, 2000). The bedrock surface of Mýrdalsjökull has been mapped by radio echo soundings (Björnsson et al., 2000). Recently Sigmundsson et al. (2010) outline their understanding of the intrusive processes based on GPS measurements, interferometric analysis of satellite radar images and seismic data recorded over several months before and during the 2010 eruptive events. However, to date no electric or electromagnetic (EM) methods have been applied to attempt imaging the resistivity structure beneath and around these two volcanoes, although EM methods are far more sensitive to fluid distribution (in this case partial melt) than any other geophysical method. Therefore, the aim of the project conducted by Iceland GeoSurvey (ISOR) and Dublin Institute for Advanced Studies (DIAS) is to investigate the resistivity structure beneath and around the Eyjafjallajökull using the magnetotelluric (MT) and transient electromagnetic (TEM) methods.

DATA COLLECTION AND PROCESSING

In July 2011, broadband MT data were collected at 26 sites around the Eyjafjallajökull and the southern part of Mýrdalsjökull (Figure 1) using MTU5/MTU5A systems from Phoenix Geophysics. Both horizontal electric field components were recorded using 100 m dipoles, and the vertical and both horizontal magnetic field components were measured using induction coils. At most sites the recording time was approximately 40 hours, and a distant remote reference site (about 150 km away) was recording during the whole survey. The obtained period range of good quality data is about 0.003 to 1,000 – 2,000 s. In addition, at 25 of the MT sites central loop TEM data were obtained using a transmitter loop of 200 m x 200 m and a 1 m^2 receiver loop with 100 windings (effective area 100 m^2).

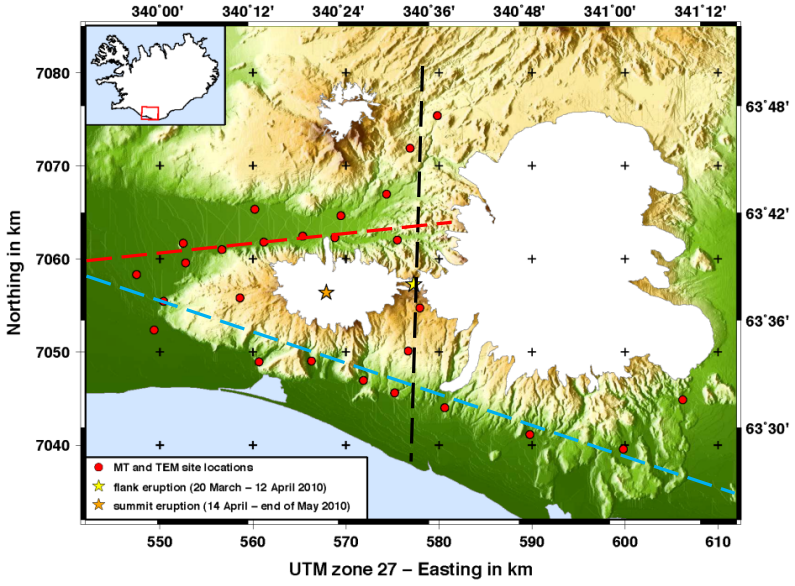

Figure 1: Map showing the locations of the 26 MT and TEM sites, flank and summit eruption sites as well as dashed lines indicating the position of cross-sections shown in Figure .

Phoenix commercial remote-reference processing software (based on Jones and Jödicke (1984)/method 6 in Jones et al. (1989)) was used to convert the time series of the magnetotelluric data into transfer functions. To obtain the best response curves combinations of electric field and magnetic field references as well as a far remote (remote reference site about 150 km away from array) and a local remote (array site that recorded at the same time) were investigated. For many sites an electric field remote reference resulted in better estimates for short periods whereas a magnetic field remote reference produced better results for long periods. Figure 2 shows apparent resistivity and phase curves as well as induction arrows using Wiese convention (Wiese, 1962) for an example site. The transfer functions were merged from electric field remote reference estimates for periods < 10 s and magnetic field remote reference estimates > 10 s. In general, the data quality is very good and the transfer functions suggest at least for the first three decades a 1D structure.

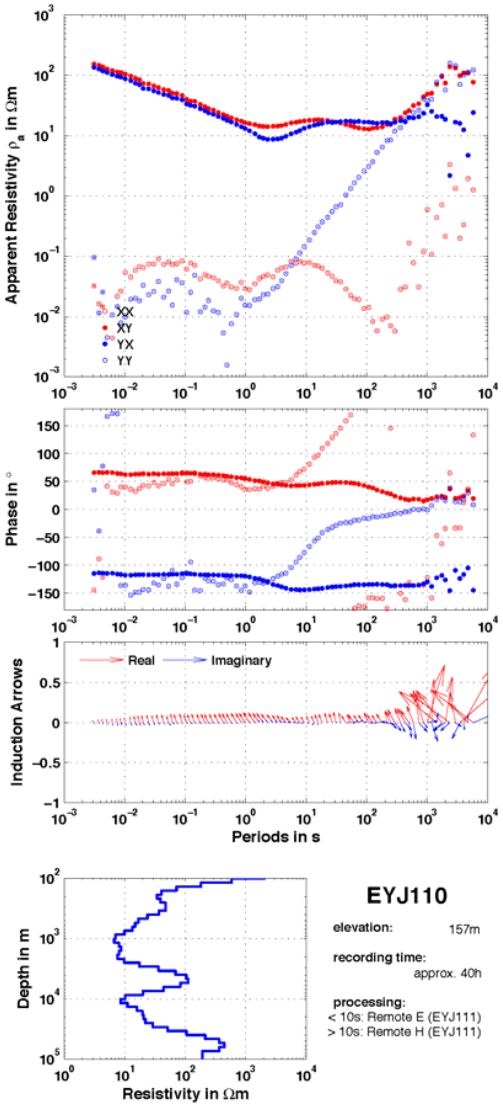

Figure 2: Response curves of an example site. Apparent resistivity curves (top), phase curves (middle) and induction arrows (bottom) in Wiese convention (Wiese, 1962) are shown. Below are information about this particular site and the obtained 1D Occam model of the invariants.

PRELIMINARY RESULTS

Small-scale, near-surface resistivity heterogeneities and topography can affect MT responses. This phenomenon is known as distortion. If the distortion is purely galvanic (as assumed for the MT case), the phase relationship between the horizontal electric and magnetic field vectors will be virtually unaffected and only the amplitudes of the observed electric field are distorted. Taken advantage of this, Caldwell et al. (2004) introduced the phase tensor approach. The graphical representation of the phase tensor is an ellipse. The principle axes of the phase tensor ellipse (ϕ_{max}, ϕ_{min}) indicate the horizontal directions of the maximum and minimum induction current, which reflects lateral variations in the resistivity structure. The phase tensor skew angle (β), and the variation of the direction of the major axis of the phase tensor ellipse can help in determining the dimensionality of the structure. In the case of an isotropic, 1D structure, $\phi_{max} = \phi_{min}$ and therefore the phase tensor will be represented by circles. In the 2D case, $\phi_{max} \neq \phi_{min}$ and the phase tensor is represented by an ellipse. For the 1D and 2D case, the phase tensor is symmetric (theoretically: $\beta = 0$), whereas for the 3D case the phase tensor is not symmetric and accordingly the skew angle will be non-zero. Figure 3 shows phase tensor maps including induction arrows for 0.5 km, 1.5 km and 7.5 km depth below surface (Niblett-Bostick penetration depth estimation). The colour of the phase tensor ellipses represent the skew angle β (left) and ϕ_{min} (right). For 0.5 km and 1.5 km the phase tensor ellipses are almost all nearly circular and therefore indicate a 1D resistivity structure in shallow depth

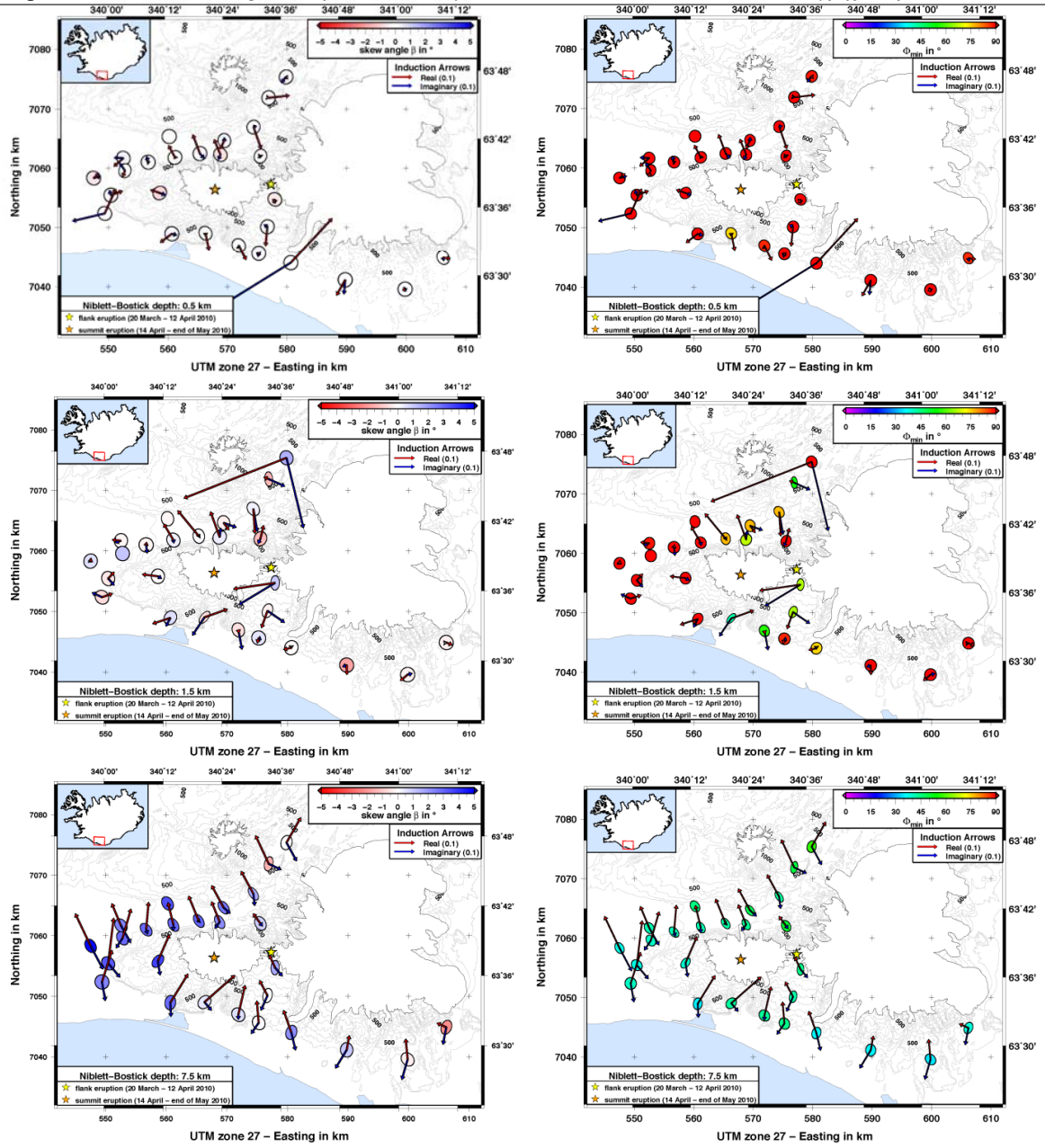

Figure 3: Maps of phase tensor ellipses and induction arrows. For three different depths (0.5, 1.5 and 7.5 km) the real (red) and imaginary (blue) induction arrows are plotted, the arrow length in the legend represents a value of 0.1. The colour of phase tensor ellipses (axes normalised by ϕ_{max}) indicates (left) the skew angle β and (right) ϕ_{min}, respectively. (Note, that the comparable large induction arrow estimates at some sites are not very reliable values as the induction arrows for these sites and these periods range, e.g., in the MT dead-band, scatter a lot.)

(conform with the statement above regarding the first three decades of the response curves in Figure 2). For 7.5 km most phase tensor ellipses are elongated indicating a more complex structure than 1D. The skew angles β are relatively small for all depth and the induction arrow lengths are very short, both indicators for low dimensionality. Large ϕ_{min} values at 0.5 km depth indicate an overall increasing conductivity with depth for the whole survey area. At 1.5 km the sites close to the eruption sites show

moderate ϕ_{min} values (i.e., less strong decrease in resistivity) while all other sites still require a strong decrease in resistivity. At greater depth (7.5 km), the ϕ_{min} values suggest rather constant resistivities or a slight increase. For shallow depth the real induction arrows (red) point away from the Eyjafjallajökull indicating a more conductive structure there compared to the surrounding. At greater depth almost all real induction arrows point away from the Atlantic Ocean. The Icelandic continental shelf has a shallow bathymetry (< 100 m) for the first few kilometres off the coast line, therefore the coast effect only affects long periods/greater depths (see also Figure 2).

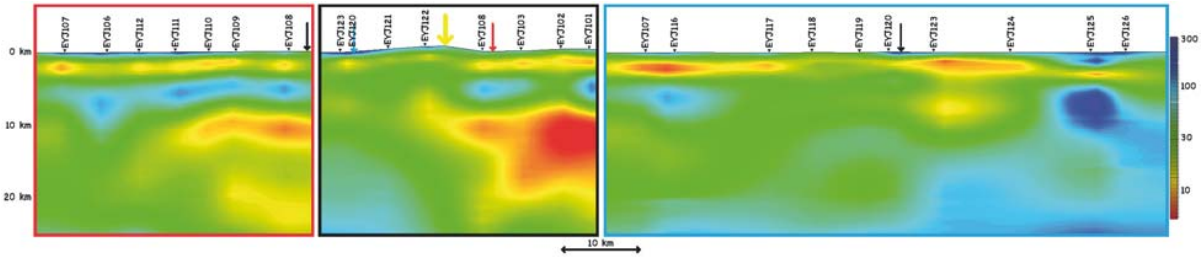

Figure 4: Cross-sections of three profiles. Cross-sections are grids (interpolation radius 3, spline weight 0, smoothing factor 4) of Occam 1D models of the invariants. The coloured boxes indicate where the profiles are located (dashed line of same colour on map in Figure 1) and intersections with other profiles are indicated by an arrow of the same colour. The yellow arrow is the flank eruption location projected onto the profile.

The above suggests that a 1D approach is valid to gain a first impression of the near surface resistivity structures. Therefore, the invariants of the MT data, i.e., geometric mean of resistivities ρ_{xy} and ρ_{yx} and arithmetic mean of phases ϕ_{xy} and ϕ_{yx}, were used to calculate 1D Occam models (Constable et al., 1987). The inversion was ran for maximum 10 iterations using 45 layers with depth limits set to 100 m (top) and 100 km (bottom). Figure 2 shows the resistivity-depth profile obtained for the example site. Such resistivity-depth profiles were calculated for all sites and most show (as in Figure 2) two conductive layers – one at about 1 – 3 km and the other one at about 10 km below surface. Figure 4 shows cross-sections of three profiles (marked by coloured dashed lines in Figure 1) along which the 1D Occam model were smoothly gridded. These cross-sections show also a shallow conductor nearly everywhere, presumably reflecting hydrothermal alteration minerals and, in some parts, a dominant second conductor below 10 km. Previous MT work in Iceland (e.g., Beblo & Björnsson, 1978; Hersir et al., 1984; Eysteinsson & Hermance, 1985) repeatedly showed a conductor in about 10 – 12 km depth nearly everywhere beneath Iceland. The conductive layer was initially interpreted to be due to partial melt in the crust and is still believed to be connected to melt, at least below some parts of the island. However, strong arguments against the presence of a considerable amount of partial melt at this depth interval have been put forward, based on a study of the attenuation of seismic waves (Menke et al., 1995) and later, Kaban et al. (2002) also concluded that considerable melt within the lower crust of Iceland is unlikely. In a recent interpretation of resistivity data from the high temperature area Hengill, SW Iceland the deep conductors are believed to reflect dikes and magma

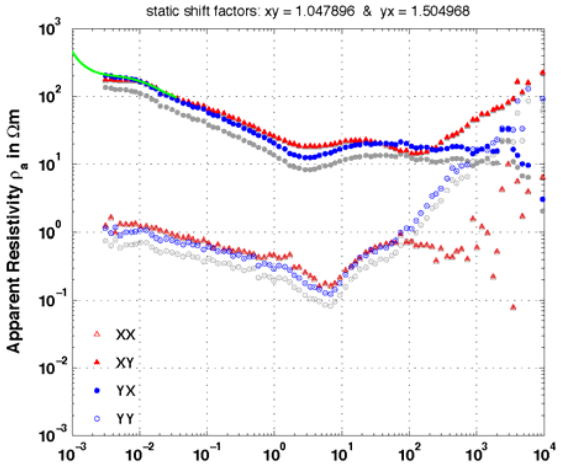

Figure 5: Apparent resistivity curves of an example site. The grey symbols represent the original data whereas the coloured are the data corrected by the static shift factors specified above based on the TEM data (green line).

intrusions and the conductive layer proposed to be due to magmatic brines trapped in ductile intrusive rocks (Árnason et al., 2010). The geological/geophysical reason of the deep-seated high conductive layer is not yet fully understood.

In a next step the obtained TEM data was used to estimate the static shift effects on the original MT data. Displaying TEM data, the apparent resistivity values are usually plotted against time in seconds. To compare the TEM data with the MT data they are plotted using the conversion by Sternberg et al. (1988), where the TEM time is divided by 0.2 to approximate a period on the scale used for MT data. For an example site Figure 5 shows the original apparent resistivity data as grey symbols and the converted TEM curve is represented by the green line. The static shift factors specified above are obtained by calculating the mode (i.e., most frequent value) of the differences in resistivity between the TEM data and each of the XY and YX components of the original MT data. The shift factor XY is applied to the XX and XY MT data and the YX factor to the YX and YY components. The corrected MT data are represented by the coloured symbols. Figure 6 shows a map of all obtained XY and YX static shift factors. Some sites show negligible static shift effects, whereas a few others have more significant effects (mainly only on one E-field direction). Three sites show a shift factor > 1 for one and < 1 for the other direction. These three sites are all located in valleys (especially the south-western one of the three is in an extremely narrow valley). The sites that have a static shift factor close to 2 for one direction are all close to a steep slope. Therefore, the static shift effects found are considered as partly caused by topography. This effect was described by Jiracek (1990).

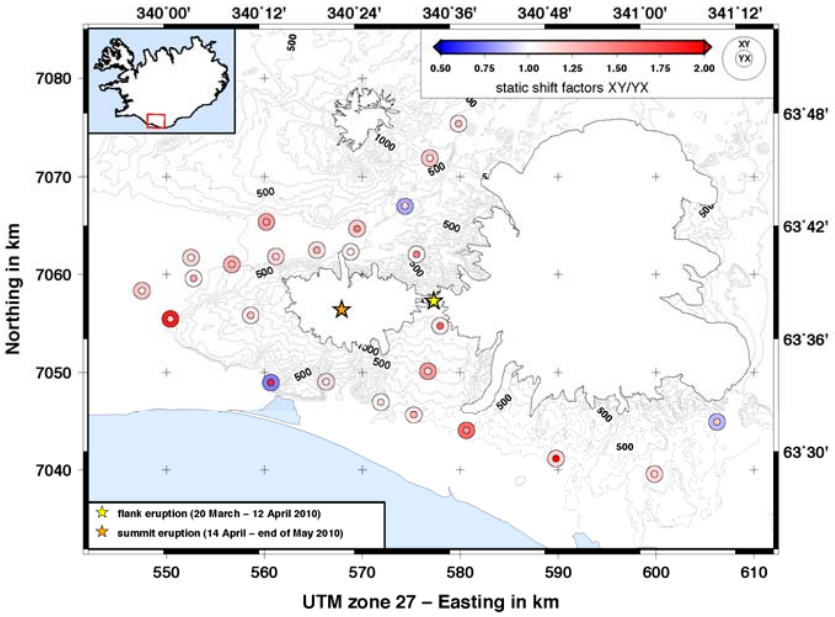

Figure 6: Map showing static shift parameters XY and YX for all sites that have MT and TEM data. The outer circle represents the XY shift factor and the inner dot the YX shift factor.

CONCLUSION & OUTLOOK

The quality of the MT data recorded is very good and all sites show 1D behaviour at short periods. The 1D Occam results (cross-sections as well as resistivity-depth profiles) show two conductive layers; one in approximately 1-3 km depth and one around 10 km depth. The later is conform with many other MT observations across Iceland (e.g., Beblo & Björnsson, 1978; Hersir et al., 1984; Eysteinsson & Hermance, 1985; Árnason et al., 2010). Using TEM data, the MT response curves are corrected for static shift, which is to some extent driven by topography.

The next steps towards a final interpretation will be distortion and strike analysis, 2D and 3D modelling. For interpretation the resistivity models obtained will be compared to other geophysical data

available (e.g., seismicity and GPS data). This study will hopefully be the beginning of a more detailed electromagnetic study of the Eyjafjallajökull and Katla volcanic systems.

ACKNOWLEDGEMENTS

We would like to thank Mark R. Muller, Halldór Örvar Stefánsson, Pálmar Sigurðsson, Sigurbjörn Bogi Jónsson, Alae-Eddine Barkaoui, Anna Wairimu Mwangi, Diego A. Badilla Elizondo, Raymond M. Mwakirani for their indispensable and indefatigable help during the fieldwork.

REFERENCES

Árnadóttir, T., H. Geirsson, S. Hreinsdóttir, S. Jónsson, P. LaFemina, R. Bennett, J. Decriem, A. Holland, S. Metzger, E. Sturkell and T. Villemin (**2008**). *Capturing crustal deformation signals with a new high-rate continuous GPS network in Iceland.* Eos, Transactions, American Geophysical Union 89(53). Fall Meet. Suppl., Abstract G43A-0650

Árnason, K., H. Eysteinsson and G.P. Hersir (**2010)**. *Joint 1D inversion of TEM and MT data and 3D inversion of MT data in the Hengill area, SW Iceland.* Geothermics, vol. 39, 13-34.

Beblo, M., and A. Björnsson (**1978)**. *Magnetotelluric investigation of the lower crust and upper mantle beneath Iceland.* J. Geophys. 45, 1-16.

Björnsson, H., F. Pálsson and M.T. Guðmundsson (**2000**). *Surface and bedrock topography of the Mýrdalsjökull ice cap, Iceland: The Katla caldera, eruption sites and routes of jökulhlaups*. *Jökull* 49, 29-46.

Caldwell, T.W., H.M. Bibby and C. Brown (**2004**). *The magnetotelluric phase tensor*. Geophysical Journal International, 158.

Constable, S.C., R.L. Parker and C.G. Constable (**1987**). *Occam's inversion: A practical algorithm for generating smooth models from electromagnetic sounding data*. Geophysics, 52(3).

Dahm, T. and B. Brandsdóttir (**1997**). *Moment tensors of micro-earthquakes from the Eyjafjallajökull volcano in South Iceland.* Geophysical Journal International, 130*.*

Einarsson, P. and B. Brandsdóttir (**2000**). *Earthquakes in the Myrdalsjökull area, Iceland, 1978–1985: Seasonal correlation and relation to volcanoes*. Jökull 49.

Eysteinsson, H. and J.F. Hermance (**1985**). *Magnetotelluric measurements across the eastern neovolcanic zone in southern Iceland.* Journal of Geophysical Research, 90.

Guđmundsson, M.T., P. Högnadóttir, A.B. Kristinsson and S. Gudbjörnsson (**2007**). *Geothermal activity in the subglacial Katla caldera, Iceland, 1999–2005, studied with radar altimetry*. Annals of Glaciology 45.

Guđmundsson, Ó., B. Brandsdóttir, W. Menke, and G.E. Sigvaldason (**1994**). *The crustal magma chamber of the Katla volcano in South Iceland revealed by 2-D seismic undershooting*. Geophysical Journal International, 119.

Hersir, G.P., A. Björnsson and L.B. Pedersen (**1984)**. *Magnetotelluric survey across the active spreading zone in southwest Iceland.* Journal Volc. Geothermal. Res. 20, 253-265.

Hooper, A., R. Pedersen and F. Sigmundsson (**2009**). *Constraints on magma intrusion at Eyjafjallajökull and Katla volcanoes in Iceland, from time series SAR interferometry*. In: Bean, C.J., Braiden, A.K., Lokmer, I., Martini, F., O'Brien, G.S. (Eds), VOLUME project, EU PF6 (No. 018471). ISBN 978-1- 905254-39-2. VOLUME Project Consortium, Dublin.

Jiracek, G.R. (**1990**). *Near-surface and topographic distortions in electromagnetic induction*. Surveys in Geophysics, 11.

Jones, A.G. and H. Jödicke (**1984**). *Magnetotelluric transfer function estimation improvement by a coherence-based rejection technique*. 54th Ann. Mtg. Soc. of Expl. Geophys., Atlanta, Georiga.

Jones, A.G., A.D. Chave, G. Egbert, D. Auld and K. Bahr (**1989**). *A Comparison of techniques for magnetotelluric response function estimation.* Journal of Geophysical Research (Solid Earth), 94(10).

Jónsson, G. and L. Kristjánsson (**2000**). *Aero-magnetic measurements over Mýrdalsjökull and vicinity*. Jökull 49.

Kaban, M,K, Ó G. Flóvenz and G. Pálmason (**2002)**. *Nature of the crust-mantle transition zone and the thermal state of the upper mantle beneath Iceland from gravity modelling*. Geophys. J. Int. (2002) 149, 281–299.

Larsen, G. (**2000**). *Holocene eruptions within the Katla volcanic system, south Iceland: characteristics and environmental impact*. Jökull 49.

Menke, W., V. Levin and R. Sethi (**1995)**. *Seismic attenuation in the crust at the mid-Atlantic plate boundary in south west Iceland.* Geophys. J. Int. 126, 175-182.

Sigmundsson, F., S. Hreinsdóttir, A. Hopper, T. Árnadóttir, R. Pedersen, M.J. Roberts, N. Óskarsson, A. Auriac, J. Decriem, P. Einarsson, H. Geirsson, M. Hensch, B.G. Ófeigsson, E. Sturkell, H. Sveinbjörnsson and K.L. Feigl (**2010**). *Intrusion triggering of the 2010 Eyjafjallajökull explosive eruption*. Nature, 468.

Sternberg, B.K., J.C. Washburne and L. Pellerin (**1988**). *Correction for static shift in magnetotellurics using transient electromagnetic soundinds*. Geophysics, 53.

Sturkell, E., P. Einarsson, F. Sigmundsson, A. Hooper, B.G. Ófeigsson, H. Geirsson, and H. Ólafsson (**2010**). *Katla and Eyjafjallajökull Volcanoes*. Developments in Quarternary Sciences, 13.

Wiese, H (**1962**). *Geomagnetische Tiefentellurik. II. Die Streichrichtung der Untergrundsstrukturen des elektrischen Widerstandes, erschlossen aus geomagnetischen Variationen*. Geofis. Pura Appl., 52.

Magnetotelluric Exploration of the Sipoholon Geothermal Field, Indonesia

Sintia Windhi Niasari[1], Gerard Muñoz[1], Kholid Muhammad[2], Edi Suhanto[2], Oliver Ritter[1]
[1]GFZ German Research Centre for Geosciences, Telegrafenberg, 14473 Potsdam, Germany
[2]Pusat Sumber Daya Geologi (PSDG), Badan Geologi, Jl. Soekarno-Hatta 444, 40122 Bandung, Indonesia

Abstract

The Sipoholon geothermal field is located in North Sumatra, Indonesia. The geothermal field is characterized by 15 hot springs situated in the Tarutung pull-apart basin and an additional 8 hot springs outside of the basin. The main difficulty in understanding the geothermal system is the temperature distributions of the hot springs, which appears to be random, based on the occurrence of 3 inactive volcanoes around the basin.

Here we report on preliminary results of two MT experiments that were carried out in Sipoholon, in December 2010 and July 2011. Data quality is generally good with the exception of sites from the populated basin area, which is noisier. Preliminary modeling results indicate a shallow high conductivity layer in the pull-apart basin area is generally caused by the sedimentary fill. Deeper conductive structure occurs east of the basin. Further data processing and modeling is necessary to decide if zones of high conductivity are related with a clay cap or hydrothermal fluids.

Introduction

Indonesia has an abundance of geothermal resources mostly associated with the volcanic arc, including Sumatra Island. On Sumatra, there are 84 known geothermal areas, but only 6 high temperature areas are under development (for electricity production). Many of the lower temperature areas have not been studied in detail and energy production from the latter is nil (Hochstein and Moore, 2008). The low-enthalpy Sipoholon geothermal field is located along the Sumatra Fault, in the Tarutung pull-apart basin, North Sumatra. Although there are several publications about this area, the geothermal system is still poorly understood. The Martimbang, Imun, and Helatoba Tarutung volcanoes are near the basin, but not inside it. It is still debated which, or whether, one of them could be a heat source for the hot springs. Other factors of the hydrothermal system are still enigmatic, for example whether faults play a role as fluid pathways, whether a sealing clay cap exists, and how water recharge into the hydrogeological system occurs.

Existing geophysical measurements carried out in this area include DC electrics, magnetic, and gravity methods. Since the spatial distribution of these measurements was insufficient, the results cannot answer how the Sipoholon hydrothermal system works. The initial MT measurements showed high resistivity beneath the graben and low resistivity east of the basin. However, only lines 4 and 5 were crossing the basin (see Figure 1), so to continue our previous research, we did additional MT field measurements covering a larger area than the first measurements. Lines A, B, C, and D cross the basin and cover the hot springs area. The

southernmost hot springs (Namora I langit) correspond to the Sarulla high enthalpy geothermal system.

The MT data of the first experiment often showed poor data quality above 4 s, to improve the situation for the second experiment, we recorded for a longer time (three days per site instead of one) and we installed a permanent remote reference site.We present data and preliminary 2D inversion result from both experiments, and briefly discuss the resistivity structure of the Sipoholon geothermal field.

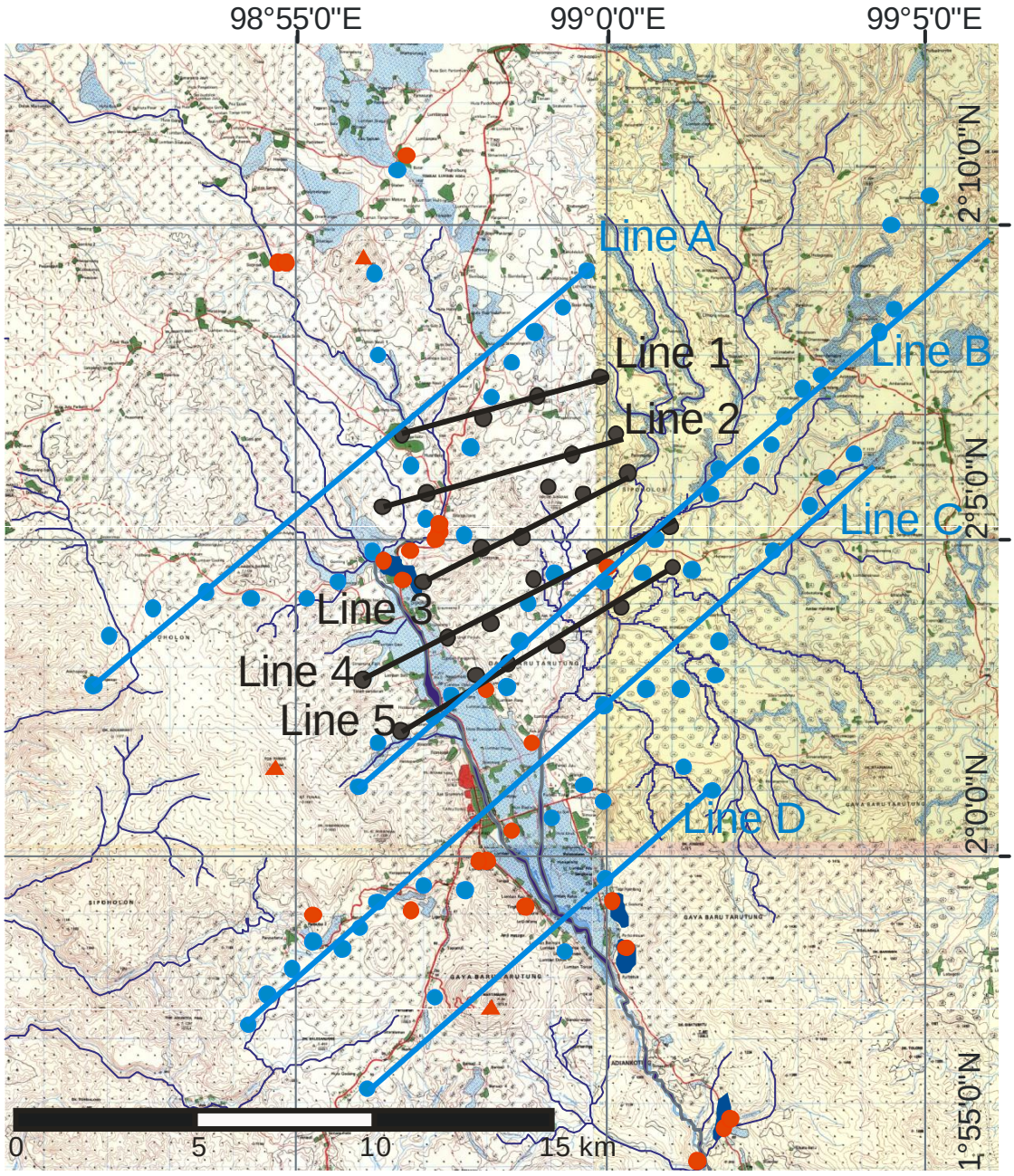

Figure 1. Location map of the study area. 26 MT sites were measured by PSDG in December 2010 (black dots). In July 2011, 71 MT sites were measured by GFZ (blue dots). Red dots mark hot springs. Red triangles are volcanoes.

Geological background

The dextral strike-slip Sumatra Fault accommodates oblique convergence between the Eurasian and Indo-Australia plates (Yeats et al, 1997 on Sieh and Natawidjaja, 2000). This 1900-km long fault consists of 19 segments (Sieh and Natawidjaja, 2000). There are thirteen pull-apart basins along the fault which occur near clusters of volcanoes, but volcanoes are rarely found inside the basins (Muraoka et al., 2010; Bellier and Sébrier, 1994). The Sipoholon pull-apart basin is dominated by major strike-slip faults along its longitudinal axis and bound by normal faults along its short-axes (Hickman, 2004). Figure 2 shows the Sipoholon and Sarulla pull-apart basins. Major fluid discharges are observed along the NW boundary normal fault in the Sipoholon pull-apart basin and the SE boundary normal fault in the Sarulla pull-apart basin. The NW boundary normal fault of the Sipoholon pull-apart basin at Ria-Ria-Sipoholon is situated on top of a travertine terrace. Muraoka et al. (2010) suggested that the NW boundary normal faults of the Sipoholon pull-apart basins play an important role as major discharge or fluid up flow zone.

Nukman and Moeck (2011) identified hot springs situated within and around the basin which are regionally controlled by NW-SE strike slip. The hot springs west of the Tarutung pull-apart basin are dominated by NE-SW trending fractures, while a NW-SE trend prevails north of the basin. The highest temperatures of 62°C (Ria-Ria Hot spring) were measured during the rainy season. However, there is no simple correlation between temperature distribution of hot springs and distance from volcanoes (Figure 3). Figure 3 also shows lineaments which were derived from SRTM (Shuttle Radar Topography Mission) high resolution digital topographic data of the Earth.

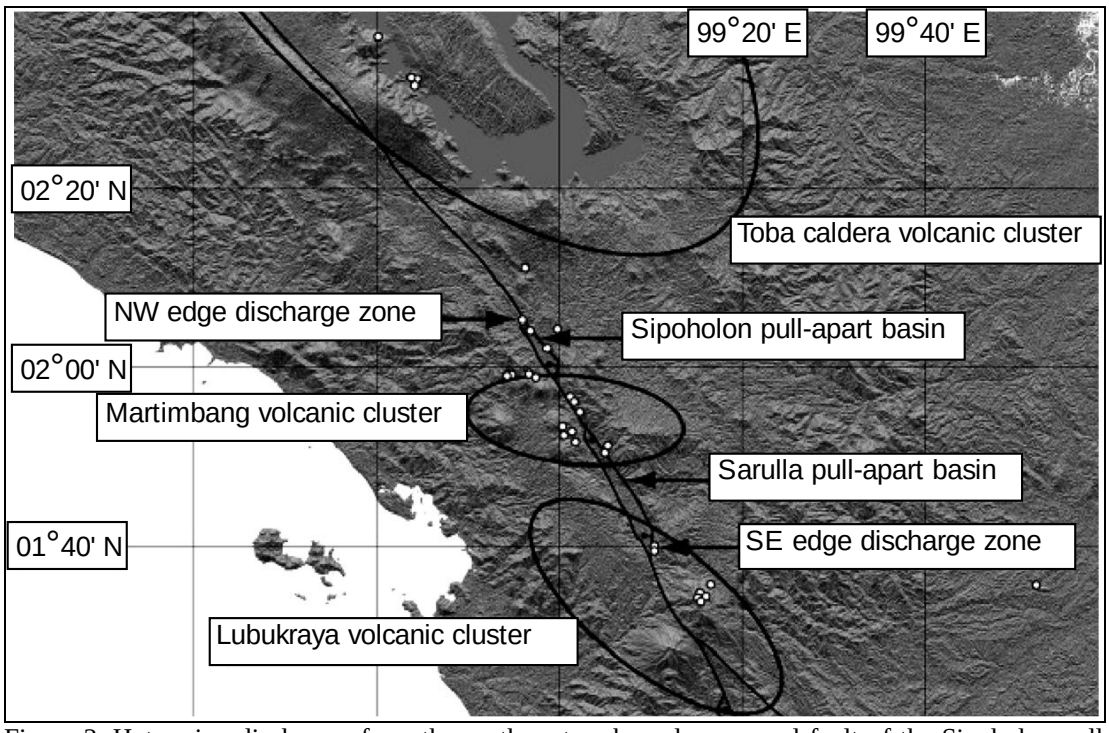

Figure 2. Hot spring discharges from the northwestern boundary normal fault of the Sipoholon pull-apart basin (Muraoka et al., 2010).

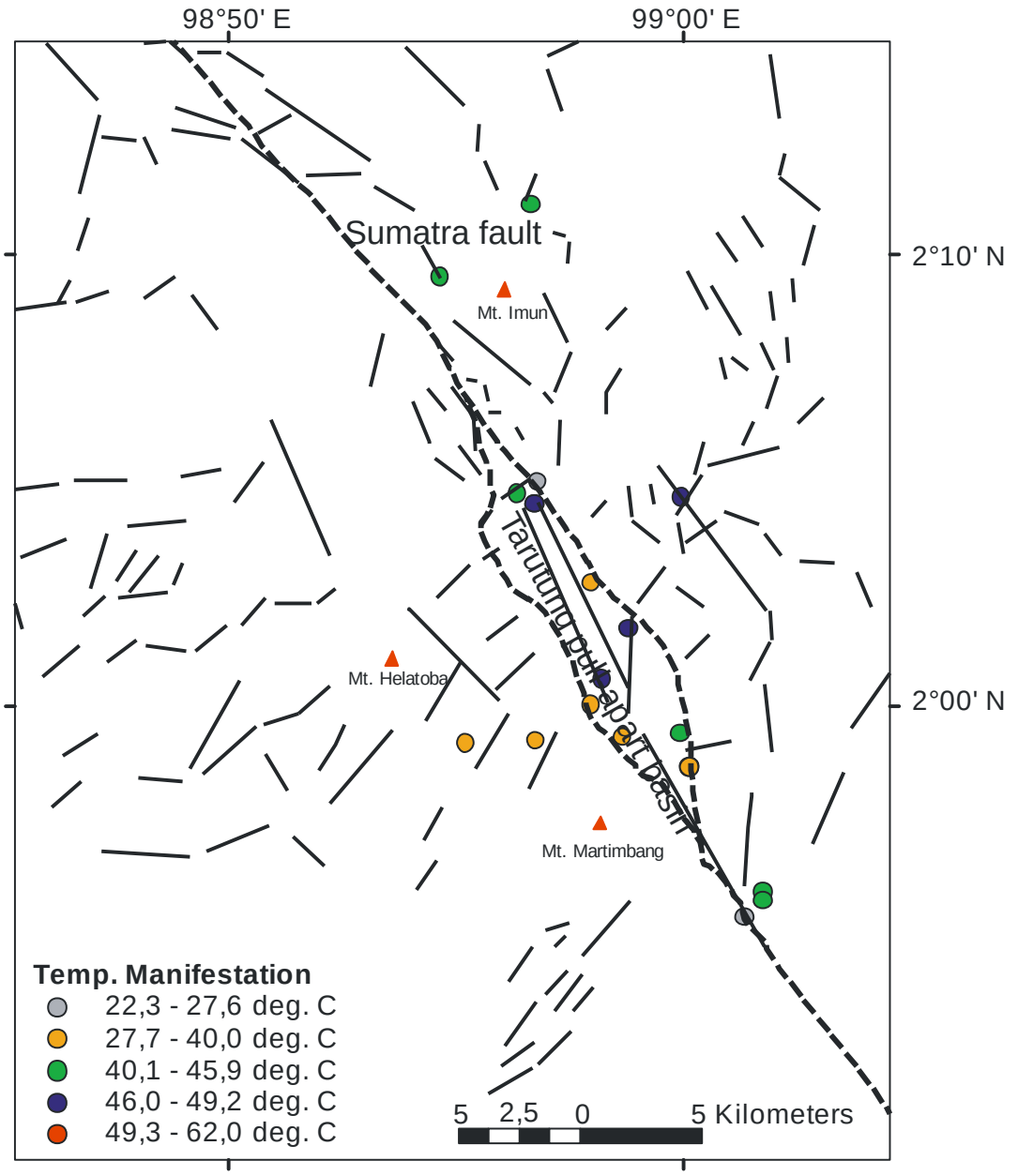

Figure 3: Tectonic lineaments derived from SRTM digital topography, drainage patterns, and field observations. Coloured dots mark locations of hot springs, temperatures after Nukman and Moeck (2011).

Magnetotelluric data processing and interpretation

The first measurements were carried out by Badan Geologi in the Sipoholon area in December 2010 using MTU 5A Phoenix instruments. Time series of Hx, Hy, Ex, and Ey were measured at 26 MT sites in the frequency range 320-0.0034 Hz for approx. 1 day. The data were processed using MT Editor from Phoenix. Some data points with larger error bars (very noisy data above 4 s) were removed by manual inspection.

For the second measurements time series of Hx, Hy, Hz, Ex, and Ey were recorded in the frequency range 1000-0,0001 Hz for approx. 3 days. For the duration of the experiment we

operated a Remote Reference site to improve the data quality. The remote reference technique can help to remove noise at sites which are close to houses, power lines or other electromagnetic noise sources. To remove noise in the short period range, particularly 50 Hz and harmonics, we applied a delay line filter.

After performing geo-electric strike analysis (Becken and Burkhardt, 2004), the data from first measurements were rotated to N47°E so that the xy polarization corresponds to the TE mode. Secondary electromagnetic fields which are elliptically polarized are generated in the presence of a regional 2-D conductivity anomaly. The regional strike direction can be then be identified from vanishing ellipticities of electric and magnetic fields, because the ellipticity remains unchanged even if the electric field at the surface is distorted by inhomogeneities. If the minimal ellipticities are close to zero, then the telluric vectors can be rotated to the coordinate system of the regional strike. We found an angle of -43° in which the ellipticity vectors are generally minimal for all periode (0,001-10 s) and for all sites (Figure 4). The 90° ambiguity can be solved as the direction seems to coincide with the direction of the Sumatra Fault which is N40±2°W in this area (Genrich et al. 2000). Some sites show deviations from the regional strike directions by more than 30°; likely these sites are affected by local shallow structures.

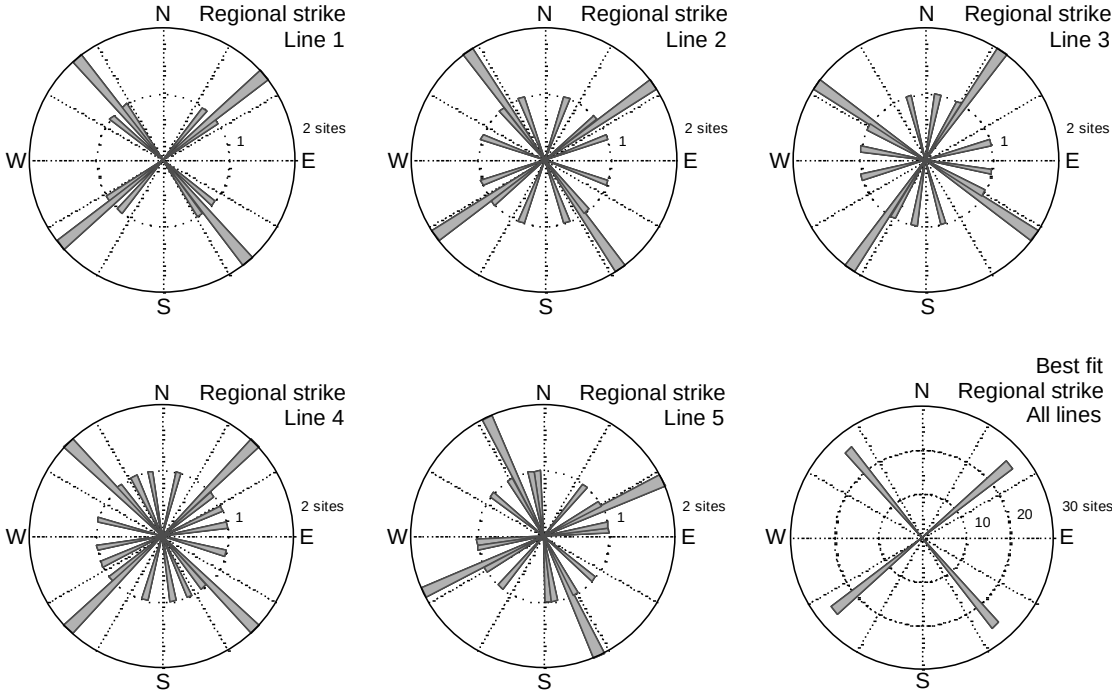

Figure 4. Rose diagrams showing the strike angle distribution of line 1, 2, 3, 4, and line 5, and the best fit regional strike angle for all lines. These were calculated for period 0,001 – 10 s.

Resistivity models were obtained along five lines (Figure 5) from 2D inversion of the rotated data, using the code of Rodi and Mackie (2001) which is included in the Winglink software package. The inversions were performed setting an error floor of 100% for TE apparent resistivity (i.e. down-weighting this component), 10% for TM apparent resistivity and 1.5°

for the phases of both modes. After an L-curve analysis, the optimal value of the smoothing parameter (τ) was found to be 10.

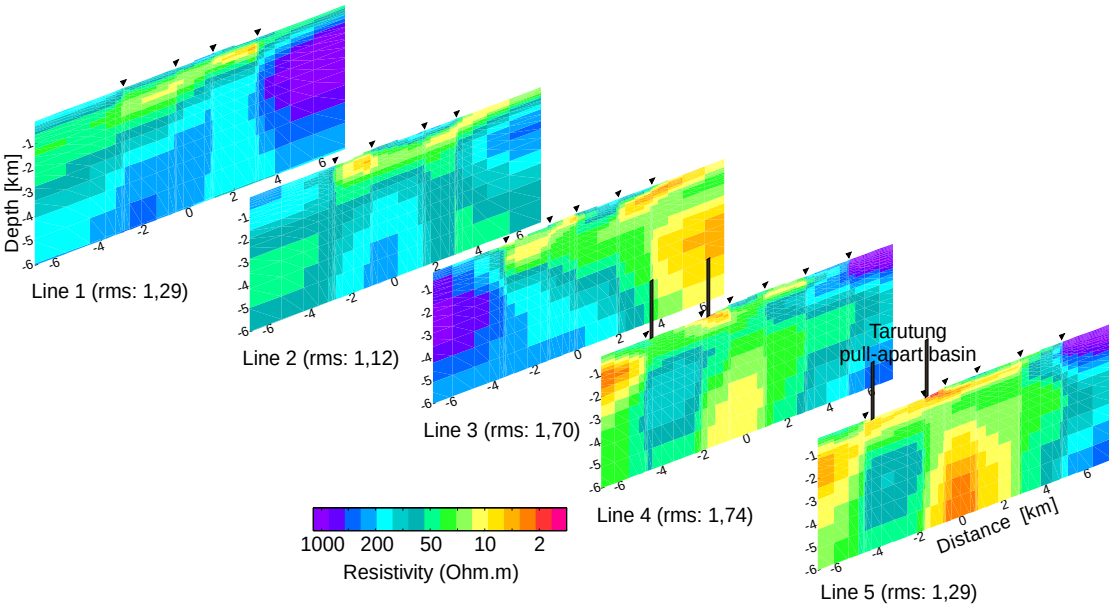

Figure 5. Resistivity models obtained from 2D inversion of the MT data of the first experiment along five lines. The black line indicates the location of the Tarutung pull-apart basin.

The results (Figure 5) indicate a shallow high conductivity layer extending down to approx. 1 km in all lines. In lines 4 and 5 the shallow conductors could correspond to unconsolidated sedimentary fill of the Tarutung pull-apart basin. This basin formed by discontinuities in the Sumatra strike slip fault and was filled with thick pyroclastic flow deposit of Toba volcano. Lines 1, 2 and 3 do not cross the graben area and hence, the 2D inversion models of those lines appear quite different to the other lines. The southernmost lines 3, 4 and 5 indicate the presence of a deeper conductive anomaly located slightly off to the east of the graben starting at 3 km depth.

Figure 6 shows 2D inversion model result from lines A, B, C, and D which include all data from the first and second measurements. Recalculation of the geo-electric strike analysis (Becken and Burkhardt, 2004) based on the entire data set, resulted in a more complicated situation for the regional strike. Data rotation depends on the distance of a site from the basin area: sites east of the basin were rotated to N327°E, sites within the basin were rotated to N343°E, and to N324°E for sites west of the basin. After rotation the xy- polarization corresponds to the TE mode. The inversion models were obtained using the code of Rodi and Mackie (2001) which is included in the Winglink software package and setting error floors to 100% for TE apparent resistivity (i.e. down-weighting this component), 10% for TM apparent resistivity and 1.5° for the phases of both modes. After an L-curve analysis, the optimal value of the smoothing parameter (τ) was found to be 3.

The 2D inversion results are still preliminary. High resistive bodies to the west of the basin area could correspond with Permian granites. Shallow high conductive zones found in the basin area could be caused by (unconsolidated) sedimentary fill. Lines B and D show these

shallow conductive zones quite clearly while their expression is weaker in lines A and C. More conductivity anomalies appear east of the Tarutung pull-apart basin. However, 3-D modeling is needed to find out if and how these conductors are connected.

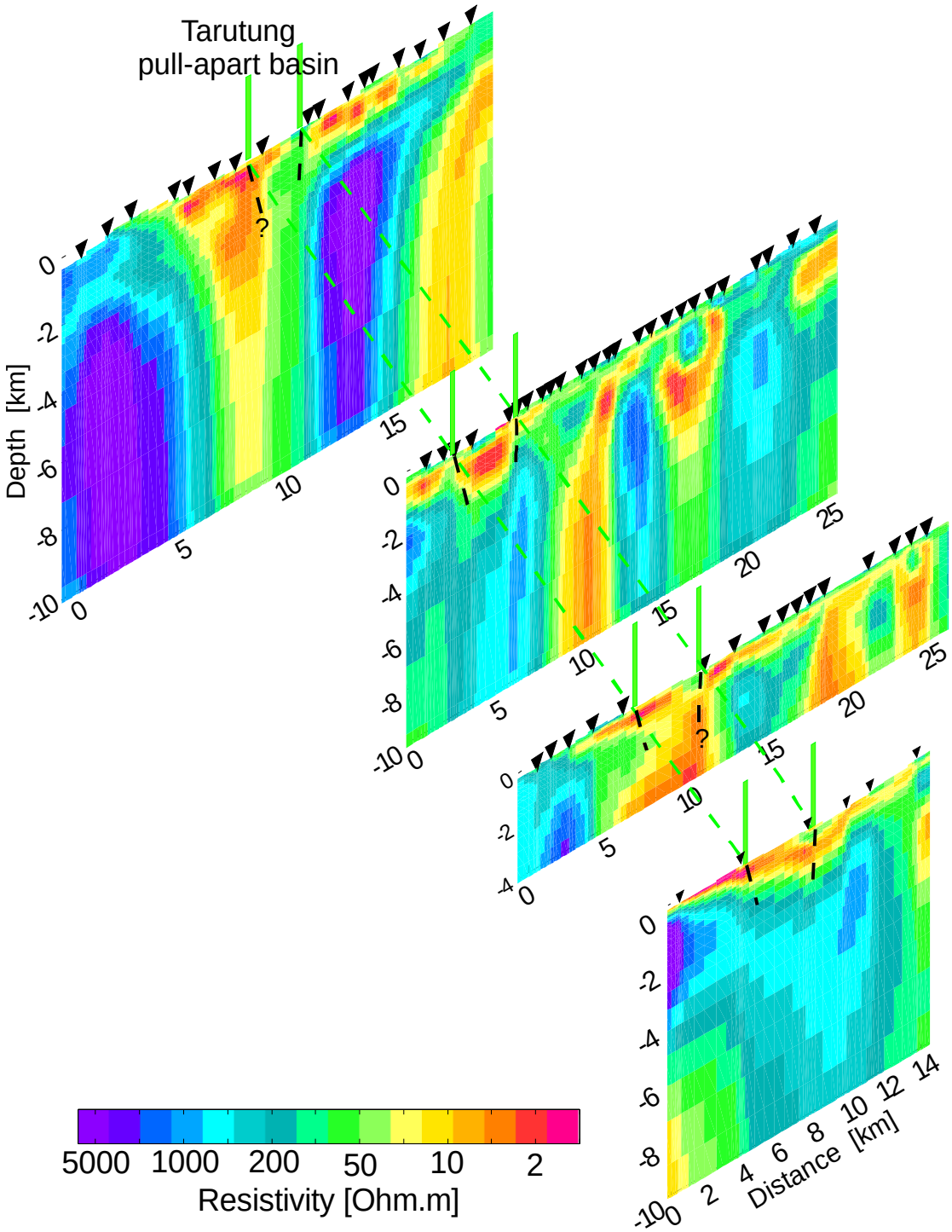

Figure 6. Resistivity models obtained after 2D inversion of the all MT data (four lines). The green bars indicate the location of the Tarutung pull-apart basin.

Acknowledgment

This work would not have been possible without field support and the cooperation of numerous colleagues from Germany (GFZ) and Indonesia (Badan Geologi, ITB, Unila). The project is funded by the German Federal Ministry of Education and Research (BMBF, 03G0753A)., the Helmholtz Centre Potsdam GFZ German Research Centre for Geosciences and Badan Geologi. MT Instruments for the field campaign in 2011 were provided by the Geophysical Instrument Pool Potsdam.

References

Becken, M. and Burkhardt, H. (2004) - An elipticity criterion in magnetotelluric tensor analysis, Geophys. J. Int., 159, 69-82.

Bellier, O. and Sébrier, M., 1994. Relationship between tectonism and volcanism along Great Sumatran fault Zone deduced by SPOT image analyses. Tectonophysics, 233:215-231

Genrich, J.F., Bock, Y., McCaffrey, R., Prawirodirdjo, R., Stevens, C.W., Puntodewo, S.S.O., Subarya, C., and Wdowinski, S. (2000) - Distribution of slip at the northern Sumatra fault system, Journal of Geophysical Research, 105, 28327-28341.

Hickman R. G., Dobson P. F., van Gerven M., Sagala B. D., and Gunderson R. P., 2004, Tectonic and stratigraphic evolution of the Sarulla graben geothermal area, North Sumatra, Indonesia, Journal of Asian earth Science 23, 435-448

Hochstein, M. P. and Moore, J. N., 2008. Preface: Indonesia: Geothermal prospects and developments. Geothermics, 37:217-219

Muraoka H., Takahashi M., Sundhoro H., Dwipa S., Soeda Y., Momita M. and Shimada K., 2010. Geothermal Systems Constrained by the Sumatran Fault and Its Pull-Apart Basins in Sumatra, Western Indonesia. Proceedings World Geothermal Congress

Nukman, M. and Moeck, I., 2011. Structural control over hot springs in Sipoholon geothermal prospect, North Sumatra, Indonesia: a preliminary data update. 2nd European Geothermal PhD Day, Iceland.

Rodi, W. and Mackie, R.L. (2001) - Nonlinear conjugate gradients algorithm for 2-D magnetotelluric inversion, Geophysics, v. 66, no. 1, 174-187.

Sieh K. and Natawidjaja D., 2000. Neotectonics of the Sumatran Fault, Indonesia. J. Geophys. Res. 105:28295-326

Yeats, R., K. Sieh, and C. Allen, The Geology of Earthquakes, 568 pp., Oxford Univ. Press, new York, 1997.

Magnetotelluric measurements across the Scandinavian Caledonides in Lapland – Finland/Norway

C. Nittinger[1], M. Becken[1], A. Rödder[2], A. Junge[2], M. Smirnov[3]

[1]University of Münster, [2]Johann Wolfgang Goethe University Frankfurt, [3]University of Oulu, Finland
E-mail: cnittinger@uni-muenster.de

Introduction

We collected magnetotelluric broad-band data along a 110 km long profile across the Caledonian Mountains in the Finland-Norway border region. The conducted survey is embedded in larger-scale magnetotelluric array measurements to study the three-dimensional structure and properties of the Fennoscandian lithosphere with electromagnetic measurements.

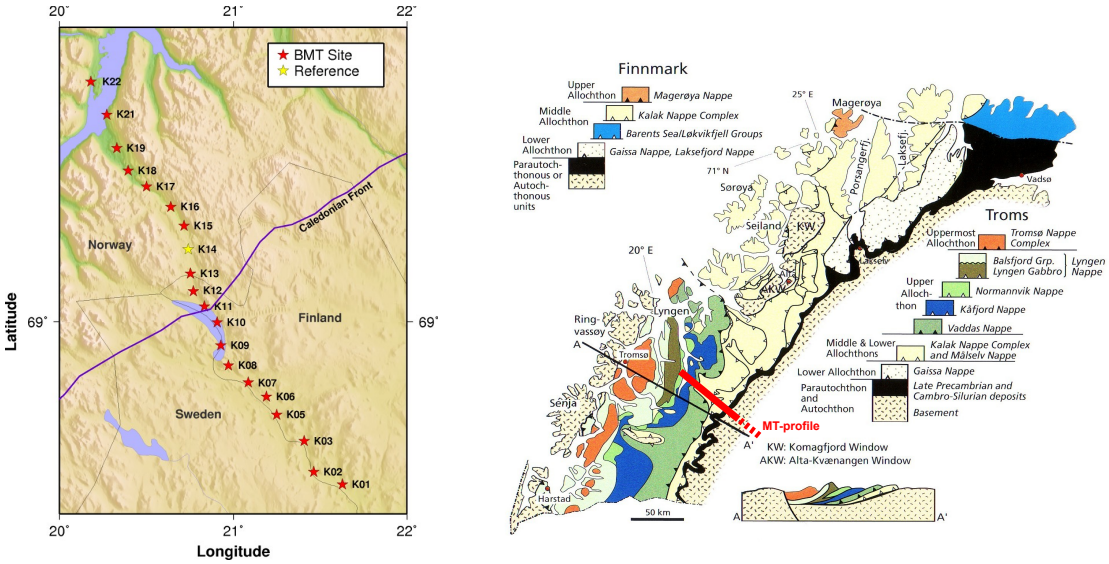

Figure 1: Site locations across the Caledonian Front in Lapland with GMTED2010 Topography (left panel) and geological map with crosssection (right panel, Ramberg et al. 2008).

The Scandinavian mountains are far from active plate boundaries and the origin of their present high altitude is unknown. Rocks that deformed during the Caledonian orogeny (400 Ma), the oldest orogeny in Europe, are exposed in the Scandes. During the Caledonian orogeny the continents Baltica and Laurentia collided and Neoproterozoic to Silurian rocks and fragments of older basement were thrusted over Baltica and the Fennoscandian shield. The thrusted sheets formed nappe piles covering late Precambrian and Cambro-Silurian deposits and the Precambrian basement. The boundary between the nappe piles and the basement is denoted as the Caledonian Front. Over much of its extent in Scandinavia, the Caledonian Front is characterized by occurrences of black-shales. These rocks have been imaged with MT in Central Sweden (Jämtland region, Korja *et al.* 2008) as a pronounced crustal conductive zone extending west of the Caledonian Front.

The purposes of this study are to characterize the electrical properties of the crust and upper mantle surrounding the Caledonian Front and to complement the regional array measurements with structures at a higher lateral resolution. Electrical resistivity is sensitive to the presence of interconnected metallic conductors and fluids and to the temperature. Fluids and temperature strongly influence the mechanical properties of rocks. Therefore, our results can also provide constraints on uplift models of the northern Scandes.

Magnetotelluric profile data across the Caledonian Front

Field work was conducted in June 2011. We measured at 20 sites along a 110km profile in NNW direction (Figure 1). The profile extends from the exposed Precambrian basement in Finland in the south to the Lyngen Fjord in the north in Norway. The profile crosses the Caledonian Front in its central part between sites K10 and K11, close to the Finnish-Norwegian border between K12 and K13 (Figure 1). The profile follows the only road in the area, which made it not always possible to place sites far away from power lines and passing traffic.

Five channel broadband MT data in the period range from 0.01 to 1000s were collected with runtimes between one to three days. One reference site K14 acquired data throughout the whole measurements for quality control and subsequent remote-reference processing.

Several noise sources along the profile distorted the collected data. Local noise was produced by passing traffic and is reflected as spikes in the H-field. A second major noise source is a pumping storage power station in the northern part of the profile. Coherent noise was produced by power-lines running parallel to the profile and by trains near Kiruna. Although the railroad is about 150 km away, the extremely high resistivities in the crust are responsible for the fact that these train signals generate large signals in our measurement area. Because of technical problems at some locations, we had to replace the local magnetic fields at these sites with remote magnetic recordings from other sites operative at the same time.

Data was processed using the robust remote reference processing code of Egbert and Booker (1986). The reference site K14 helped to eliminate local noise. Overall, the data exhibit a good quality.

To study the properties of the data more quantitatively, we applied the strike and dimensionality analysis of Becken and Burkhardt (2004), and the phase tensor method by Caldwell *et al.* (2004). Phase tensors at sites south of K10 exhibit a 1-D behavior with low phase tensor ellipticities at all periods. Sites north of the Caledonian front indicate 3-D effects, first appearing at short periods and extending to larger periods further to the north**.** At northern sites only very long periods (100-1000s) exhibit one-dimensionality.

Despite these complications, we carried out a regional strike analysis, which takes into account the effect of galvanic distortion (Becken and Burkhardt, 2004). Single-site multi-period strike estimates are depcited in the rose diagrams in Figure 2. Here, we show the results for the sites in the North and in the South separately. Southern sites (left panel) exhibit a consistent strike direction, whereas northern strike directions vary over a broad range, which reflects the three-dimensional nature of the data in this part. The global strike estimate, using all impedance data simultaneously, is +16º (clockwise from north).

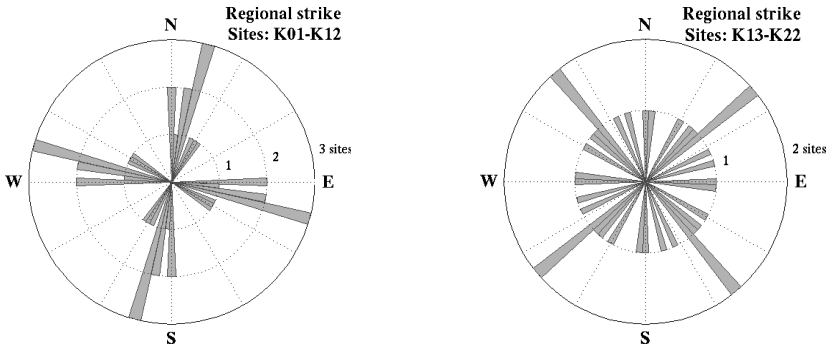

Figure 2: Results of single site multi period strike estimation of northern sites K01-K12 (left) and northern sites K13-K22 (right).

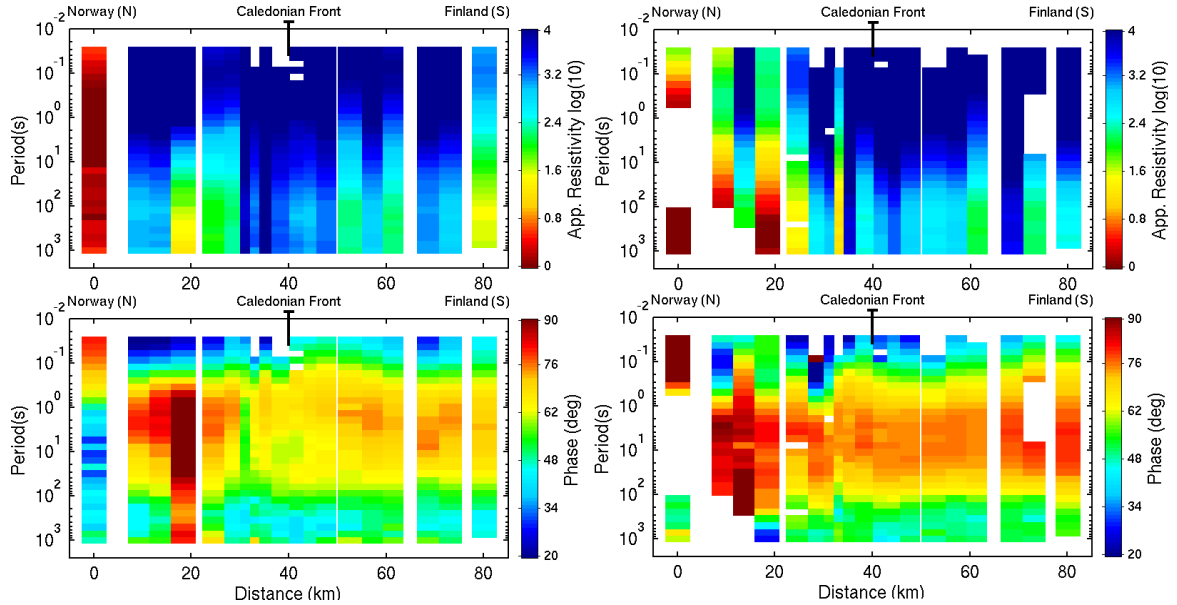

Figure 3: Pseudo-sections showing Zxy (left) and Zyx (right) apparent resisitivity (top) and Phase (bottom). Gaps are produced by masked bad datasections caused by coil failures .

Figure 3 depicts pseudo-sections of the measured off-diagonal impedances Zxy and Zyx in a coordinate system that has been rotated to -74°, according to the global strike estimate of +16°. Representative rotated transfer functions of sites K09 and K17 are shown in Figure 4. In general, the data exhibit distinct features to the north and to the south of the Caledonian Front.

The southern sites (K01-K12) in Finland have overall uniform characteristics. At short periods, the apparent resistivities are in a range of 10^4-10^5 ohm-m, and decrease to less than ~10^3 ohm-m at longer periods (100s and 1000s). Static shift maybe responsible for apparent resistivity variations in this part of the profile, resulting in resistivities up to 10^6 ohm-m at some sites. Irrespective of the rotation angle these sites also exhibit very large main-diagonal elements of the impedance tensor, with resistivities similar to those of the off-diagonal elements.

Phases of the southern sites increase from 30° to up to 80° at 1-10s and decrease with longer periods. A uniform, rotationally invariant minor phase split of 5-10° is observed between 1s and 100s. The phase quadrants of main-diagonal elements change inconsistently between sites. Tipper data of southern sites look consistent for all sites with slightly varying amplitudes and small amplitudes between 1-100s.

Sites in the northern part of the profile (K13-K22) show a more complex behavior with apparent resistivities at short periods slightly smaller than at the southern sites. At long periods apparent resistivities decrease to ~10^2 ohm-m. Compared to southern sites, much more variations can be observed between the different impedance tensor elements. Especially at sites K17,K18 and K19 phases leave the quadrant and go beyond 90° indicating more complex (3-D) resistivity structures or source effects. Tipper data of the sites in the North show strong variations and directional twists for short periods (0.03-10s). The two sites far in the north directly near the Lyngen Fjord (K21,K22) show different resistivities and phases which could be caused by technical issues or strong distortion.

In summary, the collected data set shows variations in dimensionality and complexity in the transfer functions across the Caledonian Front providing two distinct regions with several prominent features and different causes which need to be further investigated.

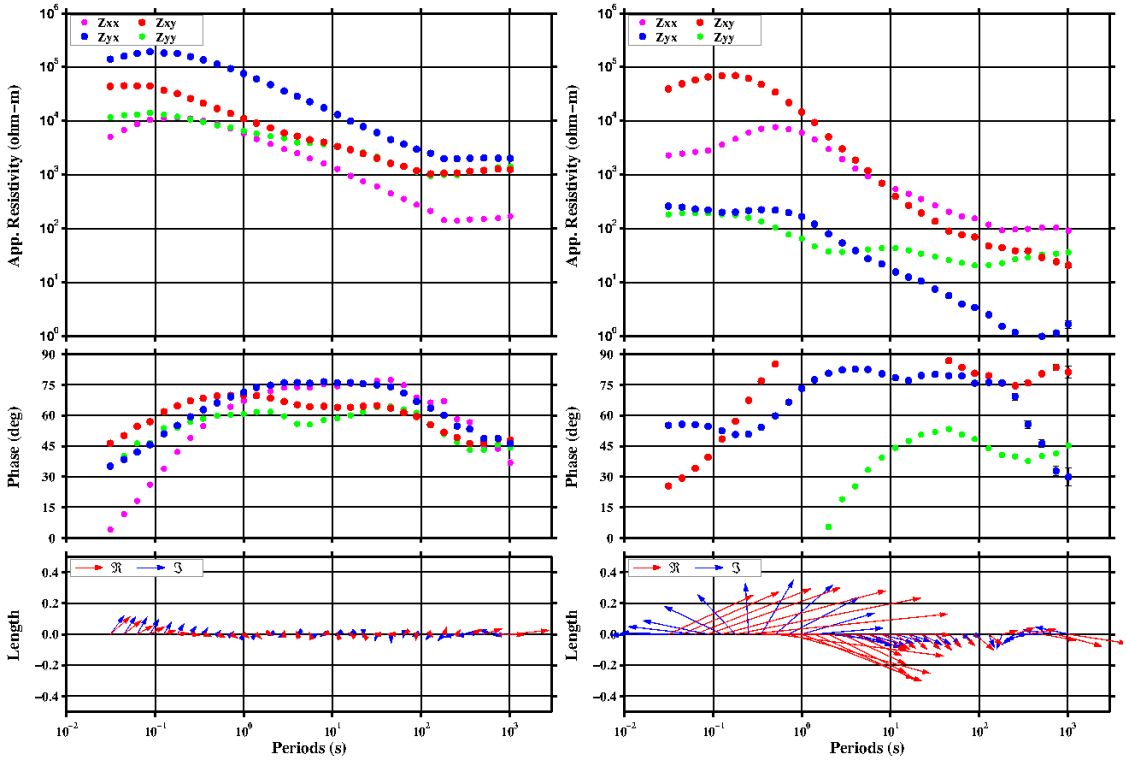

Figure 4: Rotated transfer functios of site K09 (left) on the Precambrian basement and K17 (right) north of the Caledonian Front with apparent resistivity (top) Phase (mid) and Tipper (bottom).

1-D isotropic modelling

Due to the spatial uniformity of the data on the Baltic shield, and the absence of large curve steps, as well as the results of phase tensor analysis, we initially attempted 1-D isotropic inversions of these sites. However, the presence of large off-diagonal elements is not consistent with this approach, and is addressed below in matters of 1-D anisotropic models.

Occam-type (1-D) resistivity inversion models of southern sites K01 and K06 on the Precambrian basement were calculated and are shown in Figure 5. The estimated resistivity models yield a resistivity-depth profile with slightly increasing resistivity in the upper crust (0 to 20km) and decreasing at lower crustal and upper mantle depths (~10^2-10^3 ohm-m in the mantle). Overall the models indicate a strong transition zone at 40-70km, consistent with Moho depths determined from teleseismic data. The lithopshere-astenosphere boundary is not obvious in the resistivity models.

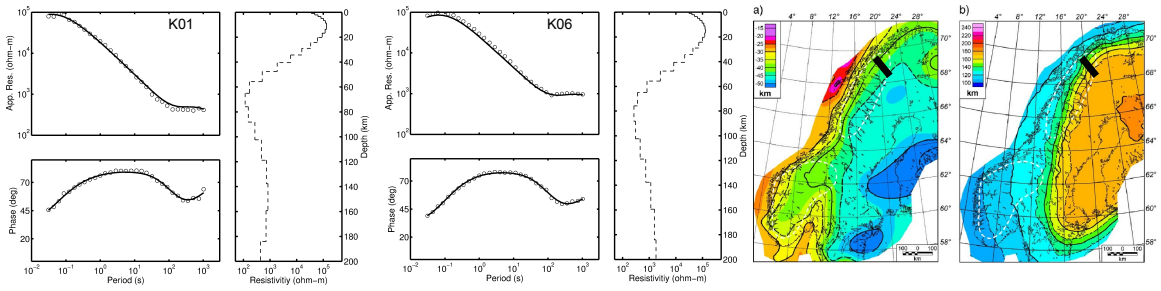

Figure 5: 1D Occam-type Inversion models of southern sites K01 (left) and K06 (middle) in comparison to (a) Moho-depth and (b) LAB as compiled by seismic/tomographics studies (Ebbing and Olesen 2005, Calgagnile 1982)

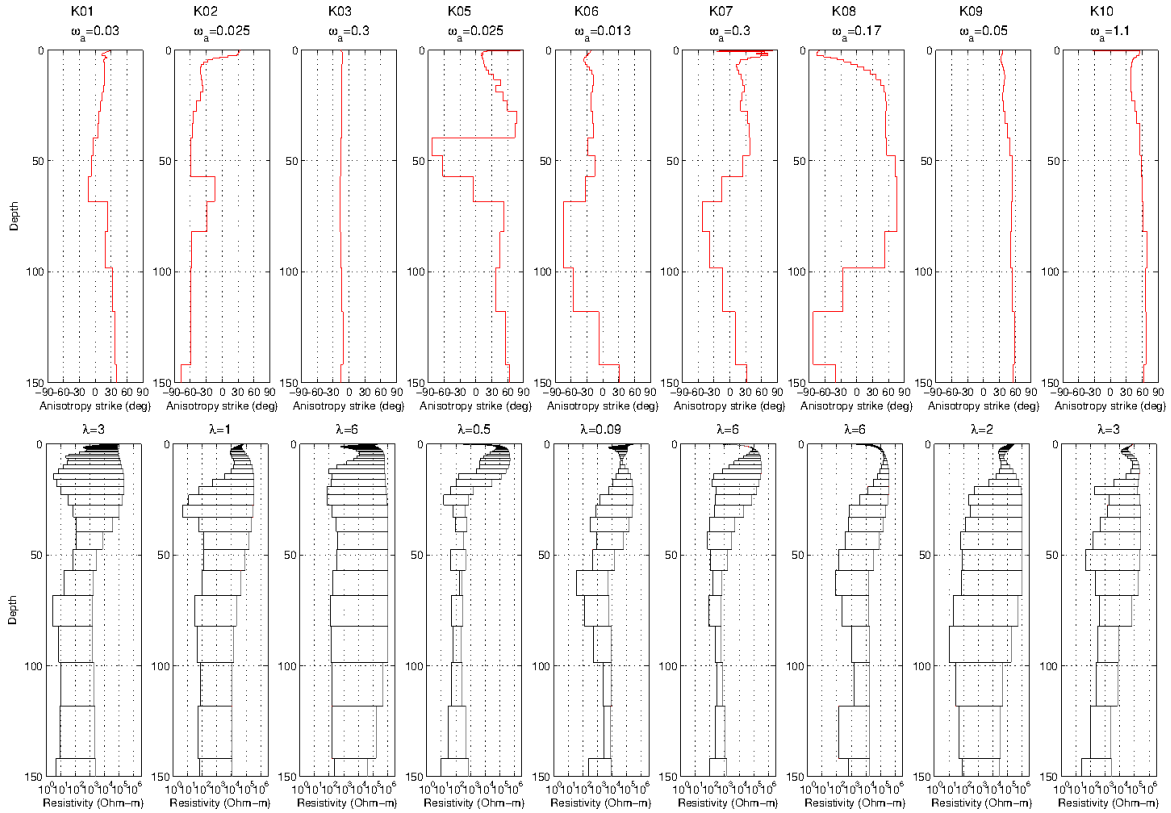

Figure 6: 1-D Anisotropy Inversion models for sites K01-K10 on the precambrian basement. Strike direction of anisotropy is shown at the top and maximum/minimum resistivites at the bottom. Anisotropy regularization is $\omega \in [0.01,1]$ and roughness penalty $\lambda \in [0.5,6]$ for the different sites.

1-D Anisotropy analysis

As described before sites on the Precambrian basement in Finland show large main-diagonal elements irrespective of the rotation angle. This behavior cannot be fully explained by galvanic distortion of a regional 1-D field over an isotropic earth. A 1-D behavior of sites south of the Caledonian Front can be reproduced by the phase tensor analysis which can not identify anisotropy.

A possible explanation for this characteristic is the presence of anisotropy. The impedance tensor over a 1-D anisotropic layered earth is full and given by

$$Z_{1\mathrm{D}\,anis} = \begin{bmatrix} Z_{xx} & Z_{xy} \\ Z_{yx} & -Z_{xx} \end{bmatrix} .$$

In general, it is not possible to find a suitable rotation angle to minimize the main-diagonal elements, as is the case for our data.

To test for 1-D anisotropic structures, we determined 1-D anisotropic inversion models using the code by Pek and Santos (2006). This program inverts for the azimuthal (horizontal) anisotropy in each layer of a 1-D layered medium. The horizontal conductivity tensor is parameterized by an effective strike angle of the anisotropy around the z coordinate axis and the two principal elements of the simplified conductivity tensor. The latter are depicted in terms of the maximum and minimum resistivities.

The 1-D models and corresponding regularization parameters for the inversion are shown in Figure 6. Similar to the 1-D isotropic models the maximum resistivities of the anisotropic models roughly show similar structures with resistivities up to 10^5 ohm-m in 20km depth, a transition zone at 40-70km depth and ~10^3 ohm-m at greater depths. Moreover minimum resistivities may indicate

anisotropic regions with anisotropy in an amount of four decades in depths of ~20km at K01-K03 or in greater depths at K09. Sites K05-K07 mostly show anisotropic regions in a range of 1-2 decades with a higher anisotropy amount in depths between 20km and 50km.

All models exhibit anisotropy at depths greater than 5-10km with very large variations in the amount of anisotropy as well as anisotropic strike directions.

For a uniform 1-D anisotropic subsurface, we would expect uniform degrees of anisotropy as well as of the anisotropy strike. This is, however, not the case for the estimated models. We found that these inconsistencies are related to different signs of the imaginary part of the main-diagonal impedances, i.e. the corresponding phases swap quadrants from site to site. One possible explanation for this behaviour can be the presence of near surface galvanic distortion.

To demonstrate this, we utilize the distortion model of Groom and Bailey (1989), who parametrize the distortion matrix in terms of the real-valued parameters *e* (*shear*), *t* (*twist*) and *a* (*distortion anisotropy*). Then, the distorted version of an 1-D anisotropic impedance tensor is given by

$$Z^{obs} = T \cdot S \cdot A \cdot Z_{1D\,anisotropic} = \begin{bmatrix} 1 & -t \\ t & 1 \end{bmatrix} \begin{bmatrix} 1 & e \\ e & 1 \end{bmatrix} \begin{bmatrix} 1+a & 0 \\ 0 & 1-a \end{bmatrix} \begin{bmatrix} Z^r_{xx} & Z^r_{xy} \\ Z^r_{yx} & -Z^r_{xx} \end{bmatrix}$$

Let us for simplicity assume for the moment that $t=a=0$, i.e. only shear is considered. Then,

$$Z^{obs} = \begin{bmatrix} 1 & e \\ e & 1 \end{bmatrix} \begin{bmatrix} Z^r_{xx} & Z^r_{xy} \\ Z^r_{yx} & -Z^r_{xx} \end{bmatrix} ,$$

and the distorted main-diagonal impedances are

$$\begin{aligned} Z^{obs}_{xx} &= e \cdot Z^r_{yx} + Z^r_{xx} \\ Z^{obs}_{yy} &= e \cdot Z^r_{xy} - Z^r_{xx} \end{aligned} .$$

It is obvious that the phase of the observed main-diagonal elements depend on the ratio of the regional off- and main-diagonal elements as well as on the shear distortion. Small variations of shear can lead to phases in a different quadrant. Similar effects can be observed for a full distortion model. Because the sign of the main-diagonal elements strongly influences the anisotropic strike to be determined by 1-D anisotropic inversion, galvanic distortion must be corrected for prior to the inversion of the full tensor. Recently, Jones (2012) proposed a decomposition procedure for a galvanic distorted 1-D anisotropic impedance tensor. We will follow his approach in order to test, if distortion removal can improve the consistency of 1-D anisotropic inversion models.

Preliminary Results and Outlook

Across the Caledonian Front variations of electrical resistivity between the Precambrian basement in the south and the nappe piles of the Caledonian orogen in the north are observed. Transfer functions of sites in the Scandinavian mountains show a 3-D behavior, including phases out of the quadrant at some locations, and indicate complex resistivity structures. In turn, the data from the Precambrian basement in Finland are more uniform. Isotropic 1-D models of these sites reveal a transition zone from resistivities of 10^5 ohm-m in the upper crust to 10^3 ohm-m in the uppermost mantle. However, the presence of large main-diagonal elements, which can not be accounted for with galvanic distortion models, indicate the presence of anisotropy in this region. Our inversion tests showed, that 1-D anisotropic models can explain the data. However, the models are inconsistent from site to site. Further tensor decomposition and distortion analysis may provide better understanding of the data, as galvanic distortion may result in wrong estimations of the anisotropy strike direction. First 2-D Inversion models were also calculated, but failed to fit the data sufficiently, especially at the northern sites near the Lyngen Fjord. The role of possible source field effects in high latitudes is also subject of further investigations.

References

Calcagnile, G., (1982) The lithosphere-asthenosphere system in Fennoscandia. Tectonophysics 90, Pages 19–35.

Caldwell, T.G., Bibby, H.M., Brown, C., (2004). The magnetotelluric phase tensor. Geophys. J. Int. 158, Pages 457–469,

Ebbing, J., Olesen, O.,(2005) The Northern and Southern Scandes – structural differences revealed by an analysis of gravity anomalies, the geoid and regional isostasy, Tectonophysics 411, Issues 1-4, Pages 73-87

Egbert, G. and Booker, J.R., (1986). Robust estimation of geomagnetic transfer functions,. Geophysical J. R. Astron. Soc. 87, Pages 173-194.

Groom, R. W., Bailey, R. C., (1989). Decomposition of Magnetotelluric Impedance Tensors in the Presence of Local Three-Dimensional Galvanic Distortion. Journal of Geophysical Research, Vol. 94, No. B2, Pages 1913-1925

Korja, T., Smirnov, M., Pedersen, L.B. and Gharibi, M., (2008) Structure of the Central Scandinavian Caledonides and the underlying Precambrian basement, new constraints from Magnetotellurics, Geophysical Journal International 175, Pages 55–69.

Jones, A. G. (2012) Distortion decomposition of the magnetotelluric impedance tensors from a one-dimensional anisotropic Earth, Geophys. J. Int. (in press)

Pek, J., Santos, F. A. M., (2006) Magnetotelluric inversion for anisotropic conductivities in layered media,Physics of the Earth and Planetary Interiors 158, Pages 139–158.

Ramberg, I. B., Bryhni, I., Nottvedt, A., K. Rangnes, (2008) The Making of a Land: The Geology of Norway, Geographical Society of Norway, Trondheim.

Acknowledgements

We wish to thank Heinrich Brasse from FU Berlin and the Geophysical Instruments Pool Potsdam (GIPP) for providing instruments as well as Josef Pek for providing the 1-D Anisotropy inversion code. Funding is provided in the framework of the TopoScandiaDeep project and from the Geophysics Institute, University of Münster.

Non-Linear Conjugate Gradient Magnetotelluric Inversion for 2-D Anisotropic Conductivities

Josef Pek[(1)], Fernando A. M. Santos[(2)] and Yuguo Li[(3)]

[(1)]Institute of Geophysics, Acad. Sci. Czech Rep., Prague, Czech Rep. (e-mail: jpk@ig.cas.cz)
[(2)]Center of Geophysics, Univ. Lisbon, Lisbon, Portugal
[(3)]College of Marine Geosciences, Ocean Univ. China, Qingdao, China

Abstract

We report on the state of the art in the development of a non-linear conjugate gradient (NLCG) version of the 2-D inverse algorithm for magnetotelluric (MT) data over structures with arbitrary electrical anisotropy. The algorithm is based on the Occam inverse strategy. As a direct solver, our 2-D finite volume forward modeling program for structures with arbitrary anisotropy is employed, which is also further used to effectively evaluate parametric sensitivities by employing the reciprocity principle. A standard Polak-Ribiere NLCG algorithm is then applied to minimize the inversion objective function which consists of a data misfit term and of regularization penalties applied to both the structure complexity and anisotropy throughout the model. The algorithm offers considerable savings to the computing time and memory demands due to both the reciprocity-based evaluation of the parametric sensitivities and on-line computation of products of the Jacobian and its transverse with a vector within the CG algorithm. Synthetic test inversions with a single anisotropic box anomaly are presented and used to discuss expected ambiguity issues in anisotropic structures. The 2-D anisotropic inversion is further applied to a small subset of experimental MT data from the contact area of the Southern Portuguese Zone and the Ossa Morena Zone in southern Portugal, and the results are compared with those obtained earlier by a 1-D inverse and 2-D direct trial-and-error modeling approach to the same data.

1 Introduction

Over the last decades, anisotropy of the electrical conductivity in the earth has become a valuable indicator of tectonic structures and processes, both fossil and recent. Large-scale electrical macro-anisotropy manifests a specific spatial arrangement of conducting fractions in the subsurface, a specific organization of conductors which are not distinguished as separate bodies by the diffusing electromagnetic field but rather sensed as an anisotropic bulk. Interpretations of electromagnetic induction data from a vicinity of the German Continental Deep Borehole (KTB) proved that suites of graphitized fossil shear zones or faults filled with saline fluids appear as highly electrically anisotropic domains throughout the whole upper crust of the area (e.g., Eisel and Haak, 1999; Eisel *et al.*, 2001). Crustal anisotropic structures were later modeled, and put into regional tectonic plots, in several regional MT studies, e.g., by Lezaeta and Haak (2003), Heise and Pous (2003) or by Weckmann *et al.* (2003), with special regard to the phenomenon of MT phases exceeding 90°. Brasse *et al.* (2008) could explain systematic deflections of long-period induction arrows over the South Chilean continental margin by regional 2-D anisotropy due to a deeply fractured, fluid-rich crust in the region. Deep sub-crustal electromagnetic investigations as well as attempts of interpreting jointly the seismic and electric anisotropy in the lithospheric and sub-lithospheric upper mantle have evolved into promising indicators of large-scale structures and deformation processes in the Earth (see, e.g., Mareschal *et al.*, 1995; Simpson, 2001; Bahr and Simpson, 2002; Hamilton *et al.*, 2006; Padilha *et al.*, 2006; Roux *et al.*, 2011; Ruiz-Constán *et al.*, 2012). See Wannamaker (2005) for a more thorough review on the electrical anisotropy and its relations to deep geological and tectonic processes.

The sample of the induction studies mentioned above clearly evidenced the existence of crustal and upper mantle electrical anisotropy. The studies also demonstrated that macro-anisotropic structures can be

often treated mathematically as earth sub-domains with continuous intrinsic anisotropy. This approximation simplifies the modeling of inductive responses considerably, as highly heterogeneous structures, often involving series of thin and highly conducting sheet-like bodies, can be modeled by a single large-scale anisotropic bulk.

Methods for the direct numerical modeling of MT fields in laterally inhomogeneous structures with arbitrary anisotropy have been around since the paper by Reddy and Rankin (1975) who presented the first finite element algorithm for 2-D structures with azimuthal electrical anisotropy. A finite volume algorithm for MT fields in 2-D structures with general biaxial anisotropy was published by Pek and Verner (1997), and the finite element version of the same algorithm was presented by Li (2002). The latter algorithm was later extended to allow for an automatic mesh adaptation in the direct simulations by Li and Pek (2008). A 3-D finite difference code for the modeling of MT fields in anisotropic structures was presented by Weidelt (1999), and a number of algorithms exist for the simulation of controlled source electromagnetic fields in 3-D generally anisotropic media (e.g., Wang and Fang, 2001; Weiss and Newman, 2002; Davydycheva *et al.*, 2003; Hou *et al.*, 2006; Zaslavsky *et al.*, 2011).

As it can be often difficult to even qualitatively suggest particular anisotropic structures that can account for specific features in the experimental MT data, inverse MT solutions for anisotropic conductivities in the earth are highly desirable. Although a few inverse algorithms for anisotropic conductivities have been presented for geoelectric and electromagnetic applications with controlled source (Pain *et al.*, 2003; Ramananjaona and MacGregor, 2010), they cannot be immediately applied to the MT case because of largely different sensitivity patterns of anisotropic media for different source types and geometries. For MT inversions for laterally non-uniform anisotropic media, two approaches have been presented so far: a 2-D inversion for a conductivity tensor aligned with the model coordinate frame by Mackie (based on the 2-D inverse code by Rodi and Mackie, 2001) and an inverse algorithm by Li *et al.* (2003) for a general conductivity tensor in the 2-D model. The latter algorithm was an attempt for a complete solution to the 2-D anisotropic MT inverse problem. The solution was based on a damped Gauss-Newton minimization of a penalized objective function and made it possible to employ non-quadratic structure and anisotropy penalties to regularize the inverse solution. Due to stability problems with practical MT data, development of the algorithm has been discontinued, but substantial portions of the work spent on that method have been included into the present version of the non-linear conjugate gradient inverse procedure.

As compared to the 2-D isotropic case, the inversion for anisotropic conductivities has to cope with increased number of parameters (by a factor of 6 for the most general anisotropy case, and by a factor of 3 in the most common case of anisotropy due to a finely laminated structure), with a more complex direct solution and sensitivity computations (coupled partial differential equations for coupled field modes in the anisotropic case), and also with a largely more complex pattern of equivalencies and ambiguities of the anisotropy parameters.

This paper reports on the current development of a non-linear conjugate gradient (NLCG) version of the 2-D inverse algorithm for magnetotelluric (MT) data over structures with arbitrary electrical anisotropy. The structure of the paper is as follows: In the following section, we present a brief description of the NLCG algorithm along with the pre-requisites necessary for its application to the anisotropic 2-D MT inversion. In Section 3, we present two simple synthetic tests of the inverse algorithm and discuss ambiguity issues in 2-D anisotropic models. Finally, in Section 4, we compare results of the anisotropic inversion applied to a small subset of practical MT data from a contact area of the Southern Portuguese Zone and the Ossa Morena Zone, southern Portugal, with those obtained for the same data set earlier by a 1-D inversion and a trial-and-error 2-D direct modeling. Section 5, Conclusion, summarizes the main results achieved.

2 NLCG Inversion Algorithm

2.1 2-D Magnetotelluric Model with Arbitrary Anisotropy

Here, we adopt the 2-D MT model with arbitrary anisotropy exactly in the form as it was introduced in (Pek and Verner, 1997). A 2-D conducting medium (earth) occupies the half-space $z > 0$ and its (structural) strike is parallel to the x-coordinate axis. The conductor is generally characterized by a symmetric, positive definite 3×3 conductivity tensor $\boldsymbol{\sigma}(\mathbf{r})$, where $\mathbf{r}$ is a position vector, $\mathbf{r} = (x, y, z)$.

Locally, i.e. in each point of the medium, an orthonormal transformation exists that diagonalizes the conductivity tensor. This transformation can be expressed through three rotations around the coordinate axes (Euler rotations), and the conductivity tensor can be generally written in the form

$$\boldsymbol{\sigma} = \mathbf{R}_z(-\alpha_S)\,\mathbf{R}_x(-\alpha_D)\,\mathbf{R}_z(-\alpha_L)\ \mathrm{diag}\{\sigma_1,\sigma_2,\sigma_3\}\,\mathbf{R}_z(\alpha_L)\,\mathbf{R}_x(\alpha_D)\,\mathbf{R}_z(\alpha_S), \tag{1}$$

where σ_1, σ_2, σ_3 are the principal conductivities, and α_S, α_D, α_L are the anisotropy strike, dip and slant, respectively. Matrix $\mathbf{R}_\xi(\alpha)$ symbolizes a rotation around the current axis ξ through the angle α. Eq. (1) is true in each point $\mathbf{r}$ of the conductor but is generally spatially dependent. The position argument $\mathbf{r}$ is omitted for brevity here and in what follows. The air layer, $z < 0$, is assumed to be filled with an ideal insulator ($\sigma_{\mathrm{air}} = 0$).

Magnetotelluric field in the model is excited by a uniform, time-harmonic plane wave originating from sources at $z \to -\infty$. We assume the time-harmonic factor of the form $\exp(-i\omega t)$ here, where $\omega = 2\pi/T$ is the angular frequency corresponding to the period T and t is time.

With the MT model described above, Maxwell's equations in the diffusive approximation reduce to a coupled pair of partial differential equations of the second order for the strike-parallel field components, E_x and H_x, of the form (Pek and Verner, 1997)

$$\frac{\partial^2 E_x}{\partial y^2} + \frac{\partial^2 E_x}{\partial z^2} + i\omega\mu_0(\sigma_{xx} + \sigma_{xy}L + \sigma_{xz}K)E_x + i\omega\mu_0 A\frac{\partial H_x}{\partial y} - i\omega\mu_0 B\frac{\partial H_x}{\partial z} = 0, \tag{2a}$$

$$\begin{aligned}\frac{\partial}{\partial y}\left(\frac{\sigma_{yy}}{D}\frac{\partial H_x}{\partial y}\right) + \frac{\partial}{\partial z}\left(\frac{\sigma_{zz}}{D}\frac{\partial H_x}{\partial z}\right) + \frac{\partial}{\partial y}\left(\frac{\sigma_{zy}}{D}\frac{\partial H_x}{\partial z}\right) + \frac{\partial}{\partial z}\left(\frac{\sigma_{yz}}{D}\frac{\partial H_x}{\partial y}\right) + \\ + i\omega\mu_0 H_x - \frac{\partial}{\partial y}(KE_x) + \frac{\partial}{\partial z}(LE_x) = 0,\end{aligned} \tag{2b}$$

where the material coefficients A, B and K, L are given by

$$A = (\sigma_{xy}\sigma_{yz} - \sigma_{xz}\sigma_{yy})/D, \quad B = (\sigma_{xz}\sigma_{zy} - \sigma_{xy}\sigma_{zz})/D,$$

$$L = (\sigma_{yz}\sigma_{zx} - \sigma_{yx}\sigma_{zz})/D, \quad K = (\sigma_{yx}\sigma_{zy} - \sigma_{yy}\sigma_{zx})/D,$$

and D is a sub-determinant of the conductivity tensor, $D = \sigma_{yy}\sigma_{zz} - \sigma_{yz}\sigma_{zy}$. In virtue of the symmetry of the conductivity tensor, we have $A = L$ and $B = K$. After solving eqs. (2), with corresponding boundary conditions, for E_x and H_x, we can obtain the complete MT field in the model by calculating the transversal field components via

$$H_y = \frac{1}{i\omega\mu_0}\frac{\partial H_x}{\partial z}, \quad H_z = -\frac{1}{i\omega\mu_0}\frac{\partial H_x}{\partial y}, \tag{3a}$$

$$E_y = \frac{\sigma_{yz}}{D}\frac{\partial H_x}{\partial y} + \frac{\sigma_{zz}}{D}\frac{\partial H_x}{\partial z} + BE_x, \quad E_z = -\frac{\sigma_{yy}}{D}\frac{\partial H_x}{\partial y} - \frac{\sigma_{yz}}{D}\frac{\partial H_x}{\partial z} + AE_x. \tag{3b}$$

Determining basic MT functions, i.e. MT impedances and vertical geomagnetic transfer functions (induction arrows), requires us to solve the above system of equations for two independent polarizations of the exciting field. Then, if a field component F is linearly related to the horizontal magnetic components through $F = T_x H_x + T_y H_y$, we easily obtain

$$T_x = \frac{F^{(1)}H_y^{(2)} - H_y^{(1)}F^{(2)}}{H_x^{(1)}H_y^{(2)} - H_y^{(1)}H_x^{(2)}}, \quad T_x = \frac{H_x^{(1)}F^{(2)} - F^{(1)}H_x^{(2)}}{H_x^{(1)}H_y^{(2)} - H_y^{(1)}H_x^{(2)}}, \tag{4}$$

where the superscripts (1), (2) distinguish MT fields for the two polarizations.

2.2 Numerical Solution to the Direct Problem

Analytical solution to Eqs. (2) has not been given yet even for the simplest 2-D models. To solve that system numerically, a standard finite volume (FV) approximation of (2) was presented by Pek and Verner (1997). Alternatively, a finite element (FE) algorithm for the same problem was developed by Li (2002).

By discretizing the system of equations (2), with the corresponding boundary conditions, on a FV mesh we arrive at a system of linear algebraic equations, $\mathbf{A}\mathbf{x} = \mathbf{b}$, for the approximate strike-parallel fields $\mathbf{u}$. The matrix $\mathbf{A}$ is a symmetric banded complex matrix which depends on the conductivities and on the geometry of the mesh. The r.h.s. vector $\mathbf{b}$ depends on the fields on the outer boundaries of the computation domain (Dirichlet boundary conditions). Remember that $\mathbf{x}$ involves both the electric and magnetic components of the MT field because of the mode coupling in anisotropic media. Remember also that, from the point of view of the inverse problem, one direct solution represents, in fact, a number of solutions computed for a suite of periods and, at each period, for two independent polarizations,

$$\mathbf{A}\mathbf{x} = \mathbf{b} \;\Leftrightarrow\; \begin{pmatrix} \mathbf{A}(T_1) & 0 & \dots & 0 & 0 \\ 0 & \mathbf{A}(T_1) & \dots & 0 & 0 \\ \vdots & \vdots & \ddots & \vdots & \vdots \\ 0 & 0 & \dots & \mathbf{A}(T_{N_{\rm per}}) & 0 \\ 0 & 0 & \dots & 0 & \mathbf{A}(T_{N_{\rm per}}) \end{pmatrix} \begin{pmatrix} \mathbf{x}^{(1)}(T_1) \\ \mathbf{x}^{(2)}(T_1) \\ \vdots \\ \mathbf{x}^{(1)}(T_{N_{\rm per}}) \\ \mathbf{x}^{(2)}(T_{N_{\rm per}}) \end{pmatrix} = \begin{pmatrix} \mathbf{b}^{(1)}(T_1) \\ \mathbf{b}^{(2)}(T_1) \\ \vdots \\ \mathbf{b}^{(1)}(T_{N_{\rm per}}) \\ \mathbf{b}^{(2)}(T_{N_{\rm per}}) \end{pmatrix}, \tag{5}$$

where T_i, $i = 1, \dots, N_{\rm per}$ are the periods for which the solution is to be calculated.

As a 2-D MT direct problem for anisotropic media is mostly of moderate size, we use Gaussian elimination procedure to solve the systems (5). For each period of the field, the elimination step is carried out in full for one polarization only and the eliminated form of the matrix $\mathbf{A}(T_i)$ is stored. This can be later used to carry out a fast elimination step for only the r.h.s. vector $\mathbf{b}^{(2)}(T_i)$ in the second polarization, without the necessity of repeating the time consuming complete elimination procedure for $\mathbf{A}(T_i)$ once again. The fast back-substitution step is identical for both polarizations. After the approximate solution $\mathbf{u}(T_i)$ has been found, transversal fields (3) are computed by using a spatial derivative procedure by Weaver *et al.* (1985, 1986) generalized to anisotropic models (see Pek *et al.*, 2003). From the solutions for both field polarizations, required MT functions are obtained easily from (4).

2.3 Computation of Parametric Sensitivities

Sensitivities of the MT fields and functions are essential parts of inverse algorithms as they allow us to find parametric changes in the model required to improve the fit between the model and observed data. Sensitivities with respect to the parameters of a 2-D anisotropic model can be evaluated by differentiating the field components or MT functions with respect to the model parameters, i.e. with respect to σ_j (or $\varrho_j = \sigma_j^{-1}$), $j = 1, 2, 3$, and α_S, α_D, α_L, eq. (1), for each specified homogeneous domain of the model. Following the ideas by Rodi (1976), Jupp and Vozoff (1977), Červ and Pek (1981) and Rodi and Mackie (2001), Pek *et al.* (2003) developed a numerical algorithm for the parametric sensitivities in 2-D MT models with arbitrary anisotropy. Starting from (5), approximate parametric sensitivities of the strike-parallel field components with respect to an arbitrary parameter p are given by

$$\frac{\partial \mathbf{x}}{\partial p} = -\,\mathbf{A}^{-1}\left(\frac{\partial \mathbf{A}}{\partial p}\,\mathbf{x} + \frac{\partial \mathbf{b}}{\partial p}\right) \equiv -\,\mathbf{A}^{-1}\mathbf{r}_p, \tag{6}$$

where $\mathbf{r}_p$ is a vector which depends on conductivities, mesh geometry, boundary conditions, as well as on the direct solution $\mathbf{x}$. Vector $\mathbf{r}_p$ is parameter (p) dependent. Since (6) is a pseudo-direct problem (i.e., it has the same matrix $\mathbf{A}$ as the direct solution, but the r.h.s. is different), we can solve it fast by making use of the eliminated form of the matrix $\mathbf{A}$ which had been stored earlier. Eq. (6) has to be solved once for each parameter p for which the sensitivity is needed.

Even more speedup in the sensitivity calculations can be achieved if reciprocity principle is applied (Rodi and Mackie, 2001; Pek *et al.*, 2003). If (6) is solved directly we obtain the parametric sensitivity with respect to p in all mesh nodes throughout the model, which mostly represents a lot of redundant information. If the sensitivities are needed for only a single index (mesh node), say δ, we can pick out that index by multiplying the complete sensitivity $\partial\mathbf{x}/\partial p$ by a vector $\mathbf{\Delta}_\delta$ which consists of zeros everywhere except at the δ-th position where it is one,

$$\frac{\partial x_\delta}{\partial p} = \mathbf{\Delta}_\delta^T\,\frac{\partial \mathbf{x}}{\partial p} = \underline{-\,\mathbf{\Delta}_\delta^T\,\mathbf{A}^{-1}\mathbf{r}_p = -\,\mathbf{\Delta}_\delta^T\,(\mathbf{A}^T)^{-1}\mathbf{r}_p} = -\,(\mathbf{A}^{-1}\mathbf{\Delta}_\delta)^T\mathbf{r}_p. \tag{7}$$

The underlined part of the formula shows where the symmetry of the normal matrix is used, $\mathbf{A} = \mathbf{A}^T$, which is a manifestation of the physical reciprocity principle in the numerical domain. By employing (7),

we obtain sensitivities with respect to *all parameters* at a single mesh node for the price of only one single pseudo-forward solution $\mathbf{q}_\delta = \mathbf{A}^{-1}\mathbf{\Delta}_\delta$. This must be solved repeatedly if the sensitivities in several nodes, with different 'pickers' $\mathbf{\Delta}$, are required. The idea of eq. (7) can be easily extended to more general 'picker' vectors which may span several mesh nodes and even depend on the model parameters. In this way, the reciprocity computations can be employed immediately to numerically evaluate parametric sensitivities of the transversal MT fields (3) and MT functions (4).

Formulas for the transversal fields (3), when numerically approximated, lead to linear interpolation filters in an, at most, 9-point vicinity of the central mesh node δ, $F_\delta = \mathbf{P}_\delta^T(\mathbf{p})\,\mathbf{x}$, for any transversal field component F (Pek *et al.*, 2003). Components of the picker vector $\mathbf{P}_\delta(\mathbf{p})$ now generally depend on the model parameters $\mathbf{p}$, but they are equal for both polarizations of the exciting field. In virtue of (7), the sensitivities of F_δ with respect to p can be computed via

$$\frac{\partial F_\delta}{\partial p} = \frac{\partial \mathbf{P}_\delta^T}{\partial p}\,\mathbf{x} + \mathbf{P}_\delta^T\,\frac{\partial \mathbf{x}}{\partial p} = \frac{\partial \mathbf{P}_\delta^T}{\partial p}\,\mathbf{x} - \mathbf{P}_\delta^T\,\mathbf{A}^{-1}\mathbf{r}_p = \frac{\partial \mathbf{P}_\delta^T}{\partial p}\,\mathbf{x} - (\mathbf{A}^{-1}\mathbf{P}_\delta)^T\mathbf{r}_p\,. \tag{8}$$

Evaluating the first term on the r.h.s. of (8) is elementary. The second term requires one pseudo-forward solution, $\mathbf{q}_\delta = \mathbf{A}^{-1}\mathbf{P}_\delta$, for each field component for which the sensitivities are needed. Once $\mathbf{q}_\delta$ is found, evaluating any sensitivity for F_δ is a matter of a simple multiplication of $\mathbf{q}_\delta^T$ with the respective vector $\mathbf{r}_p$.

Parametric sensitivities of the MT transfer functions (4) can be computed either by using (7), (8) in formulas (4) which have been differentiated directly with respect to p, or by deriving corresponding picker vectors $\mathbf{P}_{T\delta}$ for the MT functions considered. In the latter approach, we write the MT functions (4) in a general functional form, $T_\delta = f(F_{i\delta})$, where $F_{i\delta}$, $i = 1, \ldots$, symbolize field components at the δ-th mesh node for any polarization. As $F_{i\delta} = \mathbf{P}_{i\delta}^T\,\mathbf{x}$ according to what was said in the previous paragraph, we can write for the parametric sensitivities of T,

$$\begin{aligned}
\frac{\partial T_\delta}{\partial p} &= \sum_i \frac{\partial T_\delta}{\partial F_{i\delta}}\,\frac{\partial F_{i\delta}}{\partial p} = \sum_i \frac{\partial T_\delta}{\partial F_{i\delta}}\left(\frac{\partial \mathbf{P}_{i\delta}^T}{\partial p}\,\mathbf{x} - \mathbf{P}_{i\delta}^T\,\mathbf{A}^{-1}\mathbf{r}_p\right) = \\
&= \left(\sum_i \frac{\partial T_\delta}{\partial F_{i\delta}}\,\frac{\partial \mathbf{P}_{i\delta}^T}{\partial p}\right)\mathbf{x} - \left(\sum_i \frac{\partial T_\delta}{\partial F_{i\delta}}\,\mathbf{P}_{i\delta}^T\right)\mathbf{A}^{-1}\mathbf{r}_p = \left(\sum_i \frac{\partial T_\delta}{\partial F_{i\delta}}\,\frac{\partial \mathbf{P}_{i\delta}^T}{\partial p}\right)\mathbf{x} - \left(\mathbf{A}^{-1}\sum_i \frac{\partial T_\delta}{\partial F_{i\delta}}\,\mathbf{P}_{i\delta}\right)^T\mathbf{r}_p \equiv \\
&\equiv \mathbf{w}_x^T\mathbf{x} - (\mathbf{A}^{-1}\mathbf{w}_p)^T\mathbf{r}_p.
\end{aligned} \tag{9}$$

Formally, eq. (9) looks the same as (8), only with more complex coefficients. Again, we need to solve only one pseudo-forward problem to evaluate all sensitivities of the function T at the node δ.

2.4 Inverse Problem

The MT inverse problem for 2-D generally anisotropic conductivity in the earth is formulated as a minimization problem for a target functional

$$\Phi(\mathbf{p}|\lambda_s, \lambda_a, \mathbf{p}_{\mathrm{ref}}) = \Phi_d(\mathbf{p}) + \lambda_s\Phi_s(\mathbf{p}|\mathbf{p}_{\mathrm{ref}}) + \lambda_a\Phi_a(\mathbf{p}|\mathbf{p}_{\mathrm{ref}}), \tag{10}$$

where Φ_d is a misfit between the model and observed data, and Φ_s, Φ_a are structure complexity and anisotropy penalties, respectively, with respective weights λ_s, λ_a. The vector $\mathbf{p}$ aggregates the model parameters, which are in our case logarithms of the principal resistivities and the anisotropy directions, i.e. strike, dip and slant, eq. (1), or any subset of those, in each homogeneous model sub-domain selected for inversion. The vector $\mathbf{p}_{\mathrm{ref}}$ contains parameters of a reference model which gives a way how to incorporate prior information into the inverse procedure. If a reference model is introduced, the minimization parameters are $\Delta\mathbf{p} = \mathbf{p} - \mathbf{p}_{\mathrm{ref}}$ instead of $\mathbf{p}$, and the inversion searches for deviations of the parameters $\mathbf{p}$ from the reference model $\mathbf{p}_{\mathrm{ref}}$ which minimize (10). In the following we omit the reference model $\mathbf{p}_{\mathrm{ref}}$ from the notations for simplicity.

The data misfit term in (10) is defined in the least-squares sense as

$$\Phi_d(\mathbf{p}) = \left\| \mathbf{C}_d^{-1}[\,\mathbf{d}^{\mathrm{obs}} - \mathbf{d}^{\mathrm{mod}}(\mathbf{p})\,]\right\|^2 = [\,\mathbf{d}^{\mathrm{obs}} - \mathbf{d}^{\mathrm{mod}}(\mathbf{p})\,]^T(\mathbf{C}_d^{-1})^T\mathbf{C}_d^{-1}[\,\mathbf{d}^{\mathrm{obs}} - \mathbf{d}^{\mathrm{mod}}(\mathbf{p})\,], \tag{11}$$

where $\mathbf{d}^{\mathrm{mod}}(\mathbf{p})$ is a vector of modeled data for parameters $\mathbf{p}$, $\mathbf{d}^{\mathrm{obs}}$ are experimental measured data, and $\mathbf{C}_d$ is a covariance matrix of the observations. As in anisotropic modeling the secondary, diagonal

elements of the MT impedance tensor are of particular importance, we use real and imaginary parts of all four components of the impedance tensor and of both components of the vertical geomagnetic transfer functions as data items in the inversion procedure.

The two regularization terms in (10) are of crucial importance for a stabilization of the MT inversion which is an ill-posed problem (e.g., Constable *et al.*, 1987; deGroot-Hedlin and Constable, 1990). The structure complexity term of (10), $\Phi_s(\mathbf{p}|\mathbf{p}_{\rm ref})$, penalizes excessive structure in the inverse model and prevents overfitting the data by structural features that are required by only the noise component in the data. We employ only simple structure penalties in the present inverse algorithm, specifically the minimum norm penalty (Tikhonov and Arsenin, 1977), and minimum roughness and minimum curvature penalties (Constable *et al.*, 1987; deGroot-Hedlin and Constable, 1990). The minimum norm functional produces the closest model with respect to the reference model, the minimum roughness and minimum curvature functionals produce smooth electrical models that still fit the data within their error bars. All these penalties can be formally written in the same form,

$$\Phi_s(\mathbf{p}|\mathbf{p}_{\rm ref}) = \| \mathbf{L}_s(\mathbf{p}-\mathbf{p}_{\rm ref}) \|^2 = (\mathbf{p}-\mathbf{p}_{\rm ref})^T \mathbf{L}_s^T \mathbf{L}_s (\mathbf{p}-\mathbf{p}_{\rm ref}), \tag{12}$$

where $\mathbf{L}_s$ is a unit matrix, or approximation to the gradient or Laplace operators for the three considered structure functionals, respectively. The matrix $\mathbf{L}_s$ is independent of the model parameters $\mathbf{p}$ in these cases. We apply the structure penalty to each of the anisotropy parameters separately, and we use one common weight λ_s for all parameters. It seems to balance well the regularization structure terms provided the logarithms of the principal resistivities and the anisotropy angles in radians are used as model parameters. It should be emphasized here that the structure penalty in the form (12) makes best sense for homogeneous model domains arranged into a rectangular grid of cells. In what follows, our model domains for the inversion will be identical with the cells of the FD grid used in the forward modeling though the inverse algorithm alone is able to operate on any disjunct set of domains within the model. A structure penalty best suited to the general case of completely irregular blocks throughout the model is the minimum norm penalty.

The aim of introducing the anisotropy penalty term, $\Phi_a(\mathbf{p})$, in the target (10) is to supress redundant anisotropy in the structure. The anisotropy penalty aims at minimizing the difference, in the least-squares sense, between the full conductivity tensor, $\boldsymbol{\sigma}$, and its mean isotropic part defined by $\bar{\boldsymbol{\sigma}}_{\rm iso} = \frac{1}{3}(\sigma_1+\sigma_2+\sigma_3)\,\mathrm{diag}\{1,1,1\}$. It can be easily shown that this leads to an anisotropy penalty form (Pain,2003)

$$\Phi_a(\mathbf{p}) = \sum_{\rm cells} (\log\varrho_1, \log\varrho_2, \log\varrho_3) \begin{pmatrix} 2 & -1 & -1 \\ -1 & 2 & -1 \\ -1 & -1 & 2 \end{pmatrix} \begin{pmatrix} \log\varrho_1 \\ \log\varrho_2 \\ \log\varrho_3 \end{pmatrix} = \\ = \sum_{\rm cells} \left[(\log\varrho_1 - \log\varrho_2)^2 + (\log\varrho_2 - \log\varrho_3)^2 + (\log\varrho_3 - \log\varrho_1)^2 \right]. \tag{13}$$

The summation in (13) runs over all anisotropic cells, or domains, of the model that are flagged for inversion. Formally, the anisotropy functional can be again expressed as $\Phi_a(\mathbf{p}) = \mathbf{p}^T \mathbf{L}_a^T \mathbf{L}_a \mathbf{p}$, similarly as the structure complexity functional (12), but with the matrix $\mathbf{L}_a$ being effective on the resistivity variables only, not on the anisotropy angles.

Eq. (1) describes the most general, biaxial conductivity anisotropy in the space. In MT practice, however, this type of anisotropy is too general, and difficult to interpret. Anisotropy in MT is most commonly understood in terms of finely layered earth domains or sub-parallel dykes which are not sensed as separate conductors by the diffusing electromagnetic field. In such cases, simpler, uniaxial anisotropy is a more useful concept in MT interpretations rather than the general case (1).

Uniaxial electrical anisotropy can be introduced as a fixed constraint by *apriori* setting, e.g., $\sigma_1 = \sigma_2$. We can easily show that, in (1), $\mathbf{R}_z(-\alpha_L)\,\mathrm{diag}\{\sigma_l,\sigma_l,\sigma_t\}\,\mathbf{R}_z(\alpha_L) = \mathrm{diag}\{\sigma_l,\sigma_l,\sigma_t\}$, where we have introduced longitudinal and transversal conductivities, $\sigma_l \equiv \sigma_1 = \sigma_2$ and $\sigma_t \equiv \sigma_3$, respectively. Thus, the slant α_L vanishes in the uniaxial case, and we can conclude that the uniaxial anisotropy is completely described by four parameters only, two principal conductivities σ_l and σ_t (or resistivities ϱ_l and ϱ_t) and two anisotropy directions, strike α_S and dip α_D. Of course, if uniaxial anisotropy is imposed as a fixed constraint we have to consider that varying σ_l implies varying both σ_1 and σ_2 simultaneously, and we must modify the sensitivities accordingly, specifically $\partial/\partial\sigma_l = \partial/\partial\sigma_1 + \partial/\partial\sigma_2$, $\partial/\partial\sigma_t = \partial/\partial\sigma_3$. In the same way, isotropy can be introduced as a fixed constraint in certain portions of the model by

setting $\sigma_{\rm iso} \equiv \sigma_1 = \sigma_2 = \sigma_3$. The parameter $\sigma_{\rm iso}$ (or, alternatively, the resistivity $\varrho_{\rm iso}$) is the only parameter that desribes the isotropic conductivity completely. A modified sensitivity must be then considered in the isotropic case, $\partial/\partial\sigma_{\rm iso} = \partial/\partial\sigma_1 + \partial/\partial\sigma_2 + \partial/\partial\sigma_3$.

Degenerate anisotropy cases, like the uniaxial anisotropy and isotropy above, can be also imposed as soft constraints on the model structure, by modifying slightly the anisotropy penalty (13) to the form

$$\Phi_a(\mathbf{p}) = \sum_{\rm cells} \left[\lambda_{a,12}(\log\varrho_1 - \log\varrho_2)^2 + \lambda_{a,23}(\log\varrho_2 - \log\varrho_3)^2 + \lambda_{a,31}(\log\varrho_3 - \log\varrho_1)^2\right]. \qquad (14)$$

If the internal weights are, e.g., $\lambda_{a,12} \gg \lambda_{a,23} = \lambda_{a,31} = 1$, the minimization of (10) will keep the principal resistivities ϱ_1 and ϱ_2 close to equal, except for those model domains where the biaxial anisotropy is highly effective at improving the fit to the data, or at decreasing the structure complexity. Soft isotropy constraint is simply imposed by increasing the overall penalty weight λ_a in (10). Incorporating the anisotropy penalty (14) in the code is straightforward while introducing the fixed constraints requires some extra decision branches to be coded for the individual degeneracy cases.

There is a number of methods that can be used to minimize the target (10) (see, e.g., Bertsekas, 1999). Here, we use the non-linear conjugate gradient (NLCG) minimization procedure that has been a core of well-known MT inversion codes by Newman and Alumbaugh (1999) and Rodi and Mackie (2001). NLCG is a class of extensions of the linear conjugate gradient method to nonquadratic problems (e.g., Andrei, 2008). NLCG algorithms are well suited for large-scale problems due to the simplicity of their iteration and their very low memory requirements. NLCG algorithms show stable and robust convergence and do not usually fail in case of ill-posed problems, where the speed of convergence is negatively affected, however. Just as in the linear case, preconditioning can improve the convergence rate of conjugate gradients.

Without going into further theoretical details, we present the NLCG version we use in our inversion algorithm as a flowchart in Fig. 1. It is Polak-Ribière form of the NLCG procedure adopted from (Rodi and Mackie, 2001), with a direct line search employed. Minimization of the target (10) starts from an initial model p_0 in the direction of the steepest descent defined by the negative of the target gradient,

$$\mathbf{g}(\mathbf{p}|\lambda_s,\lambda_a) = -2\,\mathbf{S}^T(\mathbf{p})\,(\mathbf{C}_d^{-1})^T(\mathbf{C}_d^{-1})[\,\mathbf{d}^{\rm obs} - \mathbf{d}^{\rm mod}(\mathbf{p})] + 2\,\lambda_s\mathbf{L}_s^T\mathbf{L}_s\mathbf{p} + 2\,\lambda_a\mathbf{L}_a^T\mathbf{L}_a\mathbf{p} \text{ for } \mathbf{p} = \mathbf{p}_0, \qquad (15)$$

where $\mathbf{S}(\mathbf{p})$ is a sensitivity matrix with entries $s_{ij}(\mathbf{p}) = \partial d_i^{\rm mod}(\mathbf{p})/\partial p_j$, $i = 1,\ldots,N_{\rm dat}$, $j = 1,\ldots,N_{\rm par}$. Here, $N_{\rm dat}$ and $N_{\rm par}$ are the number of measured data items and number of model parameters flagged for inversion, respectively. Subsequent steps are carried out in conjugate gradient directions which prevents the algorithm from proceeding in slow, zigzagging steps on the slope characteristic of a pure steepest descent minimization.

An essential ingredient of the NLCG iteration step is an 1-D line search for a minimum in the conjugate gradient direction. Since the direct MT problem for 2-D anisotropic conductivities is substantially faster than the evaluation of the target gradient (15), we employ a simple golden search rule (Press *et al.*, 1986) to carry out the line search. Typical number of the line search steps is between 20 and 30 in our procedure. If the target does not decrease in the line search because of loss of conjugacy due to numerical errors the NLCG process is restarted in the steepest descent direction. If the target gradient reaches a pre-defined threshold, or if the number of iterations exceeds a user defined limit, the iteration process is terminated.

As mentioned in the previous paragraph, evaluation of the target gradient (15) is the most computer resource demanding step in the minimization procedure. Substantial time savings could be already achieved by employing the reciprocity principle in the sensitivity calculations, see eqs. (7), (8), (9). The NLCG procedure gives a possibility of saving even more time and memory at computing the gradient of the data misfit in (15) (Rodi and Mackie, 2001). This part of the target gradient requires us to compute a matrix-vector product $\mathbf{S}^T(\mathbf{p})\,(\mathbf{C}_d^{-1})^T(\mathbf{C}_d^{-1})[\,\mathbf{d}^{\rm obs} - \mathbf{d}^{\rm mod}(\mathbf{p})] \equiv \mathbf{S}^T\mathbf{v}$, where $\mathbf{v}$ is a vector of model vs. data residuals normalized by the data covariance matrix. The i-th component of this product is

$$(\mathbf{S}^T\mathbf{v})_i = \sum_{j=1}^{N_{\rm dat}} \frac{\partial d_j^{\rm mod}(\mathbf{p})}{\partial p_i}\, v_j = \sum_{j=1}^{N_{\rm dat}} \left[\,\mathbf{w}_{xj}^T\,\mathbf{x} - (\mathbf{A}^{-1}\mathbf{w}_{pj})^T\mathbf{r}_{p_i}\,\right] v_j =$$

$$= \left(\sum_{j=1}^{N_{\rm dat}} v_j\mathbf{w}_{xj}\right)^T \mathbf{x} - \left(\mathbf{A}^{-1}\sum_{j=1}^{N_{\rm dat}} v_j\mathbf{w}_{pj}\right)^T \mathbf{r}_{p_i} \equiv \mathbf{W}_{xi}^T\,\mathbf{x} + (\mathbf{A}^{-1}\mathbf{W}_p)^T\mathbf{r}_{p_i}\,, \qquad (16)$$

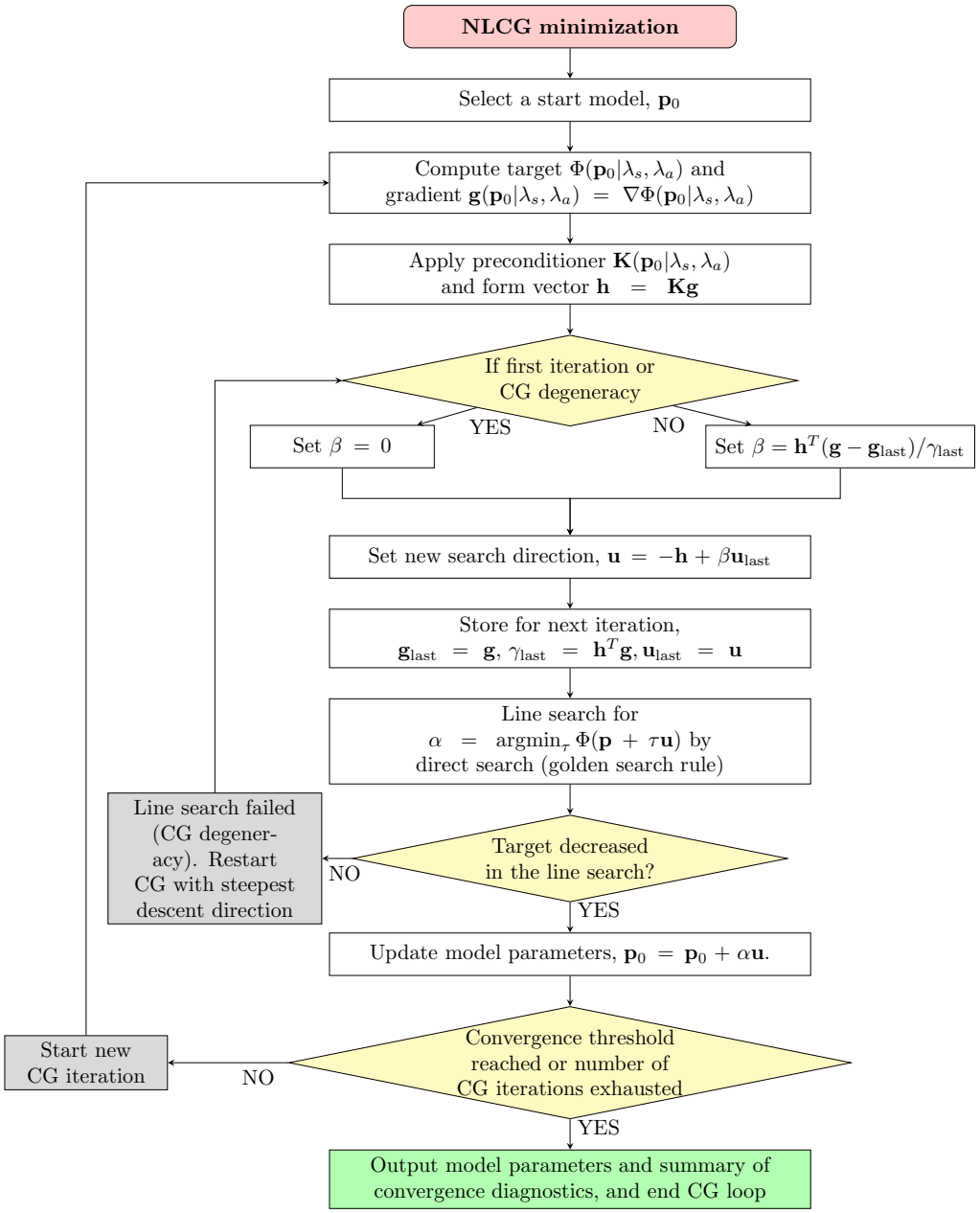

Figure 1: Flowchart of the NLCG minimization algorithm as applied to the MT inversion for 2-D anisotropic conductivities.

where eq. (9) has been used to express the sensitivities of $d_j^{\text{mod}}(\mathbf{p})$ (MT model responses) with respect to the parameter p_i. Since the vectors $\mathbf{w}_{pj}$, $j = 1,\ldots,N_{\text{dat}}$, are characteristics of the MT function $d_j^{\text{mod}}(\mathbf{p})$ only, and not of the particular p_i, we can evaluate them in the course of the forward problem solution and accumulate them, with weights v_j (data residuals), into the sum $\sum_{j=1}^{N_{\text{dat}}} v_j\mathbf{w}_{pj} = \mathbf{W}_p$. Only one pseudo-forward solution is then needed, $\mathbf{A}^{-1}\mathbf{W}_p$, for all the sensitivity computations. The vectors $\mathbf{W}_{xi}$, $i = 1,\ldots,N_{\text{par}}$, must be, however, computed for each p_i individually, but it is an easy operation. To summarize, eq. (16) says that computing the matrix-vector product $\mathbf{S}^T\mathbf{v}$ (i) does not need the elements of the sensitivity matrix $\mathbf{S}$ to be evaluated explicitly and stored, and, (ii) requires only one pseudo-forward

solution, and then, for each parameter p_i, $i = 1, \ldots, N_{\mathrm{par}}$, two vector-vector multiplications.

We use a simple Jacobi pre-conditioning to improve the convergence rate of the NLCG procedure (e.g., Newman and Boggs, 2004). In this case, the pre-conditioning matrix is an inverse diagonal of the approximate Hessian,

$$\mathbf{K}(\mathbf{p}|\lambda_s, \lambda_a) = \left\{\text{diagonal of } \left[\mathbf{S}^T(\mathbf{p})(\mathbf{C}_d^{-1})^T(\mathbf{C}_d^{-1})\mathbf{S}(\mathbf{p}) + \lambda_s \mathbf{L}_s^T\mathbf{L}_s + \lambda_a \mathbf{L}_a^T\mathbf{L}_a\right]\right\}^{-1}. \tag{17}$$

In our runs, we found that applying the pre-conditioning improved the convergence of the NLCG minimization and prevented the iterations to terminate prematurely due too small target gradients. Unfortunately, we must evaluate the individual sensitivities explicitly (though not to store them) to use the pre-conditioner (17), which does not allow us to fully exhaust the time-saving advantage implied by eq. (16) above. Therefore, we do not compute the pre-conditioner (17) in each iteration step, but update it only after a couple of iterations, typically after 5 to 10 steps in our algorithm. Fig. 2 shows the effect of the pre-conditioning for an inverse run by comparing convergence curves for both non-pre-conditioned and pre-conditioned NLCG with various update rates. The convergence is monitored as a function of iterations and of the computation time.

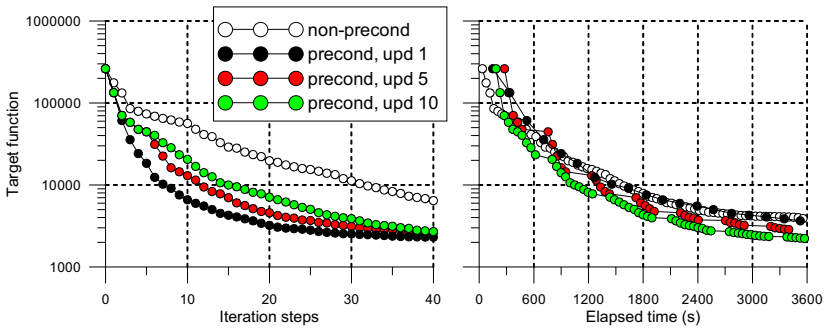

Figure 2: Effect of pre-conditioning on the NLCG iteration process. Pre-conditioned process is shown for several update rates of the pre-conditioner, specifically for updates at each iteration (upd 1), after every 5th (upd 5) and after every 10th iteration (upd 10). Left plot monitors the convergence as a function of the iteration number, right plot as a function of the computation time. The reference PC workstation was based on an Intel Core i7-940 processor and was equipped with 6 GB of RAM. Intel Visual Fortran v. 11 compiler was used to compile the code.

3 Synthetic tests

3.1 Simple 2-D Anisotropic Box Anomaly in a Uniform Host

3.1.1 Anomaly with Uniaxial Anisotropy and Anisotropy Strike only

We carried out a series of synthetic tests of the inverse MT procedure for 2-D structures with arbitrary anisotropy with very simple models in order to assess the performance of the code, as well as to indicate basic ambiguity patterns in 2-D anisotropic structures. A first test was run with synthetic data generated by a simple block anomaly, size 10×10 km^2, embedded in a uniform host half-space. The top of the anomaly is situated 2 km beneath the surface. Geometry of this test model has been adopted from (Rodi and Mackie, 2001). The host medium is isotropic, with resistivity $\varrho_{\mathrm{host}} = 300$ Ωm. The anomalous block is characterized by uniaxial anisotropy, with principal resistivities $\varrho_1 = \varrho_3 = 10$ Ωm and $\varrho_2 = 100$ Ωm and with anisotropy strike $\alpha_S = 30°$. No dip or slant are considered. Physically, the anomaly may be interpreted as a lamelar structure, with parallel vertical conducting lamelas deflected by 30° with respect to the structural strike of the model. Experimental data are simulated at seven equispaced sites above the anomalous body for 10 logarithmically equidistant periods from the range of 0.01 to 300 s. We add Gaussian noise to the data, with zero mean and a standard deviation equal to 2.5% of the maximum

module from all four impedance elements. An absolute standard deviation of 0.01 is used to add noise to geomagnetic transfer functions (induction arrows). The size of the inverse problem was: 1350 model cells, 5400 model parameters, 560 data items.

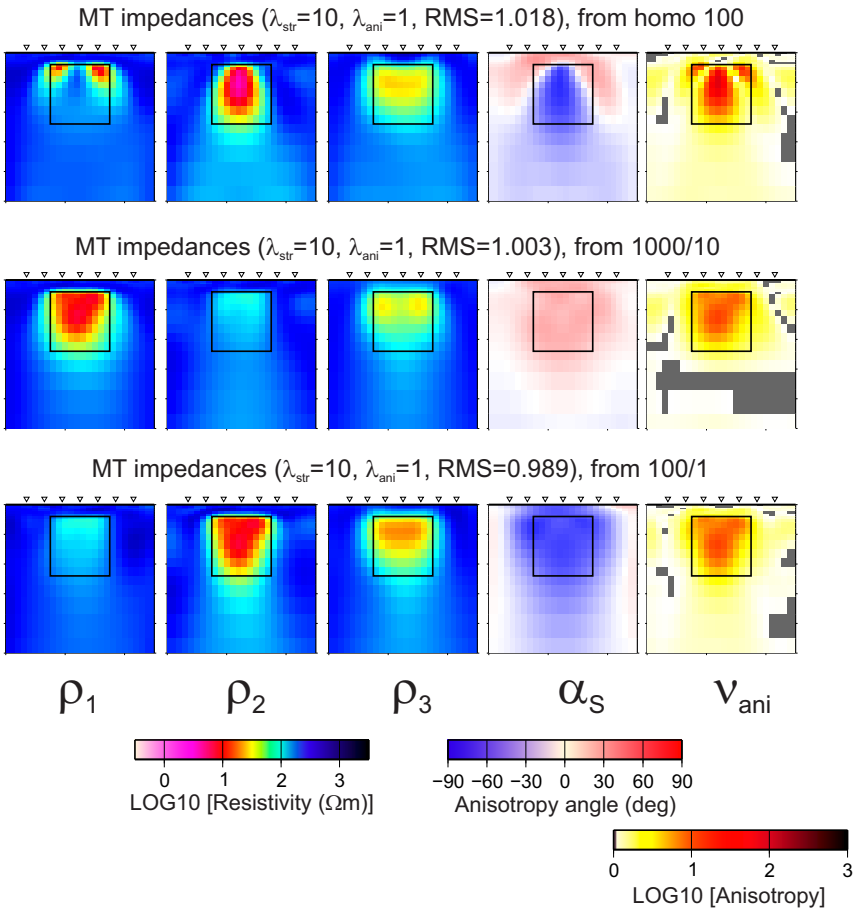

Figure 3: Three patterns of inverse models from simulated MT data for a box anomaly with uniaxial anisotropy and anisotropy strike. The models were obtained from different initial models but with the same regularization weights, $\lambda_s = 10$ and $\lambda_a = 1$. The black square shows the position of the anisotropic anomalous body. The triangles on the surface indicate observation sites. The size of the model section displayed is 25×25 km^2. The panels show, from the left to the right, the three principal resistivities, ϱ_1, ϱ_2, ϱ_3, from the inversion, the anisotropy strike α_S, and the anisotropy ratio defined as $\nu_{\text{ani}} = \varrho_{\max}/\varrho_{\min}$, where $\varrho_{\min}$, $\varrho_{\max}$ are, respectively, the minimum and maximum principal resistivities in model cells. The gray zones in the anisotropy plots indicate model domains with small anisotropy, $\varrho_{\max}/\varrho_{\min} < 1.1$. The RMS indicated for each model is computed by RMS $= \sqrt{\Phi_d(\mathbf{p})/N_{\text{dat}}}$.

In 1-D case, this type of structure is the most general anisotropic structure that can be restored from MT data, with the exception of the vertical resistivity, ϱ_3, which is principally indistinguishable in layered media (Pek and Santos, 2006). In 2-D, the vertical resistivity does affect the MT curves, but simulation studies have shown that its effect is concentrated immediately above the anomalous box and is very weak as compared to the effect of the horizontal resistivities. Thus, we can expect only very poor resolution of the 2-D inversion with respect to the vertical resistivity.

In fact, inverse runs applied to the simulated data typically show three patterns of resulting models, displayed in Fig. 3. The first pattern shows heterogeneous anisotropy within the anomaly, with $\varrho_{\max} = \varrho_1 > \varrho_2$, strike $\alpha_S = 30°$, in the top corners of the anomalous body, and $\varrho_{\max} = \varrho_2 > \varrho_1$, strike $\alpha_S = -60°$, in the body central zone. Both those zones reproduce the horizontal anisotropy correctly, but the

transition between them inside the body evidently represents an excessive structure. Though it seems to be an effect of underregularization of the model, the pattern is pervasive enough and is likely to be connected with a deep local minimum in the parameter space. The other two patterns are as expected, with only the min/max resistivites swapped. The vertical resistivity is not recovered correctly in any of the models, and is evidently result of an interplay of the starting model and of the regularization.

Figure 4 shows a complete suite of inverse results for our test model with various regularization weights, $\lambda_s \in \{1, 10, 100, 1000\}$ and $\lambda_a \in \{0, 1, 10, 100\}$. To avoid visually disturbing jumps between different quasi-equivalent model types (see Fig. 3), we started all inversion runs from the same oversmoothed model obtained from a uniform host, $\varrho_0 = 100$ Ωm, with $\lambda_s = 1000$, $\lambda_a = 10$. For small penalties, we evidently obtain models with excessive granularity and anisotropy. For strong anisotropy penalization, the recovered conductive domain becomes thinner and concentarted along the top edge of the true anomaly. The horizontal anisotropy is best recovered with the weights λ_s, λ_a close to 10 and 1, respectively. This agrees with the positions of the corresponding solutions on the L-surface (Fig. 5, left), which was suggested earlier for estimating the optimum regularization weights in 1-D anisotropic inversions (Pek and Santos, 2006).

3.1.2 Anomaly with Uniaxial Anisotropy and Anisotropy Strike and Dip

Anisotropy dip is known to be an unresolvable parameter in the 1-D anisotropic MT model unless additional information on the principal resistivites is available. A layer with the longitudinal and transversal resistivities ϱ_l and ϱ_t, respectively, and anisotropy dip α_D is sensed by MT soundings as an azimuthally anisotropic layer (i.e., with $\alpha_D = 0°$) with the horizontal resistivity (e.g., Pek and Santos, 2002)

$$\varrho_d = \varrho_l \cos^2 \alpha_D + \varrho_t \sin^2 \alpha_D. \tag{18}$$

Even for a known dip α_D, the principal resistivities ϱ_l, ϱ_t cannot be found uniquely unless one of the principal resistivities or the anisotropy ratio is known. The bottom left panel in Fig. 6 shows $\varrho_y - \varrho_z$ (transversal vs. longitudinal) equivalency lines for various dips α_D for a 1-D anisotropy model with true $\varrho_y = 100$ Ωm, $\varrho_z = 10$ Ωm, and $\alpha_D = 60°$. Any resistivity pair on any of the α_D-labeled curves produces the same horizontal resistivity ϱ_d, and is thus indistinguishable from MT data in the 1-D case.

In a 2-D case, the above equivalency is not theoretically justified, though the models equivalent in the 1-D case produce very similar MT curves also in 2-D. In Fig. 6, a few curves are demonstrated for a square 2-D anomalous body with various dipping anisotropies which would be completely equivalent in 1-D case. For the period of 30 s, the 2-D MT curves are between 20 and 30 Ωm in resistivities and between 120 and 125° in phases immediately above the anomalous body. These differences are very small, in spite of the largely different generating models. Therefore, a poor resolution of the dip by a 2-D anisotropic inversion can be expected.

One more feature of dipping anisotropy in laterally non-uniform structures should be mentioned, namely a slight asymmetry of the MT curves above the anomaly with anisotropy dip. This feature does not appear in 1-D media. Because of poor resolution with respect to the dip, this asymmetry often translates into an asymmetry of the conductivity distribution within the earth. This is clearly demonstrated in Figs. 7a and b where inversion results are shown for synthetic data from the box model in Fig. 6. In Fig. 7a, the data were inverted only for principal resistivities and anisotropy strike, the dip was fixed at $\alpha_D = 0°$. The data were fit successfully, but the recovered anisotropic conductor is shifted considerably towards the right-hand side margin of the true anomaly. Fig. 7b results from the inversion for both the principal resistivities, anisotropy strike as well as dip. A forced lamelarity of the anisotropy is demonstrated in Fig. 7c by increasing the internal anisotropy penalty weight $\lambda_{a,12}$ from 1 to 100 in (14).

Effect of extending the inverted data set by vertical geomagnetic transfer functions (induction arrows, tippers) is demonstrated in Fig. 7d. The geomagnetic data do not improve the inversion considerably as compared to Fig. 7b, they perhaps focus and centre the recovered anomaly marginally better. An attempt of employing the geomagnetic data as a source of directional information in the anisotropic inversion failed completely. Fig. 7e shows results of the inversion of the main, off-diagonal impedances jointly with the geomagnetic transfer functions, with diagonal impedances omitted. The anisotropy was not recognized properly by those data, and neither the principal resistivities nor the characteristic anisotropy directions were recovered satisfactorily.

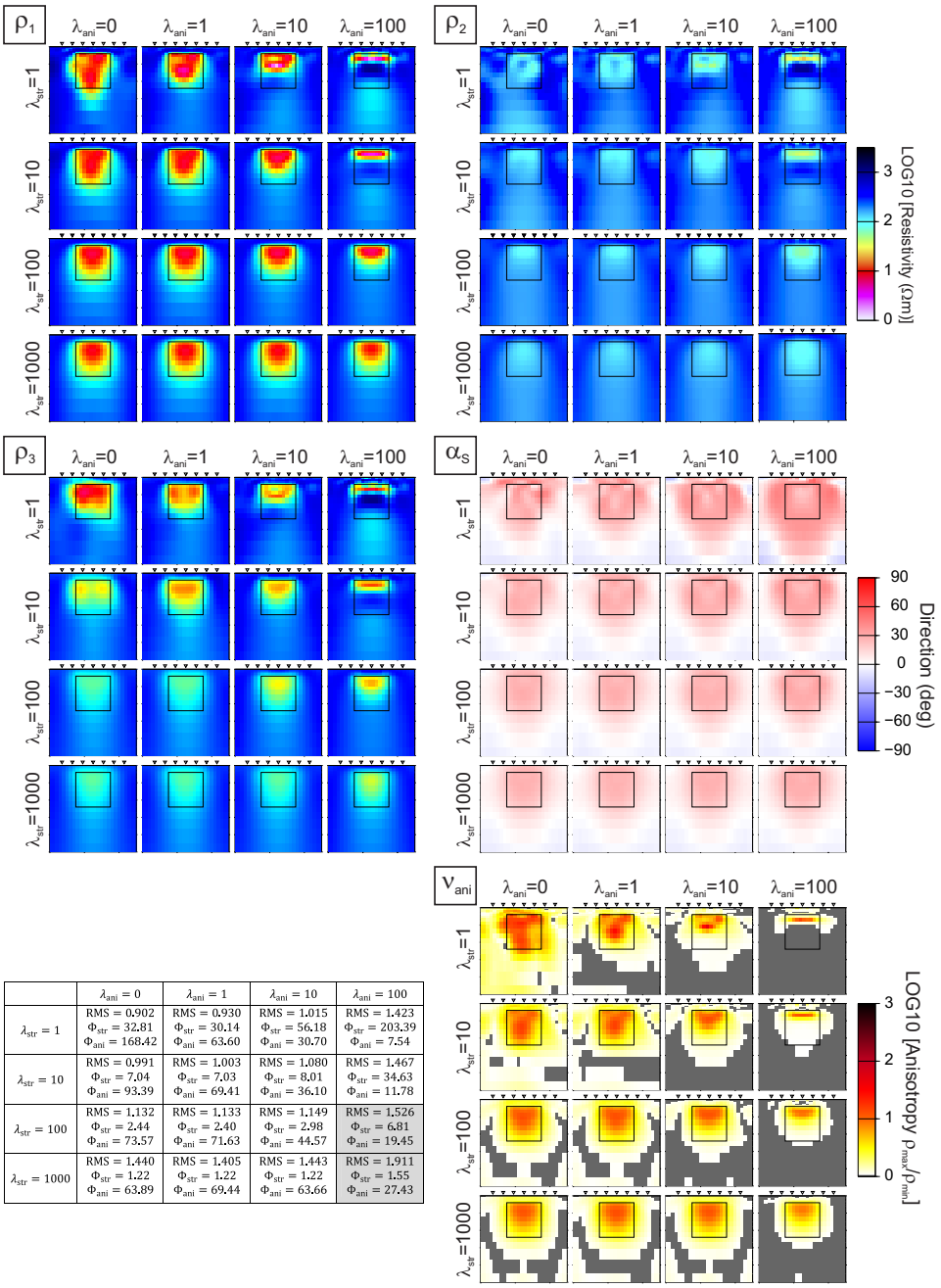

	$\lambda_{ani} = 0$	$\lambda_{ani} = 1$	$\lambda_{ani} = 10$	$\lambda_{ani} = 100$
$\lambda_{str} = 1$	RMS = 0.902 Φ_{str} = 32.81 Φ_{ani} = 168.42	RMS = 0.930 Φ_{str} = 30.14 Φ_{ani} = 63.60	RMS = 1.015 Φ_{str} = 56.18 Φ_{ani} = 30.70	RMS = 1.423 Φ_{str} = 203.39 Φ_{ani} = 7.54
$\lambda_{str} = 10$	RMS = 0.991 Φ_{str} = 7.04 Φ_{ani} = 93.39	RMS = 1.003 Φ_{str} = 7.03 Φ_{ani} = 69.41	RMS = 1.080 Φ_{str} = 8.01 Φ_{ani} = 36.10	RMS = 1.467 Φ_{str} = 34.63 Φ_{ani} = 11.78
$\lambda_{str} = 100$	RMS = 1.132 Φ_{str} = 2.44 Φ_{ani} = 73.57	RMS = 1.133 Φ_{str} = 2.40 Φ_{ani} = 71.63	RMS = 1.149 Φ_{str} = 2.98 Φ_{ani} = 44.57	RMS = 1.526 Φ_{str} = 6.81 Φ_{ani} = 19.45
$\lambda_{str} = 1000$	RMS = 1.440 Φ_{str} = 1.22 Φ_{ani} = 63.89	RMS = 1.405 Φ_{str} = 1.22 Φ_{ani} = 69.44	RMS = 1.443 Φ_{str} = 1.22 Φ_{ani} = 63.66	RMS = 1.911 Φ_{str} = 1.55 Φ_{ani} = 27.43

Figure 4: 2-D anisotropic inversion of noisy synthetic data generated by a model with a square anisotropic box ($\varrho_1 = \varrho_3 = 10$ Ωm, $\varrho_2 = 10$ Ωm, $\alpha_S = 30°$) embedded in a homogeneous halfspace ($\varrho_{\text{host}} = 300$ Ωm) for different structure and anisotropy penalty weights. For detailed description of the model sections, see caption to Fig. 3. The table in the bottom left panel summarizes the structure and anisotropy penalties of the resulting models as well as their RMS's. Models with RMS > 1.5 are grayed.

3.1.3 Isotropic Anomaly

Another important test consists in checking any spurious anisotropy produced by the anisotropic inversion if data due to an isotropic structure are inverted. We consider the same 2-D box model as above but

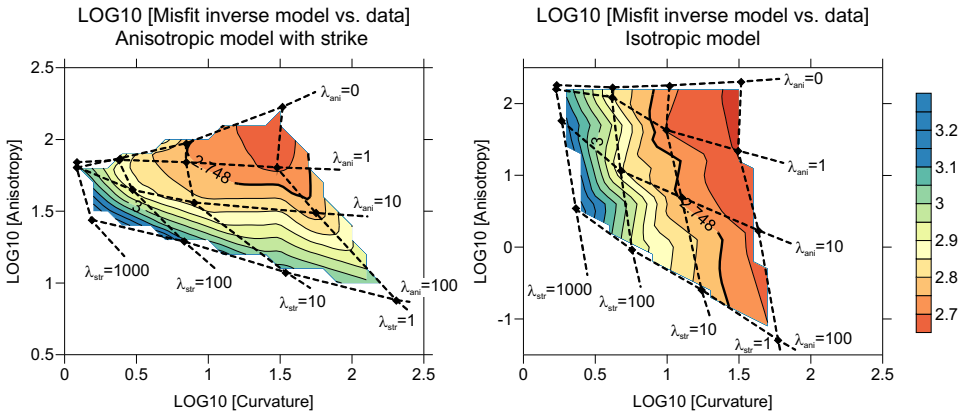

Figure 5: Regularization L-surfaces for the inversion of an anisotropic box data (left plot) and for its isotropic version (right). The dashed lines connect model points with the same structure and anisotropy penalty weights. The bold isoline marks a misfit contour of 760 which corresponds to the RMS = 1.000.

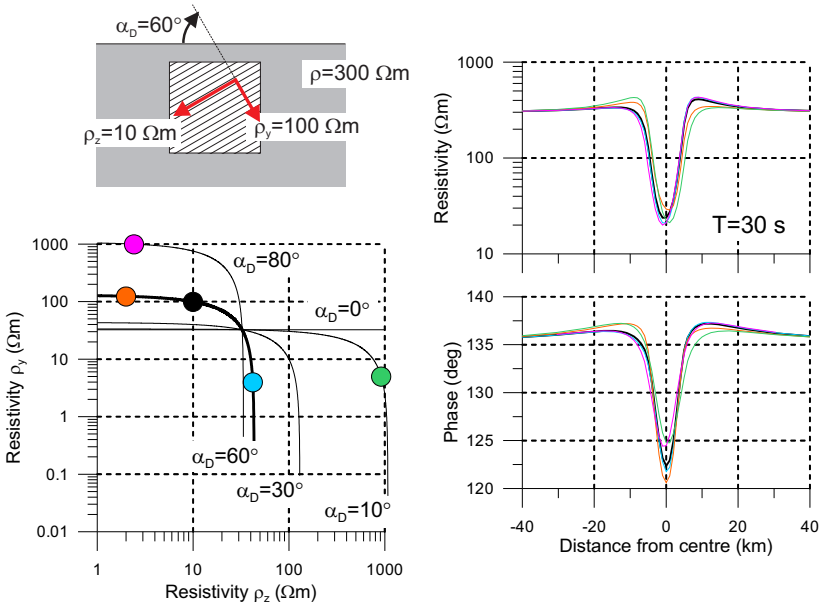

Figure 6: 2-D box model with dipping anisotropy (top left panel) and MT apparent resistivity and phase curves for a series of models with various principal resistivities ϱ_y, ϱ_z and anisotropy dips α_D which would be exactly equivalent in 1-D case (right panels). The bottom left panel shows lines of pairs of the resistivities ϱ_y, ϱ_z which are equivalent for indicated dips α_D in 1-D case. The colored circles correspond to anisotropy parameters which produced the 2-D MT curves in the right panels.

with an isotropic anomaly with $\varrho_{\text{iso}} = 10$ Ωm. The top panel in Fig. 8 shows models provided by a standard isotropic inversion for several structure penalty weights. The same inversion runs were then carried out for three principal resistivities aligned with the model coordinate frame. The anisotropy angles were omitted here since no reason existed to include them for data which did not contain any significant diagonal impedance elements. Results of the anisotropic inversion are displayed in the bottom panel of Fig. 8. Clearly a superior result is obtained with $\lambda_s = 100$ and $\lambda_a = 10$, though the data are

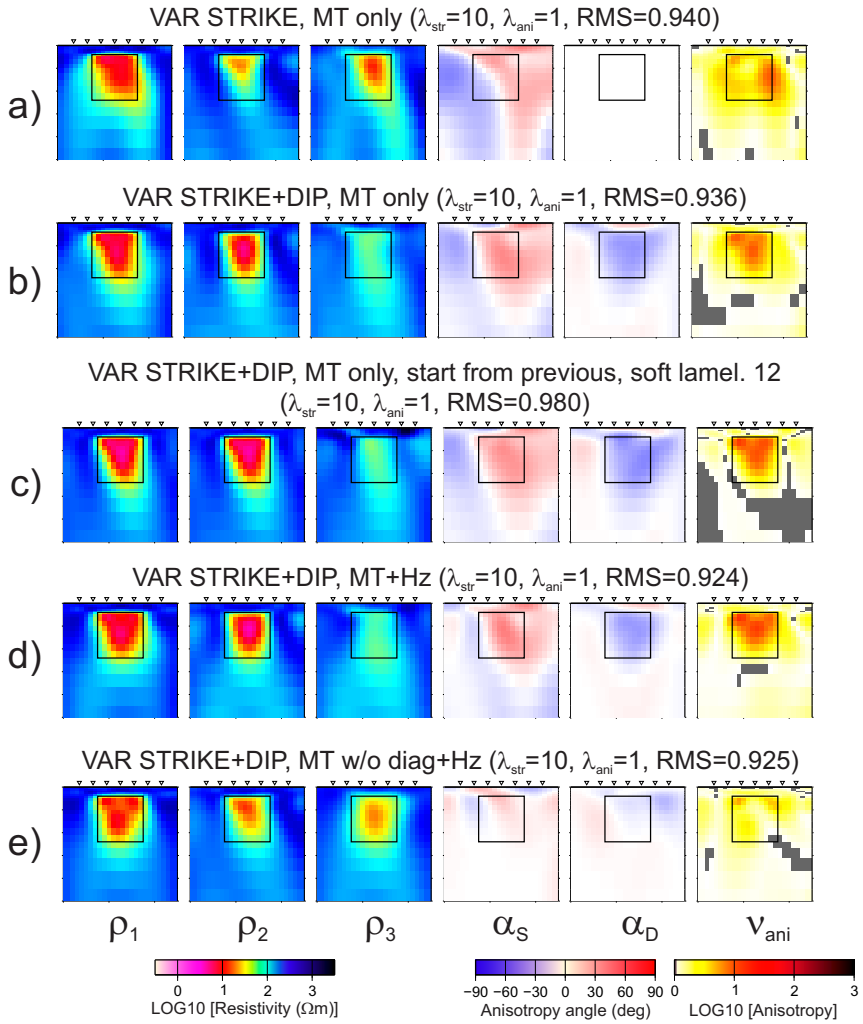

Figure 7: 2-D anisotropic inversion of synthetic MT data generated by the model with dipping anisotropy from Fig. 6. a) Inversion of MT impedances for three principal resistivities and anisotropy strike; dip is fixed at $\alpha_D = 0°$. b) Inversion of MT impedances for three principal resistivities and anisotropy strike and dip. c) The same as b) but with a soft constraint applied to minimize the difference between the resistivities ϱ_1 and ϱ_2 (forced lamelarity of anisotropic domains). d) The same as b) but the inverted data set was extended by vertical geomagnetic transfer functions (induction arrows). e) The same as d) with diagonal impedances left out from the inverted data set.

slightly underfitted in this case (RMS = 1.130). With smaller structure and zero anisotropy penalties, we observe both considerable spurious anisotropy as well as structural instability. For large penalties, new spurious anisotropy may appear due to the fact that the yx MT curves (H-mode) can be fitted satisfactorily with less conductivity (i.e., with less structure) than the xy (E-mode) curves. The vertical resistivity, ϱ_3, evidently gives the most variable images due to the low sensitivity of the MT fields with respect to this paramter.

The L-surface for this synthetic test is shown in the right-hand side panel in Fig. 5. The shape of this surface is slightly different from that for the anisotropic case studied earlier. As we cannot worsen the model complexity and data misfit by strengthening the anisotropy penalty applied to isotropic data, the L-surface does not show a target increase for large anisotropy penalties as it is the case for anisotropic data.

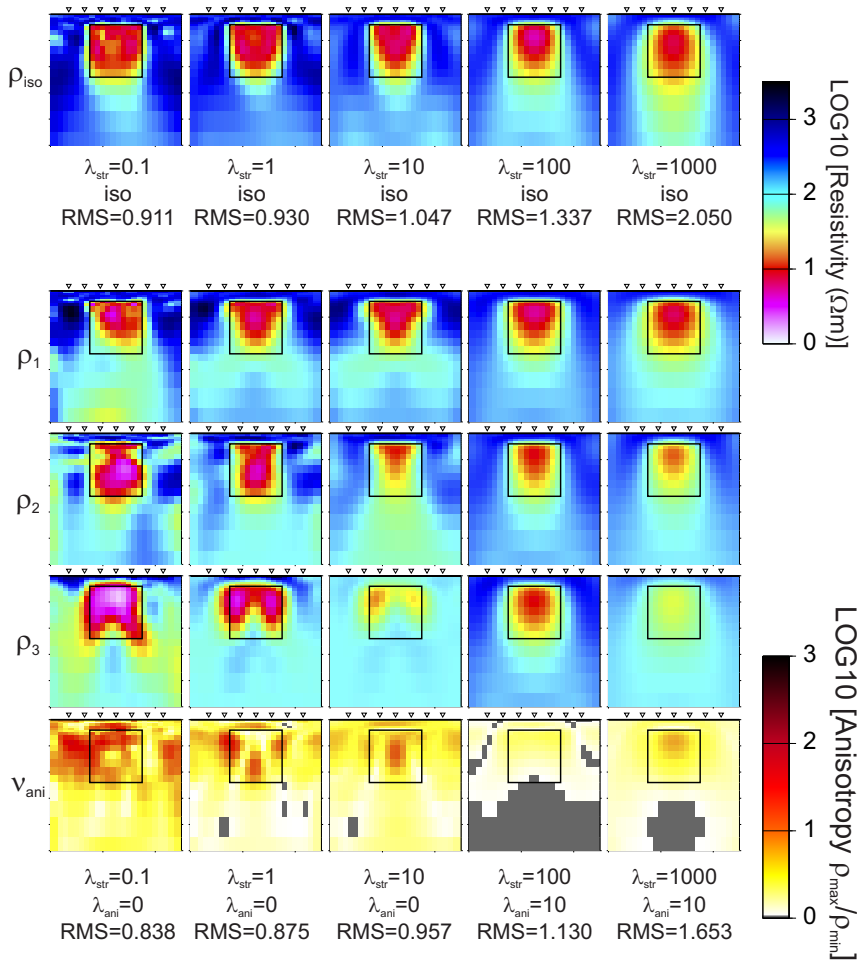

Figure 8: Top: Isotropic inversion for isotropic conductivity in a square box anomaly for several structural penalties. Bottom: Anisotropic inversion for three principal resistivities aligned with the model coordinate frame for the same data as above for several pairs of structure and anisotropy penalties.

3.2 Near-Surface Anisotropic Distorter above a Discordant Anisotropic Layer

A special class of anisotropic models are structures with highly anisotropic, near-surface bodies which act as strong MT distorters by virtue of chanelling the telluric currents in a direction generally oblique with respect to the structural strike. Such distortions may even result in MT phases rolling out of their natural quadrant (Pek, 2009), and may be a source of convergency difficulties for the NLCG inversion procedure. Here we only briefly visit a synthetic test for MT data generated by a model consisting of a near-surface, highly anisotropic block ($\varrho_1 = \varrho_3 = 1$ Ωm, $\varrho_2 = 100$ Ωm, $\alpha_s = 20°$) in the uppermost crust underlain by a mid- to lower-crustal layer with increasing anisotropy from the left to the right and discordant anisotropy strike, $\alpha_S = -20°$. Complete parameters of the model are shown in the bottom right panel in Fig. 9. The model produces the out-of-quadrant phases but only for rotated data, not in the model coordinate frame.

The inversion was run for all three principal resistivities and for the anisotropy strike. The size of the inverse problem was: 950 model cells, 3800 model parameters, 1440 data items. Results of the inversion are shown in Fig. 9 for the regularization weights $\lambda_s = 10$, $\lambda_a = 3$. RMS of the final model is 1.060. The inverse model captures the true structure satisfactorily, especially parameters of the near surface distoring body. The resistive part of the deep layer to the left is shifted towards the surface but its anisotropy to the right is recovered well both as to the size and geometrical position. The part of the layer immediately

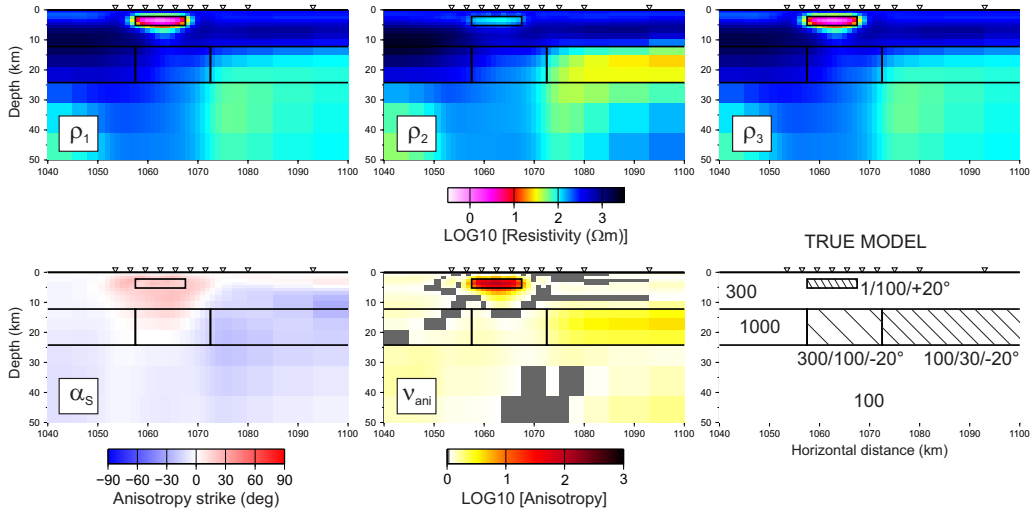

Figure 9: Inversion of noisy synthetic MT data generated by a model of a shallow, strongly anisotropic anomaly and a layer of moderate anisotropy increasing from the left to the right beneath the anomalous block. The panels show the principal resistivities (ϱ_1, ϱ_2, ϱ_3, top panels), anisotropy strike and anisotropy ratio (α_S, ν_{ani}, bottom panels) recovered by the inversion. The bottom rightmost panel shows the geometry and parameters of the data generating (true) model, resistivities are given in Ωm. The regularization weights used are $\lambda_s = 10$, $\lambda_a = 3$. The inverse model's RMS is 1.060.

beneath the distorter is not sensed properly, which could be expected.

This model test presents an exercise with a more complex anisotropic structure, which could be recovered sufficiently well by the NLCG inverse procedure. For this kind of models with mixed anisotropy strikes one open question still remains, specifically that of misdetermined structural strikes for the 2-D modeling.

4 Field Data: MT Data from Southern Portugal

In our previous paper on the 1-D MT inversion for anisotropic media, we tested the developed method on practical data from southern Portugal, from the transition of two southernmost prominent zones of the Iberian Variscides, the Southern Portuguese Zone (SPZ) and the Ossa Morena Zone (OMZ) (Pek and Santos, 2006). A long and narrow belt of mafic and ultramafic rocks lines up at the border between these zones. Those rocks are currently interpreted as an ophiolite complex (Badajoz Acebuches Ophiolite Complex, BAOC). In the Portuguese mainland the BAOC represents the southern border of the Beja Igneous Complex (BIC) deformed in the vicinity of the Ferreira-Ficalho thrust (Figueiras *et al.*, 2002). Without further repeating the geological background of the area, detailed in (Pek and Santos, 2006), it has been concluded that the geological context of the study area is greatly favourable to the presence of anisotropic structures at upper to middle crust depths. References to the presence of anisotropic black schists in south Iberia, as well as to the anisotropic behaviour of MT data can be found in (Pous *et al.*, 2004).

Pek and Santos (2006) modeled a small subset of data from a large-scale broad-band MT experiment in southern Portugal (Almeida *et al.*, 2001) which crosses the contact area between the SPZ and OMZ. They used a 1-D inversion procedure for anisotropic structures and 2-D trial-and-error forward modeling to fit the MT impedances. Though excellent fit was achieved earlier by 2-D inverting the principal MT curves, some specific features in the data suggested that non-negligible non-2-D effects influence the MT field, especially those related to the diagonal impedance elements (Pek and Santos, 2006). Anisotropy was adopted as a possible mechanism for explaining the non-2-D features in the data, though other reasons cannot be excluded either, particularly static distortions or off-profile 3-D effects.

Without attempting any deeper interpretation of the above MT data, we only want to demonstrate here how the trial-and-error modeling by Pak and Santos (2006) compares with results of the 2-D anisotropic

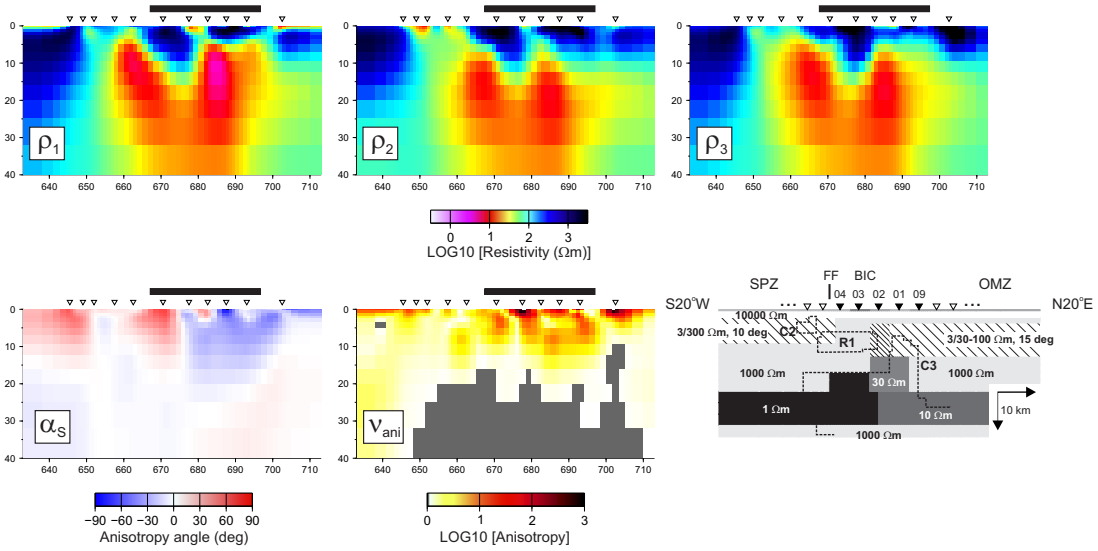

Figure 10: Inverse 2-D anisotropic model from a subset of MT data across the contact area between the SPZ and OMZ, southern Portugal. The model was obtained with regulariztion penalty weights $\lambda_s = 300$, $\lambda_a = 100$. The size of the model was: 1701 model cells, 8505 model parameters, 792 data items. The bottom right panel repeats the model obtained by a combined 1-D anisotropic inversion and 2-D trial-and-error forward modeling by Pek and Santos (2006). The black lines above the plots indicate the section of the profile which was modeled in the paper by Pek and Santos (2006) (sites 04, 03, 02, 01, 09 in the original model). See the text for the acronyms.

inversion of the same data subset. We present one of the inverse anisotropic models in Fig. 10. All three principal resistivities, anisotropy strike and dip were inverted in this case. A significant dip was detected only in the conductive channel between two resistors in the central part of the profile which may indicate vertical current channeling in this zone. In other domains of the model, the dip is featureless, and therefore is not displayed in Fig. 10.

The interpreted principal resistivities in Fig. 10 are very similar to each other, and we would rather conclude that the underlying structure is isotropic. The main structures revealed by the inversion do coincide well with the results of the isotropic inversion by Almeida *et al.* (2001), which are indicated in the bottom left model in Fig. 10 by dashed contours labeled C2, R1, C3. Only the localized conductor C2 by Almeida *et al.* (2001) is substantially larger in our model and interconnected with deep crustal conductors. This can be explained by the structure being oversmoothed due to large structural penalty imposed ($\lambda_s = 300$). In fact, this conductor becomes more focused if the structure penalty is relaxed, but for the price of unrealistically increased anisotropy in other parts of the model.

Effect of the anisotropy in the model is mainly seen in improved fit to the secondary, diagonal impedances, which are non-symmetric ($Z_{xx} + Z_{yy} \neq 0$) and cannot be thus explained in terms of a purely 2-D model. Similarly as in the trial-and-error result, the anisotropy is practically completely concentrated in the first 10 km layer of the model. A strong anisotropic feature is observed beneath the BIC and seems to represent a sub-vertical current channel because of $\varrho_1 \approx \varrho_2 \ll \varrho_3$ and a large dip in this zone. The originally strongly anisotropic continuous layer modeled beneath the SPZ in the SW of the profile is not necessarily supported by the new 2-D model, and may occur due to a strong effect of the conductor C2. The moderately anisotropic layer beneath the OMZ in the NE part of the profile does appear in the inverse model in the basement of the continuous crustal resistor. The anisotropy strike in this layer is, however, of opposite sign in comparison with the original model. Some of the very shallow anisotropy is likely to be due to static distortions in the MT curves which could not be removed completely, especially from the diagonal impedances. Interference of the static shifts with anisotropy is one of the questions still open to further investigations.

5 Conclusion

We presented an algorithm for the 2-D inversion of magnetotelluric data for conductivity distributions with arbitrary anisotropy. The inversion is based on a Polak-Ribière version of the NLCG algorithm with a simple Jacobi pre-conditioning, and is the same procedure as Rodi and Mackie's (2001) technique used for isotropic inversion. We tried to show all the algorithmic issues of the anisotropic inversion and demonstrate all of them working together. Though the synthetic tests carried out in this contribution were only very simple, they could demonstrate basic features of the anisotropic inversion as well as an overview of ambiguities and quasi-equivalencies that may appear at interpreting anisotropic models. Though the most significant ambiguity issues known from 1-D magnetotellurics (sensitivity w.r.t. the vertical conductivity, ambiguities for dipping anisotropies) cannot be theoretically justified in 2-D structures, they are manifested in practice by poor resolution and by quasi-equivalencies of certain model parameters in 2-D anisotropic sections. This situation as well as missing theoretical results cause that a lot more weight is put on numerical experiments and tests in 2-D MT situations.

As regards the outputs of the synthetic tests, we could arrive at following conclusions: (i) similarly as in the 1-D case, the most reliable inversion results are obtained for structures with azimuthal anisotropy, (ii) vertical resistivity is almost indistinguishable in 2-D models though it cannot be omitted completely because of its irreplaceable role in the forward modeling step; forcing lamelar or tubular anisotropy may be a baypass for coping with the unresolved vertical conductivity, (iii) similarly as in 1-D MT case, anisotropy dip is an unresolvable parameter unless additional structural information is available; effect of the true dip increases if anisotropy strike increases (i.e., if lamelas dip in the direction close to the structural strike); if false dip is fixed in the inverse procedure in such a case, the recovered anisotropy strike may be not correct, (iv) care must be taken if resistivities from dipping structures are interpreted; the resistivities may be not correct due to the action of the structure/anisotropy penalties.

With regard to practical data, we could arrive to a satisfactory fit of the experimental data in a few cases. Nevertheless, verifying the models cannot be based on the MT fit alone, and will require additional support from other geodata. Moreover, a number of more or less algorithmic questions remains still open, e.g., (i) how much do static distortions and 3-D off-profile effects in MT data interfere with 2-D anisotropic interpretations, (ii) how much significant is a correct determination of the 2-D structural strike for the 2-D anisotropic inversion if varying or mixed anisotropy strikes mask the true structural axis of homogeneity, (iii) how oblique anisotropies are interpreted by the 2-D inversion, especially those producing out-of-quadrant anomalous MT phases.

Acknowledgements

Financial support of the Czech Sci. Found. to this work, under contract No. P210-10-2227, is highly acknowledged.

References

Almeida, E., Pous, J., Monteiro Santos, F., Fonseca, P., Marcuello, A., Queralt, P., Nolasco, R., and Mendes-Victor, L.: Electromagnetic imaging of a transpressional tectonics in SW Iberia. *Geophys. Res. Lett.*, **28** (2001), 439–442.

Andrei, N.: 40 conjugate gradient algorithms for unconstrained optimization. A survey on their definition. *ICI Technical Report* No. 13/08, March 14, 2008.

Bahr, K., and Simpson, F.: Electrical anisotropy below slow- and fast-moving plates: Paleoflow in the upper mantle? *Science*, **295** (2002), 1270–1272.

Bertsekas, D. P., and Bertsekas, D. P.: *Nonlinear Programing*. Athena Scientific, 2nd edition, 1999, 794 pp.

Brasse, H., Kapinos, G., Li, Y., Mütschard, L., Soyer, W., and Eydam, D.: Structural electrical anisotropy in the crust at the South-Central Chilean continental margin as inferred from geomagnetic transfer functions. *Phys. Earth Planet. Inter.*, **173** (2009), doi:10.1016/j.pepi.2008.10.017.

Constable, S. C., Parker, R. L., and Constable, C. G.: Occam's inversion: a practical algorithm for generating smooth models from EM sounding data. *Geophysics*, **52** (1987), 289–300.

Červ, V., and Pek, J.: Numerical solution of the two-dimensional geomagnetic induction problem. *Studia geoph. et geod.* (1981), **25**, 69–80.

Davydycheva, S., Druskin, V., and Habashy, T.: An efficient finite-difference scheme for electromagnetic logging in 3D anisotropic inhomogeneous media. *Geophysics*, **68** (2003), 1525–1536.

deGroot-Hedlin, C., and Constable, S. C.: Occam's inversion to generate smooth, two-dimensional models from magnetotelluric data. *Geophysics*, **55** (1990), 1613–1624.

Eisel, M., and Haak, V.: Macro-anisotropy of the electrical conductivity of the crust: A magnetotelluric study from the German Continental Deep Drilling site (KTB). *Geophys. J. Int.*, **136** (1999), 109–122.

Eisel, M., Haak, V., Pek, J., and Červ, V.: A magnetotelluric profile across the German Deep Drilling Project (KTB) area: Two- and three-dimensional modeling results. *J. Geophys. Res.*, **106** [B8] (2001), 16061–16073.

Figueiras, J., Mateus, A., Gonalves, M.A., Waerenbourgh, J., and Fonseca, P.: Geodynamic evolution of the South Variscan Iberian Suture as recorded by mineral transformations. *Geodinamica Acta*, **15** (2002), 45–61.

Hamilton, M. P., Jones, A. G., Evans, R. L., Evans, S., Fourie, C. J. S., Garcia, X., Mountford, A., Spratt, J. E., and the SAMTEX Team: Electrical anisotropy of South African lithosphere compared with seismic anisotropy from shear-wave splitting analyses. *Phys. Earth Planet. Inter.*, **158** (2006), 226–239.

Heise, W., and Pous, J.: Anomalous phases exceeding 90° in magnetotellurics: Anisotropic model studies and a field example. *Geophys. J. Int.*, **155** (2003), 308–318.

Hou, J., Mallan, R. K., and Torres-Verdn, C.: Finite-difference simulation of borehole EM measurements in 3D anisotropic media using coupled scalar-vector potentials. *Geophysics*, **71** (2006), G225–G233.

Jupp, D. L. B., and Vozoff, K.: Two-dimensional magnetotelluric inversion. *Geophys. J. Roy. Astr. Soc.*, **50** (1977), 333–352.

Lezaeta, P., and Haak, V.: Beyond magnetotelluric decomposition: Induction, current channeling, and magnetotelluric phases over 90 degrees. *J. Geophys. Res.–SE*, **108** (2003), Art. No. 2305.

Li, Y.: A finite-element algorithm for electromagnetic induction in two-dimensional anisotropic conductivity structures. *Geophys. J. Int.*, **148** (2002), 389–401.

Li, Y., Pek, J., and Brasse, H.: Magnetotelluric inversion for 2D anisotropic conductivity structures. In Hoerdt, A., and Stoll, J. B., Eds., *Proceed. 20th Colloq. "Electromagnetic Depth Investigations"*, Königstein, 29. 9.–3. 10. 2003, DGG, pp. 250–259.

Li, Y., and Pek, J.: Adaptive finite element modelling of two-dimensional magnetotelluric fields in general anisotropic media. *Geophys. J. Int.*, **175** (2008), 942–954.

Mareschal, M., Kellett, R. L., Kurtz, R. D., Ludden, J. N., Ji, S., and Bailey, R. C.: Archean cratonic roots, mantle shear zones and deep electrical anisotropy. *Nature*, **375** (1995), 134–137.

Newman, G. A., and Alumbaugh, D. L.: Three-dimensional magnetotelluric inversion using non-linear conjugate gradients. *Geophys. J. Int.*, **140** (2000), 410–424.

Newman, G. A., and Boggs, P. T.: Solution accelerators for large-scale three-dimensional electromagnetic inverse problems. *Inverse Problems*, **20** (2004), S151–S170.

Padilha, A. L., Vitorello, I., Pádua, M. B., and Bologna, M. S.: Lithospheric and sublithospheric anisotropy beneath central-southeastern Brazil constrained by long period magnetotelluric data. *Phys. Earth Planet. Inter.*, **158** (2006). 190-209.

Pain, C., Herwanger, J. V., Saunders, J. H., Worthington, M. H., and Oliveora, C. R. E.: Anisotropic resistivity inversion. *Inverse Problems*, **19**, 1081–1111.

Pek J., and Verner, T.: Finite-difference modelling of magnetotelluric fields in two-dimensional anisotropic media. *Geophys. J. Int.*, **128** (1997), 505–521.

Pek, J., and Santos, F. A. M.: Magnetotelluric impedances and parametric sensitivites for 1-D generally anisotropic layered media. *Computers & Geosciences*, **28** (2002), 939–950.

Pek, J., Santos, F. A. M., and Li, Y.: Parametric sensitivities for 2-D anisotropic magnetotelluric model.

In Hoerdt, A., and Stoll, J. B., Eds., *Proceed. 20th Colloq. "Electromagnetic Depth Investigations"*, Königstein, 29. 9.–3. 10. 2003, DGG, pp. 240–249.

Pek, J., and Santos, F. A. M.: Magnetotelluric inversion for anisotropic conductivities in layered media. *Phys. Earth Planet. Inter.*, **158** (2006), 139–158.

Pek, J.: Effects of electrical anisotropy on magnetotelluric data: modelling and experiments. In *Modern methods of electromagnetic data measurement, processing and interpretation* (pp. 110–135), V. V. Spichak (Ed.), LIBROKOM Publ., Moscow 2009, 304 pp. (in Russian).

Pous, J., Munoz, G., Heise, W., Melgarejo, J.C., and Quesada, C.: Electromagnetic imaging of Variscan crustal structures in SW Iberia: the role of interconneted graphite. *Earth Planet. Sci. Lett.*, **217** (2004), 435–450.

Press, W. H., Flannery, B. P., Teukolsky, S. A., and Vetterling, W. T.: *Numerical recipes: the art of scientific computing*. Cambridge University Press, NY, USA, 1986.

Ramananjaona, C., and MacGregor, L.: 2.5D inversion of CSEM data in a vertically anisotropic earth. *J. Phys.: Conf. Ser.*, **255** (2010), doi:10.1088/1742-6596/255/1/012004.

Reddy, I. K., and Rankin, D.: Magnetotelluric response of laterally inhomogeneous and anisotropic media. *Geophysics*, **40** (1975), 1035–1045.

Rodi, W. L.: A technique for improving the accuracy of finite element solutions for magnetotelluric data. *Geophys. J. Roy. Astr. Soc.*, **44** (1976), 483-506.

Rodi, W., and Mackie, R. L.: Nonlinear conjugate gradients algorithm for 2-D magnetotelluric inversion. *Geophysics*, **66** (2001), DOI:10.1190/1.1444893.

Roux, E., Moorkamp, M., Jones, A. G., Bischoff, M., Endrun, B., Lebedev, S., and Meier, T.: Joint inversion of long-period magnetotelluric data and surface-wave dispersion curves for anisotropic structure: Application to data from Central Germany. *Geophys. Res. Lett.*, doi:10.1029/2010GL046358

Ruiz-Constán, A., Galindo-Zaldivar, J., Pedrera, A., Arzate, J. A., Pous, J., Anahnah, F., Heise, W., Monteiro Santos, F. A., and Marín-Lechado, C.: Deep deformation pattern from electrical anisotropy in an arched orogen (Betic Cordillera, western Mediterranean). *Geology*, **38** (2010), 731–734.

Simpson, F.: Resistance to mantle flow inferred from the electromagnetic strike of the Australian upper mantle. *Nature*, **412** (2001), 632–635.

Tikhonov, A. N., and Arsenin, V. Y.: *Solution of ill-posed problems*. Winston and Sons, 1977, 285 pp.

Wang, T., and Fang, S.: 3-D electromagnetic anisotropy modeling using finite differences. *Geophysics*, **66** (2001), 1386–1398.

Wannamaker, P. E.: Anisotropy versus heterogeneity in continental solid earth electromagnetic studies: fundamental response characteristics and implications for physicochemical state. *Surv. Geophys.*, **26** (2005), 733-765.

Weaver, J. T., Le Quang, V. B., and Fischer, G.: A comparison of analytical and numerical results for a two-dimensional control model in electromagnetic induction - I. B-polarization calculations. *Geophys. J. R. astr. Soc.*, **82** (1985), 263–278.

Weaver, J. T., Le Quang, V. B., and Fischer, G.:, 1986. A comparison of analytical and numerical results for a 2 D control model in electromagnetic induction - II. E-polarization calculations. *Geophys. J. R. astr. Soc.*, **87** (1986), 917–948.

Weckmann, U., Ritter, O., and Haak, V.: A magnetotelluric study of the Damara Belt in Namibia. 2. MT phases over 90 degrees reveal the internal structure of the Waterberg Fault/Omaruru Lineament. *Phys. Earth Planet. Inter.*, **138** (2003), 91–112.

Weidelt, P.: 3-D conductivity models: Implications of electrical anisotropy. In Oristaglio, M., and B. Spies, Eds., *Three-dimensional electromagnetics*, Geophys. Dev. Series, 7, Soc. Explor. Geophys., Tulsa, OK, 119–137, 1999.

Weiss, C. J., and Newman, G. A.: Electromagnetic induction in a fully 3-D anisotropic earth. *Geophysics*, **67** (2002), 1104–1114.

Zaslavsky, M., Druskin, V., Davydycheva, S., Knizhnerman, L., Abubakar, A., and Habashy, T.: Hybrid finite-difference integral equation solver for 3D frequency domain anisotropic electromagnetic problems. *Geophysics*, **76** F123 (2011), DOI:10.1190/1.3552595.

Maximum resolution of conductivity structures in Magnetotellurics

Annika Rödder, Andreas Junge

Institute of Geosciences, Department of Geophysics,
Goethe-University Frankfurt, Germany
contact: roedder@geophysik.uni-frankfurt.de

Introduction

In Magnetotellurics (MT) the model resolution depends on the depth of the anomaly, the period and the conductivity distribution. Often it is difficult to resolve structures smaller than the skindepth, but sometimes it is even difficult to resolve larger structures. Therefore we investigated the maximum resolution for depth and for lateral directions. Inspired by the checkerboard test used in seismic inversions [*Lévěque et al.* 1993] we calculated 2D models with periodic lateral resistivity contrasts. Then the model responses are also periodic. Thus a spatial Fourier transformation of the response functions should reveal a significant peak in the Fourier spectrum at the wavelength of the lateral anomalies. All models for this study were calculated with *COMSOL Mulitphysics 4.2*.

Modeling

The anomalous resistivity structure $\rho_{mod}(x, z)$ is shown in Fig.1 according to

$$\rho_{mod} \propto \frac{(1 + cos(x \cdot k_x))}{2} \text{ for } z_{min} \leq z \leq z_{max}, \quad (1)$$

with profile position x and wavenumber $k_x = 2\pi/\lambda$ and wavelength λ (anomaly-width). The depth z of upper anomaly boundary is z_{min} and z_{max} marks the lower boundery.
Both the anomaly-width λ (see upper and lower plots in Fig.1) and the thickness d of the anomaly are varied. For $\lambda = 20km$ the anomaly's upper boundary was fixed at$12km$, $8km$ and $4km$ depth, for $\lambda = 50km$ it started in $40km$ depth and was shifted by steps of $5km$ up to a depth of $5km$. Magnetotelluric transfer functions for the TE- and TM-mode were calculated along the profile at the surface with a sampling rate of 5km for a period range of $0.1s$ to $1000s$. The profilelength was eight times the anomaly-width. If the structure is resolved well for a given period, it is possible to identify the oszillation of the amplitudes of the apparent resistivity $\rho_a(x)$ and phases $\Phi(x)$ along the profile. This variation has

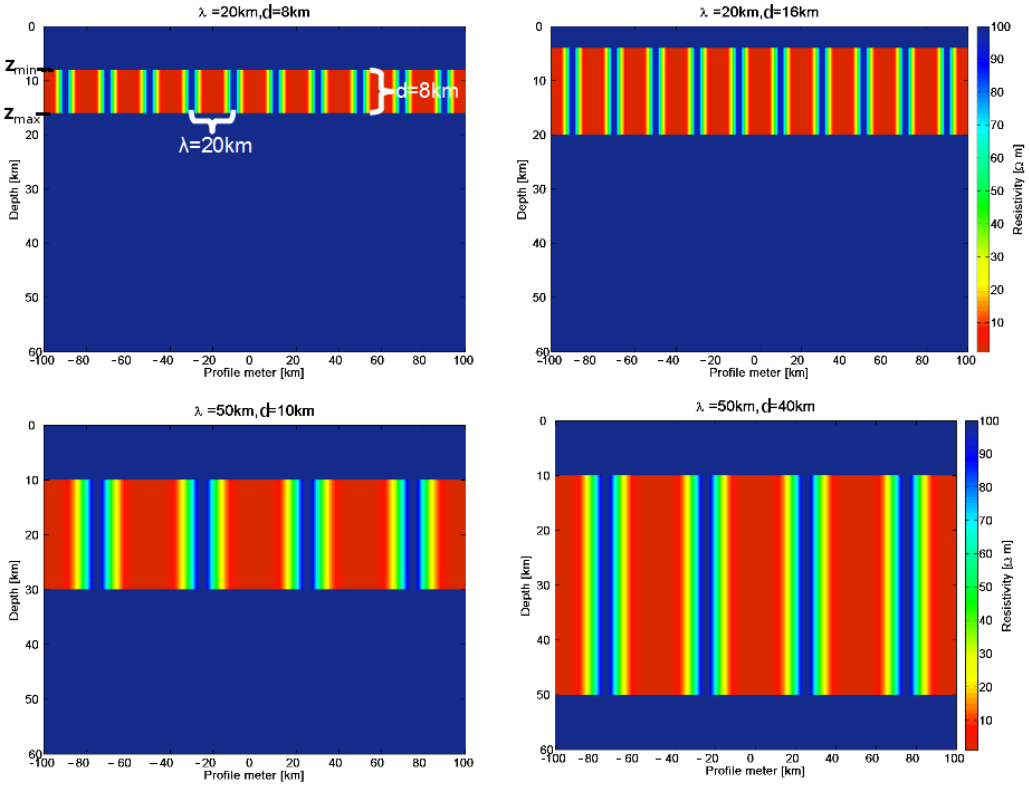

Figure 1: *Four models with different resistivity structures depending on the anomaly-width λ, the anomaly-depth z_{min} and the thickness d. The background resistivity is $100\Omega m$. Resistivities vary between the background resistivity (blue) and $1\Omega m$ (red). Their size and position is calculated via eq.1. a) $\lambda = 20km$, $d = 8km$, $z_{min} = 8km$; b) $\lambda = 20km$, $d = 16km$, $z_{min} = 4km$; c) $\lambda = 50km$, $d = 10km$, $z_{min} = 10km$; d) $\lambda = 50km$, $d = 45km$, $z_{min} = 10km$.*

the same period as that of the anomaly structure. Spatial Fourier transformations of $\rho_a(x)$ and $\Phi(x)$ were calculated for each period. The Fourier coefficients are sensitive even to very small periodic signals. If this method is not able to detect the periodic structure anymore, a smaller anomaly with the same parameters and bounded lateral extension will neither be resolved. The amplitude of the Fourier spectrum is picked directly as the anomaly period is known. Furthermore, the signal-to-noise-ratio (s/n) is calculated. The noise level was calculated from the background spectrum omitting the anomaly's peak. If the (s/n) is equal or less than one, structures cannot be resolved.

Results

As the resistivity structure influences the phases stronger than the apparent resistivities, only the results of the phases are shown (Fig. 2-4). The upper plots represent the TE-mode, the lower plots the TM-mode. The left part shows the amplitudes of the anomalous peak, the right part shows the logarithm of the signal-to-noise-ratio.
In Fig.2 the anomaly-width is $\lambda = 20km$ and the period is $1s$ in Fig. 2a) and $1000s$ in Fig. 2b). The models are calculated for anomaly-thicknesses $8km$, $12km$ and $16km$ and for depths of $4km$, $8km$ and $12km$. For the period of $1s$ the anomalous phases in $-4km$ depth are $3°$ for the TE-mode and $4-4.5°$ in the TM-mode. The (s/n) values vary between $3-8$ in TE- to $10-16$ in TM-mode. For greater depth the values approximates one for the phases and the signal-noise-ratios. This effect is independent of the anomaly thickness.

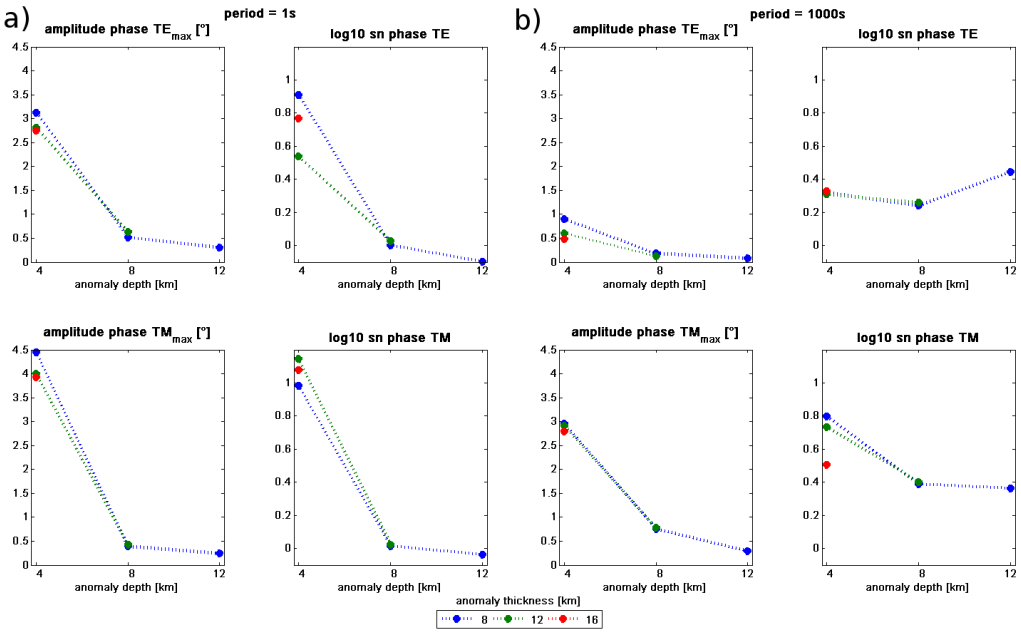

Figure 2: *Amplitudes and $log_{10}(s/n)$ of the phases of TE-(top) and TM-mode (bottom). The anomaly-width was $\lambda = 20km$, the depth of the upper anomaly-boundary was varied between $4km$, $8km$ and $12km$ depth (x-axis). The color refers to the anomaly-thickness.* ***Fig. 2a)*** *shows the model results for the period of $1s$,* ***Fig. 2b)*** *shows the results for a period of $1000s$. Highest amplitudes ($3°$-$4°$) are achieved for the lowest anomaly-depth for the period of $1s$, but do not depend on the thickness of the structure. In this case the (s/n) varies between 3 and 15 for the lowest depth and decreases to one. For $1000s$ the maximum amplitudes vary between $0.5°$ and $0.9°$ for the TE-mode and are around $3°$ in the TM-mode. For deeper anomalies the amplitude decreases. The s/n ratio for all combinations is smaller than for a periode of $1s$, but in this case it does not decrease to one but stays on level of 1.7 to 2.8 which indicates a better resolution for greater depths (as expected for a higher period).*

The right part of Fig.2 shows the results for the same model but for a period of $1000s$. Here the phases show the same behavior as for $1s$. The highest phases of $0.5 - 0.9°$ for TE- and $2.7 - 3°$ for TM-mode occur for the shallow depth of $4km$ whereas for greater depths the values decrease to zero. Regarding the signal-to-noise-ratio, the general behavior is not the same as for the smaller period. Although the maximum values are lower than those for $1s$, they keep a constant level of 1.8 to 2.8 instead of decreasing to one.

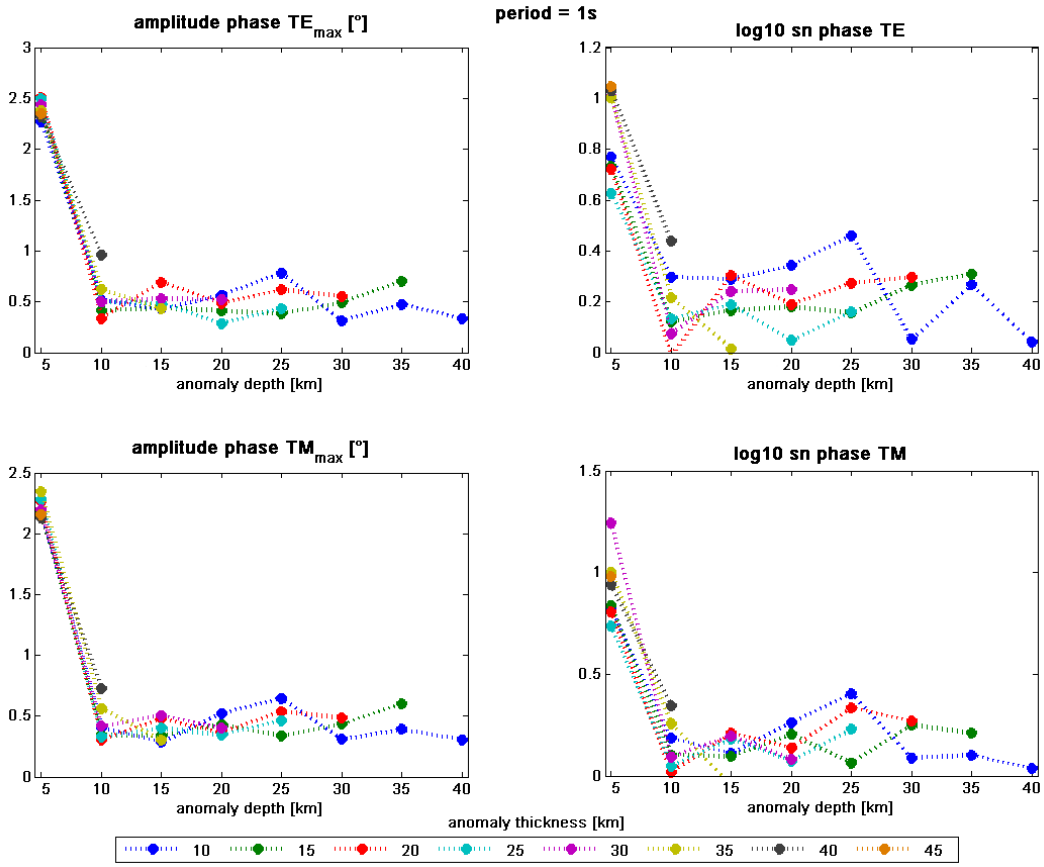

Figure 3: *Amplitudes (left) and $log_{10}(s/n)$ (right) of the phases of TE-(top) and TM-mode (bottom) for a period of $1s$ and the anomaly-width of $\lambda = 50km$. The anomaly-depth is plotted on the x-axis and varies from $5km$ in steps of $5km$ up to $40km$ depth. The anomaly-thickness varies between $10km$ and $45km$ also in steps of $5km$. As for the smaller λ in Fig.2 there are only high amplitudes and (s/n) values for the smallest depth and afterwards they decrease for all thicknesses.*

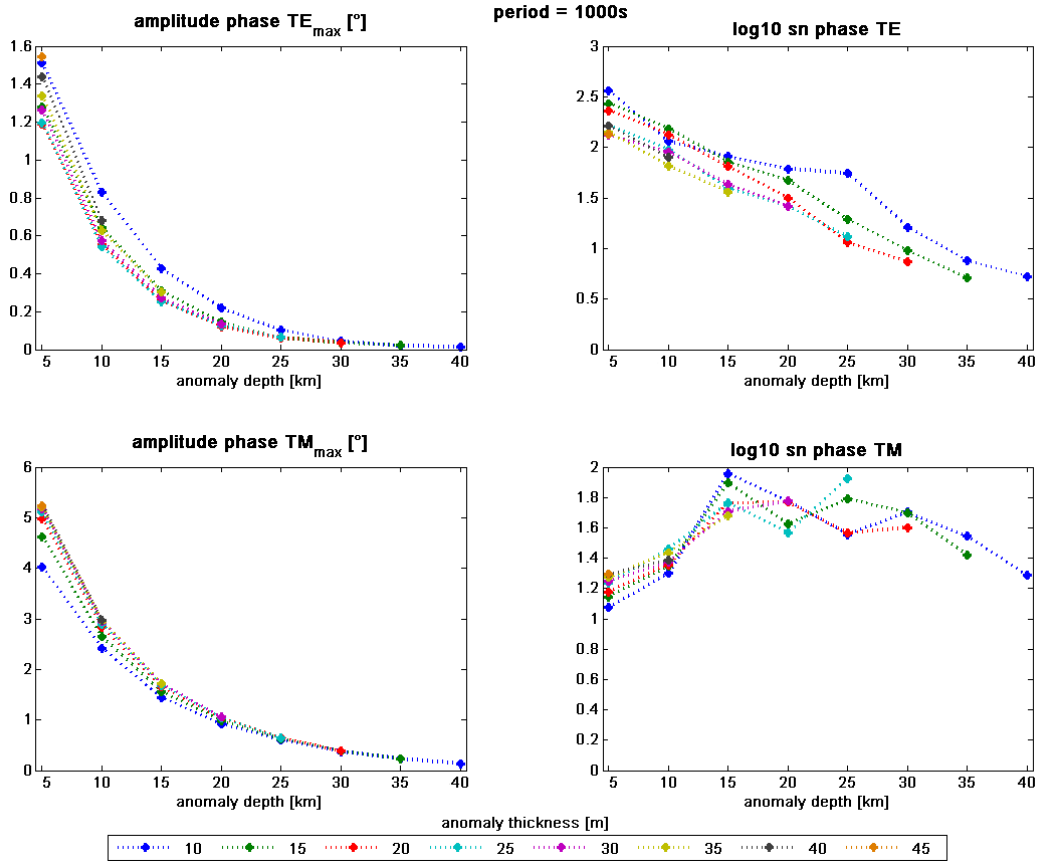

Figure 4: *Amplitudes (left) and* $\log_{10}(s/n)$ *(right) of the phases of TE-and TM-mode for a period of* $1000s$*. The models are the same as described in Fig.3. The maximum amplitudes for the TE-mode are* $1.2-1.6°$ *and for TM-mode* $4-5°$*. The* (s/n) *decreases from* $100-300$ *to* 4 *for the greatest depth in TE-mode. In TM-mode the* (s/n) *starts at* $10-20$ *for the smallest depth, has its maximum at* $15km$ *depth with* $40-100$ *and varies for greater depths between* 25 *and* 60*.*

The second example shown here is a model with the anomaly-width of $\lambda = 50km$. The anomaly-depth varies from $5km$ to $40km$ in steps of $5km$. The anomaly-thickness also varies in the same steps but starting with $10km$ up to $45km$. Fig.3 shows the results for a period of $1s$. As in Fig.2 the highest values occur for the lowest depth with 2°-2.5° for the phases and $4-16$ for the signal-noise-ratio. For greater depth those values decrease close to one. The result of this model for the period of $1000s$ is shown in Fig.4. As before the highest phases occur for the shallow depth with 1.2° to 1.6° for the TE-mode and 4° to 5° for the TM-mode. The phases for greater depths decrease to zero again. But regarding the signal-to-noise-ratio the maximum resolution in the TM-mode is at $15km$ with ratios of 40 to 100. The values for all depths are higher than 16. In the TE-mode the (s/n) values decrease with depth but the smallest value with 5 is still larger than for the smaller period.

Conclusion

The models show a good resolution of the periodic structure for shallow anomalies. In our models this effect does not depend on the period or on the anomaly-thickness. Furthermore, the signal of the TM-mode is usually higher than that of the TE-mode. The largest signals and signal-noise-ratios were achieved for higher periods from $10s$ to $1000s$.
This method seems to be promising to study the resolution of resistivity anomalies in magnetotellurics. More models have to be calculated with different anomaly sizes and depths, and also the resistivity contrast and the station spacing at the surface should be varied. In this manner we hope to find a limiting value for the maximum resolution which can be used to define the cell size within models. Thus the number of degrees of freedom in models could be reduced significantly and the running time of forward models or inversions could be optimized. Additionally, this method is a good approach to study the model sensitivities for different MT parameters.

References

Lévěque, J.-J., L. Rivera and G. Wittlinger, On the use of the checkerboard test to assess the resolution of tomographic inversions, *Geophys. J. Int.*, *115*, 313–318, 1993.

2D and 3D inversion of MT data from the continental collision zone in the Pamir and Tien Shan, Central Asia

P. Sass*, O. Ritter*, A. Rybin**, and V. Batalev**
*Helmholtz Centre Potsdam GFZ, German Research Centre for Geosciences
**Research Station of the Russian Academy of Sciences, Bishkek, Kyrgyzstan

1 Introduction

A disputed question in geodynamics is the mode of deformation and ultimate fate of lithosphere in collisional mountain building. The Pamir – Tien Shan region in Central Asia may be the best location on Earth to observe lithospheric deformation during orogeny in progress. This mountain range and high plateau formed at the tip of the western Indian promontory through Cenozoic shortening of a magnitude similar to the adjacent Himalaya-Tibet system. The Pamir – Tien Shan orogenic belt hosts some of the deepest active intra-continental subduction zones on Earth and absorbs the highest strain rate over the shortest distance that is manifested in the India–Asia collision zone. The multi-disciplinary Tien Shan – Pamir Geodynamic Program (TIPAGE) combines numerical geodynamic modeling, structural geology, geo-thermochronology and petrology with multiple passive source geophysical experiments, i.e. a seismic and a magnetotelluric (MT) survey in Kyrgyzstan and Tajikistan, predominantly along a 350 km long N-S profile. The MT method is sensitive to electrically conductive regions in the crust and mantle, which often imply the presence of fluids. Hence, with MT we address crucial topics such as crustal flow and fluid release by continental subduction processes.

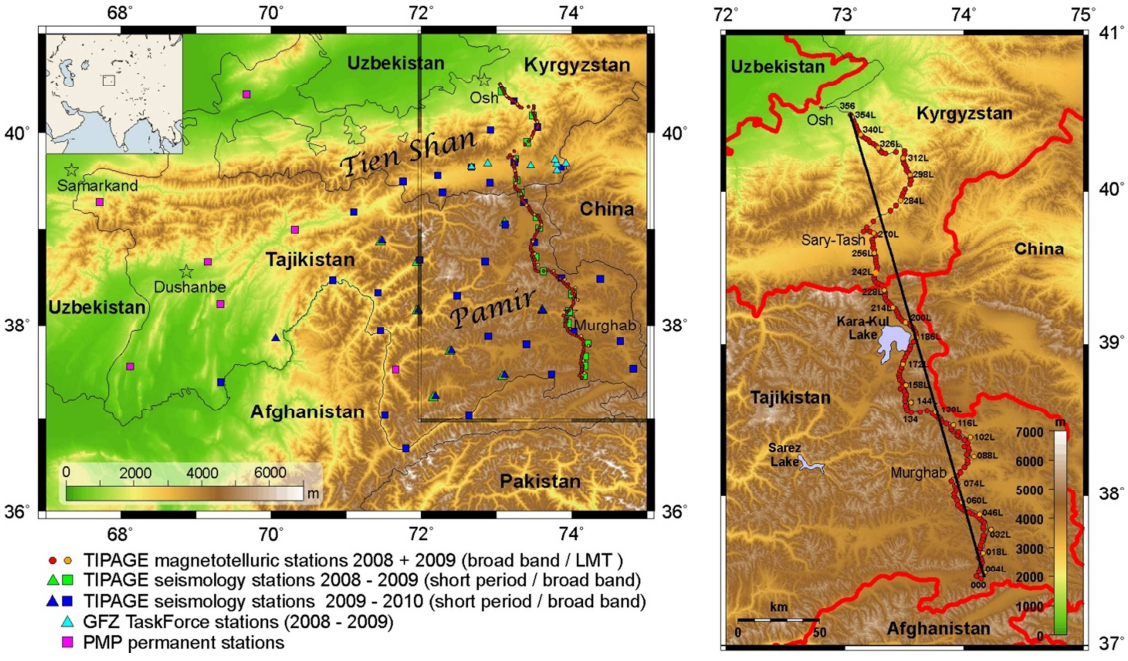

Figure 1: Overview map with all TIPAGE stations (MT + seismology, left) and the location the TIPAGE MT profile (right). Labeled sites mark positions of combined long period (LMT) and broad band (BB) stations, dots show BB-only stations.

Figure 1 shows two overview maps of the TIPAGE area. The left map shows all TIPAGE stations including seismological sites, the right map presents only the magnetotelluric profile

area. MT data was recorded in two field campaigns in 2008 and 2009 along a 340 km long corridor from southern Tajikistan to Osh in Kyrgyzstan across the Pamir Plateau and southern Tien Shan mountain ranges. In total there are 178 MT stations, whereof 26 combine broad band (10^{-3} s - 10^{3} s) and long period (up to 10^{4} s) recordings.

2 Data Analysis and Results

2.1 Data Processing

At each of the MT stations we recorded five channel electromagnetic data: two horizontal magnetic and electric fields and the vertical magnetic field. We used the robust, remote-reference EMERALD data processing package (Ritter 1998, Weckmann 2005, Krings 2007) to obtain apparent resistivity, phase and induction vector data. Particularly in the sparsely populated northern Pamir region, data quality was excellent; figure 2 shows two examples of transfer functions from sites 052 on the Pamir plateau and site 228 which is close to the Tajik – Kyrgyz border. Curves of both sites were obtained after applying standard single-site processing (for station locations, see figure 1).

Nevertheless, many of the TIPAGE MT stations from Kyrgyzstan are affected by anthropogenic electromagnetic noise and needed to be processed in a more sophisticated and individual way in order to improve the data quality. Figure 3 shows a representative example of noise-affected data of the station 288 from a more densely populated Tien Shan mountain valley in the northern profile part. The standard single site processing yields highly scattered and noisy data curves especially for the periods of the ”dead band” between 1 s and 10 s (Figure 3, left diagram). The quality of this and many other station data could be improved using the remote reference processing technique whereat the undisturbed source fields at a remote site which is recording simultaneously are used to clean the signal. The right diagram of figure 3 was gained after a remote reference processing of site 288, using station 222 as the remote site. The data quality improves significantly.

Apparent resistivity and phase data of all sites are plotted as pseudo-sections in figure 4, in which the amplitude and phase values are color-coded. For the pseudo-section presentation, the data are already rotated according to the geo-electric strike (see below) into TE (currents perpendicular to strike) and TM modes (currents parallel to strike). As a preparatory measure for 2D inversion, some of the more noisy data points were masked; we also removed some data points exhibiting phase values >90° (at long periods), as they are indication for the presence of 3D structures.

The vertical magnetic transfer functions can be used to investigate lateral variations of conductivity. Often they are visualized as induction vectors. In the Wiese convention (Wiese 1962), they tend to point away from good conducting zones. This convention was used in figures 2 and 3. Maps views of the real and imaginary parts of induction vectors at different periods are shown in figure 5.

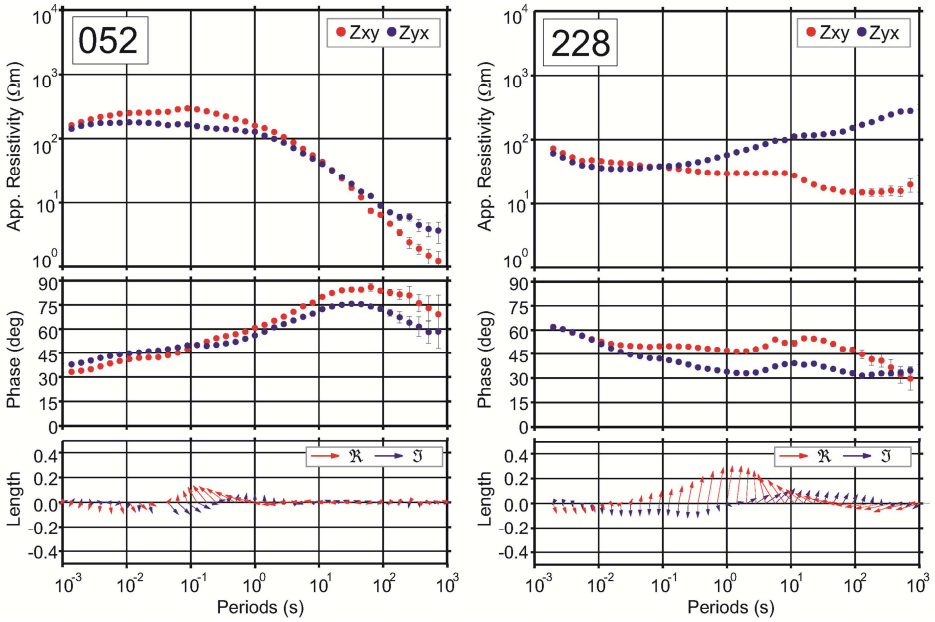

Figure 2: Examples of high-quality curves of apparent resistivity, phases and induction vectors of station 052 (left diagram) and station 228 (right diagram). For station location, see figure 1.

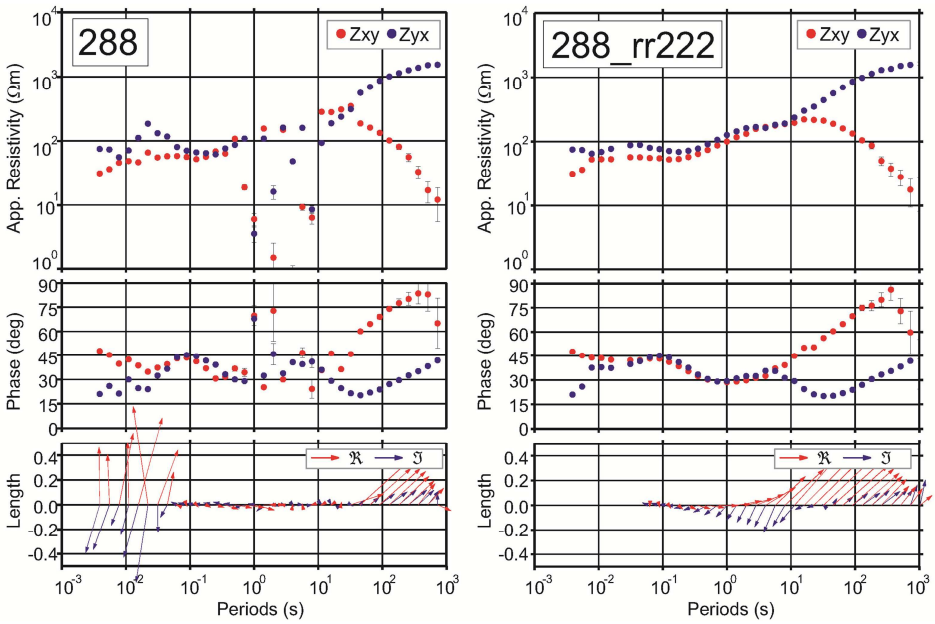

Figure 3: Apparent resistivity, phases and induction vectors of station 288 after the standard single site processing (left diagram) and the remote reference processing using station 222 as the remote site (right diagram).

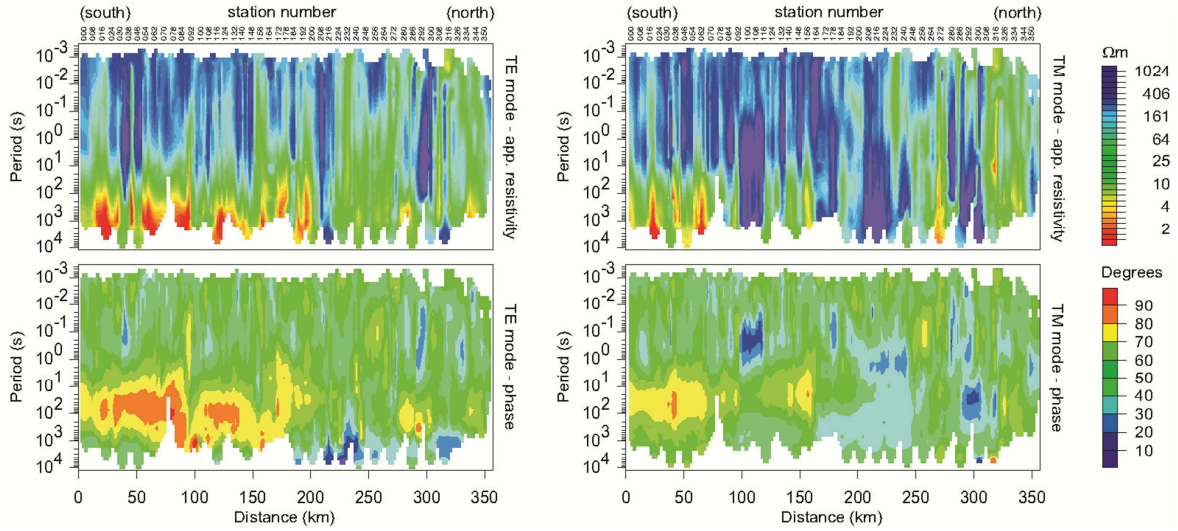

Figure 4: Pseudosections of apparent resistivity and phases of all stations, TE mode (left) and TM mode (right). Noisy data points and phases > 90° are removed.

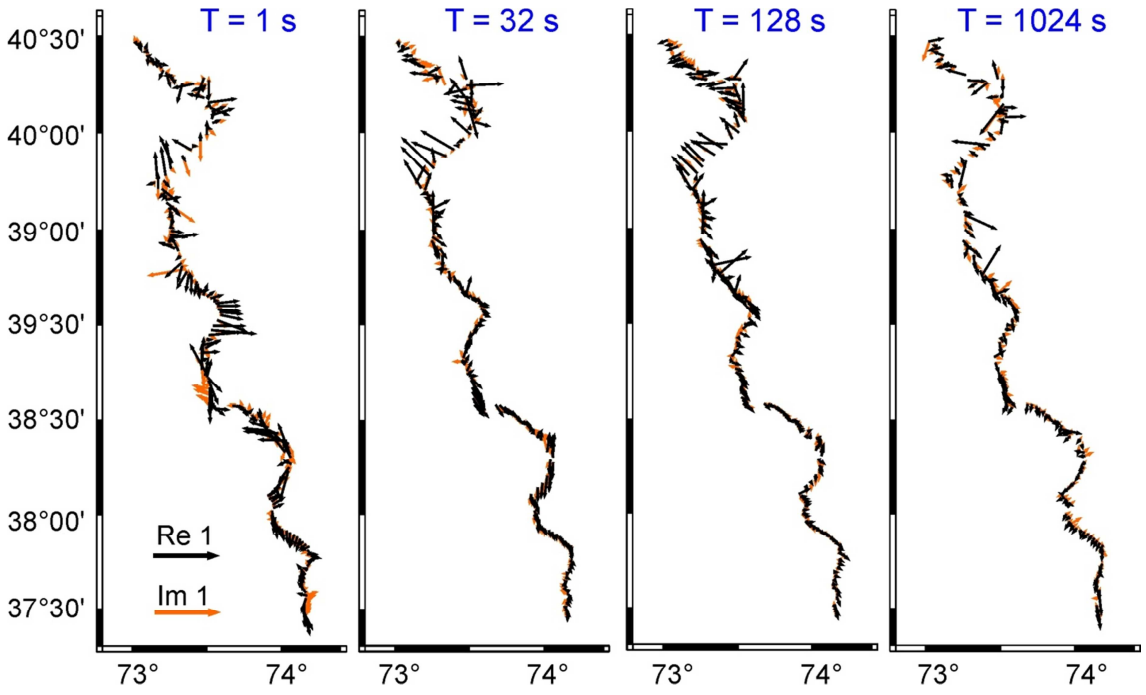

Figure 5: Maps of induction vectors (real and imaginary part) of each station at different periods from T = 1 s (left) to T = 1024 s (right). The arrows are plotted according to the Wiese convention (Wiese 1962) and tend to point away from good conducting zones.

2.2 Strike Detection

We performed a strike direction analysis after Becken and Burkhard (2004). The obtained rose diagrams include cardinal points and are shown in figures 6 and 7. The gray shaded areas, which point in a certain direction of the diagram, represent stations with a certain direction of main current flow at the considered frequencies. The bigger the length of the gray area in a certain direction, the more stations have a dominating current flow in this direction. The principal 90° ambiguity of the impedance tensor strike analysis results in the cross-shaped diagrams and can be resolved by using the induction vectors (figure 5). In figure 6, the left diagram was obtained using only the short period data between 0.0001 s and 1 s which penetrates only the upper crust (depth less than 10 km). The average strike direction is predominantly W-E. When analyzing the longer periods (10 s - 10000 s) we obtain a dominating strike direction of approximately -15° to -20° N (figure 6, right diagram), which shows the dominating strike in middle to lower crustal levels. This picture is generally consistent with the predominant geological and tectonic trend in the area and justifies 2–dimensional inversion of the data. However, a more detailed analysis in figure 7 provides information about the spatial distribution of the strike directions at different periods and for different profile parts. This compilation exhibits larger variability in the strike directions. At the shortest periods, the strike directions scatter. This could hint at the influence of local 3D structures but could also be due to local 1D condition for which strike directions are undetermined. The strike at longer periods is generally more uniform along the profile, though some scattering is present.

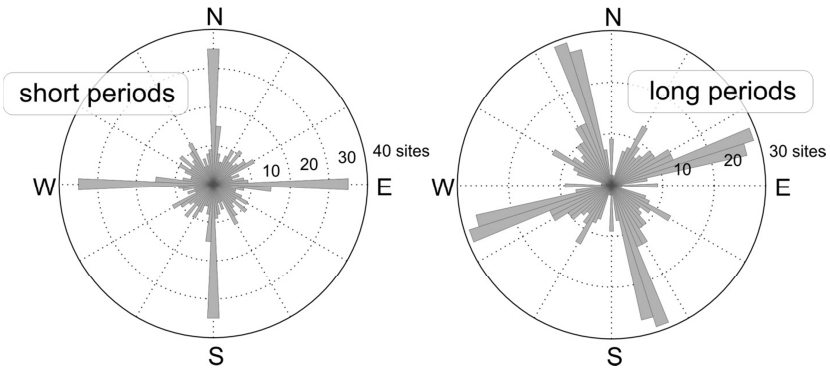

Figure 6: Electrical strike direction analysis, including all stations and a period range 0.0001 s - 1 s (left diagram) and 10 s - 10000 s (right diagram). The diagrams show the number of stations with a certain direction of the main current flow (Becken & Burkhard, 2004). Longer periods include deeper layers.

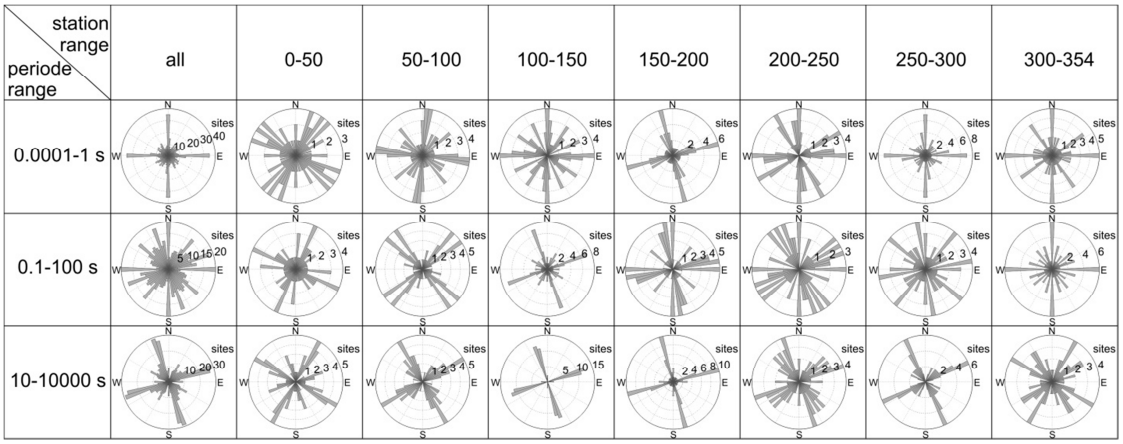

Figure 7: Electrical strike direction analysis for different periods (rows) and station ranges (columns).

A non-dimensional rotationally invariant parameter to characterize the complexity of subsurface structures is the skew of the impedance tensor defined by Swift (1967) or Bahr (1988). A 1D or 2D conductivity distribution results in a skew value of 0, whereas greater values indicate the presence of 3D structures. Practically, a value of 0.2 to 0.3 is still considered as small and generally consistent with 2D assumptions. Pseudosections of the skewness in Figure 8 show values below 0.3 for most stations and periods. Skew values > 0.4 occur at stations 60 to 90 for longer periods, where we also observed phases >90°. Large skew values towards the northern end of the profile are likely caused by anthropogenic noise.

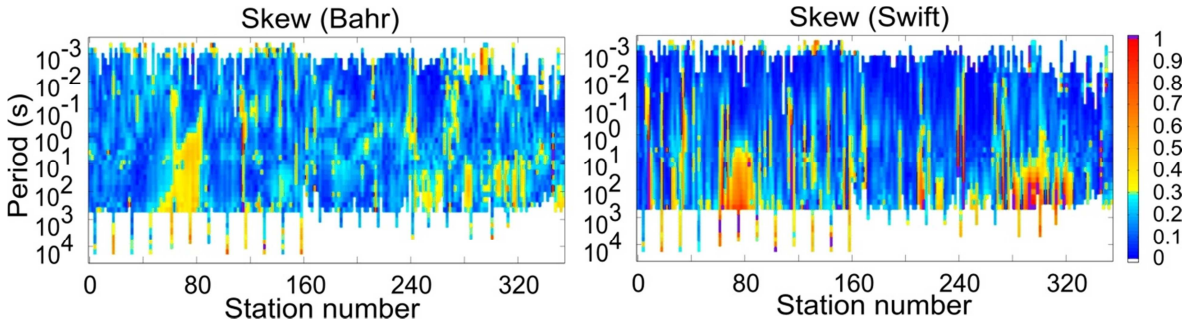

Figure 8: Pseudosection of the skewness in the definition of Swift (left) and Bahr (right). Blue colors indicate skew values below 0.3, which are considered to be compatible with 2D assumption (Swift 1967, Bahr 1988).

2.3 2D Inversion

To solve the 2D magnetotelluric inverse problem we used an algorithm based on a regularized, nonlinear conjugate gradients (NLCG) scheme (Rodie and Mackie, 2001), implemented in the WinGLink software package (version 2.20.09).

After rotation of the data by -105° (see prev. section and figure 6) the x-direction of the data, which prior to the rotation pointed northwards, shows now to WSW-direction, parallel to the dominating strike. For the 2D inversion, all stations locations were projected onto the profile line marked in Figure 1 (right hand side).

To probe at least some parts of the solution space we varied systematically some of the inversion parameters, including starting model, frequency range, error floors and data weighting. An important aspect of this particular inversion scheme is finding the most appropriate smoothness (regularization) factor. Plotting the roughness vs. the RMS of inversion results with different settings of the smoothing parameter τ yields a Pareto front, which is shown in Figure 9. The best value of τ, as an optimum trade-off between coherent structures and data misfit, is found close to the kink of the Pareto front; here we choose τ = 30.

The result of the 2D inversion can be found in Figure 10 together with the topography and major tectonic features. To obtain this model we used only the longer period data between 0.1 s and 10000 s. Due to grid size restrictions, we had problems fitting the shorter periods, so the upper 5 to 10 km are not resolved in this model.

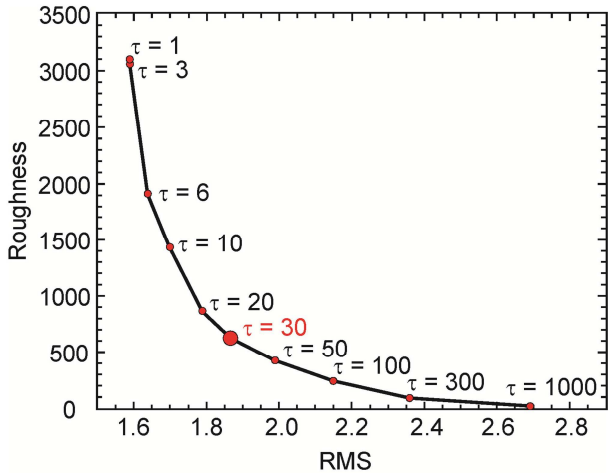

Figure 9: Pareto front: roughness vs. RMS for a range of smoothing parameters τ; here, a reasonable choice is τ = 30.

For the inversion we concentrated on fitting the phase curves rather than the static-shift-affected apparent resistivity curves by setting large error floors for the TE-mode apparent resistivity (see Figure 10 for the inversion settings). The fit of both phase curves and the TM mode resistivity is fairly good, resulting in a total RMS of 1.87. Detailed diagrams of the RMS errors for every component are given in figure 11. The RMS values were calculated according to

$$RMS(d) = \sqrt{\frac{1}{N_d} \cdot \frac{1}{(err_d)^2} \cdot \sum_{n=1}^{N_d} \left[\ln(d_{n,obs}) - \ln(d_{n,calc})\right]^2} \ ,$$

where d indicates a data component (e. g. certain data mode and certain station), N_d the number of data points for component d (e. g. number of periods), err_d the estimated error for the component d, $d_{n,obs}$ and $d_{n,calc}$ are the observed (measured) and calculated (model response) data points, respectively. The very low RMS values for ρ_{TE} in figure 11 are caused by the extremely high pre-set error floor values. The lowermost diagram of figure 11 shows a comparison of RMS given by WinGLink and the total values calculated manually. The bias which is present at the RMS values of WinGLink and our calculation varies between different models, but the WinGlink RMS are always lower than ours. We are not sure how the RMS is calculated in WinGLink, but the absolute RMS value is less important than the general trend of the data misfit distribution, which is in good agreement in the two RMS curves.

The models reveal a generally resistive upper crust for the Pamir plateau and several regions of high conductivity at lower crustal levels. Below the Pamir plateau we observe prominent conductive structures at depths of approx. 20 km – 40 km. The absolute values for resistivity and depth ranges of these conductors are in the same range as observed from the Tibetan plateau which were interpreted as zones of lower crustal flow (Bai et al., 2010).

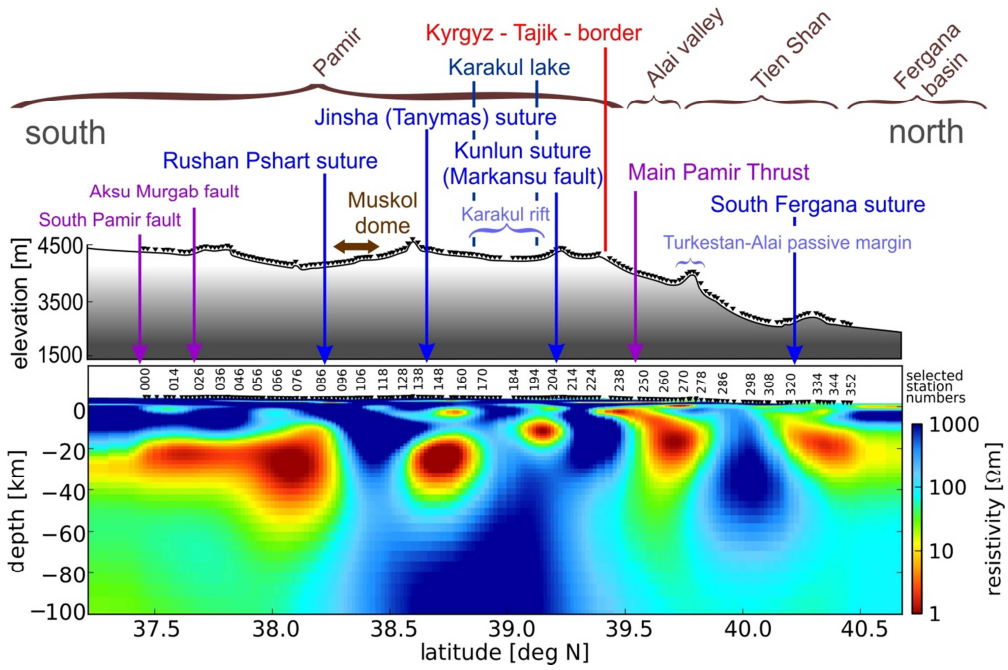

Figure 10: 2D inversion result, truncated at a depth of 100 km. Also shown are the topography and the main tectonic features (Schwab & Ratschbacher, 2004 and Robinson, 2007). The model was obtained using the 2D inversion algorithm of Rodie and Mackie (2001), convergence was achieved with 400 iterations. Settings (WinGLink): joint inversion for TE + TM + Hz mode, 156 x 176 cells, τ = 30, R_{start} = 100 Ωm, weighting: α = β = 1, H = V = 500, error floors: ρ_{TE} = 10000%, ϕ_{TE} =1.5°, ρ_{TM} = 30%, ϕ_{TM} =1.5°, T_{yz} =0.05. RMS = 1.87.

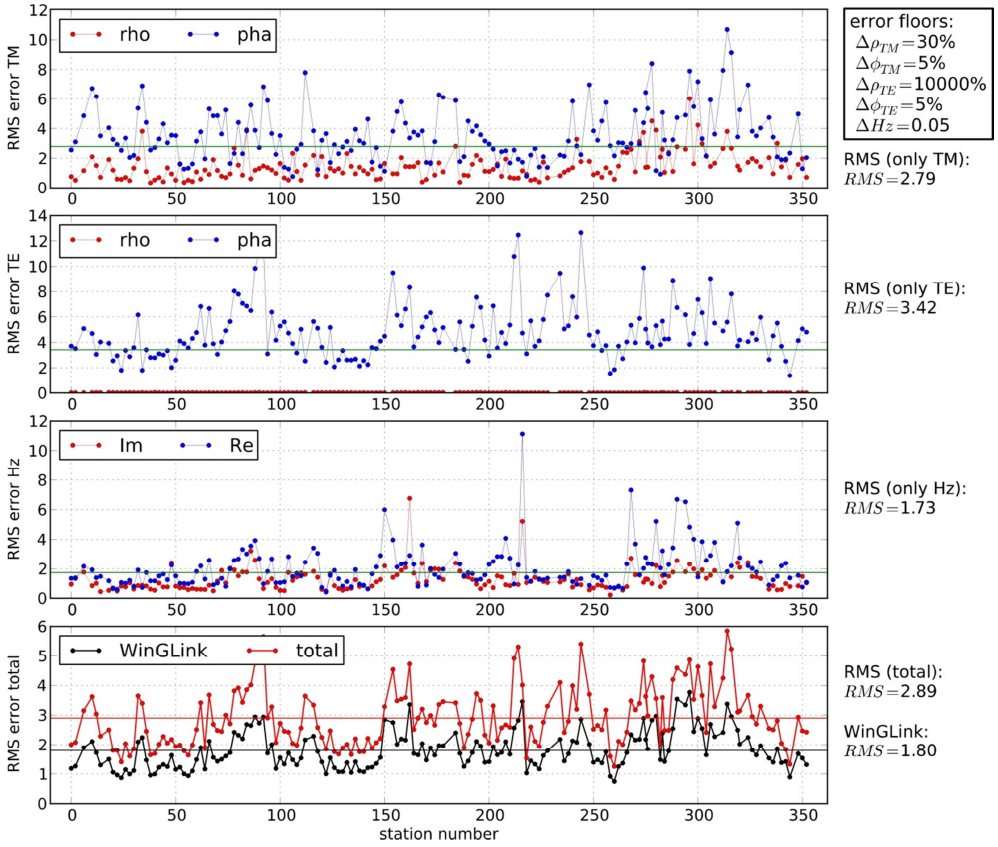

Figure 11: RMS error for each data mode and every station of the 2D model in figure 10. Error floors used for calculation of the RMS values are shown in the box. The lowermost diagram shows a comparison of RMS given by WinGLink and the total values calculated manually.

2.4 3D Inversion

Preliminary 3D inversion was performed using the parallelized version of ModEM (Egbert & Kelbert 2012). Figure 12 exhibits smaller scale resistive features in the upper layers but also some prominent conductors at approximately 20 km depth. The slices also show that the inversion modifies only cells in the vicinity of the profile. The area affected increases with increasing induction range (larger periods). Comparison of a slice through the 3D model with the corresponding 2D model (Figure 13) clearly shows that the main conductivity features are visible in both models. This is remarkable considering that the 3D model was calculated using only a subset of stations and a different grid. While these preliminary 3D results confirm our 2D inversion model, more 3D inversion will be a major part of our future work.

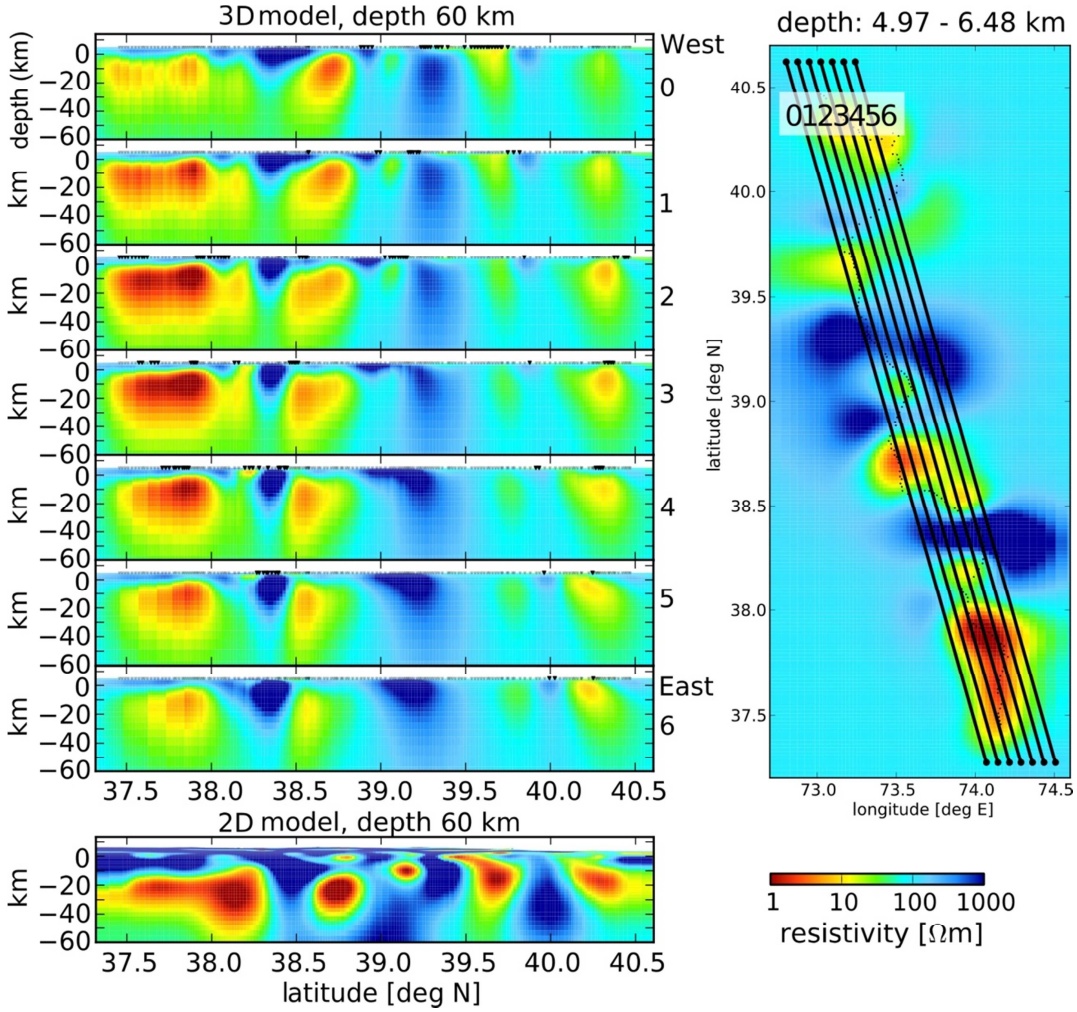

Figure 12: Vertical slices through a 3D model to a depth of 60 km. Location of the slices are shown in a map view on the right hand side. Section 0 is the westernmost slice, section 6 is the easternmost slice. For comparison, the 2D model from figure 10 is plotted below the 3D model slices. Most of the major features appear in both inversion images.

2.5 Topography Influence

Topography can have an influence on magnetotelluric data and inversion results. Electromagnetic field lines are “compressed” by concave topographies and “stretched” by convex structures (Fox 1980). Consequently, a higher potential difference of the electric field over a certain distance is measured in valleys in comparison to measurements on ridges, which causes valley to appear as too restive valleys and ridges appear as too conductive. As the TIPAGE area is dominated by mountains, it is crucial to check the influence of the topography on the inversion results. Therefore, we constructed a 3D model with layers reproducing the real topography and a homogeneous conductivity distribution in the rest of the model space. We used an algorithm for computing the magnetotelluric response of three-dimensional earth models, which is implemented in the 3D-forward-module of the WinGLink package (Mackie et al., 1993). We calculated the model response of this 3D topography model at places of our receiver stations. Taking this response as station data we inverted it in the 2D scheme. The result is displayed in figure 13. All conductivity structures in the inversion originate only from topography. The starting model was a 100 Ωm half space. Maximum differences between inversion result and the starting model (100 Ωm) are approximately ± 80 Ωm. Hence, the influence of topography on the real data, were resistivity varies over more than four orders of magnitude, is minor. Please note the different color scales in figure 13 and in the model plots in figures 10 and 12. In order to compare the influence of topography on the model with the influence of some subsurface resistivity distribution, in figure 14 the same color scale is used as in the model plots.

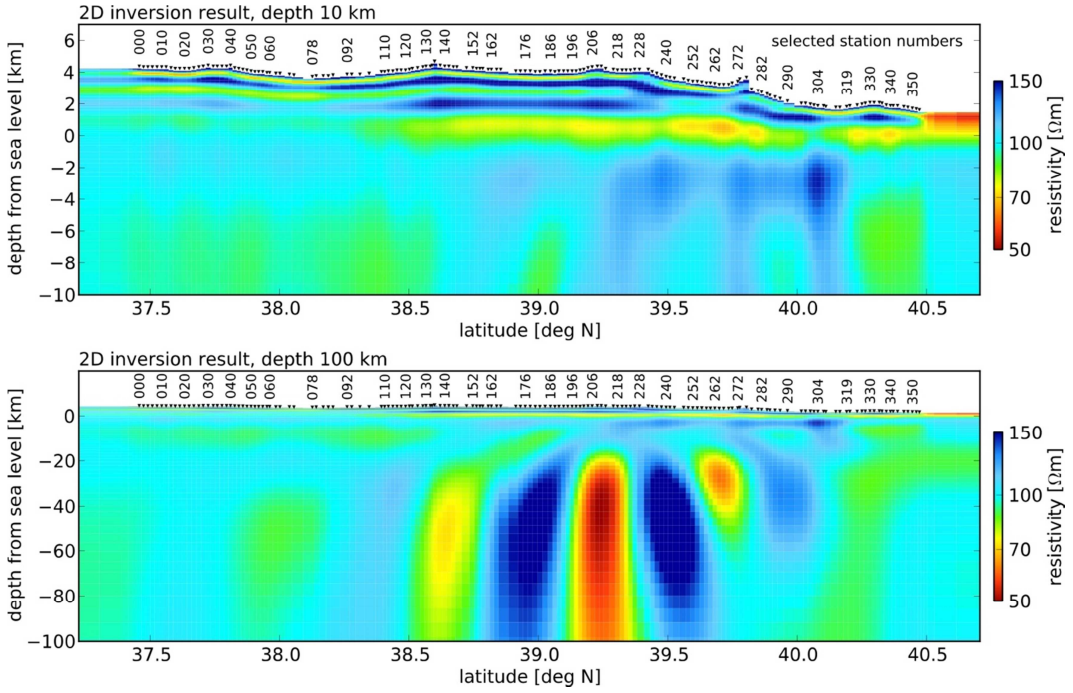

Figure 13: Topography influence on TIPAGE MT data. Upper plot: shallow layers down to -10 km depth below NN, lower plot: deep layers 0-100 km depth. The models were obtained after a 2D inversion of a 3D forward response of the modeled topography at places of MT stations. The color scale is chosen to amplify changes from a 100 Ωm half space.

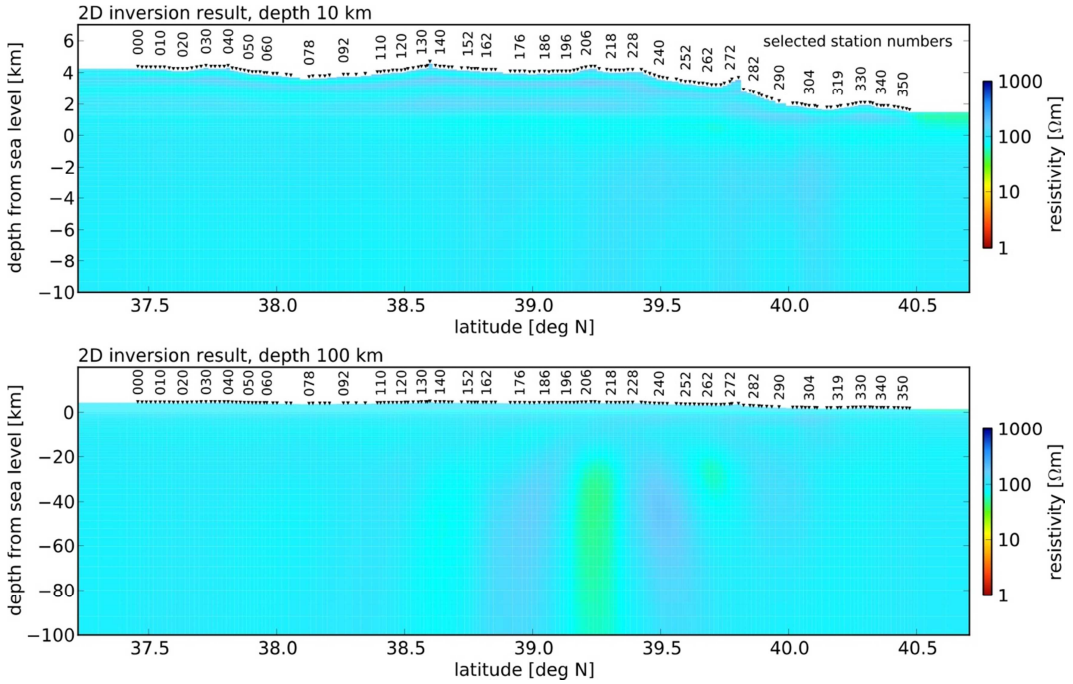

Figure 14: Similar as in figure 13, but now using the same color scale as in figures 10 and 12. The artificial subsurface features created by the inversion are due to topography. However, the contrasts are rather weak and have little influence on the inversion result.

Acknowledgements

The MT field team: Employees and students of the International Research Center, Russian Academy of Sciences, Bishkek and from Germany: D. Brändlein, X. Chen, T. Krings, A. Nube, M. Schüler, K. Tietze, C. Twardzik and G. Willkommen.

Dr. V. E. Minaev, Dr. N. Radjabov, Dr. I. Oimahmadov, Prof. A. R. Faiziev: Institute of Geology, Academy of Sciences of the Republic of Tajikistan, Dushanbe.

Dr. B. Moldobekov, Prof. H. Echtler, Dr. A. Mikolaichuk: Central Asian Institute for Applied Geosciences, Bishkek.

Dr. S. K. Negmatullaev: PMP International / Seismic Monitoring Network in Tajikistan, Dushanbe.
Prof. L. Ratschbacher: University of Freiberg, Germany and all other German colleagues participating in this project.

We very gratefully acknowledge substantial funding which we received from the DFG and GFZ. Seismic and magnetotelluric instruments were provided by the GFZ Geophysical Instrument Pool (GIPP).

References

Bahr, K. (1988), Interpretation of the magnetotelluric impedance tensor: regional induction and local telluric distortion. J. Geophys., 62:119–127.

Bai, D. et al. (2010), Crustal deformation of the eastern Tibetan plateau revealed by magnetotelluric imaging, Nature Geoscience 3, 358 – 362

Becken, M. and Burkhardt, H. (2004), An ellipticity criterion in magnetotelluric tensor analysis. Geophysical Journal International, 159: 69–82.

Egbert, G. and Kelbert, A. (2012), Computational Recipes for EM Inverse Problems. Geophysical Journal International, 189, 1.

Fox, R.C., Hohmann, G.W., Killpack, T.J., and Rijo, L. (1980), Topographic effects in resistivity and induced-polarisation surveys. Geophysics, 45, 75–93.

Krings, T. (2007), The influence of Robust Statistics, Remote Reference, and Horizontal Magnetic Transfer Functions on data processing in Magnetotellurics. Diploma thesis, Westfälische Wilhelms-Universität Münster and GeoForschungsZentrum Potsdam.

Mackie, R. L., Madden, T. R. , and Wannamaker, P.E. (1993), Three-dimensional magnetotelluric modeling using difference equations; theory and comparisons to integral equation solutions. Geophysics 58(2): 215-226

Ritter, O., Junge, A. and Dawes, G. (1998), New equipment and processing for magnetotelluric remote reference observations. Geophysical Journal International, 132: 535–548.

Robinson A. C. et al. (2007), Cenozoic evolution of the eastern Pamir: Implications for strain-accommodation mechanisms at the western end of the Himalayan-Tibetan orogen, GSA Bulletin, v. 119, no. 7/8, p. 882–896

Rodi, W., Mackie, R. (2001), Nonlinear conjugate gradients algorithm for 2-D magnetotelluric inversion, Geophysics 66: 174-187

Schwab, M., et al. (2004), Assembly of the Pamirs: Age and origin of magmatic belts from the southern Tien Shan to the southern Pamirs and their relation to Tibet, Tectonics, 23, TC4002

Swift, C. M. (1967), A Magnetotelluric Investigation of an Electrical Conductivity Anomaly in the Southwestern United States. PhD thesis, Massachusetts Institute of Technology, Cambridge, Massachusetts, USA.

Weckmann, U., Magunia, A., and Ritter, O. (2005), Effective noise separation for magnetotelluric single site data processing using a frequency domain selection scheme. Geophysical Journal International, 161: 635–652.

Wiese, H. (1962), Geomagnetische Tiefentellurik Teil ii: Die Streichrichtung der Untergrundstrukturen des elektrischenWiderstandes, erschlossen aus geomagnetischen Variationen, Pure and Applied Geophysics, 52: 83–103

Tiefe Erkundung des Leinetal-Störungssystems mit geoelektrischen und elektromagnetischen Messungen

Gerlinde Schaumann, Thomas Günther, Michael Grinat & Robert Meyer

Leibniz-Institut für Angewandte Geophysik (LIAG), Hannover

gerlinde.schaumann@liag-hannover.de

Kurzfassung

In einem Teilprojekt des niedersächsischen Forschungsverbund-Projektes gebo (Geothermie und Hochleistungsbohrtechnik, www.gebo-nds.de) wird die Eignung gleichstromgeoelektrischer und elektromagnetischer Verfahren zur Erfassung von Störungszonen in geothermisch relevanten Tiefen untersucht. Als Studiengebiet zur beispielhaften Erkundung einer geologischen Störungszone in Niedersachsen wurde der Leinetalgraben südlich von Northeim gewählt. Dabei wurde anfänglich der Schwerpunkt auf Tiefen gelegt, die mit der Standardausrüstung der verwendeten Methoden erreicht werden können, um prinzipiell die Erfassung einer Störungszone zu erkunden. In einem weiteren Schritt wurden die Standardausrüstungen im Hinblick auf eine größere Erkundungstiefe erweitert. Im Studiengebiet wurden bislang die Multielektroden-Geoelektrik in einer Wenner-Anordnung mit verschiedenen Elektrodenabständen, großskalige Dipol-Dipol-Experimente unter Einsatz einer neuen Hochstromquelle und die Transientelektromagnetik mit unterschiedlichen Sendespulengrößen bis zu 1000 m Kantenlänge und einem leistungsstarken Sender eingesetzt. Die zweidimensional ausgewerteten Geoelektrikdaten zeigen Strukturen, die klar den aus geologischen Informationen bekannten Segmenten der Störungszone zugeordnet werden können. Die eindimensionale Inversion der transientelektromagnetischen Sondierungen liefert unterschiedliche Leitfähigkeitsmodelle beiderseits der Störung, wobei Tiefen bis maximal 1000 m erreicht werden. Für die Interpretation der Messdaten werden außerdem seismische Strukturinformationen herangezogen, die insbesondere in die Auswertung der Geoelektrikdaten als strukturelle Bedingungen einfließen.

1. Einleitung

Elektrische und elektromagnetische Methoden werden bei geothermischen Fragestellungen eingesetzt, da die elektrische Leitfähigkeit ein wichtiger Parameter für die Erkundung geothermischer Reservoire ist. Insbesondere in Hochenthalpiegebieten werden diese Methoden erfolgreich angewendet, da hier charakteristischerweise hohe Leitfähigkeiten auftreten (Spichak & Manzella 2009). Diese Methoden sollen in dem Teilprojekt „Elektrische und elektromagnetische Erkundung geologischer Störungszonen“ auf ihre Anwendbarkeit unter Sedimentbedingungen wie im norddeutschen Becken untersucht werden. Als ein möglicher „Reservoirtyp“ werden hier speziell geologische Störungszonen mit Wegsamkeiten für hydrothermale Fluide angesehen. Ziel des Projektes ist eine Erfassung der Störungszonen von der Oberfläche bis in geothermisch relevante Tiefen (im norddeutschen Becken etwa 3 bis 7 km Tiefe). In dem vorliegenden Beitrag wird der derzeitige Stand der Untersuchungen dargestellt.

Im Studiengebiet Leinetalgraben, wo eine bekannte Störungszone an der Erdoberfläche ausstreicht, kamen zunächst die Multielektroden-Geoelektrik mit verschiedenen Elektrodenabständen und die Transientelektromagnetik (TEM) mit Standardauslagen auf einem Profil zum Einsatz. Zwei großskalige Dipol-Dipol-Experimente unter Einsatz einer Hochstromquelle sowie die TEM mit großen Sendespulenauslagen und einem leistungsstarken Sender wurden danach auf einem weiteren Profil eingesetzt. Desweiteren erfolgten auch seismische Messungen sowie Messungen mit der Methode der Spektralen Induzierten Polarisation, die in weiteren Teilprojekten innerhalb von gebo bearbeitet werden.

2. Messgebiet Leinetal und Messkampagnen 2010 und 2011

Im Messgebiet stehen die für die geothermische Nutzung im Norddeutschen Becken interessanten Sandsteinschichten des Mesozoikums an der Oberfläche an. Die Grabenschultern werden aus Muschelkalk und Buntsandstein gebildet, während im Grabeninneren überwiegend die Gesteine des Keuper und des Lias anstehen (Musmann et al. 2012, Tanner et al. 2010, Reyer 2008, siehe Abb. 2.1).

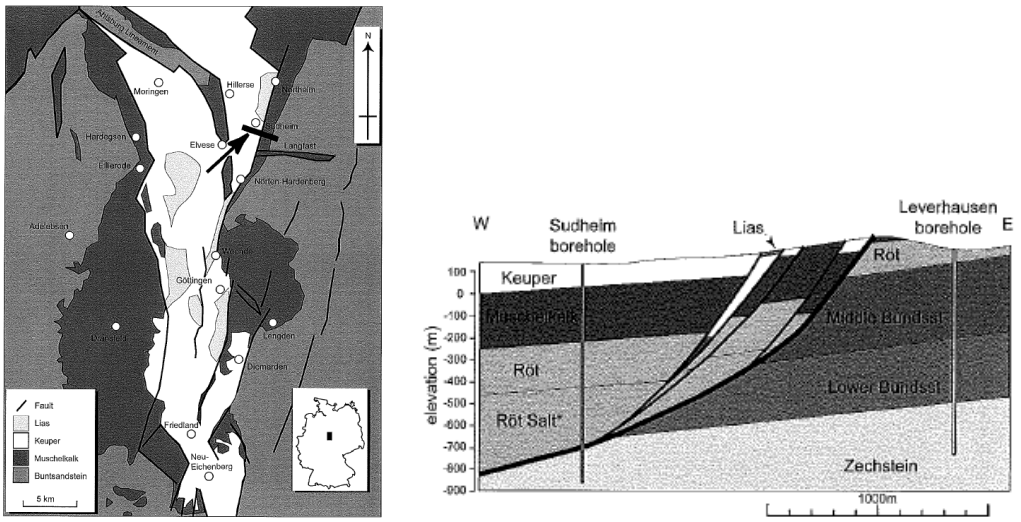

a) b)

Abbildung 2.1: Geologie des Leinetalgrabens südlich von Northeim (Tanner et al. 2010) (a). Die schwarzen Linien bezeichnen Störungslinien in diesem Gebiet. Der Pfeil deutet auf den Schnitt (schwarzer Balken), der in (b) dargestellt ist. Dieser Schnitt wurde u.a. mit Hilfe der Bohrungen Sudheim 2 (im Westen, hier: Sudheim borehole) und Sudheim 1 (im Osten, hier: Levershausen) erstellt, vgl. auch orangefarbene Symbole in Abb. 2.2.

Die Messprofile, in deren Nähe auch seismische Messungen durchgeführt wurden (Musmann et al. 2012), befinden sich auf den Feldern zwischen Northeim und Sudheim (Abb. 2.2). Auf Profil 1 wurde die Multielektroden-Geoelektrik in einer klassischen Wenner-Anordnung mit zwei verschiedenen Elektrodenabständen (2 m und 5 m) im Mai 2010 eingesetzt. Die TEM-Messungen wurden mit Sendespulen von 100 m bis 200 m Kantenlänge mit dem Gerät terraTEM durchgeführt.

Auf Profil 2a wurde 2010 ein großskaliges Dipol-Dipol-Experiment unter Einsatz einer Hochstromquelle (1000 V, bis 50 A) durchgeführt. Das Profil der Hochstrom-Geoelektrik läuft von der Bundesstraße B3 über den östlichen Rand des Leinetals, welches hier durch den Höhenzug des Wieter begrenzt wird und setzt sich noch wenige hundert Meter nach Osten fort. Die Strom-Dipole hatten eine Länge von 200 m und 400 m sowie Abstände von 200 m, die Messung der Potentialdifferenzen erfolgte mit Dipolen von 50 m Länge. Dabei war der maximale Abstand zwischen Stromdipol und Potentialelektrodendipol ca. 2 km und die Gesamtprofillänge betrug ca. 2,5 km. Für die TEM-Messungen wurden auf Profil 2a fünf quadratische Sendespulen mit 50 m und drei mit 400 m Kantenlänge in Inloop- und Coincident-loop-Konfiguration eingesetzt, wobei die Mittelpunkte der großen Spulen sich etwas nördlich der Profillinie befinden (Schaumann et al. 2011). Dabei kam der leistungsstarke Sender terraTX-50 (max. 96 V, max. 50 A) zum Einsatz. Aufgrund mangelnder Datenqualität der Messungen östlich des Wieter werden diese hier nicht betrachtet. Profil 2b ist eine Zusammenstellung mehrerer TEM-Messungen mit der großen Sendespule mit 1000 m Kantenlänge. Hierbei wurde nur die Empfangsspule versetzt (Fixed-Transmitter-Anordnung), (Schaumann et al. 2012).

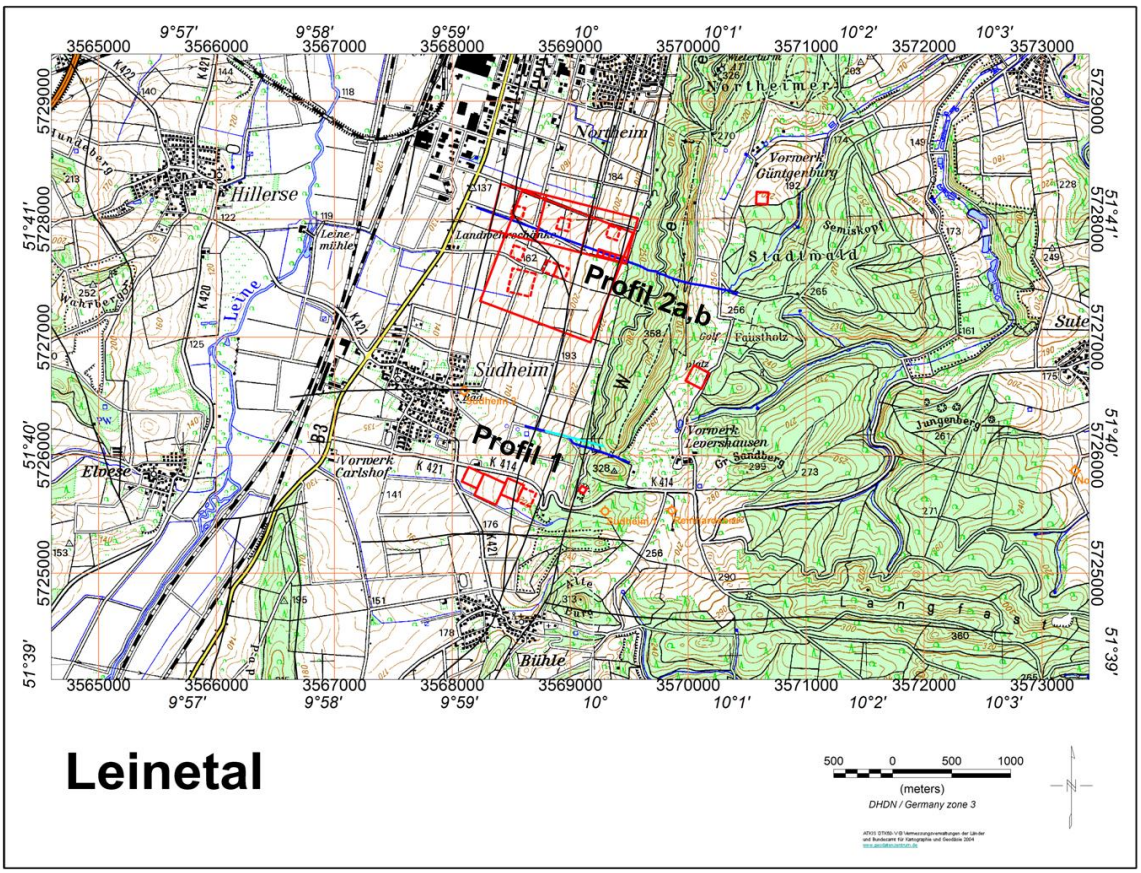

Abbildung 2.2: Karte des Messgebietes im östlichen Leinetal südlich von Northeim, TEM: rote Quadrate (Sendespule Tx durchgezogene Linien, Empfangsspulen Rx gestrichelte Linien auf den Profilen 2a und b), DC-Profile: blaue u. hellblaue Linien, orangefarbene Symbole: Bohrungen, vgl. Sudheim 2 und Sudheim 1 von Abb. 2.1., schwarze Linien: aus der Geologie bekannte Störungslinien, die Hauptstörungslinie streicht westlich des Wieter aus.

3. Eindimensionale Simulationsrechnungen für die Transientelektromagnetik

Beispielhaft für die im Projekt ausgeführten Modelluntersuchungen werden hier vier Abbildungen gezeigt, auf denen für eindimensionale Modelle mit gut leitenden Schichten in unterschiedlichen Tiefen der Einfluss der verwendeten Sendespule gezeigt wird. In Abb. 3.1 sind Transienten für eine Sendespule der Kantenlänge 200 m dargestellt, wie sie über dem angegebenen Modell zu erwarten wären. Dabei liegt eine gut leitende Schicht von 5 Ohm*m mit einer Mächtigkeit von 10 m einmal in 350 m Tiefe, einmal in 600 m Tiefe. Abb. 3.2 zeigt ebenfalls Transienten für diese Modelle, allerdings für eine Sendespule der Kantenlänge 1000 m. Die Transienten wurden durch eine eindimensionale Vorwärtsmodellierung für eine Inloop-Anordnung erzeugt (Weidelt 1984). Bei dem für Feldmessungen verwendeten terraTEM-Gerät liegt der letzte mögliche Zeitkanal zur Registrierung eines Transienten bei 475 ms.

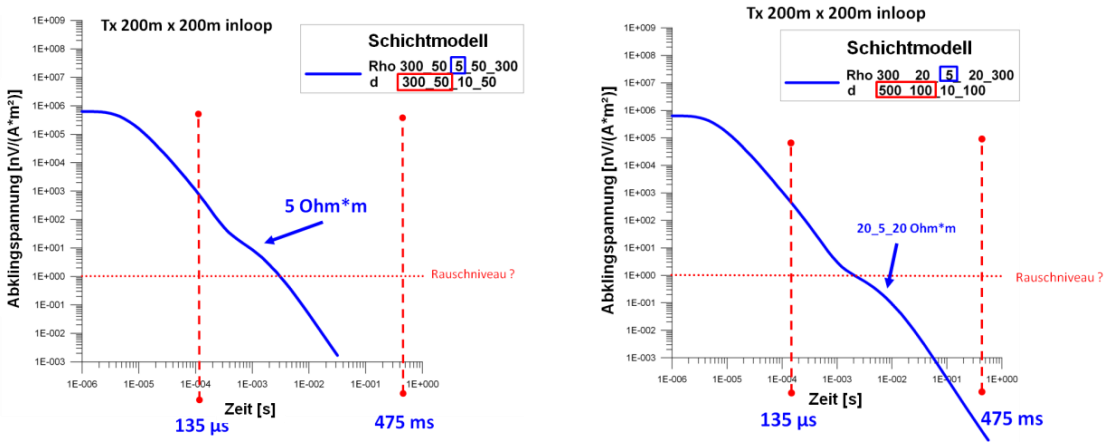

Abbildung 3.1: Abklingkurve für eine quadratische Sendespule der Kantenlänge 200 m für das angegebene Schichtmodell. Dabei liegt eine Schicht geringen Widerstands (hier 5 Ohm*m) mit einer Mächtigkeit von 10 m in 350 m bzw. 600 m Tiefe.

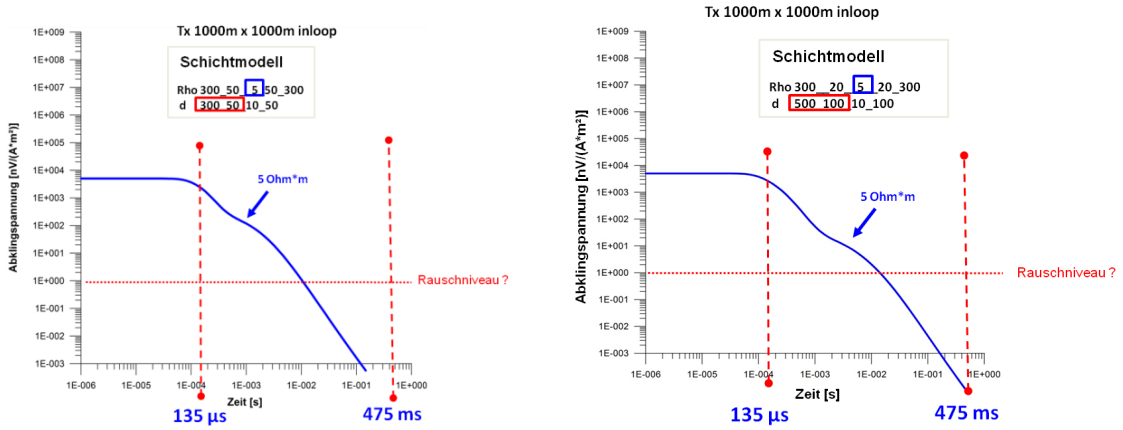

Abbildung 3.2: Abklingkurve für eine quadratische Sendespule der Kantenlänge 1000 m für das angegebene Schichtmodell. Dabei liegt eine Schicht geringen Widerstands (hier 5 Ohm*m) mit einer Mächtigkeit von 10 m in 350 m bzw. 600 m Tiefe.

Für die Detektion des guten Leiters (Abb. 3.1), ist unter Berücksichtigung eines typischen Rauschniveaus die Stärke des Sendedipolmomentes entscheidend. Bei einer Vergrößerung der Fläche der Sendespule (Tx) von 40.000 m² (Abb. 3.1) auf 1.000.000 m² (Abb. 3.2) kann mittels des Transienten (innerhalb eines geräteabhängigen Zeitfensters, hier bis 475 ms) diese leitfähige Schicht in 600 m Tiefe zwischen schlechter leitenden Schichten gut erfasst werden. Allerdings ist für die große Sendespule der Transient erst nach ca. 135 µs auswertbar. Dagegen können die mit den kleineren Sendespulen gemessenen Transienten bereits zu deutlich früheren Zeiten ausgewertet werden und geben damit auch Informationen über die Leitfähigkeiten oberflächennäherer Schichten. Damit müssen für eine Interpretation der Schichten von Oberflächennähe bis in größere Tiefen die Ergebnisse beider Spulenanordnungen zusammen ausgewertet werden.

4. Ergebnisse

4.1. Ergebnisse der TEM

Während auf Profil 1 die Erkundungstiefe bei der TEM aufgrund der kleineren Messauslagen auf etwa 200 m bis 300 m beschränkt ist (Abb. 4.1), wurden auf den Profilen 2a und 2b größere Tiefen durch die Verwendung größerer Sendespulen und mit höheren Dipolmomenten erzielt. Für alle TEM-Stationen wurde eine 1D-Inversionsrechnung mit dem Programm WinGLink durchgeführt. Die 1D-Modellierung liefert auf Profil 2a für die 400 m-Sendespulen Schichtmodelle bis ca. 900 m Tiefe (Abb. 4.2). Allerdings wird das Modell ab etwa 800 m Tiefe unsicher, da die Datenqualität nicht ausreichend ist.
Auf Profil 2b (Abb. 4.3) liegt die erzielte Tiefe bei über 1000 m. Hier ist ebenfalls die mangelnde Datenqualität eine limitierende Größe, jedoch ist die Eindringtiefe gegenüber Abb. 4.2 deutlich größer geworden. Sämtliche Messungen im Leinetal sind durch ein geringes Signal/Rauschverhältnis nachteilig beeinflusst. Dadurch können verlässliche Aussagen über die Verteilung der elektrischen Leitfähigkeit für Tiefen von mehr als 1000 m in diesem Gebiet nicht getroffen werden. Die in allen drei Abbildungen angedeutete gestrichelte rote Linie zeigt einen möglichen Verlauf der Störungszone an, falls diese sich mit erhöhter elektrischer Leitfähigkeit charakterisieren lässt.

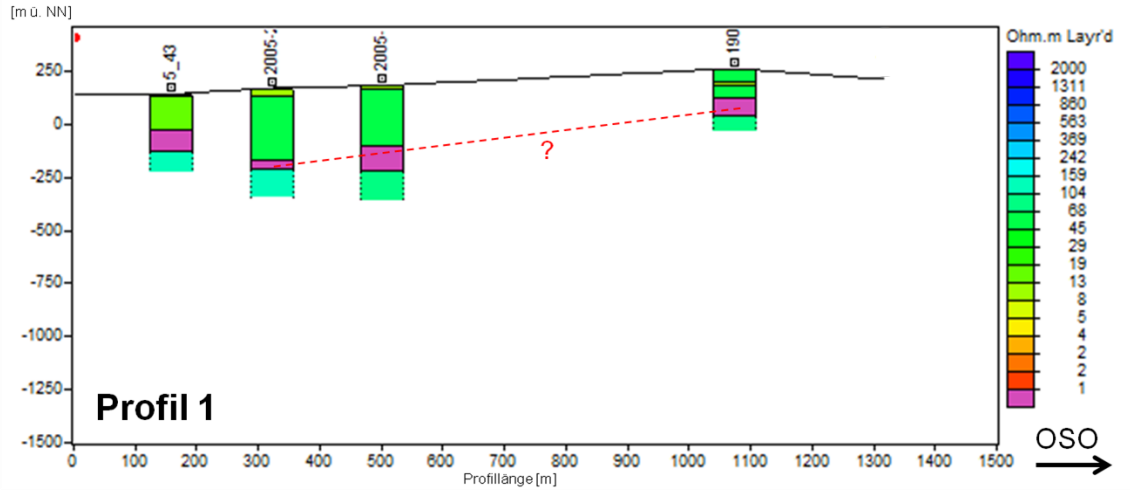

Abbildung 4.1: 1D-Inversionsergebnisse der TEM-Stationen auf Profil 1.

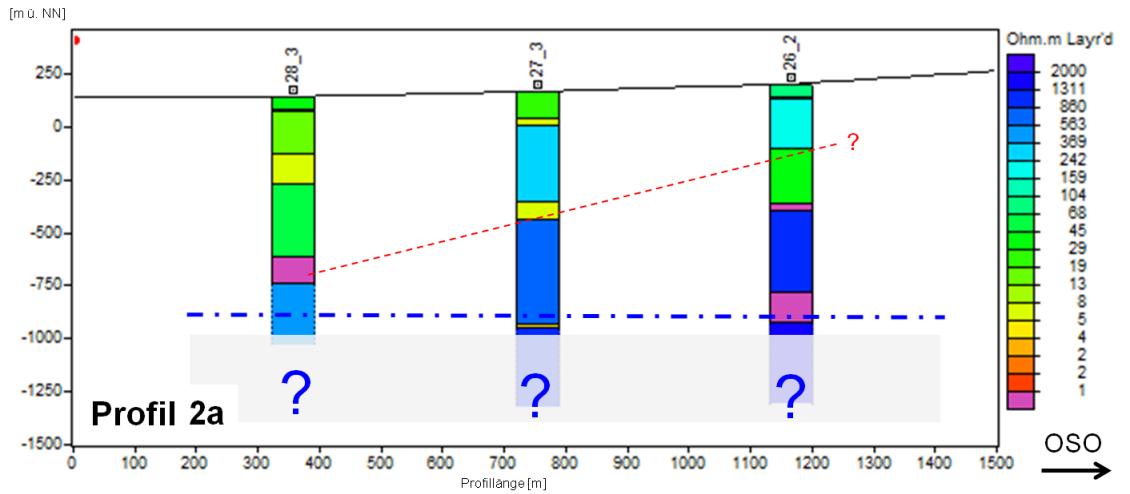

Abbildung 4.2: 1D-Inversionsergebnisse der TEM-Stationen auf Profil 2a.

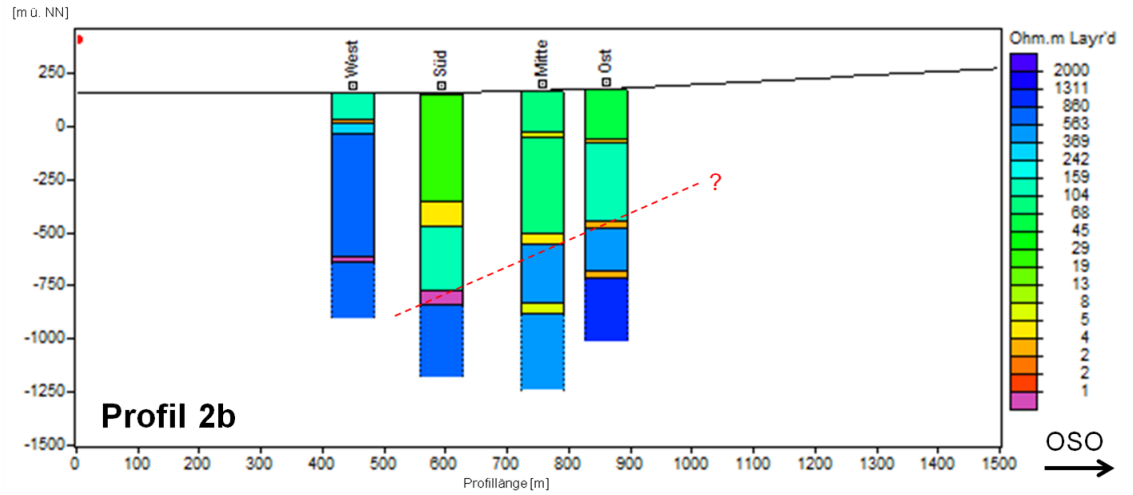

Abbildung 4.3: 1D-Inversionsergebnisse der TEM-Stationen auf Profil 2b.

4.2 Ergebnisse der Geoelektrik

Sämtliche DC-Daten wurden zweidimensional mit dem 2D-Programm BERT von Günther et al. (2006) mit unstrukturierten Dreiecks-Gittern ausgewertet. Mittels Finiter Elemente kann die Topographie nachgebildet werden und beliebig geformte Elektroden können modelliert werden, was mit strukturierten Gittern nicht möglich ist. Grenzen, die sonst glatt sein müssen, sind hier stückweise glatt. Damit können bekannte Strukturen a priori berücksichtigt werden (Günther & Rücker 2006).

Die Abb. 4.4 zeigt die Ergebnisse auf Profil 1 von Messungen in Wenner-Elektrodenanordnung mit einem Elektrodenabstand von 2 m (hellblaue Linie in Abb. 2.2) und 5 m (dunkelblaue Linie in Abb. 2.2). Im Vergleich wird sofort die Erweiterung der Eindringtiefe von etwa 100 m auf fast 300 m deutlich. Die Auflösung im oberflächennahen Bereich ist naturgemäß bei den kleineren Elektrodenabständen feiner. Hier können komplizierte Strukturen, wie sie von der Geologie vermutet werden, erfasst werden und spiegeln sich in der Abfolge von gut und schlecht leitenden Bereichen wider. Dabei wird deutlich, dass sich die geologischen Einheiten nicht durch Bereiche einheitlichen Widerstandes darstellen lassen (vgl. Abb. 1b). Die Störungszone deutet sich bereits durch den Übergang in einen großen Bereich mit hohen spezifischen Widerständen an (schwarzer Pfeil).

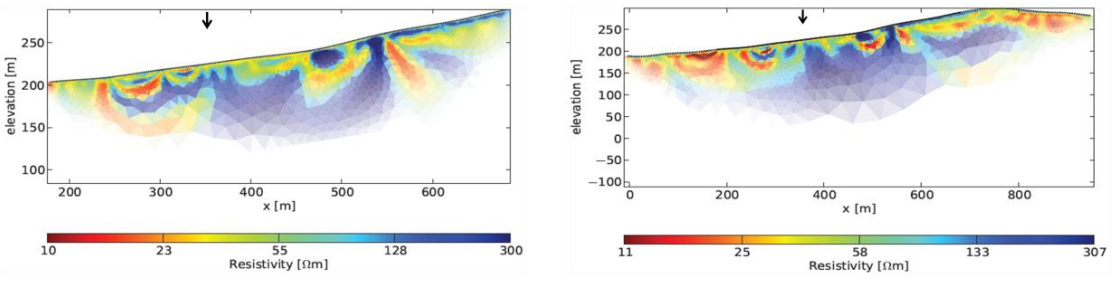

a) b)

Abbildung 4.4: 2D-Inversionsergebnis von Messungen mit einer Wenner-Elektrodenanordnung mit 2 m Elektrodenabstand auf Profil 1 (a) und aus der Kombination von Messungen mit 5 m Elektrodenabstand (b). Der schwarze Pfeil zeigt auf den Bereich, in dem die Hauptstörungszone an der Erdoberfläche ausstreicht.

Abb. 4.5a zeigt die Ergebnisse entlang Profil 2 (Dipol-Dipol-Auslagen, dunkelblaue Linie in Abb. 2.2). Hier wird im direkten Vergleich zu Profil 1 sofort die Erweiterung der Eindringtiefe auf fast 700 m deutlich. Abb. 4.5b zeigt das 2D-Inversionsergebnis unter Einbezug seismischer Strukturinformationen (Musmann et al. 2012), die als Linien in die Netzgenerierung eingehen und keinen Beitrag in der Regularisierung liefern (Günther et al. 2012).

Die zweidimensional ausgewerteten Geoelektrikdaten zeigen eine klare Trennung von unterschiedlich leitfähigen Bereichen westlich und östlich der Störungszone. Der Verlauf der Störungszone mit der Tiefe ist deutlich erkennbar.

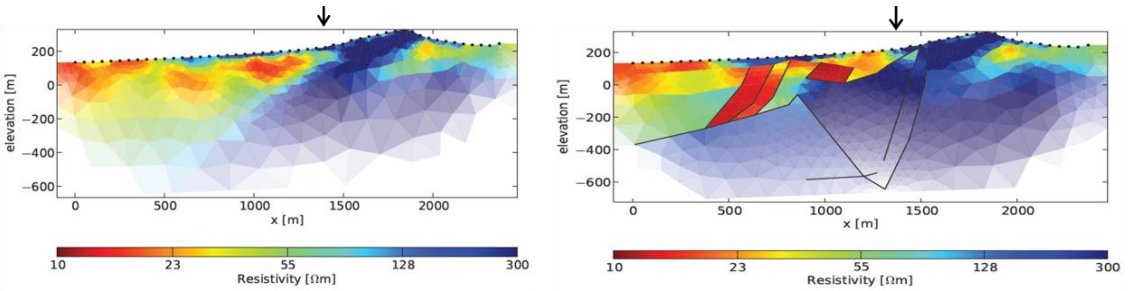

Abbildung 4.5: 2D-Inversionsergebnis der großskaligen Geoelektrik-Messungen auf Profil 2 ohne (a) und mit (b) Einbezug seismischer Strukturinformationen. Der schwarze Pfeil zeigt auf den Bereich, in dem die Hauptstörungszone an der Erdoberfläche ausstreicht.

5. Zusammenfassung

Die Erweiterung bzw. Modifikation des jeweiligen Messaufbaus hat bei beiden Methoden (DC und TEM) eine größere Eindringtiefe im Leinetal ermöglicht. Dies konnte am Beispiel der Untersuchung der Störungszone entlang des östlichen Grabenrandes gezeigt werden. Es konnte außerdem gezeigt werden, dass die nicht standardmäßigen großen Auslagen beider Methoden hier zur Klärung des Verlaufs der Störungszone in größerer Tiefe herangezogen werden können. Für die Auswertung wurden seismische Strukturinformationen in die Interpretation insbesondere der Hochstrom-Geoelektrik einbezogen. Die Ergebnisse der 2D-Auswertung der Gleichstromgeoelektrik und der 1D-Auswertung der TEM liefern gemeinsam Anhaltspunkte für den möglichen Verlauf dieser Störungszone. Während die Geoelektrik die Unterschiede in den spezifischen Widerständen westlich und östlich der Störungszone deutlich zeigt, werden in den TEM-Ergebnissen die gut leitenden Schichten zwischen ca. 500 m und 800 m Tiefe als Hinweis auf die Störungszone interpretiert. Dies bedarf noch weiterer Klärung. Dazu sollen noch mögliche äquivalente Modelle betrachtet werden, die mit den DC-Ergebnissen und den seismischen Strukturen korrelieren.

Eine Studie mit Simulationsmodellen, wobei Schichten in unterschiedlicher Tiefe, Mächtigkeit und Leitfähigkeit betrachtet werden, soll Aufschluss darüber geben, welche Schichten mit entsprechendem Messaufbau der angewendeten Methoden noch aufgelöst werden können.

Mit einer Verdopplung der Auslagenlängen bei den Dipol-Dipol-Messungen auf Profil 2 und einem maximalen Abstand von Einspeisepunkt und Elektrodenauslage von ca. 6 km, deren Auswertung noch nicht abgeschlossen ist, werden Eindringtiefen bis ca.1000 m erwartet (hier nicht dargestellt), aber auch, dass oberflächennahe Aussagen nur noch näherungsweise gemacht werden können. Bei der Eindringtiefe der DC im Leinetal wird damit eine Verdreifachung im Vergleich zu dem ersten Einsatz der Standard-Wenner-Anordnung erwartet.

Referenzen

Günther, T. & Rücker, C. 2006. A general approach for introducing information into inversion and examples from dc resistivity inversion. Ext. Abstract, EAGE Near Surface Geophysics, 04.09.-06.09.2006, Helsinki.

Günther, T., Rücker, C. & Spitzer, K. 2006. 3-d modeling and inversion of dc resistivity data incorporating topography - part II: Inversion. Geophys. J. Int., 166(2), 506–517.

Günther, T., Schaumann, G., Musmann, P. & Grinat, M. 2011. Imaging of a fault zone by a large-scale dc resistivity experiment and seismic structural information. Ext. Abstr., 17th EAGE Near Surface Meeting, 12.09.-14.09.2011; Leicester, UK.

Musmann, P., Günther, T., Buness, H. & Thomas, R. 2012. Reflexions- und refraktionsseismische Erkundung zur Bestimmung der P-Wellen-Geschwindigkeitsverteilung eines Störungssystems im Leinetalgraben. Poster auf der 72. Jahrestagung der Deutschen Geophysikalischen Gesellschaft, 05.03.-08.03.2012, Hamburg.

Reyer, D. 2008. Geologische Kartierung im Bereich der östlichen Grabenrandstörung des Leinetalgrabens südlich von Sudheim. Unveröffentlichte Diplomkartierung, Georg-August-Universität Göttingen, 78 p.

Schaumann, G., Grinat, M. & Günther, T. 2011. Tiefe Erkundung des Leinetal-Störungssystems mit geoelektrischen und elektromagnetischen Messungen. Poster auf der 71. Jahrestagung der Deutschen Geophysikalischen Gesellschaft, 21.02.-24.02.2011, Köln.

Schaumann, G., Günther, T., Meyer, R. & Grinat, M. 2012. Erweiterung der Erkundungstiefe bei geoelektrischen und elektromagnetischen Messungen im Leinetal. Poster auf der 72. Jahrestagung der Deutschen Geophysikalischen Gesellschaft, 05.03.-08.03.2012, Hamburg.

Spichak, V. & Manzella, A. 2009. Electromagnetic sounding of geothermal zones. Journal of Applied Geophysics 68, p. 459-478.

Tanner, D., Albero, F., Leiss, B. & The GGG (GeothermieGruppeGöttingen) 2010. Modelling the Geothermal Potential of the Eastern Border of the Leinetal Graben, Lower Saxony. Z. geol. Wiss. 38 (1) 2010, p. 61-68, Berlin.

Weidelt, P. 1984. Bericht über Inversion transient-elektromagnetischer Messungen über geschichtetem Untergrund. Archiv-Nr. 96720. Bundesanstalt für Geowissenschaften und Rohstoffe, Hannover.

Solving the Electromagnetic Inverse Problem Using Krylov Subspace Methods

M. Scheunert[1], M. Afanasjew[1,2], R.-U. Börner[1], M. Eiermann[2], O. G. Ernst[2], K. Spitzer[1]

[1]*Institute of Geophysics, TU Bergakademie Freiberg, Germany,*
[2]*Institute of Numerical Analysis and Optimisation, TU Bergakademie Freiberg, Germany*

1 Summary

Krylov subspace methods are well-known as iterative solvers for linear systems of equations. Using the same basic projection methodology these can also be used to approximate the solution of least squares problems, while avoiding the explicit construction of the sensitivity matrix. We point out how Krylov subspace methods such as CGNR – as well as its more robust variant LSQR – take into account the least squares origin of the normal equations, thereby ameliorating the ill-conditioning inherent in the inverse problem. These observations are illustrated with examples from the inversion of 3-D helicopter electromagnetic data. The research is carried out in an interdisciplinary project called 'AIDA – From Airborne Data Inversion to In-Depth Analysis'.

2 Introduction

In the context of geophysical inversion problems Krylov subspace methods such as the conjugate gradient method are often applied directly to the normal equations. It is often neglected that variants of these methods, mainly differing in their numerical stability, are designed as a solver for the actual minimisation problem. We aim at examining the theoretical fundamentals of two selected approaches and their application to an example of airborne electromagnetics.

3 Fundamental Relations

We consider a real-valued least squares problem

$$\|\boldsymbol{r}\|_2^2 = \|\boldsymbol{d} - \boldsymbol{J}\boldsymbol{m}\|_2^2 \to \min_{\boldsymbol{m}}, \tag{1}$$

where

$$\boldsymbol{J} \in \mathbb{R}^{N\times M}, \boldsymbol{d} \in \mathbb{R}^N, \boldsymbol{m} \in \mathbb{R}^M. \tag{2}$$

The vector $\boldsymbol{m}$ solves (1) and the normal equations

$$\boldsymbol{J}^\top \boldsymbol{J}\boldsymbol{m} = \boldsymbol{J}^\top \boldsymbol{d}, \tag{3}$$

at the same time. The residual for $\boldsymbol{m}_0$, which is an arbitrary approximation of $\boldsymbol{m}$, reads

$$\boldsymbol{J}^\top \boldsymbol{r}_0 = \boldsymbol{J}^\top (\boldsymbol{d} - \boldsymbol{J}\boldsymbol{m}_0). \tag{4}$$

Using the squared linear system of normal equations, Krylov subspaces can be expressed as a sequence of ascending bases

$$\mathcal{K}_k(\boldsymbol{J}^\top \boldsymbol{J}, \boldsymbol{J}^\top \boldsymbol{r}_0) = \operatorname{span}\{\boldsymbol{v}_1, \ldots, \boldsymbol{v}_k\}, \tag{5}$$

with

$$\boldsymbol{V}_k = [\boldsymbol{v}_1, \ldots, \boldsymbol{v}_k] \quad \text{and} \quad \boldsymbol{V}_k^\top \boldsymbol{V}_k = \boldsymbol{I}. \tag{6}$$

The method of building this basis (Hermitian Lanczos process) is determined by a recursive algorithm that generates a sequence of orthonormal basis vectors $\boldsymbol{v}_k$ of $\mathcal{K}_k(\boldsymbol{J}^\top \boldsymbol{J}, \boldsymbol{J}^\top \boldsymbol{r}_0)$. We now consider two different Krylov subspace methods, CGNR and LSQR. The essential differences between both methods are the approaches used to generate $\boldsymbol{V}_k$ and to extract a unique solution. While the CGNR method applies the Lanczos process to $\boldsymbol{J}^\top \boldsymbol{J}$ and therefore uses a projection of $\boldsymbol{J}^\top \boldsymbol{J}$ the LSQR method is based on an extended matrix

$$\boldsymbol{A} = \begin{bmatrix} \boldsymbol{I}_N & \boldsymbol{J} \\ \boldsymbol{J}^\top & \boldsymbol{0}_M \end{bmatrix}, \tag{7}$$

that results in a projection of $\boldsymbol{J}$.

Note that the condition number $\operatorname{cond}(\boldsymbol{J}^\top \boldsymbol{J}) = \operatorname{cond}(\boldsymbol{J})^2$, which is also reflected in the slope and range of the singular value distribution shown in Figure 1. A representation of the solution is expressed in terms of a linear combination of these basis vectors, exploiting that in general $N \gg k$

$$\boldsymbol{m} \approx \boldsymbol{m}_0 + \boldsymbol{V}_k \boldsymbol{y}_k \ \in \ \boldsymbol{m}_0 + \mathcal{K}_k(\boldsymbol{J}^\top \boldsymbol{J}, \boldsymbol{J}^\top \boldsymbol{r}_0). \tag{8}$$

4 Basic Concepts

While the considered Krylov subspace methods use different starting points to iteratively generate bases with variants of the Lanczos process, they are very similar in nature of their essential concepts.

- The methods project large-scale problems to a sequence of nested Krylov subspaces of sufficiently low dimension such that the projected problems can be solved with direct methods.
- The action of the system matrix on the generated orthonormal bases are expressed using a much smaller representation matrix (Lanczos decomposition).
- Different selection criteria (constraints) are then used to extract an approximate unique solution from the Krylov subspace.
- Iterative updating schemes are based on implicit triangular or orthogonal factorisation of the projected matrix.

Within the derived algorithms $\boldsymbol{J}^\top$ or $\boldsymbol{J}^\top \boldsymbol{J}$ is never calculated explicitly since only products with either $\boldsymbol{J}^\top$ or $\boldsymbol{J}$ are required.

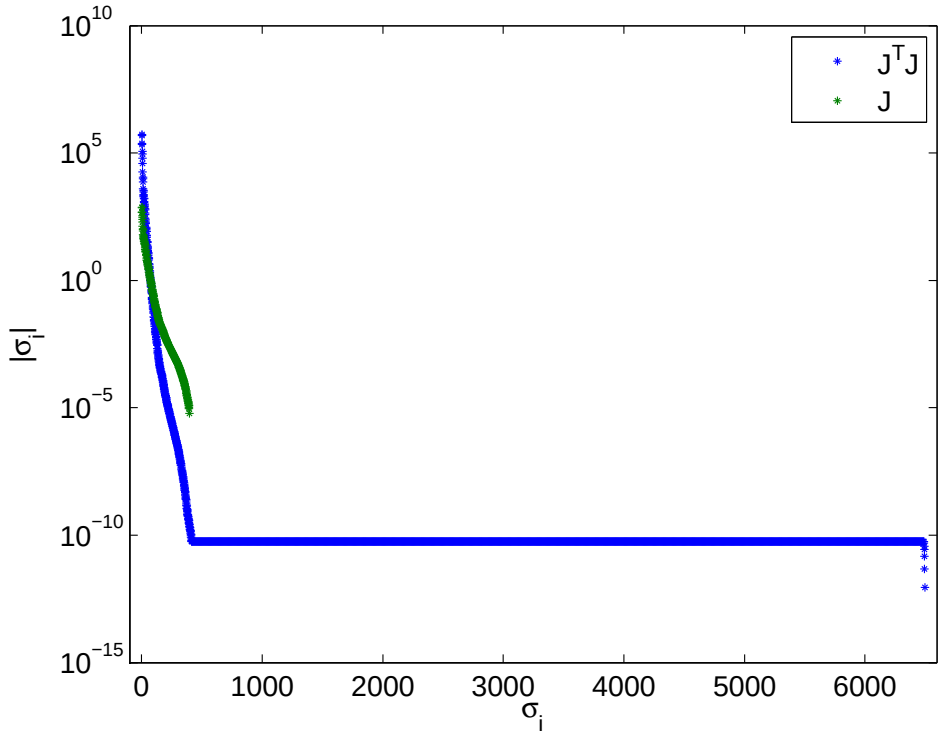

Figure 1: Singular value distribution of the matrices $\boldsymbol{J}$ and $\boldsymbol{J}^\top\boldsymbol{J}$

5 CGNR method

For the construction of the basis $\mathcal{K}_k(\boldsymbol{J}^\top\boldsymbol{J}, \boldsymbol{J}^\top\boldsymbol{r}_0)$, the CGNR method utilises the normal equations

$$\boldsymbol{A}\boldsymbol{m} = \boldsymbol{b}, \tag{9}$$

with

$$\boldsymbol{A} = \boldsymbol{J}^\top\boldsymbol{J}, \quad \boldsymbol{b} = \boldsymbol{J}^\top\boldsymbol{d} \quad \text{and} \quad \boldsymbol{s}_0 = \boldsymbol{J}^\top\boldsymbol{r}_0 = \boldsymbol{b} - \boldsymbol{A}\boldsymbol{m}_0. \tag{10}$$

The application of the Hermitian Lanczos process in order to generate an orthonormal basis $\boldsymbol{V}_k$ leads to a decomposition of the matrix $\boldsymbol{A}$

$$\boldsymbol{A}\boldsymbol{V}_k = \boldsymbol{V}_k\boldsymbol{T}_k + \delta_{k+1}\boldsymbol{v}_{k+1}\boldsymbol{e}_k^\top. \tag{11}$$

$\boldsymbol{T}_k \in \mathbb{R}^{k\times k}$ is a tridiagonal matrix, resulting from the symmetry and positive (semi)definiteness of $\boldsymbol{J}^\top\boldsymbol{J}$ and δ is a scaling factor for the vector $\boldsymbol{v}$. A unique solution that originates from the Krylov subspace is obtained by the definition of an additional constraint

$$\boldsymbol{m}_k \in \boldsymbol{m}_0 + \boldsymbol{V}_k\boldsymbol{y}_k \quad \text{s.t.} \quad \boldsymbol{b} - \boldsymbol{A}\boldsymbol{m}_k \perp \mathcal{K}_k(\boldsymbol{A}, \boldsymbol{s}_0) \quad \text{(orthogonal residual)}. \tag{12}$$

Now the initial problem of size $M \times M$ can be expressed by a projected problem of size $k \times k$:

$$\begin{aligned}
\boldsymbol{0} \overset{!}{=} \boldsymbol{V}_k^\top (\boldsymbol{b} - \boldsymbol{A}\boldsymbol{m}_k) &= \boldsymbol{V}_k (\boldsymbol{b} - \boldsymbol{A}[\boldsymbol{m}_0 + \boldsymbol{V}_k \boldsymbol{y}_k]) = \boldsymbol{V}_k^\top (\boldsymbol{s}_0 - \boldsymbol{A}\boldsymbol{V}_k \boldsymbol{y}_k), && (13)\\
&= \boldsymbol{V}_k^\top \left(\boldsymbol{s}_0 - \left(\boldsymbol{V}_k \boldsymbol{T}_k + \delta_{k+1} \boldsymbol{v}_{k+1} \boldsymbol{e}_k^\top\right) \boldsymbol{y}_k\right), && (14)\\
&= \boldsymbol{V}_k^\top \left(\delta_0 \boldsymbol{V}_k \boldsymbol{e}_1 - \boldsymbol{V}_k \boldsymbol{T}_k \boldsymbol{y}_k + \delta_{k+1} \boldsymbol{v}_{k+1} \boldsymbol{e}_k^\top \boldsymbol{y}_k\right), && (15)\\
\boldsymbol{T}_k \boldsymbol{y}_k &= \delta_0 \boldsymbol{e}_1, && (16)
\end{aligned}$$

where

$$\boldsymbol{V}_k \perp \boldsymbol{v}_{k+1}, \quad \boldsymbol{V}_k^\top \boldsymbol{V}_k = \boldsymbol{I} \quad \text{and} \quad \boldsymbol{s}_0 = \delta_0 \boldsymbol{v}_1. \tag{17}$$

Solving the resulting linear system using a Cholesky decomposition finally permits the formulation as an iterative process. Within the whole algorithm $\boldsymbol{J}^\top \boldsymbol{J}$ is never calculated explicitly since only products with either $\boldsymbol{J}^\top$ or $\boldsymbol{J}$ are required.

6 LSQR method

In contrast to CGNR the LSQR method is based on an extended linear system

$$\boldsymbol{A}\boldsymbol{u} = \boldsymbol{b}, \tag{18}$$

where

$$\boldsymbol{A} = \begin{bmatrix} \boldsymbol{I}_N & \boldsymbol{J} \\ \boldsymbol{J}^\top & \boldsymbol{0}_M \end{bmatrix}, \quad \boldsymbol{u} = \begin{bmatrix} \boldsymbol{r} \\ \boldsymbol{m} \end{bmatrix}, \quad \boldsymbol{b} = \begin{bmatrix} \boldsymbol{d} \\ \boldsymbol{0} \end{bmatrix} \quad \text{and} \quad \boldsymbol{s}_0 = \begin{bmatrix} \boldsymbol{r}_0 \\ \boldsymbol{0} \end{bmatrix} : \boldsymbol{r}_0 = \boldsymbol{d} - \boldsymbol{J}\boldsymbol{m}_0. \tag{19}$$

By (formally) applying the Hermitian Lanzcos process to this system, two orthonormal bases $\boldsymbol{W}_k$ and $\boldsymbol{V}_k$ can be generated, which together form the Krylov subspace

$$\mathcal{K}_{2k}(\boldsymbol{A}, \boldsymbol{s}_0) = \left\{ \begin{bmatrix} \boldsymbol{w} \\ \boldsymbol{v} \end{bmatrix} : \boldsymbol{w} \in \mathcal{K}_k(\boldsymbol{J}\boldsymbol{J}^\top, \boldsymbol{r}_0), \boldsymbol{v} \in \mathcal{K}_k(\boldsymbol{J}^\top \boldsymbol{J}, \boldsymbol{J}^\top \boldsymbol{r}_0) \right\}. \tag{20}$$

Two coupled decompositions, both are based on the matrix $\boldsymbol{J}$ itself, can therefore be arranged

$$\begin{aligned}
\boldsymbol{J}\boldsymbol{V}_k &= \boldsymbol{W}_k \boldsymbol{H}_k + \beta_{k+1} \boldsymbol{w}_{k+1} \boldsymbol{r}_1^\top = \boldsymbol{W}_{k+1} \boldsymbol{H}_{k+1}, && (21)\\
\boldsymbol{J}^\top \boldsymbol{W}_{k+1} &= \boldsymbol{V}_k \boldsymbol{H}_k + \alpha_{k+1} \boldsymbol{v}_{k+1} \boldsymbol{r}_1^\top = \boldsymbol{W}_{k+1} \boldsymbol{H}_{k+1}. && (22)
\end{aligned}$$

Here $\boldsymbol{H}_k$ is a bidiagonal matrix and α and β normalise the vectors $\boldsymbol{v}$ and $\boldsymbol{w}$ respectively.
The definition of a further constraint

$$\boldsymbol{m}_k \in \boldsymbol{m}_0 + \boldsymbol{V}_k \boldsymbol{y}_k \quad \text{s. t.} \quad \|\boldsymbol{d} - \boldsymbol{J}\boldsymbol{m}_k\|_2^2 \to \min_{\boldsymbol{m}_k} \quad \text{(minimal residual)}, \tag{23}$$

leads to a projected problem which now has the size of $k+1 \times k$

$$\begin{aligned}
\|\boldsymbol{r}_K\|_2^2 = \|\boldsymbol{d} - \boldsymbol{J}\boldsymbol{m}\|_2^2 = \|\boldsymbol{d} - \boldsymbol{J}(\boldsymbol{m}_0 + \boldsymbol{V}_k \boldsymbol{y}_k)\|_2^2 &= \|\boldsymbol{r}_0 - \boldsymbol{J}\boldsymbol{V}_k \boldsymbol{y}_k\|_2^2, && (24)\\
&= \|\beta \boldsymbol{W}_{k+1} \boldsymbol{e}_1 - \boldsymbol{W}_{k+1} \boldsymbol{H}_{k+1} \boldsymbol{y}_k\|_2^2, && (25)\\
\|\beta \boldsymbol{e}_1 - \boldsymbol{H}_{k+1} \boldsymbol{y}_k\|_2^2 &\to \min_{\boldsymbol{y}_k}, && (26)
\end{aligned}$$

exploiting

$$\boldsymbol{r}_0 = \beta_0 \boldsymbol{W}_{k+1} \boldsymbol{e}_1 \quad \text{and} \quad \|\boldsymbol{H}_{k+1} \boldsymbol{z}\|_2^2 = \|\boldsymbol{z}\|_2^2. \tag{27}$$

To end up with an iterative algorithm, this minimisation problem can be solved using the QR decomposition. The LSQR method also requires only products with either $\boldsymbol{J}^\top$ or $\boldsymbol{J}$.

7 Numerical Examples

To verify the theoretical aspects both methods have been implemented to solve the 3D inversion problem for helicopter electromagnetic data. We use a finite difference forward operator and apply it to the secondary field approach of Maxwell's curl-curl equation. The primary field of a vertical dipole source is computed analytically. The parameter distribution is based on a coarse grid which acts as a starting point for the adaptively refined modelling grid. In summary, we observe an underdetermined problem consisting of 395 data points and 6496 model parameters. The resulting least squares problem based on the minimisation of magnetic fields is approximated using the Gauss-Newton method. To avoid the inverse crime we apply a different finite difference code for generating the synthetic data so that the resulting data error stays below 4 %.

The convergence rates of both Krylov methods applied to the first Gauss-Newton step are shown in Figure 2. Due to the fact that the LSQR method is based on the better-conditioned matrix $\boldsymbol{J}$, this results in a slightly better convergence rate. In combination with a well-defined terminating condition, therefore a reduction of the required iteration steps could be achieved.

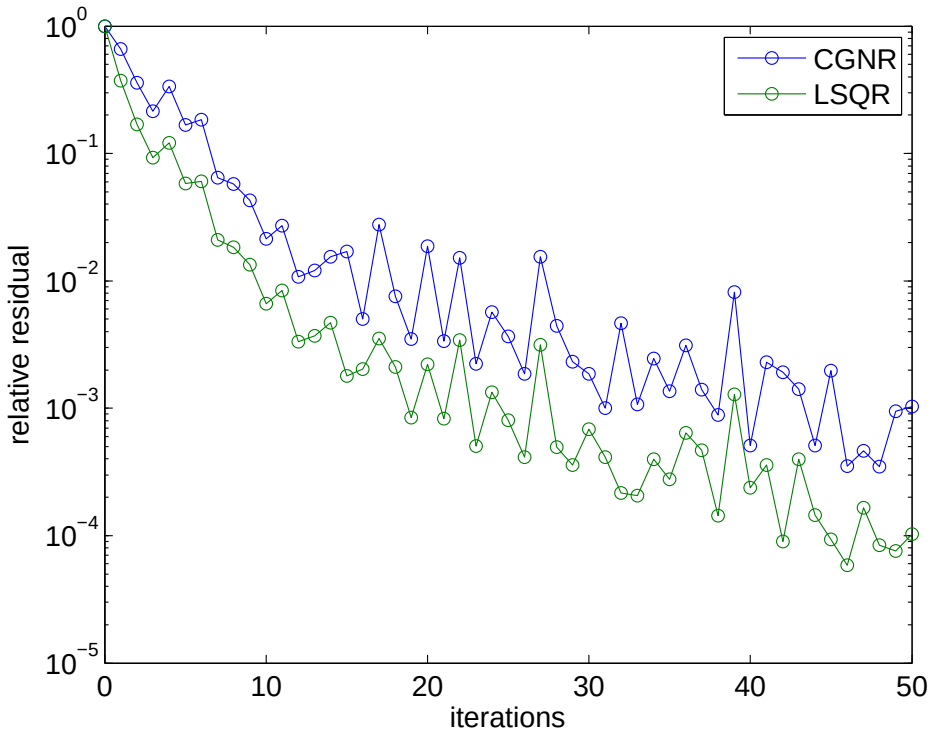

Figure 2: Relative residuals resulting from LSQR solving the least squares problem as well as CG solving the normal equation, in each case for the first Gauss-Newton iteration

8 Conclusion

Two Krylov subspace methods for solving the linear equation systems arising from least squares minimisation problems have been investigated. Both approaches differ in how they generate an orthonormal basis. The improved convergence rate of the LSQR method, mainly resulting from its inherent numerical stability, could be demonstrated for a minimisation problem which is typical, e. g., in large scale 3-D helicopter electromagnetic applications.

9 Acknowledgements

This research has been funded by the German Ministry of Education and Research BMBF and the German Research Foundation DFG under the Geotechnologien Programme, grant 03G0735D.

References

[1] Hestenes, M.R. and Stiefel, E. “Methods of Conjugate Gradients for Solving Linear Systems”. In: *Journal of Research of the National Bureau of Standards* 49. 6 (1952), pp. 409–436.

[2] Paige, C.C. and Saunders, M.A. “LSQR: An Algorithm for Sparse Linear Equations and Sparse Least Squares”. In: *ACM Transactions on Mathematical Software* 8. 1 (1982), pp. 43–71.

MARINE CONTROLLED SOURCE ELECTROMAGNETIC METHODS FOR GAS HYDRATE ASSESSMENT: NEW INSTRUMENTATION AND FIRST RESULTS FROM THE BLACK SEA TEST CRUISE

Katrin Schwalenberg, Martin Engels
Bundesanstalt für Geowissenschaften und Rohstoffe (BGR)
Stilleweg 2
30655 Hannover
GERMANY

ABSTRACT

The electrical conductivity of the seafloor derived from marine controlled source electromagnetic (CSEM) data can be related to the gas hydrate concentration and distribution within the stability zone, and can provide valuable information for resource assessment. Gas hydrates are electrically resistive in contrast to the conductive pore fluid and may significantly increase the bulk resistivity where they occur in sufficient quantities.
The marine electromagnetic group at BGR has developed a new, seafloor-towed, electrical multi-receiver system that consists of a transmitting dipole and four receiving dipoles at increasing offsets, sensitive to depths relevant for gas hydrate evaluation from the seafloor to some hundred meters below. The system was successfully deployed on a test cruise on RV Poseidon in water depth of 1335 m over known gas hydrate targets in the Danube Delta, and in shallow water on the upper rim of the Danube Canyon. Inversion of the data reveals highly anomalous resistivity which at least for the deep water deployment can be explained with a combination of fresh pore water and the presence of gas hydrates in the sediments.

Keywords: gas hydrates assessment, marine controlled source electromagnetics, Black Sea

1. Introduction

Marine controlled source electromagnetics (CSEM) has become an important exploration tool for submarine energy resources such as oil and gas (e.g. Constable and Srnka, 2007). Recently, there have been also a number of case studies using CSEM methods for submarine gas hydrate studies (Yuan and Edwards, 2000, Schwalenberg et al., 2005, Weitemeyer et al., 2006, 2011, Schwalenberg et al., 2010a, b).
Gas hydrates are ice-like compositions of water and methane molecules, and are stable at high pressure and low temperature conditions. These conditions are found along most continental margins, in permafrost grounds and deep lakes. The global budget of methane stored in hydrate is vast, probably in the order of all other conventional hydrocarbon energy resources (oil, gas, coal). Yet, estimates differ considerably (Burwicz, 2011, Milkov 2004) and the assessment of substantial gas hydrate deposits in marine sediments is still an ambitious exploration problem. The extent of the gas hydrate stability zone (GHSZ) in the marine environment depends on water depth (pressure) and the regional heat flow (temperature). Marine gas hydrates typically occur in water depths exceeding about 500 m and extend from the seafloor to some hundred meters below. Within the GHSZ gas hydrate formation has been observed as isolated pellets in pore space, along grain contacts, filling fissures and cracks, or in solid layers from centimeter to 10^{th} of meter scale. A wide range of techniques is used to assess the extent and concentration of gas hydrate deposits including mapping of the bottom simulating reflector (BSR) using reflection seismic data, seismic velocity analysis, heat flow, seafloor compliance, water column imaging of methane flares and plumes, seafloor sampling, geochemical and microbiological analyses, and ocean drilling. These methods operate on different scales and address different processes. Besides of seismic and ocean drilling most of these methods are confined to the very shallow seafloor section.
Marine CSEM is an exploration method sensitive to the entire gas hydrate stability zone. The electrical conductivity of the seafloor derived from marine CSEM data can be related to the presence of resistive hydrocarbons, and can provide valuable information for resource assessment. Gas hydrates are electrically resistive in contrast to the conductive pore fluid and may significantly increase the bulk resistivity where they occur in sufficient quantities.

Here we report on first results from the western Black Sea using a newly developed, bottom-towed electric dipole-dipole system. Instrument development and the survey was part of the German gas hydrate program SUGAR- submarine gas hydrate reservoirs.

2. Electrical Resistivity of Gas Hydrate

The replacement of conductive pore fluid with resistive gas hydrate increases the formation resistivity. Thus, the electrical resistivity of the seafloor derived from marine CSEM data can be related to the presence of gas hydrate. A simplified approach to estimate the gas hydrate content of a reservoir is given by Archie's empirical law (Archie, 1942):

$$\rho_f = a\rho_\omega \phi^{-m} S_\omega^{-n},$$

with ρ_f: formation resistivity, ρ_ω: pore water resistivity, ϕ: sediment porosity, S_ω: pore water saturation, S_h=(1- S_ω): gas hydrate fraction, *a*, *m*, *n*: coefficient, cementation factor, saturation factor.

Archie's law is defined for porous media and may provide false estimates when gas hydrate has formed in sub-parallel fissures and cracks causing a local anisotropy. This could be the case in borehole measurements (e.g. Cook et al., 2010, Ellis et al., 2011). However, for larger sediment volumes covered by the diffusive propagation of electromagnetic fields for source-receiver offsets exceeding 100 m, Archie's law may provide a useful estimate of the average gas hydrate content of the surveyed area. The presence of free gas which is also resistive cannot be ruled out by marine CSEM data alone, but is believed to play a minor role as it will mainly result in the formation of gas hydrate within the gas hydrate stability field, and would also cause a seismic signature. The exclusion of chloride during hydrate formation increases the pore water conductivity and may, at least in parts, compensate the higher formation resistivity due to the presence of gas hydrate. In this case, the gas hydrate concentration derived from CSEM may be even underestimated.

Table 1 lists the fractional gas hydrate concentration for some formation resistivities for a typical set of Archie's parameter. This demonstrates that the formation resistivity is a robust indicator for high gas hydrate concentrations while low concentrations (< 5%) may be difficult to resolve from CSEM data alone.

Gas hydrate Fraction	Formation Resistivity
0 %	1.2 Ωm
5 %	1.33 Ωm
20 %	1.88 Ωm
40 %	3.33 Ωm
70 %	13.33 Ωm

Table 1. Background porosity ϕ:=50%, ρ_ω= 0.3 Ωm, a=1, n=m=2.

3. HYDRA – a new Bottom-Towed Time-Domain CSEM System

The towed CSEM system follows a simple principle: the electromagnetic signal generated by the current transmitter propagates with time away from the source dipole. The diffusion process is faster (less damping) through the resistive seafloor than through the conductive seawater. Each receiver dipole records the voltage of the ambient electric field. Amplitude and waveform of the electric field depend on the sub-seafloor resistivity and can be interpreted in terms of sediment properties such as gas hydrate or fluid content.

The marine electromagnetic group at BGR has developed a new, seafloor-towed, electrical, dipole-dipole system (Figure 1). The design of the system is based on a previous system built at the University of Toronto for gas hydrate mapping. This older system consists of two receiving dipoles towed in-line behind a transmitting dipole and was used to study gas hydrates in Cascadia (Yuan and Edwards, 2000), Schwalenberg et al., 2005), Chile (Schwalenberg et al., 2006), and New Zealand (Schwalenberg et al., 2010a, b).

HYDRA, the new BGR system, consists of a horizontal electrical transmitting dipole, 100m long, and four receiver units with horizontal, 10 - 20 m long receiving dipoles which are connected inline along a data

cable at offsets from 150 m to 750 m. An instrument platform called the 'pig' is attached to the front end of the array. It hosts the control unit, a CTD sensor measuring seawater conductivities and sound velocities, and an acoustic transponder system to get the seafloor position of the pig. The pig also serves as a depressor to keep the array on the seafloor while towing along profiles.

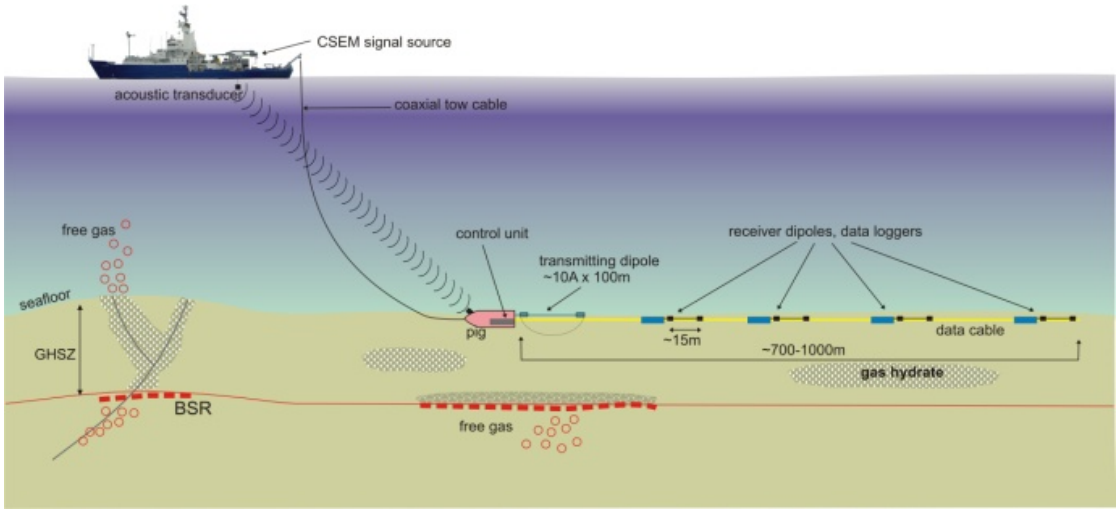

Figure 1: Set-up of HYDRA, the new BGR bottom towed CSEM System

Receiver units and the control unit are battery powered with a lifetime of about 72 h and have their own data logger and front end electronics inside a stainless steel pressure cylinder. Data are collected and stored locally on 4GB micro SD cards at a sampling frequency of 10 kHz. Control and receiver units are synchronized with a 1pps signal sent from the control unit along the data cable to the receiver units. At this stage data were only available after instrument recovery through an USB connection. Housekeeping data, i.e. compass, 3-axis accelerometer and temperature inside the pressure cylinder, are recorded every second. The receiving dipoles have a pair of Ag/AgCl electrodes attached to the data cable behind the receiver unit pressure cylinders.

The source signal is generated by a current transmitter onboard the research vessel and is sent down to the transmitting dipole on the seafloor via the coaxial deep-tow cable. The signal form is typically a square wave with a period between two and six seconds, but any signal waveform i.e. sine, ramp can be applied. Transmitted currents and voltages are recorded with the control unit. The current transmitter has two output ranges for shallow (40A, 200V) and deep water applications (13A, 1000V). Sediment investigation depths from the seafloor to 100 m – 350 m below can be achieved with the set-up which covers the area of interest of the gas hydrate stability zone.

Figure 2: Deployment procedure: The CSEM system is deployed over the aft deck of the research vessel. The 'pig' an instrument platform and plough is picked up last by the A-frame and lowered to the seafloor.

The system is deployed over the aft deck and aligned on the seafloor while the ship is slowly moving forward at a speed around one knot. A cable length of about three times the water depth is paid out to ensure that the system remains on the seafloor while being dragged on the seafloor. Data are recorded continuously while towing, but the array is stopped for some minutes because data quality improves considerably when the array does not move on the seafloor.

4. Danube Delta Geology and CSEM survey area

The Black Sea is a quasi closed marginal sea with unusual sediment thickness of up to 19 km in the western basin, and 10-12 km in the eastern basin. Anoxic conditions favor the generation of hydrocarbons. Methane seeps have been frequently observed, particularly at the shelf edge outside the gas hydrate stability field. The existence of gas hydrates has been inferred through seismic mapping of the bottom simulating reflector (BSR) and direct sampling.

The sediment input is particularly high in the area of the Danube Fan in the northwestern part of the Black Sea. Seismic data analyzed by Popescu et al. (2006) and Baristeas (2006) show widespread areas of BSRs and multiple BSRs which are interpreted as paleo BSRs caused by past sea level changes. Thus, the gas hydrate potential is expected to be particularly high in the Danube fan.

The CSEM experiments were part of the test cruise on RV Poseidon (Leg POS405) in December 2010 to test new instrumentations and systems developed in the SUGAR project (Bialas et al., 2011). The survey area was located around the Danube Fan in Romanian Waters, about 100 nm southeast of Constanta (Figure 4).

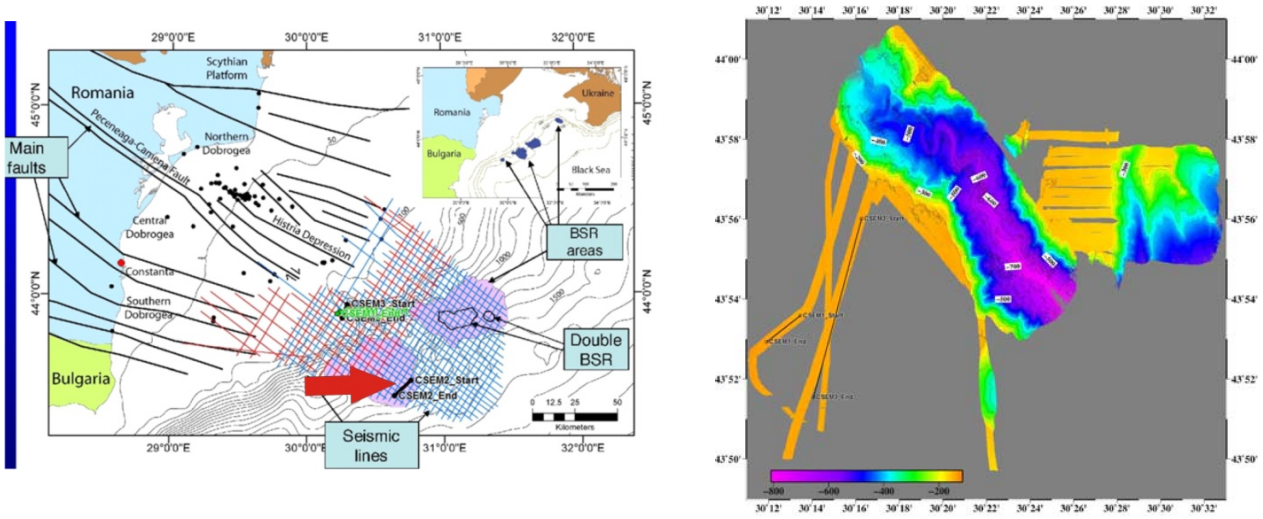

Figure 4: Working area of the SUGAR test cruise in the Danube Delta, Black Sea. The new towed CSEM system was deployed over potential gas hydrate areas along profile 2 (red arrow, left) in 1335 m water depth.BSR areas are marked in violet (map updated from Baristeas, 2006). The right figure shows a bathymetric map of the Danube fan (Bialas et al., 2011) with the two shallow water profiles.

5. Black Sea CSEM Experiment

HYDRA, the new CSEM system, was deployed three times along three profiles. Two deployments were completed on the upper shelf edge of the Danube Canyon in water depths around 100 m thus outside the hydrate stability zone. One profile was conducted in water depths of 1335 m over an area with bottom simulating reflectors (BSRs) indicating the presence of gas hydrates. The CSEM survey parameters are summarized in Table 2.

Nr.	Set-up / Offsets	Profile Coordinates	Water Depth
1	Pig – TX – RX1 Offset: T-R1: 156.13m	Start: 43:50.95N / 30:13.54E End: 43:56.11N / 30:18.47	107m
2	Pig – TX – RX1 – RX2 – RX3 – RX4 Offsets: T-R1: 151.08m (only late time) T-R2: 253.90m (only late time) T-R3: 396.76m T-R4: 745.03m	Start: 43:28.33N / 30:38.94E End: 43:55.19N / 30:21.42	1323-1350m
3	Pig – TX – RX1 – RX2 – RX3 Offsets: T-R1: 151.08m (only late time) T-R2: 253.90m (saturated) T-R3: 399.50m	Start: 43:52.79N / 30:14.39E End: 43:53.38N / 30:20.93	106m

Table 2: CSEM survey parameter, including number of receivers, transmitter receiver offsets, profile coordinates and water depths.

6. Data Processing

CSEM data recorded with the electrical dipole-dipole system are time series of the ambient electric field recorded at each receiver unit, and the transmitted current recorded with the control unit. Figure 5a shows a filtered data example from the second deployment in deep water with four receivers. The top panel shows the current signal, a square wave with a peak-to-peak Amplitude of +/- 10 A and a period of 4s. The data of R1 and R2 show spikes when the current polarity is switched. These distortions decrease with distance from

the transmitter and have been identified to be caused by inductive cross talk from the strong transient current signal to the data cable. The distortions propagate via the data cable to the following receivers where they get picked up by the receiver dipoles parallel to the data cable. The last receiver dipole is not attached to the data cable and displays much cleaner data beside of the smaller signal amplitudes.

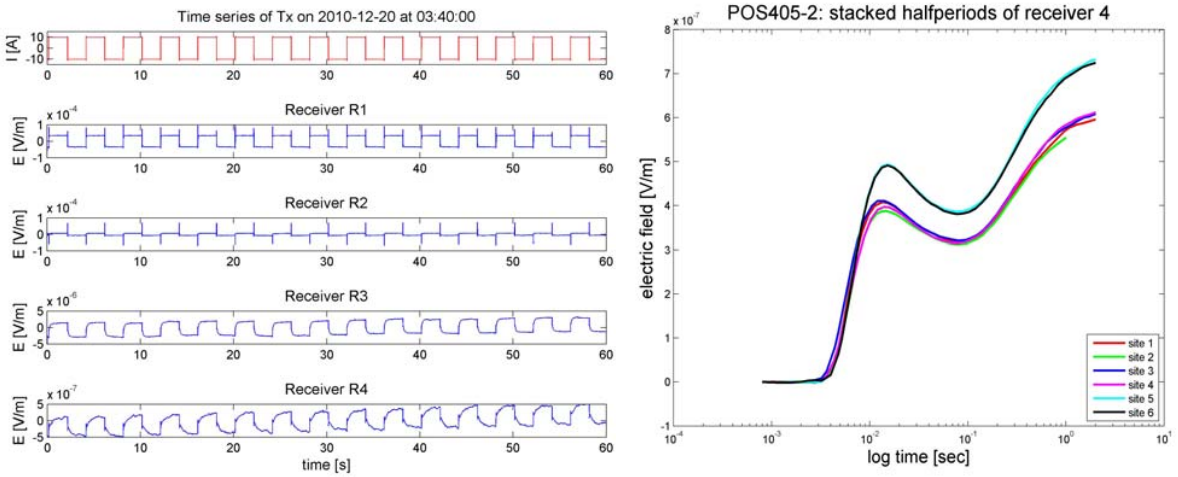

Figure 5a (left figure): Data example from the Black Sea cruise. The top panel shows the source signal recorded at the control unit. The lower panels show the data from four receivers. Figure 5b (right figure) shows stacked data from six sites along the profile recorded with the last receiver R4 at an offset of 745m. The source dipole moment was 10 A x 100 m for sites 1-4 and 12 A x 100 m for sites 5 and 6. The data (stacked halfperiods) show a very pronounced double-bump which is indicative for a strong conductivity contrast between seawater and a very resistive sub-seafloor. The first bump is caused by the part of the signal propagating through the resistive seafloor. The second rise at late times (>0.5 s) is the part of the signal through the seawater. The stacked data are used as input to obtain the 1-D layered inversion results.

Data processing includes the following steps:

(1) LP filtering: The original time series recorded with 10 kHz sampling rate shall be decimated in the second step to e.g. 2.5 kHz. Before decimation, the time series is low pass filtered using a zero phase Butterworth filter with a cut-off frequency equal to the Nyquist frequency of the decimated time series. This filtering does not remove information but internal high frequency noise from the electronics in the 4-5 kHz range (beat frequencies). Furthermore, distortions by inductive cross talk are reduced for receivers (e.g. completely for R3 in Figure 5a).

(2) Averaging and decimation: Data are first averaged by a running mean from 10 kHz to e.g. 2.5 kHz and then decimated. This downward averaging increases resolution and improves data quality.

(3) Offset and drift correction: Removal of DC offsets and electrode drifts can be relevant within a period. Therefore, a quadratic drift correction of each period has been applied by approximating a linear trend to the differences of both neighbour periods.

(4) Stacking: At each site along a profile the time series is divided in half-periods. Using an iterative scheme, two thirds of all half-periods but not more than 100 are selected in terms of minimum standard deviation against the stacked half-period.

(5) Data picking: From the stacked receiver transients and their standard deviations, and the current signal or system response data are picked linearly at early times and logarithmically at late times using maximal 50 picks in total. For some receiver transients early times were discarded because they are particularly affected by inductive noise from the transmitter.

The picked system responses, and receiver data and standard deviations are the input in the subsequent inversion.

7. Data Inversion

We used a code supplied by C. Scholl (pers. communication) that offers 1D Marquardt-type and Occam-type inversion strategies. Data inputs in the inversion are the stacked and picked receiver transients and data errors at each site along the profile where the array was stationary on the seafloor, the corresponding system responses, and a starting model. The starting model consists of the thickness and conductivity of the water layer taken from the CTD (conductivity, temperature, density) sensor inside the "pig" and which are fixed in the inversion, and the resistivities and thicknesses of the underlying model.

The first step in the inversion is the calculation of the halfspace resistivity for the data of each receiver at each waypoint using Marquardt-type inversion. This is shown in Figures 6 and 8. The apparent resistivity is an average value of the sediment volume between transmitter and receiver at each waypoint and displays lateral variations along the profiles.

Secondly, if data of more than one receiver can be used we apply a layered starting model and jointly use the data of receivers at different offsets covering the same waypoints to receive the lateral and also the vertical resistivity distribution. Figure 7 shows a result for the second deployment with four receivers.

8. Preliminary Results from the Black Sea

Profile POS405-1

CSEM Profile 1 is located in 106 m water depth on the southern upper slope of the Danube Delta. Due to bad weather conditions and a short time window only one receiver was towed at an offset of 156 m behind the transmitter. The data have been processed following the procedure described above. The apparent resistivity profile derived from the data shows almost constant halfspace resistivities around 5 Ωm (not shown here).

Profile POS405-2

Profile POS405-2 is located in 1335 m water depth over an area with known BSRs. Data at six waypoints have been analyzed along the 2.5 km long profile. The complete system set-up with four receivers was used for the deployment. The early time transients of the first two receivers are severely distorted by inductive noise generated by the transmitter signal as described above. Thus only late time responses were used in the inversion for these data sets. Fig. 6 shows the apparent resistivity profiles derived for each receiver using Marquardt-type inversion. The respective RMS profiles are plotted on top. The apparent resistivities increase with offset from the transmitter indicating increasing resistivities at depth. RMS misfits are around 1 for small offsets increasing slightly for larger offsets where a halfspace model is not anymore explaining all data within its error bars.

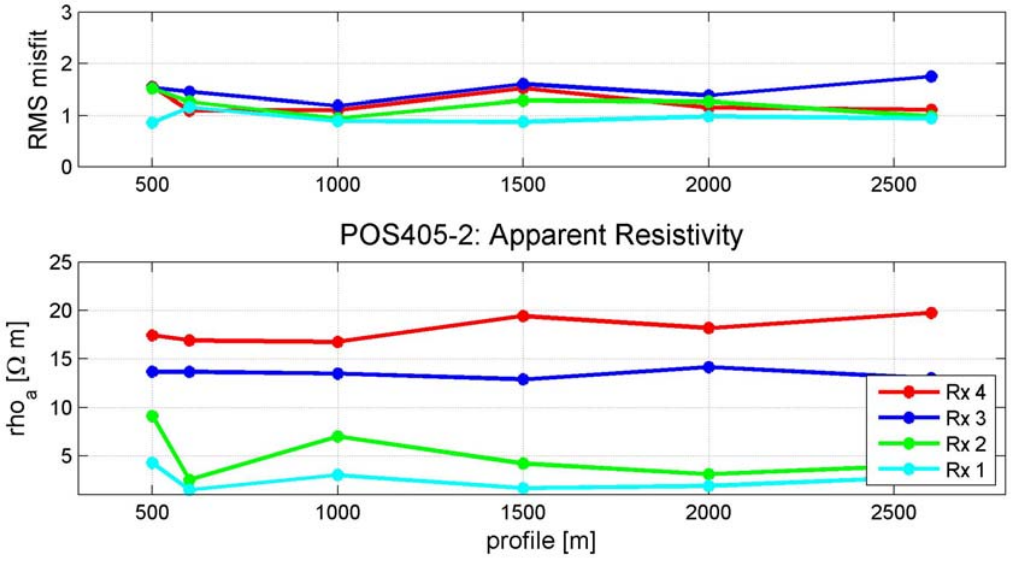

Figure 6. Halfspace inversion results along profile POS405-2 in 1335 m water depth over BSRs. Apparent resistivities increase with increasing offsets averaging over a larger and deeper induction space.

Figure 7 shows two inversion results using data from three receivers (R2, R3, R4), and a starting model with 10 layers and Occam-type inversion (top) or a three-layer starting model and Marquardt-type inversion (bottom) with RMS misfits on top. Both models show a highly resistive layer ($\rho > 30$ Ωm) at depth(100-250 mbsf for the Occam models with fixed layer geometry, 50-150mbsf for the Marquardt models). The Marquardt models show a conductive layer in the first 50 mbsf with resistivities around 3 Ωm while the Occam models show a very thin resistive layer at the seafloor on top of the 3 Ωm layer. For both models the lateral resistivity distribution is uniform to a first approximation. We conclude, the resistivities are clearly elevated along profile POS405-2 with the highest resistive zone at depths between 50 and 200 mbsf.

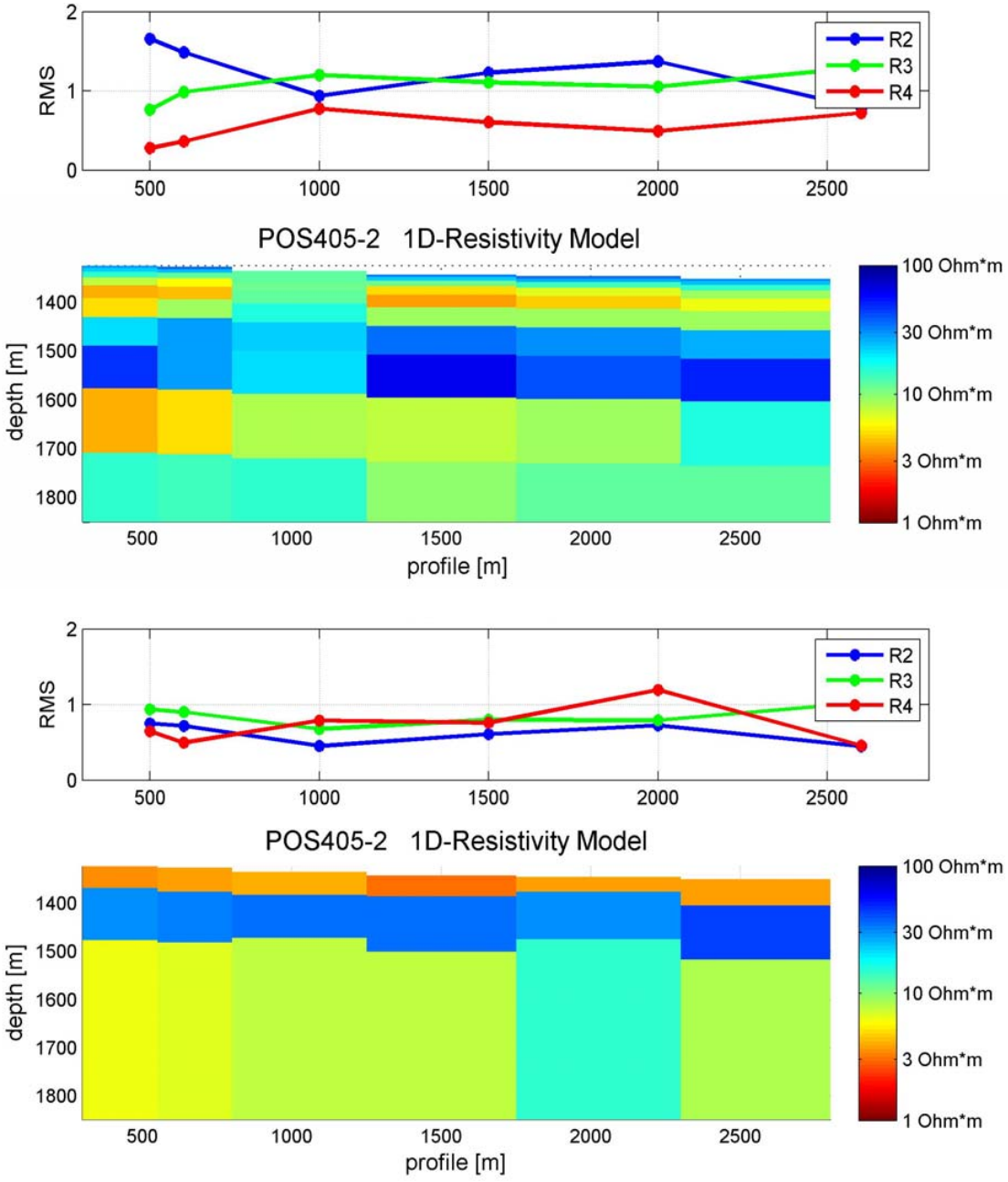

Figure 7. Occam- (top) and Marquardt-type (bottom) inversion results along profile POS405-2 in 1335 m water depth over BSRs. Both models show a resistive layer at different depths which is possibly caused by a combination of gas hydrate filling pore space as indicated by BSRs and fresh pore water as proposed by Popescu et al. (2006) and CTD measurements.

Profile POS405-3

Profile POS405-3 is located in vicinity to profile POS405-1 on the upper rim of the Danube Canyon (Fig. 4). HYDRA with three receivers was towed along the seven km long profile (see table 2). Electrodes of R2 drifted out of range, thus no data could be used from the second receiver. Early time data of receiver R1 were distorted by transmitter noise as described above, therefore, only late time responses are used in the inversion. Figure 8 shows the inverted halfspace resistivity profile for R1 and R3. The profile shows an increase in apparent resistivity for the last receiver from ~7 Ωm to the NE to ~16 Ωm at the SW end of the profile. A good data fit of all models is expressed by rms values around and below 1. The high apparent resistivity of 16 Ωm is in the order of the apparent resistivity observed along the deep water profile POS405-2. However, profile POS405-3 is clearly outside the gas hydrate stability field, thus gas hydrate can be ruled out to contribute to the high resistivity. However, free gas migrates even to the shallow areas in the Danube delta where many methane seeps are mapped. Therefore, a candidate for the high resistivity might be free gas or fresh water lenses.

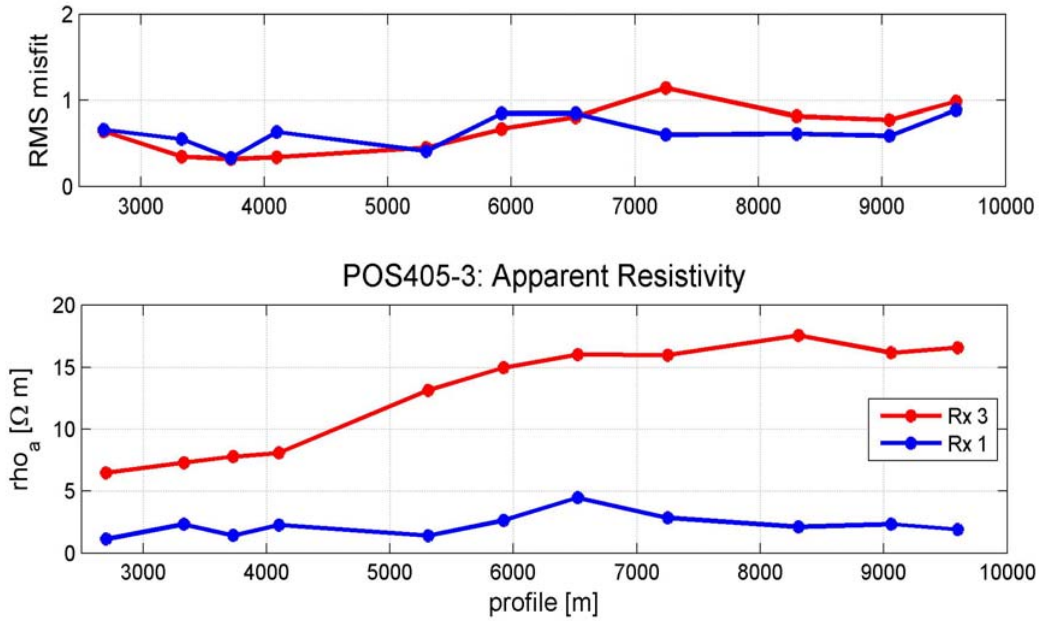

Figure 8. Halfspace inversion results along profile POS405-3 in 106 m water depth. Apparent resistivities of the last receiver (offset 399.50 m) increase from 7 Ωm in the first part to about 16 Ωm in the second much more resistive part.

9. Discussion

Two explanations may account for the anomalously high resistivities along the deep water profile POS405-2: Fresh pore water and the presence of gas hydrate which both increase the formation resistivity. Popescu et al. (2006) point out low porewater salinities observed in DSDP 42B drilling in the central Black Sea. Our CTD sensor also measured sea-bottom resistivities of 0.43 Ωm, and the presence of gas hydrate is indicated by wide spread bottom simulating reflectors in the area (Popescu et al., 2006). If the resistive layer shown in Figure 7 is present in all areas where the BSR is already mapped, large amounts of gas hydrates may have accumulated in the Danube delta.

The interpretation of the two shallow water profiles is more difficult. Apparent resistivities along profile POS405-1 with one receiver at offset 156 m are about 5 Ωm, while they are between 1.5 and 5 Ωm for receiver 1 at offset 151 m along nearby profile POS405-3, and increase from 6 to 17 Ωm for receiver 3 at offset 399.50 m. Thus there is a discrepancy between the apparent resistivities derived at short offsets. However, we think that the resistivities around 5 Ωm along profile POS405-1 are more reliable, because the whole transient was used in the inversion which results in more robust inversion results. Profile POS405-3 is clearly located outside the gas hydrate stability field. Thus, the high resistivities at R3 at the SW end cannot be explained with gas hydrate. We assume that free gas may have accumulated at deeper levels along the profile. Active venting of free gas from the seafloor has been frequently observed in acoustic data on the upper shelf edge around the Black Sea (Naudts et al., 2006). The high resistivities may indicate deeper gas-filled sediments, and the gas migrates along faults to the seafloor.

Archie's law can be used to approximate the sediment porosity and gas hydrate saturation from the resistivities. With a=1, m=n=2, ρ_f = 5 Ωm, ρ_ω=0.5 Ωm (inversion result of profile 1) and S_ω = 1 (no gas hydrate) we resolve a sediment porosity ϕ of 32 %. This is a very low porosity value for shallow seafloor sediments, and could be due to wrong settings of Archie parameters a, m, and n, or due to the presence of another resistive phase (i.e. free gas), or Archie's law is simply not applicable. Instrument errors and wrong offset readings should be also present in the other data sets. However, at this time we don't have a better estimate for Archie's parameter. If we take the 32 % as a background porosity for the deep water profile, we obtain with ρ_f = 17 Ωm an average gas hydrate saturation of 46 % for the deep water profile.

ACKNOWLEDGEMENT

The development of HYDRA was supported by project SUGAR - Submarine Gas Hydrate Deposits, BMBF Grant 03G0688A. We thank the Captain and Crew of RV Poseidon for technical assistance. University of Toronto and Geomar supplied ship time for first instrument tests. All electronics have been developed in productive cooperation with MAGSON GmbH, Berlin. C. Scholl, Fugro-EM, Berlin, is thanked for supplying his 1-D CSEM inversion code.

REFERENCES

Baristeas N. Seismische Fazies, Tektonik und Gashydratvorkommen im nordwestlichen Schwarzen Meer. Diplomarbeit, Universität Hamburg, 2006. 106 pages.

Bialas J (ed). POS 405 Cruise Report, 7-22 December 2010.

Burwicz EB, Ruepke LH, Wallmann K. A new global gas hydrate budget based on numerical reaction-transport modeling and a novel parameterization of Holocene and quarternary sedimentation. Proceedings of the 7th ICGH, Edinburgh, Scotland, July 17-21, 2011.

Constable S, Srnka LJ, 2007. An introduction to marine controlled-source electromagnetic methods for hydrocarbon exploration. Geophysics; 72(2):WA3-WA12.

Edwards RN, 1997. On the resource evaluation of marine gas hydrate deposits using sea-floor transient electric dipole-dipole methods. Geophysics; 62(1):63-74.

Edwards RN, Schwalenberg K, Willoughby EC, Mir R, Scholl C, 2010. Marine Controlled-source Electromagnetics and the Assessment of Seafloor Gas Hydrate. In: Riedel M, Willoughby EC, Chopra S, editors. Geophysical Characterization of Gas Hydrates. SEG Geophysical Developments Series No. 14, 149-160.

Ellis M., Evans RL, Hutchinson D, Hart P, Gardner J, Hagen R, 2008. Electromagnetic Surveying of Seafloor Mounds in the Gulf of Mexico. Mar. Pet. Geol.,doi:10.1006/j.marpet.geo.2007.12.006.

Milkov AV, 2004. Global estimates of hydrate-bound gas in marine sediments: how much is really out there? Earth Science Reviews, 66, 183-197.

Naudts L, Greinert J, Artemov Y, Staelens P, Poort J, Van Rensbergen P, De Batist M, 2006. Geological and morphological setting of 2778 methane seeps in the Dnepr paleo-delta, northwestern Black Sea. Marine Geology, 227, 177-199.

Popescu I, DeBatist M, Lericolais G. Nouze H, Poort J, Panin N, Versteeg W, Gillet H, 2006. Multiple bottom –simulating reflectors in the Black Sea: Potential proxies of past climate conditions. Marine Geology, 227, p163-176.

Popescu I, Lericolais G, Panin N, De Batist M, Gillet H, 2007. Seismic expression of gas and gas hydrates across the western Black Sea. Geo-Mar Lett. DOI 10.1007/s00367-007-0068-0.

Schwalenberg K, Haeckel M, Poort J, Jegen M, 2010. Evaluation of gas hydrate depsoits in an active seep area using marine controlled sourc electromagnetic: Results from Opouawe Bank, Hikurangi Margin, New Zealand. Marine Geology, 272, 79-88.

Schwalenberg K, Wood W, Pecher I, Hamdan L, Henrys S, Jegen M, Coffin R, 2010. Preliminary interpretation of electromagnetic, heat flow, seismic, and geochemical data for gas hydrate distribution across Porangahau Ridge, New Zealand. Marine Geology, 272, 89-98.

Schwalenberg K, Willoughby E, Mir R, Edwards RN, 2005. Marine gas hydrate electromagnetic signatures in Cascadia and their correlation with seismic blank zones. First Break, 23, 57–63.

Weitemeyer KA, Constable SC, Key KW, Behrens JP, 2006. First results from a marine controlled-source electromagnetic survey to detect gas hydrates offshore Oregon. GRL, 33.

Yuan J, Edwards, RN, 2000. The assessment of marine gas hydrates through electrical remote sounding: Hydrate without a BSR? Geophys. Res. Lett., 27, 2397-2400.

3D Airborne Electromagnetic Mapping of Groundwater Salinisation and Lithology along the Staßfurt-Egeln Anticline, Germany

Bernhard Siemon, Tatjana Kerner

Bundesanstalt für Geowissenschaften und Rohstoffe (BGR), Stilleweg 2, D-30655 Hannover

bernhard.siemon@bgr.de, *www.aerogeophysik.de*

Summary

A number of destructive effects of the subsiding surface at the Staßfurt-Egeln salt anticline in central Germany were caused by collapses of abandoned salt mine pits, the dissolution of salt in the mines and the pump-driven drainage system. These man-made effects increased the effect of natural salt solution along the south-western side of the Staßfurt-Egeln anticline. In order to investigate possible consequences of salt-mine flooding the German Federal Ministry of Education and Research funded the research project 'Dynamic processes in flooded or abandoned salt mines and their overburden'. As an example for this multidisciplinary research project, the area of the 1200-year-old town of Staßfurt, where the world's first potash mine was opened in 1852, was selected.

BGR conducted an airborne geophysical survey covering the salt anticline in summer 2007. Helicopter-borne frequency-domain electromagnetic, magnetic and radiometric data were simultaneously collected over an area of 470 km^2 at a line spacing of 100 m. The aim of this survey was to acquire extensive electrical conductivity data sets showing the regional hydrogeological and geological structures down to about 100 m depth.

The electromagnetic data, inverted to layered-earth resistivity models, revealed several hydrogeologically important features such as the distribution of salt water, areas of salt-water rise, buried paleo channels and freshwater influents. In addition to that areas with distinct conductivity anomalies, interpreted as evidence of potential groundwater recharge (low conductivity) or salinisation zones (high conductivity), were selected for more detailed high-resolution ground geophysical studies. The airborne electromagnetic data were also used as input for 3D geological and hydrogeological modelling and served as base-line data for a hydrogeological drilling programme.

Introduction

The German Federal Ministry of Education and Research (BMBF) funded under the program 'Research for Sustainability' (FONA) the research project 'Dynamic processes in flooded or abandoned salt mines and their overburden' in order to investigate possible consequences of salt-mine flooding. From 2006 to 2010 an interdisciplinary network of universities, research institutes and industries investigated the risk potential of land subsidence, surface wetting and sinkhole development in salt bearing formations associated with abandoned mining. Main target was the identification and characterization of the mechanisms of existing dissolution-subsidence features in order to develop strategies to predict future subsurface destabilisation processes that endanger communities.

As an example, the area of the 1200-year-old town of Staßfurt, Germany, where the world's first potash mine was opened in 1852, was selected for this multidisciplinary research project. A number of destructive effects of the subsiding surface were caused by collapses of parts of the abandoned salt mine 'Leopoldshall' and the dissolution of salt in the mines and the adjacent areas. In addition to this, the effect of salt solution on the south-western side of the Staßfurt-Egeln salt anticline contributed to the rate of subsidence and caused the development of sinkholes even before the mining started. A pump-driven drainage system has been working for decades increasing the risk of new collapse structures below the town by dissolution of rock salt (Gerardi, 2010).

Following the recommendations of a previous BMBF-funded project in the Staßfurt area (Knödel et al., 2002), the recent project aimed to make a detailed geological, hydrogeological, geomechanical, and geochemical study in order to better understand the processes causing subsidence and possible damage. Conducted by the German Federal Institute for Geosciences and Natural Resources (BGR), one of the 10 sub-projects comprised geological modelling (Dresbach et al., 2010) in conjunction with airborne and ground geophysical surveys.

This paper focuses on some of the airborne results published by Siemon & Kerner (2011). These as well as further airborne and ground geophysical results were also published by Siemon & Kerner (2010), Siemon et al. (2012) and Krause et al. (2010).

Helicopter-borne survey

In summer 2007, BGR conducted an airborne geophysical survey covering the Staßfurt-Egeln salt anticline (Fig. 1). Helicopter-borne frequency-domain electromagnetic, magnetic and radiometric as well as position data were simultaneously collected (Siemon et al., 2010). The survey area (467 km²) was covered with 161 NW-SE lines at 100 m spacing and 33 SW-NE tie lines at 1 km spacing totalling to 5100 line km. Topographic elevations derived from the position data along the survey lines vary between 60 m within the Bode valley near the town of Staßfurt up to 220 m in the western part of the survey area (Fig. 1).

The aim of this airborne survey was to acquire extensive data sets showing the regional (hydro-) geological structures down to about 100 m depth in order to support and check the 3D geological and hydraulic modelling. Particularly helicopter-borne electromagnetics (HEM) is very useful for mapping both the groundwater mineralisation (Siemon et al., 2009) and the lithology (Jordan & Siemon, 2002).

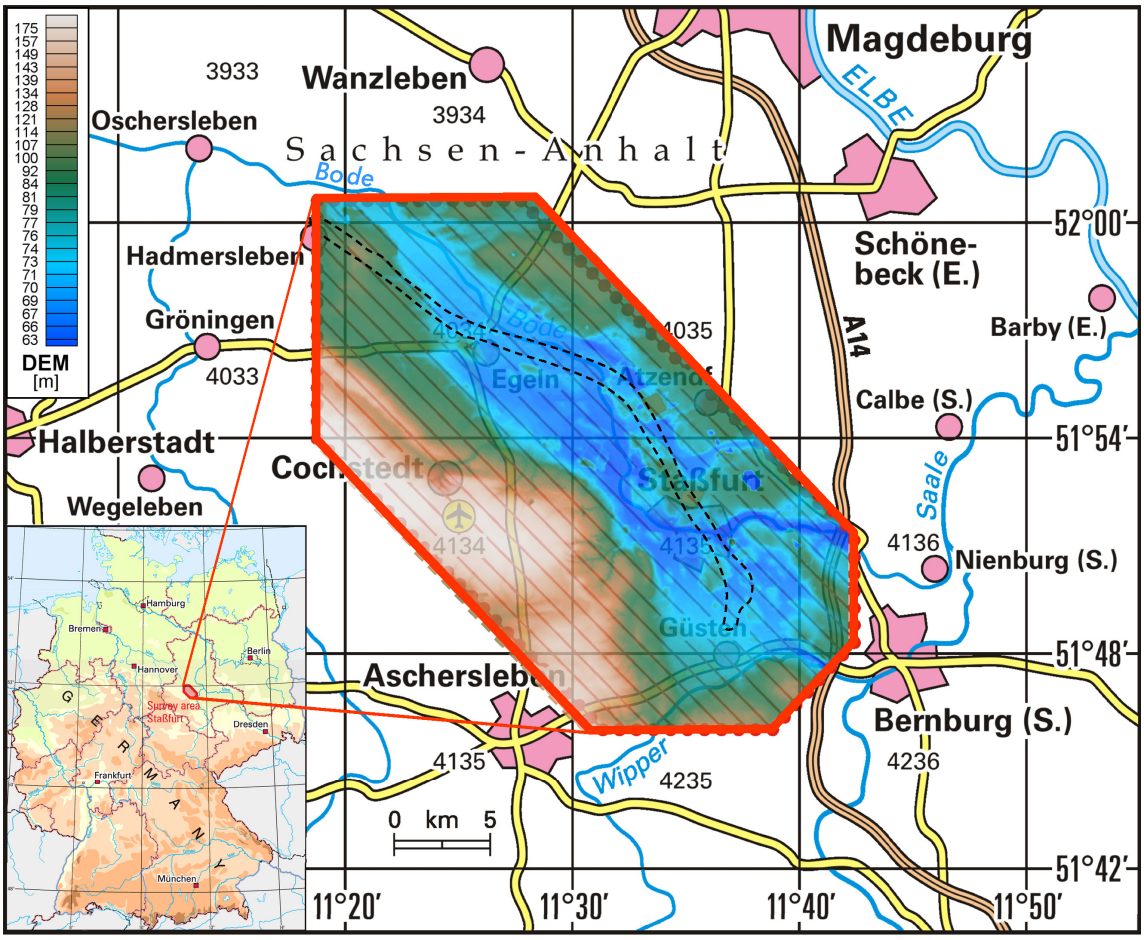

Figure 1 *Location of the survey area Staßfurt (thick red line) in central Germany. The coloured map shows the topographic relief derived from the helicopter-borne survey (Siemon et al., 2010). The dashed black line outlines the cap rock of the Staßfurt-Egeln anticline (after LAGB, 2001).*

Results

The six-frequency (387 Hz – 133 kHz) electromagnetic data were inverted to homogeneous as well as layered-earth (1D) resistivity models using algorithms described by Sengpiel & Siemon (2000). The 1.3 million four-layer 1D resistivity models – displayed as vertical resistivity sections and horizontal resistivity maps – reveal a number of important hydrogeological features such as the distribution of salt water close to the town of Staßfurt, areas of salt-water rise, buried palaeo channels and freshwater influents as well as Mesozoic to Quaternary lithological units (Siemon et al., 2011).

The principal resistivity distributions in the entire survey area are shown in Fig. 2 exemplarily at depths of 10 m and 40 m below ground level (bgl). Outside the Staßfurt-Egeln anticline, which in fact is a depression due to erosion processes, the resistivities correlate fairly well with Mesozoic units: high, medium and low resistivities indicate limestones (blue, $\rho > 60$ Ωm), sandstones (green to blue, $\rho = 20$–60 Ωm) and mudstones (yellow to light green, $\rho = 10$–20 Ωm), respectively. The resistivities on both sides of the salt ridge are caused by Tertiary and Quaternary sediments having a variable clay content (predominantly sandy: green to blue, $\rho > 20$ Ωm; predominantly clayey: orange to light green, $\rho = 5$–20 Ωm). The cap rock appears resistive (dark green to blue, $\rho > 40$ Ωm) as long it is saturated with freshwater. Very low resistivities (red, $\rho < 5$ Ωm) indicate brackish or saline water.

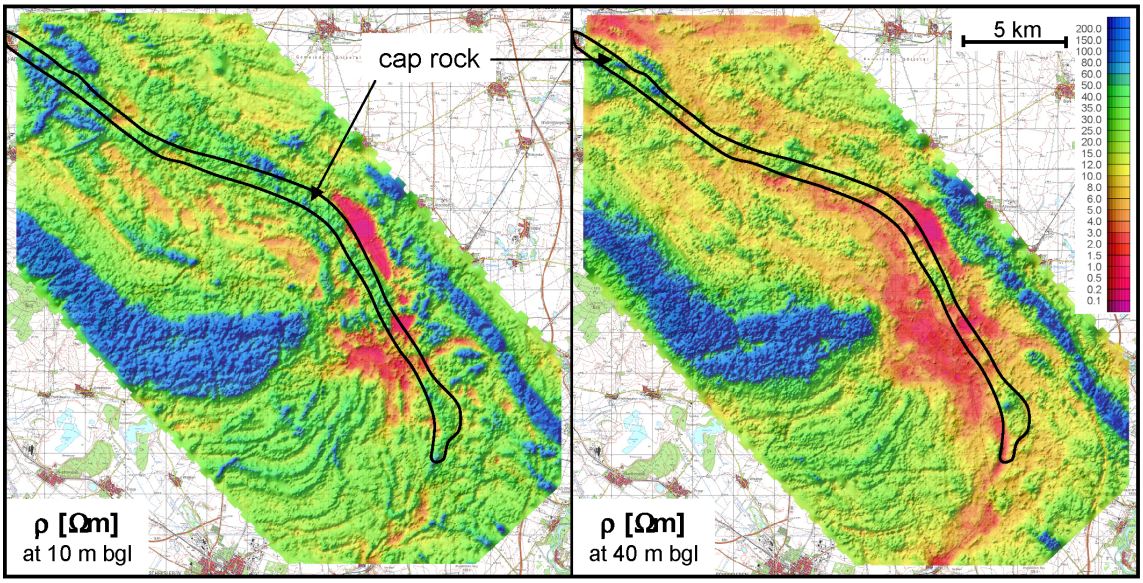

Figure 2 *Resistivity distributions in the survey area Staßfurt at 10 and 40 m depth below ground level on top of a topographic map (DTK50-V, 2005).*

Salt-water occurrences

The contribution of the lithology to the resistivities derived from HEM data is often negligible if the groundwater is saline. Normally, very low resistivities of less than 3 Ωm are not observed in freshwater-saturated sediments. Therefore, the depth to salt-water occurrences were derived from 1D resistivity models at places where the resistivity of a model layer drops below 3 Ωm. Fig. 3 shows that shallow salt water occurs at the tailings ponds and the soda dumpsite as well as at some places between Hecklingen and Staßfurt. Particularly along the south-western slope of the salt ridge and corresponding to the deep-seated salt pits, salt water was revealed below 40 m depth.

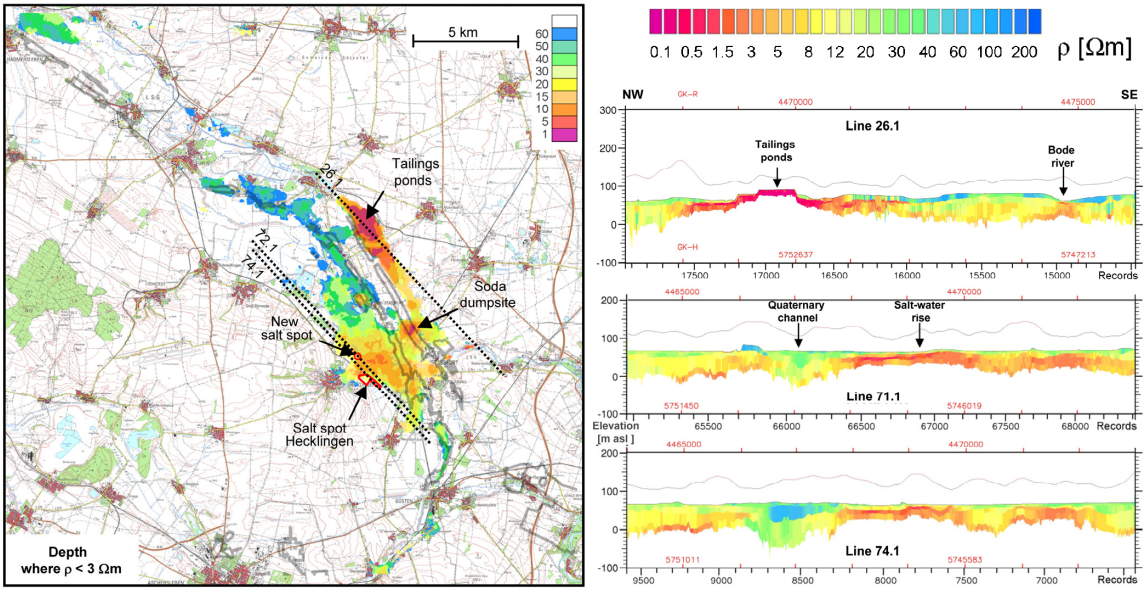

Figure 3 *Depth to salt-water occurrences derived from 1D models with ρ < 3 Ωm on a topographic map (DTK50-V, 2005) and the boundaries (grey lines, LAGB) of the salt pits (left); excerpts of resistivity sections showing conductive salt-water occurrences and resistive Quaternary deposits (right).*

Buried valleys

Quaternary palaeo channels refilled with glacial deposits affect the dynamic hydrogeological system of the investigation area. The resistive structures 1 and 2 (ρ = 50–150 Ωm) crossing the Staßfurt-Egeln salt anticline (Fig. 4) consist of porous sediments (sand, gravel). They are clearly distinguishable from conductive Tertiary silt, clay and lignite layers (ρ = 5–20 Ωm). Structure 3 indicates the salinisation of the Bode river valley.

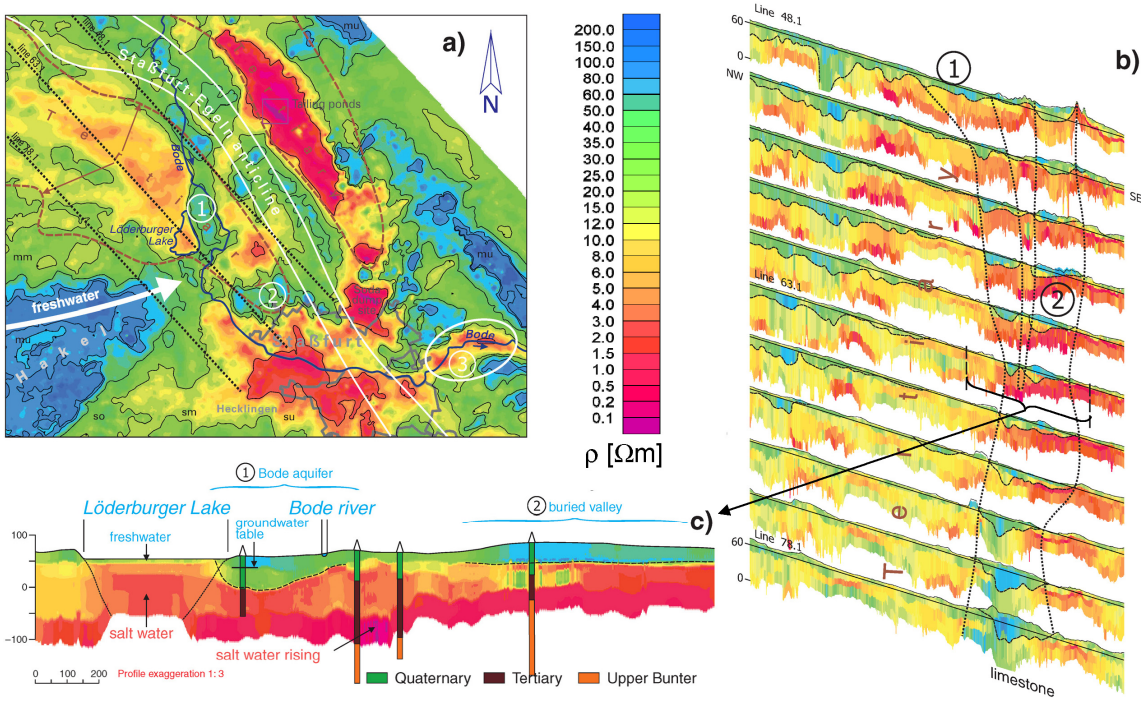

Figure 4 *Resistivity map and sections indicating buried valleys: a) resistivity distribution at 10 m depth below surface, b) every third vertical resistivity section of lines (48.1–78.1), c) short portion of line 63.1 with boreholes (Λ) provided by LAGB and interpretation.*

Conclusions

Airborne geophysics, particularly HEM, proved to be a very useful tool for investigating the geology und hydrogeology of the survey area down to about 100 m depth. The airborne results supported and proved 3D geological and hydraulic modelling which are essential to understand the dissolution and subrosion processes being responsible for the subsidence of the Staßfurt area. Due to the detailed pattern of subsurface geophysical parameters the spatial airborne data also provided information on appropriate locations for ground follow-up studies such as new boreholes, hydrological measuring sites and ground geophysical investigations.

Acknowledgements

We thank the German Federal Ministry of Education and Research for funding the project (BMBF 02C1476), BGR for the permission to publish the results, EAGE for their invitation to publish the results in First Break, and particularly all those colleagues at BGR, LAGB and other institutes involved in the “Staßfurt Project” for providing information on geology and hydrogeology and for their numerous discussions on the interpretation of the airborne results.

References

Dresbach, C., Pusch, M., Mingerzahn, G., Fleig, S., Hammer, J. und Behlau, J., 2010. 3D-Modelle der Kali- und Steinsalzbergwerke des Staßfurter Sattels und geologisches 3D-Modell der Region Staßfurt. In: Gerardi, J. (2010), 46–62, Hannover.

DTK50-V, 2005. Digitale Topographische Karte 1:50000. Bundesamt für Kartographie und Geodäsie, Frankfurt am Main.

Gerardi, J. (Hrsg.), 2010. Staßfurt 2010 – Erkennen, analysieren, bewerten und prognostizieren der zukünftigen Entwicklung der Bergbaufolgeschäden. Forschungsverbundvorhaben "Dynamik abgesoffener oder gefluteter Salzbergwerke und ihres Deckgebirgsstockwerks". Exkursführer und Veröffentlichungen der DGG (EDGG), 244, pp 265, Hannover.

Jordan, H. und Siemon, B., 2002. Die Tektonik des nordwestlichen Harzrandes – Ergebnisse der Hubschrauber-Elektromagnetik. Z. dt. geol. Ges., 153/1, 31-50, Stuttgart.

Knödel, K., Lux, K.-H., Seifert, G., Voigt, H.-J., Lauterbach, M. und Schuck, A., 2002. Maßnahmen der nachhaltigen Gefahrenabwehr für Altlasten in Gebieten mit bergbaubedingten Destabilisierungsvorgängen am Beispiel der Stadt Staßfurt. BMBF-Verbundvorhaben, Abschlussbericht.

Krause, Y, Noell, U., Furche, M. und Grissemann, C., 2010. Der Beitrag hochauflösender Geophysik zur hydrogeologischen Charakterisierung von Destabilisationsprozessen in Bergschadensgebieten am Beispiel der Stadt Staßfurt. In: Gerardi (2010), 82–91, Hannover.

LAGB, 2001. Geologische Übersichtskarte (GÜK) von Sachsen-Anhalt 1:400.000, Landesamt für Geologie und Bergwesen von Sachsen-Anhalt (LAGB).

Sengpiel, K.-P. and Siemon, B., 2000. Advanced inversion methods for airborne electromagnetic exploration. Geophysics, 65, 1983-1992.

Siemon, B., Christiansen, A.V., and Auken, E., 2009. A review of helicopter-borne electromagnetic methods for groundwater exploration. Near Surface Geophysics, 7, 629–646.

Siemon, B. und Kerner, T., 2010. Möglichkeiten der Aerogeophysik zur hydrogeologischen Erkundung der Umgebung des Staßfurt-Egelner Sattels. In: Gerardi, J. (2010), 230–233, Hannover.

Siemon, B. and Kerner, T., 2011. Airborne geophysical investigation of the environment of abandoned salt mines along the Staßfurt-Egeln anticline, Germany. 73rd EAGE Conference & Exhibition incorporating SPE EUROPEC 2011 – Vienna‘11, 23.-26.5.2011, Vienna, Austria, P136.

Siemon, B., Kerner, T., Ibs-von Seht, M. und Pielawa, J., 2011. Interpretationsbericht zur Befliegung Staßfurt, Juni – August 2007. BGR-Bericht, Archiv-Nr. 0129769, 47 S., Hannover.

Siemon, B., Kerner, T., Ibs-von Seht, M., Voß, W., Rehli, H.-J., und Pielawa, J., 2010. Technischer Bericht zur Befliegung Staßfurt, Juni – August 2007. BGR-Bericht, Archiv-Nr. 0128730, Hannover.

Siemon, B., Kerner, T., Krause, Y. and Noell, U., 2012. Airborne and ground geophysical investigation of the abandoned salt mine environment along the Stassfurt-Egeln Anticline, Germany. First Break, 30 (2), 41–51.

Helicopter-borne electromagnetics (HEM) at the Elbe estuary in Northern Germany

Annika Steuer[1], Bernhard Siemon[1], Malte Ibs-von Seht[1], Uwe Meyer[1] and Helga Wiederhold[2]

[1]*Federal Institute for Geosciences and Natural Resources (BGR), Hannover, Germany*
[2]*Leibniz Institute for Applied Geophysics (LIAG), Hannover, Germany*
annika.steuer@bgr.de

Abstract

Helicopter-borne electromagnetic investigations provide a high potential for a comprehensive mapping of the upper hundred metres of the subsurface. The relevance for hydrogeological questions is given by the determination of resistivity models for revealing the distribution of sandy and clayey as well as saltwater and freshwater saturated sediments.

The survey area to the north-west of the City of Hamburg covers the estuary of the Elbe river. Here, the aquifers and their potential salinization were intended to be mapped. Parts of the results of this survey area are involved in the project KLIMZUG-NORD, in which the Technical University Hamburg-Harburg investigates the environmental effects of climate change on the estuary of the Elbe river. Due to current climate change scenarios a sea level rise in the North-Sea region is predicted and, consequently, the water level of the Elbe river will rise in an area affected by a changing sea level. That entails an intrusion of brackish water into the surrounding freshwater aquifers. Such scenarios are investigated by hydraulic flow models. Existing geological information will be complemented spatially by electrical resistivity models derived from HEM data to a geological structural model. This will be related to hydrological parameters and should therefore serve as a base for a hydraulic modelling.

Introduction

The problem of groundwater salinization is becoming increasingly important within the context of groundwater extraction and treatment, and is a latent risk for the sustainable use of aquifers. The intrusion of seawater is a natural source of coastal groundwater salinization (green colours, Figure 1). Onshore salinization is attributable to the leaching of salt domes close to the earth's surface and the upwelling of deep saline water. These natural sources of salinization are exacerbated by man-made hydraulic activities such as groundwater extraction and drainage systems. Further risks are the long-term rise in sea level, storm floods, and – in some areas – flooding caused by tsunamis. These events

will also have an impact on the distribution of saltwater in the subsurface and can also jeopardise aquifers used to produce potable water.

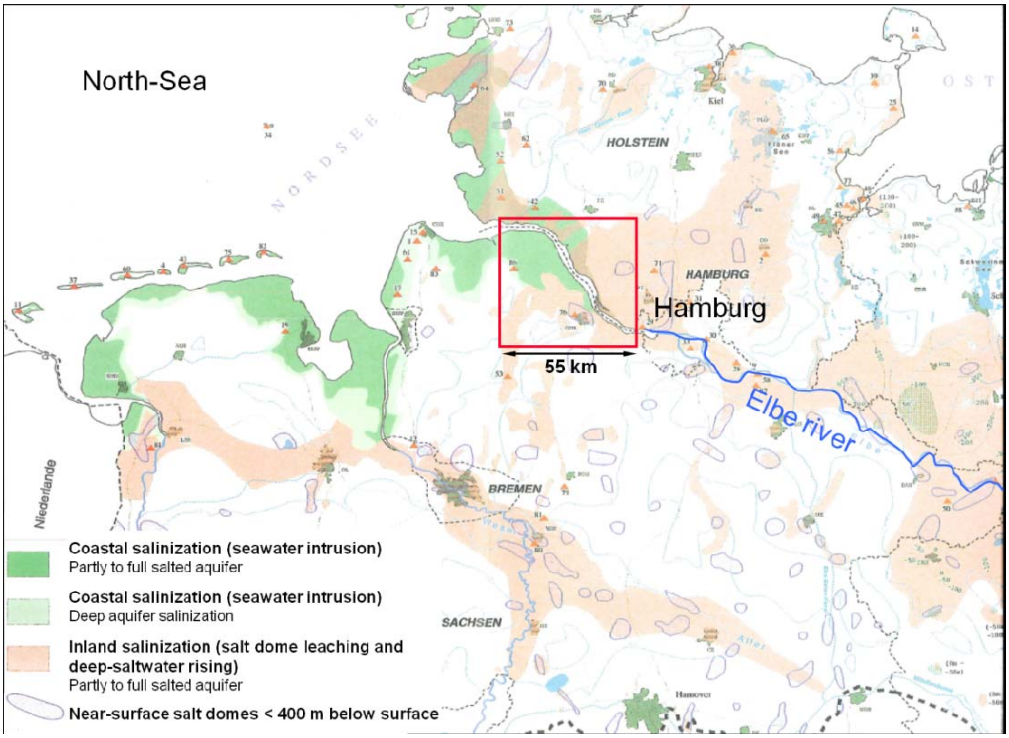

Figure 1: *Distribution of groundwater salinization in the North-German Plain (modified after Grube et al., 2000). The natural source of the coastal salinization is seawater intrusion (green colours), and of the inland the leaching of salt domes (red colours) which reach at places the surface. Hydraulic intervention by groundwater extraction and artificial drainage increase the effect of the natural sources. The red box marks the survey area at the Elbe estuary.*

Airborne geophysical surveys enable huge areas to be surveyed almost completely in a relatively short time at economic cost. The results can generally be used for geological and hydrogeological mapping. Particular the data collected by airborne electromagnetic surveys is important for hydrogeological interpretation as the derived electrical conductivities reveal the distribution of sandy and clayey sediments as well as salinization zones and freshwater occurrences down to depths of the upper hundred metres (*Siemon et al., 2009; Steuer et al., 2009a; Siemon et al., 2012*).

In 2008 and 2009, the Federal Institute for Geosciences and Natural Resources (BGR) carried out airborne geophysical measurements for saltwater-freshwater investigations in cooperation with the Leibniz Institute for Applied Geophysics (LIAG) in frame of the project D-AERO (*Wiederhold et al., 2008; Steuer et al., 2009b; Schaumann et al., 2010; Steuer et al., 2010*). In ten different survey areas located at the German North-Sea coast 13 400 and 4500 line kilometres were flown using helicopter-borne electromagnetics in frequency-domain (HEM) and time-domain (HTEM), respectively (*Wiederhold et al., 2010*). One aim of D-AERO is, to build a data set as a reference to monitor climate or man-made induced changes of the saltwater/freshwater interface at the German North-Sea coast.

The BGR airborne geophysical system

The helicopter-borne system operated at the BGR enables simultaneous measurements of three geophysical methods: electromagnetics, magnetics and gamma-ray spectrometry (Figure 2). The electromagnetic and magnetic sensors are housed in a 10 m long tube, which is towed by a Sikorsky S-76B helicopter on parallel flight lines about 30–40 m above ground level.

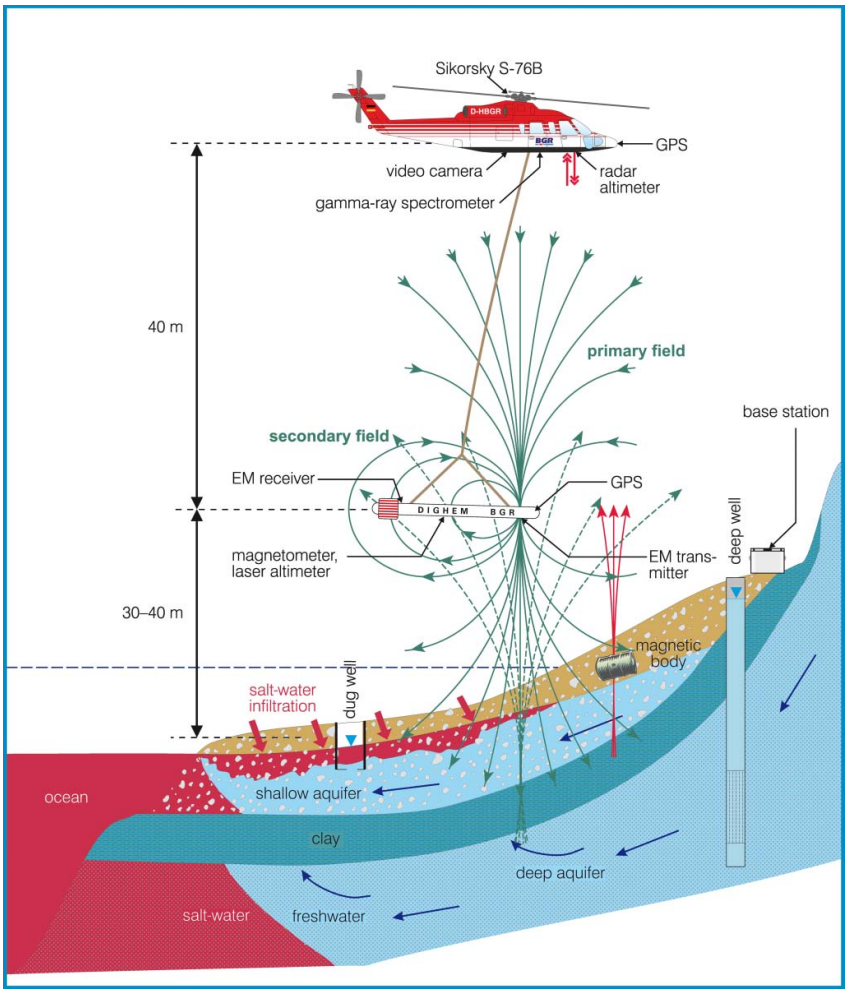

Figure 2: *BGR helicopter-borne geophysical system and a hydrogeological situation typical for coastal areas (Siemon and Steuer, 2011).*

The electromagnetic system is a RESOLVE system (manufactured by Fugro Airborne Surveys) consisting of six transmitter-receiver coil pairs. The transmitter signals, the primary magnetic fields, induce eddy currents into the subsurface which depend on the electrical conductivity distribution. The relative secondary magnetic fields from these induced currents are measured at the receiver coils in parts per million (ppm) as they are related to the primary fields. The use of different frequencies ranging from 387 Hz to 133 kHz enables the investigation of different depths: High frequencies resolve the shal-

lower parts of the subsurface and lower frequencies the deeper parts. The depth of investigation also depends on the subsurface conductivity distribution: The higher the conductivity the lower the penetration of the electrometric fields into the subsurface. Typical maximum investigation depths of the RESOLVE system range from about 30 m (saltwater saturated sediments) to about 150 m (freshwater saturated sandy sediments or hard rock).

In addition to the electromagnetic measurements, the earth's magnetic field and the natural gamma radiation of the earth's surface are recorded. These measurements can be used to interpret the structure of the earth's crust and the mineral composition of the shallowest soil layers, respectively. The joint interpretation of this data supports three-dimensional modelling of the subsurface and is also used as a basis for planning and activities in many environmental and economic disciplines, *e.g.* for regional planning, development of water utilization and water protection concepts.

Modelling of the electromagnetic data

The in-phase (I) and quadrature (Q) components of the measured secondary magnetic fields are generally converted into resistivities (inverse of conductivity) based on half-space models. Apparent resistivity ρ_a [Ωm] and centroid depth z*[m] of a homogeneous half-space (Figure 3, Model 1) are derived from the data of each single frequency (f). The half-space models are used to derive appropriate starting models for the one-dimensional (1D) inversion.

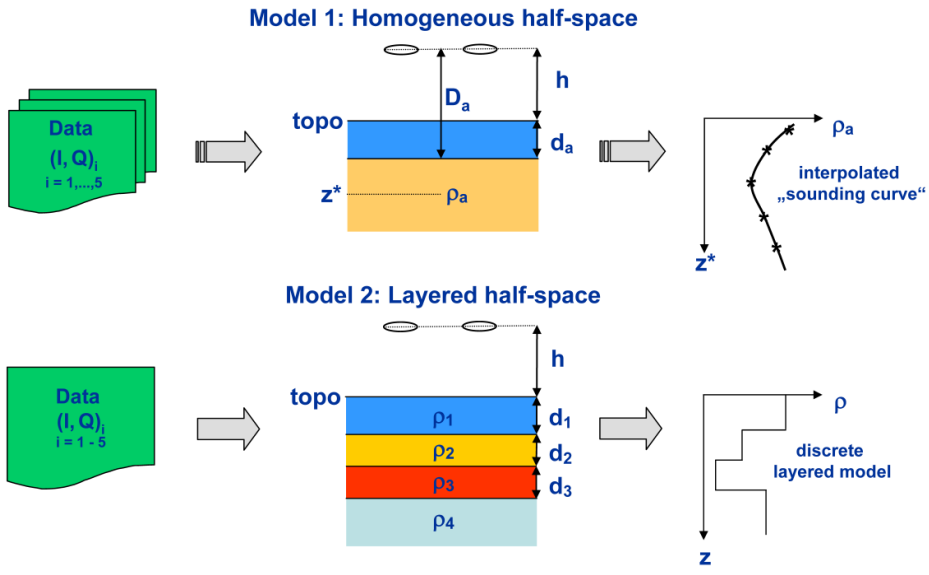

Figure 3: *HEM inversion scheme based on the model of a homogeneous half-space and of a layered half-space model (Siemon and Steuer, 2011).*

A Marquardt–Levenberg inversion procedure iteratively calculates the model parameters, resistivity and thickness of the model layers (Figure 3, Model 2), from the data of all frequencies available (*Sengpiel and Siemon, 2000*). The inversion procedure stops when a given threshold (*e.g.* 10%) is reached, which is defined as the differential fit of modelled and measured HEM data.

The results of the 1D inversion are presented as vertical resistivity sections (VRS) and resistivity maps. The VRS are constructed by placing the resistivity models for each sounding along a survey profile next to each other using the topographic relief (in m above sea level) as base line.

The survey

The helicopter-borne survey at the estuary of the Elbe river to the north-west of Hamburg (Figure 1, red box) took place in July and October 2008 and from March to April 2009 and covered an area of about 2000 km². The nominal flight-line spacing was 250 m for the 209 lines (W-E) and 2500 m for the 19 tie-lines (N-S) resulting in a total survey line length of more than 8500 km (Figure 4a).

In this area, the aquifers and their potential salinization were intended to be mapped. Parts of the results of this survey are involved in the project KLIMZUG-NORD (www.klimzug-nord.de), where the Technical University Hamburg-Harburg investigates the environmental effects of climate change on the estuary of the Elbe river (*Palm and Steuer, 2010*).

Figure 4b shows the digital elevation model (DEM, derived from SRTM data) where the higher-lying Geest ridge (brown) and the Marsch (blue) are displayed.

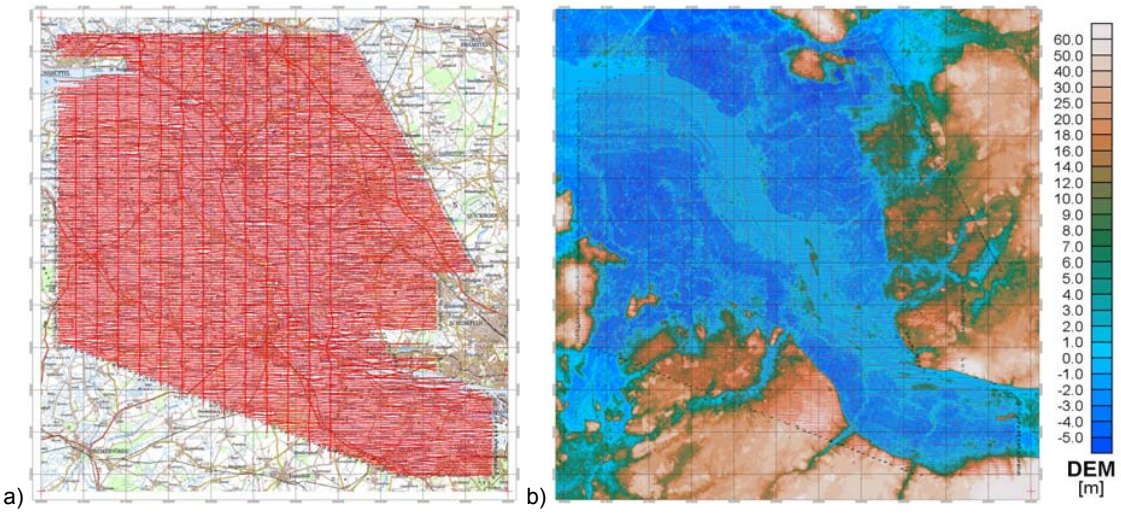

Figure 4: *a) The flight lines are displayed as red. b) Digital elevation model based on SRTM data.*

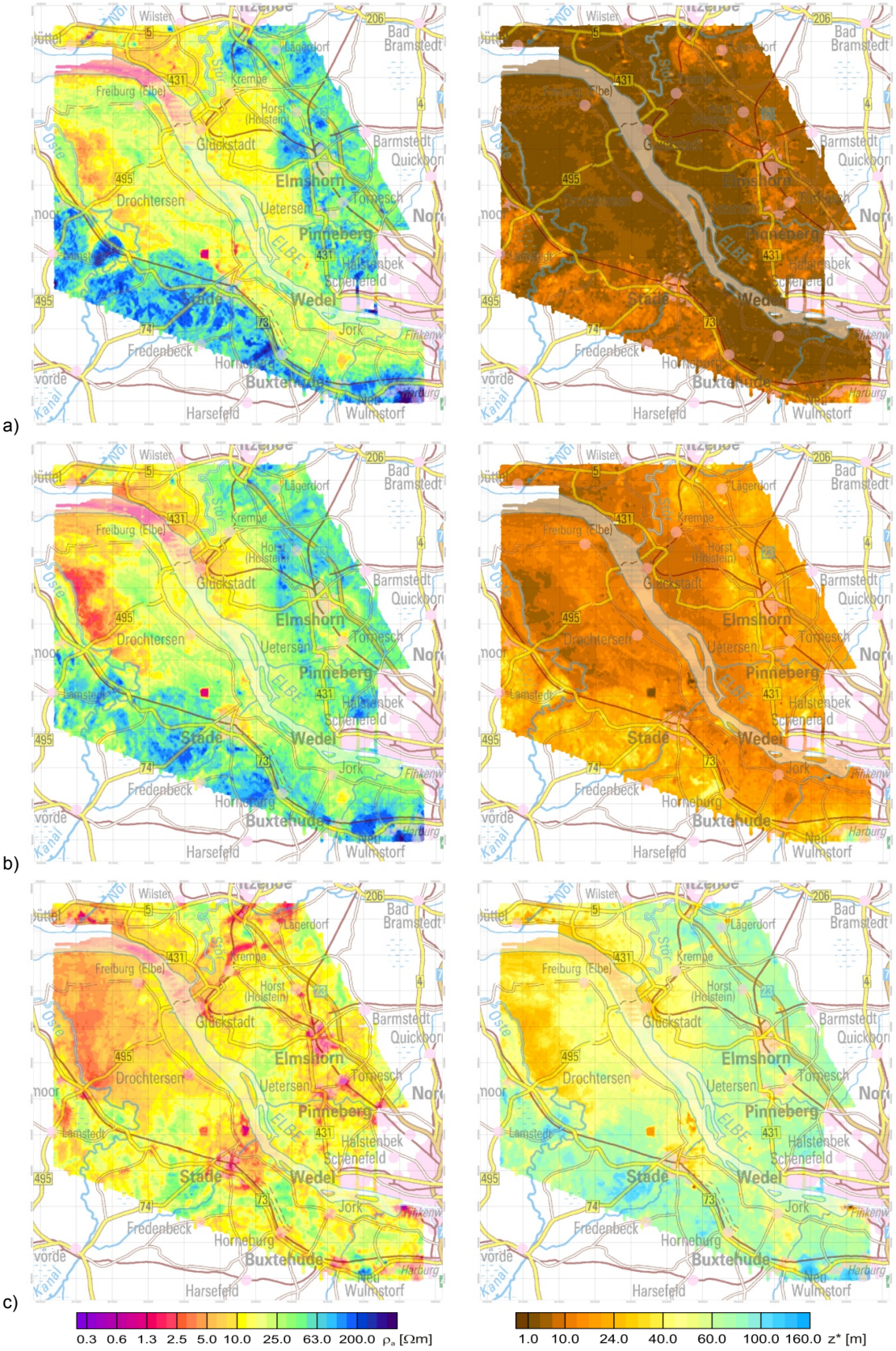

Figure 5: *Apparent resistivity (ρ_a) and centroid depth (z*) maps of a) 133 kHz, b) 8 kHz and c) 387 Hz.*

The apparent resistivity and centroid depth maps provide a first overview on the resistivity structure (Figure 5). Here, the Geest ridge (high-lying hinterland consisting of pleistocenic moraine sediments) appears resistive, whereas the Marsch (plain holocenic wet land, alluvium) appears conductive (Figure 5a and 5b). The investigation depth increases with decreasing frequency and reaches 160 m at places (Figure 5c).

The resistivity maps derived from the 1D inversion are shown in Figure 6 at selected depths of 2, 7, 14 and 25 m below sea level (bsl). On the near surface map conducting Marsch sediments appear (Figure 6, 2 m). In the northern part of the survey area the distribution of the saltwater intrusion of the Elbe river into the Quaternary aquifer was mapped (Figure 6, 25 m).

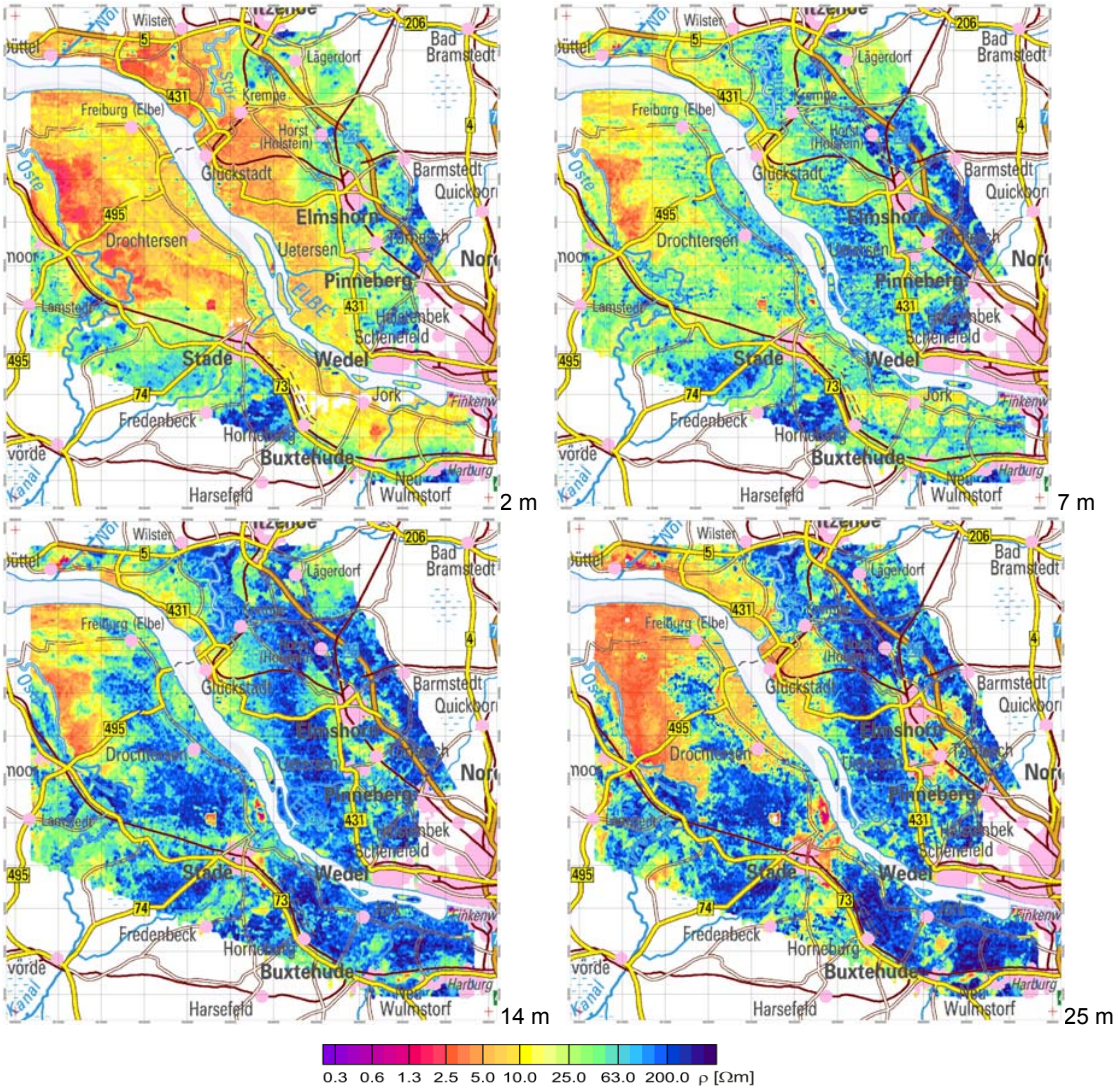

Figure 6: *Resistivity (ρ) maps at selected depths of 2, 7, 14 and 25 m bsl as result of 1D inversions.*

Saltwater-rising zone

An electrical conductivity anomaly of about 2 km diameter was detected in the southern part of the survey area (black circle in Figure 7) at a place where anthropogenic sources could be excluded. This anomaly could be caused by clay or saltwater saturated sediments. The latter is presumable as analyses of waters from drainage channels and rain ponds in that area show high NaCl concentrations (150-724 mg/L).

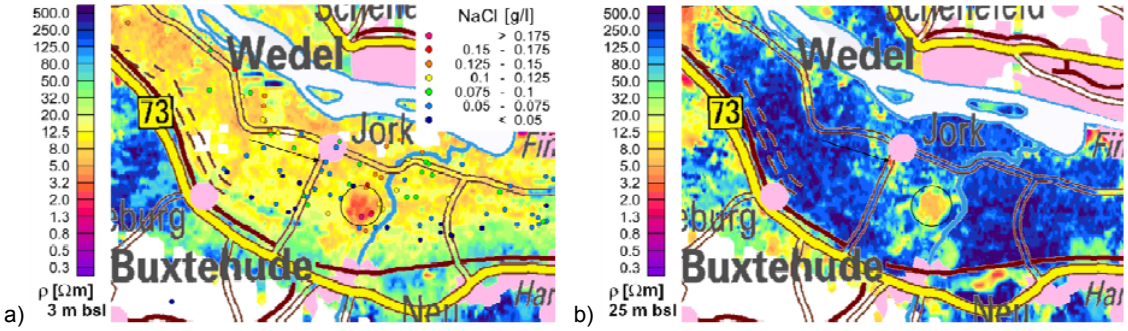

Figure 7: *Resistivity maps at selected depths of a) 3 m bsl and b) 25 m bsl as result of a 1D inversion. Additionally NaCl concentrations (Koepcke, 2010) of surface water samples are displayed in a).*

The electrical conductivity anomaly is located in the Marsch area between the higher lying Geest ridge in the South and the Elbe river in the North, as shown in the digital elevation map (Figure 8a). Below the anomaly a Quaternary valley is assumed, which is carved more than 200 m deep into the Miocene layering (Figure 8b).

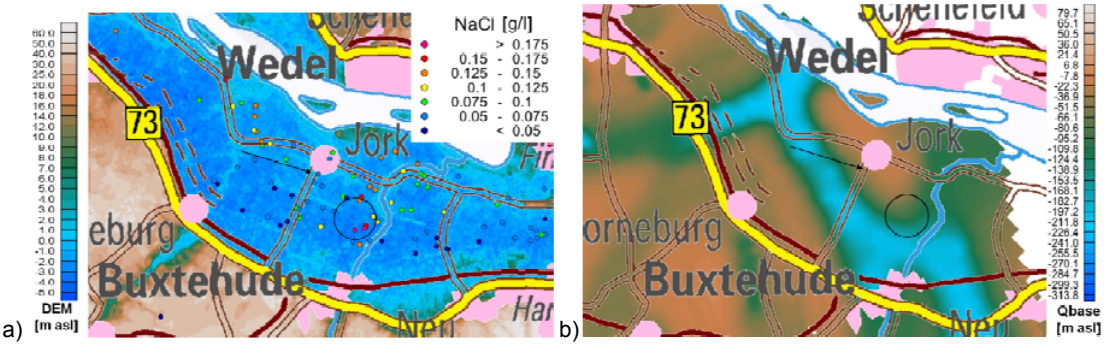

Figure 8: *a) Digital elevation model based on SRTM data. b) The map of the Quaternary base (LBEG, 2009) is the result of the interpolation of a few boreholes. The resistivity anomaly is located at the edge of a Quaternary valley which runs from south-east to north-west.*

Hydrogeological interpretation

Salinizations of the Miocenic aquifer are known in that region in places. The Miocenic aquifer is locally in hydraulic contact with the upper Quaternary aquifers by Quaternary valleys. At that places a rise of highly minerilized groundwater may occur depending on the groundwater potential differences. In the Elbe estuary region some of such risings are documented by *Grube et al. (2000)*. Figure 9 shows this hydrological situation schematically.

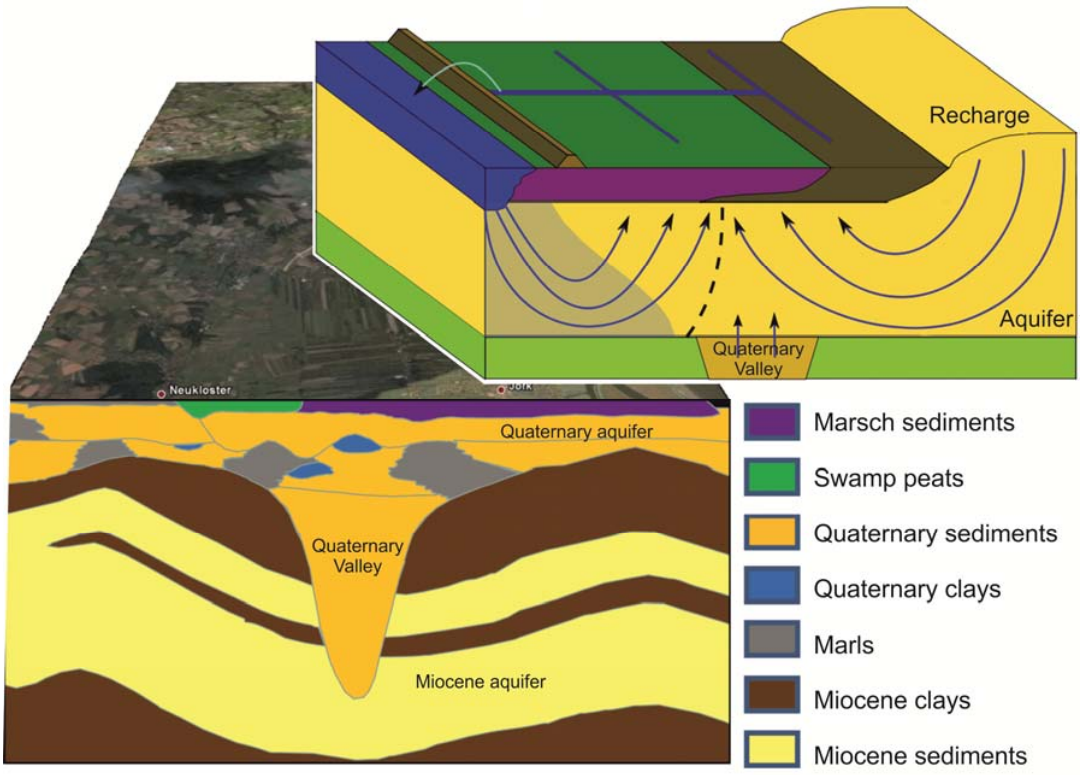

Figure 9: *Hydrogeological scheme of the survey area (modified after Palm and Steuer, 2010).*

Conclusions

The HEM method proved to be an efficient tool for resistivity mapping and revealed following results at the Elbe estuary: The Geest ridge and the swamp belt are characterized by high resistivities at the highest frequency of 133 kHz, whereas lower resistivities occur in the Marsch area. In the northern part of the survey area the distribution of saltwater intrusion was mapped. The investigation depth reaches 160 m in the southern part of the survey area. Here, a significant resistivity low obviously not affected by anthropogenic sources was detected by HEM and identified as saltwater-rising zone by water analyses and hydrogeological considerations.

References

Grube A., Wichmann, K., Hahn, J.and Nachtigal, K.H. (2000): Geogene Grundwasserversalzung in den Poren-Grundwasserleitern Norddeutschlands und ihre Bedeutung für die Wasserwirtschaft (Band 9), DVGW-Technologiezentrum Wasser (Ed.), Karlsruhe, ISSN 1434-5765, 203 p.

Koepcke, D. (2010): Landwirtschaftskammer (LKW) Niedersachsen, Obstbauversuchsanstalt (OVA) Jork, personal communication.

LBEG (2009): NIBIS® Kartenserver, Quartärgeologische Übersichtskarte von Niedersachsen 1:500000 - Tiefenlage der Quartärbasis, Landesamt für Bergbau, Energie und Geologie, Hannover, http://nibis.lbeg.de/cardomap3/#, last access: 02.04.2012.

Palm, J. and Steuer, A. (2010): Kartierung und Interpretation von Salzwasseraufstiegen mit HEM-Daten in der Elbmarsch, LIAG Austauschsitzung, Hannover, 03.-04.11.2010.

Schaumann, G., Steuer, A., Siemon, B., Wiederhold, H. and Binot, F. (2010): Die deutsche Nordseeküste im Fokus aeroelektromagnetischer Untersuchungen, Teilgebiete Langeoog mit Wattenmeer und Elbemündung. In: Ritter, O. & Weckmann, U. (Ed.) *Proceedings of the 23rd Schmucker-Weidelt-Colloquium for Electromagnetic Depth Research*, Potsdam, ISSN 0946-7467, 177–187.

Sengpiel, K.-P. and Siemon, B. (2000): Advanced inversion methods for airborne electromagnetic exploration. *Geophysics*, Vol. 65, No. 6, 1983–1992.

Siemon, B., Christiansen, A.V. and Auken, E. (2009): A review of helicopter-borne electromagnetic methods for groundwater exploration. *Near Surface Geophysics*, 7, 629–646.

Siemon, B. and Steuer, A. (2011): Airborne geophysical investigation of groundwater resources in northern Sumatra after the tsunami of 2004. In: Mörner, N.-A. (Ed.) *The tsunami threat – research and technology*, InTech, Rijeka, ISBN 978-953-307-552-5, 575–594.

Siemon, B., Kerner, T., Krause, Y. and Noell, U. (2012): Airborne and ground geophysical investigation of the abandoned salt mine environment along the Stassfurt-Egeln Anticline, Germany. *First Break*, 30 (2), 41–51.

Steuer, A., Siemon, B. and Auken, E. (2009a): A comparison of helicopter-borne electromagnetics in frequency and time-domain at the Cuxhaven valley in Northern Germany. *Journal of Applied Geophysics*, 67, 194–205.

Steuer, A., Siemon, B., Schaumann, G., Wiederhold, H., Meyer, U., Pielawa, J., Binot, F. and Kühne, K. (2009b): The German North Sea Coast in Focus of Airborne Geophysical Investigations. – AGU Fall Meeting 2009, San Francisco, USA.

Steuer, A., Siemon, B. and Grinat, M. (2010): The German North Sea Coast in Focus of Airborne Electromagnetic Investigations: The Freshwater Lenses of Borkum. In: Ritter, O. & Weckmann, U. (Ed.) *Proceedings of the 23rd Schmucker-Weidelt-Colloquium for Electromagnetic Depth Research*, Potsdam, ISSN 0946-7467, 188–197.

Wiederhold, H., Binot, F., Kühne, K., Meyer, U., Siemon, B. and Steuer, A. (2008): Airborne geophysical investigation of the German North Sea Coastal Area. – 20th Salt Water Intrusion Meeting 2008, Naples, USA.

Wiederhold, H., Siemon, B., Steuer, A., Schaumann, G., Meyer, U., Binot, F. and Kühne, K. (2010): Coastal aquifers and saltwater intrusions in focus of airborne electromagnetic surveys in Northern Germany. – 21th Salt Water Intrusion Meeting 2010, Azores, Portugal.

Joint inversion of ground based and helicopter-borne electromagnetic data

Sudha[1], Bülent Tezkan[1] and Bernhard Siemon[2]

[1]Institute für Geophysik und Meteorologie, Universität zu Köln
[2]Bundesanstalt für Geowissenschaften und Rohstoffe, Geozentrum Hannover

Abstract:

The use of ground-based electromagnetic methods (Transient Electromagnetics (TEM) and Radiomagnetotellurics (RMT)) is increased in last decades for hydrogeological purposes. However, airborne electromagnetic methods were also proposed as a possible tool for near surface investigations due to the capability to cover large areas in short time. By jointly inverting different kinds of geophysical measurements at a site, the ambiguity inherent in different geophysical methods can be avoided. In order to couple spatial data from frequency-domain helicopter-borne electromagnetics (HEM) with electromagnetic measurements from ground geophysics, a common 1D joint inversion algorithm for HEM, TEM and RMT data is developed. The depth of investigation of HEM data is rather limited compared to time-domain EM sounding methods on the ground. In order to improve the accuracy of model parameters of shallow depth as well as of the deeper crust, the HEM, TEM, and RMT measurements are combined using numerical joint inversion methodology. The 1D joint inversion algorithm is verified for the synthetic data of HEM, TEM and RMT. The proposed concept of the joint inversion takes advantage of each single method, which provides the capability to resolve near surface (RMT) and deeper electrical conductivity structures (TEM). Furthermore, the joint inversion is realized for the field data (HEM and TEM) measured in the Cuxhaven area, Germany.

Keywords: Joint inversion, helicopter-borne electromagnetics, transient electromagnetics, radiomagnetotellurics.

1. INTRODUCTION

Geophysical data inversions often suffer from uncertainties and non-uniqueness. To obtain a unique and meaningful model, inverted models are constrained by using the information from various sources. The constraints could be the information from the local geology and lithology, sequential and joint inversion of two or more data sets belonging to the same structure. As the sensitivity of two data sets for resistive and conductive structures is different, therefore, the joint inversion helps in overcoming the limitations of two data sets.

Auken *et al.* (2006) have discussed the current trends in near-surface electrical and electromagnetic methods and briefly summarized the rapid improvements in electrical and electromagnetic methods in past few decades. Applications of TEM and DC resistivity as well as airborne electromagnetic methods were reviewed by several authors (Matias *et al.* 1994, Nobes 1996, Pellerin 2002, Tezkan 1999, Siemon *et al.* 2009, Harinarayana 1999) for solving variety of problems related to hydrogeological investigations. For the simple geological structure, where

one dimensional models are fairly valid for actual representation of the earth structures, these methods suffer from inherent difficulties in establishing layer thicknesses and resistivities from the measured data alone. Ambiguities in inversion, non-uniqueness and electrical equivalence are the common problems associated with these methods. These problems can be minimized either by constraining the inverted model by a-priori information or by using joint inversion of two or more independently generated data sets. In joint inversion, inherent weakness of one type of data set is compensated by the strength of the other data set (Raiche *et al.* 1985, Vozoff and Jupp 1975). Thus, the joint inversion can improve the inverted model and also reduces the non-uniqueness in the final model. This has been demonstrated by Vozoff and Jupp (1975) for magnetotelluric (MT) and Schlumberger soundings, and Gómez-Treviño and Edwards (1983) for controlled-source EM with Schlumberger sounding.

As EM methods are based on the propagation of EM fields, both, ground-based and airborne electromagnetic (AEM) measurements are feasible. Recent examples for helicopter-borne groundwater investigations with frequency-domain systems are given in Siemon *et al.* (2004; 2007) and Steuer *et al.* (2008), and with time- domain systems in: Jørgensen *et al.* (2006), Kjærstrup and Erfurt (2006), and Scheer *et al.* (2006).

Different EM methods can be jointly used to reduce the layer equivalences, which are an inherent problem in EM modeling, and thus enhance model resolution. Meju *et al.* (1999) combined vertical electrical soundings (VES), TEM and audio magnetotellurics (AMT) to map an aquifer in the Parnaiba Basin in the northeast of Brazil and showed that a combination of different methods helps to overcome the equivalence problem. HEM and TEM have been successfully combined for hydrogeological investigations, e.g., by Fitterman and Deszcz-Pan (2001) for saltwater mapping in the Everglades National Park in Florida, USA, and by Stadtler *et al.* (2004) for groundwater studies in Namibia.

In the present paper, the joint application of ground-based and helicopter-borne electromagnetic methods is used. The focus of this work is the joint inversion of ground-based and airborne electromagnetic methods. The idea is that the capability to resolve the near surface structures with RMT method is higher; however, deeper electrical conductivity structures can be well resolved by TEM. On the other hand, HEM provides better lateral coverage. Therefore, the joint inversion of HEM, TEM and RMT would yield quasi-2D images of the electrical conductivity over a large depth interval along a profile.

2. THEORY

Equivalence is a well known problem in the interpretation of electromagnetic data. Therefore, it can happen that the individual inversion results of different methods are different. In that case, it is difficult to combine these results. Joint inversion of these data sets is likely to give more consistent and reliable results in comparison with the individual inversion of these data sets. In literatures two different approaches have been used for joint inversion: first is sequential or multi-sequential inversion in which the output of one data set is used as an input for the other set to constrain the inverted model (Jupp and Vozoff, 1975). This is not a joint inversion in the strict sense. The second approach jointly inverts different data sets belonging to the same subsurface structure. For this purpose the objective function is defined by adding the error functional corresponding to the different data sets (Jupp and Vozoff, 1975, Kaikkonen and Sharma, 1998).

To obtain this, the data sets, the model functions and the Jacobian matrices of these methods are combined to acquire only one set of model parameters.

$$\mathbf{y} = \begin{pmatrix} \mathbf{y}(HEM) \\ \mathbf{y}(RMT) \\ \mathbf{y}(TEM) \end{pmatrix}, \qquad \mathbf{J} = \begin{pmatrix} \mathbf{J}_1(HEM) \\ \mathbf{J}_2(RMT) \\ \mathbf{J}_3(TEM) \end{pmatrix}, \qquad \mathbf{f} = \begin{pmatrix} \mathbf{f}_1(HEM) \\ \mathbf{f}_2(RMT) \\ \mathbf{f}_3(TEM) \end{pmatrix} \tag{1}$$

where $\mathbf{y}$ is the measured data vector and $\mathbf{f}$ is the computed response, and $\mathbf{J}$ is the Jacobian matrix. The Jacobian matrix is the parameter sensitivity matrix.

An important point in the joint inversion is the weighting of the used measuring methods with respect to each other. Appropriate weights are defined to the parameters influence matrix (Sensitivity matrix) for each data set (Vozoff and Jupp, 1975). The weight (w_i) indicates the importance of i^{th} data point and the resultant sensitivity matrix becomes

$$J_{ij} = w_i \frac{\partial f_i}{\partial m_j}. \tag{2}$$

For M-layer earth model with

$$\begin{aligned} &\rho_i \geq 0; \quad i = 1, \ldots, M+1, \\ &h_i > 0; \quad i = 1, \ldots, M. \end{aligned} \tag{3}$$

In log domain, the parameters are

$$\begin{aligned} &x_j = \log \rho_j \quad for\ j = 1, \cdots, M+1, \\ &x_{j+M+1} = \log h_j \quad for\ j = 1, \cdots, M. \end{aligned} \tag{4}$$

The elements of the matrix, when we use relative errors, can hence be written as

$$J_{ij} = w_i \frac{\partial f_i}{\partial m_j} = \frac{1}{f_i} \frac{\partial f_i}{\partial \log \rho_j} = \frac{\rho_j}{f_i} \frac{\partial f_i}{\partial \rho_j}. \tag{5}$$

Or,

$$\frac{1}{f_i} \frac{\partial f_i}{\partial \log h_j} = \frac{h_j}{f_i} \frac{\partial f_i}{\partial h_j}. \tag{6}$$

In this manner the Jacobian is made scale free, and since the relative error will be proportionate, different kinds of data will equally influence the correction that improves the current model (Vozoff and Jupp, 1975).

To analyze the stability of joint inversion, V-matrix, damped error bounds, damping factors and *importances* are used. These parameters are well-defined by Jupp and Vozoff (1975) and the same definition is used in the present work.

3. RESULTS

The 1D numerical inversion codes (Scholl, 2005), which were developed by the Cologne geophysics group as a tool for the interpretation of individual methods (TEM, RMT), are extended to accomplish the 1D single and joint inversion with HEM data. Inversion of ground-based and helicopter-borne electromagnetic data is carried out using the two different strategies of inversion; Occam and Marquardt inversion. To obtain a reliable estimate of the model parameters, individual sounding data were initially inverted using Occam's inversion scheme. Occam's method with first and second order smoothness constraints generates over-parameterized smoothest model from the measured data (Constable *et al.* 1987) using minimum norm inversion. For detailed analysis of the quality of inversion, Marquardt's inversion (Marquardt 1963, Levenberg 1944) technique was implemented using Singular Value Decomposition (SVD).

The 1D joint inversion algorithm for ground-based and helicopter-borne electromagnetic methods was first verified on the synthetic data and thereafter on field data. For this purpose, noise free synthetic data was generated for a five layered medium. The 1D single and joint inversion results for these data sets are discussed in the following sections.

3.1. 1D joint inversion of synthetic HEM and TEM data

At first, the joint inversion scheme is validated on synthetic HEM and TEM data derived for a five-layer model (Fig. 1(a) and 1(b)). The 1D Occam and Marquardt single and joint inversions were carried out for the data sets. No Marquardt inversion, however, was possible for HEM data of this example as the number of frequencies was less than that of model parameters. Here, 'Occam R1' and 'Occam R2' refers to the first and second order derivatives of smoothness constraints that were used in the Occam's inversion. In the zones, in which these two models were consistent and/or approximately the same, the obtained resistivity values were well resolved. The zones, where the two model results (Occam R1 and Occam R2) were not concurrent, were assumed as the unreliable zone.

The 1D single HEM inversion results for Occam's first and second order smoothness are consistent up to 80 m and infer a smooth model (Fig. 1(a)), which can be interpreted as four-layer model. However, HEM could not see the last layer (fifth layer) and the thickness of the fourth layer was also not resolved. This is due to the limitation of the depth of investigation of the lowest frequency. On the other hand, the TEM inversion results for Occam's first and second order smoothness constraints are consistent up to 200 m depth and infer a smooth model, which can be well represented by five layers. This has been confirmed by Marquardt inversion as well.

SVD analysis indicates a five layer model for TEM sounding data. However, the inherent weakness to resolve near surface layer of TEM data is reflected in the inverted model, the *importance* of first layer resistivity (0.54). The *importance* values for third layer resistivity and thickness are 0.09 and 0.08 respectively, which indicates that the layer is irrelevant (Table 1).

The joint inversion result has significantly improved the small eigen values present in the individual inversions. A five layer model with same resistivity values for each layer was selected as starting model for joint inversion (Fig. 2). But from the SVD analysis the importance value for the resistivity and thickness of the third layer indicates that this layer is irrelevant. However, the

first rather resistive (70 Ωm) and thin (3 m) layer was not resolved in the joint inversion due to the used frequency range for HEM. Therefore, only four layers were resolved in the joint inversion of HEM and TEM data. To resolve the first layer, it is required to use the shallow subsurface data, which can be measured from the other geophysical measurements suitable for shallow subsurface such as RMT.

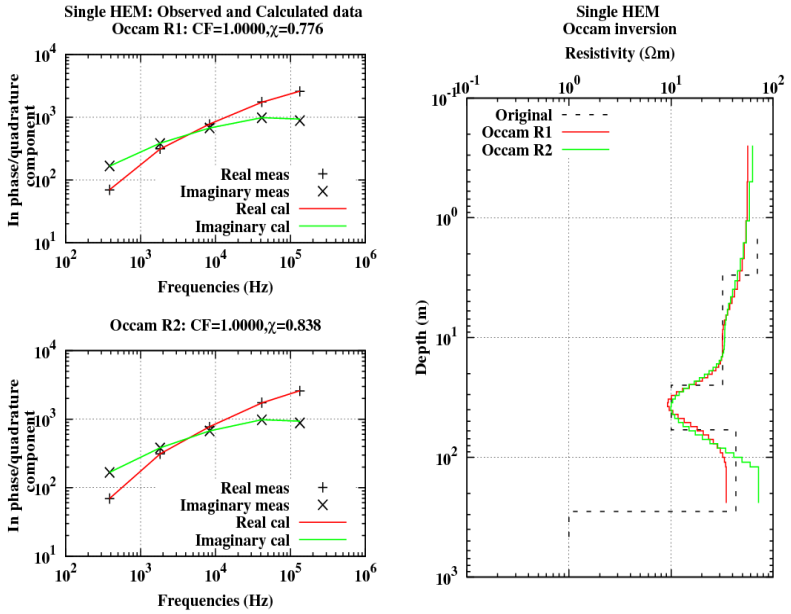

(a)

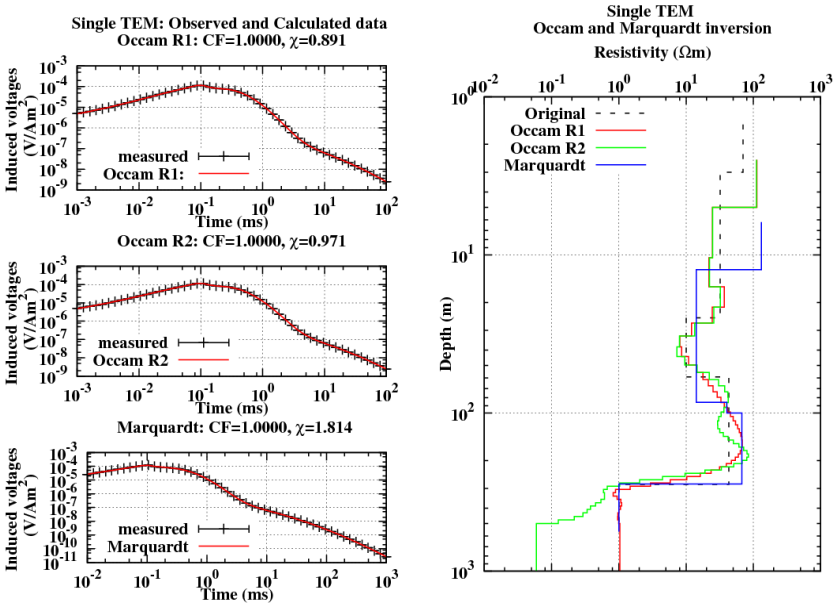

(b)

Figure 1: *Synthetic five-layer model data and its fitting for single Occam and Marquardt inversion; (a) HEM and (b) TEM.*

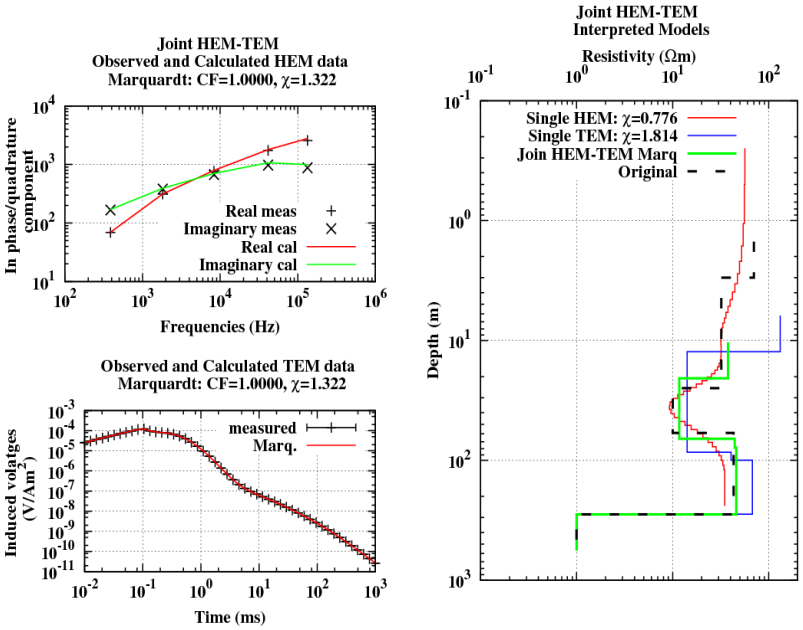

Figure 2: The joint inversion of HEM and TEM data and their fitting is displayed along with the original synthetic model.

Table 1: *Model parameter and importance values for 1D Marquardt single (TEM and RMT) and joint (HEM-TEM and HEM-TEM-RMT) interpreted five-layer model.*

Original synthetic model parameters	Single TEM inversion result		Single RMT inversion result		Joint HEM-TEM inversion result		Joint HEM-TEM-RMT inversion result	
	Model parameter values	Importances	Model parameter values	Importances	Model parameter values	Importances	Model parameter values	Importances
ρ_1 =70 Ωm	131.0584	0.5390	69.5021	0.9994	37.5017	1.0000	61.4740	1.0000
ρ_2 =32 Ωm	14.1269	0.9993	32.2785	0.9993	11.6988	0.9964	29.8819	1.0000
ρ_3 =10 Ωm	40.3728	0.0884	11.3787	0.7815	44.2405	0.0873	9.5836	0.9940
ρ_4 =43 Ωm	67.3762	0.7003	20.4584	0.0256	45.7891	0.9804	40.2462	0.9945
ρ_5 =1 Ωm	1.0050	1.0000	20.2444	0.0092	1.0010	1.0000	0.9942	0.9999
h_1 =3 m	12.3944	0.9987	3.0130	0.9966	20.7141	0.9972	4.8476	0.9999
h_2 =22 m	73.1684	0.9831	23.4694	0.9940	45.4053	0.9757	21.2994	0.9983
h_3 =34 m	14.2965	0.0759	20.2348	0.0718	12.2806	0.0627	30.3809	0.9750
h_4=224 m	181.2711	0.9938	20.0192	0.0003	204.4274	0.9970	227.6416	0.9996

3.2. 1D joint inversion of synthetic HEM, TEM and RMT data

To resolve the shallow subsurface structure, the code has been extended for the joint inversion of HEM-TEM-RMT (Fig. 3(a) & (b)). Same five-layer model was used to generate noise free synthetic RMT data. To avoid the repetition of the same information, the individual HEM and TEM inversion results are not presented again. The individual RMT inversion shows better matching with the original model for the upper layers. The inversion of RMT from Occam's first

(Model R1) and second (Model R2) order smoothness constraints (Fig. 3(a)) shows that the models start deviating after 20 m depth, which indicates the maximum depth (20 m) up to which the inverted models are reliable. The interpreted results of RMT data infer the three-layer model of the subsurface up to 20 m. RMT data could resolve only a three-layer model due to the limited frequency range. All the model parameters corresponding to the top three layers are well resolved and represented by *importance* greater than 0.8 (Table 1).

Fig. 3(b) shows the 1D jointly inverted model of HEM, TEM and RMT data. Albeit the starting model was a homogeneous half-space, the interpreted model is in good agreement with the original model. It has improved the damping factor (> 0.96) and parameter *importance* (> 0.98). In the joint inversion all nine parameters are important in the five-layer model (Table 1). The error bounds for layer parameters (resistivities and thicknesses) are narrower, which indicate that the common error due to equivalence problem in the inversion of electromagnetic data has been reduced.

The correlation between the layer resistivities and thicknesses of the jointly inverted model to the original model has been significantly improved in the HEM-TEM-RMT joint inversion in comparison with the individual inversions except for the top layer. The first layer shows better fitting with the original model in case of individual RMT inversion in comparison with the joint inversion. This can be due to the bad fitting of the data for higher frequencies. As the same RMT data showed good fitting in individual inversion, while it got bad when jointly inverted with HEM and TEM data. In the previous section, however, we have already analyzed that the first layer was not resolved by any of the used methods (HEM, TEM). This shows that an appropriate weighting is necessary to enhance the model resolution from shallow to the deeper structures. We are still working on this theme.

3.3. 1D joint inversion of HEM and TEM field data

After successful validation of the joint inversion algorithm on synthetic data, it is applied to field data. No RMT field data are available from the sites, which were already investigated by HEM and TEM; therefore only the joint inversion of HEM-TEM is tested on field data (Fig. 4).

Field data, which have been used here, were archived and interpreted by BGR Hannover (Steuer, 2008). The aim of this survey was to deliver substantiated knowledge and understanding of the structural and hydraulic properties, to focus on the vulnerability due to surface contamination and other human impacts, and to investigate interactions with saltwater intrusions and other groundwater reservoirs.

Thirty nine pairs of HEM and TEM sounding data were selected from this area for individual and joint inversion. Individual Occam's inversion for HEM data infers a general three to four layer model (Fig. 4(a) & (b)). Although, the reliability of the model is improved in the joint inversion, yet, it retains the general character of the model obtained from individual inversion.

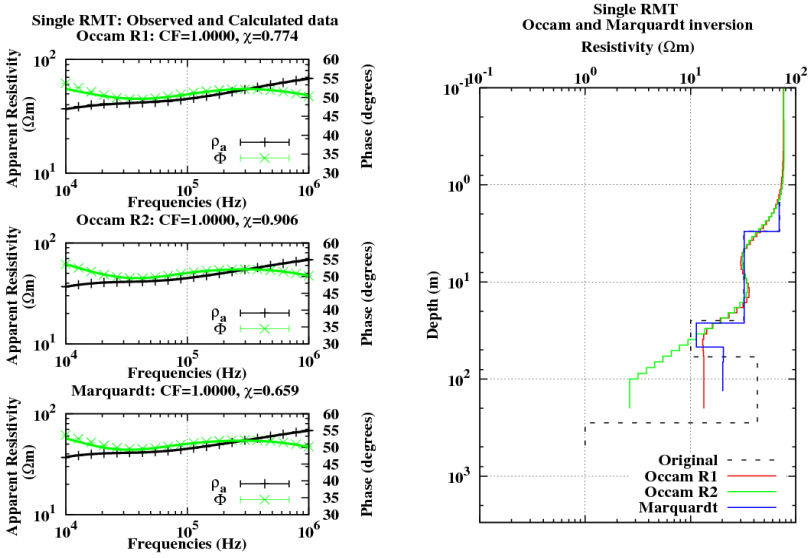

(a)

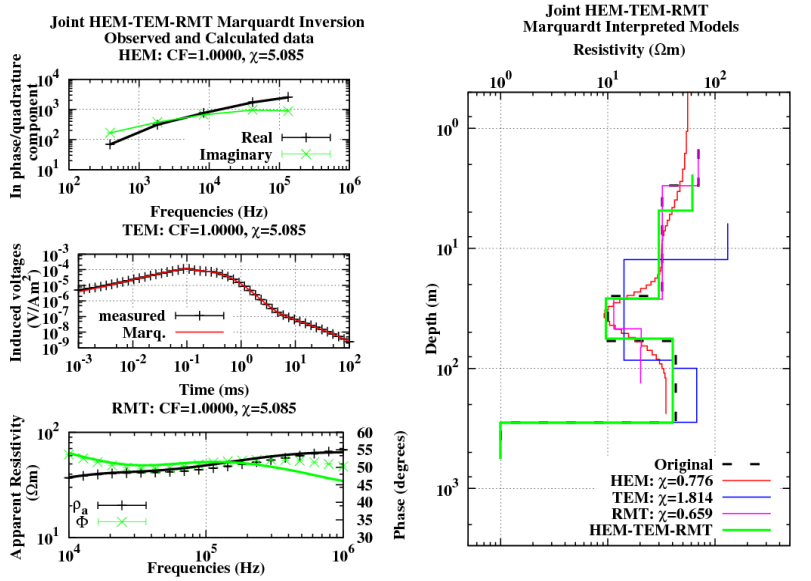

(b)

Figure 3: The synthetic five-layer model data and its fitting for single Occam and Marquardt inversion is shown in the upper plot (a) for RMT. The joint inversion of HEM, TEM and RMT data and their fitting is displayed in the lower plot (b).

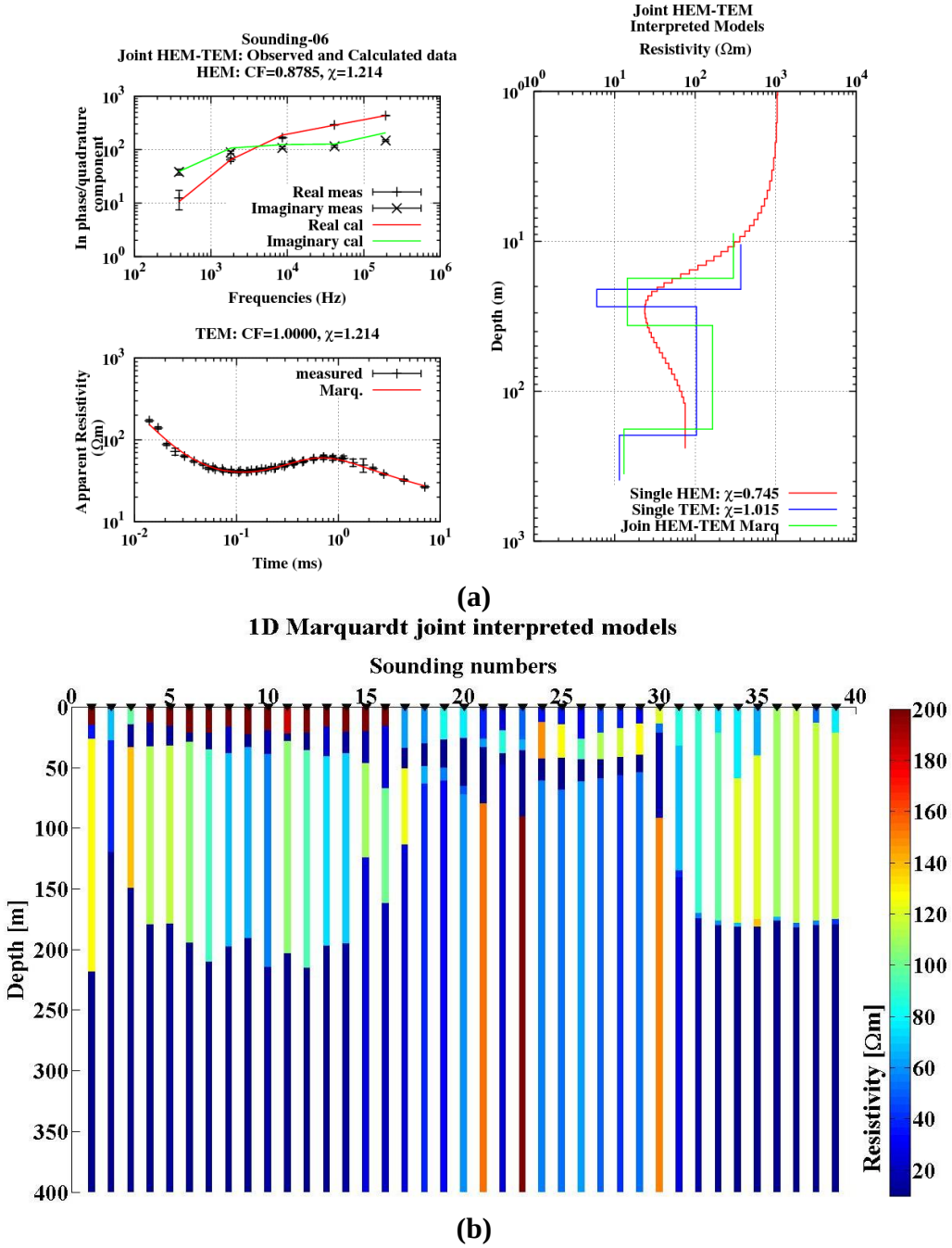

Figure 4: 1D Marquardt joint inversion for HEM and TEM field data sets from Cuxhaven (Germany) measured by BGR (Steuer, 2008). The fitting of the HEM and TEM data is shown for one sounding as an example in the upper plot.

Similar SVD analysis was performed for all data sets. It has been found that the results are consistently improved in all cases for the joint inversion. The HEM and TEM data and its fitting is shown for one sounding as an representative example (Fig. 4(a)).

4. CONCLUSIONS

The 1D numerical inversion codes, which have been used for the interpretation of single methods (TEM and RMT), are extended to do the single and joint inversion with HEM data. The joint inversion is tested for synthetic data (HEM, TEM and RMT) and field data (HEM and TEM). The resolution of model parameters is enhanced in joint inversion. To validate the code on field data, additional RMT measurements will be carried out on the sites, which were already investigated by HEM and TEM.

REFERENCES:

Auken E., Pellerin L., Christensen N. B. and Sørensen K., "A survey of current trends in near-surface electrical and electromagnetic methods", *Geophysics* **71(5)** G249 (2006).

Constable S. C., Parker R. L. and Constable C. G., "Occam's inversion: A practical algorithm for generating smooth models from electromagnetic sounding data", *Geophysics* **52(3)** 289 (1987).

Fitterman, D. V. and M. Deszcz-Pan, "Using airborne and ground electromagnetic data to map hydrologic features in everglades national park", in Proceedings of the Symposium on the Application of Geophysics to Engineering and Environmental Problems SAGEEP 2001, Denver (Colorado), *Environmental and Engineering Geophysical Society*, 2001.

Gómez-Treviño E. and Edwards R. N., "Electromagnetic soundings in the sedimentary basin of southern Ontario - A case history", *Geophysics* **4(8)** 311 (1983).

Harinarayana T., "Combination of EM and DC measurements for upper crustal studies", *Surveys in Geophysics* **20(3-4)** 257 (1999).

Jørgensen F., Johnsen R., Pedersen J., Christensen J. F. and Sandersen P. B. E., "Tyrsting valley, in Groundwater Resources in Buried Valleys – a Challenge for Geosciences", edited by R. Kirsch, H.-M. Rumpel, W. Scheer, and H. Wiederhold, Chapter 5.2, 181–190, Leibniz Institute for Applied Geophysics (LIAG), Hannover, Germany, 2006.

Jupp D. L. B. and Vozoff K., "Stable iterative methods for the inversion of Geophysical data", *Geophysical Journal of Royal and Astrnomical Society* **42** 957 (1975).

Kaikkonen P. and Sharma S. P., "2-D nonlinear joint inversion of VLF and VLF-R data using simulated annealing", *Journal of Applied Geophysics* **39** 155 (1998).

Kjærstrup M. and Erfurt P., "Bording valley, in Groundwater Resources in Buried Valleys a Challenge for Geosciences", edited by R. Kirsch, H.-M. Rumpel, W. Scheer, and H. Wiederhold, 171–179, Leibniz Institute for Applied Geophysics (LIAG), Hannover, Germany, 2006.

Levenberg K., "A method for the solution of certain non-linear problems in least squares", Quarterly of *Applied Mathematics* **2** 164 (1944).

Marquardt D. W., "An algorithm for least-squares estimation of non-linear parameters", *SIAM Journal* on *Applied Mathematics* **11** 431 (1963).

Matias M. S., Marques da Silva M., Ferreira P. and Ramalho E. "A geophysical and hydrogeological study of aquifers contamination by landfill", *Journal of Applied Geophysics* **32** 155 (1994).

Meju M. A., Fontes S. L., Oliveira M. F. B., Lima J. P. R., Ulugergerli E. U. and Carrasquilla A. A., "Regional aquifer mapping using combined VES-TEMAMT/ EMAP methods in the semiarid eastern margin of Parnaiba, Brazil", *Geophysics* **64(2)** 337 (1999).

Nobes D. C., "Troubled water: Environmental applications of electrical and electromagnetic methods", *Surveys in Geophysics* **17** 393 (1996).

Pellerin L., "Applications of electrical and electromagnetic methods for environmental and geotechnical investigations", *Surveys in Geophysics* **23** 101 (2002).

Raiche A. P., Jupp D. L. B. and Vozoff K., "The joint use of coincident loop transient electromagnetic and Schlumberger sounding to resolve resistive layers", *Geophysics* **50** 1618 (1985).

Scheer W., Kröger J., Kirsch R. and Zarth M., "Ellerbeker Rinne, in Groundwater Resources in Buried Valleys – a Challenge for Geosciences", edited by R. Kirsch, H.-M. Rumpel, W. Scheer, and H. Wiederhold, 205–226, Leibniz Institute for Applied Geophysics (LIAG), Hannover, Germany, 2006.

Scholl C., "The influence of multidimensional structures on the interpretation of LOTEM data with one-dimensional models and the application to data from Israel", Ph. D. Thesis, Institute of Geophysics and Meteorology, University of Cologne, Germany, 2005.

Siemon B., Christiansen A. V. and Auken E., "A review of helicopter-borne electromagnetic methods for groundwater exploration", *Near Surface Geophysics* **7** 629 (2009).

Siemon B., Eberle D. and Binot F., "Helicopter-borne electromagnetic investigation of coastal aquifers in North–West Germany", *Zeitschrift für Geologische Wissenschaften* **32(5/6)** 385 (2004).

Siemon B., Steuer A., Meyer U. and Rehli H. J., "HELP ACEH—a post-tsunami helicopter-borne groundwater project along the coasts of Aceh, Northern Sumatra", *Near Surface Geophysics* **5** 231 (2007).

Stadtler C., Fielitz F., Röttger B., Schildknecht F., Siemon B. and Voß W.,"Hubschrauber-(HEM) und Transientelektromagnetische (TEM) Messungen zur Grundwassererkundung in Namibia", in Abstract Book of the 64th Annual Meeting of the German Geophysical Association (DGG 2004), Berlin, HGP09, 2004.

Steuer A., "Joint application of ground-based transient electromagnetics and airborne electromagnetic", Ph.D. Thesis, University of Cologne, 2008.

Steuer A., Siemon B. and Eberle D., "Airborne and Ground-based Elecrtomagnetic Investigations of the Fresh-water Potential in the T sunami-hit Area Sigli, Northern Sumatra", *Journal of Environmental and Engineering Geophysics* **13(1)** 39 (2008).

Tezkan B., "A review of environmental applications of quasistationary electromagnetic techniques", *Surveys in Geophysics* **20** 279 (1999).

Vozoff K. and Jupp D. L. B., "Joint inversion of Geophysical data", *Geophysical Journal of Royal and Astronomical Society* **42** 977 (1975).

Resolution of 3D elongated deep conductive bodies embedded in a 2D background conductivity structure by 3D and 2D magnetotelluric inversion

Kristina Tietze[1,2], Oliver Ritter[1,2]

1 Helmholtz Centre Potsdam - German Research Centre For Geosciences GFZ, Department 2, Section 2.2, Telegrafenberg, 14473 Potsdam

2 Free University Berlin, Department of Earth Sciences, Malteserstr. 74-100, 12249 Berlin

Contact: kristina.tietze@gfz-potsdam.de

Summary

In recent years, 3D inversion has become a practical, if still computationally demanding, tool for interpreting MT data. This interpretation approach appears to hold great promise by overcoming the simplifications necessary to force the 3D nature of the real world into 2D models and thus producing more realistic and truthful images of the subsurface. In a series of geologic situations, however, we can identify a 2D regional structure in which local 3D structures are embedded. Based on synthetic data, we explore the resolution of an elongated highly conductive zone (HCZ) with varying along-strike extents embedded in a 2D regional resistivity structure with 3D and 2D inversion algorithms.

Our results show that both inversion approaches recover the HCZ for large along-strike extents; for shorter extents, surprisingly 2D inversion better recovered the subsurface structures. In presence of high conductivity contrasts and wide conductivity contrasts 3D inversion can fail to resolve structures of predominantly 2D character. In 2D inversion, the weak 3D nature of the ocean included in the synthetic model impaired the impedance-only inversion results for short HCZ extent and problems occurred if phase values below 5° were present in the data set.

Introduction

With advancing computational resources, three-dimensional (3D) inversion techniques have become practical in recent years and are now a more widely used tool for magnetotelluric (MT) data interpretation. A number of 3D inversion programs using various approaches for both forward modelling and inversion have been developed (e.g. Mackie *et al.* 2001; Siripunvaraporn *et al.* 2005a; Egbert & Kelbert 2012). Several studies applying 3D inversion algorithms to synthetic and field data show clear advantages over a 2D data interpretation as no restrictions on the dimensionality of the subsurface structure apply (e.g. Newman *et al.* 2003; Patro & Egbert 2011; Siripunvaraporn *et al.* 2005b). If data contains 3D structures, 2D interpretation of the data set can result in misleading subsurface models. Ledo (2005) outlined the dangers of 2D inversion of 3D structures depending on the orientation of the 3D structure relative to a 2D background structure.

3D and 2D inversion of a real-world data set from the San Andreas fault (SAF) in central California revealed a pronounced zone of high conductivities (HCZ) at depths of 15 – 30 km which extends parallel to a regional 2D background resistivity structure (Becken *et al.* 2008b, 2011; Tietze & Ritter *subm.*). Differences between 3D and 2D results are related to conductance, location, and shape of the HCZ. We used a 3D synthetic test model comprising the dominant structures of the survey area to investigate various aspects of 3D and 2D inversion related to the specific subsurface structure. Here, we focus on the impact of a varying finite along-strike extent of the HCZ on the outcome of 3D and 2D inversion.

3D and 2D forward modelling

The SYNPRK model (Fig. 1) comprises dominant structures of the survey area near Parkfield as revealed by 2D and 3D inversion: A highly conductive (1 Ωm) 20 km wide and 25 km high zone (HCZ) with its top at 17 km depth is embedded in a background structure mimicking a highly resistive Pacific Plate (2000 Ωm) and an intermediately resistive American Plate (200 Ωm). The elongated HCZ is located approximately 30 km southwest of the surface trace of the SAF. The top layers of the model comprise sedimentary material (3 Ωm) of varying thickness (2.2 km, 6.8 km). The Pacific Ocean (0.3 Ωm) is included according to bathymetry. The HCZ was modelled with along-strike extents of 258 km, 554 km, and 1150 km symmetric to the station array; the SYNPRK-h model variant lacks the HCZ. 3D synthetic data were calculated for a regular site layout with profile distances of 10 km, even site spacing of 10 km along the profiles and with 18 logarithmically distributed periods between 0.08 s and 11,000 s. 3 % Gaussian noise was added to the synthetic data prior to inversion. For 3D forward modelling we used ModEM3D (Egbert & Kelbert 2012) and WinGLink (Mackie *et al.* 1994).

In all modelling steps, the coordinate systems for model grid and data are identical. The *x*-axis is aligned with strike of the regional SYNPRK conductivity structure and *y* points parallel to the profiles (cf. Fig. 1). In this coordinate system, tangential-electric and tangential-magnetic modes

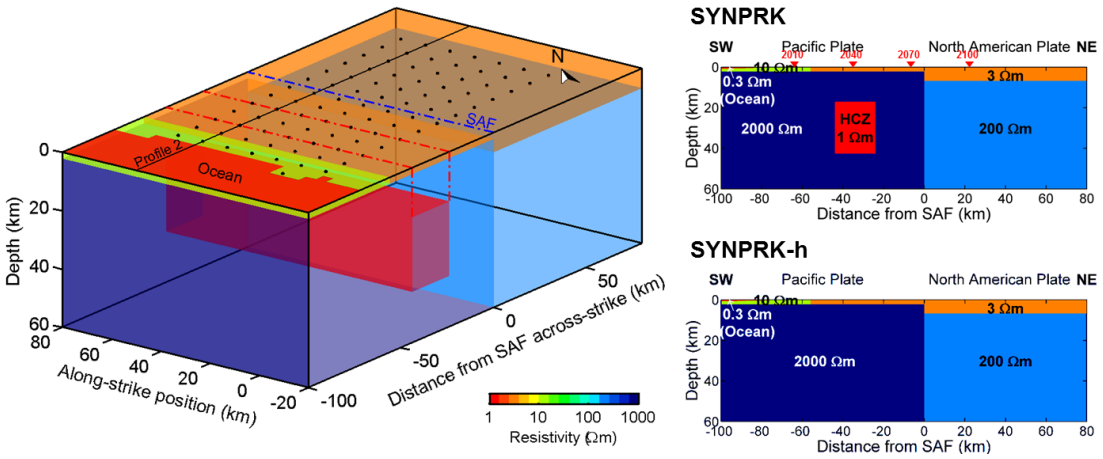

Figure 1: The SYNPRK resistivity model includes the main structural features revealed by 2D and 3D inversion of magnetotelluric data from the San Andreas fault near Parkfield, California. We investigated the impact of the along-strike extent of the HCZ. The highly conductive zone (HCZ) extends 268 - 1150 km along-strike; the Pacific Ocean is integrated according to true bathymetry. All other structures extend to the model edges. For the SYNPRK-h variant, the HCZ was removed.

of the 3D SYNPRK data set maximally separate. For the SYNPRK-h variant, Phase Tensor beta values (Caldwell *et al.* 2004) are small at all periods (Fig 2), which illustrates that the ocean constitutes only weak 3D effects (cf. Fig. 3). The 3D characteristic of the HCZ shows as elevated beta values at sites above the HCZ for periods between 100 s and 2000 s yielding maximum values at 181 s for an along-strike extent of 268 km and at 724 s for 1150 km (Fig. 2). As the data set is predominantly 2D we only consider components Zxy, Zyx, and Ty in the following.

Comparing FWD responses at selected sites, the impact of the HCZ can be identified for periods > 10 s (Fig. 4). The impact is limited to the Zxy and Ty components, which constitute the 2D TE

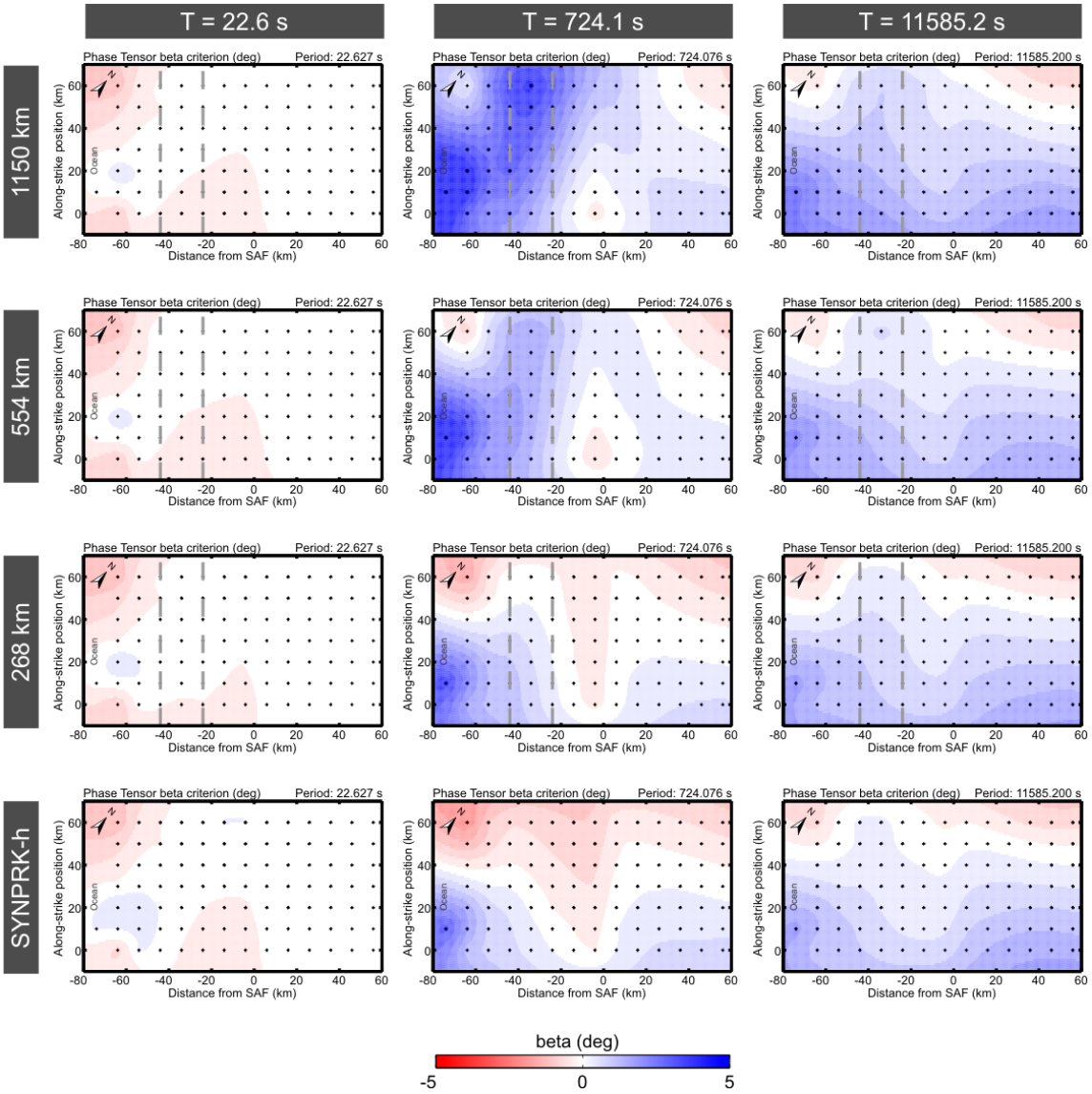

Figure 2: Phase tensor beta values for the SYNPRK model variants. Beta values significantly deviating from zero at intermediate periods (724 s) at sites above the HCZ illustrate the 3D characteristic of the HCZ. Consistently small beta values of the SYNPRK-h data (lowermost panel), illustrate the predominant 2D nature of the background structure.

mode. Zyx data are only marginally affected by the HCZ; the 3D Zyx-responses are not distinguishable in Fig. 4. For increasing along-strike extent of the HCZ, the 3D FWD responses for Zxy and Ty gradually change their shape towards a bound which resembles the response of an infinite, truly 2D HCZ. The Zxy and Ty responses for an infinite HCZ and a 2D ocean obtained with 2D FWD modelling (Rodi & Mackie 2001) along profile 2 (cf. Fig. 1) appear inconsistent with the 3D response behaviour at first sight. Also the yx-phase minima between 10 s and 1000 s are consistently weaker expressed in the 2D response. Comparing 3D FWD responses obtained with ModEM3D and WinGLink (Mackie et al. 1994) for the SYNPRK model we were able to exclude side effects from grid setup or other aspects of the 3D FWD calculation. In fact, the response differences originate from the 3D effect of the Pacific Ocean, which is mainly caused by the strike axis of the continental margin lying at an angle to the strike of the 2D SYNPRK structure (cf. Fig. 3). When modelling the 3D SYNPRK structures with a purely 2D ocean, where strike of bathymetry is parallel to the SYNPRK structures, 3D results are consistent with the 2D WinGLink result for an infinite HCZ (not shown).

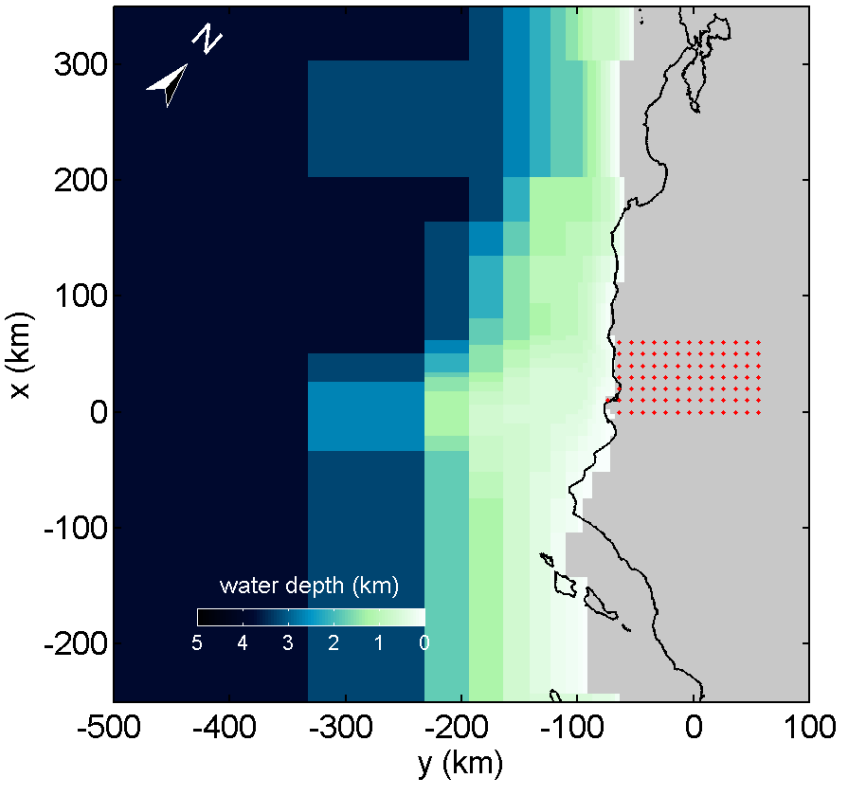

Figure 3: Bathymetry of the Pacific Ocean in the SYNPRK model. In the vicinity of the site array (red dots) the strike direction of the bathymetric fabric and the continental margin is oblique to the SYNPRK structure (aligned with model grid). Thus, the conductive sea water body has some 3D impact on the data.

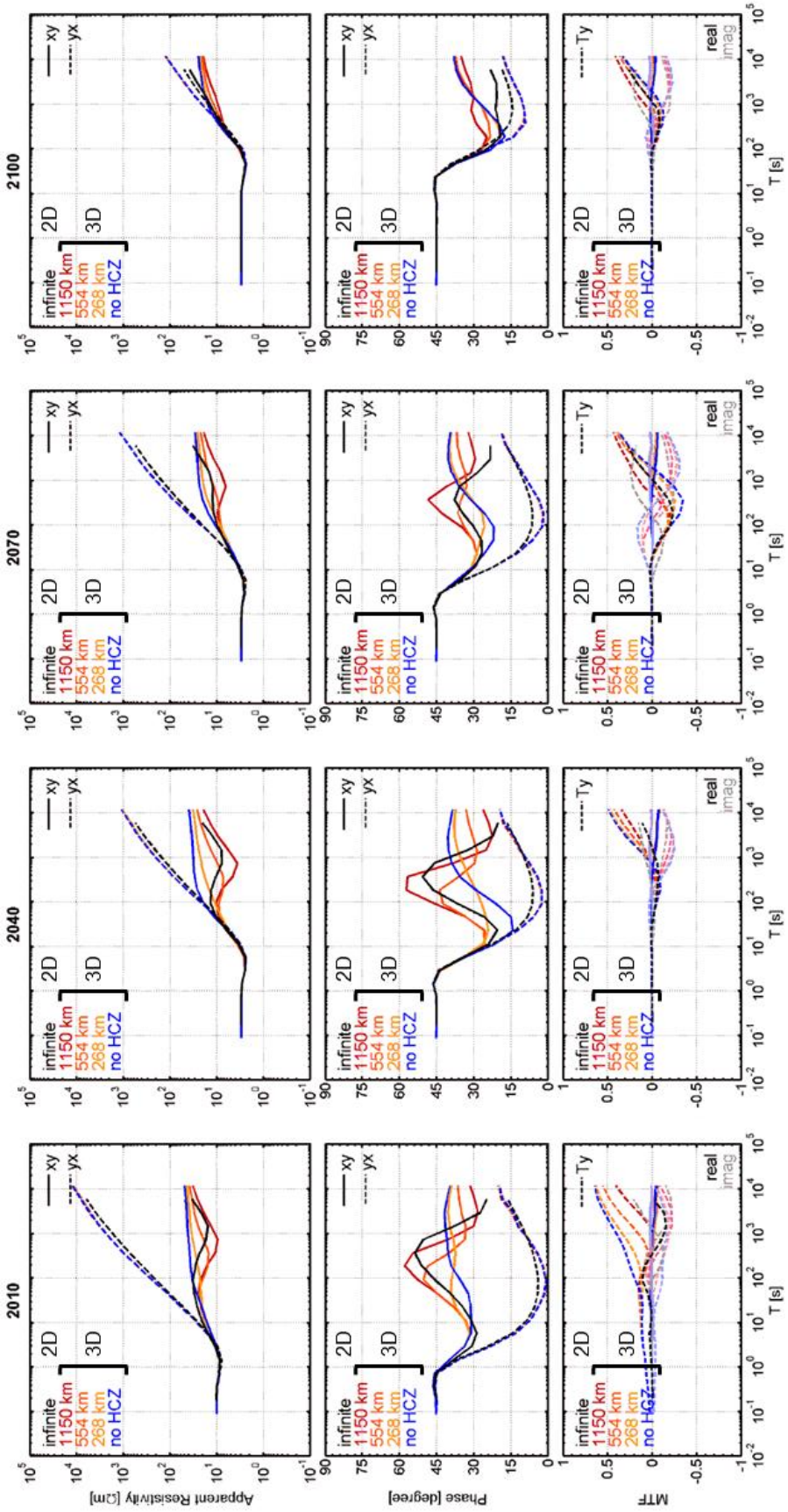

Figure 4: FWD responses along profile 2 for different along-strike extents of the HCZ, for site locations see Fig. 1. The impact of the HCZ manifests at periods > 10s at sites in the vicinity of the HCZ and periods > 100 s towards the inland end of the survey array and is limited to the Zxy and Ty components. For finite along-strike extents, ModEM3D response curves smoothly vary. The 2D WinGLink response for an infinite HCZ, however, does not fit into the pattern because of the 2D approximation of the 3D bathymetry.

3D and 2D inversion results

For 3D inversion (ModEM3D) we used off-diagonal impedances Zxy and Zyx, and/or the across-strike vertical magnetic transfer function (VTF) component (Ty) of all 92 array sites. Error floors are set to 3 % for impedances and 0.02 for Ty. The central model domain comprising the station array and the coastal area was horizontally discretized by a 4 km × 4 km mesh of 10 Ωm. A resistivity of 0.3 Ωm was assigned to the ocean cells and this model domain was kept fixed at all times during the inversion. Model covariances (regularization parameters) were set to 0.4, 0.2, and 0.3 for *x*-, *y*-, and *z*-directions, respectively, enforcing a higher regularization along-strike. Further details concerning the inversion parameters are described in the methods section in the appendix.

With 3D inversion the along-strike extent of the HCZ must exceed 500 km in order to be reliably revealed by both impedances and VTFs (Fig. 5). This is related to the inversion scheme of ModEM3D which penalizes deviations from a prior model. Thus, recovering the large range of conductivities of the SYNPRK model is a challenge, in particular, if homogeneous starting models are used. In all inversion models of the SYNPRK data set, a number of "additional" cells with high conductivity attached to the ocean can be observed. Obviously, the inversion tries to construct the desired resistivity contrast between coast and the seafloor. In terms of finding a minimal model norm, it is less costly to change some of the more conductive cells than a much larger volume of resistive cells, which would be necessary to recover the high-resistive Pacific Plate of the SYNPRK model extending beneath the ocean. However, the full intensity of the resistivity contrast is not reproduced; overall misfits close to the theoretical target of 1.0 cannot be achieved for inversion of SYNPRK impedance data which are sensitive to the absolute resistivity level. For the shortest along-strike extent, the impact of the HCZ is too low compared to the misfit due to the insufficient reproduction of the conductivity contrast along the coast.

For impedance-only inversion, the resistivity level beneath the station array and the top of the HCZ are well resolved. The location of the HCZ is shifted slightly inland with respect to the original position, as the artificial coastal conductor simulates some of the signature of the HCZ in the impedance data. In contrast, Ty-only inversion successfully recovers the lateral boundaries of the HCZ, as VTFs are particularly sensitive to horizontal conductivity changes. Due to the very low resistivities of the starting model, the HCZ is located at too shallow depth. When using higher resistivity values for the starting model, the HCZ is not resolved. Inverting for impedances and VTFs jointly, 3D inversion makes use of the strengths of either data type and well recovers both the location of the HCZ and the surrounding resistivity structure.

With 2D inversion using the algorithm of Rodi & Mackie (2001) recovering blocks with even shorter lateral extensions is successful (Fig. 6). We used standard inversion parameters (see methods section) and error floors of 10% for resistivities, 2% (0.6°) for phases, and 0.02 for Ty. Analogue to 3D modelling, bathymetry along profile 2 was integrated into the starting model and kept fixed (τ = 10,000) during inversion. Starting resistivities were 200 Ωm for Ty-only inversion and 50 Ωm for apparent resistivity/phase and joint inversions.

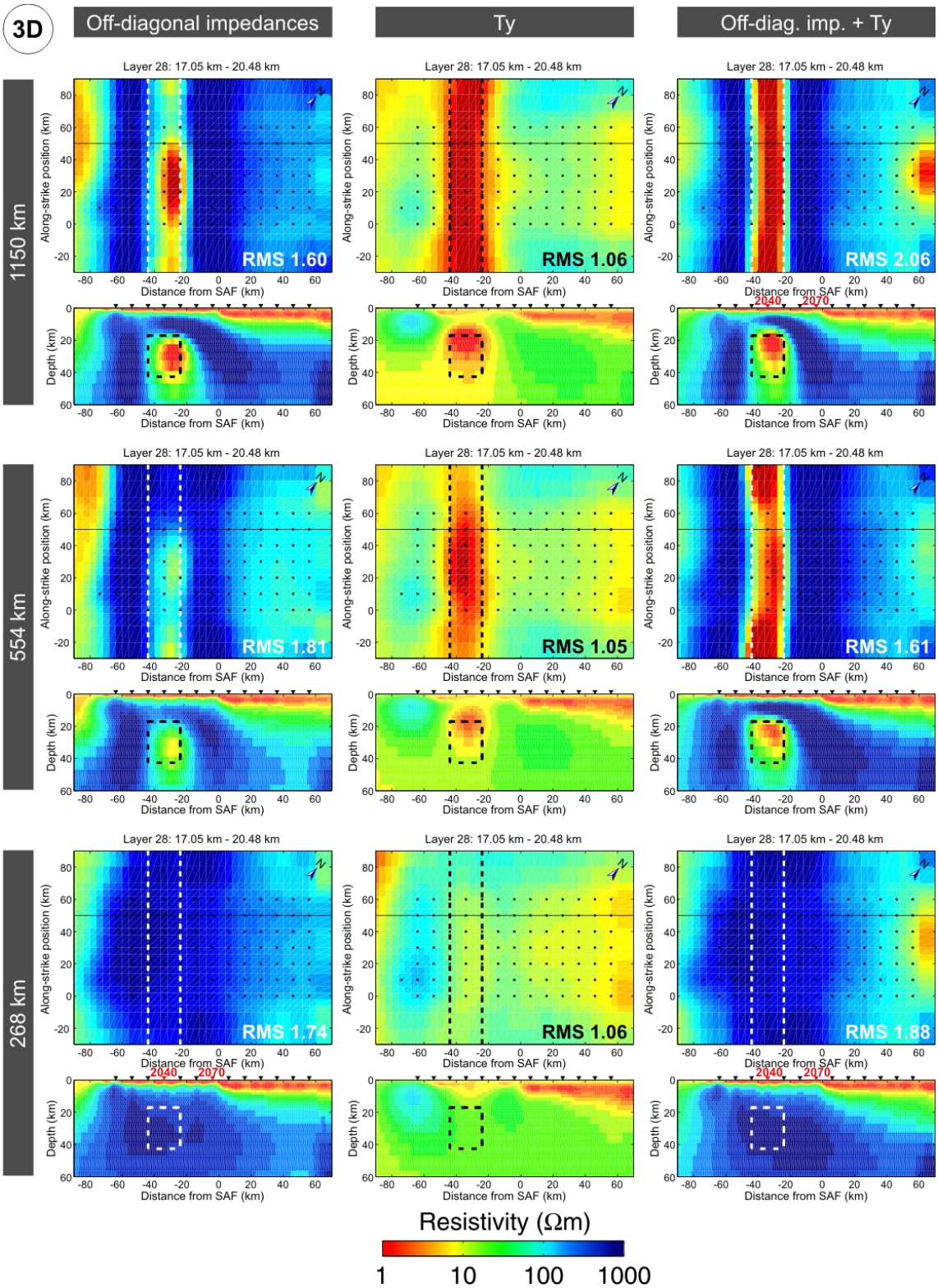

Figure 5: 3D inversion results as horizontal slices at the top of the HCZ (17 km) and along profile 2 (cf. Fig. 1). For 3D inversion the along-strike extent of the HCZ (dashed outline) must exceed 500 km to be recovered with some certainty. Insufficient recovery of the high conductivity contrast along the coastline and beneath the ocean, expressed in high final overall RMS values, inhibits resolving shorter HCZ versions.

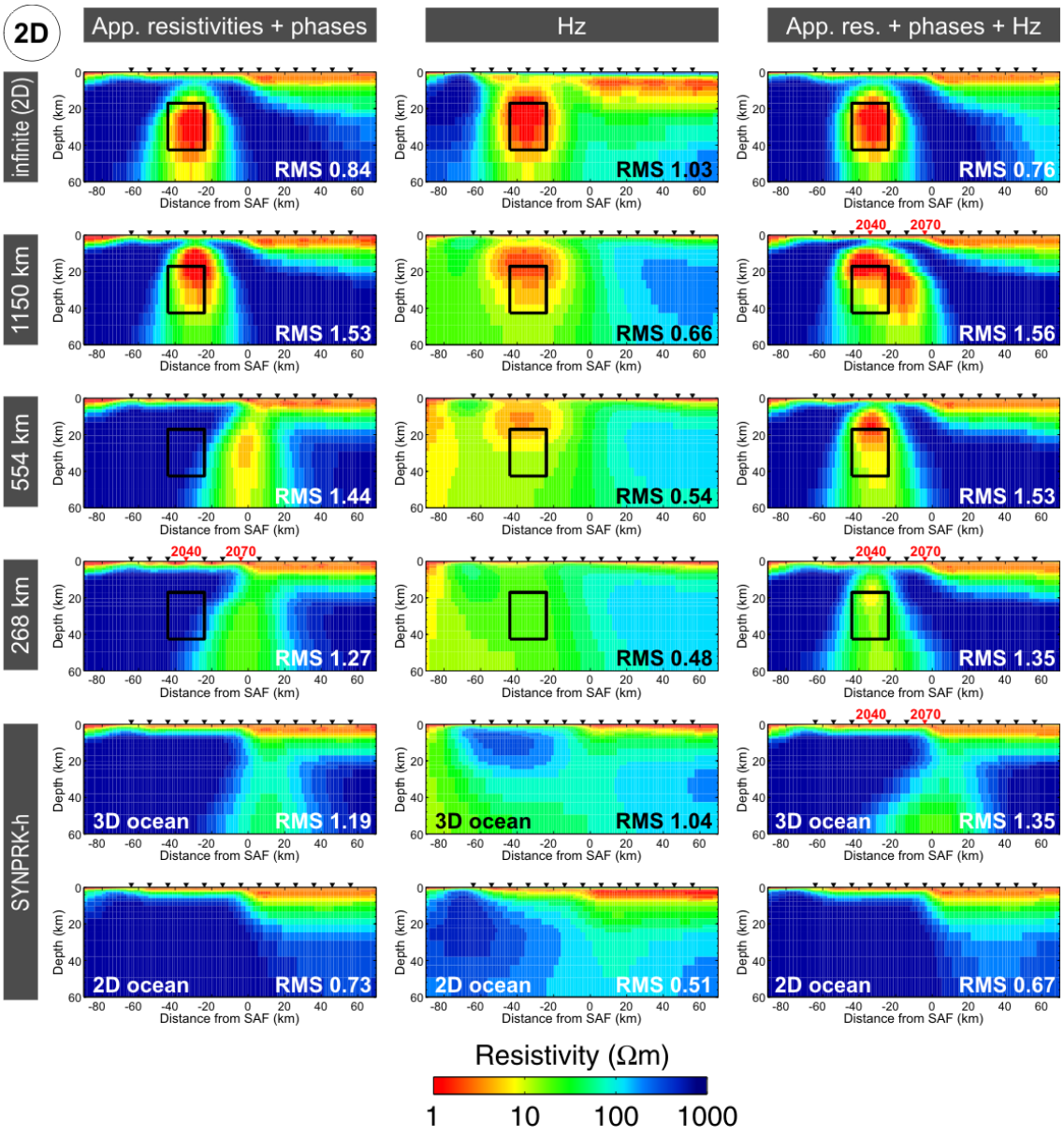

Figure 6: 2D inversion along profile 2 (cf. Fig 1) can recover the HCZ for all along-strike extents. Reliable images of the SYNPRK structure are, however, only achieved for joint inversion of apparent resistivities, phases, and VTFs. The shift of the HCZ towards the SAF and the blurred conductive region imaged beneath the SAF for the SYNPRK-h variant are related to the 3D characteristic of the bathymetry. In general, the HCZ is imaged at too shallower depth, if 3D modelling responses were inverted. Responses from sites marked in red are shown in Fig. 7.

Using only apparent resistivities (left column in Fig 6), the location of the HCZ is only well recovered for the variant with the longest extension. For shorter along-strike extents, the HCZ is shifted towards the SAF. Also for the SYNPRK-h variant which lacks the HCZ, 2D inversion images an artificial conductive region beneath the SAF. FWD modelling tests showed hardly any difference to completely homogeneous highly resistive deeper structures. This unexpected result is related to the 3D characteristic of the Pacific ocean (cf. Fig 4). Inverting the SYNPRK-h response comprising a 2D ocean, the continuous high resistivities of the deep subsurface are imaged correctly (lowermost panel in Fig 6). Ty-only inversion of the SYNPRK data, reliably

reveals the HCZ and its lateral position. The varying along-strike extent of the HCZ only affects the Ty-amplitude, which is largest for a HCZ length of 1150 km. However, even for the shortest along-strike extent considered here, the induction vectors still point nearly parallel to the profiles, the finite extent of the HCZ does not yet influence the VTFs. Thus, the behaviour of the profile-parallel Ty component is still consistent with an infinite 2D HCZ of decreased conductance. Hence, the image of the HCZ becomes weaker with shorter HCZ extent. Joint inversion of apparent resistivities, phases, and Ty successfully recovers the HCZ even for 258 km along-strike extent. All 2D inversion results of data comprising a 3D ocean, however, image the HCZ at too shallow depths.

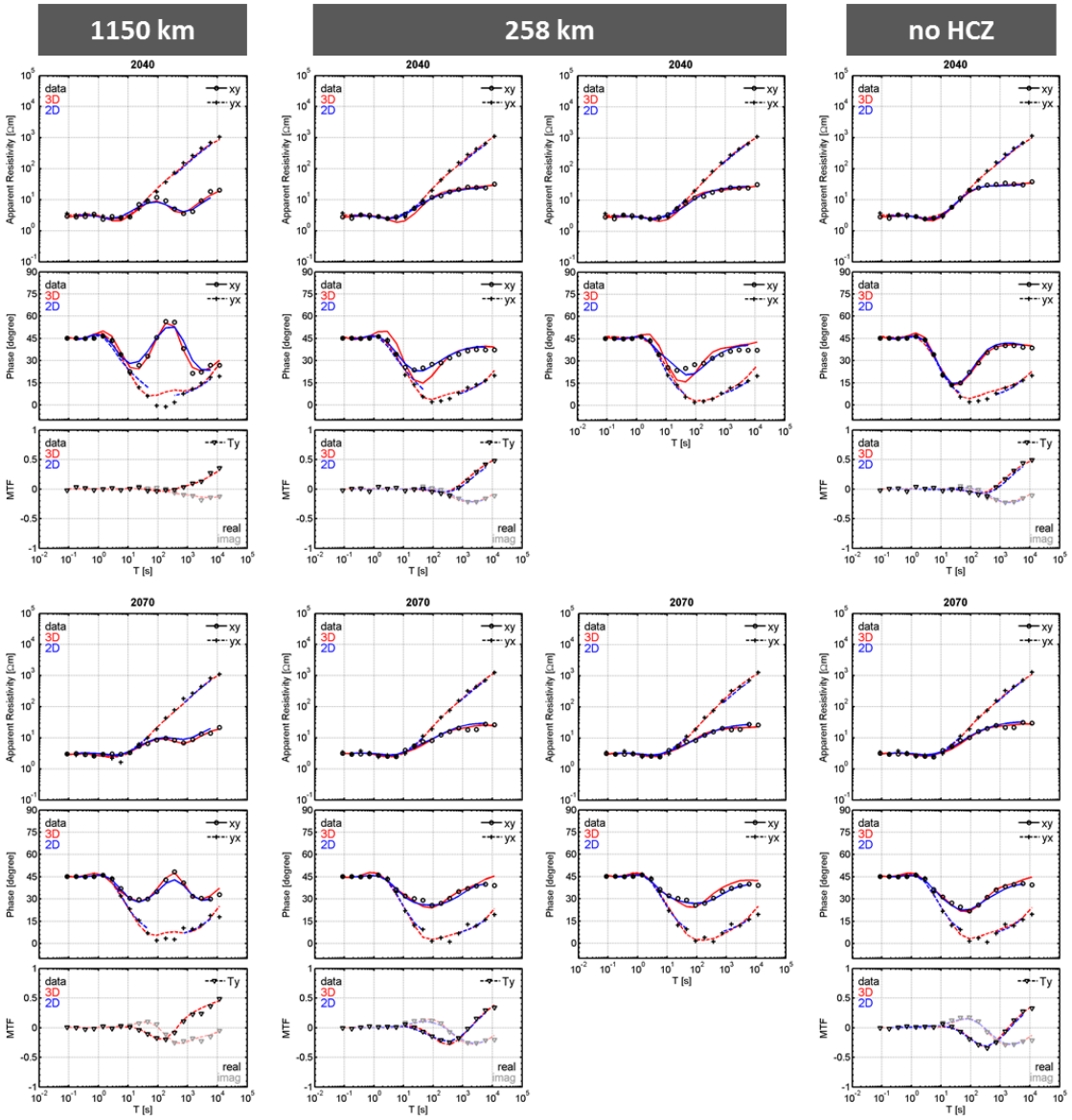

Figure 7: Comparison of 3D and 2D responses for joint (all) and impedance-only (258 km) inversion results. Site locations are marked in Figs 5 and 6. 3D and 2D data fits generally are of similar quality. For the shortest HCZ extent (258 km), 3D xy-phases between 1 s and 100 s systematically differ and indicate the absence of the HCZ in the inversion result. The blurred conductive region replacing the HCZ in 2D impedance-only result, however, does not have a significant effect on the data fit. Phase values below 5° had to be omitted in 2D inversion (see text).

The data fits of 3D and 2D inversion results are mostly of similar quality (Fig. 7). Where 3D inversion fails to recover the HCZ for the shortest along-strike extent of 258 km (middle column), 2D inversion responses better reflect the SYNPRK data. However, in order to successfully invert the data set in 2D, we had to exclude not only yx-phases below 0° but also those close to 0° which occur in the period range between 10 s and 200 s (gaps in 2D inversion responses). The 3D FWD responses contain phases which are very close to, but above 0°; phase values below 0° result from the Gaussian noise added to the impedance data prior to inversion. If yx-phases between 0° and 5° are not masked, 2D inversion fails to converge and introduces misleading artificial structures beneath affected sites (Fig. 8). We tested various modifications of the 2D resistivity structures, e.g. enhancing or decreasing resistivity contrasts between the Pacific Plate and the surrounding structures. It seems that there is a level of saturation for the 2D FWD modelling of high conductivity contrasts as we could not achieve yx-phase values below 3°.

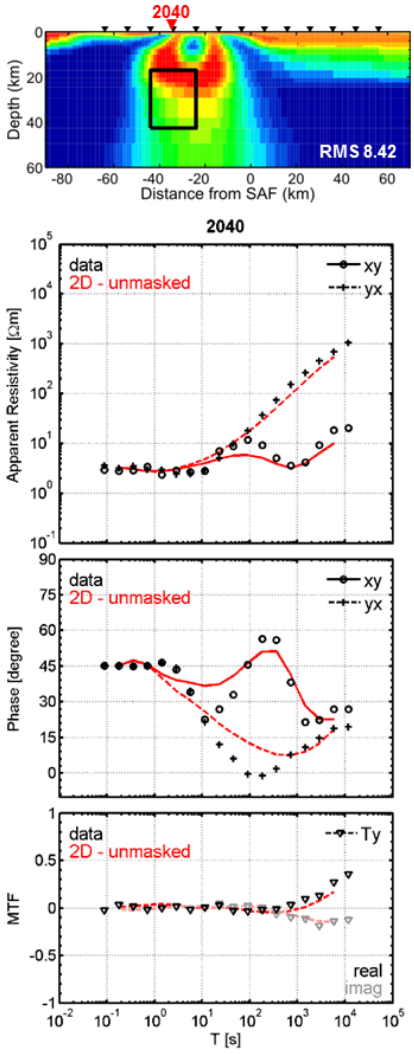

Figure 8: 2D inversion results of SYNPRK-1150 km. If yx-phase values close to or below zero are not masked, 2D inversion introduces artificial structures and fails to converge.

Discussion and conclusions

In most cases, both 3D and 2D inversion recovered the 3D HCZ successfully. The reliability of the subsurface structure depends on the inverted quantities. Best results were achieved for joint inversion of impedance-derived quantities and VTFs, particularly for 2D inversion. However, we encountered some unexpected obstacles for both inversion approaches.

For 3D inversion the largest challenges are the required wide range of resistivities and the strong conductivity contrasts of the SYNPRK model. The insufficient reproduction of extended zones of high resistivities beneath the ocean in the 3D inversion models impaired and partly inhibited resolution of the HCZ at depth.

2D inversion, using a different regularization scheme, detects even shorter versions of the structure. Inverting responses including a 3D ocean, the HCZ is systematically located at too shallow depth and artificial conductive structures appear. 2D inversion fails if phase values below 5° are not masked.

In conclusion, the advantages of joint inversion and both 3D and 2D modelling approaches should be used complementarily to render a comprehensive interpretation of the entire data set.

References

Becken, M., Ritter, O., Bedrosian, P. A. & Weckmann U., 2011. Correlation between deep fluids, tremor and creep along the central San Andreas fault, *Nature*, 480, 87—90.

Becken, M., Ritter, O., Park, S. K., Bedrosian, P. A., Weckmann, U. & Weber, M., 2008. A deep crustal fluid channel into the San Andreas Fault system near Parkfield, California, *Geophys. J. Int.*, 173, 718—732.

Caldwell, T. G., Bibby, H. M. & Brown, C., 2004. The magnetotelluric phase tensor, *Geophys. J. Int.*, 158, 457—469.

Egbert, G. D. & Kelbert, A., 2012. Computational Recipes for Electromagnetic Inverse Problems, *Geophys. J. Int.*, in press.

Ledo, J., 2005. 2-D versus 3-D Magnetotelluric data interpretation, *Surv Geophys*, 27, 111—148.

Mackie, R.L., Rodi, W. & Watts, M.D., 2001. 3-D magnetotelluric inversion for resource exploration, in *Proceedings of the 71st Annual International Meeting,* SEG, Expanded Abstracts, pp. 1501—1504.

Mackie, R. L., Smith, J. T. & Madden, T. R., 1994. Three-dimensional electromagnetic modeling using finite difference equations: The magnetotelluric example, *Radio Sci.,* 29, 923—935

Newman, G. A., Recher, S., Tezkan, B. & Neubauer, F. M., 2003. Case History: 3D inversion of a scalar radio Magnetotelluric field data set, *Geophysics*, 68, 791—802.

Rodi, W. & Mackie, R. L., 2001. Nonlinear conjugate gradients algorithm for 2-D magnetotelluric inversion, *Geophysics*, 66, 174—187.

Siripunvaraporn, W., Egbert, G., Lenbury, Y. & Uyeshima, M., 2005a. Three-dimensional magnetotelluric inversion: data-space method, *Phys. Earth Planet. Inter.*, 150, 3—14.

Siripunvaraporn, W., Egbert, G. & Uyeshima, M., 2005b. Interpretation of two-dimensional magnetotelluric profile data with three-dimensional inversion: synthetic examples, *Geophys. J. Int.*, 160**,** 804—814.

Tietze, K. & Ritter, O.. 3D magnetotelluric inversion in pratice, subm. to *Geophys. J. Int.*

Methods

3D modelling and inversion

The 3D model mesh consists of 50 × 70 × 57 cells in the two horizontal and the vertical directions, respectively, with the x-axis pointing towards N41°W. The central part of the mesh comprises 20 × 40 × 57 horizontally even-sized cells with an edge length of 4 km. On all four sides, the central domain is padded by 15 planes with cell sizes increasing laterally by a factor of 1.3. The vertical thickness is 25 m for the first layer and successively increases by a factor of 1.2 with depth. For the examples shown here, identical grids were used for FWD modelling and inversion.

2D modelling and inversion

The 2D inversion results shown here were achieved using a grid with approx. uniform horizontal spacing of 2 km. Smoothing parameter τ was set to 10 combined with horizontal (α=1.0) and vertical (β=1.5) weighting. 2D FWD modelling was conducted on the same grid as well as on a grid, which was refined in the vicinity of conductivity contrasts and sites.

DC resistivity FE modelling and inversion in view of a parallelised Multi-EM inversion approach

Julia Weißflog[1], Felix Eckhofer[2], Ralph-Uwe Börner[1], Michael Eiermann[2], Oliver G. Ernst[2], Klaus Spitzer[1]

[1]Institut für Geophysik und Geoinformatik
[2]Institut für Numerische Mathematik und Optimierung
TU Bergakademie Freiberg (Germany)

Summary

We present current research associated with a common project of the TU Bergakademie Freiberg and the Deutsches Geoforschungszentrum Potsdam (GFZ). The aim of this project is to exploit the distinct sensitivity patterns of different EM methods to enhance the resolution. Here, we focus on combining the direct current and the transient electromagnetic method. Further methods to be integrated are magnetotellurics and controlled-source EM. For this purpose, we have properly reimplemented our finite element secondary field DC forward modelling approach on unstructured grids and proved its theoretical convergence rate of $\mathcal{O}(h^2)$. We derive expressions for the Jacobian with respect to their efficient calculation in an inversion process and examine the spatial sensitivity pattern in order to design a coherent DC/TEM set-up.

Keywords: DC resistivity, finite element method, secondary field approach, sensitivity matrix

1 Introduction

The project *Three-dimensional Multi-Scale and Multi-Method Inversion to Determine the Electrical Conductivity Distribution of the Subsurface Using Parallel Computing Architectures* (Multi-EM) addresses the combination of different electromagnetic methods in a joint inversion approach to exploit their individual advantages. In Freiberg, we focus on the transient electromagnetic (TEM) and the DC resistivity method.

A prerequisite for any inversion strategy is an efficient forward modelling algorithm as outlined, e. g., by Rücker et al. (2006). Therefore, we have implemented a new DC resistivity forward operator in MATLAB using finite elements on unstructured tetrahedral grids that can easily be combined with our already existing TEM software (Afanasjew et al., 2010). This code enables us to deal with even complex topography and to extract the derivatives, which are crucial for the inversion while retaining full control over the assembly process of the system matrix.

To avoid degradation of the rate of convergence due to singularities in the source terms we deploy a secondary field approach.

For simplicity, we will apply a regularised Gauss-Newton method in view of a combination of different electromagnetic methods in one inversion algorithm.

2 DC Resistivity Modelling

DC resistivity modelling requires the discretisation of the equation of continuity:

$$-\nabla \cdot (\sigma \nabla \phi) = I\delta(\boldsymbol{x} - \boldsymbol{x}_0), \tag{1}$$

with ϕ as the electric potential, a given distribution of conductivity $\sigma(\boldsymbol{x})$ (cf. Figure 1) and a point source (electrode) A of strength I located at $\boldsymbol{x}_0 \in \mathbb{R}^3$.

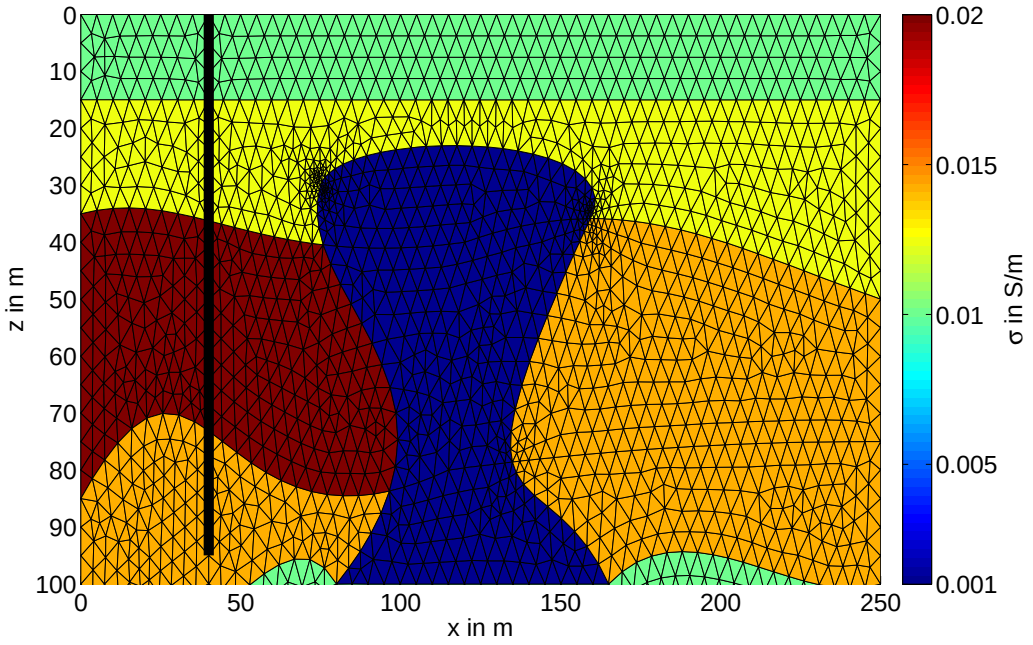

Figure 1: Used model with the source electrode A located along a borehole at $x = 40\,\mathrm{m}$

Finite elements enable us to deal with complex structures and permit extraction of the the derivatives with respect to the model parameters from the system matrix $A(\boldsymbol{\sigma})$ in a straightforward manner. Obtaining all entries of $A(\boldsymbol{\sigma})$ requires the evaluation of the following integral for each tetrahedron K that belongs to the grid:

$$a_K(\phi_j, \phi_i) = \sigma_K \int_K \nabla\phi_j(\boldsymbol{x}) \cdot \nabla\phi_i(\boldsymbol{x})\, d\boldsymbol{x},$$

with the basis functions ϕ_i and ϕ_j and the conductivity σ_K of the tetrahedron K.
Within the assembly process, $a_K(\phi_j, \phi_i)$ has to be transformed onto the reference element $\hat{K}$. The transformation reads

$$\boldsymbol{\xi} = B_K^{-1}(\boldsymbol{x} - \boldsymbol{b}_k),$$

with

$$B_K = \begin{bmatrix} x_1 - x_4 & x_2 - x_4 & x_3 - x_4 \\ y_1 - y_4 & y_2 - y_4 & y_3 - y_4 \\ z_1 - z_4 & z_2 - z_4 & z_3 - z_4 \end{bmatrix} \quad \text{and} \quad \boldsymbol{b}_K = \begin{bmatrix} x_4 \\ y_4 \\ z_4 \end{bmatrix},$$

which leads to

$$a_K(\phi_j, \phi_i) = \sigma_K \int_{\hat{K}} \left(B_K^{-T} \hat{\nabla} \hat{\phi}_j(\boldsymbol{\xi}) \right) \cdot \left(B_K^{-T} \hat{\nabla} \hat{\phi}_i(\boldsymbol{\xi}) \right) |\det B_K| \, d\boldsymbol{\xi}.$$

3 Secondary Field Approach

Singularities in the source terms decrease the convergence rate of the finite element approximation. To avoid this, we apply a secondary field approach. The decomposition of the total potential ϕ into primary (ϕ_p) and secondary potential (ϕ_s) yields the following equation:

$$\begin{aligned} -\nabla \cdot (\sigma \nabla \phi_s) &= \nabla \cdot (\sigma_s \nabla \phi_p) \\ &= \nabla \cdot (\sigma \nabla \phi_p) - \nabla \cdot (\sigma_0 \nabla \phi_p) \end{aligned} \tag{2}$$

with an anomalous conductivity $\sigma_s(\boldsymbol{x}) = \sigma(\boldsymbol{x}) - \sigma_0$. The discrete representation of equation (2) reads

$$A(\boldsymbol{\sigma})\boldsymbol{u}_s = -A(\boldsymbol{\sigma})\boldsymbol{u}_p + \sigma_0 A(\mathbf{1})\boldsymbol{u}_p, \tag{3}$$

where, in addition to $A(\boldsymbol{\sigma})$, only the matrix $A(\mathbf{1})$ has to be assembled. For multiple sources there is no need to reassemble any matrix. The primary potential is calculated analytically for a homogeneous halfspace:

$$\boldsymbol{u}_p = \boldsymbol{u}_p(\boldsymbol{x}_i) = \frac{I}{2\pi\sigma_0 ||\boldsymbol{x}_i - \boldsymbol{x}_0||}. \tag{4}$$

In Table 1 on page 3, we illustrate the efficiency of the secondary field approach for regular grid

DOFs	L_2-error e	α - Rate of Convergence	L_2-error e	α - Rate of Convergence
	Total field		*Secondary field approach*	
427	1.073763e0	-	4.745951e-1	-
3017	3.570459e-1	1.59	1.322951e-1	1.84
22681	1.657142e-1	1.11	3.382799e-2	1.97
175889	1.061691e-1	0.64	8.465897e-3	2.00

Table 1: L_2-error and convergence ($e(h) = \mathcal{O}(h^\alpha)$) with and without secondary field approach

refinements in terms of an improved convergence rate of an error measure $e(h) = \mathcal{O}(h^\alpha)$ where h is the maximum element diameter of the given mesh.

4 Calculating Sensitivities

To apply any inversion strategy we need to calculate the sensitivity or Jacobian matrix $J = \frac{\partial \boldsymbol{u}}{\partial \boldsymbol{\sigma}}$ which contains the derivatives of the discrete potential $\boldsymbol{u}$ with respect to all entries in $\boldsymbol{\sigma}$.
Considering the secondary potential, we differentiate (3) with respect to the model parameters using the product rule:

$$\begin{aligned}\frac{\partial A(\boldsymbol{\sigma})}{\partial \sigma_i}\boldsymbol{u}_s + A(\boldsymbol{\sigma})\frac{\partial \boldsymbol{u}_s}{\partial \sigma_i} = \dots \\ \dots - \frac{\partial A(\boldsymbol{\sigma})}{\partial \sigma_i}\boldsymbol{u}_p - A(\boldsymbol{\sigma})\frac{\partial \boldsymbol{u}_p}{\partial \sigma_i} \\ + \frac{\partial \sigma_0 A(\mathbf{1})}{\partial \sigma_i}\boldsymbol{u}_p + \sigma_0 A(\mathbf{1})\frac{\partial \boldsymbol{u}_p}{\partial \sigma_i}.\end{aligned} \tag{5}$$

$\frac{\partial A(\boldsymbol{\sigma})}{\partial \boldsymbol{\sigma}}$ is a three-way tensor, where the number of slices equals the number of parameters in $\boldsymbol{\sigma}$ and slice i belongs to the derivative with respect to σ_i. For example the first slice of $A(\boldsymbol{\sigma})$ belongs to the partial derivative with respect to σ_1 (Figure 2).

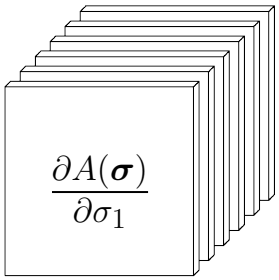

Figure 2: Slices of tensor $\frac{\partial A(\boldsymbol{\sigma})}{\partial \boldsymbol{\sigma}}$

Depending on whether σ_i is equal to the conductivity σ_0 around the source or not, several terms vanish and the derivatives differ only in an additional term $\frac{1}{\sigma_0}\boldsymbol{u}_p$, which is added if $\sigma_i = \sigma_0$:

$$\begin{aligned}\frac{\partial \boldsymbol{u}_s}{\partial \sigma_i} = - A(\boldsymbol{\sigma})^{-1}\left(\frac{\partial A(\boldsymbol{\sigma})}{\partial \sigma_i} \cdot (\boldsymbol{u}_p + \boldsymbol{u}_s)\right) \\ + \frac{1}{\sigma_0}\boldsymbol{u}_p.\end{aligned} \tag{6}$$

The derivative of the primary potential $\boldsymbol{u}_p$ is equal to zero for $\sigma_i \neq \sigma_0$, otherwise we derive (4) and arrive at

$$\frac{\partial \boldsymbol{u}_p}{\partial \sigma_0} = -\frac{1}{\sigma_0}\boldsymbol{u}_p. \tag{7}$$

Hence, if we add the sensitivities for the primary and secondary potential, we get the following expression regarding the total potential $\boldsymbol{u}$:

$$J = -A(\boldsymbol{\sigma})^{-1} \left(\frac{\partial A(\boldsymbol{\sigma})}{\partial \boldsymbol{\sigma}} \times_2 (\boldsymbol{u}_p + \boldsymbol{u}_s) \right). \tag{8}$$

The i-th ($i = 1 \dots n_{\text{parameters}}$) column of J contains the sensitivities with respect to the i-th parameter and the k-th ($k = 1 \dots n_{\text{DOFs}}$) row contains the sensitivities for the k-th electrode position M.

5 Numerical Experiments

To show the influence of embedded conductive or resistive bodies in a homogeneous halfspace on the resolution of the pole-pole configuration, we have carried out sensitivity studies. The current source and sink electrode, A respectively, is located at $x = 40\,\text{m}$ and $z = 95\,\text{m}$, whereas the potential electrode M is located at $x = 120\,\text{m}$ and $z = 0\,\text{m}$.

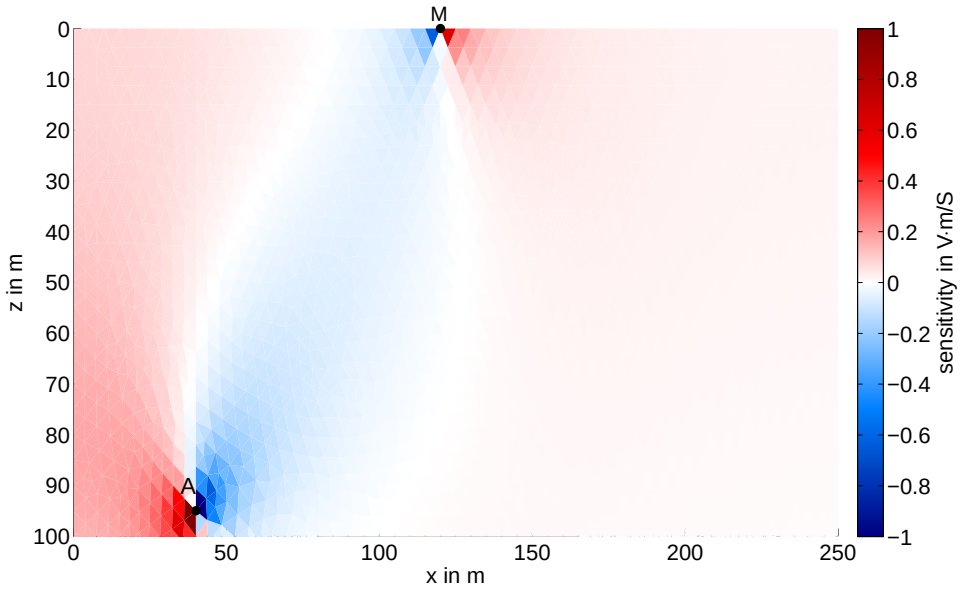

Figure 3: Sensitivities for a homogeneous halfspace

For the homogeneous halfspace we see the well-known shape of negative sensitivity between A and M (Spitzer, 1998). In Figure 4, the body causes serious distortions of the sensitivity pattern.

6 Conclusion

We have successfully reproduced the expected sensitivities using our new 3D DC forward operator. First inversions using the reference model (cf. Figure 1) appear to be working well and will be reported in detail later.

Preliminary tests using the MATLAB Parallel Computing Toolbox yield promising results regarding future plans for a parallel code.

With this re-development we have created a perfect basis to join the MATLAB-based forward modelling codes for both DC and TEM.

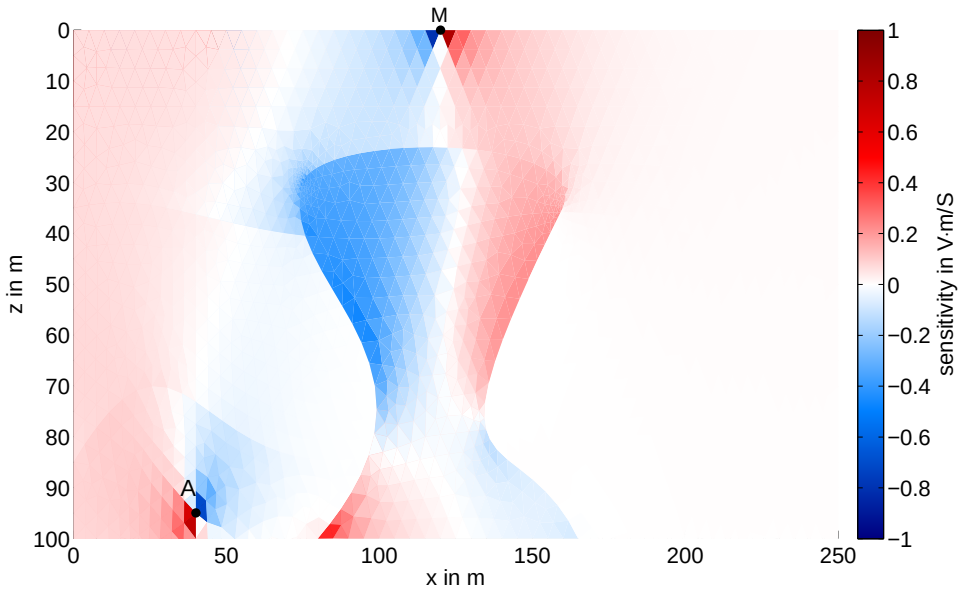

Figure 4: Sensitivities for the model from Figure 1

7 Acknowledgements

This project is funded by the German Ministry of Education and Research (BMBF) and the German Research Foundation (DFG) under the Geotechnologien Programme, grant 03G0746A,B.

References

Afanasjew, M., Börner, R.-U., Eiermann, M., Ernst, O., Güttel, S., & Spitzer, K. (2010, Sep 18 – 24, 2010, Giza, Egypt). 2D Time Domain TEM Simulation Using Finite Elements, an Exact Boundary Condition, and Krylov Subspace Methods, Expanded Abstract. *Proceedings:* 20^{th} *International Workshop on Electromagnetic Induction in the Earth*, 4p.

Rücker, C., Günther, T., & Spitzer, K. (2006). Three-dimensional modelling and inversion of DC resistivity data incorporating topography – I. Modelling. *Geophys. J. Int.*, *166*, 495–505.

Spitzer, K. (1998). The three-dimensional DC sensitivity for surface and subsurface sources. *Geophys. J. Int.*, *134*, 736–746.

Studies of A Fault Structure Using Electromagnetic Techniques in Mygdonian Basin, Northern Greece

Widodo, Bülent Tezkan, Marcus Gurk

widodo@geo.uni-koeln.de

Institute of Geophysics and Meteorology, University of Cologne
Zülpicher Str. 49a D-50674 Köln, Germany

Abstract.
The Volvi basin is located in an alluvial valley 45 km northeast of the city of Thessaloniki in Northern Greece. It is a neotectonic graben (6 km wide) structure with increasing seismic activity where the large 1978 Thessaloniki earthquake occurred. The seismic response at the site is strongly influenced by local geological conditions. Therefore, the European test site "Euroseistest" for studying site effects of seismically active areas is installed in the Volvi-Mygdonian Basin.
The ambient noise measurements from the east area of Euroseistest give strong implication for a complex 3-D tectonic setting. Hence, near surface electromagnetic (EM) measurements are carried out to understand the location of the local active fault and the top of the basement structure of the study area. The Radiomagnetotelluric (RMT) and Transient electromagnetic (TEM) measurements were carried out on eight profiles, 443 RMT and 104 TEM soundings were realized. The inverted RMT and TEM data show generally a four layer model. The layers are indicated as metamorphic and sediment rocks, which are in detail: marly silty sand with gravel (>> 100 Ωm), marly silty sand with clay (50 - 100 Ωm), sandy clay (30 – 50 Ωm) and silty sand (10 - 30 Ωm) with varying thickness. Due to the high resistivity of the top layer, the skin depths of the RMT soundings are around 35 m. The TEM data gives detail information of the lower structure down to a depth of 200 m.
The joint and sequential inversion of RMT and TEM data proves to be an effective tool to investigate complex geological structures. The 1-D and 2-D interpretation of RMT and TEM data, respectively, indicate a local fault structure and helps in explaining the direction of the fault structure. In order to understand the conductivity distribution of fault structure, 3-D modeling of RMT data was realized. According to the analyses, a normal fault is located next to the Euroseistest site, with a strike direction of N 70° E.

Keywords: Site Effect; Active Fault; Radiomagnetotelluric; Transient Electromagnetic; Northern Greece.

INTRODUCTION

It is well known that earthquake generally produces several damages. Moreover, if it occurs near densely populated area, it is required additional efforts to provide the detailed knowledge on active faulting, shear wave velocities and its correlation with seismicity in concerned area. Faults are not usually isolated structures mechanically, however they exist within a population of faults and they may interact each other through their stress fields. Destructive resulting from the large earthquake implication effect has been widely reported during recent years, such as the case of Izmit and Duzce earthquake in Aceh, North Sumatera earthquake in Indonesia [1] and Pacific coast in Japan in 2011 [7]. Prior to an earthquake hazard, it is important to evaluate the behavior of earthquake faults, the expected objective being the assessment of the future seismic hazard.

The study area is located in the epicenter area of 1978 earthquake, between Langada and Volvi lakes [11], ca. 45 km northeast of Thessaloniki (Northern Greece) (Figure 1). It has been well established that the strong ground motion of such a seismic event causes irregularly distributed modification to the local geology. Different geophysical methods have been applied in this area [2], however detail information of fault structures has not been verified so far. Ambient noise measurements from the area east of the Euroseistest experiment give strong implication for a complex 3-D tectonic setting. Therefore we carried out near surface EM studies to understand the distribution of the active faulting and the top of basement structure of this particular area.

Joint TEM and RMT inversion has been successfully applied to geological and engineering problems in the past [9]. The RMT method has low penetration depth and therefore gives information of the surface layers, whereas the TEM method gives detail information of the lower structure of the investigated area. Hence, a joint interpretation of RMT and TEM data will produce a good resolution of resistivities and thicknesses, in shallow and in deeper parts of the subsurface.

(a).

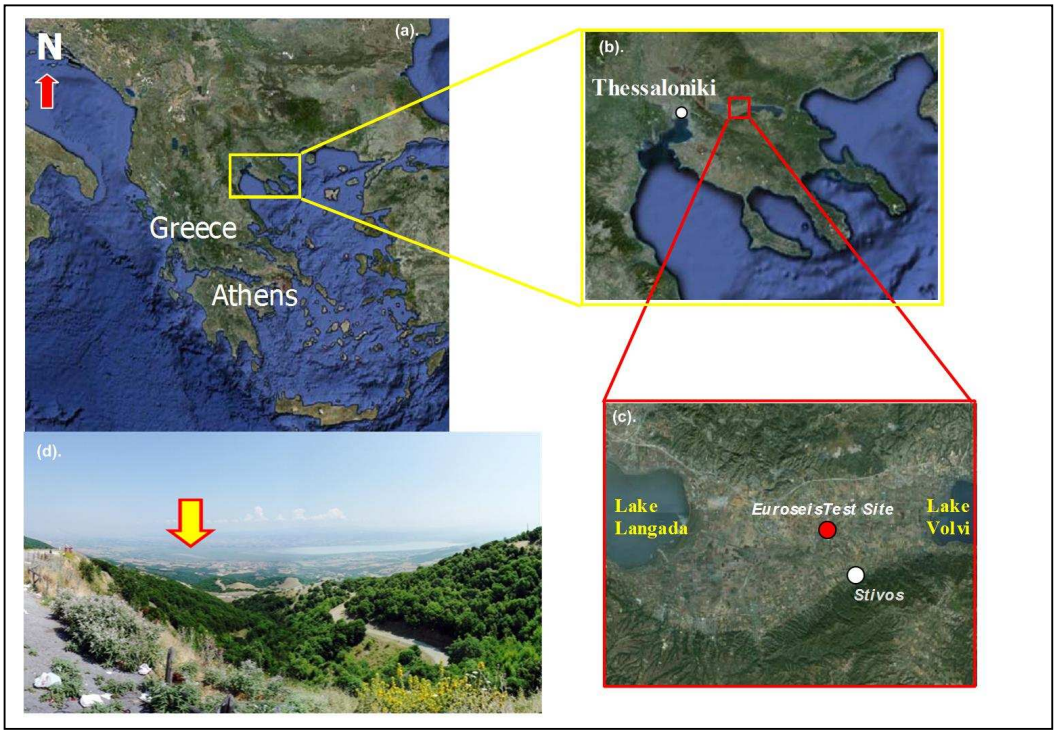

(b).

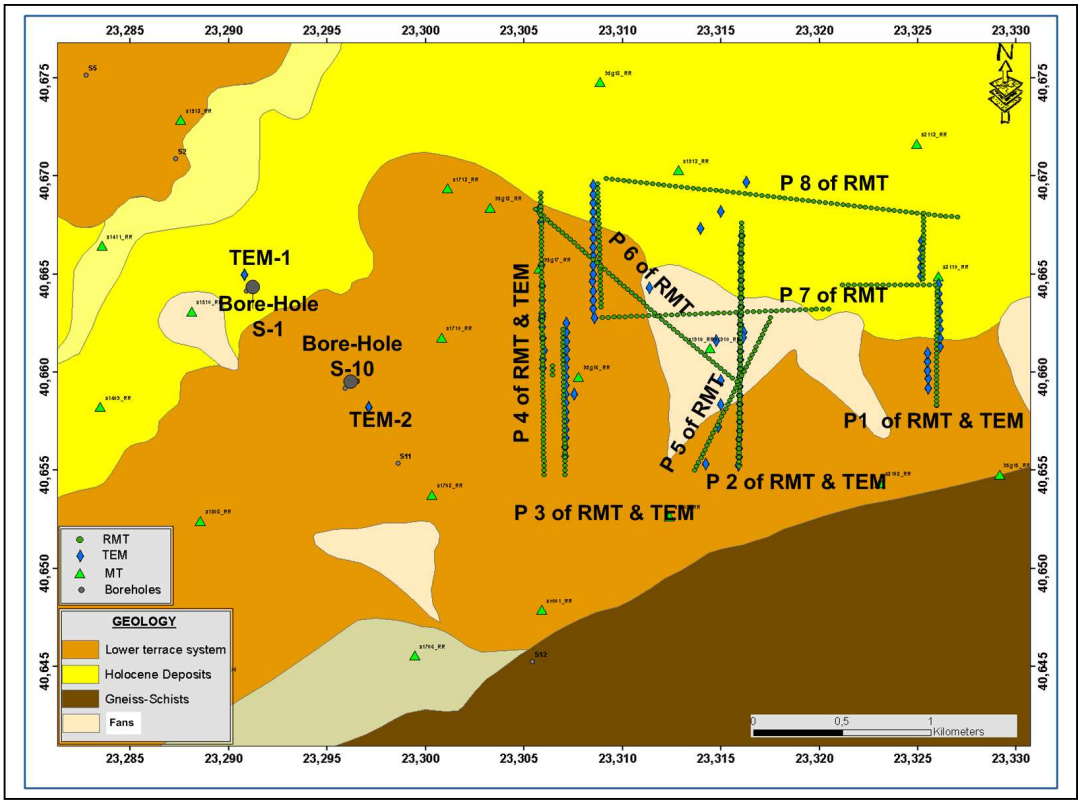

FIGURE 1. (a) Research area located on the northeast of EUROSEIST TEST (red circle) between two lakes(red square): Langada and Volvi Lake, Thessalonikhi, Northern Greece. (b) geology of the study area, location of RMT station (●), TEM station (◆) and location of boreholes (●). The green triangles (▲) show MT measurement conducted by prior researcher.

RMT MEASUREMENTS AND INTERPRETATION

The RMT measurements were carried out on six profiles as indicated in Figure 1b. Parameter of the survey design is listed in Table 1. The RMT of profile 1 is along 1600 m with direction N 0^o S, whereas the direction of profile 2 is located N60^o S. The direction of profile 3 in this area is N0^o S with length of 1400 m, which are perpendicular to the radio transmitters. The RMT profiles 4,5 and 6 are along 1100 m until 1700 m with direction N 0^o S, whereas the profiles 7 and 8 are located N 100^o S, which are parallel to the direction of available radio transmitters. The RMT-F system consists out of two magnetic sensors (induction coils, 30 cm length), a preamplifier for the electrical channels, two electrical antennae and a recorder. It is a four channel instrument (Ex, Ey, Hx, Hy) with the capability of estimating the full impedance tensor [8].

In order to calibrate the geophysical measurements with the lithology, TEM data at our reference site (TEM-1) was correlated with borehole data (Figure 1). This analysis allows identifying characteristic strata based on the electrical conductivity.

The modeling of RMT data was done by using 2-D inversion techniques (Figure 2). The 2-D inversion was performed with the 2-D Mackie code [4], the 1-D inversion was done with the Marquardt and Occam algorithm. Prior to any 2-D modeling, the penetration depth have been estimated using the ρ* (z*) transformation [6]. Penetration depths are found to be around 35 m.

TABLE 1. Parameter of RMT Survey Design

RMT Profile	Length [m]	Distance [m]	Orientation	Transmitter azimuth
Profile 1	1600	25	N0^oS	N60^oE
Profile 2	1000	25	N60^oS	N60^oE
Profile 3	1400	25	N0^oS	N60^oE
Profile 4	1100	25	N0^oS	N60^oE
Profile 5	1400	25	N0^oS	N60^oE
Profile 6	1700	25	N0^oS	N60^oE
Profile 7	1400	25	N0^oS	N60^oE
Profile 8	1500	25	N100^oS	N60^oE

As an example, we explain the RMT model of profile 2 and profile 5 in detail. This model (Figure 2) shows high resistivities on the top layer (more than 100 Ω m) which correlates to the marly silty sand of the borehole data.

The RMT 2-D inversion model of profiles 2 and 5 indicates metamorphic rock (marly salty sand) in a depth of 0 - 5 m (Figure 2). Beneath this layer, profile meters 0 – 350 m and 600 – 1200 are represented by conductive layers with resistivities less than of 50 Ωm interpreted as silty marly clay. The fault structure is found underneath profile meters 400 – 600 m in the 2-D model of profile 2 in the Volvi Basin. It can be cleary seen at 10 to 25 m depth represented by marly silty sand with resistivity of 50 – 100 Ωm. 2-D model of profile 5 which resolves a normal fault structure. It can be cleary seen at profile meters 300 – 500 m containing marly silty sand. Meanwhile, at more than 10 m depth, the layer adjacent to contains conductive material namely silty clay marly (10 - 30 Ωm). Both layers are the same resistivity as the layer identified with the fault structure at profile 2. Thus, it can be concluded that the 2-D models of profile 2 and profile 5 are mutually supportive and fit to each other (Figure 2).

Figure 3 and Figure 4 show a comparison between measured and calculated data at selected stations and frequencies at profile 2 and 5. Generally, measured and calculated data is having good fit considering a complex and inhomogeneous geological structure of research area. Some misfits which are associated as 3-D effect.

In order to provide detail information about fault structure continuity, 2-D model of all profiles have been correlated to the geological map (Figure 5). Profile 1 indicates two layers with a lateral conductivity contrast; the conductive layer is associated with Holocene deposit while the resistive layer is associated with lower terrace deposit.

The differences are shown between 2-D models and geological map in profile 3 and profile 6 crossing (see blue arrows at Figure 5). Those two models show consistent result by having conductive layers and associated with Holocene deposit. However, geological map indicate structures are associated with lower terrace deposit. In this case, RMT model can improve geological map, the layer was mapped previously as lower terrace deposit and now it can be attributed to fans.

Distribution of fault structure can be seen at profile 2 and profile 5 which indicate a normal fault structure. Meanwhile, profile 1 also indicates a normal fault structure at profile of 100 - 350 meters at depth more than 5 meters. Based on correlation between all 2-D conductivity models and geological map, it can be known that strike direction of the fault structure is N 70° E (red arrow at Figure 5).

TEM SOUNDINGS

In order to overcome the resolution problem of TEM soundings for near surface structures, we carried out RMT soundings at each TEM location to use this additional information in the following joint inversion. The TEM measurements were carried out on four profiles (Figure 1).

The distance between stations is depending on the accessibility of the area. 104 loop-loop measurements (Transmitter (Tx): 50 m x 50 m and Receiver (Rx): 10 m x 10 m) were performed during this campaign.

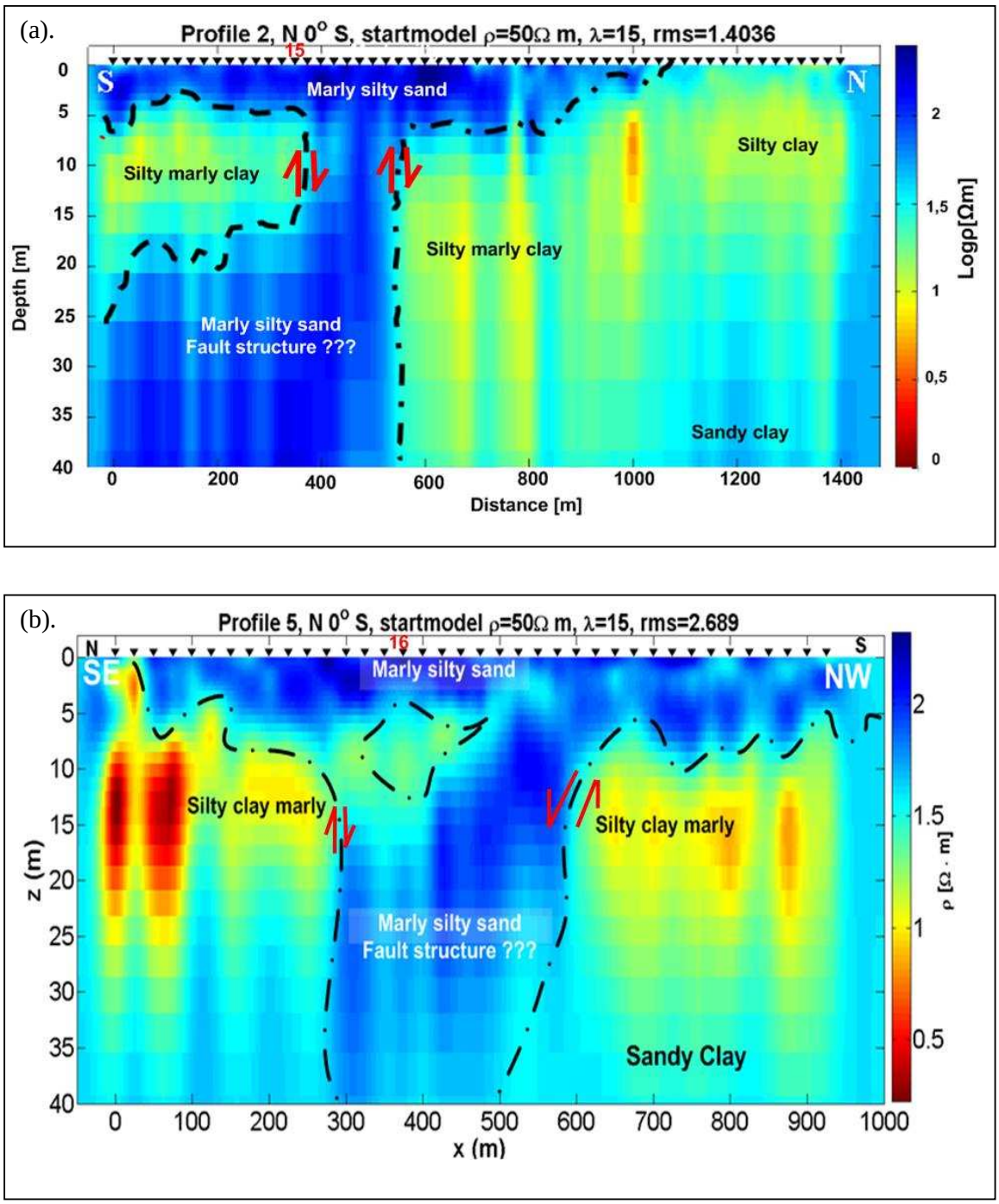

Figure 2. (a) 2-D Conductivity models of profile 2 and the location at station 15 . (b) 2-D Conductivity models of profile 5 and the location at station 16. Red arrows indicate the normal fault structure.

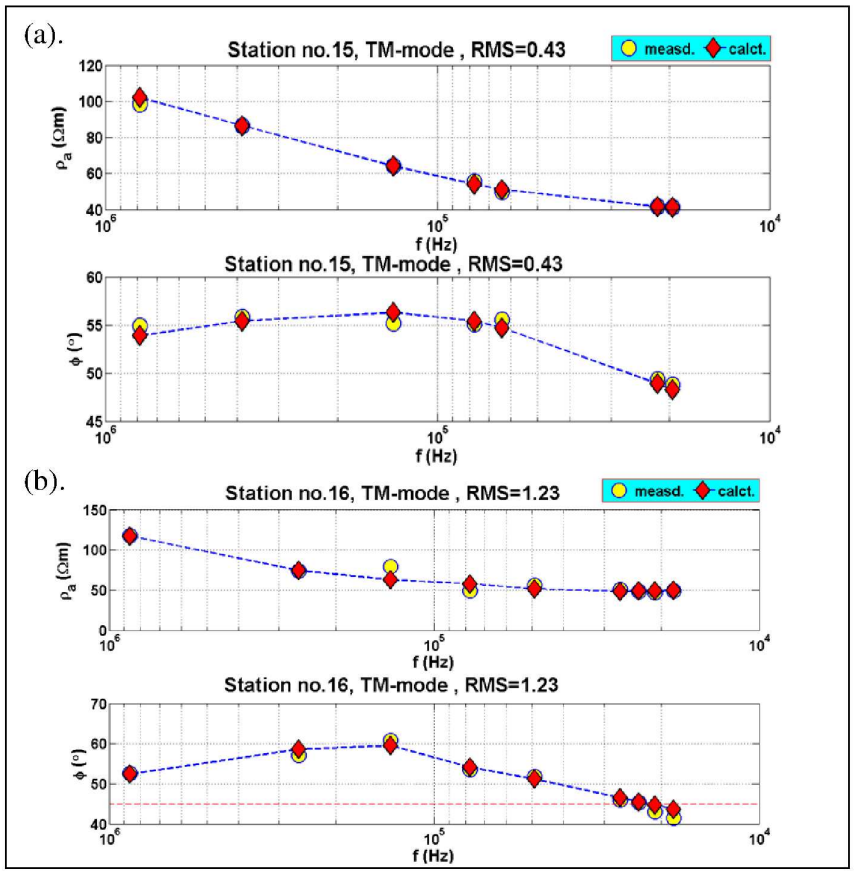

FIGURE 3. Data fitting of measured (yellow circles) and calculated (red tetrahedrons) for selected stations (a) at station 16 for profile 2 (top) and (b) station 15 for profile 5 (bottom) .

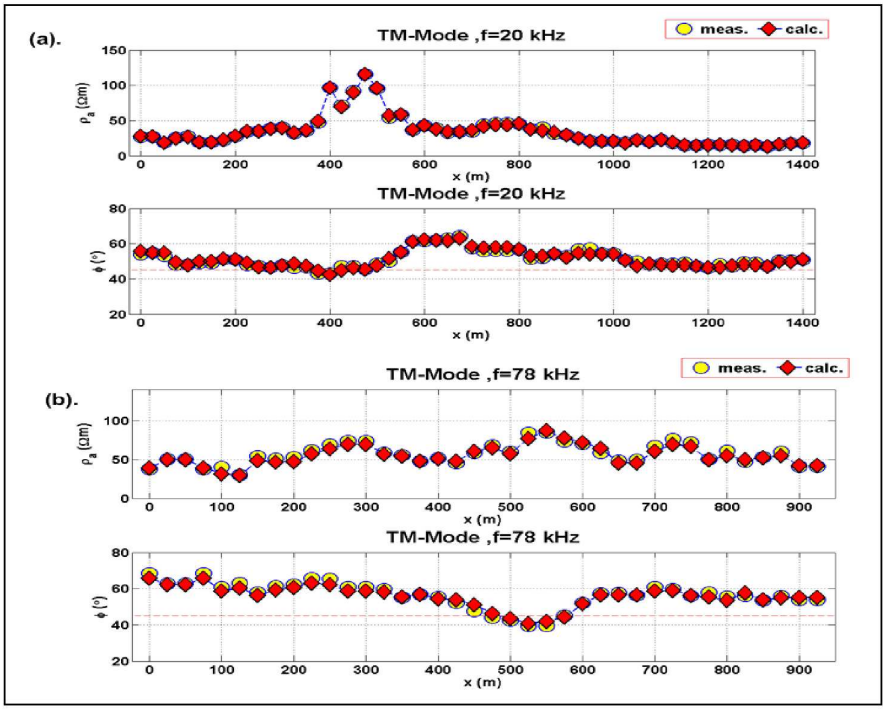

FIGURE 4. Data fitting of measured (yellow circles) and calculated (red tetrahedrons) for selected frequencies (a) at frequency 20 kHz for profile 2 (top) and (b) frequency 78 kHz for profile 5 (bottom) .

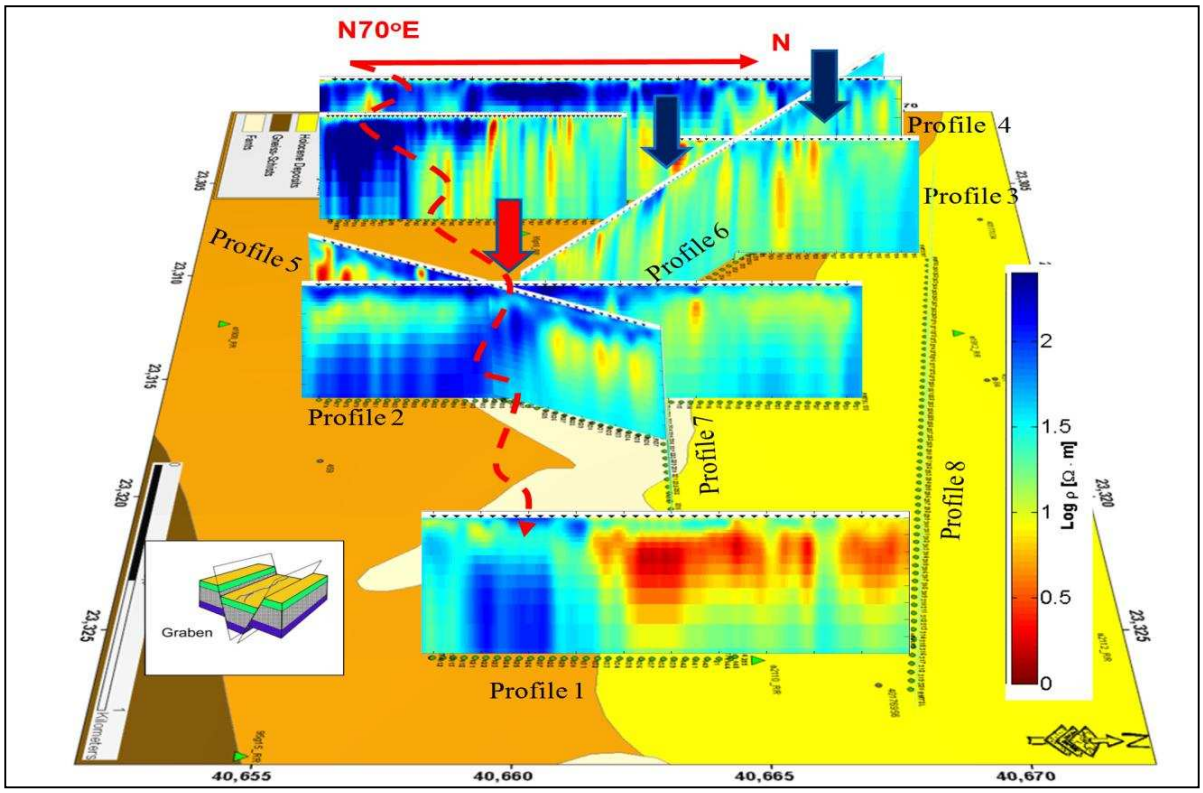

FIGURE 5. Correlation of 2-D model of RMT data with geological map. The dashed red lines show strike direction of fault structure namely N 70 E. Red arrows indicate the normal fault structure in research area (inset). Blue arrows show an area in which geological map is different from RMT models.

Parameter of the survey design is listed in Table 2. TEM data obtained using the Zonge NT 20 transmitter and the Zonge GDP32 receiver.

TABLE 2. . Parameter of TEM Survey Design

RMT Profile	Length [m]	Site distance [m]	Profile Orientation
Profile 1	850	50	N0°S
Profile 2	1350	50	N0°S
Profile 3	1500	50	N0°S
Profile 4	850	50 - 250	N0°S

The penetration depth of TEM methods depends on the time after the transmitters current is switched off [10]. The diffusion process of the transient electromagnetic induction field can be visualized using the smoke ring concept.

JOINT AND SEQUENTIAL INVERSION OF RMT AND TEM DATA

The RMT conductivity models can resolve the surface structure down to a depth (z) of 35 m 8 (Figure 2 and Figure (6a)). On the other hand,. Due to the low conductivity (metamorphic rock), the penetration depth of TEM is small enough to resolve the surface structure ($z < 10$ m), however it can resolve the deeper structure down to 200 m depth (Figure (6b)). In this kind of circumstance, joint inversion of RMT and TEM data is recommended. There are two techniques of joint inversion will be applied [9]. First is sequential inversion in which the output of RMT data set is used as an input for starting model of TEM inversion. The second approach is inverting two data sets, RMT and TEM, simultaneously in the inversion process. The joint interpretation and sequential inversion process were realized using the Marquardt algorithm.

The interpretation of the 1-D RMT model between station 49 – 70 resolves of the top layer (Figure 6 (a)) and the TEM 1-D model (Figure 6 (b)) shows the bottom of boundary layers of fault structure in this area more distinctly, however the top layers of TEM stations 49 - 70 cannot be resolved well because the top layer has a high resistivity value (> 80 Ωm) addressed as metamorphic rock from our reference borehole. Figure 6(c) shows the sequential model of TEM inversion. The structure of top layer at depth down to 40 m has identical features as RMT model while at depth below 40 m, the model represents TEM structure.

Joint inversion can increase the number of model parameters, some of which cannot be resolved separately (Figure 6(d)). The importance parameters were calculated for the model resistivities and thicknesses [3], which is plotted in Table 3. It shows

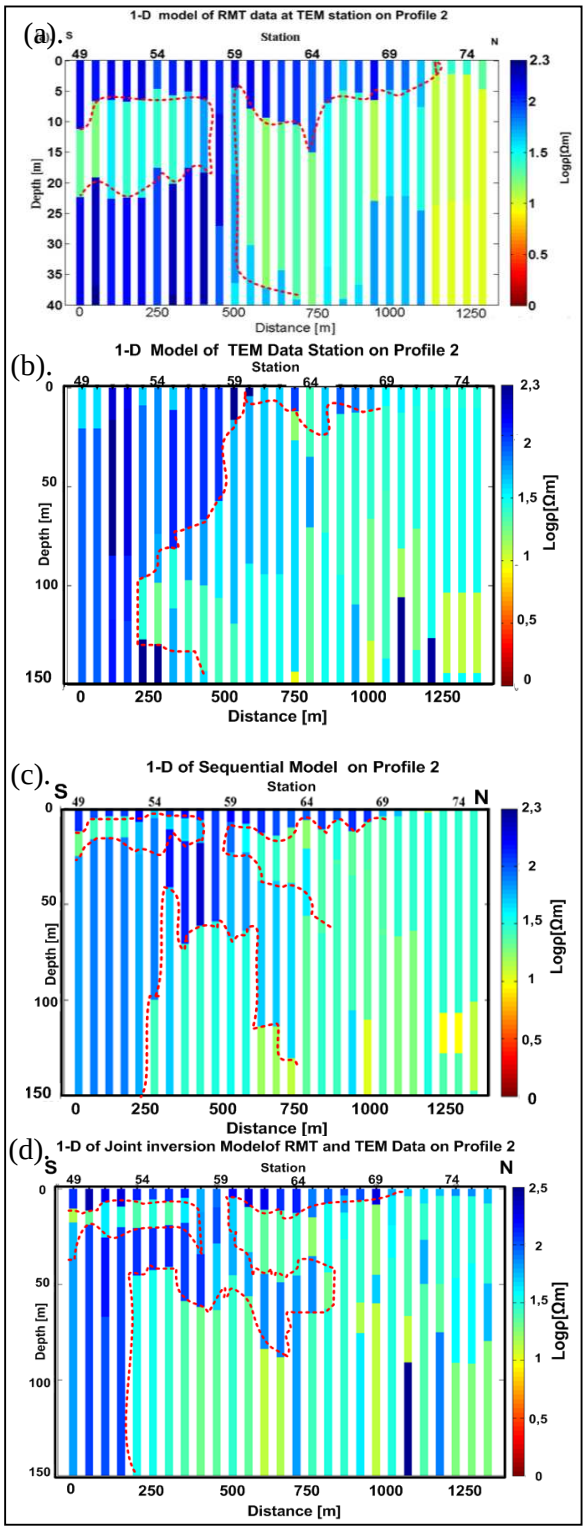

FIGURE 6. One dimensional models at profile 2 (a) Single RMT data (b) Single TEM data (c) Sequential . (d) Joint Inversion of RMT and TEM data.

the parameter (ρ_1, ρ_2, h_1) as a result of the individual single/joint inversions. Values between 0 (unimportant) and 1 (important) are calculated. The resetivities of the inversion of TEM data first and second layers (ρ_1, ρ_1) are well resolved for all models with importances of more than 0.8. However, the first layer thickness of single TEM cannot be resolved with importance of 0.58, but it is resolved well by joint inversion (importance 0.97).

TABLE 3. Model and Importance Parameter of RMT, TEM and Joint Inversion at Station 74 (Figure 6).

	RMT	Imp	TEM	Imp	Joint	Imp
ρ1[Ωm]	65.63	0.86	41.97	0.88	67.28	0.92
ρ2[Ωm]	30.37	0.87	39.26	0.99	31.75	0.92
h1[m]	3.9	0.94	62.4	0.58	3.45	0.97
RMS[%]	0.5		0.6		1	

TABLE 4. Model Resistivities Obtained from the RMT , Sequential and Joint Data for the Selected Stations at depth 14 – 20 m (second layer).

Station	RMT[Ωm]	Sequential[Ωm]	Joint[Ωm]
49	20.44	17.6	17.6
56	47.9	50.24	39.6
58	47.9	50.24	39.6
60	44.1	39.4	25.5
64	16.68	16.75	15.1
68	12.36	25.8	18.49
72	12.01	31.07	27.24
74	11.2	29.10	31.75

TABLE 5. Model Resistivities Obtained from the TEM, Sequential and Joint Data for the Selected Stations at depth 75 – 90 m (third layer).

Station	TEM[Ωm]	Sequential[Ωm]	Joint[Ωm]
49	78.6	83.56	64.4
56	20.56	42.52	21.6
58	26.76	34.16	22.82
60	45.5	30.44	23.10
64	38.5	38.34	28.1
68	24.9	29.11	13.3
72	16.9	18.28	25.02
74	29.16	29.67	18.27

The model resistivities of the second layer (between 14-20 m) obtained from 1-D models of RMT data are in good agreement with the joint and sequential inversion models (Table 4). The model resistivities from 1-D models of TEM data are also compatible with sequential and joint inversions (Tabel 5).

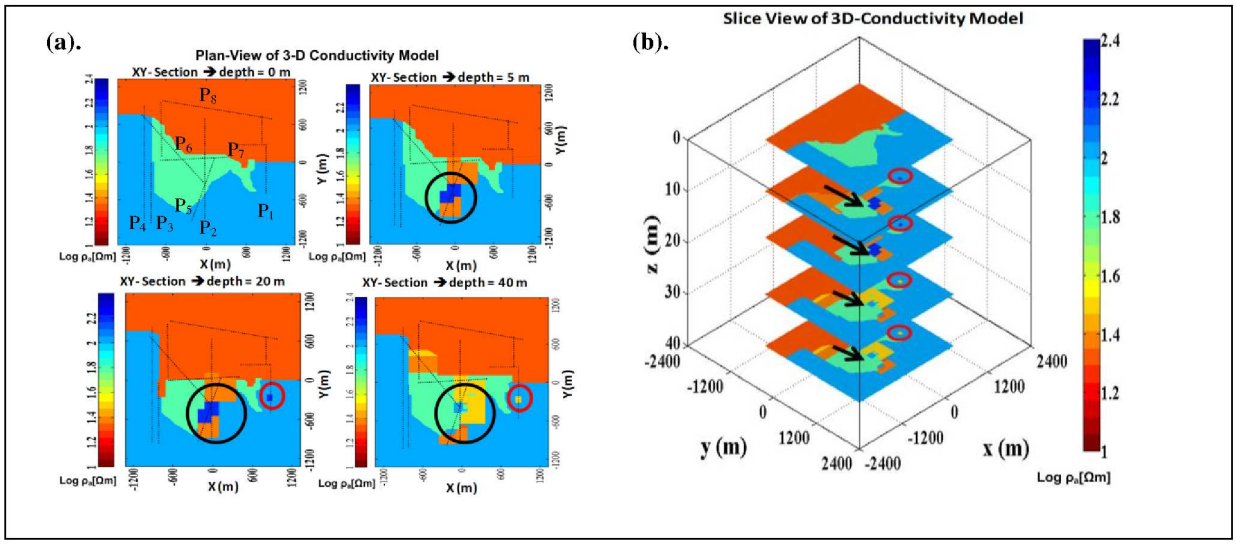

FIGURE 7. (a) 3-D forward modeling for all RMT profiles (P_1 = Profile 2 ,…, P_8 = Profile 8). The blue circles indicate fault structure in the profile 2 and 5. The red circles constitute fault structure in the profile 1 (b) Slice view of 3-D conductivity model. The black arrows indicate fault structure in the profile 2 and 5. The red circles constitute fault structure in the profile 1

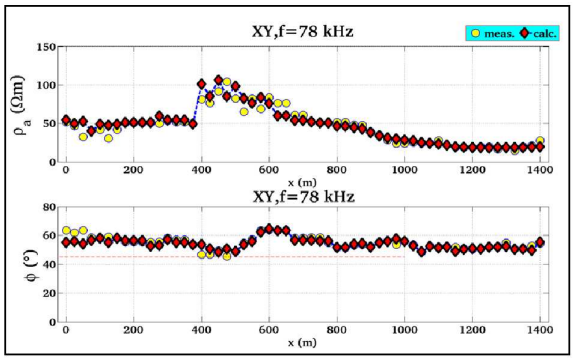

FIGURE 8. Data fit of Zxy impedance value between measured (yellow circles) and 3-D response (red diamonds) at frequency 79 kHz of profile 2.

3-D MODELING of RMT DATA

Due to complex geological structure in the research area , the 3-D modeling can provide clear information of fault structure. On the other hand, 3-D modeling gives representative model for all conductivity in the research area. In this case, the 3-D forward modeling is constructed using 2-D conductivity model and geology as priori information.

For 3D modeling of RMT data, the 3D modeling algorithm of Mackie code [8] was used. The overall number of cells in 3-D forward model is 2,178,000 (nx=220 cells, ny=220 cells and nz= 45 cells) in connection with the width of the research area modeled by 2.4 km x 2.4 km. Three dimensional mode calculated by trial and error procedure.

Three dimensional model describes the location of graben structure which lies at a depth of about 5 m up to 25 m (Figure 7). The 3-D model can fit with 2-D measured data, simultaneously. As an example, the fitting between measured data and 3-D forward modeled for profile 2 is seen in Figure 8.

CONCLUSIONS

The inversion of RMT and TEM data indicates a normal fault structure with a strike direction of approximately N 70 E. The RMT and TEM models generally show four layers according to their resistivity values. We address them as to be metamorphic and sediment rocks, which are marly silty sand with gravel (>> 100 Ωm), marly silty sand with clay (50 - 100 Ωm), sandy clay (30 – 50 Ωm) and silty sand (10-30 Ωm). The RMT data was interpreted using 2-D inversions technique that results in a good fitting between observed and calculated data. Due to the high resistivity of the top layer, the skin depths of the RMT soundings are around 35 m. The TEM data gives detail information of the lower structure down to a depth of 200 m. 3-D modeling clearly describes the existence of a fault structure in the northeast of the Volvi basin. The correlation between measured data and estimated 3-D data is having good compatibility. Three dimensional models provide a detailed description of the normal fault structure at depth about 5 up to 25 m or with thickness of 20 m. The joint interpretation and RMT data proved to be an effective tool to investigate complex geology structures.

ACKNOWLEDGMENTS

This research was financed by the Marie Curie project: IGSEA – Integrated Nonseismic Geophysical Studies to Assess the Site Effect of the EUROSEISTEST Area in Northern Greece – PERG03-GA-2008-230915 {REF RTD REG/T.2 (2008)D/596232}.

REFERENCES

1. Ghobarah, A., M. Saatcioglu, and I. Nistor, The impact of 26 december 2004 earthquake and tsunami on structures and infrastructure, Engineering Structures, Elsevier, 28, 312-326, 2006.
2. Gurk.M, Savvaidis A.S., Bastani M., Tufa Deposit in the Mygdonian Basin (Northern Greece) studied with RMT /CSTAMT, VLF & Self-Potential, EMTF Kolloqium, June, 2007.
3. Jupp, D.L.B. and K. Vozoff, stable iterative methods for the inversion of geophysical data, Geophys.J.R.astr.soc., 42,957-976, 1975.
4. Mackie R., Rieven S., Rodi W., User Manual and Software Documentation for two-dimensional of magnetotelluric data, Cambridge Massachusetts, USA, 1997.
5. Mackie, R. and J. Booker, Documentation for mtd3fwd and d3mt, Masschutes Institute of thechnology, Cambridge, Massachusets 02139, July 1999.
6. Schmucker, U., Erdmagnetische Variationen und die elektrische Leitfahigkeit in tieferen Schichten der Erde. Sitzungsber. Mitt. Braunschw Wiss. Ges. Sonderh., 4:45-102, 1979.
7. Takahashi, T., M. Goto, H. Yoshida, H. Sumino and H. Matsui, Infectious diseases after the 2011 great east japan earthquake, Journal of Experimental & Clinical Medicine, 4, 20-23, 2012.
8. Tezkan, B., and Saraev, A., A new broadband Radiomagnetotelluric instrument: Application to near surface investigation, Near surface Geophysics, 6.243-250, 2008.
9. Tezkan, B., M. Goldman, S. Greinwald, A.Hordt, I.Muller, F.M. Neubauer and H.G. Zacher, A joint application of radio magnetotellurics and transient electromagnetic to the investigation of a waste deposit in Cologne (Germany), Applied Geophysics, 34, 199-212,1995.
10. Parasnis, D. S., Principle of applied geophysics (4^{th} ed.): Chapman and Hall, London, 402p, 1986.
11. Papazachos,B.C., Papazachou, C., The Earth quake of Greece, Ziti Publications , Thessaloniki, 1997.

Preparation for 3D magnetotelluric inversion using the all-at-once approach

Wenke Wilhelms, Ralph-Uwe Börner, and Klaus Spitzer
TU Bergakademie Freiberg

Introduction

The all-at-once inversion approach requires no explicit forward calculation, because the forward modelling equations are incorporated in the objective function as constraints. This leads to a huge, so-called Karush-Kuhn-Tucker (KKT) system, which is solved in each step of the iteration procedure to update model parameters, Lagrangian multipliers, and data - all at once. Still, the forward problem needs detailed consideration, because the system matrix of the forward problem is necessary to calculate first and second derivatives to set up the KKT matrix.
As a first step, we have investigated the 1D problem. The resulting models are comparable with those of a traditional Gauss-Newton inversion. However, as expected, the Gauss-Newton method converges more slowly than the all-at-once approach, because the latter, as a Newton type scheme, takes into account second derivative information. In the process of developing a 3D all-at-once inversion code, a 3D finite difference forward operator could already be tested successfully using the 3D-2 COMMEMI model.
This paper describes the current state of our investigations. In the first section of this article, we therefore explain the governing equations of the forward problem. The second part deals with the formulation of the inverse problem using the all-at-once approach. 1D inversion results for synthetic magnetotelluric data collected at the surface of a layered halfspace will be discussed in section three. After that, we introduce the 3D magnetotelluric forward operator and show how to build up the KKT matrix, essentially, by incorporating the system matrix of the forward problem and its derivatives. The last part of the article gives an outlook to what will be done next to achieve a working 3D magnetotelluric inversion code.

Forward problem

For magnetotellurics the behaviour of the electric field $\mathbf{E}$ in a 3D earth is described by the homogeneous curl-curl equation

$$\nabla \times \nabla \times \mathbf{E} + i\omega\mu_0\sigma\mathbf{E} = 0, \tag{1}$$

with ω as the angular frequency, i as the imaginary unit, σ as the electrical conductivity and μ_0 as the induction constant. Using the secondary field approach this equation changes to

$$\nabla \times \nabla \times \mathbf{E}^s + i\omega\mu_0\sigma\mathbf{E}^s = -i\omega\mu_0(\sigma - \sigma_0)\mathbf{E}^p, \tag{2}$$

where σ_0 is a background conductivity model, usually a layered or a homogeneous halfspace having an analytical solution. The total electric field $\mathbf{E}$ is the sum of both, primary and secondary electric fields $\mathbf{E}^p$ and $\mathbf{E}^s$. The primary electric field $\mathbf{E}^p$ is a function of depth z and the secondary electric field $\mathbf{E}^s$ vanishes on the boundary Γ of the model. The right-hand side of eq. 2 represents the sources of the secondary field. Together with appropriate Dirichlet boundary conditions the curl-curl equation is discretized on a finite-difference grid providing the forward operator $\mathbf{A}(\boldsymbol{m})$ in the forward problem

$$\mathbf{A}(\boldsymbol{m})\boldsymbol{u} = \boldsymbol{b}(\boldsymbol{m}) \tag{3}$$

with $\boldsymbol{m}$ as a vector containing logarithmic model parameters $m_i = log\sigma_i, i = 1,...,M$, and M as the total number of model cells. The right-hand side vector $\boldsymbol{b}$ contains boundary values. The vector $\boldsymbol{u}$ denotes

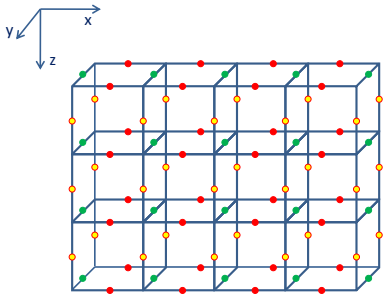

Figure 1: Staggered finite-difference grid: Red, green and yellow dots, respectively, mark the locations of x-, y- and z-components of the electric field $\mathbf{E} = \mathbf{E}^p + \mathbf{E}^s$.

the complex secondary electric field $\mathbf{E}^s = [\mathbf{E}^s_x, \mathbf{E}^s_y, \mathbf{E}^s_z]^T$ within the whole discretized region. Fig. 1 shows a finite difference grid with the degrees of freedom (dofs) located on the edges of the model cells. Red dots stand for the x-components, green dots mark the locations of the y-components, and yellow dots stand for the z-components of the electric fields $\mathbf{E}^p$ and $\mathbf{E}^s$. Since we have measured data $\boldsymbol{d}$ only at the earth's surface we need an observation matrix $\mathbf{Q}$ to extract the corresponding data from the model response $\boldsymbol{u}$ and calculate the residual $\boldsymbol{r}$:

$$\boldsymbol{r} = \mathbf{Q}\boldsymbol{u} - \boldsymbol{d}. \tag{4}$$

Inverse problem

The all-at-once approach is based on Newton's method. As described by Haber, Ascher, and Oldenburg (2000) the Lagrangian $\mathcal{L}$ is formed by setting up the optimization problem in a constrained form. In doing so, the forward problem is incorporated using Lagrange multipliers $\boldsymbol{\lambda}$ in the objective function:

$$\mathcal{L}(\boldsymbol{u}, \boldsymbol{m}, \boldsymbol{\lambda}) = \frac{1}{2}||\mathbf{Q}\boldsymbol{u} - \boldsymbol{d}||^2 + \frac{\beta}{2}||\mathbf{W}(\boldsymbol{m} - \boldsymbol{m}_{\text{ref}})||^2 + \boldsymbol{\lambda}^T[\mathbf{A}(\boldsymbol{m})\boldsymbol{u} - \boldsymbol{b}(\boldsymbol{m})]. \tag{5}$$

The first term on the right-hand side is the data residual and the second one is a regularisation term. For minimizing the Lagrangian via Newton's method, the gradient $\nabla\mathcal{L}$ and the Hessian $\nabla^2\mathcal{L}$ need to be calculated. The gradient is a vector containing the partial derivatives of $\mathcal{L}$ with respect to all three parameters $\boldsymbol{u}$, $\boldsymbol{m}$ and $\boldsymbol{\lambda}$:

$$\nabla\mathcal{L} = \begin{pmatrix} \mathcal{L}_{\boldsymbol{u}} \\ \mathcal{L}_{\boldsymbol{m}} \\ \mathcal{L}_{\boldsymbol{\lambda}} \end{pmatrix} = \begin{pmatrix} \mathbf{Q}^T(\mathbf{Q}\boldsymbol{u} - \boldsymbol{d}) + \mathbf{A}^T\boldsymbol{\lambda} \\ \beta\mathbf{W}^T\mathbf{W}(\boldsymbol{m} - \boldsymbol{m}_{\text{ref}}) + \mathbf{G}^T\boldsymbol{\lambda} \\ \mathbf{A}\boldsymbol{u} - \boldsymbol{b} \end{pmatrix} \quad \text{with} \quad \mathbf{G} = \partial_m\mathbf{A} \cdot \boldsymbol{u}. \tag{6}$$

The Hessian $\nabla^2\mathcal{L}$ (or KKT matrix $\mathcal{H}_{KKT}$) contains the second derivatives of the Lagrange function with respect to all three parameters:

$$\mathcal{H}_{KKT} = \begin{pmatrix} \mathcal{L}_{\boldsymbol{u},\boldsymbol{u}} & \mathcal{L}_{\boldsymbol{u},\boldsymbol{m}} & \mathcal{L}_{\boldsymbol{u},\boldsymbol{\lambda}} \\ \mathcal{L}_{\boldsymbol{m},\boldsymbol{u}} & \mathcal{L}_{\boldsymbol{m},\boldsymbol{m}} & \mathcal{L}_{\boldsymbol{m},\boldsymbol{\lambda}} \\ \mathcal{L}_{\boldsymbol{\lambda},\boldsymbol{u}} & \mathcal{L}_{\boldsymbol{\lambda},\boldsymbol{m}} & \mathcal{L}_{\boldsymbol{\lambda},\boldsymbol{\lambda}} \end{pmatrix} = \begin{pmatrix} \mathbf{Q}^T\mathbf{Q} & \mathbf{K} & \mathbf{A}^T \\ \mathbf{K}^T & \beta\mathbf{W}^T\mathbf{W} + \mathbf{R} & \mathbf{G}^T \\ \mathbf{A} & \mathbf{G} & \mathbf{0} \end{pmatrix} \tag{7}$$

with $\mathbf{G} = \partial_m \mathbf{A} \cdot \boldsymbol{u}, \qquad \mathbf{K} = \partial_m \mathbf{A}^T \cdot \boldsymbol{\lambda}, \qquad \mathbf{R} = \partial_m \mathbf{G}^T \cdot \boldsymbol{\lambda}.$

The Newton method then reads

$$\mathcal{H}_{KKT} \cdot \begin{pmatrix} \boldsymbol{\delta u} \\ \boldsymbol{\delta m} \\ \boldsymbol{\delta \lambda} \end{pmatrix} = - \begin{pmatrix} \mathcal{L}_{\boldsymbol{u}} \\ \mathcal{L}_{\boldsymbol{m}} \\ \mathcal{L}_{\boldsymbol{\lambda}} \end{pmatrix} \tag{8}$$

with $\boldsymbol{\delta u}$, $\boldsymbol{\delta m}$, and $\boldsymbol{\delta \lambda}$ as parameter updates.
$\mathcal{H}_{KKT}$ is a blockwise singular matrix where only cross-diagonal blocks are invertible. As a part of a large but sparse linear system of equations, it can be transformed into a positive definite matrix. The permuted Hessian $\mathcal{H}$ results from a permutation of block rows and columns that results in the following equation:

$$\mathcal{H} \cdot \begin{pmatrix} \boldsymbol{\delta u} \\ \boldsymbol{\delta \lambda} \\ \boldsymbol{\delta m} \end{pmatrix} = - \begin{pmatrix} \mathcal{L}_{\boldsymbol{\lambda}} \\ \mathcal{L}_{\boldsymbol{u}} \\ \mathcal{L}_{\boldsymbol{m}} \end{pmatrix} \tag{9}$$

$$\text{with} \quad \mathcal{H} = \begin{pmatrix} \mathbf{A} & \mathbf{0} & \mathbf{G} \\ \mathbf{Q}^T\mathbf{Q} & \mathbf{A}^T & \mathbf{K} \\ \mathbf{K}^T & \mathbf{G}^T & \beta \mathbf{W}^T\mathbf{W} + \mathbf{R} \end{pmatrix}. \tag{10}$$

After each Newton iteration the inversion produces updates for all three different types of model parameters:

$$\begin{pmatrix} \boldsymbol{u}_{n+1} \\ \boldsymbol{m}_{n+1} \\ \boldsymbol{\lambda}_{n+1} \end{pmatrix} = \begin{pmatrix} \boldsymbol{u}_n \\ \boldsymbol{m}_n \\ \boldsymbol{\lambda}_n \end{pmatrix} + \begin{pmatrix} \boldsymbol{\delta u} \\ \boldsymbol{\delta m} \\ \boldsymbol{\delta \lambda} \end{pmatrix}. \tag{11}$$

Thus, explicit forward modelling after each iteration is not necessary.

Inversion results for the 1D magnetotelluric problem

Starting point is a horizontally layered halfspace consisting of four layers with resistivities $\rho = [250, 25, 200, 10]\Omega$m and thicknesses $h = [600, 1400, 3800, 4000]$m and a homogeneous substratum with $\rho = 25\,\Omega$m. In Figs 2 and 4 this model is indicated as a red line. Using Wait's algorithm (Wait, 1953), synthetic data were calculated analytically, which served as input into the all-at-once inversion. Starting model is a homogeneous halfspace with $\rho = 90\,\Omega$m (green line in Figs 2 and 4).
Fig. 2 shows the inversion results for the all-at-once (marked blue) and the Gauss-Newton method for comparision. Both models agree well. The KKT results were obtained after 8 iterations and 18.9 s of computing time on a desktop computer (8 GB RAM, processor: Intel Core 2 CPU 6600 2.4 GHz). Results of the Gauss-Newton inversion were obtained after 40 iterations and 19.3 s of computing time on the same machine. Fig. 3 shows the sounding curves for the final KKT inversion model in terms of ρ_a (a) and phase (b) (blue line). They match the analytical solution of the true model very well (red asterisks) with a maximum deviation of 0.1 % for the resistivity ρ_a and 0.03 degrees for the phase.
Figs 4 and 5 show inversion results and sounding curves for KKT and Gauss-Newton in the same way as in Figs 2 and 3. This time, however, 1 % of random noise was added to the data. All model parameters are still resolved quite well except for the resistivity of the substratum. The sounding curves in Fig. 5, therefore, exhibit significant deviations from the analytical solution up to 7 % for the resistivity ρ_a and 1.2 degrees for the phase mainly at the long period end, which is associated

with small sensitivities. It is straightforward to assume that the added noise affects low sensitivity regions more seriously than well resolved regions. This assumption is corroborated by the fact that the reconstructed resistivity of the substratum remains closer to the one of the starting model (green line in Fig. 4). In other words, the noise may easily mask the weak information that originates from low resolution areas.

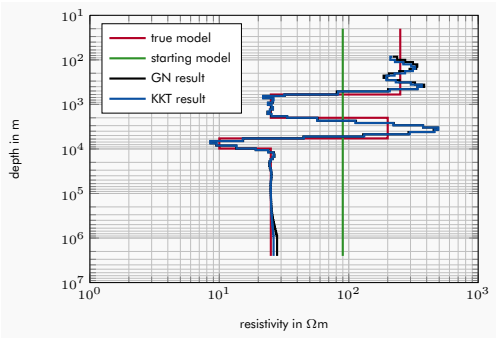

Figure 2: Inversion results for the all-at-once approach (blue) and a Gauss-Newton scheme (black) using synthetic data for a 1D layered halfspace.

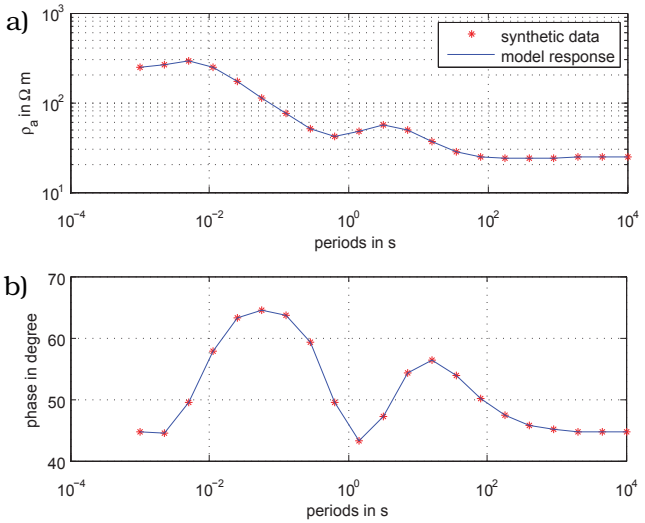

Figure 3: Sounding curves obtained from evaluation of the true model and the KKT result as depicted in Fig. 2.

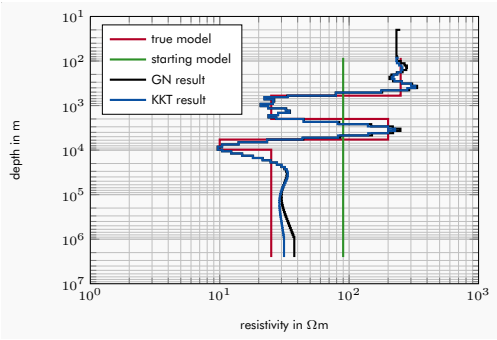

Figure 4: Inversion results for the all-at-once approach (blue) and a Gauss-Newton scheme (black) using synthetic data for a 1D layered halfspace with 1 % random noise.

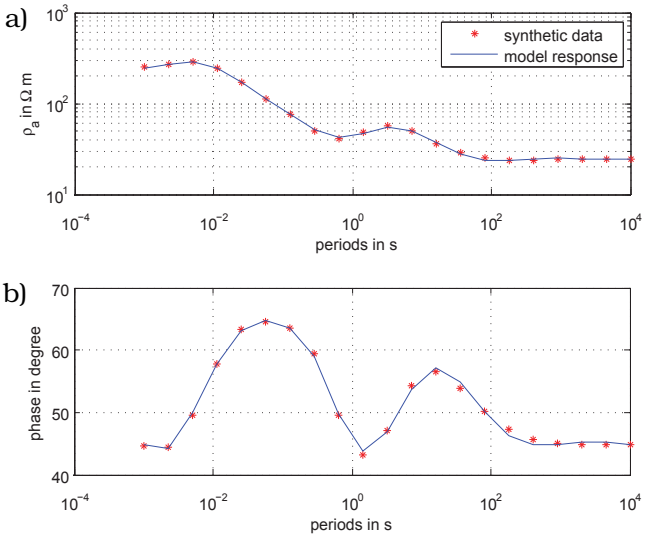

Figure 5: Sounding curves obtained from evaluation of the true model and the KKT result as depicted in Fig. 4.

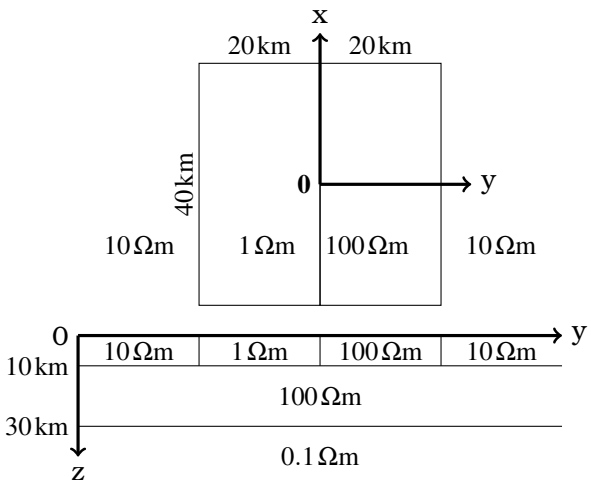

Figure 6: 3D-2 COMMEMI model

3D forward modelling results

The essential step towards a 3D inversion is incorporating a 3D forward operator into the inversion scheme. For simplicity we use a finite-difference discretization, which is easy to code and easy to handle at the same time. To verify its proper functioning, we use the well known results from the 3D-2 COMMEMI model (Zhdanov & Weaver, 1997), which is depicted in Fig. 6. Fig. 7 shows simulation results for this model at $x = 0$ and for a period of $T = 100\,\mathrm{s}$. The diagrams show real und imaginary parts of the normalized electric fields for two polarisation directions: polarisation 1 (a, c) with the incident magnetic field oriented in y-direction and polarisation 2 (b, d) with an incident magnetic field in x-direction. Our simulation results (blue lines) are compared with those obtained with an integral equation code (red dots) by Xiong (1992). The agreement is generally good. Deviations at large parameter contrasts, e.g. at $y = 0$, probably originate from the rather coarse grid used by Xiong.

Outlook

The upcoming challenge is to handle the enormous size of the KKT system for the 3D magnetotelluric problem. In the case of the 3D-2 COMMEMI model our problem size is $N = 260{,}000$ dofs for one frequency and, therefore, the size of the system matrix $\mathbf{A}$ is $\mathbb{C}^{N\times N}$. A realistic case would include at most ten frequencies per decade which means 2,6 million dofs per decade. At this stage – for a real 3D environment – it is not possible to store the corresponding KKT matrix $\mathcal{H}_{KKT}$ with an estimated size of $(3N)^2$. There are strategies to circumvent the storage of the huge KKT system, e.g., by using reduced Hessian methods (Biros & Ghattas, 2005; Haber & Ascher, 2001).
Our experiences with the KKT system so far lead to the conclusion that a 3D all-at-once inversion of magnetotelluric data seems to be possible.

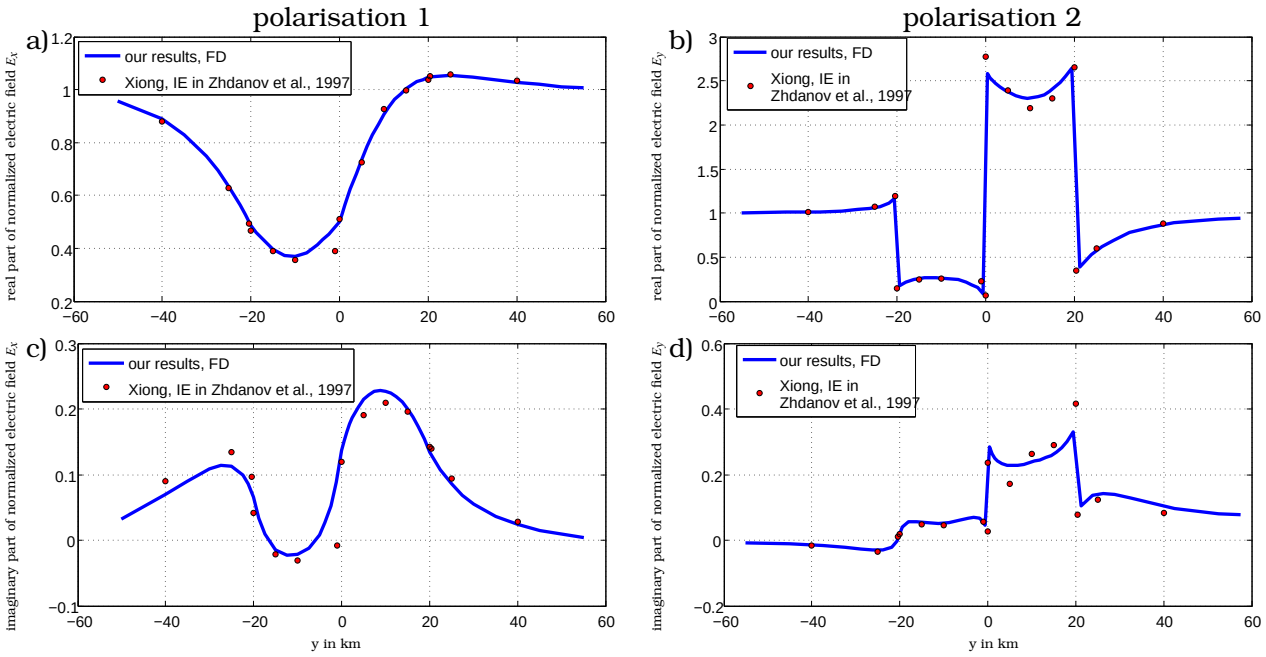

Figure 7: 3D forward modelling results for the COMMEMI model 3D-2 at a period of $T = 100\,\mathrm{s}$ for polarisation 1 (a, c) and polarisation 2 (b, d). Upper diagramms (a, b) show real parts of the normalized electric fields, lower ones (c, d) show imaginary parts.

References

Biros, G., & Ghattas, O. (2005). Parallel Lagrange-Newton-Krylov-Schur methods for PDE-constrained optimization. Part I: The Krylov-Schur solver. *SIAM Journal of Scientific Computing*, *27*, 687 - 713.

Haber, E., & Ascher, U. M. (2001). Preconditioned all-at-once methods for large, sparse parameter estimation problems. *Inverse Problems*, *17*, 1847 - 1864.

Haber, E., Ascher, U. M., & Oldenburg, D. (2000). On optimization techniques for solving nonlinear inverse problems. *Inverse Problems*, *16*, 1263 - 1280.

Wait, J. R. (1953). Propagation of radio waves over a stratified ground. *Geophysics*, *20*, 416 - 422.

Xiong, Z. (1992). Electromagnetic modeling of 3-D structures by the method of system iteration using integral equations. *Geophysics*, *57*, 1556 - 1561.

Zhdanov, M. S., & Weaver, J. T. (1997). Methods for modelling electromagnetic fields. *Journal of Applied Geophysics*, *37*, 133 - 271.

A new meshfree method for magnetotelluric modelling

Jan Wittke, Bülent Tezkan

University of Cologne - wittke@geo.uni-koeln.de

Introduction

The magnetotelluric method (MT) is well established in geophysical prospecting. It is based on measuring the natural magnetic and electrical fields on the surface of the earth. With these measurements one can relate the spatial field variations to the electrical conductivity distribution of the subsurface. Through a comparison of the horizontal components of the electric fields with the magnetic fields on the surface one can probe the conductivity structure up to depths of several tens of kilometers [21, 11, 17].
To interpret the measured data sets a large number of numerical software has been written. Some of them utilize the well known finite element method (FEM) to simulate the electrical and magnetic fields for a given conductivity structure. The first programs were developed by Coggon [4] and Wannamaker et al. [25]. Over the past twenty years, a lot of effort has been made to develop this numerical method as efficiently and accurately as possible. There are several formulations to compute a numerical stable solution of Maxwell's equations [eg. 2, 20], but the finite element method heavily relies upon the chosen finite-dimensional subspace in which the similar discrete problem of a continuous operator problem exists. Therefore, one must choose among other things the correct type [18] and size [5, 14] of elements to compute the most accurate solution for the physical problem. However, even though the FEM is known as a robust and accurate method, it also has some drawbacks. Spectral pollution [8, 9, 10] and/or time consuming remeshing techniques [7, 5, 14] are some critical issues when FEM is chosen for electromagnetic simulation.
Meshless methods were developed to overcome some of these problems. Over the last decade several meshless or meshfree methods have been proposed. One of the first is the smooth particle hydrodynamics (SPH) which is often used in computational astrophysics

[15]. Belytschko et al. [1] developed the element-free galerkin method. They used the moving least squares (MSL) approximation to construct shape functions using locally distributed nodes. The point interpolation technique developed by Wang et al. Wang et al. [24] uses interpolation and the derived shape functions possess the Kroneker delta property. One type uses the radial basis interpolation (RPIM) [22, 23] so the underlaying method avoids an explicit mesh structure for the numerical solution of the differential equation. The flexibility in the node distribution allows complex geometries and also fast adaptive node placing algorithms [12, 13].
In this work the RPIM method is used to compute the electromagnetic fields generated by a transverse electric (TE) plane-wave excitation for a given two-dimensional conductivity structure.
In the next section we present the model and the differential equation to be solved. Afterwards we introduce the numerical method employed to solve it. At the end we show numerical results and draw the conclusion.

The differential equations and boundary conditions

For the transverse-electric polarization the equation is given by [6]

$$\frac{\partial^2 E_y}{\partial x^2} + \frac{\partial^2 E_y}{\partial z^2} = k^2 E_y \tag{1}$$

with $k^2 = i\omega\mu_0\sigma$. E_y is the scalar electric field in the strike direction, σ the electrical conductivity in S/m, ω the radian frequency in rad/s and $\mu_0 = 4\pi 10^{-7} H/m$ the magnetic permeability of the vacuum. On the outer boundaries of the given model we applied Dirichlet boundary conditions from analytical 1D solutions from the left-hand and right-hand sides of the model. For our purpose we have to calculate the apparent resistivity ρ_a and phase ϕ

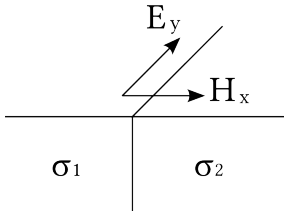

Figure 1: Model and the directions of the fields

$$\rho_a^{TE} = \frac{1}{\omega\mu}\left|\frac{E_y}{H_x}\right|^2 \quad \text{and} \quad \phi^{TE} = arg\left(\frac{E_y}{H_x}\right)$$

To solve these equations we determine the magnetic field H_x perpendicular to the electric

field with

$$H_x = \frac{1}{\omega\mu}\frac{\partial E_y}{\partial z}$$

Meshless fomulation

Due to the formalism of the used meshless method, we derive a weak formulation of the given PDE (1). We integrate the residual of (1) multiplied with a weight function w over the model domain Ω

$$\iint\limits_{\Omega} \left(\frac{\partial^2 E_y}{\partial x^2} + \frac{\partial^2 E_y}{\partial z^2} - k^2 E_y \right) w \, d\Omega$$

The Dirichlet boundary conditions have to be fulfilled by the interpolation of E_y. Now we use the Galerkin method, where the weight and shape functions are the same. So we can approximate E_y with a linear combination of the meshless shape functions Φ_i and the E_{yi} values at the nodes

$$E_y^h = \sum_{i=1}^{N} \Phi_i E_{y\,i} \tag{2}$$

and finally derive the linear system

$$\left[\mathbf{K} - k^2\mathbf{A}\right]\mathbf{E_y} = \mathbf{0} \tag{3}$$

with:

$$K_{ij} = \iint\limits_{\Omega} \frac{\partial \Phi_i}{\partial x}\frac{\partial \Phi_j}{\partial x} + \frac{\partial \Phi_i}{\partial y}\frac{\partial \Phi_j}{\partial y} \; d\Omega \tag{4}$$

$$A_{ij} = \iint\limits_{\Omega} \Phi_i \Phi_j \; d\Omega \tag{5}$$

We can now calculate E_y at any point in the model domain Ω if we solve (3) and then use (2). The next chapter shows how the meshless shape functions are constructed.

The radial point interpolation method (RPIM)

If we use a meshfree method we do not need to represent the model domain Ω with a mesh. Instead we use arbitrarily distributed nodes to represent the domain Ω and its boundary Γ. At these nodes an approximation of E_y is computed. For constructing the

shape functions Φ we use the radial function interpolation [3, 26]. Consider a set of N nodes (samples) and a point $\boldsymbol{x} \in \mathbb{R}^2$ where we want to interpolate over the given samples $(x_1, y_2, u_1(x_1, y_1)) \ldots (x_N, y_N, u_N(x_N, y_N))$.

We can derive a interpolation function $u^h(\mathbf{x})$ as a linear combination of radial basis functions (RBF) ϕ and the interpolation weights λ

$$u^h(\mathbf{x}) = \sum_{i=1}^{N} \lambda_i \phi(|\mathbf{x} - \mathbf{x}_i|) + P(\mathbf{x}) \quad (6)$$

with the constrains

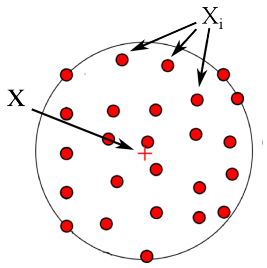

Figure 2: RBF interpolation

$$u^h(\mathbf{x}_i) = u(\mathbf{x}_i) \quad and \quad \sum_{i=1}^{N} \lambda_i P(\mathbf{x}_i) = 0$$

we can build the interpolation system

$$\begin{pmatrix} \phi & \mathbf{P} \\ \mathbf{P}^T & \mathbf{0} \end{pmatrix} \begin{pmatrix} \lambda \\ \mathbf{b} \end{pmatrix} = \begin{pmatrix} \mathbf{u} \\ \mathbf{0} \end{pmatrix} \quad (7)$$

If we solve this system for λ_i and b_i we can interpolate the given values at any point $\mathbf{x}$ with the surrounding nodes and the interpolation function (6). Note that we add a polynomial $P(x)$ to the interpolation function (6) to be able to reproduce a linear field exactly [19].

The matrix elements ϕ_{ij} in (7) and $\phi(|\mathbf{x} - \mathbf{x}_i|)$ in (6) are radial basis functions (RBF).

Table (1) lists three possible RBFs. They all have in common that their function value only depends on the distance between two points.

For our purpose we use the multiquadratic RBF. To derive the RPIM-shape functions we write the interpolation function (6) as

Name	RBF
Linear	$\phi(r) = cr$
Gaussian	$\phi(r) = e^{-cr^2}$
Multiquadratic	$\phi(r) = (c^2 + r^2)^{\frac{1}{2}}$

Table 1: Radial Basis Functions

$$\mathrm{u}^h(\mathbf{x}) = \sum_{i=1}^{N} \lambda_i \phi(|\mathbf{x} - \mathbf{x}_i|) + \sum_{j=1}^{m} p_j(\mathbf{x}) b_j = \mathbf{R}_N^T(\boldsymbol{x})\mathbf{a} + \mathbf{p}^T(\mathbf{x})\mathbf{b}$$

so the ansatz results in a linear system

$$\mathbf{u} = \mathbf{R}_N\mathbf{a} + \mathbf{Q}_m\mathbf{b} \tag{8}$$

with the contrains

$$\mathbf{Q}_m\mathbf{a} = \mathbf{0}$$

the matrix $\mathbf{Q}_m$ consists of:

$$\mathbf{Q}_m = \begin{pmatrix} 1 & x_1 & y_1 & xy_1 \\ 1 & x_2 & y_2 & xy_2 \\ \vdots & \vdots & \vdots & \vdots \\ 1 & x_N & y_N & xy_N \end{pmatrix}$$

when for a 2D case a polynomial basis $\mathbf{p}^T(\mathbf{x}) = [1\ x\ y\ xy]$ is chosen. The matrix $\mathbf{R}_N$ in (8) is invertible [3] so equation (8) can be transformed into

$$\mathbf{a} = \mathbf{R}_N^{-1}\mathbf{u} - \mathbf{R}_N^{-1}\mathbf{Q}_m\mathbf{b}$$

with the abbreviations:

$$\mathbf{S_a} = \mathbf{R_N^{-1}}\left[1 - \mathbf{Q}_m\mathbf{S}_b\right]$$

$$\mathbf{S}_b = \left[\mathbf{Q}_m^T\mathbf{R}_N^{-1}\mathbf{Q}_m\right]^{-1}\mathbf{Q}_m^T\mathbf{R}_N^{-1}$$

the interpolation function (6) can be expressed as

$$u^h(\mathbf{x}) = \left[\mathbf{R}^T(\mathbf{x})\mathbf{S}_a + \mathbf{p}^T(\mathbf{x})\mathbf{S}_b\right]\mathbf{u} = \mathbf{\Phi^T}(\mathbf{x})\mathbf{u}$$

with the derived RPIM shape functions $\mathbf{\Phi^T}(\mathbf{x}) = \begin{bmatrix} \Phi_1(\mathbf{x}) & \Phi_2(\mathbf{x}) & \dots & \Phi_N(\mathbf{x}) \end{bmatrix}$. The derivatives of the interpolation function can be directly computed by calculating the derivations of the shape functions.

To solve the arising integrals in (4) and (5) we use a 6-point Gaussian quadrature rule.

Numerical results

The new RPIM method in magnetotelluric simulation for the E-polarisation are now investigated and compared to finite differences [16], finite element [25] software and Comsol a commercial FEM package. First we consider a simple model (see Figure 3) with a $1:10$ conductivity contrast. The results are shown in Figure (4). We solve the model for a period of $T = 0.01\,s$ and a $50\,m$ spacing between the stations and regular spaced meshless nodes. For comparison the Mackie and Wannamaker models also have a spacing of $50\,m$ between the (FD/FEM) nodes in their mesh. The Comsol solution was computed with quadrilateral elements also with a size of $50\,m$.

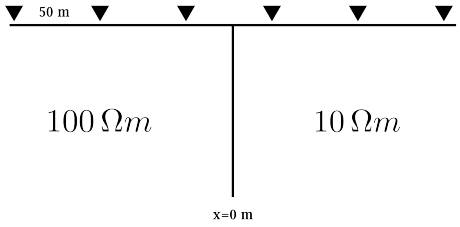

Figure 3: Simple Model

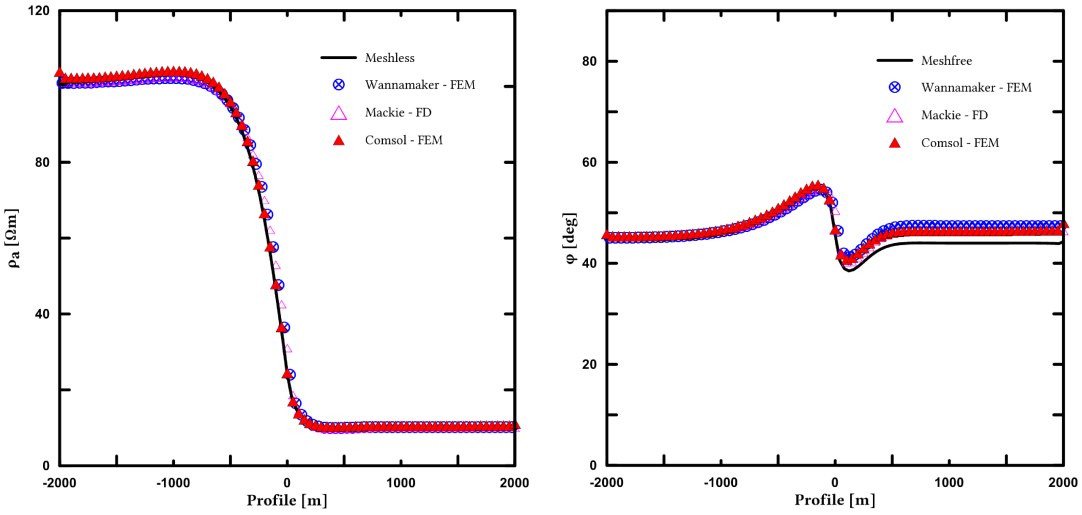

Figure 4: Computed apparent resistivity an phases for the simple model

The second model we computed is a simple prism, shown in Figure (5)

It is also a $1 : 10$ conductivity contrast and the dimension of the prism is $100\,m \times 200\,m$ The prism is of low resistivity $(10\,\Omega m)$ relative to its host $(100\,\Omega m)$. We also computed several solutions in comparison with the RPIM solution. The results are shown in Figure (6). We also solve the model for a period of $T = 0.01\,s$ and a $50\,m$ spacing between the stations and regular spaced meshless nodes. For comparison the Mackie and Wannamaker models also have a spacing of $50\,m$ between the (FD/FEM) nodes in their mesh. The Comsol solution was computed with quadrilateral elements also with a size of $50\,m$.

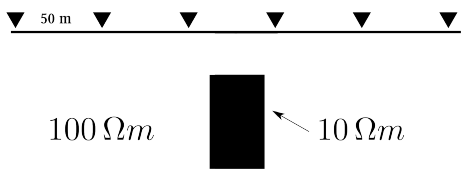

Figure 5: Simple prism model

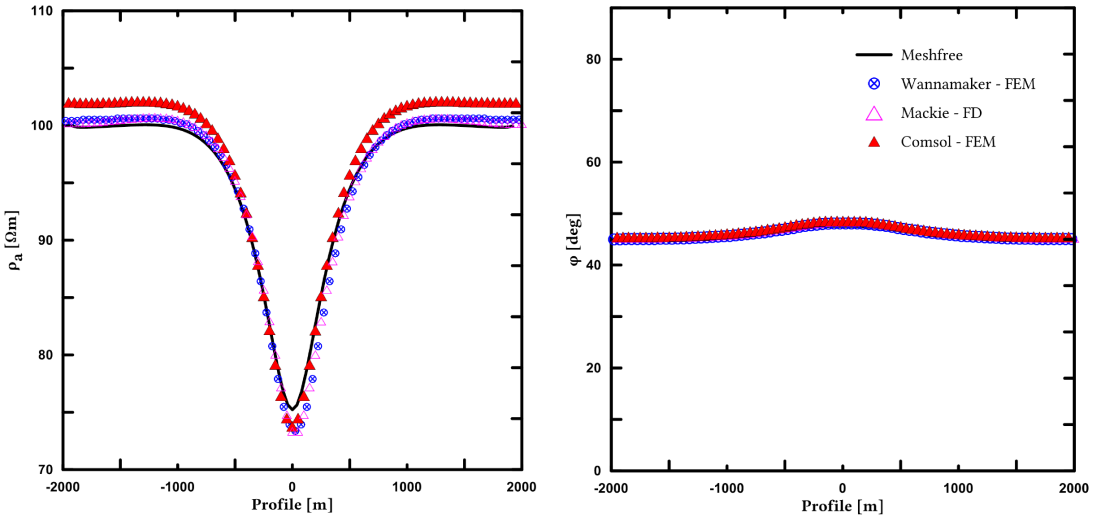

Figure 6: Computed apparent resistivity an phases for the simple prism model

Conclusion

The radial point interpolation method (RPIM) has been investigated with respect to magnetotelluric modelling. It has been validated on two numerical examples in com-

parison to established numerical software. The results show a good agreement to these programs so the presented formulation has proven to be well suited for the simulation of electromagnetic fields. It is the first time that the meshless numerical method has been adapted to simulate electromagnetic fields in computational geophysics. This approach shows a great flexibility because a mesh for representing the model domain is avoided. The next step towards will be a critical convergence and computation time analysis. With a view to inverse electromagnetic problems this method shows great capabilities to improve actual methods in computational electromagnetic geophysics.

References

[1] T. Belytschko, Y. Y. Lu, and L. Gu. Element-free galerkin methods. *International Journal for Numerical Methods in Engineering*, 37(2):229–256, 1994. ISSN 1097-0207.

[2] O. Biro and K. Preis. On the use of the magnetic vector potential in the finite-element analysis of three-dimensional eddy currents. *IEEE Transactions on Magnetics*, 25(4):3145–3159, 1989.

[3] M.D. Buhmann. *Radial basis functions: theory and implementations*, volume 12. Cambridge Univ Pr, 2003.

[4] J. H. Coggon. Electromagnetic and electrical modelling by the finite element mrthod. *Geophysics*, 36:132–155, 1971.

[5] A. Franke, R. U. Börner, and K. Spitzer. Adaptive unstructured grid finite element simulation of two-dimensional magnetotelluric fields for arbitrary surface and seafloor topography. *Geophysical Journal International*, 171(1):71–86, 2007.

[6] G. W. Homann. *Electromagnetic Methods in applied Geophysics*, chapter Nummerical Modeling for Electromagnetic Methods of Geophysics, pages 313–361. SEG, 1988.

[7] T.J.R. Hughes, J.A. Cottrell, and Y. Bazilevs. Isogeometric analysis: Cad, finite elements, nurbs, exact geometry and mesh refinement. *Computer Methods in Applied Mechanics and Engineering*, 194(39-41):4135–4195, 2005. ISSN 0045-7825. doi: 10.1016/j.cma.2004.10.008.

[8] F. Ihlenburg and I. Babuška. Finite element solution of the helmholtz equation with high wave number part i: The h-version of the fem. *Computers & Mathematics with Applications*, 30(9):9–37, 1995. ISSN 0898-1221. doi: 10.1016/0898-1221(95)00144-N. URL http://www.sciencedirect.com/science/article/pii/089812219500144N.

[9] Frank Ihlenburg and Ivo Babuska. Finite element solution of the helmholtz equation with high wave number part ii: The h-p version of the fem. *SIAM J. Numer. Anal.*, 34(1):315–358, February 1997. ISSN 0036-1429. doi: 10.1137/S0036142994272337. URL http://dx.doi.org/10.1137/S0036142994272337.

[10] B.N. Jiang, J. Wu, L.A. Povinelli, United States. National Aeronautics, and Space Administration. The origin of spurious solutions in computational electromagnetics. *Journal of computational physics*, 125(1):104–123, 1996.

[11] A.A. Kaufman and G.V. Keller. *The magnetotelluric sounding method*. Elsevier, Amsterdam, 1981.

[12] T. Kaufmann, C. Fumeaux, and R. Vahldieck. The meshless radial point interpolation method for time-domain electromagnetics. In *Microwave Symposium Digest, 2008 IEEE MTT-S International*, pages 61–64. IEEE, 2008.

[13] T. Kaufmann, Y. Yu, C. Engström, Z. Chen, and C. Fumeaux. Recent developments of the meshless radial point interpolation method for time-domain electromagnetics. *International Journal of Numerical Modelling: Electronic Networks, Devices and Fields*, 2012.

[14] K. Key and C. Weiss. Adaptive finite-element modeling using unstructured grids: the 2d magnetotelluric example. *Geophysics*, 71(6):G291–G299, 2006.

[15] L. B. Lucy. A numerical approach to the testing of the fission hypothesis. *Astronomical Journal*, 82:1013–1024, 1977.

[16] R.L. Mackie, T.R. Madden, and P.E. Wannamaker. Three-dimensional magnetotelluric modeling using difference equations - theory and comparisons to integral equation solutions. *Geophysics*, 58:215–226, 1993.

[17] M.N. Nabighian. *Electromagnetic Methods in Applied Geophysics*, volume 1 & 2. Society of Exploration Geophysicists, Tusla, 1987.

[18] J. C. Nedelec. Mixed finite elements in r3. *Numerische Mathematik*, 35:315–341, 1980.

[19] MJD Powell. The theory of radial basis function approximation in 1990. *Advances in numerical analysis*, 2:105–210, 1992.

[20] C. Schwarzbach. *Stability of Finite Element Solutions to Maxwell's Equations in Frequency Domain.* PhD thesis, TU Bergakademie, 2009.

[21] K. Vozoff. *Magnetotelluric Methods,*, volume 5 of *Geophysics Reprint Series*. Society of Exploration Geophysicists, Tusla, 1985.

[22] JG Wang and GR Liu. A point interpolation meshless method based on radial basis functions. *International Journal for Numerical Methods in Engineering*, 54(11): 1623–1648, 2002.

[23] JG Wang and GR Liu. On the optimal shape parameters of radial basis functions used for 2-d meshless methods. *Computer Methods in Applied Mechanics and Engineering*, 191(23):2611–2630, 2002.

[24] JG Wang, GR Liu, and YG Wu. A point interpolation method for simulating dissipation process of consolidation. *Computer Methods in Applied Mechanics and Engineering*, 190(45):5907–5922, 2001.

[25] P. Wannamaker, J. A. Stodt, and L. Rijo. Pw2d - finite element program for solution of magnetotelluric response of two-dimensional earth resistivity structure. Technical report, University of Utah, 1985.

[26] H. Wendland. *Scattered data approximation*, volume 17. Cambridge Univ Press, 2005.

Investigation of the Azraq Basin in the Eastern Desert of Jordan using Integrated Geoelectrical Techniques

P. Yogeshwar[1], B. Tezkan[1], A. Haroon[1]
[1]Institute of Geophysics and Meteorology, Cologne, Germany
Email: yogeshwar@geo.uni-koeln.de, CRC-806: Our Way to Europe, www.sfb806.de

The Eastern Mediterranean has been the passageway for human migration between Africa, the Middle East, the Balkans and Europe. The Azraq basin in the eastern desert of Jordan has been a major spot for human settlements since the middle Pleistocene. The former lake in the basin center has developed to a hyper-saline alluvial mudflat, the Qa' Al Azraq. In the mudflat thick sequences of alluvial sediments are deposited. Such sediment successions are promising archives used for reconstructing the paleoclimate.
We utilized the Transient Electromagnetic (TEM), the Direct Current Resistivity (DCR) and the Radiomagnetotelluric (RMT) methods to identify suitable borehole locations in the area for the paleoclimatical reconstruction. Two transects were investigated from the edge of the basin to the basin center.
The data sets of the three methods are interpreted by 1D Marquardt and Occam inversion. Furthermore, the DCR data is interpreted by a 2D smoothness constraint inversion. Previously uncertain geological boundaries are determined by the geoelectrical models along both transects.

1 Introduction

The Collaborative Research Centre 806 (CRC 806) *Our Way to Europe* concerns the history of mankind. It is designed to capture the complex nature of dispersal of modern man from Africa to Western Eurasia, and particularly to Europe. The CRC 806 concentrates on the time span between the dispersal of modern man from Africa (190,000 B.P.) and the permanent establishment in Central Europe (40,000 B.P.). The CRC 806 investigates archaeological sites, terrestrial and aquatic archives in the source region of modern man, along trajectories of dispersal and in sink areas (Fig. 1). It is a multidisciplinary project established at the Universities of Cologne, Bonn and Aachen [SFB-806, 2012].

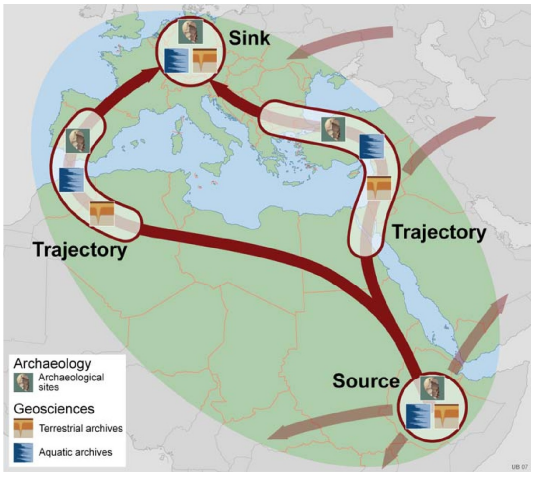

Figure 1: *Study areas of the CRC 806: the source region, trajectories and sink areas [SFB-806, 2012].*

The Eastern Mediterranean has been the passageway for human migration between Africa, the Middle East, the Balkans and Europe. In particular the Jordan rift valley served as a trajectory of dispersal of modern man [SFB-806, 2012].
The Azraq area is located 100 km east of Amman, in the eastern desert of Jordan (Fig. 2). The area around the former oasis Qa' Al Azraq has been a major spot for prehistoric settlements since the middle Pleistocene [Gerard et al., 1975; Copeland, 1988; Byrd, 1988]. The former shorelines of the Qa' Al Azraq mudflat are littered with stone artifacts, which were also found during the geophysical field survey.
Very promising archives for paleoclimatical reconstruction are sediment successions accumulated in dry clay lakes. Davies [2005] has analyzed a 31 m long core from the Qa' El Jafr basin in the south of Jordan and provided paleoclimate data for the Jordan Plateau. Ahmad [2010] interpreted the paleoclimate and paleoenvironment by dating bulk organic matter from the Azraq area. Abed et al. [2008] suggest the presence of a varying fresh to brackish water lake throughout the history, covering an area of roughly 13,000 km^2 around 330,000 B.P. The former lake in the center of the Azraq Basin has developed to a 10×10 km^2 big hyper-saline alluvial mudflat, the Qa' Al Azraq. During rainy season it is partly covered by water. In the basin center thick sequences of alluvial sediments, consisting mostly of clay intermixed with various evaporates, are deposited.
The Azraq area is of enormous economical importance to Jordan, due to its mineral deposits and groundwater resources. Approximately one third of the freshwater supply for Jordan's capital city Amman is provided from the Azraq Area [Ibrahim, 1996].
El-Kaysi and Talat [1996] and El-Waheidi et al. [1992] studied the condition of the shallow aquifer system and the interface of the fresh-brackish water zone utilizing Schlumberger vertical electric soundings.

In the present studies, previously uncertain depths of geological boundaries are determined and from that, suitable borehole locations for the paleoclimatical re-

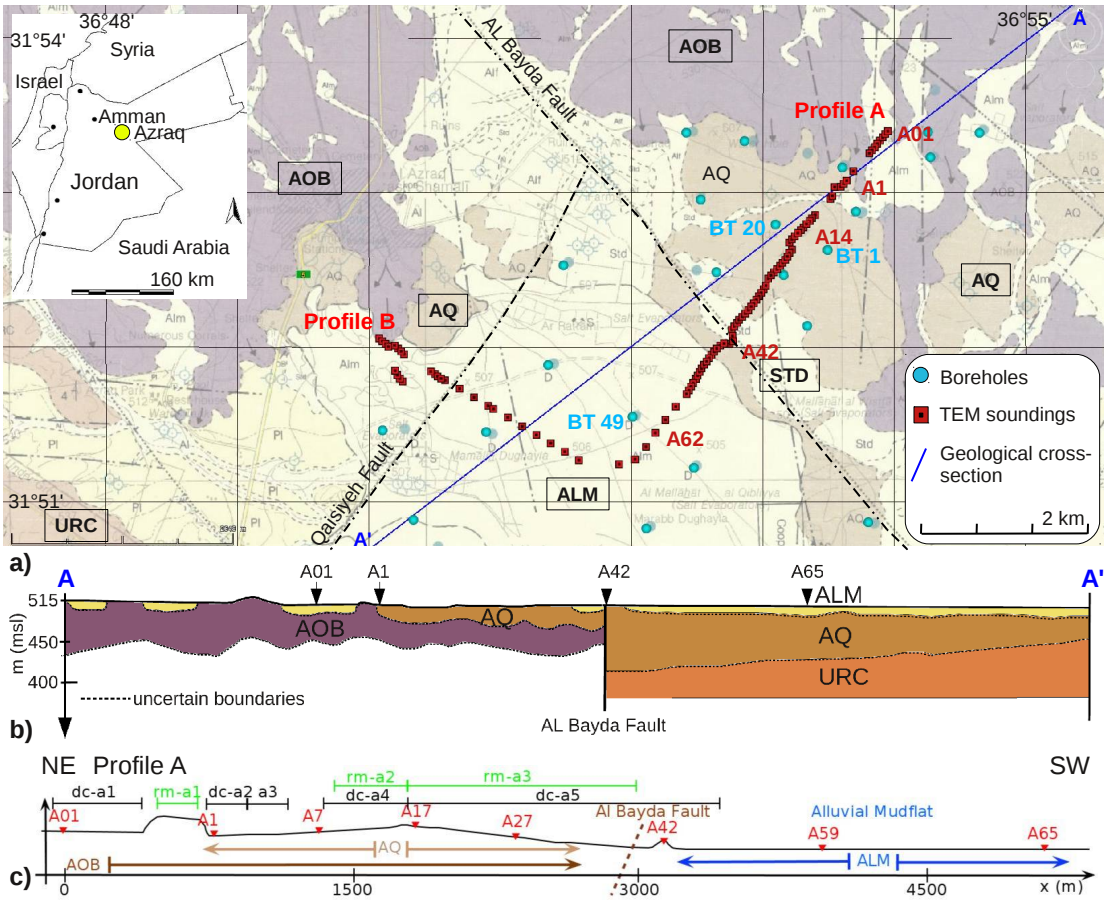

Figure 2: *(a) Geological map of the survey area. (b) Geological cross section for AA' (Modified after Ibrahim [1996]). The TEM stations are marked with red squares and labeled A01 to A65. (c) Schematic sketch of DCR and RMT profiles investigated on profile A. TEM stations are marked as red triangles, DCR profiles are marked black and RMT profiles green. AQ: Azraq Quaternary Formation, AOB: Abed Olivine Phyric Basalt, URC: Umm Rijam Chert Limestone Formation, ALM: Alluvial Mudflat.*

construction are identified. Two transects, 5 km and 3 km long, were investigated from the edge of the basin to the basin center, crossing three geological formations. We utilized the Transient Electromagnetic (TEM), the Direct Current Resistivity (DCR) and the Radiomagnetotelluric (RMT) methods.
The TEM data is interpreted by 1D Marquardt and Occam inversions and stitched together as a 2D section for the complete profile. For the time being, the RMT data is interpreted for selected stations in a similar manner as the TEM data. The DCR data is interpreted in 2D using a smoothness constraint inversion. The geoelectrical models are calibrated with lithological information available in the survey area.

2 Geology and hydro-geology of the study area

The geological features occurring in the Azraq area are briefly described in Ibrahim [1996].
The Azraq basin is a tectonic structural depression. It covers an area of 30×50 km^2, oriented from northwest to southeast, situated roughly 500 m above mean sea level. It is bounded by two major fault systems, the Fuluq fault in the north and the As Sirhan fault in the south.
The 10×10 km^2 Qa' Al Azraq in the basin center is bounded by faults from all sides. In the northeast the Al Bayda fault is present and in the northwest the Qaisiyeh fault (Fig. 2).
Four geological formations are described in the study area and were investigated during the geophysical field survey.

1. The Abed Olivine Phyric Basalt (AOB) stems from the earliest volcanism in the area. It is most abundant, highly fractured and forms irregular shaped boulders. It outcrops in the northern area.

2. The Umm Rijam Chert Limestone Formation (URC) outcrops in the northeast and southwest and forms the base of the mudflat.

3. The Azraq Quaternary Formation (AQ) consists of clay, intermixed with various evaporates and

fragments of gravel, limestone and basalt. The top surface is a present erosion and deposition surface, partly covered by alluvial sediments. At station A42 the AQ is covered by the Dasha Silt Dunes (STD).

4. The Alluvial Mudflat (ALM) in the basin center consists of soft, silty hyper saline clays intermixed with various evaporates. Beneath the ALM quaternary sediments of the AQ formation are present. The depth down to the URC formation is roughly 80 m [El-Kaysi and Talat, 1996].

These formations are displayed in the geological map (Fig. 2(a)). In the cross-section in Fig. 2(b), the depth of the geological boundaries are uncertain and therefore marked as dotted lines.

Three Aquifer systems were defined in the basin [Ibrahim, 1996]. The ground water occurrence in the upper aquifer system is complex, due to to the high lithological variability. The ground water level ranges between 250 m depth in the northern lava fields and less than 6 m in the Qa Al' Azraq. The main groundwater recharge is from the north.
Due to high evaporation the groundwater is hypersaline inside the alluvial mudflat with an electrical resistivity of around 2 Ωm.
The upper aquifer is extensively exploited for agricultural purpose and freshwater supply for Jordan's capital Amman. The extreme groundwater discharge has lead to a drastic decline of the ground water table.

3 Field measurement and data interpretation

Two transects were investigated from the edge of the mudflat to the center. Profile A is oriented from northeast to southwest and has a total length of 5130 m. Profile B is oriented from northwest to southeast and has a length of 3250 m.
The TEM measurements were carried out utilizing a NT-20 transmitter and a GDP32 receiver unit [Zonge, 2002]. A total of 102 stations were investigated (Profile A: 74 stations, Profile B: 28 stations). In general the station distance was 50 m between each consecutive station, depending on the availability of space and probable noise sources (e.g. 50 Hz powerlines) in the field. On the mudflat the station distance was increased to 200 m. The transmitter loop size was 50×50 m^2 and the receiver loop (single turn) was 10×10 m^2.
We measured in two modes: NanoTEM (NT) and ZeroTEM (ZT). The NanoTEM mode records 31 logarithmic equidistant values of the induced voltage in a time window from t =7.28E-07 to 1.91E-03 s. Setting the device to ZeroTEM mode allows to record from t =3.81E-05 to 2.43E-02 s.
Profile A was additionally investigated with DCR and RMT. The DCR measurements were performed using an ABEM SAS 4000 multi-electrode system [ABEM, 2010]. The length of the Wenner array was decided, depending upon the availability of space. Five DCR profiles (dc-a1 to dc-a5, (Tab. 1)) were investigated and are displayed in Fig. 2(c).

DCR profile	dc-a1	dc-a2	dc-a3	dc-a4	dc-a5
length (m)	400	200	150	600	1700
El. sep. (m)	2.5	2.5	2.5	5	5

Table 1: *DCR profiles investigated on the profile A.*

The RMT measurements were performed with the RMT-F device from the University of Cologne [RMT-F, 2005; Tezkan and Saraev, 2007; Tezkan, 2009]. Three RMT profiles were investigated on profile A (length: rm-a1= 150 m, rm-a2= 350 m, rm-a3=1320 m) with a distance of 10 m between consecutive stations (Fig. 2(c)). Usually seven distinct frequencies were available in the range from 10 kHz to 1 MHz in the E-polarization (TE-mode). The strike direction was assumed in southeast direction, i.e. aligned with the Al Bayda fault. Therefore, transmitters associated with the electric field directions perpendicular to the profile and parallel to the assumed strike direction were assumed as the E-polarization.

3.1 Data processing

Due to the self- inductance of the TEM transmitter loop, the current turn-off is not instant. The transmitter turn-off time (ramp time) depends on the current, the loop size and the subsurface resistivity distribution. For the configuration used during the field survey the ramp time was 3.5 μs in NanoTEM and 56 μs in ZeroTEM mode [Zonge, 2002].
The relation between a linear current turn-off function and the induced voltage was described by Fitterman and Anderson [1987]. We removed the effect of the linear ramp by applying a parameterized deconvolution of the measured signal and the current turn-off function. Afterwards both, the Nano- and ZeroTEM transients are stitched together to one long transient [Lange, 2003; Helwig et al., 2003; Hanstein, 1992]. Data points with standard deviations higher than $\Delta d = 3\%$ are removed.
The DCR and RMT data is edited visually for data outliers. In particular for DCR, data points with high standard deviations are removed from the apparent resistivity pseudosection. We assumed a percentage error of $\Delta d = 3$ % for the DCR and RMT data.
The processed TEM, DCR and RMT data for station A14 on profile A is presented in Fig. 3. The TEM data is transformed from induced voltages into late-time-apparent resistivities [Ward and Hohmann, 1988]. From the TEM and DCR data a resistor in the depth is indicated, which is not indicated by the RMT data, due to an insufficient depth of investigation for the lowest available frequency.

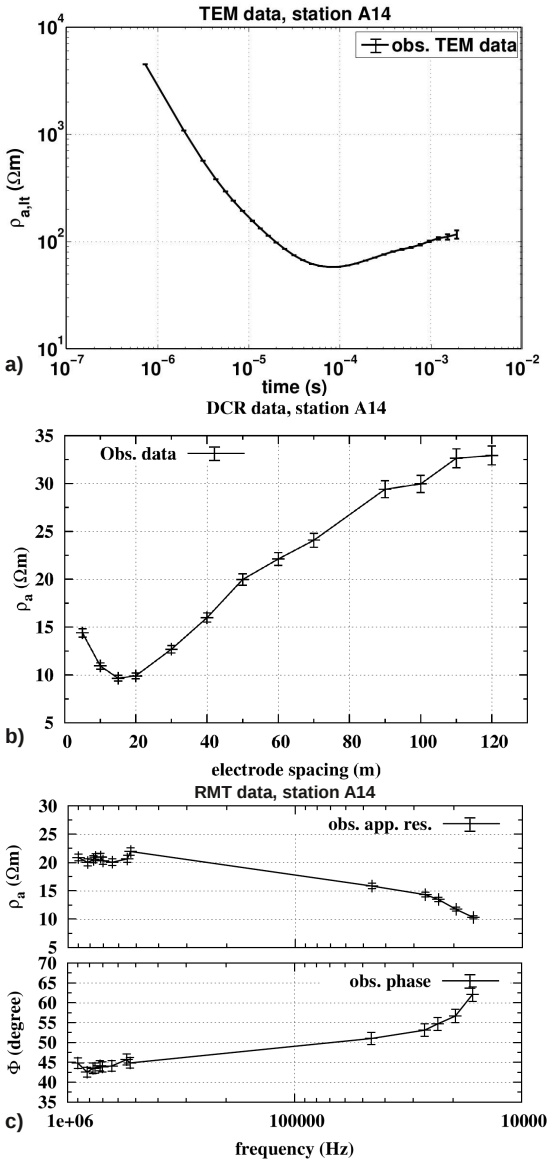

Figure 3: *(a) TEM, (b) DCR and (c) RMT data observed on profile A, station A14.*

3.2 1D interpretation of the data

The observed data is analyzed using a 1D inversion. We use the Occam scheme implemented for the first (Occ R1) and second order smoothness (Occ R2) constraint of the model [Constable et al., 1987]. The first and second order Occam inversion models generally differ in zones, where the model is not supported by the data. In order to obtain a layered earth model, Marquardt inversions are performed, too [Scholl, 2005; Menke, 1984]. For both, Occam and Marquardt inversion, a homogeneous halfspace model is used as an initial guess. The number of model layers for the Marquardt inversion is derived from the result of the particular Occam inversion model.
The obtained Marquardt best-fit and the corresponding equivalent models for station A14, investigated on the AQ formation, are displayed in Fig. 4(a),(b) and (c). The 1D results for station A62 on the mudflat is displayed in Fig. 4(f).
Besides calculating equivalent models, another possibility for the model resolution appraisal is to analyze the resulting matrices of a singular value decomposition of the generalized inverse during the Marquardt inversion [Scholl, 2005]. The importance of each model parameter is calculated according to Menke [1984]. The closer the value is to one, the better the model parameter is resolved.
The data fit is estimated according to the Root Mean Square (RMS)

$$RMS = \sqrt{\frac{1}{N}\sum_{i=1}^{N}\frac{(d_{i,obs}-d_{i,calc})^2}{(d_{i,obs})^2}} \qquad (1)$$

where $d_{i,obs}$ is the observed data, $d_{i,calc}$ the calculated data and N is the number of data points.
The depth of investigation (DOI) of the TEM method, is estimated according to Spies and Frischknecht [1991]:

$$\delta_{doi} = 0.5\left(\frac{IA\bar{\rho}}{\eta}\right) \qquad (2)$$

where I is the transmitted current, A the transmitter loop size and $\bar{\rho}$ is the mean resistivity of the overlying subsurface. We assume that the transients were always recorded until the noise level is reached, therefore η corresponds with the induced voltage value of the last recorded time point.
The obtained 1D models for station A14 (Fig. 4(a) to (c)) are matching well and validate each other. Especially the TEM and DCR models coincide. Further more the Marquardt and Occam models are well comparable.
According to the model parameter importances, the first layer of the TEM model (Fig. 4(c)) is not resolved separately. The third layer resistivity shows acceptable equivalence and is resolved with an importance of 0.38. The last layer resistivity and depth is resolved again well ($Imp > 0.8$).
The RMT model in Fig. 4(a) is reliable down to a depth of 15 m, due to the limited depth of investigation. Therefore, the last layer ist not significant. The latter is clear, due to the low importance values for the last layer, the huge equivalence and the differing of the two Occam models in a depth of 15 m.
The Marquardt and Occam models for station A62 are coinciding. Nevertheless, the resistivities of the second and fourth layer are not resolved, according to the Marquardt inversion models.

3.2.1 Correlation with borehole lithological data

Lithological borehole data was available from a bentonite drilling project in the Azraq area [Ibrahim, 1996; Ala'li, 1993]. The geoelectrical models are compared and calibrated with the lithological data. The locations of the boreholes used (BT-1 and BT-49) are

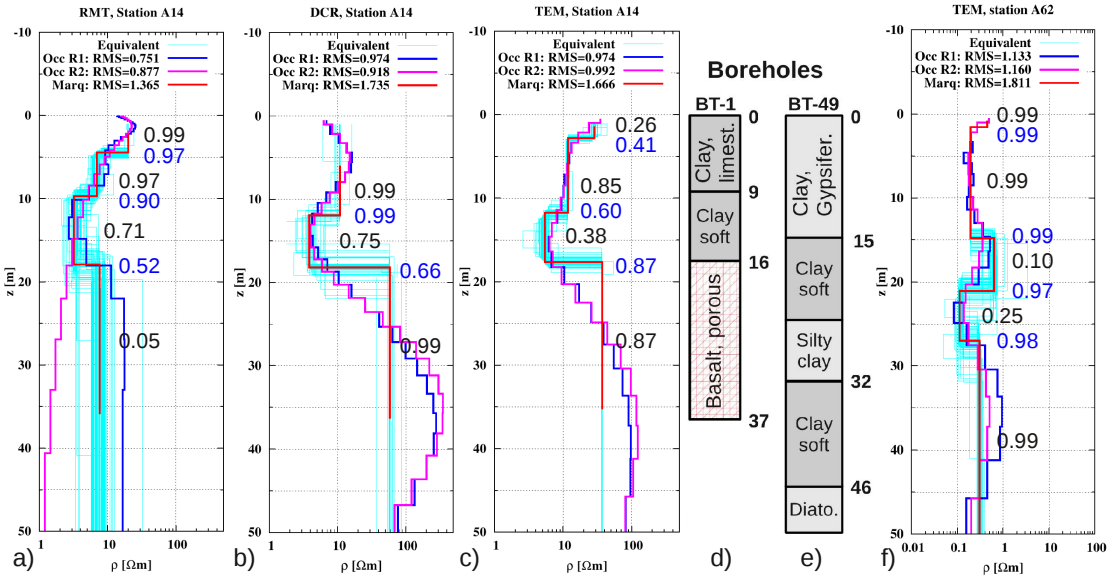

Figure 4: *1D inversion models of (a) TEM, (b) DCR and (c) RMT data for station A14 obtained on the AQ formation. Borehole lithological information for (d) BT-1 on the AQ formation and (e) BT-49 on the mudflat (Shown on the geological map (Fig. 2)). 1D inversion models of (f) the TEM data for station A62 on the mudflat. The importance for each layer resistivity and thickness is displayed in black and blue, respectively.*

displayed in Fig. 2.

According to the borehole data of BT-1 (Fig. 4(d)), the topmost 12 m of the model for station A14 consists of a clay layer intermixed with evaporates, pieces of limestone, chert, gravel and plant roots. The resistivity range is between 10 to 20 Ωm. Below, a soft clay layer is present with a resistivity of around 3 Ωm. In a depth of 16 m the basalt is clearly detected with a resistivity of around 40 to 100 Ωm. The basalt is highly porous and intermixed with gypsiferous material [Ibrahim, 1996].

The TEM resistivity model for station A62 on the alluvial mudflat is calibrated with lithological data from borehole BT-49 (Fig. 4(e)), which consists of layers of hyper-saline gypsiferous clay, soft clay, silty clay and diatomite. Both models, Marquardt and Occam, correlate quite well with the lithological data. However, the resistivity contrasts for the TEM models are small and the equivalent models indicate poorly resolved layers with resistivities ranging between 0.1 and 1 Ωm.

3.3 2D interpreted sections

We have calculated the TEM late-time apparent resistivity ($\rho_{a,lt}$) and the first order time derivative (Fig. 5(b) and (c), respectively). There are some data gaps along the profile, due to topography, streets and a powerline. Between $x = 750$ and 1000 m along the profile line a more conductive zone is visible at approximately $t = 10^{-4}$ s. Southwest of the Al Bayda fault, $\rho_{a,lt}$ decreases strongly to around 0.5 Ωm.

The first order time derivative of $\rho_{a,lt}$ visualizes a probable resistivity increase in the depth. Fig. 5(b) indicates a resistive structure in the depth between $x = 0$ and 3000 m, starting at approximately $t = 10^{-4}$ s. The increase of the $\rho_{a,lt}$-values obviously stems from the basalt layer. On the alluvial mudflat, northwest of station A42, only a slight increase of $\rho_{a,lt}$ is visible for very late times, indicating a resistor in the depth.

The calculated 1D TEM inversion models are stitched together as a 2D section for all 74 stations along profile A (Fig. 6(a) and (b)). We did not apply any constraints between neighbouring models or fix regions with a-priori information.

The 2D stitched section for the Marquardt 4 layer models and the Occam R2 models are displayed in Fig. 6(a) and (b), respectively. Both 2D sections are matching very well.

In a depth of 495 m amsl the basalt layer is present. It is slightly dipping downwards towards southwest and ends at the Al Bayda fault. The top of the basalt is precisely determined by the stitched TEM models. From $x = 700$ m to 3000 m a quite thin soft clay layer is present above the basalt, which is also described in the lithological information (Fig. 4). The top surface layer with a resistivity of 6 to 25 Ωm coincides with the clay layer, intermixed with pieces of chert, limestone and gravel. The quaternary sediments above the basalt stream belong to the AQ-formation.

Southwest of the Al Bayda fault the alluvial mudflat begins. It contains of hyper-saline clays. The resistivity varies between 0.1 and 1 Ωm. A slight layering is visible from the 2D stitched Occam models inside the ALM. Although the resistivity contrast is small it is continues in lateral direction. Apparently this layering coincides with the different type of clays described in the lithological information (Fig. 4). As supported by the time derivative of the first order late-time apparent resistivity, a slight increase of the

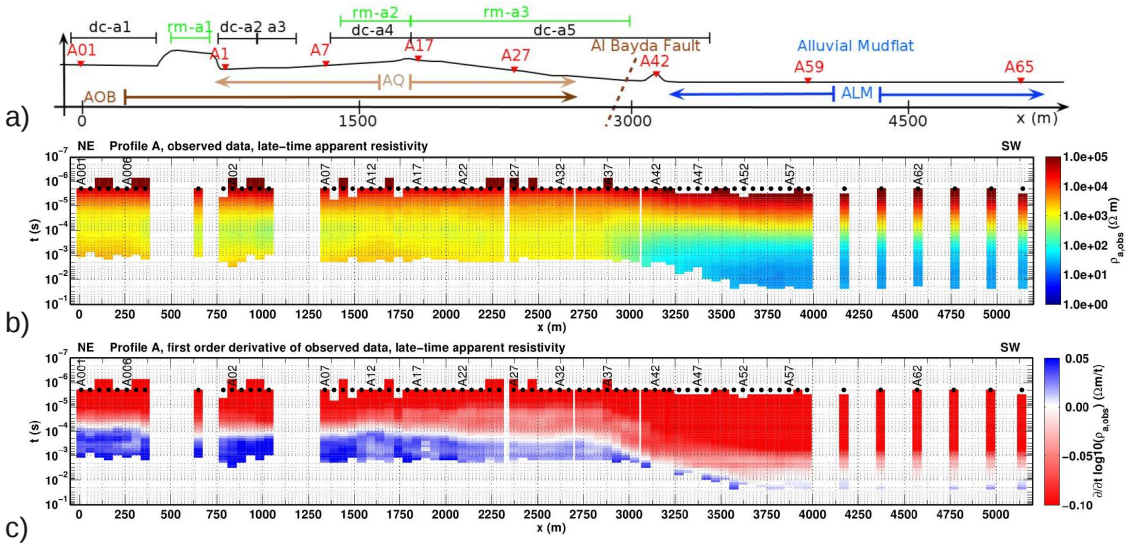

Figure 5: *(a) Schematic sketch of the investigated profiles along Profile A. 2D section of (b) TEM late-time apparent resistivity data and (c) first order time derivative of TEM late-time apparent resistivity data.*

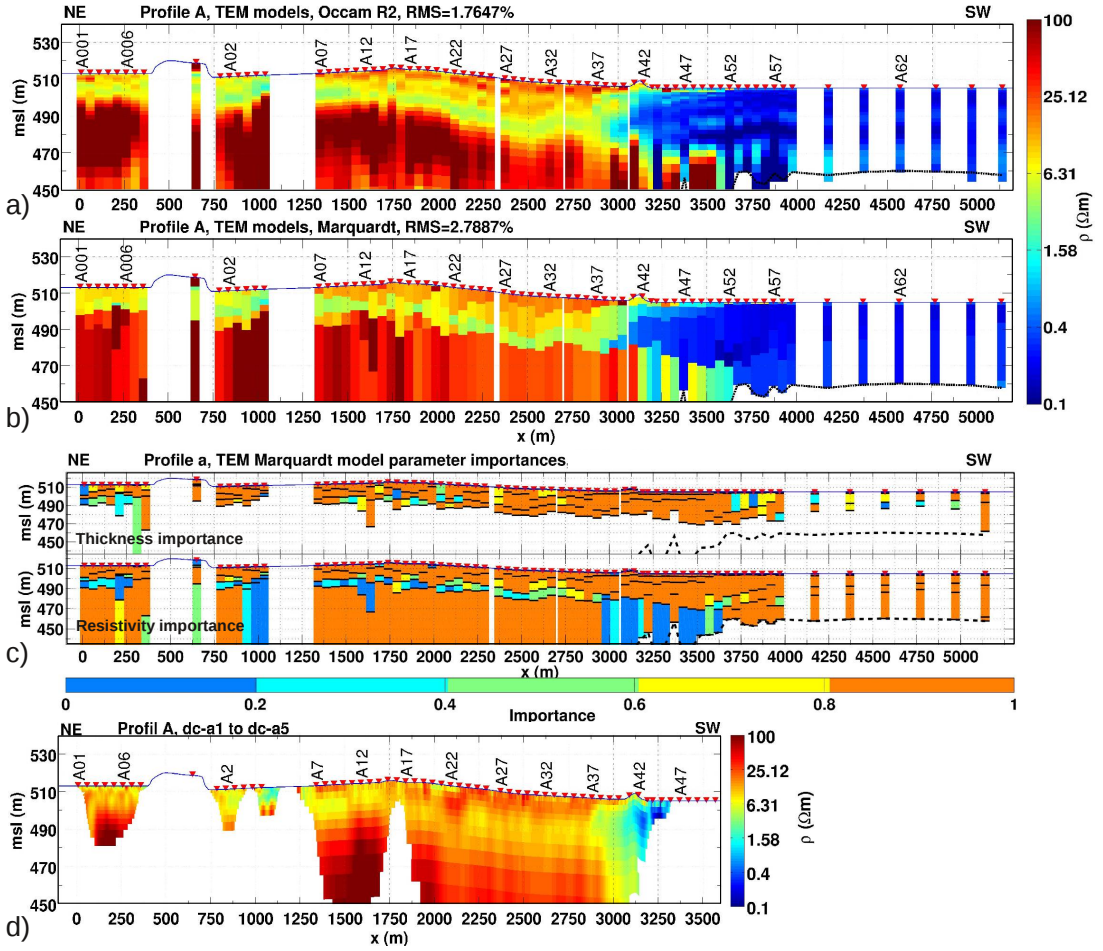

Figure 6: *1D inversion results stitched together as a 2D section for (a) the Marquardt models (b) the Occam R2 models. (c) 2D section of the importances of each layer thickness and resistivity for each station. (d) 2D DCR inversion models. The DOI is plotted as a dotted line in the TEM models inside the mudflat.*

model resistivity is visible in a depth of 480 m amsl. From the geological cross section, the deposited alluvial sediments inside the mudflat are followed by quaternary sediments of the AQ formation, which are also present northeast of the mudflat. Most likely the slight increase in resistivity in about 480 m amsl, is related to the top of the AQ formation. Deeper resistivity information is not available, due to a limited DOI of roughly 50 m on the mudflat (Fig. 6(a),(b)).
In the transition zone, close to the Al Bayda fault, the subsurface becomes highly two-dimensional and a 1D interpretation becomes inadequate. From both, the data and the models, it is not clear if the basalt stream continues after $x = 3000$ m towards southeast until $x = 3600$ m. Therefore we have calculated the importances for each layer resistivity and thickness (plotted as a 2D section in Fig. 6(c)). According to the latter, the top of the last layer is well resolved, whereas the resistivity is not resolved in the transition zone.
The data for all 74 stations is fitted with a glabal RMS of 1.76% for the Occam models and 2.79% for the Marquardt models.

The DCR data is inverted in 2D using a second order smoothness constraint inversion algorithm by Günther [2004]. The smoothness parameter is determined automatically in each inversion iteration by the L-curve criterion [Hansen and O'Leary, 1993]. We have masked the zones in the models which are not supported by the data.
The DCR profiles (dc-a1 to dc-a5) are plotted along profile A in Fig. 6(d). For the large Wenner arrays (dc-a1, dc-a4 and dc-a5) the basalt stream is well detected. The overlying clay layer is represented a bit more resistive than in the stitched TEM models (Fig. 6(b)). The transition zone is visible at around $x = 3000$ m along the profile line. Further southwest, DCR measurements were not possible due to technical problems. Therefore, the continuation of the basalt southwest of the Al Bayda fault is unclear from the DCR result.

4 Conclusions

Two long transects were investigated in the Azraq area from the edge of the Qa Al' Azraq to the center, utilizing three geophysical methods: TEM, DCR and RMT.
The TEM data is analyzed in detail. A 5 km long 2D subsurface resistivity section is derived from stitched Occam and Marquardt inversion models. The resulting models are appraised by equivalent modelling and inversion statistics (i.e. model parameter importances). The DCR data is interpreted in 2D and the obtained models validate the 2D stitched TEM section.
Three geological formations are investigated in the study area. Previously uncertain geological boundaries are determined by the geophysical results. Especially the depth down to the basalt stream is detected, which is a limitation for probable future drilling projects. A geological layering inside the alluvial mudflat could be identified, which also coincides with the lithological data. The transition zone between the basalt stream and the alluvial mudflat is resolved, although the subsurface is highly two-dimensional and the 1D interpretation becomes critical.
The Azraq area has a tremendous importance to Jordan, due to its mineral and water resources. This study provides additional geological information. Furthermore it is a basis for future drilling projects.

5 Acknowledgement

The project is funded by the DFG and hosted in the frame of the CRC-806 "Our Way to Europe", established at the Universities of Cologne, Bonn and Aachen. We gratefully thank the Natural Resources Authority, Jordan and especially Tahsin Talat for great support in the field work, the tough organization and the hospitality.

6 References

Abed, A. M., Yasin, S., Sadaqa, R., Al-Hawari, Z., 2008. The paleoclimate of the eastern desert of jordan during marine isotope stage 9. Quaternary Research 69, 458–468.

ABEM, 2010. Terrameter SAS 4000 / SAS 1000 Instruction Manual. ABEM Instrument AB, printed matter no. 93109 Edition.
URL http://www.abem.se/software.php

Ahmad, K. I., 2010. Organic chemistry of Al-Azraq basin, Jordan, an interpretation of paleoenvironment and paleoclimate using bulk organic matter. Ph.D. thesis, University of Missouri-Kansas City.

Ala'li, J., 1993. Exploration for Bentonite and other Minerals in Azraq Depression. Tech. rep., Natural Recources Authority, Geology Directorate, Economic Geology Division, Amman.

Byrd, B. F., 1988. Late Pleistocene settlement diversity in the Azraq basin. Paleorient 14/2, 257–264.

Constable, S. C., Parker, R. L., Constable, C. G., 1987. Occam's inversion: a practical algorithm for generating smooth models from EM sounding data. Geophysics 52, 289–300.

Copeland, L., 1988. Environment, chronology and lower-middle-paleolithic occupations of the Azraq basin, Jordan. Paleorient 14/2, 66–75.

Davies, C., 2005. Quaternary paleoenvironment and potential for human exploitation of the Jordan plateau interior. Geoarchaeology: An International Journal 20/4, 379–400.

El-Kaysi, K., Talat, T., 1996. Geoelectrical survey in the Azraq mudflat area. Tech. rep., Natural Resources Authority, Geophysics and Technical Service Department, Geophysics Division, Amman.

El-Waheidi, M., Merlanti, F., Pavan, M., 1992. Geoelectrical resistivity survey of the central part of Azraq basin (Jordan) for identifying saltwater/freshwater interface. Journal of Applied Geophysics 29, 125–133.

Fitterman, D., Anderson, W., 1987. Effect of Transmitter Turn-Off Time on Transient Soundings. Geoexploration 24, 131–146.

Gerard, A. N., Price, N. S., Copeland, L., 1975. A survey of prehistoric sited in the Azraq basin, eastern Jordan. Paleorient 3, 109–126.

Günther, T., 2004. Inversion Methods and Resolution Analysis for the 2D/3D Reconstruction of Resistivity Structures from DC Measurements. Ph.D. thesis, Technische Universität Bergakademie Freiberg.

Hansen, P. C., O'Leary, D. P., 1993. The use of the l-curve in the regularization of discrete ill-posed problems. SIAM Journal of Scientific Computing 14, 1487–1503.

Hanstein, T., 1992. Iterative und parametrisierte Dekonvolution für LOTEM Daten. In: Protokoll über das 14. Kolloquium Elektromagnetische Tiefenforschung. Dt. Geophys. Gesellschaft, p. 163–172.

Helwig, S. L., Lange, J., Hanstein, T., 2003. Kombination dekonvolvierter Messkurven zu einem langen Transienten. In: Protokoll über die 63. Jahrestagung der Deutschen Geophysikalischen Gesellschaft. Dt. Geophys. Gesellschaft.

Ibrahim, K., 1996. The Regional Geologoy of Al Azraq Area. Hashemite Kingdom of Jordan, Geological Mapping Division, Natural Resources Authority, Bulletin 36.

Lange, J., 2003. Joint Inversion von Central-Loop-TEM und Long-Offset-TEM Transienten am Beispiel von Messdaten aus Israel 2002. Master's thesis, Universität zu Köln, Institut für Geophysik und Meteorologie.

Menke, W., 1984. Geophysical data analysis: discrete inverse theory. Academic Press inc.

RMT-F, 2005. RMT-F1 and SM25 user manual. Microkor and St. Petersburg University.

Scholl, C., 2005. The influence of multidimensional structures on the interpretation of LOTEM data with one-dimensional models and the application to data from Israel. Ph.D. thesis, Universität zu Köln, Institut für Geophysik und Meteorologie.

SFB-806, January 2012. OUR WAY TO EUROPE-Culture-Environment Interaction and Human Mobility in the Late Quaternary. Online.
URL http://www.sfb806.uni-koeln.de/

Spies, B. R., Frischknecht, F. C., 1991. Electromagnetic Sounding. In: Nabighian, M. N. (Ed.), Electromagnetic methods in applied geophysics. Vol. 2. Soc. Expl. Geophys., Ch. 5.

Tezkan, B., 2009. Radiomagnetotellurics, in Groundwater Geophysics, A Tool for Hydrogeology, 2nd Edition. Springer-Verlag, Ed. by R. Kirsch, Ch. 10, pp. 295–316.

Tezkan, B., Saraev, A., 2007. On the 2D inversion of radiomagnetotelluric data (10 kHz-1 MHz) for shallow investigations observed by a newly developed device. Near Suface Geophysics 6, 245–252.

Ward, S. H., Hohmann, G. W., 1988. Electromagnetic theory for geophysical applications. Soc. Explor. Geophys., eM, theory.

Zonge, Mai 2002. GDP-32 II Multifunction Receiver Operation Manual. Zonge Engineering and Research Organization.
URL http://www.zonge.com/RxManuals.html

Liste der Autoren